Kinetic Monte Carlo Study of Charge and Exciton Transport in Organic Solar Cells

Kinetische Monte Carlo Studie von Ladungs- und Exzitonentransport in Organischen Solarzellen

Waldemar Kaiser

Professur für Simulation von Nanosystemen für Energieumwandlungen
Fakultät für Elektrotechnik und Informationstechnik
Technische Universität München

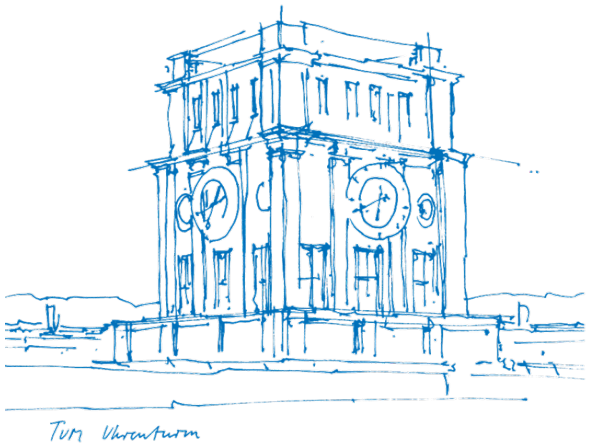

TECHNISCHE UNIVERSITÄT MÜNCHEN
FAKULTÄT FÜR ELEKTROTECHNIK UND INFORMATIONSTECHNIK
PROFESSUR FÜR SIMULATION VON NANOSYSTEMEN FÜR ENERGIEUMWANDLUNGEN

Kinetic Monte Carlo Study of Charge and Exciton Transport in Organic Solar Cells

Waldemar Kaiser

Vollständiger Abdruck der von der Fakultät für Elektrotechnik und Informationstechnik der Technische Universität München zur Erlangung des akademischen Grades eines

Doktors der Naturwissenschaften (Dr. rer. nat.)

genehmigten Dissertation.

Vorsitzende(r): Prof. Dr. Bernhard Wolfrum
Prüfer der Dissertation:
1. Prof. Dr. Alessio Gagliardi
2. Prof. Dr. David Egger

Die Dissertation wurde am 30.09.2020 bei der Technische Universität München eingereicht und durch die Fakultät für Elektrotechnik und Informationstechnik am 07.04.2021 angenommen.

Dedicated to my family and friends. Für meine Familie und Freunde.

Abstract

Harvesting energy from solar power is probably the most promising way to meet society's growth in energy demand in an environmentally friendly and sustainable manner. Existing photovoltaic (PV) panels are based on highly optimized silicon technologies. However, the production of silicon solar cells requires plenty of energy because of high-temperature processing techniques. Also, the amount of silicon needed to absorb light efficiently is a major drawback. Recent research has been focused on novel material systems such as organic semiconducting polymers and small molecules or highly efficient perovskites. This new generation of materials provides several advantages: their large absorption coefficients combined with direct bandgaps make these materials ideal candidates for thin-film solar cells.

Organic semiconductors show favorable characteristics for usage within optoelectronic devices such as high absorption coefficients, mechanical flexibility, low weight, tunability of optical and electrical properties, as well as low-temperature and low-cost processability. While organic light-emitting diodes are already widely used, a deeper understanding of the transport of charge carriers and excitons is required to improve organic solar cells (OSCs). Organic semiconductors have low dielectric constants in the range of 3 to 4, which causes the creation of strongly bound Frenkel excitons upon light absorption. Additionally, the lack of long-range order in solution-processed OSCs leads to strong localization of charges and excitons. The low lifetime and short diffusion lengths of excitons require a highly intermixed, three-dimensional bulk heterojunction morphology to induce efficient exciton dissociation. If excitons reach the donor:acceptor interface, they can be dissociated into charge transfer (CT) states where the electron and the hole reside on adjacent molecules. Efficient separation of CT states into a free electron and a free hole is crucial for photocurrent generation. Finally, charges need to be transported through the amorphous organic semiconductors and highly intermixed blends towards the electrodes.

While the working principle may sound simple, several aspects still are puzzling. Due to the complex interplay of charge carriers and excitons in the complex three-dimensional morphology, numerical models, including the microscopic structure of OSCs, are required to understand the device physics. Existing drift-diffusion (DD) models are limited to 1D-simulations and lead to convergence problems at higher dimensions. Also, DD calculations assume immediate equilibration of charge carriers within the energetic density of states. This limits the accuracy in the description of the device physics, especially on fast timescales and short length scales. Thus, a 3D kinetic Monte Carlo (kMC) model is developed to capture the non-equilibrium dynamics of charge carriers and excitons within the complex morphology. This thesis studies several aspects of charge and exciton transport within OSCs and presents novel methodologies to improve the accuracy and computational demand of kMC simulations.

Solution-processed organic semiconductors are amorphous materials that show a strong disorder in molecular orbital energies and in the spatial arrangement of the molecules. Most existing kMC models represent the organic material by a cubic lattice, where each lattice site represents one quantum state. However, this does not capture the realistic structure of organic semiconductors. An off-lattice kMC model based on the Voronoi tessellation is developed to overcome this limitation and represent accurate molecular structures. The off-lattice kMC is further embedded in a multiscale simulation

framework to compute charge carrier mobilities for realistic thin film morphologies with structural disorder obtained from molecular dynamics.

kMC simulations of most electronic and electrochemical systems require extensive computational resources due to the large time disparities of the competing physical processes. Device characteristics, which may depend heavily on the slowest processes, are hardly accessible within reasonable simulation times. Scaling algorithms must understand that a system is being trapped within a small portion of the phase space. Such algorithms recognize if multiple fast transitions are executed without gaining new information on the slow processes. Most studies either have entirely neglected or decoupled particle transport from competing reactions. We tackled this issue by developing a novel acceleration scheme that detects critical regions in the material during the initialization step. Efficient downscaling of the fast rates was achieved with acceleration in CPU-times and accuracies of orders of magnitude beyond state-of-the-art accelerated superbasin kMC.

OSCs show high losses in the open-circuit voltage of up to 1.0 V. Existing studies employ one-dimensional, effective medium DD simulations to study the origin of the voltage losses. Their main conclusion is that losses are due to non-radiative recombination and energetic disorder. However, the role of the morphology and the detailed electronic structure at the donor:acceptor interface is not well understood. In this thesis, the effect of the interfacial disorder on the open-circuit voltage is studied using 3D kMC simulations. It is shown that the interface disorder is the dominating part of the open-circuit voltage. Correlating the energy landscape by increasing the order at the interface significantly enhances the open-circuit voltage.

Typical OSCs are based on highly intermixed donor:acceptor blends to enhance the dissociation of low-lifetime singlets into free charge carriers. While OLEDs employ well-studied techniques to convert triplets into singlets, such exciton management is not well understood in OSCs. In this work, the kMC model incorporates accurate singlet and triplet dynamics as well as the intersystem crossing of singlets into triplets. While the population of triplet states in typical organic semiconductors is negligible, phosphorescent sensitizers can be used to enhance the intersystem crossing of singlets into long-living triplet excitons. The presented simulations show a significant enhancement in diffusion length and lifetime and an efficiency increase.

Existing thermodynamic investigations highlight the role of disorder, localization, and the dimensionality of the material on the free energy barrier. However, these analyses are based on an equilibrium description. The validity of equilibrium descriptions, and hereby the role of non-equilibrium states, has been questioned in recent years. Here, a novel non-equilibrium thermodynamic description on the free energy barrier of CT state dissociation is developed. The results show an interesting connection between the separation of CT states with the entropy.

One of the main unsolved challenges of OSCs is the transport of charge carriers in the presence of mixed and isolated phases. Dilute donor OSCs, i.e., OSCs with donor concentrations below the percolation threshold, represent ideal test systems for the study of hole transport in isolated phases. Even at donor concentrations of 0.1 wt% substantial photocurrent can be observed. Several physical mechanisms have been suggested to explain the transport of charge carriers in isolated phases: tunneling, back transfer, or even percolation. Here, the origin of hole transport is studied for polymer and small molecule dilute donor. It is shown that back transfer dominates for low donor concentrations below 5 wt%, while tunneling can lead to substantial photocurrent at higher donor concentrations.

Zusammenfassung

Die Erzeugung elektrischer Energie aus der Sonnenstrahlung ist möglicherweise der vielversprechendste Weg den wachsenden Energiebedarf der Gesellschaft auf umweltfreundliche und nachhaltige Weise zu decken. Bestehende Photovoltaik (PV)-Module basieren auf hochoptimierter Siliziumtechnologie. Die Herstellung von Silizium-Solarzellen erfordert einen hohen Energieverbrauch aufgrund von Hochtemperatur-Verarbeitungsschritten. Zudem stellt die groSSe Menge an benötigtem Silizium zur effizienten Lichtaufnahme einen groSSen Nachteil dar. Jüngste Forschung konzentriert sich auf neuartige Materialsysteme wie beispielsweise organische halbleitende Polymere und Moleküle oder hocheffiziente Perowskite. Diese neue Generation von Materialien bieten signifikante Vorteile: Ihre groSSen Absorptionskoeffizienten in Verbindung mit direkten Bandlücken machen diese Materialien zu idealen Kandidaten für Dünnschichtsolarzellen.

Organische Halbleiter besitzen günstige Eigenschaften für den Einsatz in optoelektronischen Bauelementen, wie hohe Absorptionskoeffizienten, mechanische Flexibilität, geringes Gewicht, Abstimmbarkeit der optischen und elektrischen Eigenschaften sowie eine kostengünstige Verarbeitung bei niedrigen Temperaturen. Während organische Leuchtdioden bereits weit verbreitet sind, bedarf es für den Einsatz in organische Solarzellen (OSCs) ein tieferes Verständnis des Transports von Ladungsträgern und Exzitonen. Organische Halbleiter haben niedrige Dielektrizitätskonstanten im Bereich von 3 bis 4, was zur Bildung stark gebundener Frenkel-Exzitonen in Folge der Photonenabsorption führt. Zusätzlich bedingt das Fehlen einer langreichweitigen Ordnung in Lösungs-prozessierten organischen Solarzellen eine starke Lokalisierung von Ladungen und Exzitonen. Die geringe Lebensdauer und kurze Diffusionslängen der Exzitonen erfordern eine stark durchmischte, dreidimensionale Heterostruktur für eine effiziente Dissoziation der Exzitonen. Wenn Exzitonen die Donor:Akzeptor-Grenzfläche erreichen können sie in Ladungstransfer (CT)-Zustände dissoziieren, in denen sich das Elektron und das Loch auf benachbarten Molekülen befinden. Eine effiziente Trennung der CT-Zustände in ein freies Elektron und ein freies Loch ist für die Photostromerzeugung entscheidend. SchlieSSlich müssen die Ladungen durch die amorphen organischen Halbleiter und stark durchmischte Heterostruktur zu den Elektroden transportiert werden.

Das Funktionsprinzip mag einfach klingen, doch einige Eigenschaften sind noch immer ungeklärt. Aufgrund des komplexen Zusammenspiels von Ladungsträgern und Exzitonen in der komplexen dreidimensionalen Morphologie sind numerische Modelle für ein besseres Verständnis der Physik von organischen Solarzellen erforderlich. Bestehende Drift-Diffusions (DD)-Simulationen basieren auf 1D-Modellen und leiden unter Konvergenzproblemen in höheren Dimensionen. AuSSerdem gehen DD-Berechnungen von einem unmittelbaren Gleichgewicht der Ladungsträger innerhalb der energetischen Zustandsdichte aus. Dies schränkt die Genauigkeit bei der Beschreibung der Bauelementphysik ein und vernachlässigt kritische Eigenschaften auf kurzen Zeit- und Längenskalen. Daher wird ein 3D kinetisches Monte Carlo (kMC) Modell entwickelt, um die Nichtgleichgewichtsphysik von Ladungsträgern und Exzitonen innerhalb der komplexen Morphologie zu erfassen. In dieser Arbeit werden verschiedene Aspekte des Ladungs- und Exzitonentransports innerhalb von OSCs untersucht und neue Methoden zur Verbesserung der Genauigkeit und des Rechenaufwands von kMC-Simulationen vorgestellt.

Lösungsbasierte organische Halbleiter sind amorphe Materialien, die eine groSSe Variation der molekularen Orbitalenergien und der räumlichen Anordnung der Moleküle aufweisen. Die meisten

existierenden kMC-Modelle beschreiben das organische Material durch ein kubisches Gitter, wobei jede Gitterstelle einen Quantenzustand darstellt. Dies erfasst jedoch nicht die realistische Struktur von organischen Halbleitern. Um diese Beschränkung zu überwinden und genaue Molekülstrukturen darzustellen, wird ein generalisiertes kMC-Modell auf Basis einer Voronoi-Tessellierung entwickelt. Das kMC-Modell wird in Multiskalen-Simulationen integriert, um Ladungsträgermobilitäten für realistische Dünnschichtmorphologien mit struktureller Unordnung zu berechnen. Diese Morphologien werden aus Molekulardynamik-Simulationen gewonnen.

kMC-Simulationen vieler elektronischer und elektrochemischer Systeme erfordern umfangreiche Berechnungsressourcen aufgrund der groSSen Zeitunterschiede konkurrierender physikalischer Prozesse. Bauteileigenschaften, die stark von den langsamsten Prozessen abhängen, sind innerhalb vernünftiger Simulationszeiten kaum zugänglich. Skalierungsalgorithmen sind erforderlich um zu erkennen, dass ein System in einem kleinen Teil des Phasenraums gefangen ist. Solche Algorithmen erkennen, wenn mehrere schnelle Übergänge ausgeführt werden, ohne neue Informationen über die langsamen Prozesse zu gewinnen. Die meisten Studien vernachlässigen den Teilchentransport entweder völlig oder entkoppeln diesen von konkurrierenden Reaktionen. Ein Lösungsvorschlag zur Überwindung dieses Problems mittels eines neuartigen Beschleunigungsschema wird präsentiert. Dieses Schema erkennt kritische Bereiche im Materialsystem während des Initialisierungsvorganges. Ein effizientes Skalieren der schnellen Raten liefert eine Beschleunigung der benötigten CPU-Zeiten und mit Genauigkeiten, welche existierende Methoden um GröSSenordnungen übertrifft.

OSCs weisen hohe Verluste in der Leerlaufspannung von bis zu 1,0 V auf. Bestehende Studien verwenden eindimensionale DD-Simulationsmodelle um den Ursprung der Spannungsverluste zu untersuchen. Die wichtigsten Schlussfolgerung durch DD-Studien ist, dass die Verluste auf strahlungsfreie Rekombination und energetische Variation der Molekularorbitale zurückzuführen sind. Die Rolle der Morphologie und der detaillierten elektronischen Struktur an der Grenzfläche zwischen Donor und Akzeptor wurde jedoch nicht untersucht. Die Auswirkung der energetischen Struktur an der Grenzflächen auf die Leerlaufspannung wird mit Hilfe von 3D kMC Simulationen untersucht. Es wird gezeigt, dass die Grenzflächenstörung den gröSSten Anteil der Verluste in der Leerlaufspannung verursacht. Eine Korrelation der Molekularorbitalenergien durch Erhöhung der Ordnung an der Grenzfläche kann die Leerlaufspannung signifikant erhöhen.

Typische OSCs basieren auf stark vermischten Donor:Acceptor-Heterostrukturen zur Optimierung der Dissoziation von Exzitonen mit geringer Lebensdauer in freie Ladungsträger. Während OLEDs weit erforschte Techniken zur Umwandlung von Tripletts in Singuletts verwenden, ist ein solches Exzitonenmanagement bei OSCs nicht gut verstanden. Das entwickelte kMC-Modell modelliert die Singulett- und Triplett-Dynamik sowie die Umwandlung von Singuletts in Tripletts. Während die Population von Triplett-Zuständen in typischen organischen Halbleitern vernachlässigbar ist, können phosphoreszierende Sensibilisatoren verwendet werden, um die Umwandlung von Singuletts zu langlebigen Triplett-Exzitonen zu verbessern. Simulationsresultate weisen eine signifikante Verbesserung der Diffusionslänge und Lebensdauer sowie eine Effizienzsteigerung auf.

Bestehende thermodynamische Studien untersuchen die Rolle der Unordnung, der Lokalisierung und der Dimensionalität des Materials für die Barriere in der Freien Energie. Diese Analysen basieren jedoch auf einer Gleichgewichtsbeschreibung. Die Gültigkeit von Gleichgewichtsbeschreibungen, und damit die Rolle von Nichtgleichgewichtszuständen, wurde in den letzten Jahren in Frage gestellt. Hier wird eine neuartige thermodynamische Nichtgleichgewichtsbeschreibung für die freie Energie der CT-Zustände während des Dissoziationsvorganges entwickelt. Die Ergebnisse zeigen einen interessanten Zusammenhang zwischen der Separation von CT-Zuständen mit der Entropie.

Eine der wichtigsten ungelösten Herausforderungen der OSCs ist der Transport von Ladungsträgern in Gegenwart von gemischten und isolierten Phasen. OSCs mit Donorkonzentrationen unterhalb der

Perkolationsschwelle repräsentieren ideale Testsysteme für die Untersuchung des Löchertransports in isolierten Phasen. Selbst bei Donorkonzentrationen von 0.1 wt% wird ein erheblicher Photostrom beobachtet. Mehrere physikalische Mechanismen zur Erklärung des Ladungsträgertransportes in isolierten Phasen wurden divers diskutiert: Tunneln, Rücktransfer oder sogar Perkolation. Hier wird der Ursprung des Lochtransports für Polymerdonatoren und Donatoren basierend auf kleinen Molekülen untersucht. Die Resultate weisen eine dominante Rolle des Rücktransfers bei niedrigen Donorkonzentrationen unter 5 wt% auf, während Tunneln bei höheren Donorkonzentrationen zu einem erheblichem Photostrom beiträgt.

Contents

1 Introduction

The development of new technologies and machines are changing our daily individual as well as social life. Starting from the alarm clock in the early morning, our daily life is affected by (more or less) novel technologies: the first coffee of the day, traveling to school or work by autonomously driving metros while answering first mails or listening to the newest podcasts, studying online or being connected with customers all over the world. In the evenings, we chat with friends, facetime with our family, or watch the newest series. All these novel technologies have been developed in shortest times – but we did not reach the end yet. Artificial intelligence, connected cars, devices, the Internet of things, virtual reality – to mention a few hot topics that most probably will enter our lives in the nearest future.

We do not expect our imagination, knowledge, or capabilities to limit the progress of novel technologies – rather, it is a bigger force, our nature. Not just since Fridays for Future, many (professional or not) environmentalists shed light on the consequences of our quest for faster and better technologies for the most important resources of our life – the nature itself. All the mentioned technologies are empowered by electricity. Some powerful energy sources, such as lignite and petroleum, damage the foundation of the earth and the environmental shield that keeps our ecosystem at temperatures we can survive. Other energy sources, nuclear power plants, proved themselves a threat to millions of people (Chernobyl 1986, Fukushima 2011). Besides, such sources of nearly unlimited power can be a threat if being misused in military actions.

One of the biggest challenges in modern society is to simultaneously satisfy humanity's unlimited demand for energy while keeping the damage to nature low. Many efforts are taken to accelerate the capacity of renewable energy delivered by wind, water, biomasses, or the sun. Most notably driven by the Paris Agreement under the United Nations Framework Convention on Climate Change, politics aim to keep the increase in global average temperature to well below 2° above pre-industrial levels. This requires a fundamental rethinking of our daily energy demand and especially the development and industrialization of renewable energy sources. Renewable energies made up more than 17 % of net U.S. electricity generation in 2018. [1] More than 50 % of Germany's energy usage[2] in the first quarter of 2020 was produced by renewable energies.

Photovoltaics (PV), i.e., the conversion of sunlight into electricity, is one of the most promising technology to supply the energy demand from renewable sources. Apart from its renewability, PV systems produced 2% of the global electricity with an average of 500 GW in 2018 [1, 2]. Predictions claim that PV can cover about 10 TW as costs will become competitive with conventional electrical energy sources [2–4].

Currently, PV panels are based on highly crystalline silicon semiconductors. This is mainly due to low production cost thanks to the highly optimized wafer fabrication laboratories and scaling capabilities to mass production. However, the production of silicon solar panels requires a high amount of energy due to high-temperature processing steps that impact the carbon footprint of silicon PV. Besides, thick photoactive layers in the range of tens to hundreds of micrometers are required to efficiently absorb light due to the indirect bandgap of silicon.

[1] https://www.c2es.org/content/renewable-energy/, Accessed on the 26/04/2020

[2] Germany marks first ever quarter with more than 50 pct renewable electricity, Clean Energy Wire, R. Waldholz, Accessed on the 26/04/2020

Recent research has been focused on thin-film solar cells based on novel material systems such as cadmium telluride or copper indium gallium selenide. These are semiconductors with direct bandgap, which allows to shrink the photoactive layer thickness to a few micrometers. In addition, novel soft materials such as organic molecules, perovskites, and dyes form the class of 'third-generation PV.' This new generation of semiconducting materials provides several advantages. Their large absorption coefficients combined with direct bandgaps make these materials ideal candidates for thin-film solar cells. Low-temperature processing, such as from solution or by roll-to-roll printing, allows a cheap and environmentally friendly fabrication. Recent efforts of these third-generation PV technologies led to an improvement in record power conversion efficiency of 25.2 % for perovskite solar cells, 17.4 % in organic solar cells (OSCs), and even 29.15 % are reached within multi-junction silicon–perovskite solar cells.[3]

Despite the tremendous development of organic semiconductors and solar cells within recent years, they are not explicitly considered a replacement for inorganic semiconductors but rather serve as alternative materials for novel applications complementing inorganic PV. The advantage of OSCs above other technologies is their flexibility, light-weight, tunability, and easy fabrication [5]. These properties allow exploring novel niche markets such as wearable electronics, integration in the chassis of cars or trains, or within in windows and buildings. Thus, one could carry a renewable energy source integrated within the backpack or integrated into the city bus.

Organic semiconductors are conjugated carbon-based molecules and polymers with alternating single and double bonds. Conjugated systems contain π-bonds which are formed from overlapping p-orbitals between sp^2-hybridized carbon atoms. Charge carriers delocalize within the π-bonds, which makes the molecule conductive. While intramolecular forces make up the structure of the molecule, weak van der Waals and dipole–dipole interactions are present between molecules leading to a lack of long-range order, especially if organic semiconductors are being solution-processed. Furthermore, this fundamentally changes the nature of charge and exciton transport, significantly alters the interactions between charge carriers and strongly enhances exciton binding energies. As a consequence, the device physics of OSCs is fundamentally impacted by four parameters:

1. *Light absorption* – Plenty of organic semiconductors can be easily synthesized with chemically engineered absorption properties. Typically, organic semiconductors have a narrow absorption spectrum limiting the amount of light being converted into electrical energy. Engineering the absorption can lead to a significant increase in the performance of OSCs [6, 7].

2. *Permittivity* – Organic semiconductors have a low permittivity in the range of 3 to 4. Thus, upon light absorption, strongly bound Frenkel excitons with binding energies in the range of hundreds of meV are generated [8, 9]. To dissociate these Frenkel excitons into free charge carriers, blends of an electron donor and an electron acceptor semiconductors are employed [10–12]. The acceptor material has a high electronegativity, which provides the required driving force at the donor:acceptor interface for exciton dissociation. Moreover, the low permittivity causes poor screening of the electrostatic interaction leading to long-range Coulomb attraction of charge carriers. This may enhance undesired geminate and non-geminate recombination [10, 13] and control the separation dynamics of charge carriers [14]. Attempts of increasing the permittivity were done via side-chain engineering [15] or via blending low permittivity semiconducting donors with high permittivity molecules [16].

3. *Spatial disorder* – Solution-processed organic semiconductors, especially within the highly intermixed donor:acceptor phases of bulk heterojunction OSCs, show high spatial disorder in

[3] National Renewable Energy Laboratory, https://www.nrel.gov/pv/cell-efficiency.html, Accessed on the 17/09/2020

the molecular arrangement. This leads to a localization of charge carriers [17, 18] and limits the charge carrier mobility [19–22]. Also, large interface areas in BHJ morphologies enhance non-radiative recombination losses in the open-circuit voltage [23, 24].

4. *Energetic disorder* – Organic semiconductors, especially polymers, are mainly made up of regio-regular regions surrounded by amorphous domains [25, 26]. The molecular disorder and the lack of periodicity in the molecular arrangement leads to an Anderson localization of charge carriers [17] and confines them on quantum states, which are of the size of single to a few molecules/monomers. Thus, the electronic structure is characterized by spatially distributed quantum states with largely varying energy levels. Consequently, charge transport is dominated by hopping from one localized state to another [18, 27–29].

The presence of the low permittivity and strongly interacting, localized charge carriers within complex bulk-heterojunction morphologies of spatially disordered molecules requires a detailed understanding of the physical processes on the nanoscale to improve charge and exciton transport and to reduce energy losses by recombination. Experimentally accessing such properties requires ultrafast techniques [30] with extreme spatial resolution. However, existing experiments cannot capture both, especially for realistic thin film devices where the active layer is hidden below selective transport layers and electrodes. Numerical simulation models can complement experimental analysis to connect the experimental observations with the dynamics of charge carriers and excitons on a molecular level.

Most existing drift-diffusion (DD) models simplify the complex bulk-heterojunction morphology by using effective medium approximations [31–33], while only a few studies include realistic morphologies [34]. However, with higher dimensions, significant convergence issues may arise. Also, DD calculations assume immediate equilibration of the charge carriers within the energetic density of states and cannot capture the non-equilibrium dynamics through the active material [32, 34, 35]. This consequently does not allow any insight into fast time- and short length scales, which may be of relevance for the improvement of OSCs.

Kinetic Monte Carlo (kMC) models have been successfully applied in the recent decades to simulate the dynamics of charge carriers [29, 36, 37] and of excitons [38, 39] in organic semiconductors, recombination characteristics [13, 40–42] as well as full OSC devices [14, 43–48]. kMC allows the simulation of dynamical properties within a network of localized sites. The information about the materials enters the simulation in terms of arrangement of molecules [49] or structure of electronic states [20]. Particles, such as electrons or excitons, evolve throughout the system phase space, given by the position and energies of the sites, controlled by physical transition rates. These transition rates incorporate the underlying physics and can include spatial and energetic disorder as well as the many-body interaction under the Coulomb potential of other charge carriers. As a result, a wide range of properties from local charge carrier mobility [20, 50, 51] up to full current–voltage characteristics [46] can be studied. Thus, the usage of kMC models allows building a bridge between the molecular structures to full device models.

The objectives of this thesis address various aspects of charge and exciton transport within OSCs. To meet these objectives, the in-house developed 3D kMC model [52] is extended to allow an improved description of charge and exciton transport within organic semiconductors and solar cells. Chapter 2 presents fundamental aspects of OSCs. First, the general physics of light conversion into electricity is presented. Then, an overview of recent developments in various PV technologies and especially emerging PV materials is summarized. Section 2.3 introduces the electronic structure of organic semiconductors. Sections 2.4 and 2.5 introduce the theory of charge transport and excitons, respectively, in organic semiconductors. Finally, section 2.6 describes the structure and working principle of OSCs.

In chapter 3, the kMC model is presented. Based on the theoretical fundament of the Gillespie algorithm (section 3.1), the system setup and the physical rates are explained in sections 3.2 and 3.3, respectively.

The developed kMC model has been used to study several aspects of OSCs involving charge and exciton transport as well as the separation of charge transfer states. The following objectives are presented within this thesis.

1. By nature, kMC simulations favor processes of high transition rates. Accessing slow transitions in the presence of fast transitions requires long simulation times. Thus, device characteristics that depend on the slowest processes are hardly accessible within reasonable timescales. The goal is to develop a scaling algorithm that detects if the system is trapped within so-called superbasins [53] to make slow processes accessible. The developed algorithm and its performance is presented in Chapter 4.

2. Existing kMC models usually represent organic semiconductors by a cubic lattice where each lattice site represents one electronic state. An off-lattice kMC model based on the Voronoi tessellation is developed to capture the nature of amorphous organic semiconductors. This allows to connect the spatial arrangement of molecules and spatial variations in charge transfer integrals on the carrier mobility. The Voronoi tessellation has been further integrated within multiscale charge transport simulations to connect the spatial arrangement of molecules in thin films with the carrier mobility. This work is presented in Chapter 5.

3. Typical OSCs show high losses in the open-circuit voltage. Existing DD-based studies connect the voltage loss with non-radiative recombination and the energetic disorder. However, the role of the intermixed BHJ morphology and the electronic density of states at the interface is not fully understood. Chapter 6 studies the role of the donor:acceptor interface on the open-circuit voltage.

4. An accurate model of exciton transport is crucial to understand the sources of exciton losses within kMC studies. The next objective is to integrate accurate physical models for both singlet and triplet excitons within the kMC framework. The model has been used to study the possibility of enhancing exciton lifetime and diffusion by the population of the triplet state from singlet excitons via intersystem crossing imposed by phosphorescent sensitizers to improve the efficiency of OSCs. Further details can be found in Chapter 7.

5. A key requirement for the efficient operation of OSCs is the dissociation of charge transfer (CT) states into free charge carriers. Despite the presence of high Coulomb energies, high internal quantum efficiencies close to 100% are observed in OSCs [54]. Existing studies revealed the importance of disorder [55] and delocalization [56], entropy [57], and initial excess energy [58]. However, most of these studies rely on equilibrium methods, which are questionable due to the nonequilibrium nature of charge and exciton transport. A novel nonequilibrium thermodynamic methodology for describing the free energy barrier during the dissociation process has been developed. This study is presented in Chapter 8.

6. One crucial question has been puzzling researchers in recent years: how do charge carriers migrate in the presence of mixed and isolated phases within OSCs. Dilute donor OSCs [36, 59, 60] with donor concentrations below the percolation threshold represent ideal test systems to analyze the physical mechanism of hole transport in isolated phases. In Chapter 9, the origin of hole transport is studied for polymer and small molecule dilute donor OSCs.

2 Fundamentals of Organic Solar Cells

2.1 Physics of Solar Cells

In this section, the general working principle of solar cells is presented for the case of a p-n junction following [61, 62]. In simple words, solar cells convert radiative energy to electrical energy based on the photovoltaic effect [63]. Semiconductors exposed to light generate excited electronic states by absorption of photons of energy $h\gamma$ larger than the bandgap energy E_{gap}. The excitation results in a bound electron–hole pair, whose binding energy depends on the material structure. Separating the electron–hole pair into free charge carriers with subsequent transport to oppositely charged electrodes gives rise to an electric current. Efficient photovoltaic conversion requires the optimization of all three processes:

1. Absorption of photons
2. Separation of electron–hole pairs
3. Extraction of free charge carriers

Each of these steps will be set into a physical description in the remaining section.

2.1.1 Absorption of Photons

As mentioned above, photons require energies higher than the optical bandgap to excite electrons from the semiconductors' valence band into the conduction band. To choose materials for optimal absorption, one must (1) consider the available spectrum of photon energies irradiated from the sun, and (2) to optimize the absorbance of a semiconductor.

Figure 2.1 shows the solar irradiance $\Phi(\lambda)$, i.e. the solar power density per wavelength (energy), as a function of the wavelength. AM0 gives the solar irradiance outside of the earth's atmosphere. This spectrum corresponds to a black body radiation of the sun at temperature $T_{\mathrm{S}} = 5800\,\mathrm{K}$. Integrating the solar irradiance for all wavelengths yields a power density of $1353\,\mathrm{W\,m^{-2}}$. AM1.5 (red curve) shows the spectrum which is being observed on the surface of the earth. Usually, spectrum AM1.5 is used as a standard for measuring solar efficiency experimentally and within all simulations. It differs from the AM0 due to absorption by water, H_2O, carbon dioxide, CO_2, nitrous oxide, N_2O, methane, CH_4, fluorinated hydrocarbons, and dust in the infrared region of the spectrum. Ozone and oxygen absorb light in the ultraviolet regime. As a result, a power density of $1000\,\mathrm{W\,m^{-2}}$ is being observed on earth, also being referred to as *1 sun* in literature. However, depending on the climate conditions, reduced solar irradiance is typically observed. In Germany, an average density of $115\,\mathrm{W\,m^{-2}}$ is observed [62]. The visible spectrum, i.e., the regime of the solar irradiance that is visible to the human eye, is in the range from about 380 nm to 740 nm. Here, the AM0 and AM1.5 reach their maximum.

The capability of a semiconductor to absorb light is described by its material-dependent absorption coefficient $\alpha(\hbar\omega)$. During the absorption of a photon, energy and momentum need to be conserved. One distinguishes between direct, in which the momentum of the electron–hole system does not

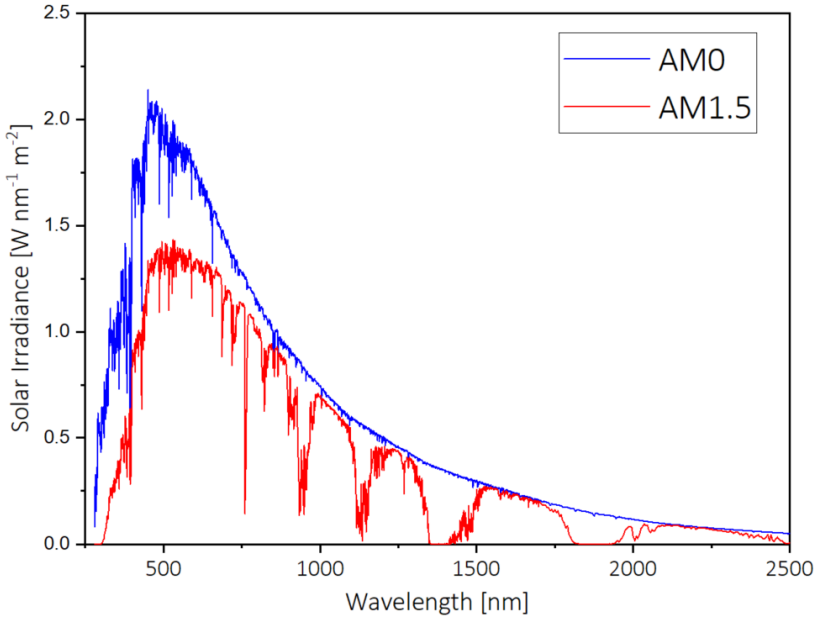

Figure 2.1 Solar irradiance as a function of the wavelength. The AM0 spectrum represents the radiation of the sun under extraterrestrial conditions without absorption in the atmosphere. The AM1.5 standard resembles solar irradiance under an incident angle of 48.19° on earth.

change, and indirect transitions, which shows a change in the momentum [61, 64]. Both transitions are visualized in a Fig. 2.2.

A direct transition describes transitions in which the initial and the final electronic state have equal momentum $\hbar\mathbf{k}$. As photons carry a negligible momentum $\hbar\mathbf{k}_\gamma \approx 0$, the momentum conservation requires that

$$\hbar\Delta\mathbf{k} = \hbar\mathbf{k}_\gamma = \hbar\mathbf{k}_f - \hbar\mathbf{k}_i \approx 0\,, \tag{2.1}$$

with $\hbar\mathbf{k}_i$ and $\hbar\mathbf{k}_f$ being the momentum before and after the transition, respectively. Energy conservation during the transition of energy $\Delta E_{i,f}$ demands

$$\Delta E_{i,f} = \hbar\omega_\gamma = E_\mathrm{C}(\mathbf{k}) - E_\mathrm{V}(\mathbf{k})\,, \tag{2.2}$$

with the photon energy $\hbar\omega_\gamma$, conduction band energy $E_\mathrm{C}(\mathbf{k})$ and valence band energy $E_\mathrm{V}(\mathbf{k})$ at wave vector $\mathbf{k}$. At the conduction band minimum (CBM) and the valence band maximum (VBM), the band dispersion can be well described by a parabolic relation with effective mass $m^*_{e/h}$. This yields

$$\Delta E_{i,f} = \left(\frac{1}{m^*_e} + \frac{1}{m^*_h}\right)\frac{\hbar^2k^2}{2} = \frac{\hbar^2k^2}{2m^*_\mathrm{komb}}\,, \tag{2.3}$$

with the combined effective mass m^*_komb. The combined density of states D_komb of the combined band structure $\Delta E_{i,f}(\mathbf{k})$ can be written as

$$D_\mathrm{komb}(\Delta E_{i,f}) = \frac{V}{2\pi^2}\left(\frac{2m^*_\mathrm{komb}}{\hbar^2}\right)^{3/2}\sqrt{\Delta E_{i,f} - E_\mathrm{gap}}\,. \tag{2.4}$$

As the absorption scales with the available number of states, we observe a root-shaped behavior:

$$\alpha(E) \propto \left(m^*_\mathrm{komb}\right)\sqrt{E - E_\mathrm{gap}}\,. \tag{2.5}$$

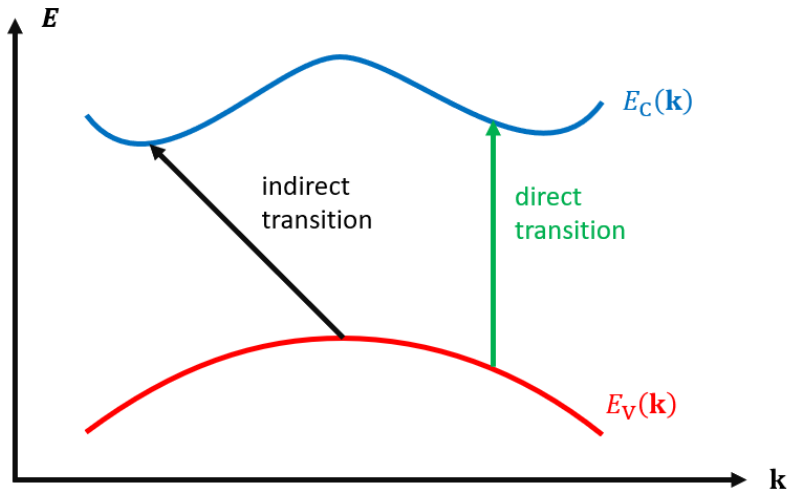

Figure 2.2 Direct and indirect interband transitions within semiconductors.

In indirect semiconductors, phonons (small energy $\hbar\Omega \ll \hbar\omega_\gamma$ and large momentum $\hbar\mathbf{q}$) play an important role in the absorption process. Indirect transitions occur by creation or annihilation of a phonon. Now, the energy and momentum conservation read

$$E_C(\mathbf{k}') = E_V(\mathbf{k}) + \hbar\omega_\gamma \pm \hbar\Omega\,, \tag{2.6}$$

and

$$\mathbf{k}' = \mathbf{k} + \mathbf{k}_\gamma \pm \mathbf{q}\,, \tag{2.7}$$

respectively. The transition matrix elements of three-particle processes are significantly smaller than the ones of two-particle processes, thus indirect processes are of minor importance for semiconductors of direct bandgap. To determine the absorption coefficient, the combined density of states needs to be calculated for each pair of bands i and k [61]:

$$D_{ik}(\hbar\omega) = \frac{1}{(2\pi)^3} \int_{\hbar\omega = E_k - E_i} \frac{\mathrm{d}S_{\hbar\omega}}{|\nabla_k \left(E_k(\mathbf{k}) - E_i(\mathbf{k})\right)|}\,. \tag{2.8}$$

These elements are maximal for bands i and k which are parallel with distance $\mathbf{k}$. An analytic equation cannot be easily derived, thus numerical methods are required to obtain the absorption coefficient. In general, a quadratic dependence of the absorption coefficient holds:

$$\alpha \propto \left(\hbar\omega - \hbar\Omega - E_{\mathrm{gap}}\right)^2\,. \tag{2.9}$$

The value of α for indirect transitions is relatively low. Thus, to absorb photons efficiently, thick photoactive layers of several 100 µm are required.

In reality, significant absorption can be already observed for slightly lower photon energies $\hbar\omega < E_{\mathrm{gap}}$. This can be explained in the presence of excitons, i.e., bound states between the excited electron within the conduction band and the remaining hole in the valence band. This electron–hole pair has certain energy E_{exc} caused by the Coulomb interaction between the positively charged hole and the negatively charged electron. One distinguishes between two types of excitons: *Wannier–Mott* and *Frenkel* excitons.

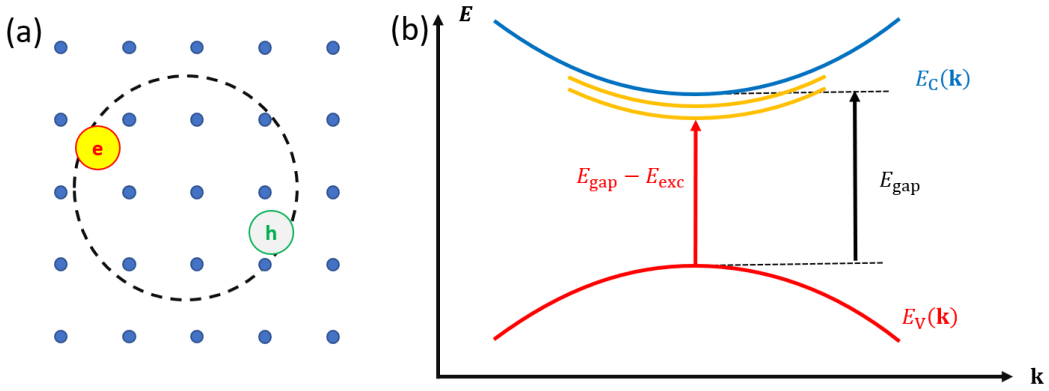

Figure 2.3 (a) Wannier–Mott exciton represented by a distant electron–hole pair. (b) Excited states within the simplified band structure. Adapted from [61].

Wannier–Mott excitons are usually observed if electrons are weakly bound to the lattice atoms. Thus, a large distance between the electron and hole are expected which gives a small binding energy $E_{exc} \approx k_B T$. Considering the binding energy by the Coulomb attraction,

$$E_{exc} = \frac{e^2}{4\pi\epsilon_0\epsilon_r \left|\mathbf{r}_e - \mathbf{r}_h\right|}, \tag{2.10}$$

with the vacuum permittivity ϵ_0, and the dielectric constant of the semiconductor ϵ_r. As typical crystalline semiconductors show $\epsilon_r \approx 10$, small binding energies are expected. Experimental values show small binding energies of 14.7 meV for silicon or 4.2 meV for gallium arsenide [61]. Figure 2.3a sketches a simplified picture of the Wannier–Mott exciton; Fig. 2.3b visualizes excitonic states within the band gap.

In contrast, Frenkel excitons are characterized by localized electron–hole pairs of small distances. In amorphous semiconductors, which are characterized by low dielectric constants, large binding energies of several 100 meV are expected.

2.1.2 Separation of Electron–Hole Pairs

Upon absorption of a photon, typically both an electron and a hole are produced. If the photon energy is at least twice the value of the bandgap, multiple exciton generation may occur. This, however, is neglected in this work. Typical inorganic solar cells are based on a pn-junction, which has been already used within first solar cells in 1954 [65]. Standard pn-junction silicon (Si) solar cells are made of a 600 µm-thick p-doped Si layer, on which a 1 µm-thick n-doped Si layer is deposited. A thin n-doped layer is required, as one desires to absorb light within the depletion layer, which will be discussed briefly in the following. The thick p-doped layer ensures mechanical stability and efficient absorption of light.

The band diagram of the pn-junction is visualized in Fig. 2.4. The fundamental structure is equal to a pn-junction, in which electron–hole pairs are generated by incoming light with photon energy $E_\gamma \geq E_{gap}$. At the interface between the oppositely doped materials, a depletion layer is formed. Electrons from the n-doped layer and holes from the p-doped layer diffuse into the oppositely doped region and partially recombine. This leads to a positive space charge in the n-doped layer, as ionized donors remain left, and a negative space charge in the p-doped layer, as ionized acceptors remain left. The resulting space charge forms an internal electric field which supports the separation of

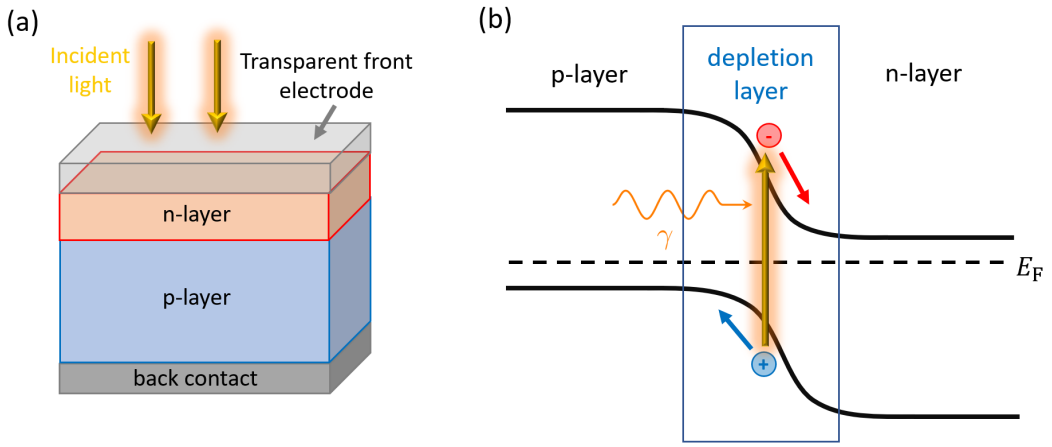

Figure 2.4 (a) The basic structure of a pn-solar cell made of a thin n-doped and a thick p-doped layer stacked between two metallic contacts. (b) Band diagram of a pn-junction. Light is absorbed in the photoactive layer. Efficient separation of charges happens in the depletion layer.

electron–hole pairs (see Fig. 2.4b). This electric field created by the diffusion of majority charges into the minority regions corresponds to a built-in potential difference across the junction.

The depletion layer is crucial for the operation of pn-junction solar cells. If an electron–hole pair is excited in the p-doped region, the probability of recombination of the photogenerated electron with the majority carriers (holes) is high. Electrons need to cross the hole p-layer to reach the n-layer. The larger the distance between the spot of generation (in the p-layer) to the depletion layer, the lower the probability of extraction at the front electrode will become. In the depletion layer, photogenerated electron–hole pairs are easily separated due to the internal electric field. Consequently, holes (electrons) reach the p-layer (n-layer) and are easily transported to the contacts.

One important measure for the motion of photogenerated charge carriers is the characteristic diffusion length. This is the average distance charges pass before recombination occurs. If the diffusion length is sufficiently large, in general, in size of the thickness of the photoactive layer, charges can be transferred to the contacts mainly by diffusion. In this scenario, one may even use a single-junction photoactive layer without any depletion region. Otherwise, an internal electric field is necessary to efficiently separate electrons and holes and subsequently drive them towards the contacts.

2.1.3 Extraction of Free Charge Carriers

Finally, an efficient charge extraction of charge carriers at contacts is crucial for the final efficiency of any type of solar cells [66]. Contacts need to provide a selectivity on which charge carriers are being extracted. Especially within diffusion-based solar cells, contact selectivity is crucial for the efficient operation. It was shown that contacts with small sensitivity can strongly limit the device efficiency [67]. Additionally, several high-efficiency photovoltaic technologies, such as halide perovskites, show a strong increase in recombination and reduction in open-circuit voltage when being in contact with contact layers [68,69]. To enhance the selectivity, frequently hole and electron transport layers are added to avoid the extraction of the oppositely charged carriers. Besides, the formation of Ohmic contacts may limit the charge extraction, such as observed in silicon solar cells [70]. It was recently shown that the built-in voltage plays a favorable role for an efficient collection efficiency [66].

Another critical requirement is the transparency of the front electrode. Light absorption within the electrode or reflection at the surface of the electrode would limit the amount of photons reaching the photoactive layer, and consequently, reduce the photocurrent. Nanostructured surfaces and anti-reflective coatings can be exploited to overcome these issues.

2.1.4 Current–Voltage Characteristics of Solar Cells

The current–voltage characteristics of a pn-junction solar cell can be derived starting from the equivalent circuit diagram (see inset Fig. 2.5). The photocurrent generated by the incident light is represented by a constant current source j_L. The pn-junction is represented by a diode, which current–voltage relation is known as

$$j_\mathrm{D}(V) = j_\mathrm{S}\left[\exp\left(\frac{eV}{k_\mathrm{B}T}\right) - 1\right] , \tag{2.11}$$

with the elementary charge e, the saturation current density j_S, Boltzmann constant k_B, and temperature T. Internal recombination losses are modeled as the shunt resistance R_SH. Contact resistance and interface losses are captured by the series resistance R_S.

From Kirchhoff's current law, one obtains the *current–voltage characteristics*

$$j(V) = j_\mathrm{L} - j_\mathrm{S}\left[\exp\left(\frac{e\,(V + jR_\mathrm{S})}{k_\mathrm{B}T}\right) - 1\right] - \frac{V + j(V)R_\mathrm{S}}{R_\mathrm{SH}} . \tag{2.12}$$

Ideally, $R_\mathrm{S} \to 0$ and $R_\mathrm{SH} \to \infty$. In such scenario, the current–voltage relation simplifies to the *ideal solar cell equation*

$$j(V) = j_\mathrm{L} - j_\mathrm{S}\left[\exp\left(\frac{eV}{k_\mathrm{B}T}\right) - 1\right] . \tag{2.13}$$

In Fig. 2.5, a typical jV-characteristics is visualized. The different regimes are defined as follows:

- At negative bias voltage, the current density approaches the generation current j_L. Here, electrons and holes can be easily separated and are transferred to the respective contact. The device dissipates power in this regime.
- At zero bias volage $V = 0\,\mathrm{V}$, the short-circuit current (j_sc) is defined. In realistic solar cells, the absolute value of j_sc is smaller than the generation current, as finite recombination is expected.
- Bias voltages between 0 V and V_oc characterize the operation regime of solar cells. Here, the solar cell generates power from the incoming photons for usage in the external circuitry. The maximum power point P_max is defined by the point in which the product of current density and voltage reaches its highest value. This is the ideal operating point for solar cells.
- At open-circuit voltage, V_oc, no net current density is observed. In this regime, the highest recombination of free charge carriers is observable.
- At voltages beyond V_oc, photogenerated charge carriers are extracted at the wrong contact. In addition, charge injection from the electrodes into the photoactive layer becomes dominant such that a normal diode-like exponential increase in the current density with rising voltage can be observed.

The power conversion efficiency (PCE) of solar cells is characterized by the ratio of the generated power, P_max, and the incoming power from the solar source, P_in:

$$\mathrm{PCE} = \frac{P_\mathrm{max}}{P_\mathrm{in}} = \frac{V_\mathrm{oc} j_\mathrm{sc} \mathrm{FF}}{P_\mathrm{in}} . \tag{2.14}$$

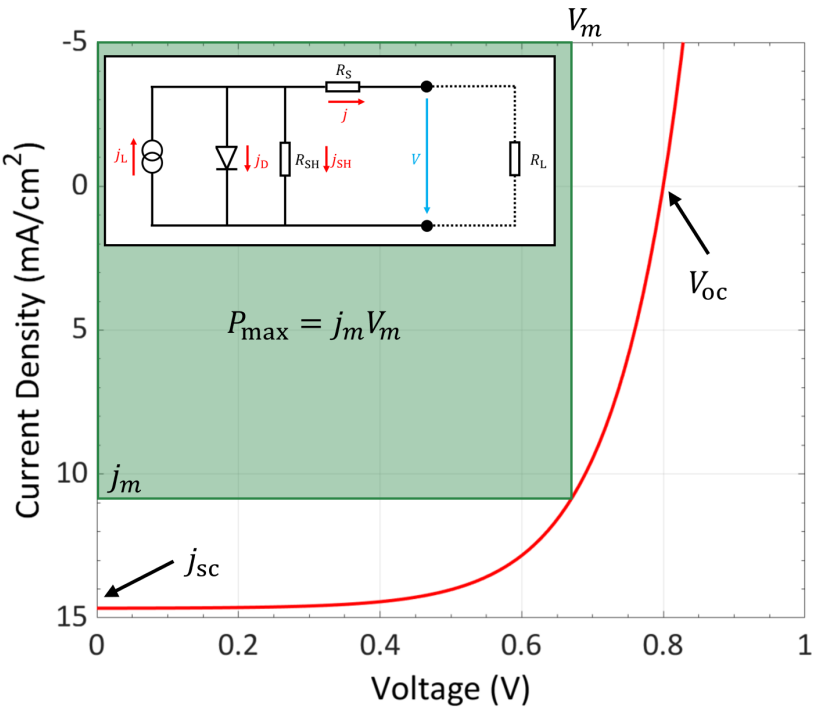

Figure 2.5 Current–voltage characteristics of a typical solar cell. The maximal power P_{max} is highlighted by the green area. The inset shows an equivalent circuit diagram.

In this relation, the generated power is expressed as the product of the open-circuit voltage, short-circuit current density and the fill factor (FF). The latter quantity describes the quality of the solar cell in terms of internal losses, while j_{sc} and V_{oc} are determined by material parameters such as the absorbance and the band gap, respectively. High FF are characteristic for low recombination losses, which is highly desirable for efficient photovoltaic operation. The input power P_{in} is given by the integral of the solar irradiance $\Phi(\lambda)$ across all wavelengths.

2.1.5 Shockley–Queisser Limit

The Shockley–Queisser limit gives the theoretical limit of the PCE of a single junction pn-junction solar cell. William Shockley and Hans J. Queisser analyzed the efficiency limit assuming that the only recombination mechanism of electron–hole pairs is radiative such that the detailed balance is fulfilled [71]. The detailed balance states that if the absorption of photons with subsequent generation of electron–hole pairs is possible, the reverse process must also be possible. That means that electrons and holes can recombine radiatively under the emission of a photon [72].

Shockley and Queisser assumed the radiation of the sun as a black-body radiator at temperature T_S, which allows us to describe the total energy density as a function of the photon frequency ν by the Planck's radiation law [71]. The second assumption in their analysis is that all photons with energy $h\nu \geq E_{gap}$ are entirely absorbed and create exactly one electron–hole pair. Subsequently, immediate relaxation of the electron to the conduction band minimum and of the hole to the valence band maximum is assumed, such that one electron and one hole at energy $eV_g = E_{gap}$ are created. Additionally, non-concentrated sunlight is assumed.

Figure 2.6 depicts the theoretical limit of the PCE derived by Shockley and Queisser at temperature $T = 300\,\mathrm{K}$. It shows a maximum PCE value of 33.7 % at $E_{gap}^{opt} = 1.34\,\mathrm{eV}$ semiconductor bandgap. For

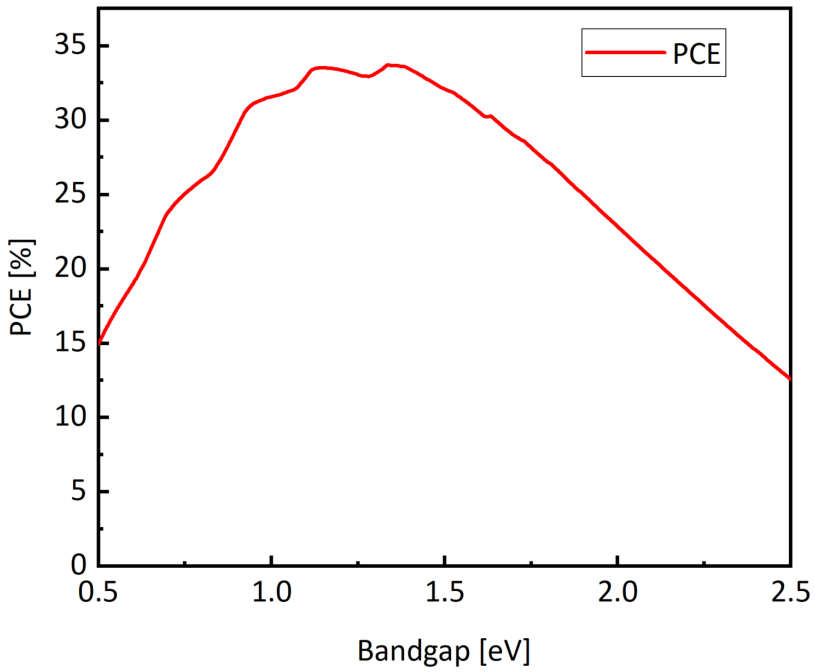

Figure 2.6 Shockley–Queisser limit for the power conversion efficiency as function of the semiconductor band gap.

bandgaps larger than $E_{\text{gap}}^{\text{opt}}$, the PCE decreases due to less absorbed photons. For smaller bandgaps, light absorption increases. However, the PCE is strongly reduced due to enhanced thermalization losses. If the temperature of the solar cell is enhanced, the maximum efficiency shifts to lower values and slightly higher bandgap. Enhancing the light intensity, e.g., using solar concentrators or mirrors, leads to a slight increase in efficiency. However, heating and enhanced recombination can be expected.

In Fig. 2.7, the contributions of the AM1.5 spectrum to the available energy as well as the energy losses for the ideal bandgap of 1.34 eV are visualized. This plot follows the equations of the original paper by Shockley–Queisser.[1] The grey area depicts the regime of the spectrum with photon energies smaller than the bandgap of the semiconductor. The available energy (blue) labels the part of the spectrum which contributes to the electrical energy. The remaining energy is lost by (red) thermalization and (yellow) extraction losses due to radiative recombination.

Several strategies are currently considered to enhance the efficiency beyond the Shockley–Queisser limit [61, 62]:

- Tandem solar cells, which consist of a stack of several photoactive semiconductor layers, allow absorbing a broader spectrum of light. Photons of high energies are absorbed in the top layer, which consists of a semiconductor of large bandgap and is transparent for the photons of lower energy. These photons are then absorbed in the bottom layer, which is made of a low bandgap semiconductor. Also, thermalization losses are reduced within each layer as the excess energy ($E_\gamma - E_{\text{gap}}$) is reduced within the individual layers with respect to single-junction solar cells.

- Solar concentration made of mirrors or optical lenses allows increasing the light intensity. This allows an increase of the efficiency beyond 40 % [73].

[1] Plots were generated using the GitHub repository `https://github.com/marcus-cmc/Shockley-Queisser-limit`

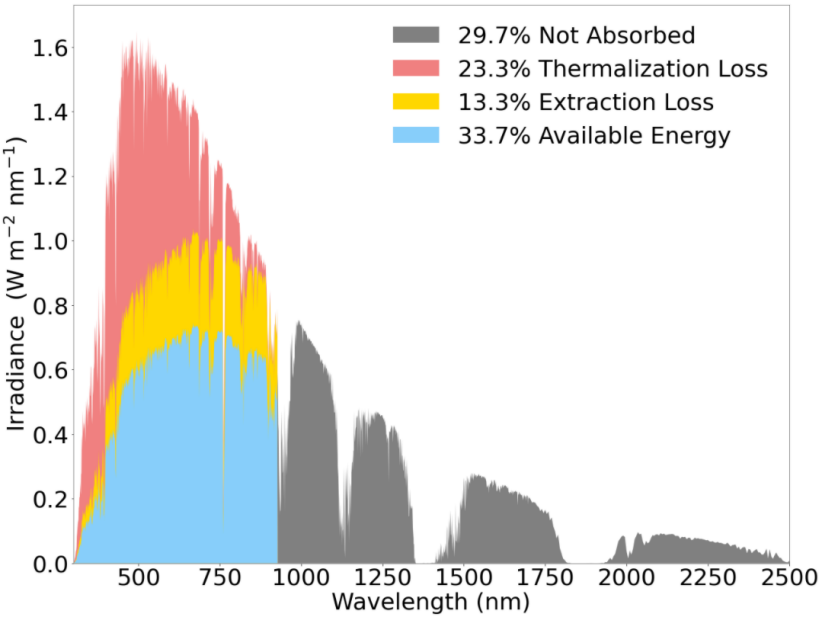

Figure 2.7 Shockley–Queisser limit for the power conversion efficiency as function of the semiconductor band gap.

- Surface structuring reduces losses due to light reflection. Pyramid-like structures allow multiple reflections of light onto the surface. Thus, the probability of light to pass the surface and reach the photoactive layer increases.

- Multiple exciton generation can be reached by down-conversion of high energy photons by introducing nanostructures with high bandgap into the photoactive layer. Also, materials with large absorption coefficients may immediately absorb photons emitted by radiative recombination before the photon leaves the active layer.

- Especially the usage of novel materials offers interesting novel photovoltaic systems. This is briefly discussed in the following section.

2.2 Emerging Photovoltaics

Within recent decades, research on novel photovoltaic technologies has flourished. The advent of nanotechnologies allows fabricating thin-film photovoltaics with high quality and control of the layer morphology and crystallinity. On the other hand, chemical synthesis of molecules allows a wide range of molecular-based photovoltaics, namely organic photovoltaics. Just a decade ago, perovskite solar cells started to fascinate researchers all over the world due to extraordinary electro–optical properties. In the following, the most recent trends are briefly summarized. Note that the focus is set on the efficiencies of non-concentrator solar cells. Typically, concentrator solar cells, i.e., solar cells with concentrated light due to e.g., optical lenses or mirrors, allow higher efficiencies as discussed within the Shockley–Queisser limit. Figure 2.8 visualizes the certified record efficiencies of existing photovoltaic technologies achieved in laboratory environment.[2]

[2] Accessed on the 17th September 2020, `https://www.nrel.gov/pv/cell-efficiency.html`

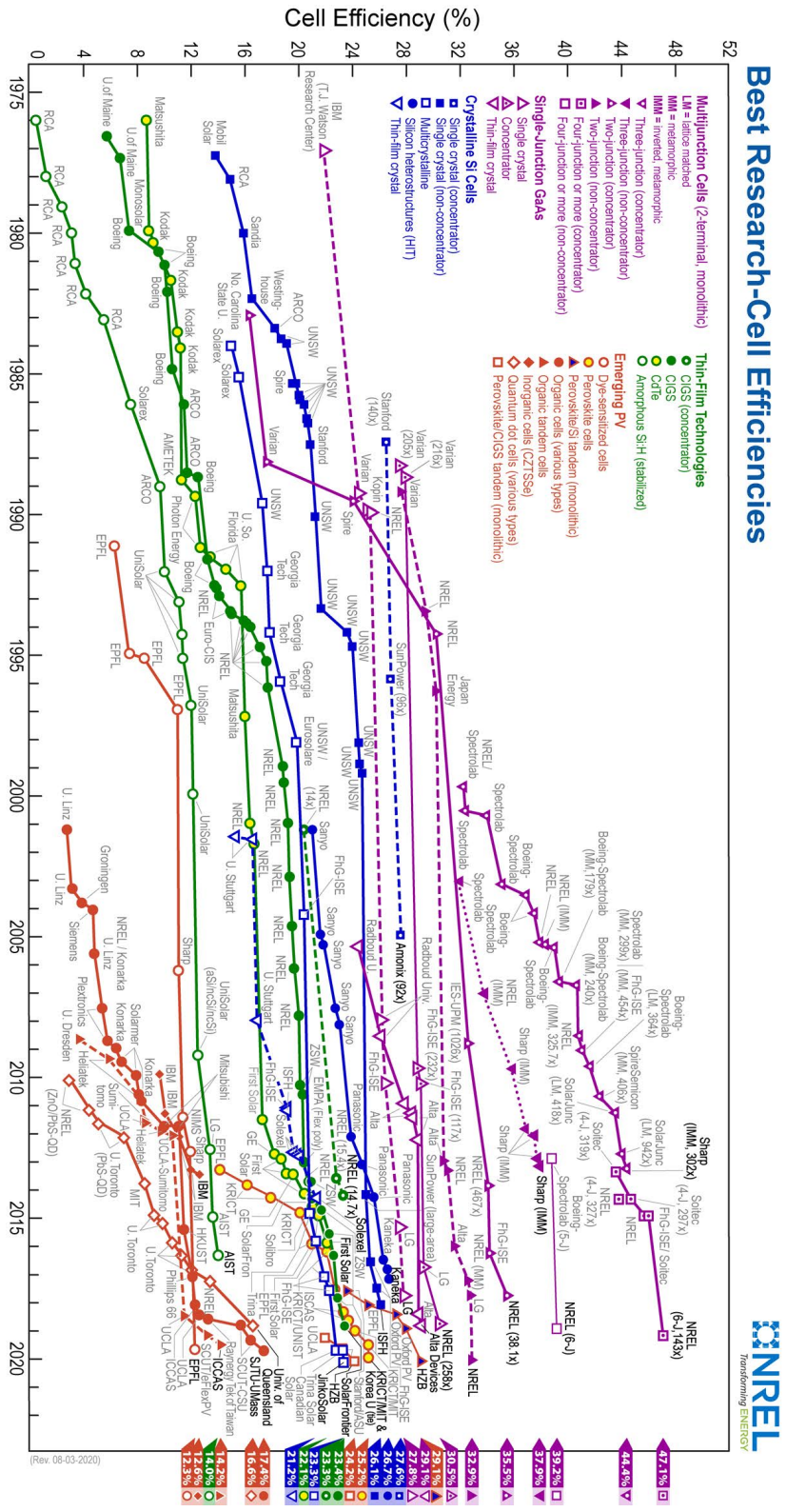

Figure 2.8 Efficiency chart of the record cell efficiencies for various material systems summarized by the National Renewable Energy Laboratory (NREL).

Classical crystalline silicon solar cells have reached efficiencies of 24 % already in 1995. Since then, only slight increases in the PCE were observed, with today's record efficiency being at 26.1 %. GaAs solar cells showed promising efficiencies beyond 20 % already in the 1970s. Nowadays, single-crystal GaAs solar cells reach record efficiencies of 27.8 %. Interestingly, for both silicon and gallium arsenide, thin-film crystalline cells reach efficiencies of 21.2 % and 29.1 %, respectively.

As mentioned in the previous subsection, tandem solar cells (multijunction cells) promise high efficiencies due to the absorption of a wider spectrum with reduced thermalization losses. Consequently, two-junction tandem solar cells reach efficiencies up to 32.9 %. One can even go further and stack more than two layers within tandem solar cells: three-junction and four-junction tandem solar cells reach record efficiencies of 37.9 % and 39.2 %. While these values are very promising, the cost for fabricating such high-quality tandem solar cells exceeds the cost of standard silicon solar cells by far.

Thin-film technologies are of interest due to the reduced amount of material and light-weight, which allows the integration in a more flexible environment. Here, especially copper-indium-gallium-diselenide (CIGS) and cadmium telluride solar cells with efficiencies of 23.4 % and 22.1 % are leading materials with significant performance increase within the recent decade. Besides, these material systems allow high stabilities.

Emerging photovoltaics, or third-generation solar cells, refer to a broad class of novel photovoltaic materials. These devices allow thin-film technologies based on material systems of high absorption coefficients and, perhaps most promising, low-cost production on large scales. Some of the most interesting material systems for third-generation cells are dye-sensitized solar cells (DSSC), also known as Grätzel cells, perovskite solar cells, and organic solar cells.

DSSCs are fundamentally electrochemical cells. A DSSC is made of a photosensitive dye attached to a mesoporous titanium dioxide anode that is immersed within a liquid electrolyte [74,75]. In DSSCs, light absorption occurs within the dyes. Subsequently, the photoexcited electron is transferred to the TiO_2, in which it migrates to the electrode. A redox couple, typically I^-/I_3^-, within the electrolyte transfers an electron to the dye [76]. The ion migrates towards the counter electrode at which it is regenerated through the interaction with a catalyst layer, typically platinum [76]. DSSCs reach record efficiencies of 12.3 %. The main advantage of DSSCs is not particularly in efficiency, but their light absorption in the visible range. This spectral region is especially present in indoor illumination spectra. Consequently, DSSCs offer interesting properties for indoor usage and may serve as an interesting candidate to power smart devices by indoor light [77]. The main challenge in DSSCs is the liquid electrolyte, which may lead to device failure in the presence of micro-cracks. The electrolyte can leak if the cell is not properly encapsulated, which may lead to corrosion within the metal electrode. Solid electrolytes may circumvent such issues [78].

Perovskites represent one of the most rapidly developing material systems for emerging photovoltaic cells [79, 80]. Perovskites are minerals made of an ABX_3 crystal structure. The most commonly studied perovskite structure is made of methylammonium lead trihalide, $CH_3NH_3PbX_3$, where X represents a halide ion such as iodine, bromine, or chlorine. Perovskites have favorable optical bandgaps for photovoltaic applications. Lead halide perovskites have gained extraordinary interest within the recent decade. Their fascinating electro(-optical) properties in combination with low-cost processability make perovskites the most promising candidate for future photovoltaic technologies as stand-alone photoactive material or in combination with other material classes within a tandem configuration. Within 10 years only, the efficiency increased from 3.8 % [81] to record-breaking values of 25.2 % in single-junction architecture [82] and 28.0 % within perovskite-silicon tandem solar cells (see NREL efficiency chart). The most critical challenges for the future development of perovskites are to ensure long-term stability, the replacement of toxic lead by non-toxic metal ions, and the reduction of recombination losses due to interfaces with the transport layers.

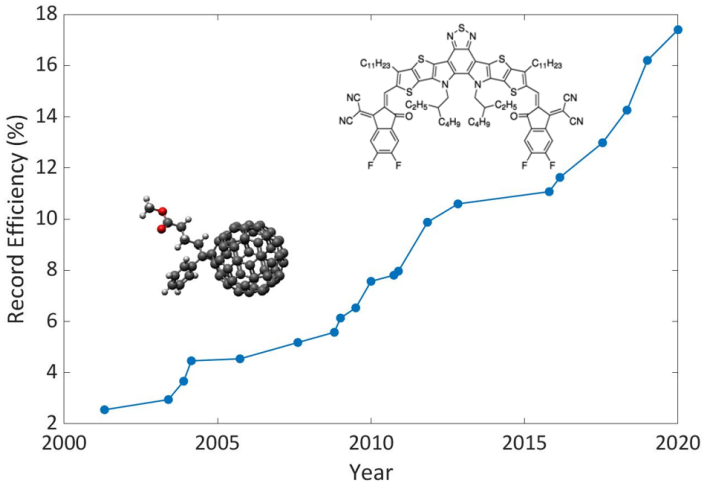

Figure 2.9 Development of the record efficiencies of single-junction organic solar cells within the recent twenty years. The left inset shows a fullerene molecule, PCBM, the standard acceptor material up to 2015. Afterward, non-fullerene acceptors have led to a tremendous increase in efficiency. The non-fullerene acceptor BTP-4F (Y6) is shown as right inset. Datapoints have been extracted from the NREL efficiency chart (see Fig. 2.8).

The main focus of this thesis is on organic solar cells (OSCs). OSCs are based on semiconducting carbon-based organic polymers or molecules which offer major advantages such as low-cost processability by roll-to-roll printing, spin- or spray-coating, which all require low temperature. Organic polymers and molecules are soft materials. Thanks to their high absorption coefficients in the range of 10^5 cm^{-1}, thin layers of up to 200 nm are sufficient to absorb the incoming light. The thin layer, in combination with the soft and flexible organic molecules, make OSCs flexible devices which are often being referred to as 'plastic solar cells.' This opens plenty of niche markets in which light-weight and flexible solar cells may be used to power consumer electronics, such as wearable electronics to charge smartphones, integration in windows and buildings, on the roof of automobiles, and many more.

The first mentionable efficiency of OSCs with a value of 3 % was reported in 2001 (see Figure 2.9). In the following years, efficiencies increased due to improved control of the donor:acceptor morphologies, molecular synthesis, and an improved understanding of the device physics. Fullerene acceptors were used for a long time with limited success. Maximum record efficiencies of 10 % were achieved within fullerene-based OSCs. In the recent decade, the usage of non-fullerene acceptors has become more and more popular. Using non-fullerene acceptors, the performance has improved tremendously since 2015 and reached a certified record efficiency of 17.6 % in single-junction solar cells [83].

The following sections introduce organic semiconductors and the working principles of OSCs. Several aspects regarding charge and exciton transport are studied within this thesis. Challenges and the recent progress are also summarized.

2.3 Electronic Structure of Organic Semiconductors

Organic solar cells are based on semiconducting organic molecules and polymers. Understanding the electronic and optical properties of organic semiconductors is vital for developing efficient optoelectronic devices based on these flexible materials. In the following, the electronic structure of organic semiconductors is outlined briefly. Excellent book references which give a more detailed description can be found in [9, 61, 84].

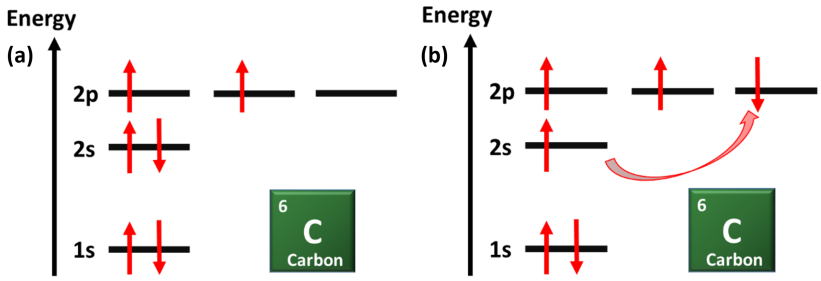

Figure 2.10 Electronic structure of atomic carbon.

Atomic carbon has six electrons, of which two occupy the 1s orbital, two are in the 2s orbital, and the remaining two electrons occupy two of the $2p_x$, $2p_y$, and $2p_z$-orbitals. In a short form, we can write the arrangement as $1s^2 2s^2 2p_x^1 2p_y^1$. The electron configuration is visualized in Fig. 2.10a. The outer shell ($n = 2$), which is made up of the 2s and the 2p orbitals, contains four electrons, i.e. carbon has four valence electrons. As the 1s and 2s orbitals are fully occupied, only the electrons in the 2p orbitals can form covalent bonds, i.e. bonds between different carbon atoms. In this scenario, carbon can form two covalent bonds with surrounding atoms. If one electron from the 2s orbital is excited to the $2p_z$ orbital (see Fig. 2.10b), then carbon could form four covalent bonds. However, the energy needed for making four covalent bonds exceeds the energy which is required for promoting the electron into the higher-lying orbital.

In the presence of other atoms such as hydrogen or additional carbon, the external forces, induced by the presence of the other atoms in proximity to the carbon atom, can compensate the energy difference between the 2s and 2p orbitals. This leads to *hybridization* of orbitals by mixing the 2s orbitals with at least one 2p orbital. Exemplary, the sp- and sp^2 hybridization are visualized in Fig. 2.11(a) and (b), respectively. If the 2s orbital mixes with only one 2p orbital, two sp-hybrid orbitals with angle 180° between each other form. The remaining two orbitals, e.g. $2p_y$ and $2p_z$ remain unchanged. Mixing of the 2s orbital with two 2p orbitals leads to three sp^2 hybrid orbitals which are planar orbitals within the xy-plane with the remaining $2p_z$ orbital being orthogonal to that plane. Finally, the 2s orbital can hybridize with all 2p orbital forming four sp^3 orbitals.

Especially sp^2 orbitals are of importance for the electronic structure of semiconducting organic molecules and polymers. Figure 2.12 visualizes the most important bonds which form if sp^2 hybridized molecules approach: σ- and π-bonds. The sp^2 orbitals form σ-bonds by splitting the orbitals into a bonding and an anti-bonding state. The σ-bonds are within the xy-plane, which leads to very planar molecules. Besides, unhybridized $2p_z$-orbitals, which are perpendicular to the xy-plane, interact, and form a weaker π-bond being above and below the plane of the σ-bond, see Fig. 2.12. σ-bonds have strong binding energies and localize the electrons strongly. The orbitals forming the σ-bond are considered localized and irrelevant for the electronic transport in organic semiconductors. On the contrary, π-orbitals are less localized and usually extend across the atoms that contribute to the π-bond. The combination of σ- and π-bonds between two atoms forms a double bond, while a simple σ-bond is a single bond. In the presence of consecutively alternating single and double bonds, as shown for polyacetylene and benzene in Figure 2.12, π-orbitals may delocalize across the whole molecule, while σ-bonds give rise to the shape of the molecule. This alternation of double- and single-bonds is known as conjugation.

The overlap of the p_z-orbitals and the sp^2 hybridized orbitals in polymers or aromatic rings leads to a change in the orbital energies. The change in the molecular orbital energies concerning the atomic orbital energies may be explained using the linear combination of atomic orbitals (LCAO).

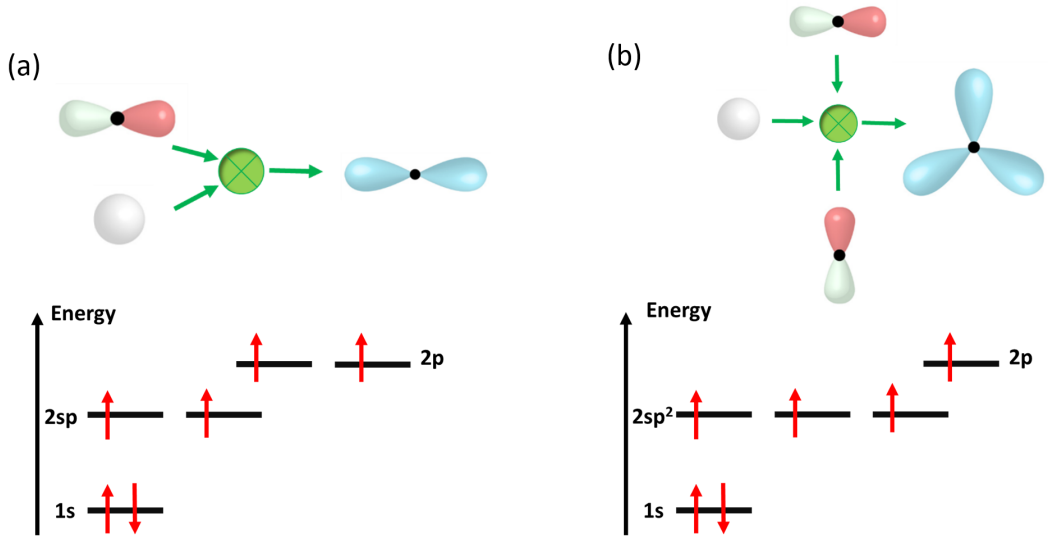

Figure 2.11 Schematic visualization of the mixing of 2s and 2p orbitals in the (a) sp-hybridization and (b) sp^2-hybridization.

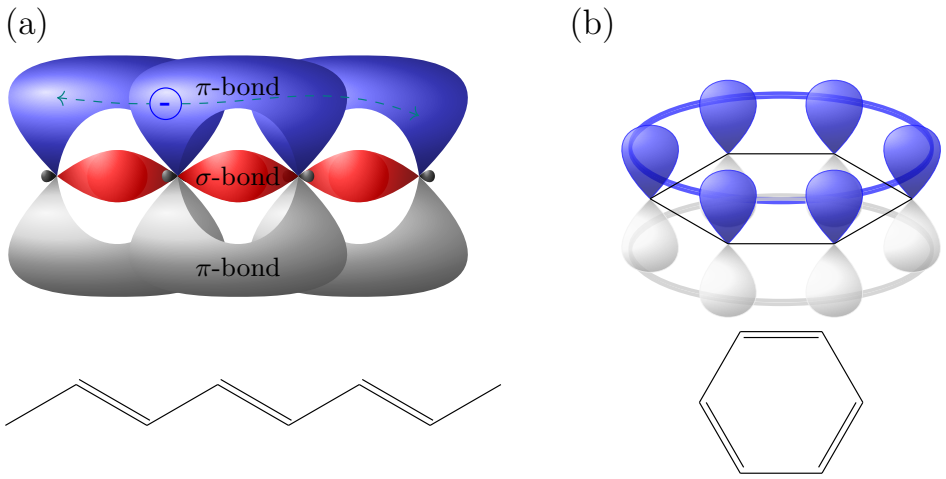

Figure 2.12 (a) Visualization of σ- and π-bonds along the chain segment of polyacetylene. (b) Formation of delocalized π-bonds in a benzene ring. The chemical structure is shown below each schematic.

As an example, the effect is briefly explained for the two 1s orbitals. Let us assume the combination of two 1s orbitals, given by ϕ_a and ϕ_b. The resulting molecular orbital can be expressed as a linear combination of the atomic orbitals, i.e. $\psi_+ = c_1\phi_a + c_2\phi_b$. However, also the combination $\psi_- = c_1\phi_a - c_2\phi_b$ is possible. The latter combination can be regarded as a destructive interference between the atomic orbitals, which leads to a reduced charge density between the nuclei. ψ_- is being referred to as anti-bonding, while ψ_+ represents a bonding orbital. The effect of bonding and anti-bonding on the energy levels is visualized in Fig. 2.13. Here, two sp^2 hybridized carbon atoms form a molecule, e.g. ethene. In general, each orbital of atom A interacts with each orbital of atom B. However, in the first approximation, the interaction between orbitals of similar energies is strongest, e.g., 1s orbital of atom A with 1s orbital of atom B. The 1s and $2sp^2$ orbitals form σ and σ^* orbitals. As 1s orbitals are close to the core of the carbon atoms, only a weak overlap is expected explaining

the small splitting between the σ and σ^* orbitals. The σ and σ^* orbitals arising from the $2sp^2$ atomic orbitals interact more strongly, leading to a large energy splitting. The splitting between π and π^* orbitals is weaker as the interaction of π-orbitals overlap further away from the internuclear axis. In this scenario, the highest occupied molecular orbital (HOMO) is defined by the π-orbital and the lowest unoccupied molecular orbital (LUMO) by the π^*-orbital.

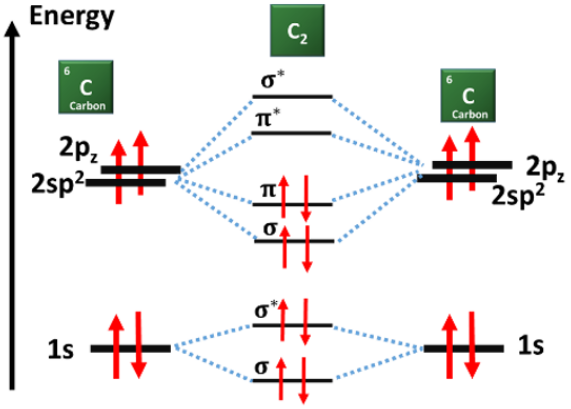

Figure 2.13 Simple energy level representation of anti-bonding σ^*/π^* and bonding orbitals σ/π from atomic orbitals for a molecule based on two sp^2-hybridized carbon atoms [84].

With respect to inorganic semiconductors, the HOMO energy is the equivalent of the valence band maximum, and the LUMO energy is equivalent to the conduction band minimum. The difference between these energies is what we call the 'bandgap,' or more accurately, the HOMO–LUMO gap. Molecules can absorb photons with energies that match the HOMO–LUMO gap. Electrons are then excited to the π^* bond, where they can move across the molecule freely. Figure 2.14 visualizes the HOMO and LUMO wavefunctions for benzene as a simple example. Benzene (Fig. 2.14) is a molecule composed of six carbon atoms arranged in a planar ring. The 120° degree angle between the carbon atoms is typical for sp^2 hybridization. The alternating double and single bonds highlight the conjugation within benzene. The HOMO and LUMO wavefunctions were calculated using density functional theory, which energies of $E_{\mathrm{HOMO}} = -6.27\,\mathrm{eV}$ and $E_{\mathrm{LUMO}} = -1.14\,\mathrm{eV}$.

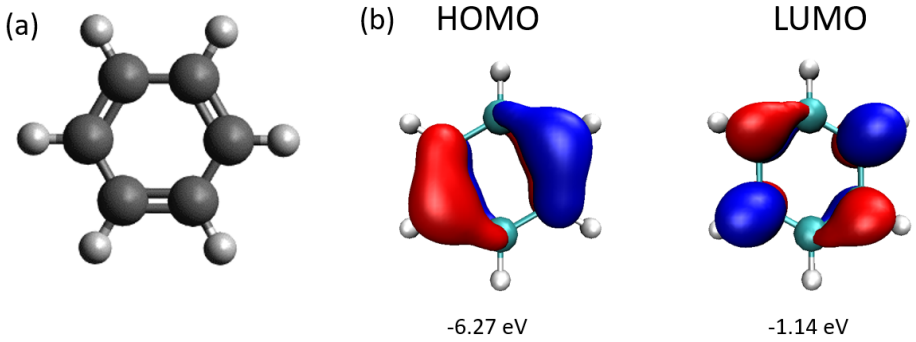

Figure 2.14 Visualization of the highest occupied molecular orbital (HOMO) and the lower unoccupied molecular orbital (LUMO) of benzene obtained from density functional theory (DFT). The visualization has been done in Visual Molecular Dynamics (VMD).

Thin films made of organic semiconductors by low-temperature processing techniques usually are strongly amorphous and lack a long-range order in the molecular arrangement. Covalent bonds within the conjugated polymer chains or aromatic rings form the main structure of the organic molecules. In the presence of other organic molecules, intermolecular interactions are present and may distort the shape of the molecule. The most relevant forces are due to van der Waals-interactions, dipole-dipole interactions, and hydrogen bonds. Often, side-chains are attached to the backbone of the conjugated segments to enhance the solubility of the molecules. All these factors induce kinks and twists of the molecule along its backbone. As organic films lack a periodic arrangement, intermolecular distances vary both dynamically and statically. As known from Anderson [17], the absence of periodic potentials within materials induces charge localization. The energetic structure of the ensemble of organic molecules can be well described by a Gaussian density of states (DOS) [85]. As discussed in the upcoming section, this determines the transport mechanisms of charge carriers and excited states in solution-processed organic semiconductors, with significant differences to traditional inorganic semiconductors.

2.4 Charge Transport in Organic Semiconductors

Computational predictions of charge transport properties in organic semiconductors are of crucial importance for understanding the electronic properties of OSCs. The nature of charge carriers and their transport mechanism within organic semiconductors is still under investigation. Currently, one distinguishes between three different transport regimes: (1) hopping regime, (2) band transport regime, and (3) an intermediate regime – the transient localization. The applicability of the different regimes can vary between the different molecules and with the processing techniques. Within amorphous semiconductors, charges localize on molecules or conjugated segments due to the structural disorder. Thus, charge transport occurs by hopping between localized conjugated segments. In contrast, crystalline organic semiconductors – such as required for high mobility transistors [86, 87] – show band-like transport. Charges are more delocalized and show properties comparable to standard inorganic semiconductor materials. This controversy is depicted in Fig. 2.15.

In the following, a concise outline of the different transport regimes is presented. The focus is set on hopping transport models as they provide the most accurate description of charge transport within amorphous organic semiconductors. A review of the different transport regimes with a focus on the computational access of the characteristic parameters is given by Oberhofer *et al.* [18].

2.4.1 Hopping Regime

Charge carriers within amorphous semiconductors are of localized nature due to the static disorder in the molecular arrangement. Also, in less disordered structure, theories predict the localization of charge carriers due to their interaction with the surrounding medium [18]. The charge causes a distortion of the molecular site and the surrounding medium, i.e., other molecules and solvents, which leads to a stabilization of localized charges and the distortion in the form of small polarons [88, 89]. Moreover, localization can be induced by nonlocal electron-phonon coupling, which is due to thermal fluctuations of the coupling between sites [90, 91].

Nobel price winner Rudolph A. Marcus has developed a seminal theory for electron transfer reactions in chemical systems during the 1950s [92]. The key problem in electron transfer within molecules is the interaction of the charge with its environment. As charges are transferred, the environment has to change in order to assist the charge transfer. The theory of the charge transfer mechanism was

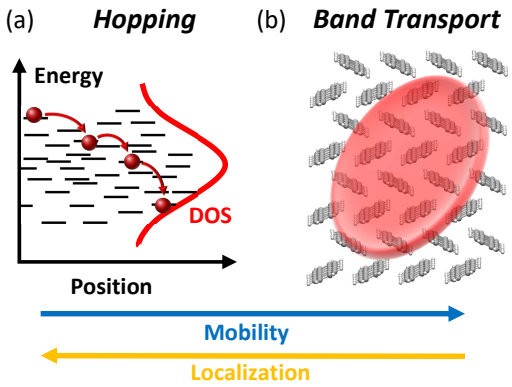

Figure 2.15 (a) Thermally-activated hopping of charge carriers between localized quantum states. (b) Band like transport of delocalized charge carriers in crystalline organic semiconductors.

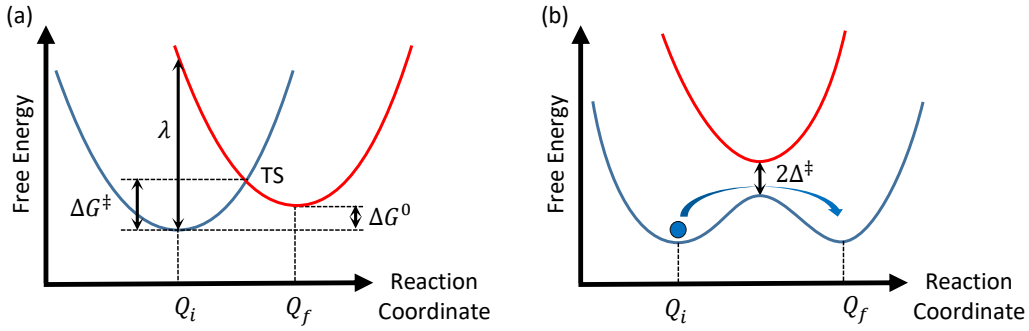

Figure 2.16 (a) Representation of the Marcus theory in the diabatic picture. (b) Lowering of the transition state barrier due to an electronic coupling $\Delta^{\ddagger}$ between the initial and final configuration (adiabatic picture).

formulated within the *Marcus theory*. The rationale of the Marcus theory is summarized following the review article by Oberhofer *et al.* [18].

Let us consider a dimer of two isoenergetic molecules A and B, an electron donor and an electron acceptor, respectively, between which charge transfer shall occur. The Marcus theory can be visualized using the two-state polaronic charge transfer model shown in Fig. 2.16a [92]. The initial configuration, i.e. a charge being on molecule A, is defined by a generalized configuration coordinate Q_i, which summarizes the initial dimer configuration and its surrounding. The final configuration is described by a generalized configuration coordinate Q_f, representing the polaronic state of the system after the charge transfer has occured. These generalized coordinates capture degrees of freedom of vibrational coordinates, i.e. internal phonon modes and the solvent molecules, i.e. external phonon modes. During the transition, distortions in bond lengths or angles can occur, which is implicitly accounted for in the chosen representation. In the harmonic approximation, changes in the nuclear degrees of freedoms lead to a parabolic variation of the free energy. The crossing point of the parabolas of the initial and the final state represents the transition state. The reorganization energy λ gives the free energy required to rearrange the initial system to match the final configuration. Energy conservation requires the charge transfer to occur at a transition state (TS) at which the initial and final polaronic states have equal free energy.

The semiclassical electron transfer rate can be obtained, starting from the transition state theory [93, 94], as

$$a_{if,\mathrm{TST}} = \nu_{\mathrm{eff}} \kappa_{\mathrm{el}} \Gamma_n \exp\left(-\frac{(\Delta G^{\ddagger} - \Delta^{\ddagger})}{k_{\mathrm{B}} T}\right), \tag{2.15}$$

with the activation energy given by $\Delta G^{\dagger} = \Delta G^{\ddagger} - \Delta^{\ddagger}$, the adiabatic correction factor $\Delta^{\ddagger}$ accounting for a finite coupling between the initial and final state, the vibrational frequency ν_{eff} along the reaction coordinate, the electronic transmission coefficient κ_{el}, and the correction Γ_n accounting for tunneling contributions, k_{B} is the Boltzmann constant, and T is the temperature. At temperatures of interest in electronic devices, typically $\Gamma_n = 1$. Within the semiclassical Landau-Zener (LZ) theory [95–97], the free energies determining the activation barrier are [98]

$$\Delta G^{\ddagger} = \frac{\left(\lambda + \Delta G^{0}\right)^{2}}{4\lambda}, \tag{2.16}$$

$$\Delta^{\ddagger} = \left\langle H_{ab}^{2} \right\rangle_{\mathrm{TS}}^{1/2} - \frac{1}{\lambda} \left\langle H_{ab}^{2} \right\rangle_{\mathrm{a}}. \tag{2.17}$$

The latter equation captures the difference between diadiabatic and adiabatic free energy surfaces (see Fig.2.16a and b, respectively). ΔG^{0} is the contribution of a free energy shift of the initial and final configuration, i.e. due to an applied electric field. $H_{ab} = \left\langle \Psi_a | \hat{H} | \Psi_b \right\rangle$ is the electronic coupling between the initial and the final diabatic configuration at the TS. The electronic transmission coefficient can be expressed in terms of the LZ theory as

$$\kappa_{\mathrm{el}} = \begin{cases} 2\left[\exp(-2\pi\gamma) - 1\right]\exp(2\pi\gamma) & \text{if } \Delta G^{\dagger} \geq -\lambda \\ 2\left[1 - \exp(-2\pi\gamma)\right]\exp(-2\pi\gamma) & \text{else} \end{cases}, \tag{2.18}$$

with

$$2\pi\gamma = \frac{\pi^{3/2} \left\langle H_{ab}^{2} \right\rangle_{\mathrm{TS}}}{h\nu_{\mathrm{eff}} \sqrt{\lambda k_{\mathrm{B}} T}}. \tag{2.19}$$

In the *adiabatic limit*, strong coupling and small reorganization energies exist between the initial and the final state [99, 100]. If the coupling is in the order of the reorganization energy, the electronic transmission coefficient κ_{el} approaches unity as $2\pi\gamma \gg 1$. Thus, we obtain a standard Arrhenius-like expression [98, 99]:

$$a_{if,\mathrm{adiab}} = \nu_{\mathrm{eff}} \exp\left(-\frac{(\Delta G^{\ddagger} - \Delta^{\ddagger})}{k_{\mathrm{B}} T}\right). \tag{2.20}$$

The prefactor consists only of the effective vibrational frequencies of the reaction coordinates.

In the *nonadiabatic limit*, the initial and final state are only weakly coupled with coupling energies much smaller than the reorganization energy $\lambda \gg H_{ab}$. Consequently, $2\pi\gamma \ll 1$ and with $\Delta^{\ddagger} << \Delta G^{\ddagger}$ we obtain [99]

$$a_{if,\mathrm{nonadiab}} = \frac{2\pi}{\hbar} \frac{\left\langle H_{ab}^{2} \right\rangle_{\mathrm{TS}}}{4\pi\lambda k_{\mathrm{B}} T} \exp\left(-\frac{\Delta G^{\ddagger}}{k_{\mathrm{B}} T}\right). \tag{2.21}$$

This is the well-known form of the Marcus rate equation. The rate is independent of the effective frequency ν_{eff} and only depends on λ, H_{ab}, and ΔG^{0}.

It is important to highlight the limitations of this polaronic model in organic semiconductors. As shown in Fig. 2.16b, a high coupling $\Delta^{\ddagger}$ reduces the activation barrier. At high coupling values, the barrier can even vanish. In case of a vanishing barrier, we cannot treat the initial and final configuration as localized states. If $\Delta G^{0} = 0$ and $\left\langle H_{ab}^{2} \right\rangle_{\mathrm{TS}} = \left\langle H_{ab}^{2} \right\rangle_{\mathrm{a}} = \left\langle H_{ab}^{2} \right\rangle$, the barrier height is given by

$$\Delta G^{\dagger} = \frac{\left\langle H_{ab}^{2} \right\rangle}{\lambda} - \left\langle H_{ab}^{2} \right\rangle^{1/2} + \frac{\lambda}{4}. \tag{2.22}$$

If $\left\langle H_{ab}^2 \right\rangle^{1/2} = \lambda/2$, the barrier vanishes and we obtain a single delocalized state across the two molecules A and B. In case of PCBM dimers ($\lambda = 140\,\text{meV}$), this happens at coupling energies of 70 meV. As shown by Gajdos *et al.*, H_{ab} in crystalline PCBM can reach values of up to 130 meV [100]. Thus, using the Marcus theorem is not applicable and accurate charge transport predictions require the usage of different transport models. In the case of amorphous organic semiconductors, coupling integrals are typically below 10 meV with $\lambda \geq 100\,\text{meV}$ and consequently Marcus theory is expected to provide accurate results for the transition rates in solution-processed optoelectronic devices.

2.4.2 Band-Transport Regime

In contrast to the hopping regime, charge carriers are assumed as delocalized within periodic crystal potentials [18, 61]. Most literature on band transport was written for inorganic semiconductors, while the literature on the transport of charge carriers in band structures of crystalline organic semiconductors is rather limited [101, 102].

The fundamental concept of band theories is Bloch's theorem. It states that electron orbitals within periodic potentials are described as a superposition of plane waves modulated by a function which accounts for the periodicity of the periodic potential:

$$\Psi_{\mathbf{k}}(\mathbf{r}) = u_{\mathbf{k}}(\mathbf{r}) \exp\left(\mathrm{i}\mathbf{k} \cdot \mathbf{r}\right) , \tag{2.23}$$

with $u_{\mathbf{k}}(\mathbf{r}) = u_{\mathbf{k}}(\mathbf{r} + \mathbf{R})$, with $\mathbf{R}$ defined by the periodicity of the crystal potential $V(\mathbf{r}) = V(\mathbf{r} + \mathbf{R})$.

The electron is described by its wavevector $\mathbf{k}$ and the band index n which it occupies. Within a semi-classical description, one can define the electron velocity by the group velocity of the wavepacket composed of Bloch functions:

$$\mathbf{v}_{\mathrm{g}} = \frac{1}{\hbar} \nabla_{\mathbf{k}} E_n(\mathbf{k}) \Big|_{\mathbf{k}=\mathbf{k}_0} . \tag{2.24}$$

The change in velocity of a charge q in the band structure of a crystal is well-defined by a Newtonian equation of motion

$$F = qE = \left(\frac{1}{m_n^*} \right)_{ij}^{-1} \frac{\mathrm{d}v_{g,j}}{\mathrm{d}t} , \tag{2.25}$$

with the effective mass describing the curvature of the band dispersion

$$\left(\frac{1}{m_n^*} \right)_{ij} = \frac{1}{\hbar^2} \left(\frac{\partial^2 E_n(\mathbf{k})}{\partial k_i \partial k_j} \right) . \tag{2.26}$$

The usage of the effective mass allows to use the classical equations of motion for the description of the transport characteristics of charge carriers within crystal potentials. Note that this approximation only holds near the conduction band minimum for electrons and valence band maximum for holes, as the band structure can be well approximated by a parabolic dispersion relation.

In realistic systems, scattering of charge carriers with phonons, impurities, and defects can occur. A frequently used methodology to describe the transport properties of an ensemble of charge carriers f under an applied electric field in presence of scattering mechanisms is the Boltzmann transport equation (BTE):

$$\frac{\partial f}{\partial t} = \left(\frac{\partial f}{\partial t} \right)_{\text{drift}} + \left(\frac{\partial f}{\partial t} \right)_{\text{diffusion}} \left(\frac{\partial f}{\partial t} \right)_{\text{scattering}} . \tag{2.27}$$

In first order approximation, the BTE can be expressed as [61]

$$\frac{\partial f(\mathbf{r}, \mathbf{k}, t)}{\partial t} = -\mathbf{v} \cdot \nabla_{\mathbf{r}} f - \frac{e}{\hbar} \left(\mathbf{E} + \mathbf{v} \times \mathbf{B} \right) \cdot \nabla_{\mathbf{k}} f + \left(\frac{\partial f}{\partial t} \right)_{\text{scattering}} . \tag{2.28}$$

Solutions of the BTE can be obtained using the relaxation-time approximation (RTA). In the RTA, all scattering processes are modeled as a relaxation with time τ:

$$\left(\frac{\partial f}{\partial t}\right)_{\text{scattering}} = -\frac{f(\mathbf{k}) - f(\mathbf{k}_0)}{\tau(\mathbf{k})} \,. \tag{2.29}$$

BTE in combination with RTA is a differential equation which can be solved if the band structure and the relaxation times of the scattering processes are known. Otherwise, Monte Carlo techniques may be applied to solve the BTE by numerical iteration in time [103].

Just within the past years, band-like transport within organic semiconductors was studied in depth. Chen *et al.* studied the temperature dependence of the charge carrier mobility in oligoacene crystals [104]. Their analysis reveals a mismatch of a simple band model with experimental data for temperatures higher than 150 K. Also, the small polaron band theory provides an inadequate description of the charge-carrier mobility. Li *et al.* showed that the band-like transport breaks down in presence of large thermal disorder at room temperature [105]. Moreover, charge carriers become localized due to electron–phonon coupling. Blülle *et al.* observed band-like temperature dependence of in-plane transport in rubrene crystals in directions perpendicular to the high mobility plane [101]. Again, the importance of dynamic disorder was pointed out.

2.4.3 Transient Localization Regime

Neither hopping nor band-like transport models can capture the charge transport characteristics in crystalline organic semiconductors. The presence of large thermal fluctuations, caused by weak intermolecular van der Waals forces, limit charge transport and can even induce charge localization. In recent years, especially the research groups of Fratini and Troisi have studied a novel transport regime, the *transient localization regime* [22, 106–109]. A relaxation time approximation has been used to describe the transient localization of the electronic wavefunction due to dynamical molecular vibrations [106].

As intermolecular vibrations are slow, Troisi and Orlandi [110] described the transport of charge carriers under localization due to scattering by molecular motion using a Born–Oppenheimer scheme. The equations of motions for electron, described by wavefunction Ψ, and the molecular degrees of freedom $\{u_i\}$ are given by

$$\mathrm{i}\hbar \left|\Psi, t\right\rangle = \hat{H}_{\text{el}}(\{u_i\} \left|\Psi, t\right\rangle \,, \tag{2.30}$$

$$\ddot{u}_i = -\omega_0^2 u_i - \frac{\partial}{\partial u_i} \left\langle t, \Psi \middle| \hat{H}_{\text{el}}(\{u_i\} \middle| \Psi, t \right\rangle \,. \tag{2.31}$$

The Ehrenfest method allows calculating the transport properties by tracking the mean-square displacement [22]

$$\Delta X^2(t) = \left\langle \Psi \right| \left[X(t) - X(0)\right]^2 \left| \Psi \right\rangle \,. \tag{2.32}$$

The time derivative of $\Delta X^2(t)$ provides the diffusivity

$$D(t) = \frac{\mathrm{d}\Delta X^2(t)}{\mathrm{d}t} \,. \tag{2.33}$$

Extracting the long time limit $D = \lim_{t\to\infty} D(t)$ allows to define the Einstein mobility $\mu = eD/(k_{\text{B}}T$ [106].

A simplified scheme based on the RTA allows to capture transport by static and dynamical disorder [22,111]. A key quantity in the RTA is the anticommutator correlation function $C(t) = \{\hat{V}(t), \hat{V}(0)\} = 2\mathrm{d}D(t)/\mathrm{d}t$. The RTA is expressed by

$$C_{\mathrm{RTA}}(t) = C_0(t) \exp\left(-\frac{t}{\tau_{\mathrm{in}}}\right), \tag{2.34}$$

with $C_0(t)$ being the correlation function for a system with static molecular disorder. The decay with timescale τ_{in} describes the destruction of quantum interference as known from Anderson localization. Fratini states that $\tau_{\mathrm{in}} \approx \omega_0^{-1}$, i.e. the timescale of molecular vibrations [106]. The diffusion coefficient can be expressed as

$$D_{\mathrm{RTA}} = \frac{L^2(\tau_{\mathrm{in}})}{\tau_{\mathrm{in}}}, \tag{2.35}$$

with $L^2(\tau_{\mathrm{in}}) = \int \exp\left(-\frac{t}{\tau_{\mathrm{in}}}\right) \Delta X_0^2(t) \tau_{\mathrm{in}}^{-1} \mathrm{d}t$ being the electron spread at $t \approx \tau_{\mathrm{in}}$. $L(\tau_{\mathrm{in}})$ captures the transient localization induced by the dynamical distortion of molecules. Finally, the mobility yields

$$\mu_{\mathrm{RTA}} = \frac{e}{k_{\mathrm{B}}T} \frac{L^2(\tau_{\mathrm{in}})}{2\tau_{\mathrm{in}}}. \tag{2.36}$$

The RTA results predict that the mobility scales with $\mu \propto T^{-2}$ from the factor $1/T$ and the temperature dependence of $L(\tau_{\mathrm{in}})$. The latter property decreases with temperature as charges become more localized with increased dynamic disorder.

To provide an example of the transient localization, Fig. 2.17 is reprinted from [106]. It shows the spread $\Delta X(t)$ of the electron wavefunction over time by the Ehrenfest method, the RTA (both include the dynamical disorder), and only static disorder. The bottom graph depicts the diffusivity $D(t)$ and labels the different regimes on the same timescales. The electron wavefunction spreads until a characteristic scattering time τ, where a diffusive behavior sets in. From ballistic transport, one expects the diffusivity to increase linearly at short timescales $t < \tau$ with saturation for $t \gg \tau$. However, the presence of disorder induces the localization of the wavefunction. After the ballistic regime, the oscillations are damped, and $D(t)$ decreases and vanishes finally in the presence of static disorder [22]. In the presence of a dynamical disorder, the results follow the localized behavior at $t < \tau_{\mathrm{in}}$. Within the RTA, $\Delta X(t)$ increases for $t \geq \omega_0^{-1}$ again. This leads to a non-zero diffusivity even at large timescales (see Fig. 2.17, bottom).

Based on the summarized approach, Fratini has summarized several strategies to improve charge carrier mobilities in crystalline organic semiconductors [106]:

1. Increase the molecular overlaps and, therefore, the charge transfer integral J
2. Reduce the electron–phonon coupling with intermolecular vibrations
3. Increase the intermolecular vibrational frequency ω_0

In a later publication [107], it was shown that the intermolecular transfer integral needs to be identical and equal in sign for each of the crystal directions, regardless of the overall value.

2.4.4 Charge Transport in Disodered Organic Semiconductors

The photoactive layer within solution-processed organic solar cells typically is strongly amorphous and shows a lack of long-range order. The molecular arrangements show strong static disorder due to large variations in distances, torsion, and orientations, consequently inducing localization of charge

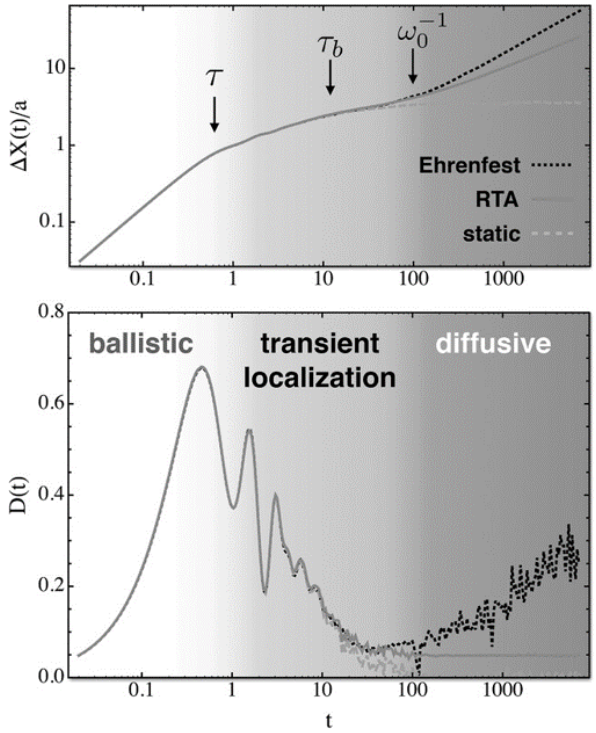

Figure 2.17 Top: Time-dependent spread $\Delta X(t)$ of the electronic wavefunction for the Ehrenfest method (black dotted curve) and the RTA (solid curve). Results for static disorder is shown by dashed lines. Bottom: Instantaneous diffusivity $D(t)$ and respective transport regimes. Reprinted with permission [106], Copyright 2020 John Wiley & Sons.

carriers. As described above, the transport of charge carriers occurs by incoherent hopping between localized quantum states in amorphous organic semiconductors [85, 112].

A seminal contribution to the description of charge transport in amorphous organic materials has been provided by Bässler within the Gaussian disorder model (GDM) [29]. He argues that charge carriers hop between localized quantum states, which are disordered in energy and space. The disorder in molecular orbital energies is captured by a Gaussian density of states (DOS)

$$g(\epsilon) = \frac{N}{\sigma\sqrt{2\pi}} \exp\left(-\frac{(\epsilon - E^0)^2}{2\sigma^2}\right) , \tag{2.37}$$

with the molecular orbital energy E^0, the energetic disorder σ, and the concentration of randomly distributed states N, also known as localization sites [29, 85].

With time, charge carriers tend to relax within the energetic DOS towards lower energy [29]. Figure 2.18 visualizes the localization sites (black lines) and the hopping process of a localized charge carrier (red dots) within a disordered organic semiconductor. The blue Gaussian indicates the DOS of occupied electronic states. Its center is shifted by $-\sigma^2/(k_\mathrm{B}T)$ towards lower energies. In thermal equilibrium, charge carriers are distributed around this level, the so-called transport energy [85, 113]. Charge carriers being at energetic states above the transport energy contribute more towards the charge transport, while charges being at states with lower energies contribute less. This is as charges move by thermally activated hopping between the localized quantum states.

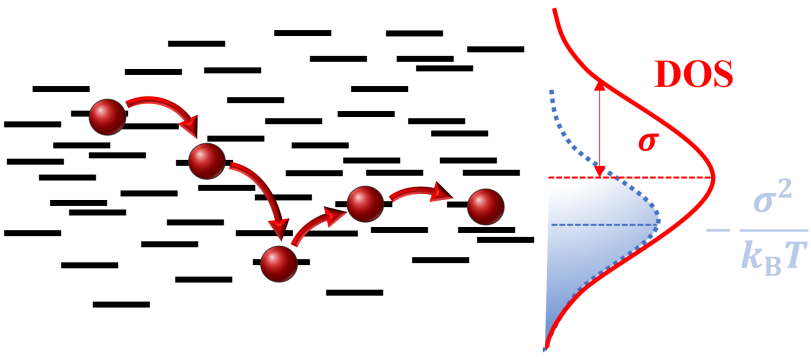

Figure 2.18 Schematic representation of charge carrier hopping in disordered organic semiconductors between localized quantum states. The density of states (DOS) and disorder σ is labeled in red. In blue, the occupied DOS is represented. The center of the occupied DOS in equilibrium is shifted by $-\sigma^2/(k_B T)$ towards lower energies.

2.5 Excitons in Organic Semiconductors

In the following section, the relevant physical fundamentals for the dynamics and interactions of singlet and triplet excitations within conjugated molecules and polymers are summarized. Excitons within organic semiconductors are typically intramolecular Frenkel-type electron-hole pairs [8]. However, also delocalized excitons are observable, especially in the presence of ordered phases [30]. Singlet excitons are excited upon the absorption of a photon, which induces the transition of an electron from the HOMO to the LUMO. Intramolecular excited states may also form from injected charge carriers, especially being critical for light generation of OLEDs, when electrons and holes enter their mutual capture radius and form a CT state. In OSCs, this usually is undesired and may be considered as a possible loss mechanism. Such electrically generated excitons show either singlet or triplet character depending on their spin arrangement.

In the following, the spin states of excitons and their respective energies are summarized. Furthermore, an overview of the excitonic processes such as generation, diffusion, dissociation, and decay is given. To understand the nature of singlet and triplet excitations, the spin properties and dynamics of singlets and triplets are presented based on the following literature [8, 9, 84, 114].

2.5.1 Singlet and Triplet Excitons

Most relevant physical properties of excited states depend on the excitation type, i.e. singlet or triplet excitation. Significant differences in lifetime and diffusion length, energies, but also in population probabilities are observed. Singlet and triplet excitons differ in their spin characteristics.

Both type of excited states are made of an electron in the LUMO and a hole in the HOMO of a molecule or a conjugated segment of a polymer. The main difference between singlets and triplets is in their electron spin, as shown in Fig. 2.19. In simple words, if the electron and the hole of the excited pair exhibit an anti-parallel (parallel) spin, a singlet (triplet) exciton is formed. Thus, the total spin adds up to zero (one) for singlets (triplets) in units of $\hbar$. The remaining orbitals of the molecule are either fully occupied (HOMO-1, HOMO-2, . . .) or fully unoccupied (LUMO+1, LUMO+2, . . .). As each fully occupied orbital contains one spin-up and one spin-down electron, its contribution to the total spin state sums up to zero. In sum, one singlet and three available triplet states exist (see Fig. 2.19).

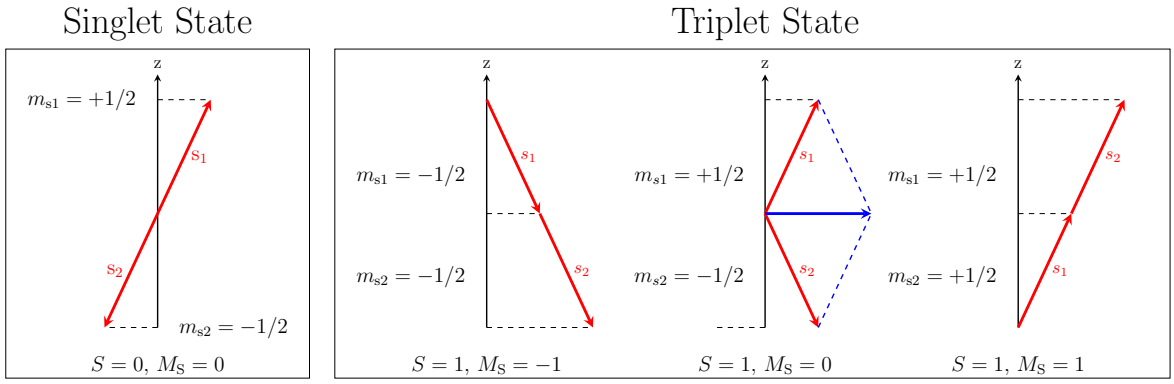

Figure 2.19 Vector diagram of the singlet state with $S = 0$, $M_S = 0$ and the triplet states with $S = 1$, $M_S = \{0, \pm 1\}$. Red arrows visualize the one-electron spin configuration. s_i and m_{si} give the eigenstates of the spin angular momentum and the z-component of the one-electron spins; S and M_S label the eigenstates of the two-particle excitation.

The involved charge carriers in the HOMO and LUMO form a two-particle system. Both the electron and the hole, labeled by index $i \in \{1, 2\}$, are characterized by their spin angular momentum with eigenvalues s_i and $m_{s,i}$. In a two-particle system, four eigenstates for the spin angular momentum operators $\hat{S}$ and its z-component $\hat{S}_z$ exist. The states of the single electron spin are given by σ^+ and σ^- with eigenvalues $s = 1/2$ with $m_s \in \{-1/2, 1/2\}$ of the spin operators $\hat{S}^2$ and $\hat{S}_z$, respectively.

Let α and β denote the spin wavefunctions of one-electron states with eigenvalues $s = 1/2, m_s = 1/2$ and $s = 1/2, m_s = -1/2$, respectively. Then, the spin wavefunctions of the two particle excitation are given by [9]

$$\Psi_{\text{spin,T+}} = \alpha_1\alpha_2 \qquad \text{yielding } S = 1, M_S = 1 \tag{2.38}$$

$$\Psi_{\text{spin,T0}} = \frac{1}{\sqrt{2}}\left[\alpha_1\beta_2 + \beta_1\alpha_2\right] \qquad \text{yielding } S = 1, M_S = 0 \tag{2.39}$$

$$\Psi_{\text{spin,T-}} = \beta_1\beta_2 \qquad \text{yielding } S = 1, M_S = -1 \tag{2.40}$$

$$\Psi_{\text{spin,S}} = \frac{1}{\sqrt{2}}\left[\alpha_1\beta_2 - \beta_1\alpha_2\right] \qquad \text{yielding } S = 0, M_S = 0 \tag{2.41}$$

The first three spin wavefunctions states are triplet states. They have spin angular momentum eigenvalue of $S = 1$ and only differ in the z-component of the spin, which takes $M_S \in \{-1, 0, 1\}$. The latter spin wavefunction represents the singlet excitation. It has $S = 0$ and only one possible arrangement with $M_S = 0$. The different configurations are visualized in Fig. 2.19. Note that the spins for triplet states are always in phase, whereas the singlet spins are 180° out of phase. It is well known that the total wavefunction of each fermionic system must be anti-symmetric with respect to the electron permutation following the Pauli exclusion principle. The spin wavefunctions for singlets (triplets) are anti-symmetric (symmetric). Consequently, the spatial wavefunction must be symmetric (anti-symmetric).

2.5.2 Energy Levels of Excitons

Significant Coulomb binding energies and exchange interaction energies are observed for excited states due to the low permittivity in organic semiconductors ($\epsilon_r \approx 3 - 4$). A schematic representation of the singlet S_1 and triplet state (T_1) energy is illustrated in Fig. 2.20. The energy difference between the

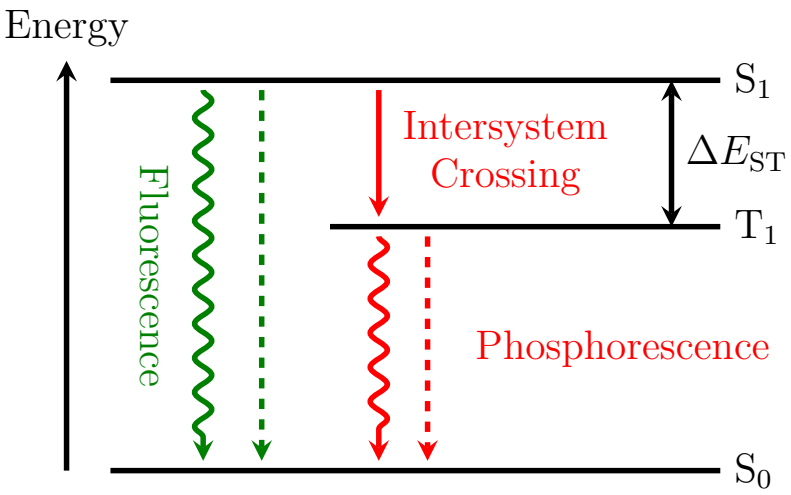

Figure 2.20 Jablonski diagram of the energy alignment of the singlet state S_1 and triplet state T_1. S_0 labels the ground state, and ΔE_{ST} gives the exchange energy. Radiative and non-radiative decay by fluorescence and phosphorescence is indicated. Singlet states can be converted to triplet states by intersystem crossing.

first singlet and triplet state is given by the exchange energy ΔE_{ST}. The exchange interaction scales exponentially with the wavefunction overlap [84]. If wavefunctions of the electron in the LUMO and the hole in the HOMO overlap, exchange energies of 0.7 eV to 1.0 eV can be observed. If the overlap occurs on different parts of the molecule, lower exchange energies of 0.2 eV to 0.5 eV are expected [9]. The exchange interaction lowers the triplet energy and increases the singlet energy [8, 115]. In π-conjugated polymers, such as P3HT, the mean electron-hole distance is measured to be less than 1 nm for singlet excitons and about 30 % less for triplet excitons [116, 117]. Exciton energy splitting in organic semiconductors is reported to be in the range of 0.6 eV to 1.0 eV [117–120]. Many triplet states T_n with higher energies than T_1 are not accessible through excitation from T_1. The wavefunction of these triplet states shows wrong symmetry for the optical excitation from T_1 and S_0. Thus, the population of the higher-lying triplet states can only occur by intersystem crossing. The population of T_4 triplet states via ISC from S_1 singlet states, e.g., was reported for bithiophene and terthiophene molecules [121].

Experimental results found a saturation of the exchange energy for increasing conjugation lengths up to 6 repeat units [117, 119, 122]. Exchange energies of 0.6 eV for polythiophene structures, to which P3HT belongs, were reported [119]. Köhler *et al.* presented exchange energies of 0.7 eV by measuring the energies of singlet S_1 and triplet T_1 for a series of organic and Pt-containing phenylene ethylenes [118]. Reducing chain length and the flexibility of the backbone result in an increased wavefunction overlap between the electron and the hole. An empirical relation for the singlet/triplet exciton energies show an inverse proportionality to the number of repeat units N within a polymer chain [8, 119]:

$$E_{s/t}(N) = E_{s/t}^{\infty} + \text{const} \cdot \frac{1}{N}, \tag{2.42}$$

with the singlet/triplet exciton energy for infinite chain length $E_{s/t}^{\infty}$. Distortion (torsion angles > 40°) in connection with short oligomer lengths (< 25 Å) also reduce the electron-hole distance and imply large exchange energies [117].

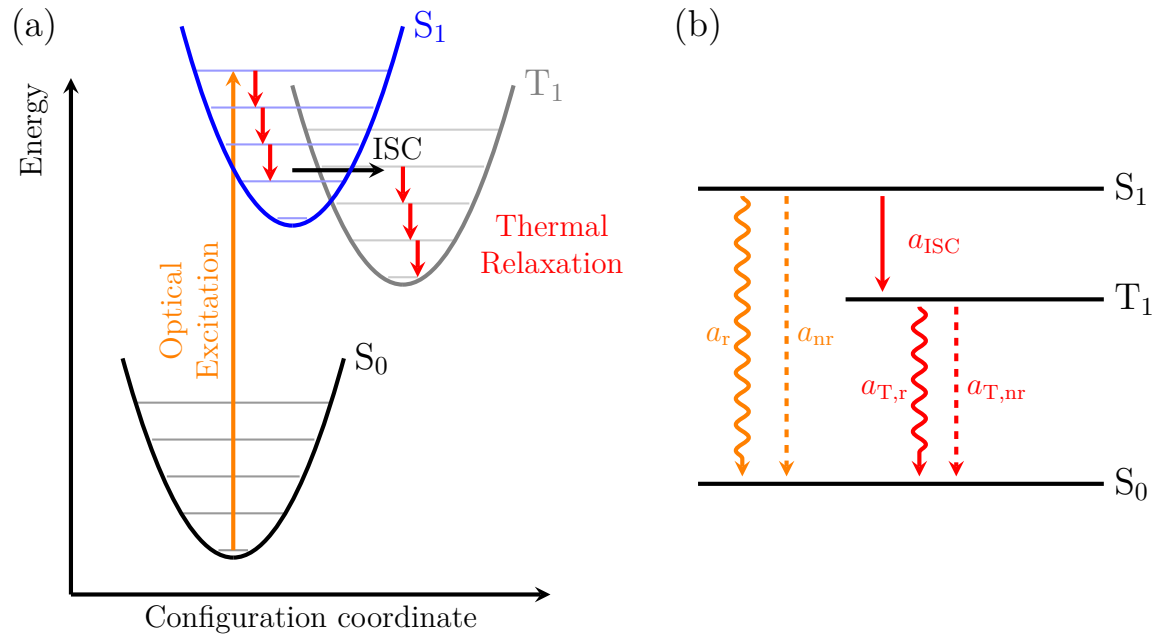

Figure 2.21 (a) Potential energy surface showing excitation from S_0 to S_1 followed by thermal relaxation and intersystem crossing to the T_1 and further thermal relaxation; (b) Energy level diagram illustrating S_1 and T_1 state and corresponding exciton rates for generation and recombination.

2.5.3 Exciton Generation

Excitons can be generated optically, i.e., by absorption of a photon or electrically due to the recombination of injected charge carriers. Also, triplet states may be populated by intersystem crossing from the singlet states in the presence of heavy element compounds. All the mentioned mechanisms will be briefly outlined in the following section.

Optical Generation

Optical excitation upon absorption of a photon leads to the formation of a singlet state as the spin of the excited electron is preserved. Energetically higher singlet states can be excited by absorption of a photon ($S_0 \rightarrow S_n$), or by absorption of two photons ($S_0 \rightarrow S_m \rightarrow S_n$). Usually, relaxation to the energetically lower singlet states is fast, and thus most models neglect energetically higher singlet states. The spin-selection rules prohibit the optical generation of triplet excitons; thus, the optical generation cannot lead to a population of triplet excitons.

Intersystem Crossing

Triplet states can be populated by *intersystem crossing* from an optically generated singlet state, as illustrated in Figure 2.21a. The intersystem crossing rate can be derived from *Fermi's golden rule* [9, 123]. It is given by

$$a_{ISC} = \frac{2\pi}{\hbar} \left\langle {}^1\psi^0 \middle| \hat{H}_{SO} \middle| {}^3\psi^0 \right\rangle [\text{FCWD}] \,. \tag{2.43}$$

Here, ${}^1\psi^0$ and ${}^3\psi^0$ denote the unperturbed singlet and triplet wavefunctions, respectively. [FCWD] is the Franck-Condon weighted density of states, i.e. the density of vibrational states in the triplet state

multiplied by the Franck-Condon vibrational overlap. In the high-temperature limit, it can be written as

$$[\mathrm{FCWD}] = \frac{1}{\sqrt{4\pi\lambda k_\mathrm{B}T}} \exp\left(-\frac{(\Delta E + \lambda)^2}{4\lambda k_\mathrm{B}T}\right), \tag{2.44}$$

where λ is the reorganization energy and ΔE is the energy difference between the initial and final states. For ISC, the reorganization energy λ gives in first approximation the change in energy between the first singlet and triplet states by switching from the singlet equilibrium to the triplet equilibrium geometry. The spin-orbit Hamiltonian $\hat{H}_\mathrm{SO}$ is given by [123]:

$$\hat{H}_\mathrm{SO} = \alpha_\mathrm{fs}^2 \sum_{\mu}^{N} \sum_{i}^{n} \frac{Z_\mu}{r_{i\mu}^3} \hat{\mathbf{L}}_i \hat{\mathbf{S}}_i \,, \tag{2.45}$$

where α_fs denotes the fine structure constant, Z_μ is the effective nuclear charge for nucleus μ, $\hat{\mathbf{L}}_i$ and $\hat{\mathbf{S}}_i$ are the orbital and spin angular momentum operators of electron i, respectively. In summary, the given Hamiltonian represents the coupling spin and orbital momentum of electron i under the influence of the nuclear field of nucleus μ [123]. As indicated in Eq. (2.43), high ISC rates are achieved in the presence of large spin-orbit coupling and considerable overlap between the singlet and triplet states wavefunctions. In Eq. (2.44), an exponential dependence on the difference in singlet and triplet energies is given. Thus, an ISC from singlet state S_1 to higher-lying vibrational modes of the triplet state with subsequent thermal relaxation to T_1 can be more efficient than direct ISC from $\mathrm{S}_1 \rightarrow \mathrm{T}_1$ [8].

In the presence of strong spin-orbit coupling, one needs to consider the conservation of the total angular momentum $\mathbf{J} = \mathbf{L} + \mathbf{S}$, being the sum of orbital angular momentum $\mathbf{L}$ and spin angular momentum $\mathbf{S}$. In the framework of perturbation theory, the first unperturbed triplet state T_1 can be mixed with one or more singlet states due to strong spin-orbit coupling. The wavefunction of the resulting perturbed triplet state T_1' is expressed as

$$\left|{}^3\psi_1'\right\rangle = \left|{}^3\psi_1^0\right\rangle + \sum_k \frac{\left\langle {}^1\psi_k^0 \middle| \hat{H}_\mathrm{SO} \middle| {}^3\psi_1^0 \right\rangle}{E(\mathrm{T}_1) - E(\mathrm{S}_k)} \left|{}^1\psi_k^0\right\rangle, \tag{2.46}$$

with $\left|{}^3\psi_1^0\right\rangle$ and $\left|{}^1\psi_k^0\right\rangle$ representing the wavefunctions of the unperturbed first triplet state and the unperturbed kth singlet state, respectively. The perturbed singlet ground state S_0' and its wavefunction $\left|{}^1\psi_0'\right\rangle$ can be expressed as:

$$\left|{}^1\psi_0'\right\rangle = \left|{}^1\psi_0^0\right\rangle + \sum_k \frac{\left\langle {}^3\psi_k^0 \middle| \hat{H}_\mathrm{SO} \middle| {}^1\psi_0^0 \right\rangle}{E(\mathrm{S}_0) - E(\mathrm{T}_k)} \left|{}^3\psi_k^0\right\rangle. \tag{2.47}$$

Due to the large energy gap between the singlet ground state S_0 and triplet states, the perturbation in the singlet ground state is negligible. The perturbation allows phosphorescence mainly by two mechanisms: (i) transition between S_0 and the singlets mixed into the triplet states; (ii) transition between the triplet excited state and the mixture of triplets into the ground state [8, 9]. The latter is less relevant as the mixing of triplet states into the ground state is small. For hydrogen-like atoms, the spin-orbit coupling Hamiltonian scales with $\hat{H}_\mathrm{SO} \propto Z^4/(n^3(l+1)(l+0.5)l)$, with quantum numbers n and l, and the atomic charge Z. Thus, strong spin-orbit coupling is obtained in the presence of heavy atoms in the molecular structure such as organometallic complexes used in OLEDs (*internal heavy atom effect*) which may also be embedded within OSCs to impose ISC [8, 115, 124, 125].

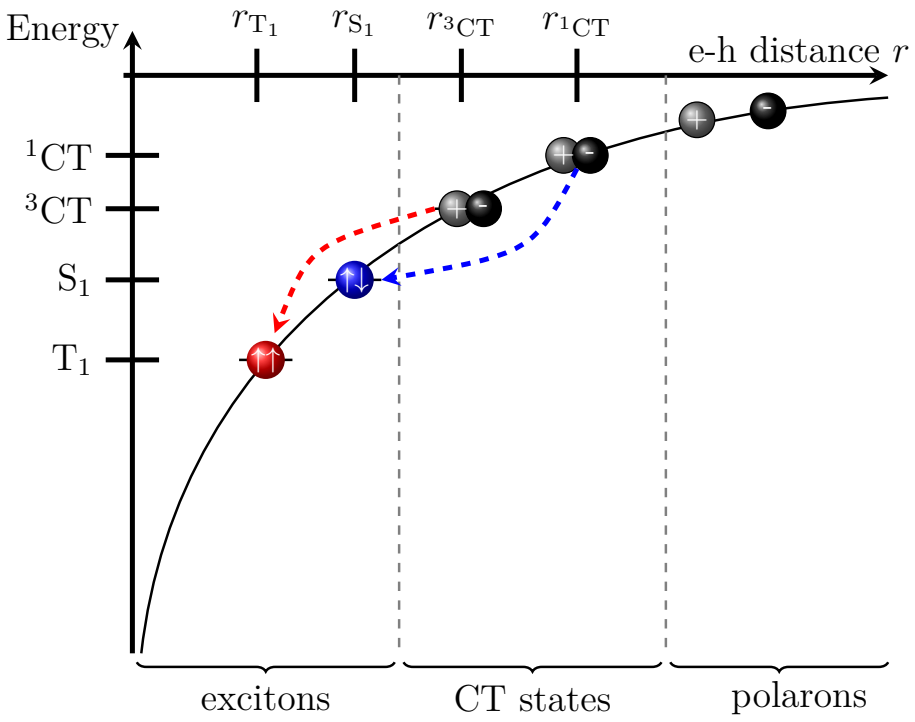

Figure 2.22 Schematic of the electron-hole recombination process forming either a singlet or triplet exciton. Free charge carriers collide and form intermediate charge transfer (CT) state of either singlet (^{1}CT) or triplet character (^{3}CT). Further, the singlet S_1 and triplet T_1 state are generated by recombination of a CT state.

The ISC efficiency is defined by the ratio of

$$\Phi_{\mathrm{ISC}} = \frac{a_{\mathrm{ISC}}}{a_{\mathrm{ISC}} + a_{\mathrm{r}} + a_{\mathrm{nr}}}, \tag{2.48}$$

where a_{nr} and a_{r} are non-radiative and radiative decay rates of singlet excitons (see Fig. 2.21b). It varies from less than 1 % for rigid organic polymers such as methyl-substituted ladder-type poly(para-phenylene), MeLPPP, to nearly 100 % for organic molecules with lone pairs states, such as benzophenone or quinoxaline [8]. In organometallic compounds, Φ_{ISC} converges to 100 % due to the high spin-orbit coupling induced by heavy metals [8, 126, 127].

Electrical Exciton Generation

Electrical generation of excitons is one possible recombination mechanism of an electron in the LUMO and a hole in the HOMO within organic semiconductors. The involved charge carriers can be injected from electrodes, by placing or removing an electron from molecular orbitals or originate from separated singlet states. Charge carriers diffuse through the active semiconductor until they enter the Coulomb radius of an oppositely charged carrier. If they get close enough, they may form a CT state of either singlet, ^{1}CT, or triplet, ^{3}CT, character. The CT state can subsequently recombine and form a singlet, S_1, or triplet, T_1, state. Figure 2.22 visualizes the electrical exciton generation by CT recombination. From a statistical point of view, three triplet states face one singlet state. Thus, singlet and triplet excitons are typically generated with a probability of 25 % and 75 %, respectively.

Electrical exciton generation is the primary mechanism allowing efficient operation of organic LEDs (OLEDs). The efficiency of OLEDs strongly depends on the type of excitons and their

recombination pathways. Only 25 % of the injected charges form fluorescent singlet excitons. OLEDs employ heavy metal-based compounds to enhance the conversion of triplet states to singlet states by intersystem crossing to achieve higher electroluminescence efficiency. Exciton mixing induced by the high spin-orbit coupling of the heavy elements activates phosphorescence and achieves up to 100 % phosphorescence efficiency [115, 128].

Experimental results for the fractions of singlets upon electrical exciton generation can be divided into two groups: small molecules and oligomers exhibit singlet fractions of ≤ 25 %, implying spin-independent recombination [8]. The singlet fraction in polymers ranges from 25 % to 80 %. In the latter case, a correlation between increasing conjugation lengths and singlet generation fraction is detected [8, 9, 129]. For increased polymer conjugation length, $^1\mathrm{CT}\rightarrow\mathrm{S}_1$ energy difference decreases which makes singlet formation more likely. In contrast, $^3\mathrm{CT}\rightarrow\mathrm{T}_n$ gets less probable.

^{3}CT states can undergo ISC to ^{1}CT states, which consecutively form a singlet exciton with high probability. The smaller the gap between the intermediate CT state and the singlet state, the higher the singlet generation fraction gets [8,115,129]. Wohlgenannt *et al.* observed a singlet fraction for different polymers in the following order: sexithienyl < poly(para-phenylene ethynylene) < poly(para-phenylene vinylene)< regio-random poly(hexylthiophene) < ladder-type poly(para-phenylene) (mLPPP) < regio-regular poly(hexylthiophene) (RR-P3HT) [130]. A singlet fraction of up to 80 % is reported for RR-P3HT [131].

2.5.4 Exciton Diffusion

Excitons move through organic semiconductors by non-radiative energy transfer from one site to another. In general, exciton transport from an excited donor to an exciton acceptor molecule occurs by two type of mechanisms: (a) a long-range electromagnetic dipole–dipole interaction, the Förster-type resonant energy transfer transfer (through-space), and (b) a short-range transfer by exchange coupling, the Dexter type energy transfer (through-bond) [132–135]. The rate for exciton transfer in organic semiconductors can be calculated starting from Fermi's Golden rule:

$$a_{\mathrm{ET}} = \frac{2\pi}{\hbar}\left|\left\langle\psi_{\mathrm{f}}\left|\hat{H}'\right|\psi_{\mathrm{i}}\right\rangle\right|^2\rho_{\mathrm{E}}\,, \tag{2.49}$$

with the density of states ρ_{E} related to the spectral overlap J between donor emission $I_{\mathrm{D}}(\lambda)$ and acceptor absorption $\epsilon_{\mathrm{A}}(\lambda)$ (see Fig. 2.23a) [9]:

$$J = \int \mathrm{d}\lambda I_{\mathrm{D}}(\lambda)\epsilon_{\mathrm{A}}(\lambda)\lambda^4\,. \tag{2.50}$$

Here, $\hat{H}'$ is the coupling Hamiltonian, which captures the electrostatic interactions of the charge distributions of the donor and acceptor molecules. The initial (Ψ_{i}) and final (Ψ_{f}) state wavefunctions are given by

$$\Psi_{\mathrm{i}} = \frac{1}{\sqrt{2}}[\Psi^*_{\mathrm{D}}(1)\Psi_{\mathrm{A}}(2) - \Psi^*_{\mathrm{D}}(2)\Psi_{\mathrm{A}}(1)]\,, \tag{2.51}$$

$$\Psi_{\mathrm{f}} = \frac{1}{\sqrt{2}}[\Psi_{\mathrm{D}}(1)\Psi^*_{\mathrm{A}}(2) - \Psi_{\mathrm{D}}(2)\Psi^*_{\mathrm{A}}(1)]\,. \tag{2.52}$$

The total coupling integral $\beta = \left\langle\psi_{\mathrm{f}}\left|\hat{H}'\right|\psi_{\mathrm{i}}\right\rangle$ can be divided into a Coulomb and an exchange contribution:

$$\beta = \beta^{\mathrm{C}} - \beta^{\mathrm{E}}\,, \tag{2.53}$$

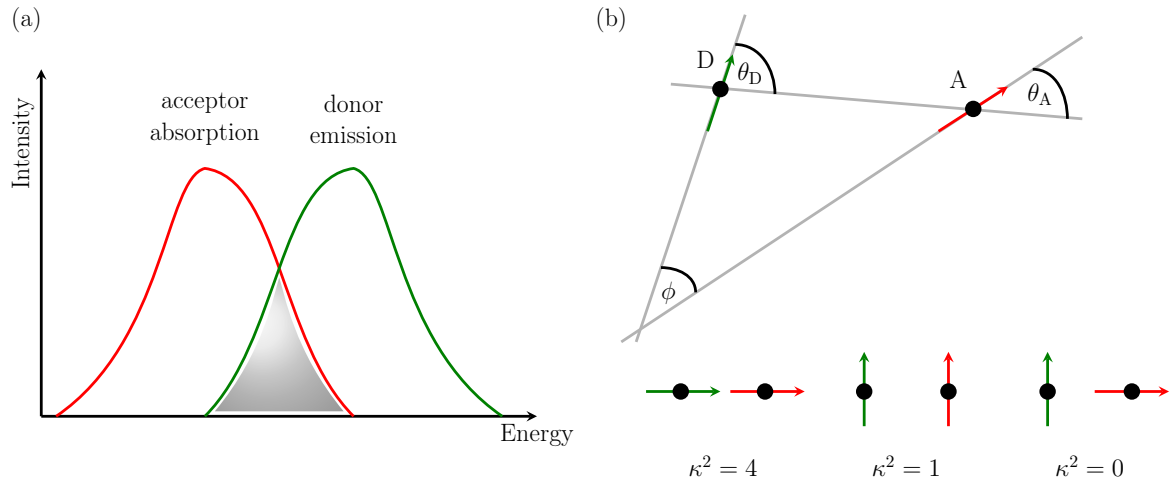

Figure 2.23 (a) Illustration of spectral overlap (gray) of donor emission (green) and acceptor absorption (red). (b) Relative orientation of donor and acceptor transition dipole moments μ_D and μ_A, respectively. The orientation factor κ for collinear, parallel, and perpendicular dipole-dipole orientation are indicated below.

with

$$\beta^C = \left\langle \Psi_D(1)\Psi_A^*(2)\middle|\hat{H}'\middle|\Psi_D^*(1)\Psi_A(2)\right\rangle, \tag{2.54}$$

$$\beta^E = \left\langle \Psi_D(1)\Psi_A^*(2)\middle|\hat{H}'\middle|\Psi_D^*(2)\Psi_A(1)\right\rangle, \tag{2.55}$$

as we deal with indistinguishable electrons e_1 and e_2. The difference between Coulomb and exchange coupling is illustrated in Figure 2.24. The meaning and consequence of both terms is outlined in the following subsections.

Förster-Type Resonant Energy Transfer (FRET)

The electrostatic Coulomb term is known as the Förster-type resonant energy transfer (FRET). Using a point–dipole approximation, as described by Förster [135], the Coulomb term is found to be directly proportional to the donor and the acceptor transition dipole moments μ_D and μ_A, respectively, and inverse proportional to the cube of donor–acceptor separation R:

$$\beta^C \propto \frac{|\mu_D||\mu_A|}{R^3}\kappa, \tag{2.56}$$

with the dipole-dipole orientation factor $\kappa = \cos\phi - 3\cos\theta_D\cos\theta_A$ which describes the relative orientation of the transition dipoles (see Fig. 2.23b). As the energy transfer rate scales with β^2, one obtains a R^{-6} dependence which captures a long-range nature of the transfer mechanism. Thus, the transition rate of non-radiative energy transfer by FRET is given by

$$a_{FRET} \propto \frac{|\mu_D|^2|\mu_A|^2}{R^6}\kappa^2. \tag{2.57}$$

The oscillator strength is approximately $f \sim |\mu|^2\hat{\nu}$, thus the rate for FRET is given by [9]

$$a_{FRET} = \frac{9\cdot\ln 10}{N_A}\frac{1}{2^7\pi^5 n^4}\frac{\Phi_D}{\tau_D^0}\frac{\kappa^2}{R^6}\int I_D(\lambda)\epsilon_A(\lambda)\lambda^4 d\lambda, \tag{2.58}$$

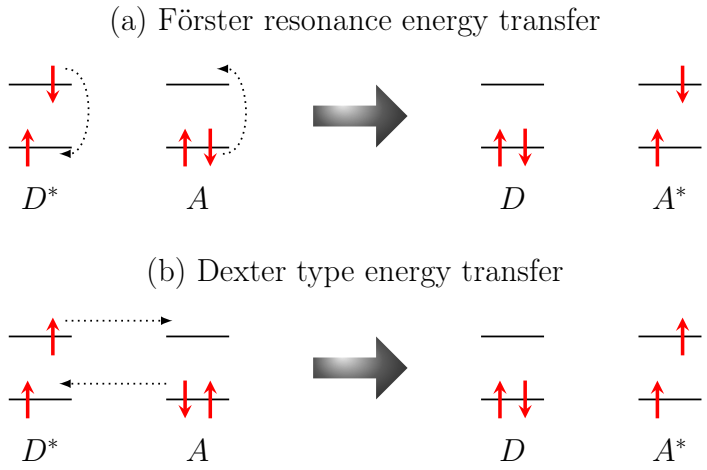

Figure 2.24 a) Förster type resonace energy transfer as non-radiative energy transfer. (b) Dexter-type energy transfer by exchange coupling. Horizontal lines illustrate the HOMO and LUMO level of exciton donor (D) and exciton acceptor (A) molecule. The asterisk label the excited state. Dotted arrows visualize the transfer and rearrangement of the electronic configuration.

where $N_\mathrm{A} = 6.02 \times 10^{23}\,\mathrm{mol}^{-1}$ is Avogadro's number, n is the refractive index of the surrounding medium, Φ_D is the fluorescence quantum yield of the donor, and τ_D^0 is the intrinsic exciton lifetime of the donor in absence of the acceptor. Using Förster radius

$$r_\mathrm{FRET}^6 = \frac{9 \cdot \ln 10}{N_\mathrm{A}} \frac{1}{2^7 \pi^5 n^4} \Phi_\mathrm{D} \kappa^2 \int I_\mathrm{D}(\lambda) \epsilon_\mathrm{A}(\lambda) \lambda^4 \mathrm{d}\lambda\,, \tag{2.59}$$

eq. (2.58) simplifies to

$$a_\mathrm{FRET} = \frac{1}{\tau_\mathrm{D}^0} \left(\frac{r_\mathrm{FRET}}{R} \right)^6 . \tag{2.60}$$

Dexter-Type Energy Transfer (DET)

The exchange contribution is known as the Dexter-type energy transfer. It has been shown that the interaction energy becomes exponentially dependent with the donor–acceptor separation R [9]:

$$\beta^\mathrm{E} \propto \exp\left(-\frac{R}{L} \right) . \tag{2.61}$$

Thus, the Dexter energy transfer rate is described by

$$a_\mathrm{DET} \propto \exp\left(-\frac{2R}{L} \right) J, \tag{2.62}$$

with L being the effective average orbital radius of the donor and acceptor states.

Energy Transfer of Singlet and Triplet Excitons

The dominating contribution to the transfer of singlet and triplet excitons can be found considering the one-electron wavefunctions $\Psi = \Psi_{\mathrm{el}}\Psi_{\mathrm{spin}}$. Assuming spin-independent interaction, the Coulomb and the exchange term can be written as:

$$\begin{aligned}\beta^{\mathrm{C}} = &\left\langle \psi_{\mathrm{el,D}}(1)\psi^{*}_{\mathrm{el,A}}(2)\middle|\hat{H}'\middle|\psi^{*}_{\mathrm{el,D}}(1)\psi_{\mathrm{el,A}}(2)\right\rangle \\ &\times \left\langle \psi_{\mathrm{spin,D}}(1)\middle|\psi^{*}_{\mathrm{spin,D}}(1)\right\rangle \left\langle \psi^{*}_{\mathrm{spin,A}}(2)\middle|\psi_{\mathrm{spin,A}}(2)\right\rangle,\end{aligned} \tag{2.63}$$

and

$$\begin{aligned}\beta^{\mathrm{E}} = &\left\langle \psi_{\mathrm{el,D}}(1)\psi^{*}_{\mathrm{el,A}}(2)\middle|\hat{H}'\middle|\psi^{*}_{\mathrm{el,D}}(2)\psi_{\mathrm{el,A}}(1)\right\rangle \\ &\times \left\langle \psi_{\mathrm{spin,D}}(1)\middle|\psi_{\mathrm{spin,A}}(1)\right\rangle \left\langle \psi^{*}_{\mathrm{spin,A}}(2)\middle|\psi^{*}_{\mathrm{spin,D}}(2)\right\rangle,\end{aligned} \tag{2.64}$$

respectively.

To obtain a non-zero contribution to the transfer rate, an overlap of wavefunctions is fundamental. The excited state wavefunction and the ground state wavefunction must have same spin multiplicity to ensure energy transfer. Equation (2.64) indicates the localization of the spin wavefunctions on two molecules for the exchange term. The Coulomb term shows localization of the spin wavefunctions on the same molecule. For singlet excitons, FRET takes place between donor and acceptor molecules with FRET radii in the range of 1 nm to 5 nm [136, 137]. For triplet excitons, the Coulomb term vanishes in the absence of spin-orbit coupling. In the presence of strong spin-orbit coupling, intermixing of singlet and triplet wavefunction occurs; consequently, triplet excitons can undergo FRET near heavy atoms. Kawamura *et al.* observed FRET in solid films doped with organometallic Ir(III)-complexes [138]. Förster radii for triplet excitons are smaller and only reach values of up to 1 nm.

Dexter-type energy transfer is a short-range mechanism caused by the requirement of significant donor-acceptor orbital overlap. As the DET rate decreases exponentially with donor-acceptor distance, it becomes unlikely for large distances. Due to the R^{-6} dependence, FRET outperforms DET for larger distances.

Role of the Energetic Disorder

The energetically disordered molecular orbitals also have a significant influence on the transport of singlet and triplet excitons. Typically, the disorder of the exciton states is represented by a Gaussian DOS. Upon diffusion throughout the organic semiconductor, excitons equilibrate towards an energy of $-\sigma^2/kT$ below the center of the Gaussian DOS [8, 114, 139]. The Gaussian width σ for exciton states is in the range of 70 meV for singlet state S_1 [140] and 40 meV for the triplet state T_1 as shown for PF2/6 polyfluorene films [141]. Due to the presence of the Gaussian DOS, exciton diffusion becomes temperature-dependent. Athanasopoulos *et al.* presented the temperature dependence of the diffusion length of singlets as a function of the energy disorder σ by kMC simulations [38]. Furthermore, Hoffmann *et al.* evaluated the triplet diffusion in disordered organic semiconductors by kMC simulations [142].

Exciton Diffusion Length

Excitons are quasi-particles with a net charge of zero, which migrate by diffusion through the semiconductor material. The characteristic diffusion length L_{D} of an excitation is given by

$$L_{\mathrm{D}} = \sqrt{2ZD\tau}, \tag{2.65}$$

where $Z \in \{1, 2, 3\}$ needs to be used for one-dimensional, two-dimensional, and three-dimensional diffusion, respectively [114]. Assuming random diffusion, D is obtained using the Smoluchowski-Einstein theory of a random walk [114]:

$$D = \frac{d^2 a_{\mathrm{ET}}}{6}, \tag{2.66}$$

where d is the average distance between initial and final molecular sites.

Singlet excitons have rather short diffusion lengths in the range of 5 nm to 20 nm within amorphous and poly-crystalline organic semiconductors [114]. Due to their longer lifetimes, triplet excitons reach diffusion lengths in the range of 10 nm to 250 nm [114]. Different methods were developed in recent years to characterize the exciton diffusion length in organic semiconductors. For singlets, exemplary methods are fluorescence quenching in bilayers, fluorescence volume quenching, exciton–exciton annihilation, microwave conductivity, and electro–optical measurements; for triplets, one can use delayed luminescence spread, remote phosphorescent sensing, and modeling of absorption transients. Detailed information on exciton characterization techniques can be found in [114].

2.5.5 Exciton Dissociation

The dissociation of an exciton into a CT state made of an electron in the LUMO and a hole in the HOMO occurs by the transfer of charges at the interface between an electron donor and an electron acceptor phase. For efficient exciton dissociation, one needs to provide a sufficient driving force to overcome the difference in the exciton binding energy and the CT binding energy. The singlet binding energy is typically defined as the difference in the electrical bandgap to the optical bandgap. The triplet binding energy can be calculated by subtracting the exchange energy ΔE_{ST} from the singlet binding energy. Typically, heterojunctions with an offset in the molecular orbital energies are employed to enhance the dissociation of excitons. Exciton dissociation occurs on a time scale of 45 fs to 100 fs for polymer-fullerene heterojunctions [114, 143–145].

2.5.6 Exciton Decay

The lifetime of excitons is limited due to radiative and non-radiative recombination. Typically, the exciton lifetime can be obtained from the recombination rates:

$$\tau = \frac{1}{a_{\mathrm{r}} + a_{\mathrm{nr}}}, \tag{2.67}$$

where a_{r} and a_{nr} denote the radiative and non-radiative decay rate, respectively. The radiative lifetime can be measured by fitting transient photoluminescence data and is given by $\tau_0 = a_{\mathrm{r}}^{-1}$. Usually, there is only one pathway for radiative decay ($S_1 \rightarrow S_0$ and $T_1 \rightarrow T_0$), while several non-radiative decay channels exist ($a_{\mathrm{nr}} = \sum_i a_{\mathrm{nr,i}}$).

Radiative decay is a vertical transition in a potential energy surface, whereas non-radiative decay is depicted by a horizontal arrow followed by a sequence of vertical relaxation processes, see Fig. 2.25. The non-radiative decay rate is given by

$$a_{\mathrm{nr}} = \left(\frac{2\pi}{\hbar}\right)\beta^2 \rho\,[\mathrm{FCWD}], \tag{2.68}$$

where β is the transfer matrix element of the transition between the initial and final state, ρ is the density of states and [FCWD] is the Franck-Condon factor [146, 147]. An exponential energy dependence for non-radiative decay rate follows [9]:

$$a_{\mathrm{nr}} \propto \exp\left(-\gamma \frac{\Delta E}{\hbar\omega}\right), \tag{2.69}$$

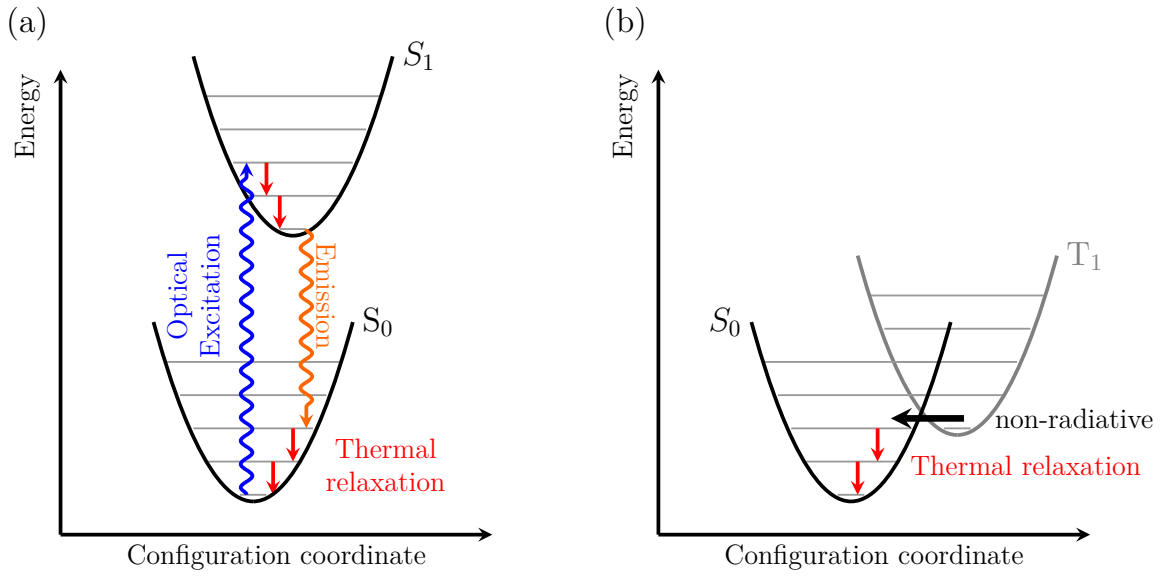

Figure 2.25 Potential energy surface representing (a) singlet and (b) triplet decay mechanisms. (a) Visualization of the excited state S_1 and ground state S_0. The green arrows show the excitation of an electron by photon absorption followed by thermal relaxation. The red arrows indicate the reverse process of photon emission by recombination of the excited state to the ground state. (b) Non-radiative decay from the first excited triplet state T_1 to the ground singlet state followed by thermal relaxation.

where ΔE is the energy difference between the excited state and the ground state, γ is a term determined by molecular parameters, and ω is the frequency of the highest vibrational mode.

In terms of radiative decay, one needs to distinguish between fluorescence of singlet excitons and phosphorescence of triplet excitons. Especially in organic semiconductors, delayed fluorescence can also occur. In the following subsections, the three radiative decay mechanisms are summarized.

Fluorescence

Singlet decay can be described by a radiative transition (fluorescence) and various non-radiative transition routes such as internal conversion, intersystem crossing, and exciton dissociation. The rate equation of the singlet exciton concentration n_s is therefore given by

$$\frac{\mathrm{d}n_s}{\mathrm{d}t} = G - \frac{1}{\tau_s} n_s, \tag{2.70}$$

with the singlet lifetime $\tau_s = \left(a_\mathrm{r} + \sum_i a_{\mathrm{nr},i}\right)^{-1}$ and the singlet generation rate G. If a single light pulse is used to generate singlets at time t_0, the time-dependence of the singlet density can be determined by

$$n_s(t) = n_s(t_0) \cdot \exp\left(-\frac{t - t_0}{\tau_s}\right). \tag{2.71}$$

Thus, we observe a monoexponential decrease in the singlet density. In the organic polymer P3HT, the optical bandgap is roughly $E_\mathrm{gap} = 1.85\,\mathrm{eV}$ [148]. Considering the exponential energy dependence for the non-radiative decay rate (Eq. (2.69)), non-radiative decay is significantly lower than the radiative decay rates. Within neat organic layers, ISC rates are usually low. Thus, by measuring the transient photoluminescence, one can obtain a good estimate of the exciton lifetime and the radiative decay rate.

Phosphorescence

The detection of phosphorescence in π-conjugated systems such as P3HT is rather difficult due to the low population probability of triplet states. In many organic semiconductors with π-conjugated backbone, the intersystem crossing rate is in the range of $10^7\,\mathrm{s}^{-1}$. Together with a singlet lifetime smaller than 1 ns, an ISC yield of less than 1 % is expected.

By incorporating heavy atoms, triplet states can be populated by ISC from the singlet state S_1. The increased ISC leads to a detectable phosphorescence quantum yield. Using this method, the first triplet energy level T_1 of the poly(phenylene-vinylene) derivative PhPPV was experimentally determined to be at 1.63 eV [149]. Xu and Holdcroft performed phosphorescence measurements on P3HT [150, 151]. They reached a sufficient population of the triplet state to measure phosphorescence and delayed, which is four orders of magnitude above the singlet lifetime, with triplet energy of $E_\mathrm{t} = 1.5\,\mathrm{eV}$ [152].

Delayed Fluorescence via Triplet-Triplet Annihilation

Delayed fluorescence (DF) can arise from another relevant loss mechanism: triplet–triplet annihilation (TTA) [9]. TTA can occur if two triplets with opposite spins collide. First reports on TTA and DF in anthracene were reported by Kepler *et al.* [153]. The spin angular momentum needs to be conserved, thus three possible reactions for TTA are possible:

$$\mathrm{T_1 + T_1 \rightarrow (TT)^*} \begin{cases} \rightarrow \mathrm{S}_n + \mathrm{S_0} \rightarrow \mathrm{S_1 + S_0} & \text{for} \quad S_\mathrm{TT} = 0 \\ \rightarrow \mathrm{T}_n + \mathrm{S_0} \rightarrow \mathrm{T_1} + S_0 & \text{for} \quad S_\mathrm{TT} = 1 \\ (\rightarrow \mathrm{Q_1 + S_0} & \text{for} \quad S_\mathrm{TT} = 2) \end{cases} . \tag{2.72}$$

Here, S_TT denotes the total spin of the resulting triplet-triplet-pair state $(\mathrm{TT})^*$. The total spin of the triplet-triplet pair state can be 0,1, or 2, which implies three possible states. In the first scenario, $(\mathrm{TT})^*$ forms a singlet state with spin angular momentum $S_\mathrm{TT} = 0$. It the energy of the triplet–triplet pair is close to or above the energy of S_1, it relaxes to the S_1 state and emits one photon, and singlet state remains left, being known as *delayed fluorescence*. If, however, the total spin of the triplet–triplet pair is $S_\mathrm{TT} = 1$, then one of the triplets is quenched non-radiatively, and a triplet exciton remains. As a final (and improbable) configuration, the triplet–triplet pair could form a quintet state Q_1 ($S_\mathrm{TT} = 2$) with twice the energy of the first excited triplet state. However, it was not observed yet [9]. This encounter is expected to induce scattering of the two triplet states. Further measurements and reports on DF and TTA can be found in refs. [8, 9, 154–156]. In OLEDs, TTA has been shown to not only lead to an energy loss but also induces an efficiency roll-off [154, 157, 158].

2.6 Organic Solar Cells

2.6.1 Working principle

The typical OSC device architecture is made of a transparent substrate, e.g., glass, representing the front contact. On top of the transparent substrate, transparent conductive oxides such as indium tin oxide (ITO) are deposited forming the anode. Its charge selectivity and the contact work function can be modified by a hole-transport layer (HTL) such as Poly(3,4-ethylenedioxythiophene)-poly(styrenesulfonate) (PEDOT:PSS). The photoactive layer of an OSC is made of an electron acceptor and an electron donor. Both small molecule and polymer semiconductors may be used for either the donor or the acceptor. Typically, a blend of two material is required two enable efficient exciton

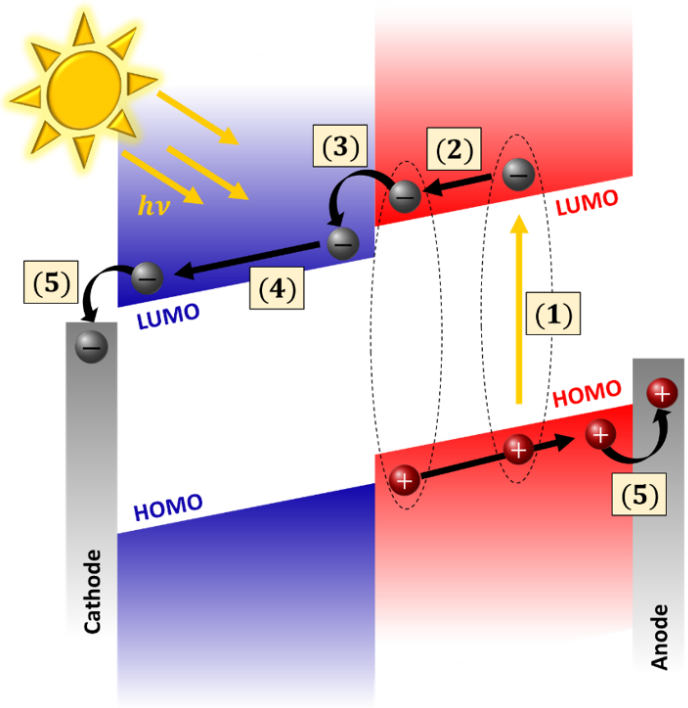

Figure 2.26 Working principle of an organic solar cell in a schematic energy diagram. The blue region visualizes the electron acceptor, the red region represents the electron donor. The key steps are indicated by numbers and describe the following steps: (1) Exciton generation by absorption of incident light. (2) Exciton diffusion towards the donor:acceptor interface. (3) Exciton dissociation by charge transfer of the electron from the electron donor to the electron acceptor. (4) Charge separation and transport towards the electrodes. (5) Charge extraction at the cathode and anode.

dissocation into free charge carriers. Finally, the cathode, e.g. aluminum (Al), is deposited on top of the photoactive layer as back electrode.

Figure 2.26 visualizes the working principle of an OSC using a simple energy diagram. The shown structure visualizes the cathode and the anode, as well as the electron donor (red) and the electron acceptor (blue). The electron acceptor is usually designed to have a lower LUMO energy compared to the electron donor. The HOMO level of the electron donor is higher than the HOMO level of the electron acceptor. The work function of the cathode Φ_c is chosen to be below the LUMO energy of the cathode; for the anode, higher work functions Φ_a than the electron donor HOMO are required to allow sufficient hole extraction. The difference in work functions $\Delta\Phi = \Phi_c - \Phi_a$ induces an internal built-in voltage at zero bias voltage.

The key steps in the conversion of solar energy into electrical energy are indicated in Fig. 2.26. A brief description of the key steps is given as follows. For detailed summaries, please be referred to [10, 11, 159].

1. A photon is absorbed in the photoactive layer. Historically, light-absorbing donor polymers were blended with fullerene molecules, which showed a rather low absorbance. In the given schematic, a photon is absorbed in the donor layer and excites a Frenkel exciton (indicated by the dotted ellipsoids). Organic semiconductors exhibit high absorption coefficients reaching up to 10^5 cm^{-1}, thus thin active layers are sufficient for efficient light harvesting [10].

2. Within OSCs, photogenerated excitons have binding energies of several hundreds of meV as the low dielectric constant between 3 and 4 causes a weak screening of the Coulomb attraction of the electron-hole pair. Thus, the photogenerated excitons cannot easily dissociate within the donor material itself. Typical operation voltages of OSCs are far too low to provide a sufficient driving force for the exciton dissociation. Excitons diffuse as neutral particles through the donor layer until reaching the donor:acceptor interface or decaying.

3. Excitons in organic solar cells have rather small diffusion lengths. Thus, if being generated far from the donor:acceptor interface, exciton decay is probable. For photogenerated singlet excitons in organic semiconductors, the lifetime is around 1 ns. Subsequently, they decay with photoluminescence as decay path. If excitons reach the donor:acceptor interface, exciton dissociation becomes probable. The offset in the LUMO energies between the electron acceptor and electron donor provides sufficient energy to support exciton dissociation. This charge transfer is reported to occur within tens of femtoseconds [160, 161]. Recently, researchers demonstrated sufficient exciton dissociation within non-fullerene based OSCs with close to zero driving force [162, 163]. In fullerene-based OSCs, a driving force is required. This controversy highlights that the need for the energy offset is still not fully understood.

4. Upon exciton dissociation, the electron resides in the acceptor phase, and the hole remains within the donor phase. Still, significant Coulomb attraction is present. This state is the so-called charge transfer (CT) state. The charge carriers need to overcome their Coulomb attraction to reach the electrodes. Several aspects support the separation, such as energetic disorder in the molecular orbital energies, entropic contributions, and delocalization. Interestingly, internal quantum efficiencies of near 100 % are observed despite the presence of the large Coulomb attraction [54].

5. If charges overcome their mutual Coulomb attraction, they migrate through the respective phase – electrons in the acceptor and holes in the donor – towards the contacts. Here, charge extraction occurs if suitable energy alignment has been chosen.

The first OSCs consisted of planar donor:acceptor heterostructures [12]. Exciton dissociation into free charge carriers is only possible at the interface. Once being separated, charge carriers can be easily transferred to the electrodes with minimized recombination properties. Due to the low diffusion length of singlets, only excitons that are generated near the interface contribute to the current densities in bilayer OSCs. All remaining excitons decay, and the excitation is lost. Thus, only a small fraction of excitons were generated. Exciton dissociation can be enhanced by intermixing the donor and acceptor phases into a bulk-heterojunction blend [10, 11]. The fine intermixing with cluster areas of 10 nm to 20 nm lead to a small mean distance from the spot of exciton generation to the interface. Thus, most excitons reach the interface and are dissociated at the donor:acceptor interface. If the intermixing is chosen too fine, migration of charge carriers is suppressed, and charge recombination is enhanced. Ideal bulk-heterojunction blends achieve a good trade-off between exciton dissociation and migration pathways towards the electrodes. In order to account for the role of the three-dimensional, intermixed morphology, three-dimensional simulation models are required. This makes kinetic Monte Carlo models highly suitable to study both structural properties as well as physical properties.

2.6.2 Efficiency Limit

Shockley and Queisser derived an efficiency limit for pn-junction solar cells based on the detailed balance [71]. The underlying assumption is that each absorbed photon with energy $h\nu \geq E_{\mathrm{gap}}$

contributes an electron and a hole at energy E_{gap}. Radiative recombination was accounted for to satisfy the detailed balance for light absorption and emission within direct semiconductors.

In contrast to traditional inorganic crystalline semiconductors, organic semiconductors are amorphous structures that have low permittivities ϵ_r and localized charge carriers. Due to the low ϵ_r, photogenerated electron-hole pairs are strongly-bound Frenkel excitons with binding energies of hundreds of milli-electronvolt. The lack of periodic structures in organic materials leads to low charge carrier mobilities in the range of $10^{-8}\,\mathrm{cm^2\,V^{-1}\,s^{-1}}$ to $10^{-2}\,\mathrm{cm^2\,V^{-1}\,s^{-1}}$, being several orders of magnitude lower than in silicon solar cells. Both of these characteristics need to be accounted for to understand realistic efficiency limits in organic solar cells.

Giebink *et al.* derived a thermodynamic efficiency limit by accounting for the exciton binding energy within general excitonic solar cells and especially within heterojunction organic solar cells [164]. Figure 2.27(a) and (c) visualize the schematic diagram of a generalized excitonic solar cell with exciton binding energy E_{B} and an organic heterojunction solar cell with additional driving force ΔG_{CT} and CT state energy $E_{\mathrm{B,CT}}$ at a donor:acceptor interface. Figure 2.27(b) and (d) visualize the respective efficiency limit as a function of the optical bandgap under 1 sun illumination. For exciton binding energies below 1.0 eV, the efficiency limit follows the Shockley-Queisser limit (black curve) for a general excitonic solar cell closely. If the binding energy exceeds 1.0 eV, a tremendous loss in efficiency is observable. The new efficiency limit for the scenario $E_{\mathrm{B}} = 1.4\,\mathrm{eV}$ gives roughly 23 %. In addition, the bandgap at maximal efficiency shifts towards lower values.

Within the heterojunction solar cells (Fig. 2.27c), Giebink *et al.* account for the driving force in the dissociation process of excitons, with binding energy E_{B}, into charge transfer states with binding energy $E_{\mathrm{B,CT}}$. To efficiently separate CT states into free charge carriers, electrons and holes need to overcome $E_{\mathrm{B,CT}}$. The Shockley-Queisser limit matches the limit $-\Delta G_{\mathrm{CT}} \to 0$. However, negligible power will be generated in the absence of a driving force that promotes exciton dissociation. An increase in $-\Delta G_{\mathrm{CT}}$ leads to a strong decrease in the efficiency limit. Typical driving forces of 0.3 eV to 0.5 eV lower the maximal efficiency to 27 % to 22 %, respectively. The energy bandgap at maximum efficiency is increased to 1.35 eV and 1.5 eV for $-\Delta G_{\mathrm{CT}} = 0.3\,\mathrm{eV}$ and $-\Delta G_{\mathrm{CT}} = 0.5\,\mathrm{eV}$, respectively. According to this model, the decrease origins from a loss in open-circuit voltage as shown in the inset in Fig. 2.27.

In the study of Giebink *et al.*, charge transport losses are neglected. Würfel *et al.* highlighted the impact of charge transport on the achievable efficiency in organic donor:acceptor solar cells [32]. Low charge carrier mobilities cause an accumulation of charge carriers within the photoactive layer. The splitting in the quasi-Fermi levels differ substantially from the externally applied voltage. Thus, the charge carrier density has been correlated to the internal voltage, while the external voltage was used as reference within the original work of Shockley and Queisser [71]. The achievable efficiency for a donor:acceptor solar cell is visualized in Fig. 2.28 for different energy alignment between the donor and the acceptor. If the bandgap of the absorbing donor material is equal to the difference $E_{\mathrm{G,eff}} = E_{\mathrm{LUMO}}(\mathrm{A}) - E_{\mathrm{HOMO}}(\mathrm{D})$, the LUMO levels of the donor and acceptor are aligned (see Fig. 2.28a). Figure 2.28b depicts the efficiency as function of $E_{\mathrm{G,eff}}$ for different charge carrier mobilities. The efficiency saturates for high carrier mobilities of $1\,\mathrm{cm^2\,V^{-1}\,s^{-1}}$ with maximum value around 26 %. Within OSCs, typical mobilities are even lower [165]. For a mobility of $10^{-4}\,\mathrm{cm^2\,V^{-1}\,s^{-1}}$, the maximum efficiency is limited at 14 % for $E_{\mathrm{G,eff}} \approx 1.6\,\mathrm{eV}$. In presence of a LUMO–LUMO offset (i.e. driving force) of 0.5 eV (Fig. 2.28c), the maximum efficiency is less than 14 % even for highest mobility values. If now charge carrier transport is poor ($\mu \approx 10^{-4}\,\mathrm{cm^2\,V^{-1}\,s^{-1}}$), maximum efficiencies of 8 % are expected.

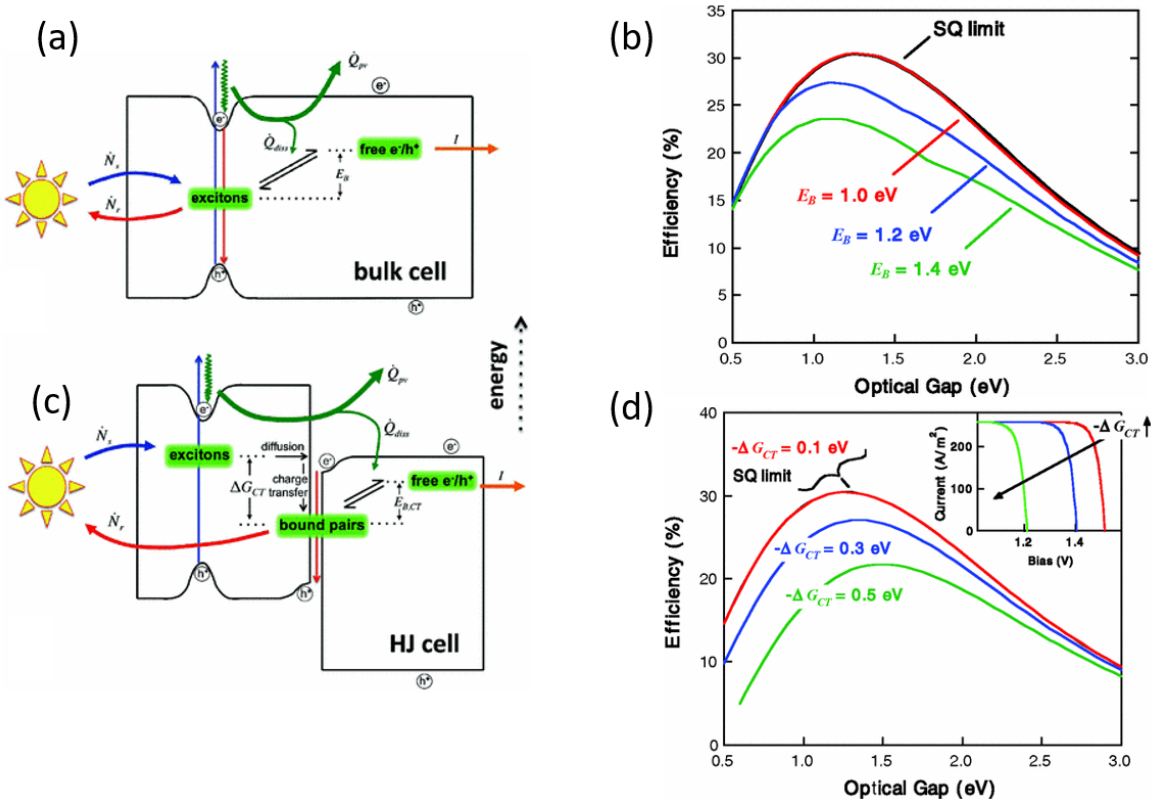

Figure 2.27 (a) Schematic diagram for a generalized excitonic solar cell in the radiative limit with exiton binding energy E_B. (b) Efficiency limit for excitonic cells as a function of the optical bandgap for different exciton binding energies E_B under 1 sun illumination. The black curve gives the Shockley-Queisser limit. (c) Donor-acceptor heterojunction cell with free energy change ΔG_{CT} which induces charge transfer of excitons into free charge transfer states with binding energy $E_{B,CT}$. (d) Maximum efficiency for an organic donor-acceptor solar cell as function of the optical bandgap and several values of the free energy for charge transfer at the heterojunction, $-\Delta G_{CT}$. The inset shows the ideal current–voltage relation for increase in $-\Delta G_{CT}$. Reprinted with permission from Giebink *et al.*, Phys. Rev. B., 83, 195326 2011 [164] Copyright (2020) by the American Physical Society.

2.6.3 Non-Fullerene Acceptors

Fullerene-based bulk-heterojunction OSCs show typical voltage losses in the range of 0.8 eV to 1.0 eV, depending on the donor material used. This limits the efficiency at approximately 10 % [10, 32]. In recent years, a tremendous performance increase was achieved thanks to the usage of non-fullerene acceptors (NFA). NFAs were synthesized with strong light absorption to complement absorption by the donor molecules. Reduced voltage losses below 0.6 V lead to an increase in record efficiencies up to 17 % [6, 166]. In recent studies, the acceptor molecule Y6 has led to fascinating results. Blended with a donor polymer PBDB-T-2F excellent performance values were reported [167]: external quantum efficiencies of 85 %, internal quantum efficiencies of 95 %, fill factors of 73 %, and overall PCEs above 15 %. Recently, Zhang *et al.* have analyzed the structure-property relations of OSCs based on the NFA Y6 [168]. As shown in Fig. 2.29, strong $\pi - \pi$-stacking of Y6 molecules has been observed from simulations and was verified to preserve in spin-coated films [168]. Such extraordinary molecular packing allows sufficient charge delocalization for both holes and electrons, as shown in Fig. 2.29e. Furthermore, this leads to exciton delocalization with long exciton lifetimes. Additionally,

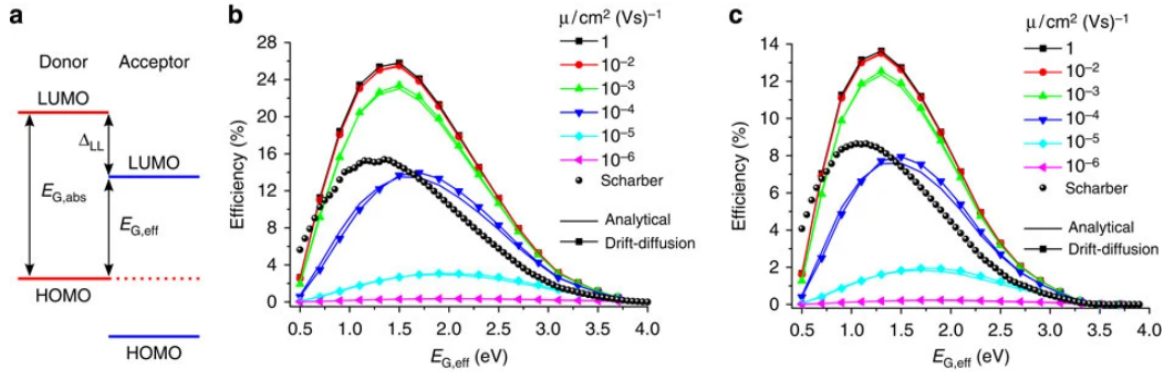

Figure 2.28 (a) Schematics of the donor:acceptor energy alignment. (b) Efficiency limit as function of the effective bandgap $E_{G,eff}$ with $E_{G,abs} = E_{G,eff}$ for different charge carrier mobilities μ. (c) Efficiency limit as function of the effective bandgap $E_{G,eff}$ with $\Delta_{LL} = 0.5\,eV$ for different charge carrier mobilities μ. Reprinted with permission from [32] under the Creative Commons Attribution 4.0.

low non-radiative voltage losses are observed due to the small energy offset between exciton and CT state energy. Such materials seem highly promising for the future development of OSCs.

Voltage losses may be further reduced by employing donor:acceptor material combinations with negligible energy-level offset. With reduced $\Delta E_{HOMO}/\Delta E_{LUMO}$, non-radiative voltage losses are strongly reduced, and open-circuit voltages may be increased. Brabec and coworkers demonstrated recently that efficient exciton splitting can occur even for low energy-level offset [169]. The key challenge to maintain high exciton separation is to provide long exciton lifetimes. They further suggest that the development of highly efficient infrared emitters will lead to long singlet exciton lifetimes. This may help to shape the future material candidates for efficient OSCs.

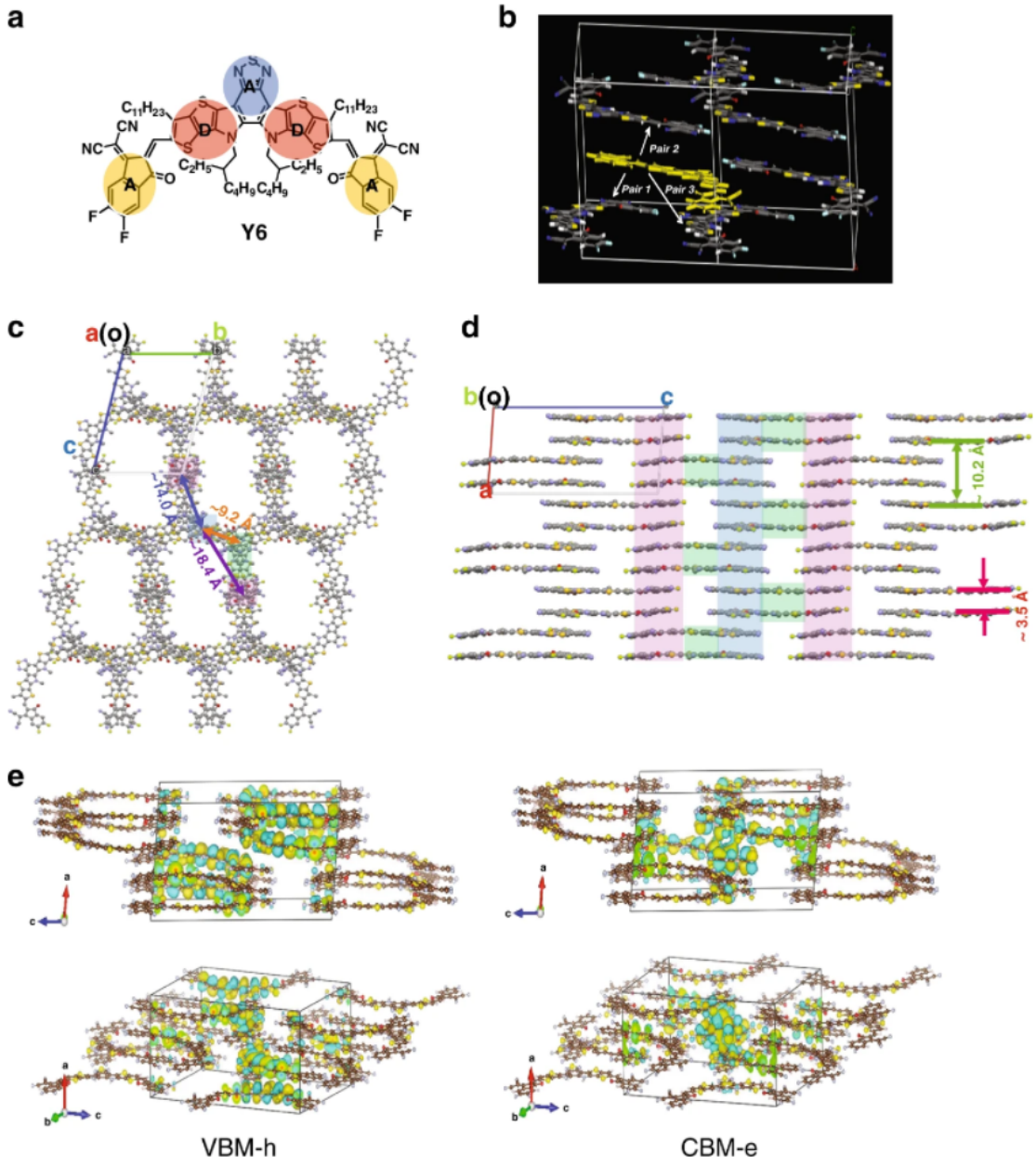

Figure 2.29 (a) Molecular structure of Y6. (b) Molecular dimers in the Y6 single crystal. (c) Top and (d) side views of the extended-crystal structure. (e) Valence band maximum (VBM) for hole (left) and conduction band minimum (CBM) for electron (right) wavefunctions at the Γ point. Reprinted with permission from [168] under the Creative Commons Attribution 4.0.

3 Kinetic Monte Carlo Algorithm for Organic Solar Cells

Computational methods allow important insight into the relationship between material properties and device characteristics. Computational methods usually cover only a distinct level of detail and focus either on atomic properties or directly analyze device characteristics. This is due to the high computational cost, which rises with increased resolution into the atomic scales. Quantum mechanical calculations are required to obtain highest accuracies, while available time-/length scales are extremely short. In contrast, device simulations such as drift-diffusion allow simulation of full devices but rely on effective material parameters. This controversy is highlighted in Fig. 3.1.

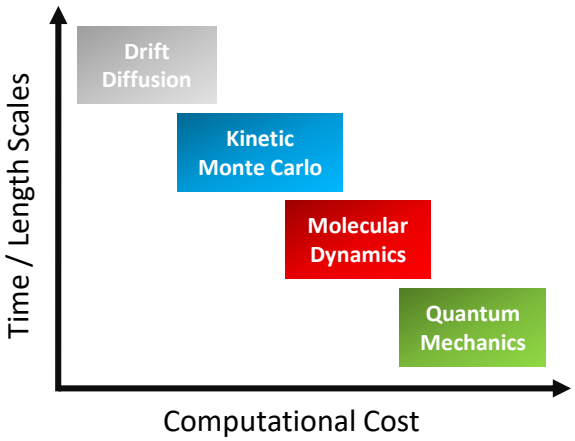

Figure 3.1 Overview of computational methods employed within multiscale device simulations.

Kinetic Monte Carlo (kMC) methods tackle problems on a mesoscopic length scale. kMC takes quantum mechanical properties, such as charge transfer integrals or distributions of molecular orbital energies, as an input and provides experimentally accessible device parameters such as charge carrier mobilities or full jV-characteristics of solar cells. Additionally, kMC simulations can unravel the importance of local variations in the morphology for the performance of solar cells. This allows us to bridge several length scales and connect the microscopic with the macroscopic world and tailor the future development of materials and interfaces.

The presented thesis is based on the kinetic Monte Carlo (kMC) solver developed within the group. The theoretical foundations of the kMC method are summarized in section 3.1. The photoactive layer needs to be represented by a set of discretized sites that contain information about the structure and material of the organic semiconductors. This is summarized in section 3.2. Finally, the implementation of the physical transition rates is presented in section 3.3. The kMC model was built on the implementation of *Tim Albes*, TUM, which is summarized in his dissertation [52].

3.1 Kinetic Monte Carlo

The time evolution of various systems of interest in science and engineering has been modeled in a deterministic manner for a long time. However, many electronic and electrochemical systems, such as organic semiconductors, require a stochastic description to account for random perturbations arising from the contact with a heat bath. Especially if systems are very small or the population of certain ionic or electronic species is low, the discreteness and randomness become significant. In the case of amorphous organic semiconductors, charge transport occurs through a series of non-adiabatic, phonon-assisted hopping events. Numerical stochastic algorithms are frequently used to analyze the system propagation in a probability space spanned by available system configurations. One of the most popular numerical methods is the *Kinetic Monte Carlo* (kMC) method. In the following, we summarize the basic concepts of the kMC method.

3.1.1 Rationale and Applications

Let $\mathcal{S} = \left\{\mathbf{x}_j | j = 1 \cdots M\right\}$ be the set of states $\mathbf{x}_j$ of a system of interest. Each state $\mathbf{x}_j$ is described by the number of particles n_k of certain species $k = 1 \cdots N$, with each particle i being at a position $\mathbf{r}_i$ and having an energy E_i. The set $\mathcal{S}$ spans a high-dimensional phase space in which the system can evolve through time. The time evolution of the probability $P(\mathbf{x}_i, t|\mathbf{x}_0, t_0)$ to find the system state, given by $\mathbf{X}(t)$, in state $\mathbf{x}_i$ at time t is given by the master equation [170, 171]:

$$\frac{\partial P(\mathbf{x}_i, t|\mathbf{x}_0, t_0)}{\partial t} = \sum_{j=1}^{M} \left[a_{j\to i}(t) P(\mathbf{x}_j, t|\mathbf{x}_0, t_0) - a_{i\to j}(t) P(\mathbf{x}_i, t|\mathbf{x}_0, t_0) \right] , \tag{3.1}$$

with $\mathbf{x}_0$ being the system state at initial time t_0. $a_{i\to j}(t)$ are the time-dependent transition rates which capture the probability of changing the system from state $\mathbf{x}_i$ to $\mathbf{x}_j$.

In many situations, the cardinality of the set of system states becomes untrackable. For example, in the presence of several interacting particle species within 3-dimensional lattices of spatial heterogeneities, the evolution of states cannot efficiently be solved with the master equation. Numerical methods have been established to obtain the evolution of the probability density using algorithmic approaches to the master equation. Especially Monte Carlo (MC) procedures are frequently used to propagate the system in the form of Markovian chains stochastically.

Monte Carlo (MC) simulations utilize random numbers to solve the evolution of stochastic systems in high-dimensional phase space. The first Monte Carlo method studied neutron diffusion in fissionable materials during the 1940s within the Manhattan Project. During that time, the Metropolis algorithm [172] was developed, which still is a convenient technique to study the relaxation and the ground-state configuration of physical systems such as spin glasses. Kinetic Monte Carlo (kMC) methods go beyond the Metropolis algorithm. The physical system is propagated between discrete states, with time information assigned to each propagation step. kMC methods do not immediately yield a solution of the master equation but provide single system trajectories through its available phase space. Averaging over multiple trajectories results in accurate probability distributions as one would obtain by solving the master equation. Often, kMC simulations are termed simulated experiments as they mimic the explicit evolution of a physical system within a sequential algorithm. While the master equation cannot be used for large systems, kMC can be used within phase spaces of arbitrary sizes accounting for complex many-body interactions such as Coulomb interactions for charged particles. kMC has gained large popularity for a variety of stochastic problems due to its simplicity and its strong capabilities, such as chemical reactions networks [173–175], crystal growth [176–178], vacancy diffusion [179–181], and charge transport in disordered materials [182].

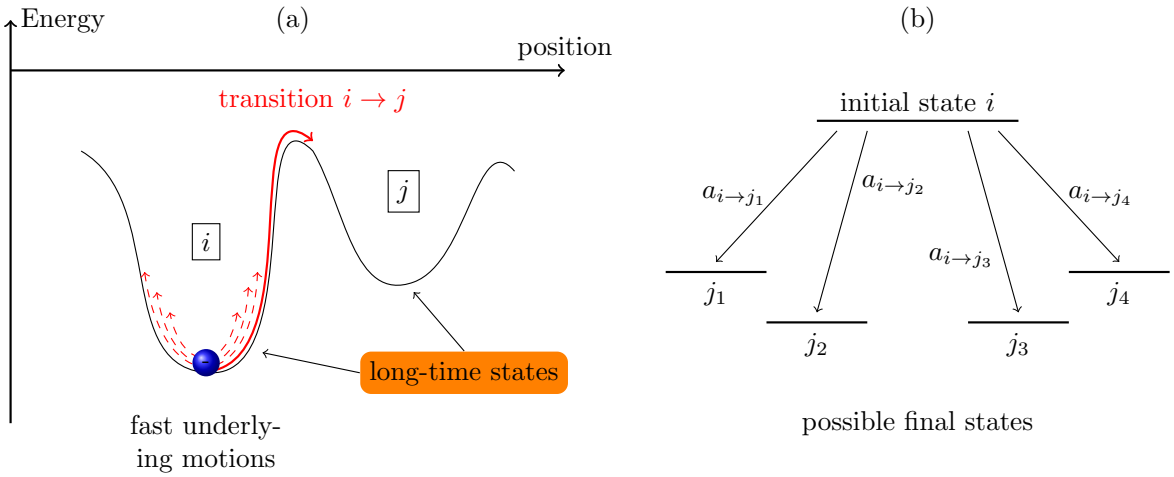

Figure 3.2 (a) Coarse-graining of the fast underlying motions into long-term system states. (b) Transition from initial state i to final states j as employed in the kMC algorithm. This figure has been published by Kaiser *et al.* [182] and is used under the Creative Commons Attribution License.

To model a photovoltaic cell, one has to identify the spatial dimensions and the timescales on which the processes determining the properties of the system occur. Compared to atomistic MD, which typically accesses timescale up to nanoseconds, the kMC method employs the concept of coarse-graining the system dynamics. A set of long-term states characterizes a system. Exemplary, fluctuations of charge carriers within a molecule occur in timescales of femtoseconds, while the hopping of charges between molecules occurs in the range of pico- to microseconds. Coarse-graining neglects the fluctuations on small timescales as they do not change our long-term states, which is the charge being located on this molecule. Accurate coarse-graining allows simulating the macroscopic system behaviors on timescales of seconds. The concept of long-term states is visualized in Fig. 3.2a. This way, kMC algorithms reach a tradeoff between accuracy and simulation time. Infrequent events such as the hopping of charge carriers between molecules are described by the transition rates a_{ij} from the initial system state i to all available final states j (see Fig. 3.2b). As shown in the master equation, these transitions modify the probability density of the system. Accurate transition rates are essential to describe the correct dynamical evolution of the system. The rates are obtained by physical laws using inputs from quantum chemical models or are fitted using experimental measurements.

3.1.2 Reaction Probability Density Function

Modern kMC algorithms are based on the early work of Gillespie [183] and Bortz *et al.* [184]. In the remaining section, we will outline the theoretical basis of the kMC algorithm following the work of Gillespie [183] closely. Assume a system of particles of different species S_i with $i = 1 \ldots N$. In kMC, each physical system can be considered as a reaction network. A variety of reactions R_μ of different order may be specified:

$$\star \longrightarrow \text{reaction product} \tag{3.2}$$

$$S_j \longrightarrow \text{reaction product} \tag{3.3}$$

$$S_j + S_k \longrightarrow \text{reaction product} \tag{3.4}$$

$$2S_j \longrightarrow \text{reaction product} \tag{3.5}$$

Reaction (3.2) represents a spontaneous creation of a particle, which can e.g. be the excitation of an electron upon absorption of a photon, or the injection of a charge from contacts. Reaction (3.3) represents a monomolecular process, e.g. the spontaneous decay of excitons or the collection of a charge carrier. Within reactions (3.4) and (3.5), bimolecular reactions are captured. This can be e.g. the recombination of an electron with a hole or the electrostatic repulsion between two ions from the same species. In principle, reactions of higher order, such as e.g. a 3-particle Auger-recombination, can be included. Each reaction R_μ is considered unidirectional, i.e. its reverse reaction is captured by another reaction R_η with $\eta \neq \mu$.

Each reaction R_μ is described by a reaction rate a_μ, which details depend on the underlying mechanism of the reaction. The hypothesis of the stochastic formulation of the reaction kinetics is that $a_\mu \delta t$ defines the average probability that a reaction R_μ, to first order in δt, occurs within the next time interval δt. To overcome the pratical difficulties of solving the master equation, we construct a *joint propability density function* (PDF) $P(\tau, \mu)$ on the space $0 \leq \tau < \infty$ and $\mu = 1, 2, \ldots, M$. This PDF is defined by $P(\tau, \mu)\mathrm{d}\tau$, which gives the probability at time t that the next reaction occurs within time interval $(t + \tau, t + \tau + \mathrm{d}\tau)$ and that this reaction is an R_μ reaction. The joint PDF can be given as the product

$$P(\tau, \mu)\mathrm{d}\tau = P_0(\tau) \cdot a_\mu \mathrm{d}\tau \,, \tag{3.6}$$

with $P_0(\tau)$ being the probability that no reaction will occur in $(t, t+\tau)$, and $a_\mu \mathrm{d}\tau$ being the probability that reaction R_μ occurs in $(t + \tau, t + \tau + \mathrm{d}\tau)$. The probability that none of the reactions $R_1, \ldots, R_m$ occurs in a time interval $(t, t + \epsilon)$ is equal to

$$\prod_{\mu=1}^{M} \left(1 - a_\mu \epsilon + O(\epsilon)\right) = 1 - \sum_{\mu=1}^{M} a_\mu \epsilon + O(\epsilon) \,. \tag{3.7}$$

If we divide $(t, t + \tau)$ in K subintervals of equal length ϵ. Then, we obtain

$$\begin{aligned} P_0(\tau) &= \left(1 - \sum_{\mu=1}^{M} a_\mu \epsilon + O(\epsilon)\right)^K \\ &= \left(1 - \sum_{\mu=1}^{M} a_\mu \tau / K + O(K^{-1})\right)^K \,. \end{aligned} \tag{3.8}$$

Taking the limit $K \to \infty$ yields

$$P_0(\tau) = \lim_{K \to \infty} \left\{1 - \left[\left(\sum_{\mu=1}^{M} a_\mu \tau + O(K^{-1})/K^{-1}\right)/K\right]\right\}^K \,, \tag{3.9}$$

which is the limit representation of the exponential function:

$$P_0(\tau) = \exp\left(-\sum_{\mu=1}^{M} a_\mu \tau\right) . \tag{3.10}$$

Finally, we arrive at the exact representation of the joint PDF:

$$P(\tau, \mu) = a_\mu \cdot \exp\left(-\sum_{i=1}^{M} a_i \tau\right) \,. \tag{3.11}$$

3.1.3 Monte Carlo Procedure

Monte Carlo procedures allow simulating the stochastic processes described by the PDF $P(\tau, \mu)$. Our implementation is based on the *Direct Method*. We split the two-variable PDF into two one-variable PDFs by

$$P(\tau, \mu) = P_1(\tau) \cdot P_2(\mu|\tau) \,. \tag{3.12}$$

The first part is defined by $P_1(\tau)\mathrm{d}\tau$ as the probability that the next reaction will occur within $(t + \tau, t + \tau + \mathrm{d}\tau)$. The PDF is given by summing $P(\tau, \mu)\mathrm{d}\tau$ over all μ:

$$P_1(\tau) = \sum_{\mu=1}^{M} a_\mu \exp\left(-\sum_{\mu=1}^{M} a_\mu \tau\right) = a_{\mathrm{sum}} \exp\left(-a_{\mathrm{sum}}\tau\right) \,, \tag{3.13}$$

with the notation $a_{\mathrm{sum}} = \sum_{\mu=1}^{M} a_\mu$ with $0 \leq \tau < \infty$. The second PDF $P_2(\mu|\tau)$ is the probability that R_μ is the next reaction which will be executed. Using Eq. (3.11) yields

$$P_2(\mu|\tau) = \frac{a_\mu}{a_{\mathrm{sum}}} \,. \tag{3.14}$$

The concept of the direct method is to calculate the time step τ according to $P_1(\tau)$ and the reaction index μ according to $P_2(\mu|\tau)$ using two random numbers r_1, r_2. One way to obtain random numbers that follow a certain probability distribution is based on the inversion method. Consider the probability function

$$F(x) = \int_{-\infty}^{x} P(x')\mathrm{d}x' \,, \tag{3.15}$$

with $F(x_0)$ being the probability that x will be less than x_0. The inversion method uses an uniformly-distributed random number $r \in (0, 1)$ to obtain x which satisfies $F(x) = r$, i.e.

$$x = F^{-1}(r) \,. \tag{3.16}$$

Thus, we obtain the time step τ from r_1 by

$$\tau = -\frac{\ln(r_1)}{a_{\mathrm{sum}}} \,. \tag{3.17}$$

$P_2(\mu|\tau)$ is a discrete probability density function. Thus, the probability is given by a summation instead of an integration:

$$F(i) = \sum_{j=-\infty}^{i} P(j) \,. \tag{3.18}$$

We choose reaction R_i for which

$$\sum_{j=1}^{i-1} P(j) < r_2 \leq \sum_{j=1}^{i} P(j) \,. \tag{3.19}$$

Inserting Eq. (3.14), the condition for the determined rate is

$$\sum_{j=1}^{i-1} a_j < r_2 a_{\mathrm{sum}} \leq \sum_{j=1}^{i} a_j \,. \tag{3.20}$$

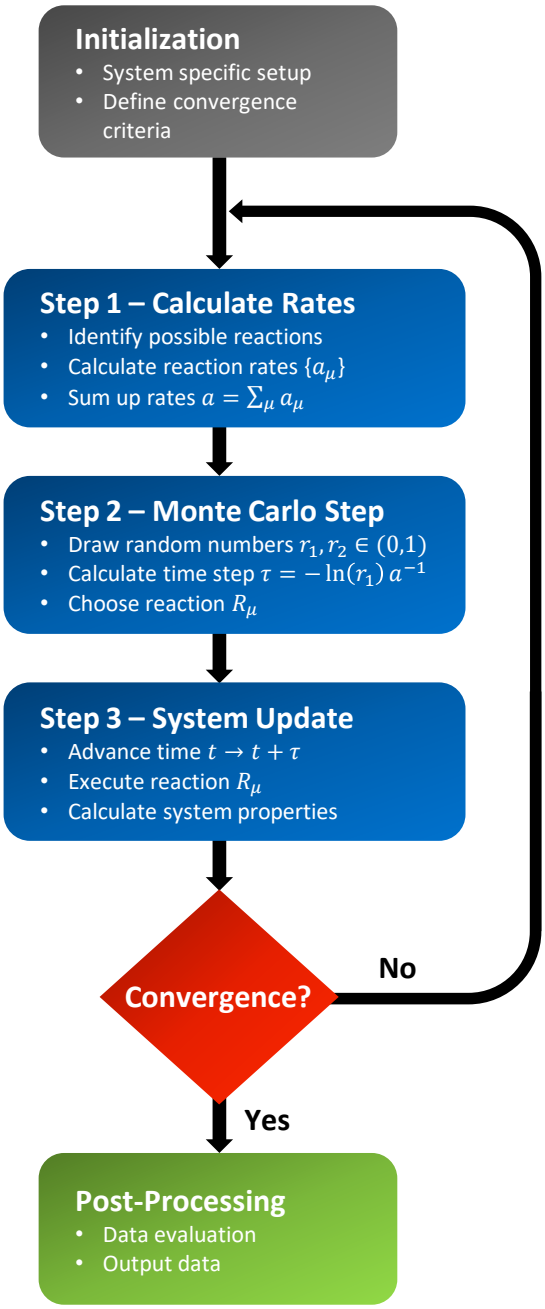

Figure 3.3 Flowchart of the Gillespie algorithm for kinetic Monte Carlo simulations.

3.1.4 Implementation

Given rates, the kMC algorithm is straightforward and can be reduced to the following scheme. Figure 3.3 visualizes the important steps of the kMC loop in a flowchart.

- Initialize the physical system and specify all node properties. Define all parameters that are required for the calculation of the transition rates. Define convergence conditions such as a stopping time $t_{\max}$.
- Identify all possible transitions $R_{i\to j}$ for the current system state $\mathbf{x}_i$ and calculate the transition rates a_{ij}. Sum up all available transition rates $a_{\text{sum}} = \sum_j a_{ij}$.
- Draw two uniformly distributed random numbers $r_1, r_2 \in (0, 1)$. r_1 gives the time passed before the transition occurs, given by
$$\tau = -\frac{\ln(r_1)}{a} \,. \tag{3.21}$$
The second number r_2 chooses the transition μ which fulfills the condition
$$\sum_{j=1}^{\mu-1} a_{ij} < a_{\text{sum}} r_2 \leq \sum_{j=1}^{\mu} a_{ij} \,. \tag{3.22}$$
- Advance the simulation time t by τ and execute transition μ.
- Check if the convergence conditions are fulfilled. If convergence is reached, the simulation stops and post-processing of the particle trajectories is performed. Otherwise, the kMC loop (Step 1-3) is repeated.

The kMC method provides a simple algorithm and can easily be applied to a variety of systems. Note that a correct description of the physical rates is crucial to obtain an accurate system evolution dynamics.

3.2 System Setup

3.2.1 Discretization of the Organic Semiconductor

The active layer of organic semiconductors within electronic devices needs to be represented by a discrete set of *sites*. Each site represents one quantum state, either a single molecule or a conjugated segment within a polymer chain. In many existing kMC models, the active layer is modeled as a cubic lattice [29, 44, 47, 185]. This allows to capture plenty of properties such as the charge carrier mobility [29], jV-characteristics in OSCs [44], or more fundamental properties such as the origin of charge transport in mixed donor:acceptor phases [36, 59]. However, organic semiconductors mostly consist of amorphous or regio-regular polymers or small molecules. A cubic lattice model may not describe all experimentally observable features in their details. The aim of developing a model representing all observable geometric features inside realistic organic thin films demands an off-lattice representation of the molecular structure. This allows including the directionality of charge transport within e.g. semi-crystalline semiconductors and spatial disorder in solution-processed organic thin films into kMC simulations. In addition, thanks to the rapidly increasing amount of computational power and powerful clusters, investigations on the detailed structure of organic materials and their influence on the physical properties using molecular dynamics (MD) have gained interest in the community [20, 186, 187]. This raises the demand of an off-lattice representation for kMC studies [29, 49, 188, 189].

For a representative model of the active organic layer, the implementation of the Voronoi tessellation is used to go beyond cubic lattice models [190, 191]. The detailed system set-up is summarized in the following:

1. **Set-up of the Simulation Box** - The dimensions of the simulation box are specified. In all simulations, an orthorhombic simulation box is specified with dimensions $a \times b \times c \in \mathbb{R}^3$. Units are specified in [nm]. One needs to specify if periodic boundaries shall be applied for each dimension.

2. **Site Distribution** - Then, the sites need to be distributed. The following options for the site distribution were implemented: (i) sites can be distributed in a cubic arrangement with constant lattice spacing a_0; (ii) sites can be distributed with equidistant spacing in every dimension, i.e. $a_0 \neq b_0 \neq c_0 \in \mathbb{R}^3$; (iii) sites are randomly distributed with a certain site density as input (n_0); (iv) sites can be loaded from an input file such as a post-processed MD snapshot to represent the center of mass of the molecules within the snapshot. Each site has a unique ID $i \in \mathbb{N}$ and the position is stored as ($\mathbf{r}_i = (x_i, y_i, z_i)^T$).

   In device simulations for OSCs, contact layers are placed on the bottom and at the top of the simulation box with equidistant spacing. So far, all OSC simulations were performed using a cubic lattice with a lattice spacing of 1 nm. Thus, the contact was also represented by a cubic grid with a spacing of 1 nm.

3. **Connectivity** - Using the Voronoi cell library of Rycroft [192], next-neighbors of each site are computed. In Fig. 3.4, the procedure is shown for the cubic lattice (left) and the non-cubic Voronoi set (right) in a simple 2D representation. Starting from an arbitrary site, the perpendicular bisectors to all neighboring sites in proximity are computed. The algorithm obtains the volume closest to the considered starting point, named Voronoi cell, as known from the Wigner-Seitz cell in periodic crystals (see Fig. 3.4,left). All neighboring sites sharing one face with the considered Voronoi cell are taken as next-neighbors. The knowledge of these is fundamental for the computation of all physical rates.

   Every Voronoi cell i is defined by its volume V_i, the IDs j to the adjacent Voronoi cells, and the interface areas A_{ij}. For the computation of the charge transport, next-neighbors need to be identified. In our method, we label neighboring cells sharing one face as next-neighbors. In Fig. 3.4, the red spheres outside of the drawn tessellation are taken as next-neighbor sites. While each site in the cubic lattice has six next-neighbors, the coordination number increases in case of a non-cubic Voronoi tessellation.

   For each site, we store a vector of pointers to the next-neighbors, the nearest-neighbor distances, the volume V_i as well as the face-areas A_{ij}. For some physical processes such as the *Variable-Range-Hopping* or *Förster-Resonant Energy Transfer*, the model needs to compute the transition rates for the particle transfer to all sites within a certain distance. Thus, a vector of neighbors within a radius of R_N is stored.

4. **Site Occupation** - The site occupation flag stores if a particle occupies the site at the current simulation time step. Additionally, the type of particles is stored. In OSCs, typical charge densities are far below the site density. Due to the low permittivity, the Coulomb interaction of particles on adjacent sites is of hundreds of meV. Thus, we only allow one particle to occupy a site at a time. This has the following consequences:

   Hopping rates to an occupied site are set to zero to avoid hopping into the already occupied site. If adjacent sites are occupied by an electron and a hole, charge recombination is activated. Otherwise, recombination is set to zero. Also, exciton generation at an occupied site is prohibited.

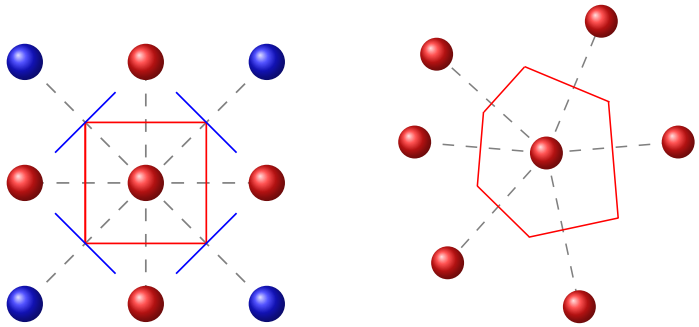

Figure 3.4 Visualization of the next neighbor generation in a cubic lattice (left) and a Voronoi tessellation (right). For most physical processes, only the nearest-neighbors, highlighted in red color, are considered. The blue lattice sites do not define the Voronoi cell, thus they are not labeled as next neighbors. Reprinted with permission from [182].

5. **Site Material** - Each site represents a quantum state of the organic semiconductors. All material parameters are stored within the site, e.g., the HOMO and LUMO energies, localization lengths, reorganization energies, Förster radius, and many more.

6. **Event Counters** - Finally, all event counters and 'analog counters' need to be specified. Here, two types of counters are distinguished: site-counters and neighbor-counters. The site-counters track all properties which occur on this site, e.g. exciton generation, exciton decay, hole/electron occupation time, and many more. Neighbor-counters track the events which occur between neighbors, such as hopping, exciton diffusion, or exciton separation.

3.2.2 Morphology Generation

Controlling the morphology of OSCs is crucial for efficient exciton dissociation at the donor:acceptor interface and charge transport to the electrodes [26, 45, 193]. After setting up the simulation box and distributing the sites, the active layer morphology has to be implemented. Here, different morphologies have been studied:

- Donor:Acceptor Bilayer
- Bulk-Heterojunction
- Planar-Mixed Heterojunction
- Polymer Chains
- Dilute Donor Morphology

The generation methods used for the mentioned morphologies are outlined in the following section.

Bilayer Morphology

The bilayer morphology is the simplest to implement. The user specifies the two materials which are used for top layer and the bottom layer, as well as the position of the interface, z_{int}. All sites with $z_i \geq z_{\text{int}}$ are assigned as the top layer material, all sites with $z_i < z_{\text{int}}$ are assigned as bottom layer.

Bulk-Heterojunction

The bulk-heterojunction morphology is generated using the Kawasaki spin-exchange algorithm [46, 52]. All sites within the photoactive layer are randomly assigned with either spin-up (↑) or spin-down (↓) flag. This flag denotes the polarity of the material. One can choose the ratio of spin-up and of spin-down materials to vary the donor:acceptor ratio. This ratio remains throughout the following steps.

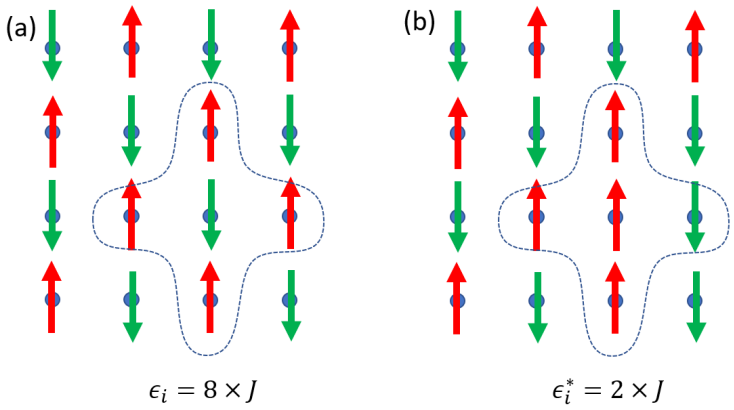

Figure 3.5 Visualization of the bulk-heterojunction generation by the spin-exchange algorithm.

A sketch of the spin-exchange algorithm is visualized in Fig. 3.5. Let us assume that the algorithm start in the fully mixed phase in which each site is surrounded by spins of other polarity (see Fig. 3.5a). The algorithm picks a random site i and one of its neighbors j. Site i is in the center of the dashed shape. All neighbors j of site i have spin-up configuration, while site i is of spin-down configuration. Now, the energy of this configuration is calculated [194]:

$$\epsilon_i = -J \sum_j \left(s_i s_j - 1 \right) \ , \tag{3.23}$$

where J is the interaction energy and the summation index j labels all neighbors of site i. The spins $s_{i/j}$ can take values of $+1$ and -1 for spin-up and spin-down, respectively. The initial configuration (Fig. 3.5a) has an energy of $\epsilon_i = 8 \times J$.

Now, the algorithm exchanges the spin of site i with a random neighbor j. If the spins of sites i and j are equal, the algorithm stops and picks another random site. Otherwise, the spins are exchanged (see Fig. 3.5b). Now, the energy of the new configuration is calculated again with result $\epsilon_i^* = 2 \times J$, which means that the spin-exchange caused a relaxation in energy by $\Delta\epsilon = \epsilon_i^* - \epsilon_i = 6 \times J$.

A Monte Carlo step decides if the spin exchange is accepted. The probability for the acceptance of the spin exchange is calculated by

$$P(\Delta\epsilon) = \frac{\exp\left(-\frac{\Delta\epsilon}{k_\mathrm{B}T}\right)}{1 + \exp\left(-\frac{\Delta\epsilon}{k_\mathrm{B}T}\right)} \ . \tag{3.24}$$

Results by Albes [52] suggest the usage of $J = 0.5 \times k_\mathrm{B}T$ for the interaction energy. In our scenario, the probability for the spin exchange is given by 99.75 %. Now, a uniformly distributed random number r_i between 0 and 1 (100 %) is chosen. If $r_i \leq P(\Delta\epsilon)$, the spin exchange is accepted. Otherwise, the spin exchange is rejected and the spins are restored with their initial configuration.

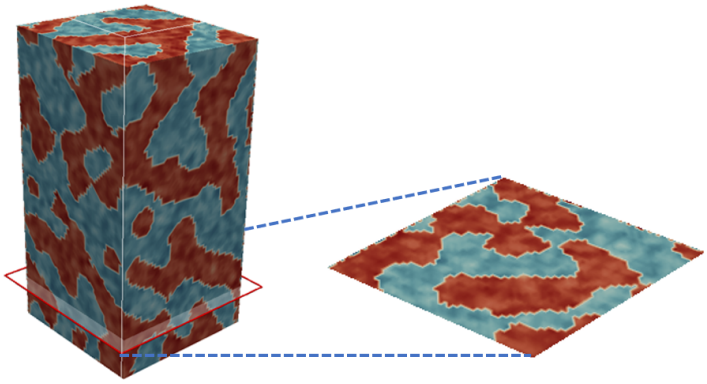

Figure 3.6 Visualization of the three dimensional bulk-heterojunction and the cross-section.

Note that the user needs to specify for each dimension if periodic boundaries need to be used. The spin-exchange algorithm is executed multiple times. To get a feeling of the required number of steps, one MC step is defined by N number of spin exchanges, where N denotes the number of sites within the active layer. Figure 3.6 visualizes the 3D morphology generated using 2000 MC steps.

Planar-Mixed Heterojunction

The planar-mixed heterojunction (PM-HJ) allows more efficient charge collection with respect to BHJ solar cells without downgrading the exciton dissociation efficiency [195]. The generation of the planar-mixed heterojunction is based on the spin-exchange algorithm. First, a BHJ is used as the initial morphology. Then, the BHJ morphology is replaced by two neat layers of thickness t at the top (donor) and the bottom (acceptor) of the morphology. To ensure a smooth morphology, the spin-exchange algorithm is run once again with reduced MC steps.

In Fig. 3.7, a PM-HJ morphology with a neat layer thickness $t = 10$ nm and 300 subsequent MC steps is visualized. The cluster size within the active layer is not changed significantly. The only changes are within the neat donor and acceptor layer at the top and bottom, respectively, of the photoactive layer.

Polymer Chains

In the following, two distinct models for polymer chains are represented. The first model is based on a self-avoiding random walk and has been presented in [182]. The second model employs a pivot algorithm implemented by Albes [52].

Polymers are composed of repeating units forming long chains. One prominent example for polymers used in OSCs is poly(3-hexylthiophene) (P3HT) [10]. Here, a generation algorithm for polymer chains is shown.

The spatial overlap of molecular orbitals leads to weaker bound and less localized electron states along polymer chains [196]. Intrachain transport along a polymer chain is usually faster than interchain transport between chains [197–199]. Vanlaeke *et al.* showed that crystallization of P3HT increases the charge carrier mobility [200]. Sirringhaus and coworkers have demonstrated that the mobility strongly depends on the orientation of crystalline domains in P3HT [201, 202]. Mollinger *et al.* studied charge transport along polymer chains which bridge crystalline domains within semi-crystalline P3HT [188]. However, the probability for leaving the chain is modeled using an effective, field-dependent exit rate

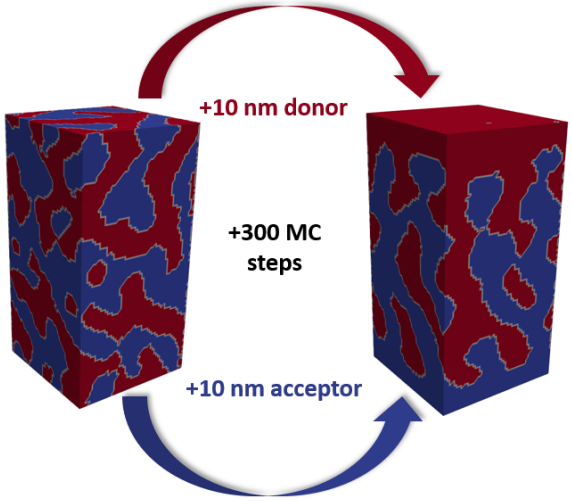

Figure 3.7 Visualization of the three dimensional planar-mixed heterojunction generated from a BHJ.

and does not include neighboring chains. To account for both interchain and intrachain transport, it is necessary to generate a morphology in which all sites along a polymer chain are connected.

Self-Avoiding Random Walk - The first algorithm for the chain morphology generation is based on a self-avoiding random walk [203]. The algorithm starts within a simulation box, in which sites are distributed arbitrarily. First, a free site is chosen, which is not yet part of a polymer chain. Starting from this site, all free nearest-neighbors are determined. Free neighbors are neighbor sites that do not belong to any polymer chain and are of the same material. A neighbor site is randomly chosen and connected to the chain. Every site stores a link to the previous and next chain elements. The free neighbors are determined from the added site, and one randomly picked site is added to the chain. This procedure is repeated until the desired chain length is reached or there are no free neighbors left.

Then a new free site is searched, and the next polymer chain is generated until the whole simulation box is filled with chains. We assume that the chain length in organic semiconductors follows a Gaussian distribution given by an average chain length l_c and a standard deviation of σ_c. The desired chain length for every single chain will then be calculated according to the Gaussian distribution function. Chain length and distribution can be measured by e.g. gel permeation chromatography [204] or static light scattering [205].

According to Carbone and Troisi [197], the orientation of the polymer chains is of importance for the overall transport characteristics of charge carriers in organic semiconductors. One distinguishes between three types of chain models: (i) Gaussian chains are flexible without preferred orientation; (ii) rigid chains that are entirely directed polymers; (iii) worm-like chain model which is a semi-flexible chains with preferred direction. The parameter $\eta \in [0, 1]$ controls the amount of stiffness, where $\eta = 0$ results in flexible Gaussian chains and $\eta = 1$ generates rigid chains. In between, the probability p_+ for connecting sites to the chain along the preferred axis is increased, while in-plain probability $p_\parallel$ or backward growth p_- is reduced. This is captured by the probability equations

$$p_+ = 1 + \eta, \tag{3.25}$$

$$p_\parallel = 1 - \eta, \tag{3.26}$$

$$p_- = \left(\frac{1-\eta}{1+\eta}\right)^2 . \tag{3.27}$$

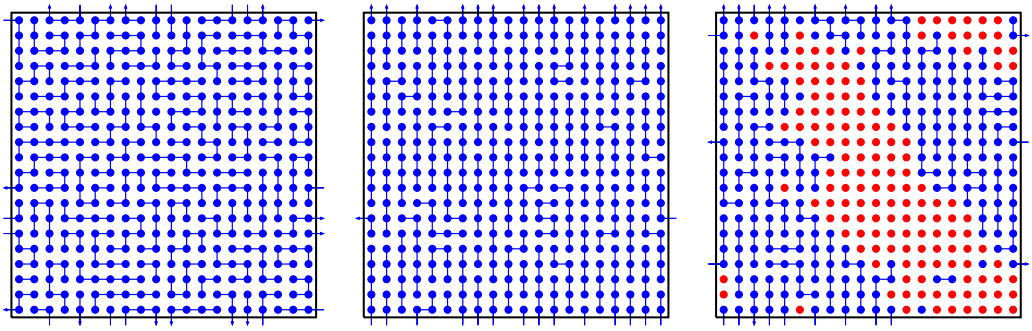

Figure 3.8 Three chain morphologies on a two dimensional 20×20 grid with an average polymer chain length of 6 monomers. Single material with Gaussian chains $\eta = 0$ (left), worm-like chains with preferred orientation $\eta = 0.9$ (middle) and chains in a BHJ where only the blue material is a polymer and the red material is small molecules (right). Reprinted with permission from [182].

Figure 3.8 visualizes (left) a single material morphology with Gaussian chains ($\eta = 0$), (mid) worm-like chains with $\eta = 0.9$, and (right) polymer chains with a BHJ morphology, where the red dots visualize acceptor molecules. The algorithm can be used in arbitrary dimensions. For non-cubic Voronoi tessellations, the distance vector to nearest-neighbor sites is decomposed into in-plane and parallel components. The probability of adding a site to the polymer is obtained by the average of Eqs. (3.25) to (3.27).

Pivot Algorithm - An alternative model to generate polymer chains is given by the Pivot algorithm [206]. This algorithm has been used to generate polymers within dilute donor OSCs within a cubic lattice [52, 59]. Let the lattice constant be a_0 and chain length $L = N \cdot a_0$, where N gives the number of monomers. The number of pivot steps p is specified as an input parameter. The workflow of the algorithm is explained following Fig. 3.9 for a chain of length $L = 6 \cdot a_0$ and $p = 3$:

1. A random pivot site, indicated by the red arrow, is picked (Fig. 3.9a).
2. Randomly pick which part of the chain, i.e. above or below the pivot site, is modified. Here, the green part is to be modified.
3. A 90° rotation is applied to all sites of the green part of the chain. The direction of the rotation is picked randomly. The blue arrow denotes the direction of the orientation.
4. Optional: If one wants to generate isolated polymer chains, the algorithm checks if the modified chain touches other chains.
5. Increment the number of executed steps k. Repeat the procedure until $k = p$.

The final polymer chain is visualized in Fig. 3.9d.

Phosphorescent Sensitizers

Incorporating phosphorescent sensitizing nanoparticles or molecules, in short PS, into organic semiconductors has led to an increased effective exciton lifetime and moreover, improved the power conversion efficiency within OSCs [207–210]. PS are generated within the simulation box as spherical regions around a random center i. All sites j with distance $r_{ij} \leq R_{\mathrm{PS}}$ are assigned to the PS. The ratio of PS to organic sites defines the volume concentration.

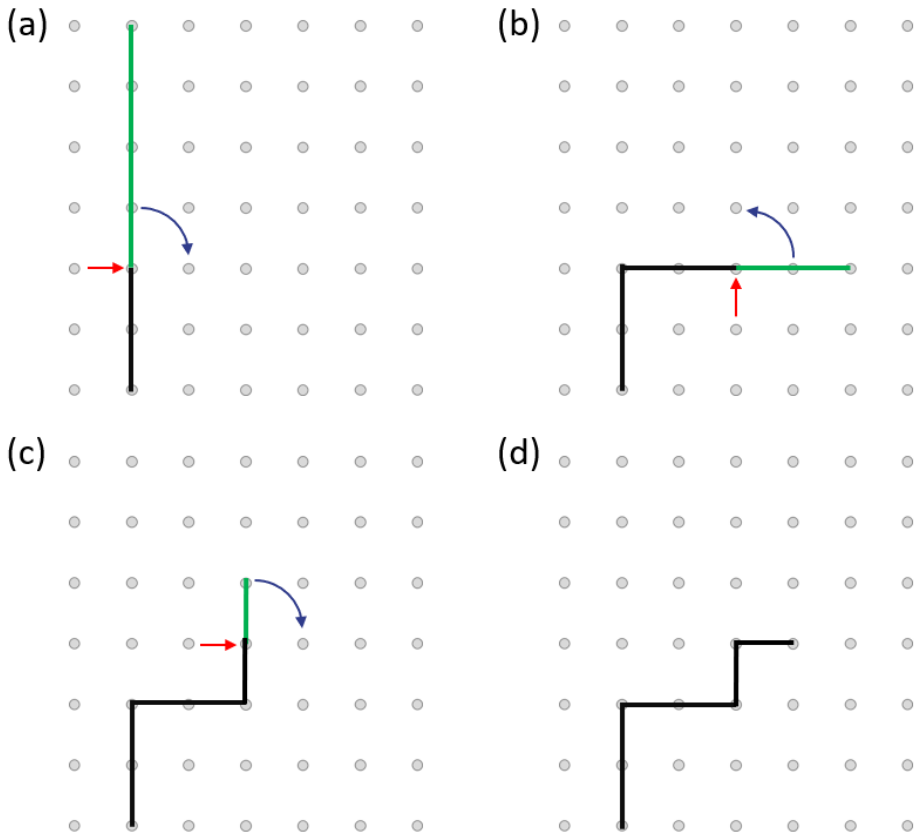

Figure 3.9 Pivot algorithm for the generation of a polymer chain of chain length $N = 6$ with 3 Pivot steps. Adapted from [52].

The strong spin-orbit coupling of the heavy elements of the PS affects excitons within its environment. Thus, a radius of r_{ISC} is specified. All sites within distance r_{ISC} to any PS site are marked as ISC sites. More information about ISC is given in the next section. A BHJ morphology with PS site with a volume concentration of 0.8 vol% is illustrated in Fig. 3.10.

3.3 Physical Process Rates

The transition rates of the physical processes are calculated during each kMC loop. All possible transitions need to be identified, and their values need to be calculated at runtime, accounting for the current system state. The rates depend on the material properties, electrostatic interaction with the environment, or the presence of interfaces or electrodes.

The model includes two classes of particles: charged particles and excitons. Charged particles are electrons and holes, while excitons include singlet and triplet excitons. Each particle stores a pointer on the node on which it is stored, its origin, charge, and the time of creation.

In the following, the transition rates for all processes and their implementation details are summarized.

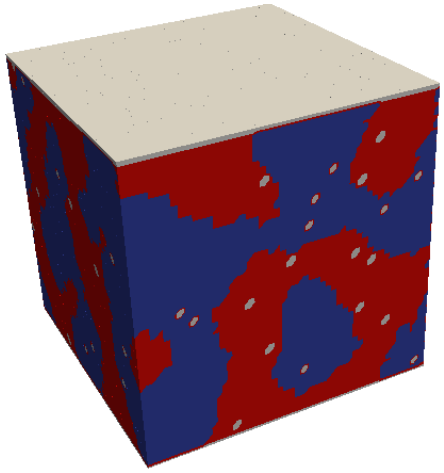

Figure 3.10 Bulk-heterojunction morphology including phosphorescent sensitizer sites (grey spheres) with a volume concentration of 0.8 vol%. Reprinted with permission from [182].

3.3.1 Charge Carrier Hopping

Miller-Abrahams Hopping

The hopping process of a charge carrier on site i to a neighbor site j can be expressed by the Miller-Abrahams equation [27]:

$$a_{\mathrm{MA}} = \sqrt{a_0^i a_0^j}\exp\left(-(\gamma_i+\gamma_j)r_{ij}\right)\begin{cases}\exp\left(-\frac{\Delta E_{ij}}{k_\mathrm{B}T}\right) & \text{if } \Delta E_{ij} > 0\\ 1 & \text{else}\end{cases}, \tag{3.28}$$

with the attempt-to-hop frequency a_0, the inverse localization radius γ, and the energy difference ΔE_{ij}. The attempt-to-hop frequency can be derived in analogy to the random walk given by

$$a_0 = \frac{6\mu k_\mathrm{B}T}{e\,l^2}\exp\left(2\gamma l\right), \tag{3.29}$$

with the mobility μ and the average site distance l. γ accounts for the tunneling character of the charge transfer and captures the overlap integral between adjacent site wavefunctions.

The energy difference in the site energies $E_{i/j}$ is given by

$$\Delta E_{ij} = E_j - E_i = \Delta E_{ij}^{\mathrm{MO}} + \Delta E_{ij}^{\mathrm{F}} + \Delta E_{ij}^{\mathrm{C}}\,. \tag{3.30}$$

The first contribution gives the difference in the molecular orbital energies - HOMO for holes and LUMO for electrons. The second term accounts for the applied bias voltage. In all simulations, a linear potential drop along the device is applied. The last term gives the difference in Coulomb energy. The Coulomb energy in OSC simulations is calculated using the Ewald summation. A detailed description of the implementation and the fundamental theory of the Ewald summation technique is summarized by [48, 52, 211].

This equation can be applied either to nearest-neighbor hopping or to the variable-range-hopping. In the latter case, long-range hopping is allowed. For high γ, long-range hopping is suppressed. Within ordered domains, low γ may allow sufficient long-range hopping.

Marcus Hopping

In his seminal Nobel price work, Marcus has introduced a theory that accounts for stronger coupling between lattice and charges [92]. Because of the low permittivity of organic materials, charges induce local polarizations in the molecules which are described by polarons. The formula for polaron transfer reads

$$a_{ij} = \frac{\left|V_{ij}\right|^2}{\hbar}\sqrt{\frac{\pi}{\lambda k_\mathrm{B} T}}\exp\left(-\frac{(\Delta E_{ij}+\lambda)^2}{4\lambda k_\mathrm{B} T}\right), \tag{3.31}$$

with the reduced Planck's constant $\hbar$, transfer integral V_{ij} and the reorganization energy λ describing the reconfiguration of the molecule due to the deformation by the charge.

The effect of a spatial disorder in disordered semiconductors is included via the site to site distance r_{ij} or the localization constant γ within the Miller-Abrahams rate and via the distance- and orientation-dependent transfer integral V_{ij} in the Marcus rate. The hopping rates are calculated for every particle and all free neighbors. If a particle already occupies a neighboring site, the hopping rate is zero.

The Miller-Abrahams rate provides a generic model for the hopping process modeling the contribution of tunneling and thermal activation by the parameters a_0, γ, and the Boltzmann term, respectively. It is used if hopping is mainly caused by single phonon-assisted tunneling between sites of energy E_i and E_j. Marcus theory accounts for multiphonon hopping processes and includes molecular details within the transfer integral and reorganization energy V_{ij} and λ, respectively. It is frequently used in multiscale studies, as for given organic molecules, the molecular positions and transfer integrals need to be calculated by molecular dynamics and quantum chemical calculations, respectively [20, 49, 212, 213].

3.3.2 Charge Injection

To simulate full device characteristics, such as current-voltage relations of OSCs, charge injection from electrodes needs to be considered. The presented kMC model includes charge injection as a thermionic injection of an electron from the Fermi level of the electrode into the LUMO of an empty site within the organic semiconductor, or by extracting an electron from the HOMO. The thermionic emission model was first studied in detail by Wolf *et al.* [214].

The injection rate of the electrode into a single unoccupied site of the photoactive layer is given as

$$a_{\mathrm{inj,e/h},i} = a_0 \exp\left(-2\gamma r_{c\to i}\right)\begin{cases}\exp\left(-\frac{E_{\mathrm{b,e/h},i}+\Delta E_i^\mathrm{C}}{k_\mathrm{B}T}\right) & \text{if } E_{\mathrm{b},i} > 0\\ 1 & \text{else}\end{cases}, \tag{3.32}$$

with the injection barrier $E_{\mathrm{b,e/h},i}$ from the electrode into the LUMO/HOMO of the adjacent site i, and the change in the Coulomb potential ΔE_i^C at site i before and after the injection of a charge. $r_{c\to i}$ gives the distance between site i and the contact layer.

For electrode C_i (anode and cathode) and for each material $\mathcal{M}_i$ that is present at the interface to the electrode layer C_i an injection rate for holes (h) and electrons (e) is summed up:

$$a_{\mathrm{inj,e/h}}^{C_i,\mathcal{M}_i} = \sum_{i\in\mathcal{M}_i \,\&\, i=\text{next-neighbor}} a_{\mathrm{inj,e/h},i}\,. \tag{3.33}$$

This is of importance to reduce the simulation time during the execution of the injection process. Once an injection rate $a_{\mathrm{inj,e/h}}^{C_i,\mathcal{M}_i}$ is picked, a random site i of material $\mathcal{M}_i$ at the interface to contact C_i is chosen and an electron/hole is injected into the LUMO/HOMO at site i. Note that due to the low

charge densities, the density of occupied sites is very low. It no free site is available, the execution of the process is forbidden and a new event is chosen.

To include the occupation of sites into the calculation of the transition rates, an update mechanism is implemented with user-defined update frequency. One can choose the number of events after which the injection rates $a_{\mathrm{inj,e/h}}^{C_i,\mathcal{M}_i}$ are updated. With this, one accounts for the Coulomb repulsion in case space charges form at the electrode-organic interface.

3.3.3 Charge Collection

Charge collection at the electrodes (anode and cathode) is enabled if a charge carrier resides on a site at the interface to the electrode. In previous studies, a constant collection rate was implemented. However, it is crucial to account for the energy barrier at the interface. As the collection of a charge is the reverse process of the injection, the same rate is used with an inversed energy barrier.

$$a_{\mathrm{inj,e/h},i} = a_0 \exp\left(-2\gamma r_{c\to i}\right) \begin{cases} \exp\left(-\frac{\Delta E_i^{\mathrm{C}} - E_{\mathrm{b,e/h},i}}{k_{\mathrm{B}}T}\right) & \text{if } E_{\mathrm{b},i} > 0 \\ 1 & \text{else} \end{cases} . \tag{3.34}$$

Once the collection is picked, the charge carrier is removed from the active layer.

3.3.4 Exciton Generation

Singlet and triplet excitons can be generated by several mechanisms. In this model, exciton generation upon light absorption, *optical exciton generation*, population of the triplet state by *intersystem crossing*, and generation by recombination of electron-hole pairs, *electrical exciton generation*, are implemented. In addition, triplet excitons may be converted to singlet excitons by triplet-triplet annihilation. Figure 3.11 visualizes the generation rates and the respective excitons, which are generated by each of the generation rates.

Optical Exciton Generation

Singlet excitons are generated optically upon absorption of a photon. Optical excitation of triplets is forbidden due to the spin selection rules. The rate of exciton generation per volume and per unit time requires to account for the attenuation of the light intensity within the photoactive and reflection at interfaces between the photoactive layer and the extraction layers. Thus, a z-dependent exciton generation rate $a_{\mathrm{opt}}(z)$ obtained by the transfer matrix method (TMM) [215–217]. Each layer in the device stack needs to be represented by the refractive index $n(\lambda)$ and the extinction coefficient $\kappa(\lambda)$ as a function of the wavelength λ. The model calculates the generation rate, light intensity, as well as reflectance and transmittance under the AM1.5 solar spectrum.

For the heterojunction morphology of OSCs, the generation rate is set equal in both the donor and acceptor material due to the lack of a complete optical model. The TMM is assuming fully homogeneous layers perpendicular to the light direction. Thus, the generation rate is calculated for each z-layer. If generation at certain z-coordinate is chosen, the x- and y-position of the photon-absorbing site are randomly chosen [13,47]. Note that the site needs to be empty, as no site is allowed to be occupied by more than one particle.

An alternative implementation is a constant exciton generation rate. This is mainly used for test purposes and for the parametrization of exciton diffusion properties. In the input file, a constant generation rate $a_{\mathrm{exg},0}$ with unit [$\mathrm{nm^{-3}s^{-1}}$] is specified. The total generation rate is calculated by

$$a_{\mathrm{exg}} = a_{\mathrm{exg},0} \times V_{\mathrm{osc}} , \tag{3.35}$$

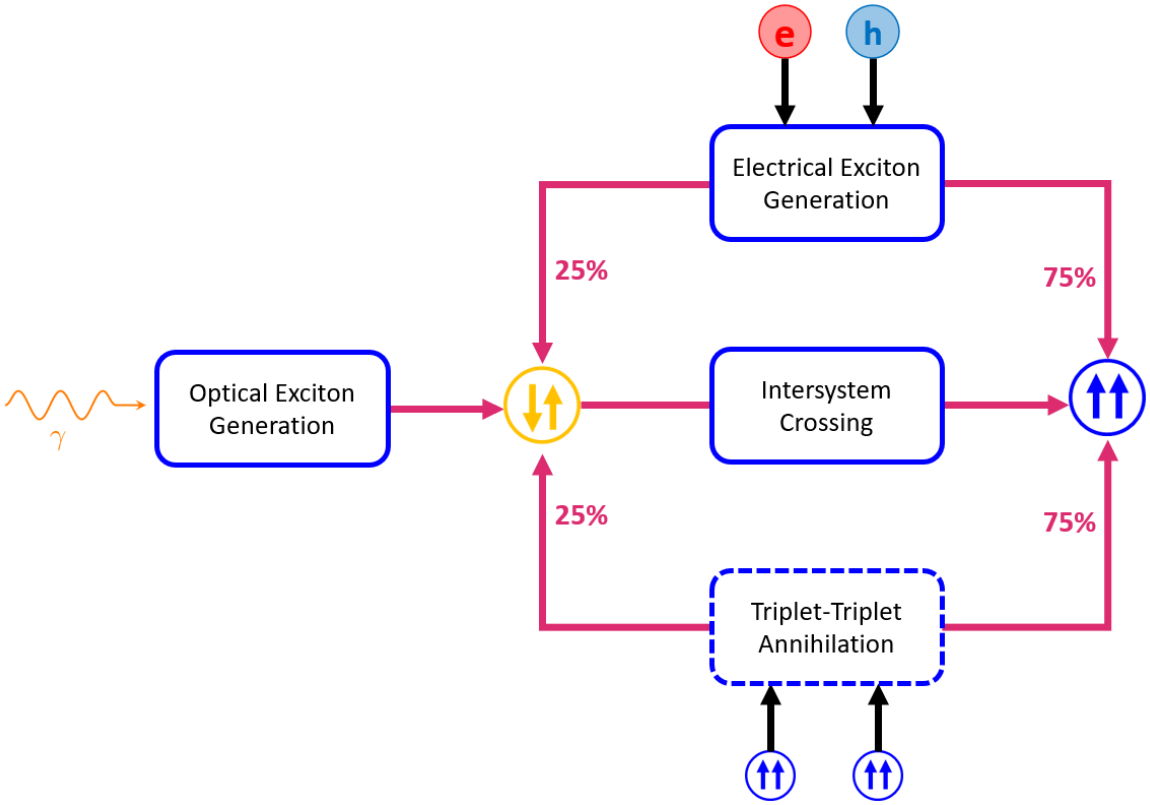

Figure 3.11 Physical processes for the generation of singlets (yellow circle) and triplets (blue circle): optical generation rate, intersystem crossing, electrical exciton generation, and triplet-triplet annihilation (TTA). Electrical exciton generation occurs upon recombination of an electron-hole pair. Absorption of a photon induces an optical exciton generation in form of a singlet exciton. TTA is labeled by dashed lines, as it is considered as a lost mechanism, but it can convert triplets to singlets.

where V_{osc} is the volume of the simulation box of the photoactive layer.

Intersystem Crossing (ISC)

The conversion of singlet into triplet excitons requires an inversion of an electron spin. In usual polymers, ISC is rather low. The usage of heavy-atom molecules can strongly enhance it due to their strong spin-orbit coupling. In our implementation, intersystem crossing is enabled within radius r_{ISC} around a phosphorescent sensitizer. When a singlet exciton resides in this radius, the intersystem crossing rate is calculated using a distance-dependent rate:

$$a_{\text{ISC}} = a^0_{\text{ISC}} \exp\left(-\frac{2r_{i\to d}}{r_{\text{ISC}}}\right), \tag{3.36}$$

with the ISC frequency a^0_{ISC}, and the distance $r_{i\to d}$ from site i and the PS residing at site d. We assume an exponential decrease in the ISC rate with the distance $r_{i\to d}$ to a PS site d to account for the attenuation of the spin-orbit coupling with distance. If ISC occurs, the singlet exciton is converted into a triplet exciton. The position of the exciton does not change.

In our implementation, we do not account for the reverse process. The reverse rate is expected to be less probable due to the exchange energy ΔE_{ST}, as visualized in Fig. 2.20. As the rate scales with $\exp\left(-\Delta E_{\text{ST}}/(k_{\text{B}}T)\right)$, the reverse ISC is expected to be much lower than the ISC rate.

Electrical Exciton Generation

Singlet and triplet excitons can be formed by electrical exciton excitation. Charge carriers, which are either injected from the electrodes or generated by exciton dissociation, may diffuse through the active layer under the electrostatic interaction with charge carriers in the environment. If an electron and a hole meet at adjacent sites, they can recombine into a singlet or triplet state depending on their spin configuration [8]. The electrical exciton generation is modeled as a hopping of an electron (hole) on a site which is occupied by a hole (electron). This charge transfer is modeled by a Miller-Abrahams rate [27]:

$$a_{\mathrm{el,gen}} = a_0 \exp\left(-2\gamma r_{ij}\right) \begin{cases} \exp\left(-\frac{\Delta E_{ij}}{k_\mathrm{B}T}\right) & \text{if } \Delta E_{ij} > 0 \\ 1 & \text{else} \end{cases}, \tag{3.37}$$

with the distance r_{ij} of the charge transfer. The involved electron and hole are labeled with a fixed spin configuration ($\uparrow$ or $\downarrow$). For the sake of simplicity, all injected holes are assigned with fixed spin-down configuration. For electrons, the spin state is chosen randomly between spin-up:spin-down states. We chose a 1:3 ratio to mimic the 1:3 ratio of singlet generation to triplet generation. The energy difference ΔE_{ij} is given by

$$\Delta E_{ij} = E_\mathrm{B}^{s/t} + E_j^\mathrm{MO} - E_i^\mathrm{MO} - E_\mathrm{CT}\,, \tag{3.38}$$

with the singlet/triplet binding energy $E_{\mathrm{B},j}^{s/t}$, the CT state energy E_CT, and the molecular orbital energies $E_{i/j}^\mathrm{MO}$ at initial site i and final site j. If an electrical generation event is picked, electron and hole are removed and a singlet/triplet exciton is generated at site j.

3.3.5 Exciton Decay

Excitons can decay radiatively, by fluorescence and phosphorescence, and non-radiatively. Singlet excitons decay radiatively within a short lifetime of nanoseconds, known as fluorescence. In contrast, triplet excitons only recombine radiatively if a spin-flip occurs. As the spin selection rules forbid a spin-flip, radiative recombination, known as phosphorescence, of triplet excitons occurs on a larger timescale of micro- to milliseconds. The decay of both types of excitons is modeled using a constant decay rate given by the inverse lifetime:

$$a_\mathrm{dec}^\mathrm{S/T} = \tau_\mathrm{S/T}^{-1}\,. \tag{3.39}$$

Within r_ISC, the triplet decay rate is raised to account for the allowed spin-flip in the presence of the high spin-orbit coupling.

3.3.6 Triplet-Triplet Annihilation (TTA)

Excited triplet states can decay monomolecularly or bimolecularly [8]. Triplet-triplet annihilation (TTA) is a bimolecular annihilation process. If two triplets meet, they form an excited triplet-triplet pair (TT^*). The spin properties of TT^* were discussed in section 2.5.6. One triplet exciton decays into the ground state, while the second triplet relaxes by non-radiative transitions to a singlet or triplet excited states $\mathrm{S}_1/\mathrm{T}_1$ depending on the spin angular momentum of the triplet-triplet pair [154, 158, 218, 219]. The relaxation occurs immediately. We consider the following processes:

$$\mathrm{T}_1 + \mathrm{T}_1 \rightarrow \mathrm{S}_0 + \mathrm{T}_1\,, \tag{3.40}$$

$$\mathrm{T}_1 + \mathrm{T}_1 \rightarrow \mathrm{S}_0 + \mathrm{S}_1\,. \tag{3.41}$$

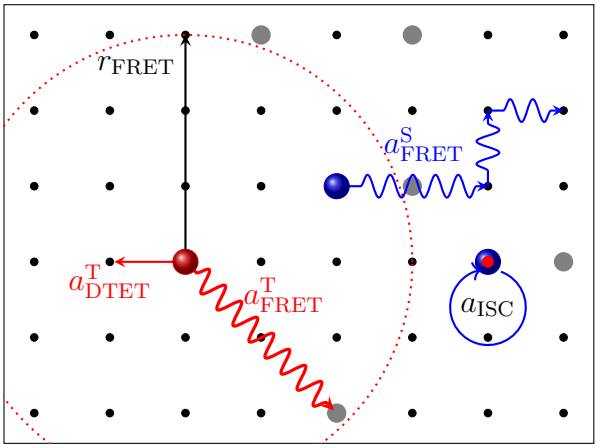

Figure 3.12 Schematic diagram illustrating the diffusion mechanisms of singlet (blue spheres) and triplet (red spheres) excitons. The black dots represent the lattice sites of the active layer. Gray dots label phosphorescent sensitizer sites. The Förster resonant energy transfer is visualized for a triplet exciton between PS sites within the Förster radius r_{FRET}. Dexter type energy transfer is possible between all adjacent sites. Intersystem crossing is visualized for a singlet exciton in proximity to the PS as a conversion of a singlet to a triplet exciton. This graph is adapted with permission from [182].

TTA is activated if two triplet excitons reside on adjacent sites or within the Förster radius of a PS site. TTA is interpreted as a triplet transfer to a site that is occupied by a second triplet. If TTA occurs, one triplet decays to the ground state. The second triplet results in a singlet/triplet with a ratio of 1:3 [154, 219]. The bimolecular TTA rate is modeled as a constant rate of a_{TTA}, which is only activated if the triplets are on adjacent sites or if two triplets reside inside the Förster radius of a PS site.

3.3.7 Exciton Diffusion

Excitons are quasi-particles with a net charge of zero. Thus, they diffuse through the organic semiconductor by energy transfer between sites. Existing kMC models account for exciton diffusion using either Förster resonance energy transfer (FRET), Dexter type energy transfer (DTET), or are based on a random walk [38, 39, 142, 220].

Here, the three transfer mechanisms are implemented: constant diffusion, FRET, and DTET. Both transfer mechanisms are shown schematically in Figure 3.12.

Random Walk

A straightforward and efficient method to include exciton diffusion is to use a constant diffusion rate [41, 48, 52]. This model sufficiently captures the exciton properties in lack of energetic disorder and if the main focus is on the properties of free charge carriers or CT states.

As the electron and hole are strongly bound in an exciton, they are spatially localized on one single site. The diffusion of this neutral particle is based on a 3D random walk described by Einstein-Smoluchowski diffusion [221, 222]. The diffusion coefficient is given by

$$D = \frac{L_{\mathrm{D}}^2}{6\tau}\,, \tag{3.42}$$

with the average diffusion length L_D and lifetime τ of an exciton before decay. The diffusion rate between neighbor sites is given by

$$a_\mathrm{cdiff} = \frac{1}{\tau_\mathrm{diff}} = \frac{6D}{r_{ij}^2}\,, \tag{3.43}$$

where r_{ij} is the distance between neighbor sites.

Förster Resonant Energy Transfer (FRET)

Singlet exciton diffusion occurs by Förster resonant energy transfer (FRET) from an excited donor to an unoccupied exciton acceptor site [8]. FRET is a long-range mechanism, described by a dipole-dipole interaction, and can occur up to several nanometers [135]. The FRET rate is given by [39, 46]

$$a_\mathrm{FRET} = \Gamma \left(\frac{r_\mathrm{FRET}}{r_{ij}}\right)^6 \begin{cases} \exp\left(-\frac{\Delta E_{ij}}{k_\mathrm{B}T}\right) & \text{if } \Delta E_{ij} > 0 \\ 1 & \text{else} \end{cases}, \tag{3.44}$$

with the exciton decay rate Γ, the Förster radius r_FRET, the distance r_{ij}, and difference in exciton binding energies $\Delta E_{ij} = E_{\mathrm{B},j} - E_{\mathrm{B},i}$ between the initial site i and the final site j. At $r_{ij} = r_\mathrm{F}$ and $\Delta E_{ij} = 0\,\mathrm{eV}$, exciton decay and FRET are equally probable.

FRET requires the excitation of an electron in the exciton acceptor site (see Fig. 2.24. For triplet excitons, this requires a spin-flip, which is forbidden by the spin selection rules [8]. Thus, the diffusion of triplet excitons by FRET is forbidden in traditional organic semiconductors [8]. Between PS sites, the spin-selection rules are lifted due to the strong spin-orbit coupling. Thus, triplet diffusion by FRET is allowed between PS sites [8, 114, 223, 224].

The energy difference ΔE_{ij} depends on the distribution of the exciton binding energies. The binding energies can be distributed following a Gaussian distribution with disorder σ_exc.

Dexter Type Energy Transfer (DET)

Dexter type energy transfer (DTET) describes the diffusion of triplet excitons between a site with negligible spin-orbit coupling [133]. It is mediated by exchange interaction between the triplet donating and triplet accepting site, which requires a strong spatial overlap of the wavefunctions. Consequently, it can only occur on short length scales [8, 225]. Its strength decays exponentially with the distance between accepting and donating sites. We model the DTET rate using a Miller-Abrahams like expression [27, 223, 225]:

$$a_\mathrm{DTET} = a_{\mathrm{D},0} \exp\left(-2\gamma r_{ij}\right) \begin{cases} \exp\left(-\frac{\Delta E_{ij}}{k_\mathrm{B}T}\right) & \text{if } \Delta E_{ij} > 0 \\ 1 & \text{else} \end{cases}, \tag{3.45}$$

with the Dexter prefactor $a_{\mathrm{D},0}$, which is used as a fitting parameter, and the inverse localization length γ for charge transport. The energetic difference ΔE_{ij} is computed in the same way as in the FRET rate.

3.3.8 Exciton Dissociation

The dissociation of excitons has been reported to occur on ultrafast timescales of $\approx$ fs [143, 160, 226]. It is of fundamental importance for OSCs to generate free charge carriers from excitons at the donor:acceptor interface. The dissociation of excitons represents the energetically inverse process of the electrical exciton generation. The dissociation is modeled as an electron or hole leaving the exciton

by a hopping process from its current site i to an adjacent site j of different polarity. Different rate expressions are implemented:

- Constant Dissociation Rate
- Dissociation by Miller-Abrahams Transfer
- Dissociation by Marcus Transfer
- Dissociation by Marcus-Levich-Jortner Transfer

The role of the driving force has been highlighted by Unger *et al.* using the Marcus rate and Marcus-Levich-Jortner expression [227].

Constant Dissociation Rate

The constant dissociation rate neglects all energetics and does not fully capture the physics of charge dissociation. Especially in the presence of large free charge densities, exciton dissociation can be even suppressed. However, constant dissociation rates are still applied in plenty of studies [47,48,59]. The transition rate is defined by the inverse of the dissociation time constant, i.e. $a_{\mathrm{diss}} = \tau_{\mathrm{diss}}^{-1}$.

Miller-Abrahams Dissociation Rate

Dissociation rate is also included as a Miller-Abrahams transfer in agreement with existing kMC studies [158, 223, 224]. Here, the energy difference is given by

$$\Delta E_{ij} = E_j^{\mathrm{MO}} - E_i^{\mathrm{MO}} + E_{\mathrm{CT}} - E_{\mathrm{B}}^{\mathrm{S/T}} \,. \tag{3.46}$$

The probability of exciton dissociation is significantly increased at donor:acceptor interfaces. Here, the molecular orbital difference $\Delta E_{\mathrm{MO}} = E_{\mathrm{MO},j} - E_{\mathrm{MO,i}}$ overcomes the high exciton binding energy.

Marcus Dissociation Rate

The Marcus transfer rate is given by:

$$a_{\mathrm{Marcus}} = \frac{|V_{\mathrm{DA}}|^2}{\hbar}\sqrt{\frac{\pi}{\lambda k_{\mathrm{B}} T}}\exp\left[-\frac{(\lambda + \Delta G_0)^2}{4\lambda k_{\mathrm{B}} T}\right] \,, \tag{3.47}$$

with the electronic couling strength V_{DA}, reorganization energy λ, and driving force ΔG_0 with

$$-\Delta G_0 = E_{\mathrm{S}} - E_{\mathrm{CT}} - \Delta E_{\mathrm{i,f}}^{\mathrm{MO}} \,, \tag{3.48}$$

with the difference in molecular orbital energies $\Delta E_{\mathrm{i,f}}^{\mathrm{MO}}$, the singlet energy E_{S}, and the CT energy E_{CT}. This expression assumes that the quantum nature of intramolecular vibrations do not need to be considered [228].

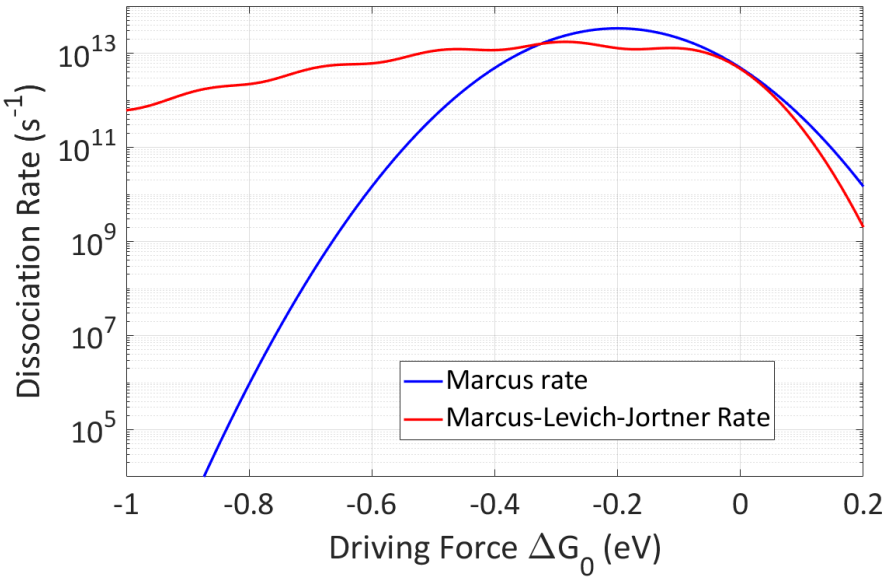

Figure 3.13 Marcus and Marcus-Levich-Jortner dissociation rate as function of the driving force ΔG_0.

Marcus-Levich-Jortner Dissociation Rate

The Marcus-Levich-Jortner (MLJ) equation is given by [228]

$$a_{\mathrm{MLJ}} = \frac{|V_{\mathrm{DA}}|^2}{\hbar}\sqrt{\frac{\pi}{\lambda_0 k_{\mathrm{B}} T}}\sum_{\nu=0}^{\infty}\frac{\exp\left(-S\right)S^{\nu}}{\nu!}\exp\left[-\frac{\left(\lambda_0+\Delta G_0+\nu\hbar\omega\right)^2}{4\lambda_0 k_{\mathrm{B}} T}\right], \tag{3.49}$$

with the Huang-Rhys parameter S, the intermolecular reorganization energy λ_0, and the mean intramolecular vibrational energy of $\hbar\omega$. The intermolecular vibrations are characterized by reorganization energy λ_0.

The energy dependence of the Marcus rate and the MLJ rate are shown in Fig. 3.13 for $V_{\mathrm{DA}} = 30\,\mathrm{meV}$, $\lambda = 0.2\,\mathrm{eV}$, $\lambda_0 = 0.1\,\mathrm{eV}$, $T = 300\,\mathrm{K}$, and $\hbar\omega = 0.186\,\mathrm{eV}$ [227, 229]. Firstly, both rates show a significant dependence on the driving force. If driving forces close to zero exist, constant dissociation rate models fail. Close to zero, both the Marcus and the MLJ rate decrease exponentially. The Marcus rate reaches its maximum if $\Delta G_0 = -\lambda$. In the MLJ-rate, the vibrational modes are clearly visible.

Unger *et al.* argued that the MLJ dissociation rate needs to be used to describe the dissociation rate for systems of large driving forces that are far in the Marcus inverted regime [227]. They justified this argumentation using experimental measurements within MeLPPP:PCBM OSCs, where efficient charge separation occurs despite the presence of large driving forces of $-0.9\,\mathrm{eV}$. At lower driving forces, Marcus and MLJ rates show similar values over a large range of energies.

3.3.9 Recombination

Recombination processes require accurate models as they determine the energy losses in open-circuit voltage and fill factor. Free electrons and holes can recombine if they form a charge transfer (CT) state, which is coupled to the ground state. In the kMC simulations, recombination is only activated if an electron and a hole reside on nearest-neighbor sites. Three different models are implemented: a constant recombination rate, radiative recombination rate, and non-radiative recombination rate. The

constant model is frequently used thanks to its simplicity, while it does not give significant physical insight.

Constant Recombination Rate - Constant recombination rate models are typically employed to limit the lifetime of CT states [13,37,230]. Typical rates that are used in kMC studies are in the range of a_{rec} =10^5 s^{-1} to 10^8 s^{-1}. Such a constant recombination model does not allow us to distinguish the recombination channels. The recombination rate is activated if an electron and a hole reside on adjacent sites, independent of the position within the active layer.

Radiative Recombination Rate - The radiative recombination rate is defined by [23,231]

$$k_{\mathrm{rad}} = \frac{64\pi^4}{3h^3c^3} n^3 \nu_{\mathrm{av}} V_{ij}^2 \Delta\mu^2 \,, \tag{3.50}$$

with the speed of light c, the solvent refractive index n, the matrix coupling element V_{ij}, the difference of dipole moments $\Delta\mu$, and the average emission frequency ν_{av}.

Non-Radiative Recombination Rate - The non-radiative recombination rate can be expressed by the Marcus-Levich-Jortner expression [23,228,231]:

$$k_{\mathrm{non-rad}} = \frac{4\pi^2}{h} V_{ij}^2 \mathrm{FC}(g) \tag{3.51}$$

with the Franck-Condon Factor weighted density of states FC(g) being defined as [231]

$$\mathrm{FC}(g) = \frac{1}{\sqrt{4\pi\lambda_S k_{\mathrm{B}} T}} \sum_{j=0}^{\infty} \frac{\exp(-S) S^j}{j!} \exp\left[-\frac{(jh\nu_\nu + g + \lambda_S)^2}{4\lambda_S k_{\mathrm{S}} T} \right], \qquad \text{with } S = \frac{\lambda_\nu}{h\nu_\nu} \,, \tag{3.52}$$

with h to be Planck's constant and j being the vibrational mode number.

FC represents the sum of the overlap between the CT state with all vibrational modes of the ground state. Each vibrational mode of the ground state offers a channel for the recombination of the CT state. Two types of vibrational modes play a role: intramolecular and intermolecular vibrational modes. Intramolecular vibrational modes are high-frequency vibrations with the reorganization energy $\lambda_\nu \gg k_B T$, thus they need to be treated quantum mechanically. On the other hand, intermolecular vibrational modes show low frequencies with $\lambda_s \leq k_B T$; thus, they are treated classically. If one treats the intramolecular vibrations also classically, the MLJ-expression corresponds to the Marcus transfer rate.

Modeling the dependence of the CT energy within the radiative and non-radiative transitions is of high relevance for the understanding of voltage losses in OSCs [23]. Fig. 3.14 visualizes both recombination mechanisms for (a) high and (b) low CT energies. Non-radiative recombination takes place from the relaxed CT state to the vibrational modes of the ground state. This is indicated by the green overlap areas. The overlap increases for reduced CT energy, which leads to an increase in the non-radiative recombination rate. The voltage loss by non-radiative recombination is given by [23]:

$$\Delta V_{\mathrm{nr}} \propto -\frac{k_{\mathrm{B}} T}{e} \left(-\frac{E_{\mathrm{CT}} - \lambda_S}{\hbar\omega} \right) \,, \tag{3.53}$$

where $\hbar\omega$ gives the vibrational mode energy, and λ_s is the vibrational energy of the solvent. This relation is known as the energy-gap law [231,232].

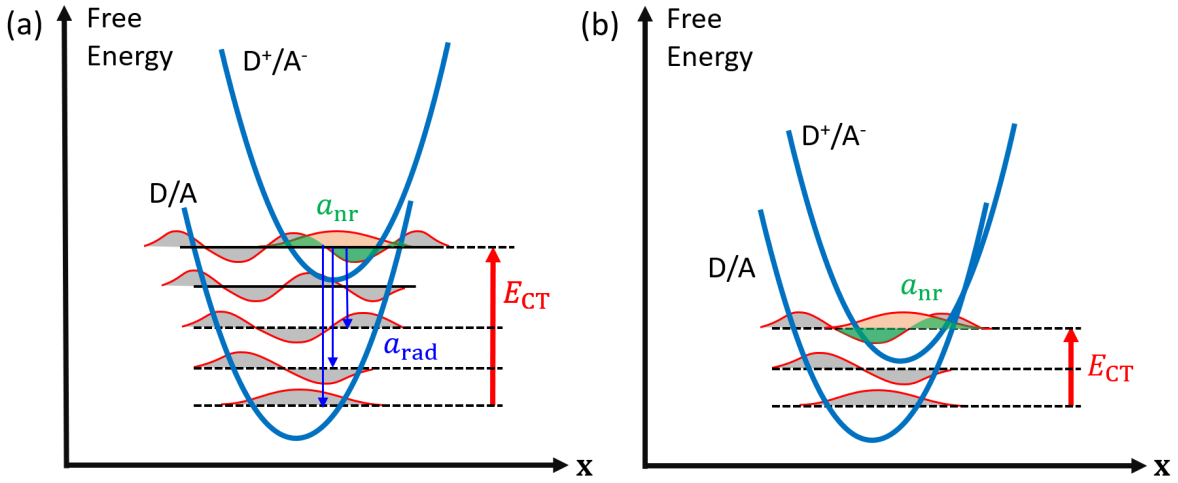

Figure 3.14 Recombination mechanism from the CT state at the donor:acceptor interface (D^+/A^-) to the ground state (D/A). The potential energies of the ground state and the excited CT are assumed as harmonic with the reaction coordinate **x**. The horizontal lines indicate vibrational modes. Non-radiative (a_{nr}) and radiative (k_{rad}) recombination rates are illustrated a for (a) high E_{CT} and (b) low E_{CT}. The transition probability, given by the wavefunction overlap of both states, is highlighted by the green area. Blue arrows indicate radiative transitions. Adapted from [23].

4 Accelerating Kinetic Monte Carlo Simulations

Kinetic Monte Carlo (kMC) simulations are frequently used to study (electro-)chemical processes within science and engineering. Significant problems concerning the computational demand arise if processes with large time disparities are competing. Acceleration algorithms are required to make slow processes accessible. Especially the accelerated superbasin kMC (AS-kMC) scheme has been frequently applied within chemical reaction networks [53]. For larger systems, the computational overhead of the AS-kMC is significant as the computation of the superbasins is done during run-time and comes with the need for large databases.

Here, a novel acceleration scheme for diffusion and transport processes within kMC simulations is proposed. Critical superbasins are detected during the system initialization. Scaling factors for the critical rates within the superbasins, as well as a lower bound for the number of sightings, are derived. The presented algorithm exceeds the AS-kMC in the required simulation time, which is demonstrate for a 1D-chain example. In addition, the acceleration scheme is applied to study the time-of-flight (TOF) of charge carriers within organic semiconductors. In this material class, time disparities arise due to a significant spread of transition rates caused by the on- and off-diagonal disorder. The acceleration scheme allows a significant acceleration up to 2-3 orders of magnitude while keeping the error of the TOF values negligible. The computational overhead is negligible, as all superbasins only need to be computed once. The developed algorithm can be easily extended to more complex transition networks to allow the study of further electronic and electrochemical processes.

Section **4.1** introduces the problem setting and sheds light on existing acceleration schemes. Section **4.2** derives the fundamental theoretical background for the acceleration scheme and introduces the algorithm as well as its implementation. Finally, section **4.3** presents the performance of the developed acceleration scheme for charge transport in 2D amorphous organic semiconductors. The implementation of the algorithm was done by *Manuel GöSSwein*, TUM, under my supervision. I have conceptualized the study and have written the manuscript.

This chapter has been reprinted from 'Acceleration scheme for particle transport in kinetic Monte Carlo methods,' *J. Chem. Phys.*, 152 (17), 2020, pp. 174106 [233], with the permission of AIP Publishing.

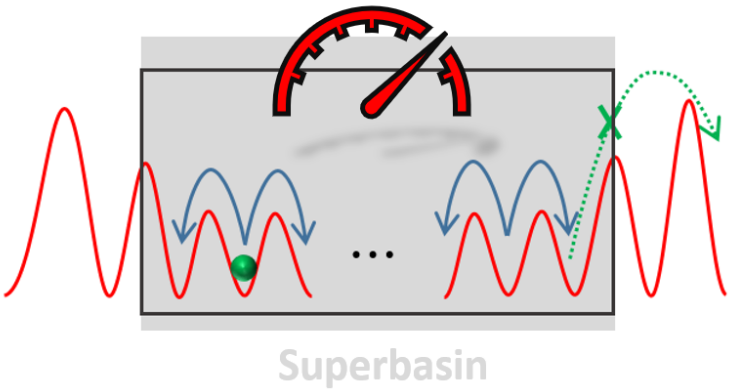

4.1 Background

Many systems of interest in science and engineering show complex stochastic and/or nonlinear behavior. The temporal evolution of these stochastic systems can be described by the master equation which models the system by a set of coupled ordinary differential equations [234]. For small systems, the master equation can be easily solved analytically. However, its applicability for large systems with a time-dependent system state $\mathbf{X}(t)$, e.g. the number of various chemical species at each position in the system of interest, is very limited. Numerical methods are required to obtain the probability density function of the system state $\mathbf{X}(t)$ or to calculate the system evolution in terms of trajectories of $\mathbf{X}(t)$ versus the time t.

Monte Carlo procedures provide a powerful method to obtain trajectories of the stochastic system state. Kinetic Monte Carlo (kMC) methods represent one special class of Monte Carlo procedures to describe the dynamics of a stochastic system. kMC simulations are frequently used within a variety of fields such as chemical reactions networks [173–175], crystal growth [176–178], vacancy diffusion [179–181], and charge transport in disordered materials [29, 50, 182, 235]. The system state in all mentioned applications is described by the number of particles n_j of certain species j, with each particle i being on a position $\mathbf{x}_i$ and having an energy E_i. The evolution of the system is described by transition rates between different system states in its phase space. The transition rates capture the physical laws which are either derived from fundamental theoretical laws or are deduced from empirical observations. Thus, kMC allows bridging different length scales between the atomistic and the device level.

Despite the manifold of capabilities and the simplicity of kMC methods, severe problems arise if the system behavior is dominated by processes occurring on different length- and/or timescales. One example where lengthscale issues may appear is the epitaxial growth of a thin film. While the important physical processes, such as the adsorption of atoms, occur on the (sub-)nanometer scale, micrometer-sized grids need to be used to be able to distinguish if smooth atomic layers or islands are formed. One method to reduce the required size of the simulated box is to introduce periodic boundary conditions (PBCs) [236, 237]. However, if the wavelength of spatial heterogeneities exceeds the computationally feasible number of sites, PBCs cannot capture the full details of the system [238]. Spatial coarse-graining has been frequently used to increase the accessible length scales [239–242].

kMC methods inherently favor events with large transition rates. If several physical processes with very different timescales compete, the faster processes (timescale t_f) will be preferably executed compared to the slow processes (timescale $t_s \gg t_f$). Approximately $N = t_s/t_f$ number of executions of the fast processes are performed before the slow process is chosen. This requires large simulation times to gain sufficient statistics of the characteristics related to the slow process. One popular example of such timescale issues is the simulation of diffusion processes within surface reactions. Typically, diffusion of the respective particles occurs on much faster timescales compared to the reaction rates. Most studies neglect the particle diffusion to keep the simulation times feasible. Timescale problems also arise if several particle species are moving with different velocities due to e.g. different masses. This occurs in all electrochemical systems, where heavy atoms/ions and light electrons are moving under their Coulomb interaction. If this Coulomb interaction is negligible, a rather simple decoupling between the particle species may appear appropriate. However, in low-permittivity materials, this needs to be reconsidered carefully.

Different acceleration schemes have been proposed to allow fast kMC simulations despite the presence of large timescale differences. One method to speed up kMC simulations is τ-leaping [243, 244]. Instead of updating the transition rates after each executed reaction, τ-leaping executes multiple transitions of a certain reaction channel within a time interval of length τ before updating the

propensity function. Thus, the system state and its transition rates are less often updated, which can lead to a substantial up-scaling of the accessible simulation time. The introduced error will be small if the state updates are relatively small [245]. For systems in which diffusion processes are relevant, an extension to the spatial τ-leaping method has been developed [246]. τ-leaping methods are frequently used in chemical reaction networks with a limited number of reaction channels [245, 247, 248]. However, its applicability to large systems with strong heterogeneity and strongly interacting particles is questionable. In these scenarios, small τs are required to keep the error low, which would lead to computational times equal or even larger than the simple 'one reaction per time step' method.

Snyder *et al.* developed the net-event kinetic Monte Carlo method to overcome large disparities in timescales [249]. Fast reversible processes are concatenated into a single net-event, where the net-event reaction rate is observed by multiplying the intrinsic transition rate with the population size of the corresponding species. This leads to a sufficient acceleration. However, this method leads to a significant reduction of the fluctuations in the properties of interest.

Another acceleration is given by the probability-weighted kMC [250]. Hereby, the probability distribution of the system states is modified by the incorporation of a weighted sampling. This increases the sampling efficiency of rare events under the loss of fluctuations in the desired properties. Here, one requires to specify the weighting for the events and requires insight into the importance of the events before running the simulations.

Chatterjee and Voter introduced an acceleration scheme based on the concept of superbasins (AS-kMC) [53]. Their algorithm recognizes system states being trapped and subsequently raises the activation barrier of frequent processes to allow the system to escape the superbasin. Their algorithm determines the superbasins dynamically by sampling the potential energy surface and storing a complete database of processes, including their number of sightings. For systems containing many states and/or particles, this will demand large databases and efficient search algorithms to determine if the system is being trapped in a superbasin. Dybeck *et al.* have modified the accelerated superbasin scheme for the acceleration of simulations of surface catalytic processes [251]. Individual processes are partitioned into reaction channels at the surface of the catalyst nanoparticles. The reaction channel is quasi-equilibrated if the difference between forward and backward transitions falls below a pre-defined limit. Once quasi-equilibrium is reached, the intrinsic rate constants of the reaction channel are reduced. Further scaling mechanisms are summarized within the review of Chatterjee and Vlachos [252].

In this work, we present a novel scaling algorithm for the acceleration of kMC simulations with the focus on particle transport and diffusion. Our algorithm conceptually is based on the work of Chatterjee and Voter [53]. Our method provides significant advantages in terms of computational time and memory demand. The number of transitions within the superbasin is tracked for each particle. If the superbasin is sufficiently sampled, we scale the transition rates of the time-critical processes for the given particle within the local (or global) superbasin. Local and global superbasins are computed during the initialization of the kMC system. Individual scaling factors are calculated for each superbasin to capture (1) their individual geometry and (2) local variations in both the potential energy surface and the rate constants. Global superbasins can also be detected using the original superbasin algorithm by sampling the entire region [53]. In contrast, our method directly detects global superbasins without the need to sample the whole superbasin region.

First, we provide the theoretical fundamentals of the scaling algorithm and derive accuracy limits. Then, the detection algorithm of superbasins, as well as the scaling procedure during runtime, are outlined. We analyze the performance of the novel acceleration scheme with respect to the AS-kMC for a simple superbasin, a 1D-chain of states. Then, we apply the scaling algorithm for one example

from our field of research, namely charge transport within organic semiconductors, and analyze the accuracy as well as the performance of the scaling algorithm.

4.2 Algorithm

4.2.1 Theoretical Background

In this section, we formulate the theoretical fundamentals of the scaling procedure. We assume that the system $\mathcal{S}$ is composed of states $i \in \mathcal{S}$ and that its evolution is described by transition rates $k_{i\to j}$ between state i and a subset of accessible states $j \in \mathcal{S}$ with $j \neq i$.

The disparity in timescales between fast and slow transitions induces a disparity in the corresponding probability fluxes. The probability flux for a transition between states i and j is defined as the product of the probability π_i of residing in state i and the transition rate $k_{i\to j}$:

$$f_{i\to j} = \pi_i k_{i\to j} \,. \tag{4.1}$$

We assume the existence of a superbasin $\mathcal{B} \subseteq \mathcal{S}$ consisting of states $i \in \mathcal{B}$. The relative complement of superbasin $\mathcal{B}$ in $\mathcal{S}$ is denoted as $\mathcal{O} = \mathcal{S} \setminus \mathcal{B}$. If $\mathcal{B}$ has reached quasi-equilibrium, we can describe the probability π_i by the Boltzmann distribution:

$$\pi_i = \frac{\exp(-\beta E_i)}{Z_{\mathcal{B}}} \,, \tag{4.2}$$

with the canonical partition function

$$Z_{\mathcal{B}} = \sum_{k\in\mathcal{B}} \exp(-\beta E_k) \,, \tag{4.3}$$

where E_i is the energy of state i, $\beta = 1/k_{\mathrm{B}}T$, k_{B} is the Boltzmann constant and T is the absolute temperature.

Using Eqs. 4.1 and 4.2, the probability flux for escaping superbasin $\mathcal{B}$ is given by

$$f_{\mathrm{es}} = \sum_{i\in\mathcal{B}, j\in\mathcal{O}} \pi_i k_{i\to j} \,. \tag{4.4}$$

Analogously, the probability flux for a frequent transition within the superbasin is given by

$$f_{\mathrm{c}} = \sum_{i,j\in\mathcal{B}, i\neq j} \pi_i k_{i\to j} \,. \tag{4.5}$$

The index highlights that these frequent transitions are considered *critical* with respect to the simulation time. Based on Eqs. 4.4 and 4.5, we can calculate the probability for an escape

$$p_{\mathrm{es}} = \frac{f_{\mathrm{es}}}{f_{\mathrm{es}} + f_{\mathrm{c}}} \,, \tag{4.6}$$

and the probability for remaining in superbasin $\mathcal{B}$

$$p_{\mathrm{c}} = 1 - p_{\mathrm{es}} \,. \tag{4.7}$$

The main advantage of our theoretical consideration with respect to the AS-kMC is the reduction of an arbitrarily large superbasin to a single escape probability p_{es}.

In general, superbasins are characterized by a low escape probability $p_{\mathrm{es}} \ll 1$ and a high critical probability $p_{\mathrm{c}} \to 1$. Based on the binomial distribution, the probability for the occurrence of N_{f} successive critical transitions is given by

$$p_{\mathrm{c}}^{N_{\mathrm{f}}} = (1 - p_{\mathrm{es}})^{N_{\mathrm{f}}} \geq \delta \,, \tag{4.8}$$

with the error measure $0 < \delta < 1$. In other words, δ specifies a confidence interval of $(1 - \delta)$. Taking the natural logarithm yields

$$N_{\mathrm{f}} \ln(1 - p_{\mathrm{es}}) \geq \ln(\delta) \,. \tag{4.9}$$

As $p_{\mathrm{es}} \ll 1$, we can simplify Eq. 4.9 by replacing the natural logarithm by its first-order Taylor expansion

$$p_{\mathrm{es}} \leq \frac{1}{N_{\mathrm{f}}} \ln\!\left(\frac{1}{\delta}\right) . \tag{4.10}$$

Relation 4.10 can be considered as an upper bound for p_{es} for being critical. Using Eqs. 4.6 and 4.7, it follows that

$$\frac{p_{\mathrm{c}}}{1 - p_{\mathrm{c}}} \geq \frac{N_{\mathrm{f}}}{\ln(1/\delta)} - 1 \,. \tag{4.11}$$

To accelerate the simulation in the presence of superbasins, the probability flux f_c of critical transitions must be lowered. This can be achieved by introducing a scaling factor $\alpha > 1$ for the transition rates within $\mathcal{B}$. Rate constants of critical transitions $k_{\mathrm{c}} \in \left\{k_{i \to j} | i, j \in \mathcal{B}\right\}$ are lowered using α:

$$k_{\mathrm{c}}^{(m)} = \frac{k_{\mathrm{c}}}{\alpha^{(m)}} \tag{4.12}$$

where the index m implies that the activation barriers in the superbasin are raised multiple times. Note, that both the forward and the reverse transtion rate between states $i \in \mathcal{B}$ and $j \in \mathcal{B}$ have to be scaled to preserve the *detailed balance*.

The concrete value for the scaling factor is determined by the relative error of the critical probability

$$\Delta p_{\mathrm{c}} = \frac{p_{\mathrm{c}} - p_{\mathrm{c}}^{(1)}}{p_{\mathrm{c}}} = \frac{(\alpha - 1) f_{\mathrm{es}}}{\alpha f_{\mathrm{es}} + f_{\mathrm{c}}} \leq \delta \,, \tag{4.13}$$

with

$$p_{\mathrm{c}}^{(1)} = \frac{f_{\mathrm{c}}/\alpha}{f_{\mathrm{es}} + f_{\mathrm{c}}/\alpha} = \frac{f_{\mathrm{c}}}{\alpha f_{\mathrm{es}} + f_{\mathrm{c}}} \,, \tag{4.14}$$

which is required to be less or equal to δ. Solving the inequality 4.13 yields an upper bound for the scaling factor α:

$$\alpha \leq \frac{\delta f_{\mathrm{c}} + f_{\mathrm{es}}}{f_{\mathrm{es}}(1 - \delta)} = \frac{1}{1 - \delta}\left(1 + \delta \frac{p_{\mathrm{c}}}{1 - p_{\mathrm{c}}}\right) . \tag{4.15}$$

Finally, Eqs. 4.11 and 4.15 can be used for calculating a conservative value for N_{f}. Inserting the smallest value of Eq. 4.11, one obtains

$$N_{\mathrm{f}} \geq \ln\!\left(\frac{1}{\delta}\right)\left(1 - \frac{1}{\delta} + \frac{1 - \delta}{\delta}\alpha\right) . \tag{4.16}$$

This can be considered as the number of critical sightings within a superbasin required to allow an accurate downscaling of the corresponding rate constants. We visualize the limits for α and N_{f} in dependence of the error measure δ and p_{c} in Fig. 4.1.

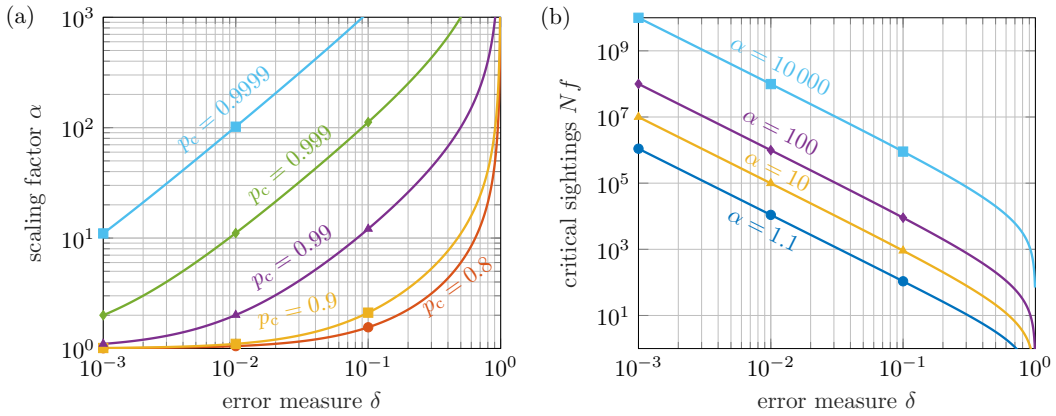

Figure 4.1 (a) Upper limits for the scaling factor α and (b) lower limits for the number of critical sightings N_f in dependence on the error measure δ. p_c gives the critical probability within a superbasin. Reprinted from [233], with the permission of AIP Publishing.

4.2.2 Implementation

As a concrete example of a diffusion process, let us consider the transport of charge carriers in organic semiconductors. In this showcase, we have to deal with two exemplary disparities in timescales:

(1) Tail states of the density of states (on-diagonal disorder) and variations in the coupling of molecules (off-diagonal disorder) induce *local* trap states for the charge carrier.

(2) Heterogeneities due to phases of different order or material blends induce *global* disparities.

At first, the set-up of the organic semiconductor model and the mentioned time disparities will be explained in detail. Subsequently, the algorithms for finding local and global superbasins will be outlined. Concluding, the integration of the scaling procedure within the rejection-free kMC algorithm will be shown.

System Set-Up

Charge transport in amorphous organic semiconductors occurs by phonon-assisted hopping between adjacent molecules or conjugated segments of polymers [18]. Hopping is strongly affected by the energies and the structure of the molecules. Both are subject to local variations due to low-temperature processing and the 'soft' nature of molecules. Molecular orbitals (MO) are affected by polarizations of surrounding molecules and strongly depend on their conjugation. Local variations in these properties affect the energies of the frontier orbitals, the highest and lowest molecular orbital energies HOMO and LUMO, respectively. Such variation is known as the on-diagonal energetic disorder. Another source of disorder is due to variations in the distance between molecules caused by the lack of structural order. Especially within non-spherical molecules, charge transport strongly depends on the orientation of adjacent molecules [212, 253]. Local variations in the coupling between molecules are often labeled as an off-diagonal disorder [29]. Charge transport in organic semiconductors is frequently modeled using the Gaussian disorder model (GDM) [29]. The GDM models charge transport by sequential hopping through a disordered lattice with an on-diagonal energetic and an off-diagonal disorder.

In this work, we analyze charge transport within a 2D-lattice of 100 nm × 100 nm with a grid spacing of 1 nm. Each lattice point describes a localized electronic state on one (or a few) molecules. We initialize a charge carrier at $x = 1$ nm and random y, and apply the voltage V_{ext} along x-direction. We

assume that the charge can only hop to nearest neighbor sites in x and y direction. Periodic boundaries are applied along y-direction. The hopping process is described by the well-known Miller-Abrahams formula [27]:

$$k_{i\to j} = \sqrt{a_0^i a_0^j}\exp\left(-\Gamma_{ij}\right)\begin{cases}1 & \text{if } \Delta E_{ij} \leq 0\\ \exp\left(-\frac{\Delta E_{ij}}{k_\mathrm{B}T}\right) & \text{else}\end{cases} \tag{4.17}$$

where $a_0^{i/j}$ is the attempt-to-hop frequency of site i/j, the overlap parameter $\Gamma_{ij} = 2\gamma r_{ij}$ which captures the overlap of the wavefunctions of sites i and j, with the inverse localization constant γ and distance r_{ij}, $\Delta E_{ij} = E_j - E_i$ denotes their difference in potential energy. The potential energy at site i is given by

$$E_i = E_i^\mathrm{MO} + E_i^\sigma + E_i^\mathrm{F}\,, \tag{4.18}$$

where E_i^MO denotes the ideal MO energy level of the used material, E_i^σ gives the energetic disorder, and E_i^F is the contribution from the external electric field.

The (on-diagonal) energetic disorder is approximated in zeroth order by a Gaussian distribution with variance σ^2. The off-diagonal disorder is captured by local variations in the overlap parameter Γ_{ij} according to Bässler [29]. In this context, we take $\Gamma_{ij} = \Gamma_i + \Gamma_j$ as the sum of the site-specific, Gaussian-distributed $\Gamma_{i/j}$ with variance Σ^2. We add a linear potential drop along the x-axis arising from an external bias voltage V_ext neglecting any contacts:

$$E_i^\mathrm{F} = \frac{x_i}{x_\mathrm{size}} q V_\mathrm{ext}\,, \tag{4.19}$$

where q is the elementary charge and x_size is the length of the material in x-direction. The x-boundary is taken as an ideal sink for the charge carrier. Once the charge reaches the upper boundary $x = 100\,\mathrm{nm}$, the charge is immediately extracted from the simulation.

The figure of merit we aim to compute is the charge carrier mobility [50]:

$$\mu(\mathbf{F}) = \frac{\langle \mathbf{v}\cdot\mathbf{F}\rangle}{|F|^2} = \frac{x_\mathrm{size}^2}{V_\mathrm{ext} t_\mathrm{TOF}}\,, \tag{4.20}$$

where t_TOF is the time-of-flight, i.e. the time a charge carrier needs to travel once across the simulation box in x-direction. For each configuration, 100 times-of-flight are calculated with and without the acceleration scheme.

We analyze two different configurations, namely (SIM1) a single amorphous material and (SIM2) a heterogeneous material stack. A sketch of the systems under investigation is shown in Fig. 4.2. SIM1 represents an organic semiconductor with on- and off-diagonal disorder σ and Σ, respectively. For the hopping of charge carriers, we use $a_0 = 10^{10}\,\mathrm{s}^{-1}$ and $\gamma = 2\,\mathrm{nm}^{-1}$. For SIM2, we add two slabs with a significantly higher attempt-to-hop frequency $a_\mathrm{g} = 1000 \times a_0$ at $20\,\mathrm{nm} \leq x \leq 40\,\mathrm{nm}$ and $60\,\mathrm{nm} \leq x \leq 80\,\mathrm{nm}$. This introduces large time disparities as the charge carrier has to cross the slab regions with high transport properties. Especially at low electric fields, the charge is expected to remain within the slab regions for a significant computational time. However, the resistivity for the charge transport is mainly determined by the regions of highest resistivity, i.e. lowest attempt-to-hop frequencies.

In SIM1, charge carriers can be trapped within a small lattice domain due to the local variation in the wavefunction overlap Γ_{ij} and by tail states in the energetic disorder. As shown in Fig. 4.2, such domains are characterized by low energy barriers in the potential energy surface surrounded by high energy barriers. Thus, SIM1 provides a model of amorphous semiconductors with *Local Superbasins*. In contrast, SIM2 represents semiconductors or semiconductor blends of varying phases or materials.

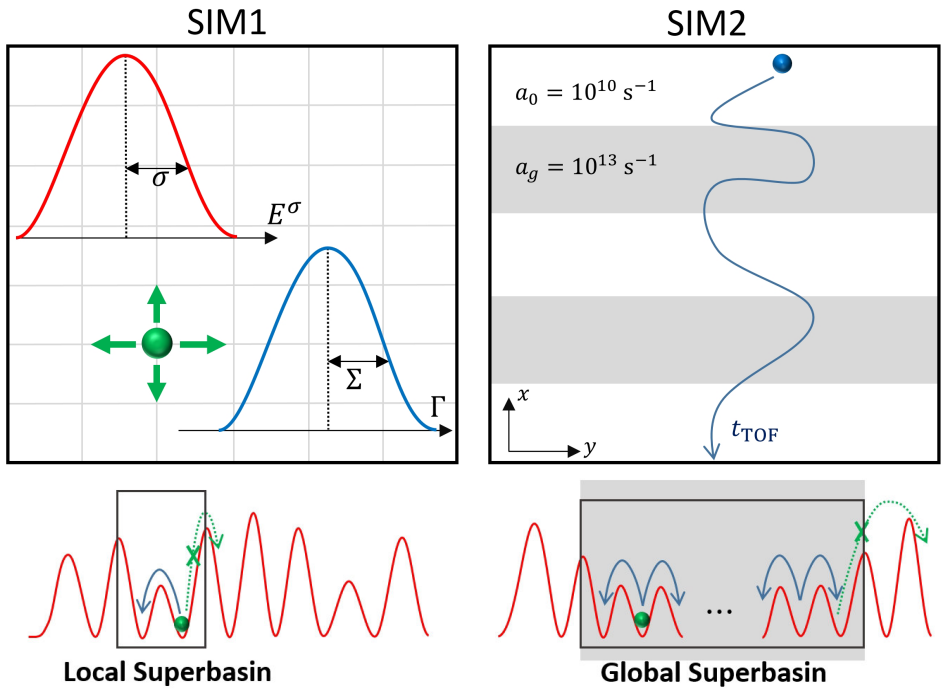

Figure 4.2 Schematic representation of the configurations SIM1 and SIM2. Hopping of charge carriers is considered to nearest neighbors only (i.e. 4 possible rates). In SIM1, an on-diagonal and off-diagonal disorder of width σ and Σ, repectively, are applied to each lattice site. In SIM2, time disparaties are induced by a heterogeneous stack of strongly different attempt-to-hop frequencies a_0/a_g. The time-of-flight t_{TOF}, i.e. the time a charge needs to travel across the structure, is tracked for each trajectory. Local and global superbasins are observed in SIM1 and SIM2, respectively. Sketches of the potential energy surface for SIM1 and SIM2 are shown to visualize the nature of superbasins within the respective system. Reprinted from [233], with the permission of AIP Publishing.

Here, large domains of strongly different transport rates are present. In SIM2, the charge has to pass the fast transport domains to contribute to the overall mobility. The fast transport domain is characterized by low activation barriers in the PES. However, the transition to the slow transport domain has a high energy barrier. The induced time disparities enhance the computational time required to calculate the times-of-flight.

Finding Superbasins

Global superbasins capture transitions which are frequent with respect to the whole system, e.g. phases of fast transport rates such as fast transport domains (grey slabs) in our study system SIM2. We detect global superbasins during the initialization procedure as follows. The procedure is explained using the GDM for charge transport as our example. Here, $\mathcal{S}$ is constituted by all lattice sites i with HOMO energy levels E_i^{MO} and position $\mathbf{r}_i$.

1. Calculate transition rates $k_{i\to j}$ for all $i, j \in \mathcal{S}$ using the Miller-Abrahams formula (Eq. 4.17) without an applied electric field ($V_{\mathrm{ext}} = 0\,\mathrm{V}$). These rates are stored as static rate constants (SRCs) for each branch $\{i \to j\}$.

2. Convert the SRC into an equivalent activation energy $E^{\mathrm{act}}_{i\to j}$ for all branches $\{i \to j\}$ using an Arrhenius relation:

$$k_{i\to j} = \frac{k_{\mathrm{B}}T}{h} \exp\left(-\frac{E^{\mathrm{act}}_{i\to j}}{k_{\mathrm{B}}T}\right), \tag{4.21}$$

   where h denotes the Planck constant.

3. Specify a threshold activation energy $\tilde{E}_{\mathrm{act}}$ to obtain branches of critical transition rates:

$$E^{\mathrm{act}}_{i\to j} < \tilde{E}_{\mathrm{act}} \to \text{global critical transition}$$
$$E^{\mathrm{act}}_{i\to j} \geq \tilde{E}_{\mathrm{act}} \to \text{non-critical transition.}$$

4. Group branches with global critical transitions that share one state.

In general, it is also possible the compare the SRCs directly with a user-defined reference rate. For some systems, it appears intuitive to set an energetic threshold as all processes are connected to activation energies and can be easily compared to e.g. the thermal energy or the lowest energy barrier within the system.

Local superbasins are described by fast transitions which are trapping the system within a small region of its phase space. Compared to global superbasins, local superbasins are defined by transitions of lower activation energy barrier with respect to their adjacent domains in phase space. We derive the local superbasins based on the critical and escape probabilities defined in the previous section. To distinguish critical from non-critical transitions, a threshold $0 < \xi < 1$ is set as an input parameter. If $p_{\mathrm{c}} > \xi$ for a certain set of states $\mathcal{B} \subseteq \mathcal{S}$, we consider $\mathcal{B}$ as a superbasin and transitions $k_{i\to j}$ with $i, j \in \mathcal{B}$ as critical transitions.

The procedure of finding local superbasins is sketched in Fig. 4.3a. The pseudocodes for the detection algorithm can be found in Algorithms 1 and 2 in the appendix A.1. We outline the detection procedure in the following paragraph closely following Fig. 4.3a.

1. Start in a system state i which is not part of a superbasin. Let us denote the initial state by the index **1** (red circle in Fig. 4.3a). Set threshold ξ. Generate an empty set $\mathcal{B}$. Add state **1** to set $\mathcal{B}$.

2. Calculate the maximum escape flux from set $\mathcal{B}$

$$f^{\mathcal{B}}_{\mathrm{es,max}} = \max_{i\in\mathcal{B}, j\in\mathcal{S}\setminus\mathcal{B}} \pi_i k_{i\to j}\,. \tag{4.22}$$

   Here, $\mathcal{B} = \{\mathbf{1}\}$. As only hopping to nearest neighbors is considered, $f^{\{\mathbf{1}\}}_{\mathrm{es,max}}$ is the maximum of the fluxes towards the 4 nearest neighbors of state **1**. Assume that state **2** (blue circle) is the destination of the maximum flux. The maximum flux is visualized by the red arrow in Fig. 4.3a.

3. Calculate the critical $p^{\mathcal{B}'}_{\mathrm{c}}$ of set $\mathcal{B}' = \mathcal{B} \cup \{\mathbf{2}\}$. If $p^{\mathcal{B}'}_{\mathrm{c}} > \xi$, branch $\{\mathbf{1} \to \mathbf{2}\}$ is labeled as a critical transition and state **2** is added to set $\mathcal{B}$ (blue rectangle). Otherwise, the procedure stops as state **1** is not part of critical transitions.

4. Again, calculate the maximum escape flux from the updated set $\mathcal{B} = \{\mathbf{1}, \mathbf{2}\}$ (Eq. 4.22). Both of states **1** and **2** have 3 nearest neighbors $j \notin \mathcal{B}$. Let us assume that the maximum escape flux from set $\mathcal{B}$ is along branch $\{\mathbf{2} \to \mathbf{3}\}$ (blue arrow). Again, we calculate the critical probability $p^{\mathcal{B}'}_{\mathrm{c}}$ with $\mathcal{B}' = \mathcal{B} \cup \{\mathbf{3}\}$. If $p^{\mathcal{B}'}_{\mathrm{c}} > \xi$, add state **3** to set $\mathcal{B}$ (green rectangle).

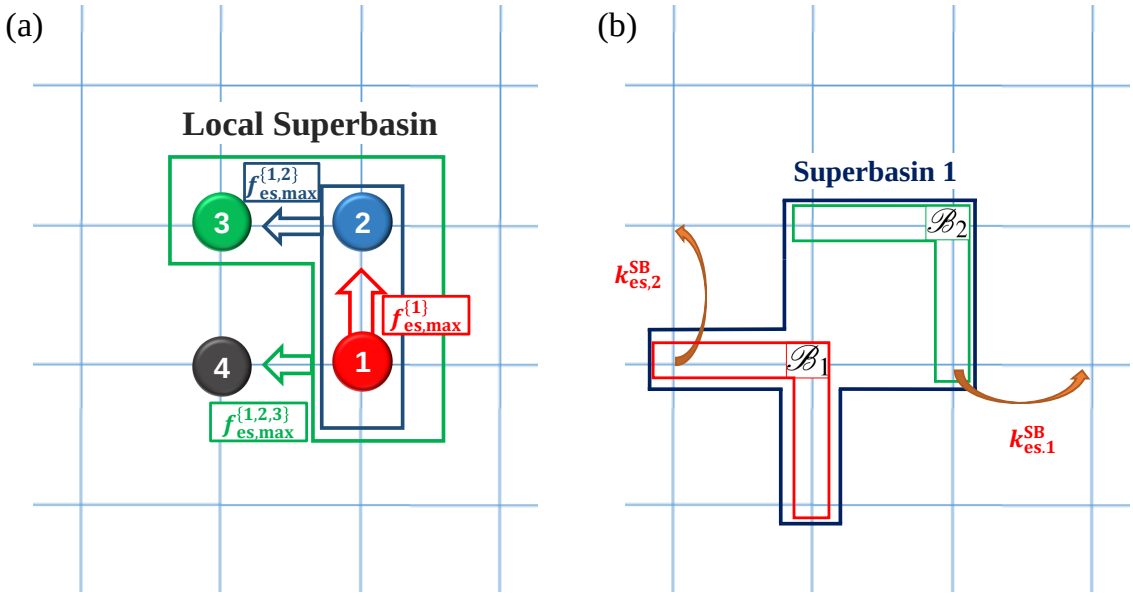

Figure 4.3 (a) Schematic representation of the algorithm *calc_local_critical_branches* for the calculation of local superbasins. The vertices and edges of the grid symbolize system states and transitions between the states, respectively. (b) Group local (global) superbasins with distance $d(\mathcal{B}_1, \mathcal{B}_2) = 1$. Two exemplary escape rates $k^{SB}_{es,i}$ of the resulting superbasin are highlighted. Reprinted from [233], with the permission of AIP Publishing.

5. Repeating step 4 yields the maximum escape flux $f^{\{\mathbf{1},\mathbf{2},\mathbf{3}\}}_{es,max}$ along branch $\{\mathbf{1} \rightarrow \mathbf{4}\}$ (green arrow). Let us assume that $p_c^{\mathcal{B}'} < \xi$ with $\mathcal{B}' = \mathcal{B} \cup \{\mathbf{4}\}$. Then, branch $\{\mathbf{1} \rightarrow \mathbf{4}\}$ does not mark a critical transition and the search of a local superbasin stops. The local superbasin is given by set $\mathcal{B}$, and all $k_{i \rightarrow j}$ with $i, j \in \mathcal{B}$ are labeled as critical transitions. Otherwise, the procedure repeats step 5 until the stopping criteria $p_c^{\mathcal{B}'} < \xi$ is fulfilled.

6. The resulting local superbasin (green box in Fig. 4.3a) consists of two critical transitions (=two branches) and three states. Now, we can calculate the escape and the critical probability for the local superbasin according to Eqs. 4.6 and 4.7, respectively.

For the final step, let us define the distance $d(\mathcal{B}_1, \mathcal{B}_2)$ between superbasins $\mathcal{B}_1$ and $\mathcal{B}_2$ as the smallest number of transitions separating $i \in \mathcal{B}_1$ and $j \in \mathcal{B}_2$. We say that $\mathcal{B}_1$ and $\mathcal{B}_2$ are adjacent superbasins if $d(\mathcal{B}_1, \mathcal{B}_2) = 1$, i.e. a single transition separates $\mathcal{B}_1$ and $\mathcal{B}_2$ (see Fig. 4.3b). To avoid possible oscillations of charges between adjacent superbasins, we connect adjacent superbasins to one single superbasin. This is done for both global and local superbasins. The scaling factor and the critical number of sightings of the resulting superbasin are calculated using Eqs. 4.15 and 4.16, respectively. The procedure is performed for all states to detect all superbasins in the system.

Now, we investigate the structure and the scaling values of the superbasins within SIM1 and SIM2. For the calculation of global superbasins, we take the equivalent activation energy of

$$\tilde{E}_{act} = -k_B T \ln\left(\frac{h}{k_B T}\sqrt{a_0 \cdot a_g}\right) . \tag{4.23}$$

We choose this particular value to cover the slab regions using the scaling algorithm. Alternatively, one could have taken a critical barrier $\tilde{E}_{act}$ slightly higher than the lowest equivalent activation barrier

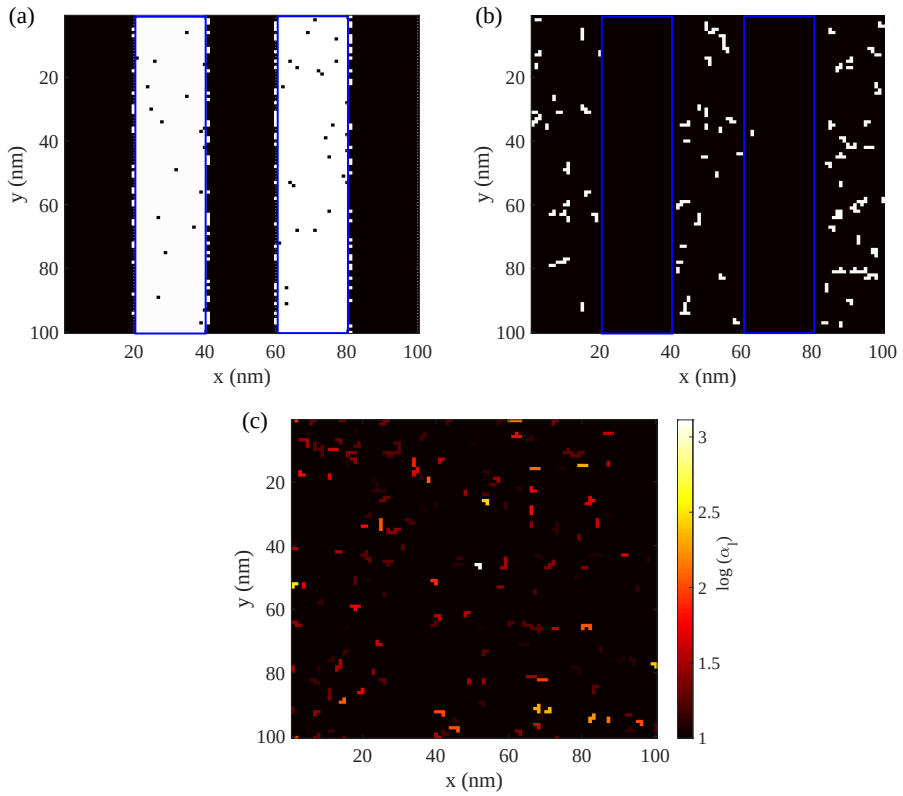

Figure 4.4 (a) Global and (b) local superbasins in the heterogeneous setup SIM2 for $\sigma = 100\,\text{meV}$ and $\Sigma = 1$. White regions mark the superbasins where the scaling algorithm is applied. The blue rectangles label the domains of high transition rates $a_g = 10^3 \times a_0$. (c) Scaling factors (in log-scale) for the local superbasins in SIM1 with $\sigma = 100\,\text{meV}$ and $\Sigma = 1$. Reprinted from [233], with the permission of AIP Publishing.

to obtain comparable global superbasins. For the calculation of the local superbasins, the scaling parameters ξ, κ, and δ are varied to analyze the sensitivity and accuracy of the algorithm.

Figures 4.4a and b show the global and local superbasins of structure SIM2, respectively. The blue rectangles mark the slab regions of fast transport properties. Here, we used $\sigma = 0.1\,\text{eV}$ and $\Sigma = 1$. In Fig. 4.4a, the white domains highlight the global superbasins. Note that there are several states within the slab regions not belonging to the superbasins. This is due to the large on- and off-diagonal disorder, which makes transitions between these states non-critical. Figure 4.4b depicts local superbasins for $\xi = 0.75$. Several superbasins of more than one critical branch are visible. This proofs that the algorithm is capable of identifying critical paths in the structure. Note that longer critical paths are to be expected within lattices of dimension $N > 2$. In Fig. 4.4c, we show the scaling factors α of each local superbasin for $\sigma = 0.1\,\text{eV}$ and $\Sigma = 1$ in SIM1. The significant off-diagonal disorder of $\Sigma = 1$ induces superbasins with scaling factors of up to $\alpha = 10^3$. Large scaling factors indicate the presence of critical transitions, which provide significant trapping of the charge carriers within unscaled kMC simulations.

Integration of the Scaling Procedure

Figure 4.5 shows the integration of the scaling procedure in the kMC loop. The Monte Carlo procedure for the calculation of transition μ and time step τ follow Gillespie's algorithm [234] and are explained

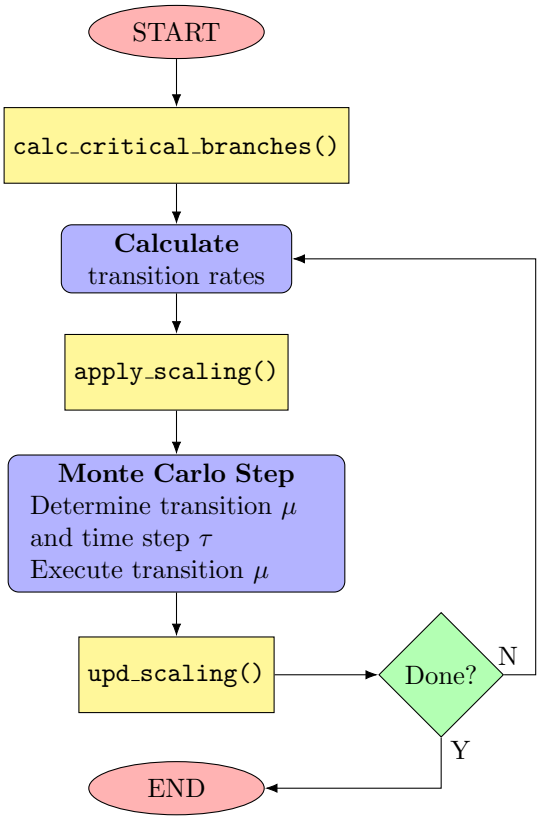

Figure 4.5 Flow chart of the kinetic Monte Carlo method. The yellow parts show the scaling subroutines. Reprinted from [233], with the permission of AIP Publishing.

in detail in our previous publication [182]. The detection algorithm for global and local superbasins is run during the initialization step. Following the execution of the Monte Carlo step, superbasin counters are updated for both the local and the global superbasins. If applicable, transition rates are scaled before the Monte Carlo step. In the remaining, we outline the integration of the scaling procedure for the example of charge transport in organic semiconductors. The pseudocodes of the procedures *apply_scaling* and *upd_scaling* are shown in Algorithms 3 and 4 (appendix A.1), respectively.

For each charge i, we store its position $\mathbf{r}_i$, a superbasin index j, a counter for the number of sightings $N_{\text{sightings},i}$ of a superbasin, scaling factor α_i and the counter for the number of scalings m_i within a superbasin.

If a charge i enters or is initialized in a superbasin $\mathcal{B}_k$, we set the counters $N_{\text{sightings},i} = 1$ and $m = 0$. In addition, the superbasin index is set and $\alpha_i = 1$ is initialized. Using α_i, the value of N_f is calculated. Now, we increment $N_{\text{sightings},i}$ for each transition of the charge within the superbasin until $N_{\text{sightings},i}$ exceeds N_f. Now, m is incremented, $N_{\text{sightings},i} = 1$ is reset, and the scaling factor is updated following

$$\alpha_i = \alpha^{m/\kappa} \,. \tag{4.24}$$

Here, α is the scaling factor of superbasin $\mathcal{B}_k$ calculated as the upper limit of Eq. 4.15. Hyperparameter κ ($m \leq \kappa$) is an integer value controlling the number of scalings which need to be performed until α is reached. This also controls the step size of the increase in alpha, which allows a conservative scaling (large κ) or a fast scaling ($\kappa = 1$). Using the updated α_i, a new value of N_f is obtained. Now, as $\alpha_i > 1$, the critical transitions of charge i in superbasin $\mathcal{B}_k$ are scaled with α_i. If the charge i leaves the superbasin, all counters and the scaling factor are reset.

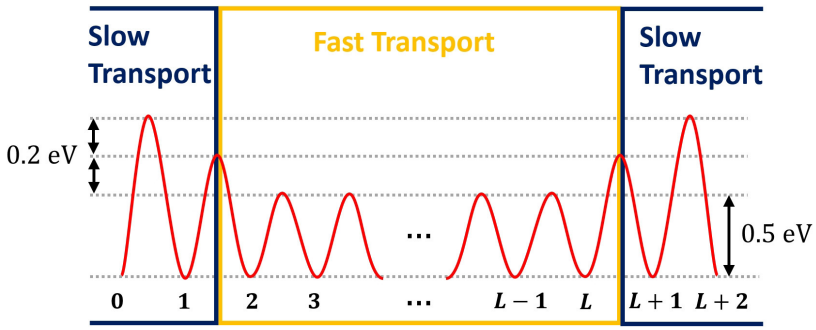

Figure 4.6 Schematic representation of the potential energy surface of the 1D-chain. The PES is shown as a solid red line. The y-axis labels the energy, while the x-axis is the reaction coordinate, i.e. the position of the particle. The transition energies between the states are $E^{\dagger}_{0,1} = E^{\dagger}_{L+1,L+2} = 0.9\,\text{eV}$, $E^{\dagger}_{1,2} = E^{\dagger}_{L,L+1} = 0.7\,\text{eV}$, and otherwise $E^{\dagger}_{i,j} = 0.5\,\text{eV}$. Reprinted from [233], with the permission of AIP Publishing.

In contrast to the AS-kMC, we use the superbasin specific value of α as upper limit of the scaling factor to avoid any disruption of the dynamics. This limit is reached if $m = \kappa$.

4.3 Results and Discussion

4.3.1 Comparison with AS-kMC

To benchmark the presented acceleration scheme, we compare its performance to the AS-kMC by Chatterjee and Voter [53]. We apply both algorithms to a one-dimensional chain of length $L + 2$, see Figure 4.6 similar to the studied system in the original AS-kMC paper. Consider the potential energy surface (PES) visualized in Fig. 4.6. The PES is set-up using the transition state energies $E^{\dagger}_{0,1} = E^{\dagger}_{L+1,L+2} = 0.9\,\text{eV}$, $E^{\dagger}_{1,2} = E^{\dagger}_{L,L+1} = 0.7\,\text{eV}$, and otherwise $E^{\dagger}_{i,j} = 0.5\,\text{eV}$. Note that we have modified the system to make it comparable with the subsequent study of transport within organic semiconductors. As shown in Fig. 4.2, the PES within fast transport domains shows lower energy barriers, i.e. higher transition rates, with respect to slow transport domains. At the interface between both domains, the prefactor of the Miller-Abrahams hopping rate is given by the geometric average $(a_0 a_g)^{1/2}$, which is captured by an intermediate energy barrier in the PES. The 1D-chain resembles these characteristics: high energy barrier for the slow transport regime, low energy barriers for the fast transport regime, and the intermediate barrier at the interface.

The transition rate between the system states is calculated by the Arrhenius-type transition rate:

$$k_{i\to j} = A \exp\left(-\frac{E^{\dagger}_{i,j}}{k_\text{B} T}\right), \tag{4.25}$$

with $A = 1\,\text{s}^{-1}$. We initialize the system at state $\lceil L/2 \rceil$ and calculate the number of steps and the time t_kMC which the system needs to leave the superbasin, i.e. to reach state 1 or $L + 2$. For each configuration we simulate 100 runs.

We vary the chain length $L \in \{10, \ldots 200\}$ and analyze the speed-up in CPU time and the error in t_kMC. For the AS-kMC, we choose the scaling parameters $\alpha = 2$, $\gamma = 2$, as proposed in the original AS-kMC paper and vary $\delta \in \{0.05,\ 0.25,\ 0.5\}$. The used parameters for our scaling method are $\delta \in \{0.05,\ 0.25,\ 0.5\}$, $\kappa = 10$, and the threshold activation energy of $\tilde{E}_\text{act} = 1.1 \times \min_{i,j\neq i} E^{\text{act}}_{i\to j}$.

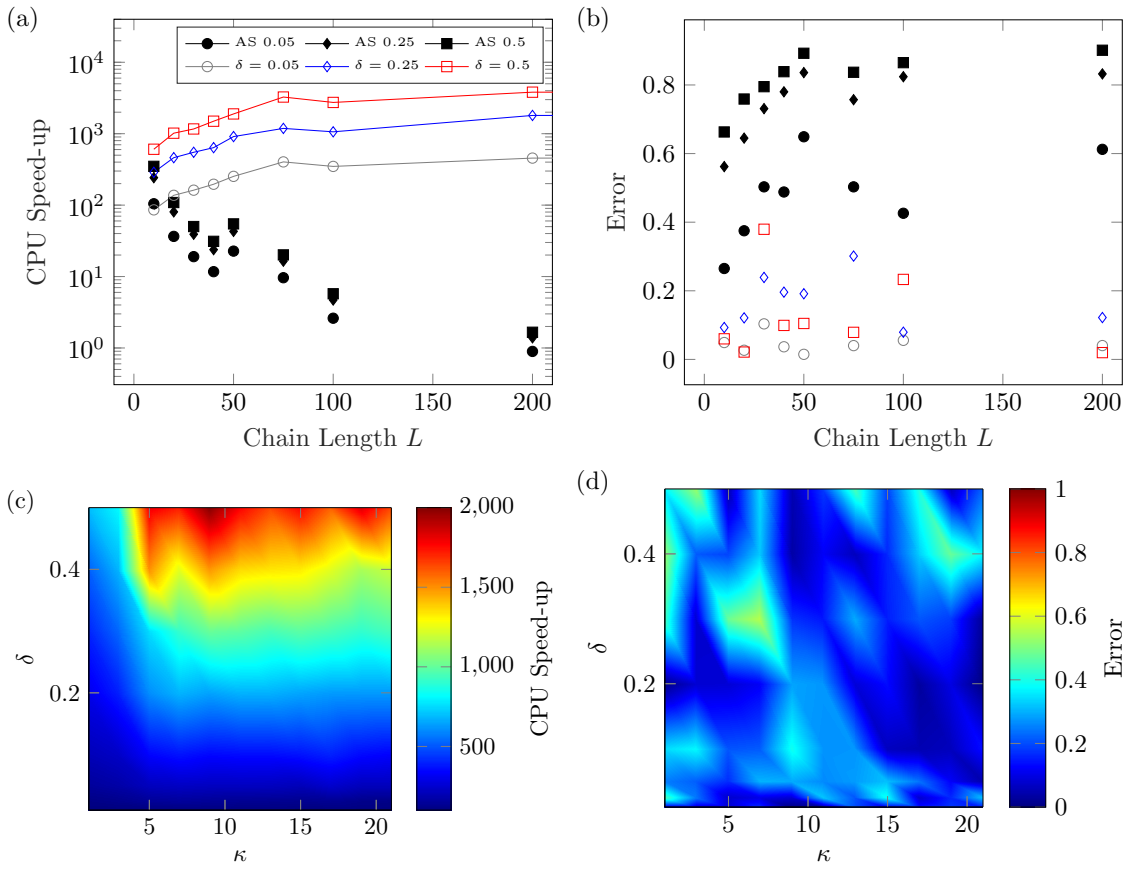

Figure 4.7 Comparison of (a) the acceleration in CPU time and (b) the error using the AS-kMC with different δ (labeled by AS δ) and our presented algorithm for the 1-dimensional chain with different δ. As a reference, a standard kMC procedure without any acceleration scheme has been used. The legend in (a) holds for both subplots. Subplots (c) and (d) present the sensitivity analysis of the CPU speed-up and the error, respectively, on the hyperparameters κ and δ for fixed chain length $L = 50$. Reprinted from [233], with the permission of AIP Publishing.

Figure 4.7 visualizes (a) the CPU speed-up and (b) the error in escape time for different chain lengths. As a reference, a standard kMC procedure without an acceleration scheme is used. We compare the AS-kMC by Chatterjee *et al.* [53]. with our presented algorithm. The AS-kMC shows best performances for small chain lengths with a CPU speed-up of 350 for $\delta = 0.5$. With rising chain length, the performance decreases due to the overhead arising from searching superbasins during runtime. The error measure rises for increasing chain lengths, with a minimum error of 0.66 at the shortest chains. In contrast, our presented acceleration method shows a high CPU speed-up within the range of 10^2 to 4×10^3, depending on the chain length and δ. Higher error measures δ give rise to larger speed-up due to larger maximum scaling factors α (see Fig. 4.1). With rising chain length, the speed-up increases slightly which is caused by the enlarged escape time of the unscaled simulations. In addition, no decrease in the speed-up with growing superbasin size is observed. Our algorithm allows a speed-up independent of the superbasin size as the main overhead is generated by the calculation of the critical regions during the initialization procedure. The error produced by the presented algorithm is smaller than the AS-kMC, with a maximum error of 0.5 for all chain lengths L. The reason for the reduced error is that the novel scaling algorithm limits the scaling factor at the maximum value of α, which is a function of δ (following Eq. 4.15). The error in the AS-kMC scales with $O(m\delta)$ when the

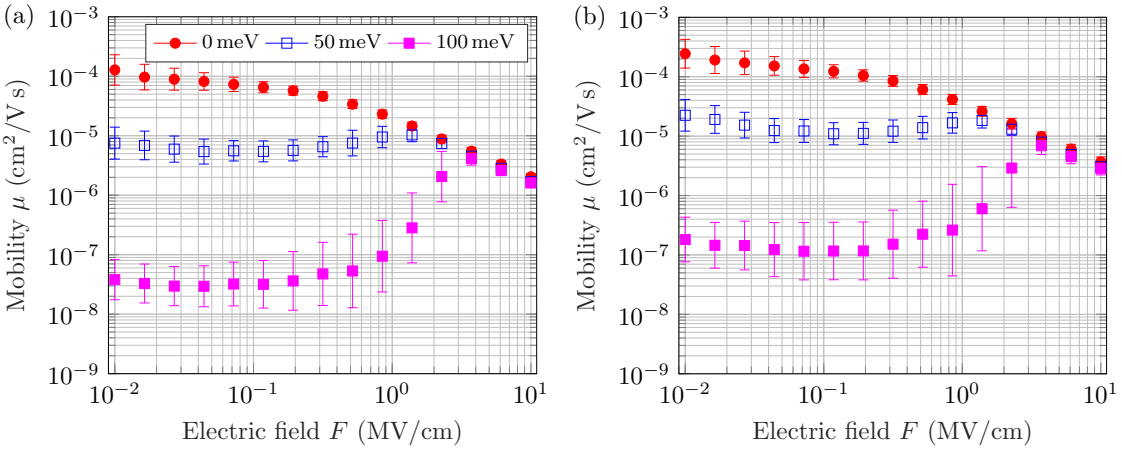

Figure 4.8 Non-accelerated mobilities for constant off-diagonal disorder $\Sigma = 1$ and varying on-diagnonal disorder σ for the (a) SIM1 and (b) SIM2 set-up. The error bars are based on a log-normal distribution of the time-of-flight values. Reprinted from [233], with the permission of AIP Publishing.

barrier are scaled m-times [53]. Thus, multiple scaling gives rise to higher errors in the AS-kMC. For small systems, the novel algorithm provides no significant advantage w.r.t. AS-KMC. However, if large superbasins are expected, our algorithm provides a significant speed-up with an accelerated sampling of the low processes. Realistic examples for large systems will be discussed in the next section in the example of SIM2.

The sensitivity of the speed-up and the error on the hyperparameters δ and κ is analyzed in Fig. 4.7c and d, respectively, for chain length $L = 50\,\text{nm}$. As shown in Fig.4.7a, the speed-up scales strongly with the error measure δ. With larger δ, fewer sightings of the superbasin are required and higher scaling factors are allowed. The hyperparameter κ denotes the number of steps the rates are scaled until the allowed limit in α is reached. Here, the choice of κ is important to achieve best performance. The absolute error remains uncritical for all over the hyperparameter set. Biggest errors are expected for large δ independent of κ.

4.3.2 Speed-up and Accuracy Analysis

Before discussing the performance improvement and accuracy, we analyze the parameter set for the organic test systems SIM1 and SIM2. Figure 4.8 depicts the field dependence of the charge carrier mobilities for (a) SIM1 and (b) SIM2 with various on-diagonal disorder σ and $\Sigma = 1$ for the unscaled simulations. The error bars are based on a log-normal distribution of the time-of-flight. The mobilities strongly decrease with rising σ and become disorder-independent for high electric fields. Due to the high off-diagonal disorder, $\mu(F)$ shows a negative field-dependence at low $F \approx 10^{-2}$ to $10^{-1}\,\text{MV cm}^{-1}$ [29]. The mobilities are slightly higher for SIM2 due to the high mobility slabs. The results can be rationalized by the Matthiessen rule as the slow and fast slabs can be considered as series resistances. Consequently, slow processes dominate the time-of-flight and μ.

Charge carrier mobilities computed using the acceleration scheme for the highest on- and off-diagonal disorder are shown in Fig 4.9. For both SIM1 and SIM2, the error of the scaling is negligible, and the mobility values are in the range of the non-accelerated mobilities. Moreover, the error bars due to the disorder in the configuration are in a comparable range. Note that the error gets smaller with decreased on- and off-diagonal disorder as fewer superbasins are present.

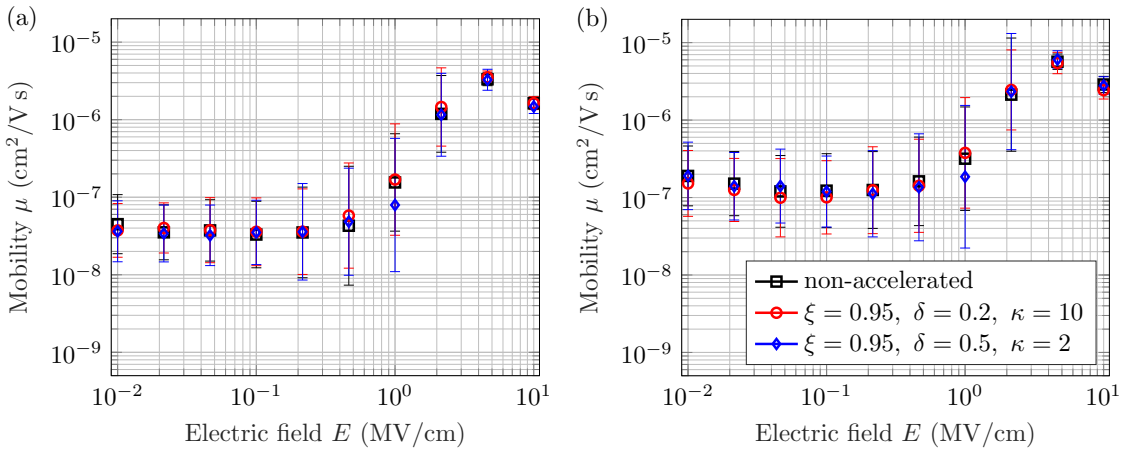

Figure 4.9 Accelerated mobilities for constant off-diagonal disorder $\Sigma = 1$ and constant on-diagnonal disorder $\sigma = 100$ meV for the (a) SIM1 and (b) SIM2 set-up. The error bars are based on a log-normal distribution of turnover frequencies. Reprinted from [233], with the permission of AIP Publishing.

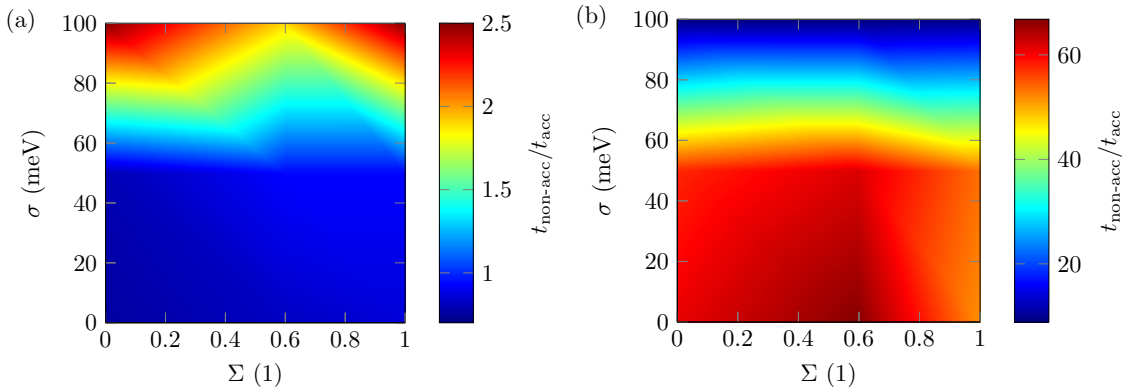

Figure 4.10 Ratio of non-accelerated to accelerated total simulation times t_{sim} and $t_{\text{sim}}^{\text{acc}}$, respectively, for the (a) SIM1 and the (b) SIM2 set-up in dependence on the on-diagonal and off-diagonal disorder σ and Σ, respectively. The scaling parameters are chosen as $\kappa = 2$, $\delta = 0.2$, and $\xi = 0.75$. Reprinted from [233], with the permission of AIP Publishing.

The CPU times needed for one mobility curve for configuration SIM2 exceed the required time for SIM1 by one order of magnitude (cf. Figures A.1 and A.3). This is due to the disparity of timescales observed in the global superbasins with respect to the slow transport domains. Figure 4.10 shows the acceleration in CPU times for (a) SIM1 and (b) SIM2. In SIM1, superbasins arise for high on- and off-diagonal energetic disorder. Here, an acceleration of factor 2.5 is achieved. For lower disorder, the superbasins are benign, i.e. charge carriers can easily escape within a few hundreds/thousands of kMC steps. In SIM2, charge carriers always have to pass the slab regions to be collected for the time-of-flight analysis. Thus, acceleration factors of up to 65 can be reached. The increase of the acceleration towards low σ is mainly caused by the reduction of local superbasins induced by tail states of the Gaussian density of states. Even for largest disorder values, an acceleration of factor 15 is achieved.

After presenting the capabilities of the algorithm, we analyze the sensitivity on the scaling parameters δ, ξ and κ. Figures A.2 (SIM1) and A.4 (SIM2) in appendix A.1 show the relative error of the times-of-flight and the acceleration in CPU times for $\sigma = 100$ meV and $\Sigma = 1$. he critical probability

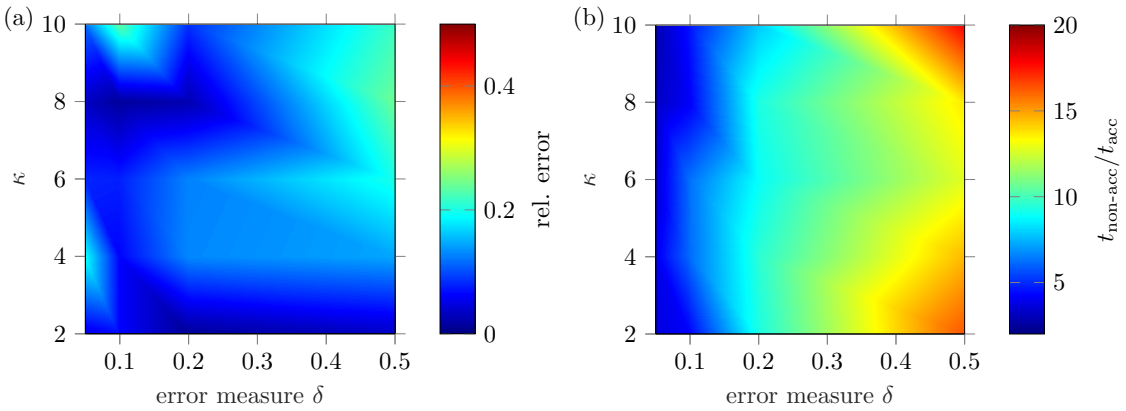

Figure 4.11 (a) Relative error of the average time-of-flight t_{TOF} in the accelerated with respect to the non-accelerated simulations. (b) Acceleration in CPU times within the acceleration scheme for calculating the full mobility curve for 100 TOFs at each voltage. The axis show the error measure δ and the scaling parameter κ. Reprinted from [233], with the permission of AIP Publishing.

ξ is an important measure for both the accuracy and the speed-up. For $\xi \to 1$, the speed-up is decreased as less transitions are captured within superbasins. For low ξ, an increased number of transitions are considered to be critical, which causes a significant acceleration. The limitation of the superbasin-specific scaling factor α leads to relative errors less than 0.5 for all hyperparameters. This connection is clearly visible for SIM1. For low $\xi = 0.75$, the speed-up is strongly increased with respect to higher ξ. The error measure δ dictates the upper boundary for α as well as the lower boundary for N_f. Thus, with a higher δ the scaling factor increases and the timescales of the system spent in the superbasin will be significantly altered.

Configurations such as SIM2 demand a higher CPU time, thus scaling for such large superbasins is of high significance. We showed for the 1D-superbasin that the AS-kMC introduces a negligible error, however the computational overhead with larger superbasins reduces the speed-up significantly. However, the acceleration using our presented method is shown to be less dependent on the system size. Figure 4.11 shows the (a) relative error and the (b) speed-up in CPU times for $\xi = 0.85$, $\sigma = 100\,\text{meV}$, and $\Sigma = 1$. In SIM2, the acceleration scheme is less sensitive on ξ as the major time disparity is not due to local but due to global superbasins (see Fig. A.4). The speed-up in CPU times strongly depends on the error measure. In most runs, the number of scalings in the superbasin reaches the upper limit given by κ. Thus, the time required to leave the superbasin is mainly dictated by δ.

Initially, the user often does not know the detailed potential energy surface of the system and might ask which superbasins might dominate and which scaling parameters to choose. The advantage of the presented scheme is that the potential superbasins are known directly after the initialization procedure. Thus, the structure can be analyzed for various parameters in advance to decide the values of the parameters based on the information given by the structure of superbasins and the magnitude of α (see Fig. 4.4).

4.4 Conclusion

We have presented a novel acceleration scheme for kinetic Monte Carlo simulations of particle transport. The developed algorithm expands the accelerated superbasin kMC (AS-kMC) by Chatterjee and Voter [53] by (i) reducing the computational overhead of the superbasin sampling and (ii) the fast detection of both local and global superbasins by sampling the potential energy surface during the

system initialization. In contrast to the AS-kMC, individual scaling factors are calculated depending on the superbasin geometry and the energetic structure. The algorithm enables an optimized kMC method by efficiently lowering the critical rates. Thus, the system can escape the corresponding superbasin and sample the slow processes efficiently.

Global superbasins are computed based on user-defined critical activation energy $\tilde{E}_{\mathrm{act}}$. Local superbasins are obtained by calculating the maximum escape flux given by the product of the state probability and the transition rates. Branches are added to the superbasin until the flux of critical rates in ratio to the escape flux decreases below a user-specified threshold probability ξ. Boundaries for the scaling factor and the number of sightings are derived based on a user-defined error measure δ and the critical probability p_{c} of the superbasin.

We have compared our algorithm with the AS-kMC using a 1D-superbasin consisting of a simple chain of sites. The presented algorithm overcomes the AS-kMC in terms of CPU speed-up by a factor of 10^3 with improved accuracy. To provide a 'real-life' example from our field of research, the accuracy of the presented acceleration scheme is investigated for the example of charge transport in amorphous organic semiconductors. We present the mobility for (1) a system of high on- and off-diagonal disorder (SIM1), and (2) a slab-like system (SIM2), where slabs of fast hopping rates are sandwiched between slabs of slow hopping rates. We are able to calculate the charge carrier mobility with accuracies in the range of statistical fluctuations, while an acceleration beyond a factor of 65 in simulation time can be achieved. Moreover, the field dependence of the mobility is fully recovered. The main advantage with respect to existing acceleration frameworks is the innovative detection algorithm of superbasins, with scaling factors depending on the structure of the superbasins. This allows the fast computation of diffusion and transport properties without significant computational overhead.

Additional Information

The acceleration scheme was implemented in MATLAB.The MATLAB code can be downloaded via GitHub https://github.com/wldmr92/pacckMC. All simulations were run on an Intel(R) Core(TM) i7-4790 CPU @3.60GHz with 4 Cores.

5 Charge Carrier Mobility in Disordered Organic Semiconductors

Charge transport plays a fundamental role for the efficient operation of several (opto-)electronic devices such as organic field effect transistors and organic solar cells. One of the characteristic measures of charge transport is the charge carrier mobility μ. In contrast to their inorganic counterpart, solution-processed organic thin films are usually strongly disordered. The lack of periodicity leads to localized quantum states which are strongly disordered in their spatial arrangement and their energies. Charge carriers propagate through these localized states by incoherent hopping. Thus, the mobility strongly depends on the detailed arrangement of the states in the position-energy phase space. Experimental studies allow the measurement of the mesoscopic carrier mobilities, but do not provide insight into the charge transport on the nanoscale. Numerical models provide insight into the relation between the morphology and charge mobilities.

This chapter studies the role of the energetic and the spatial disorder on the charge carrier mobility in organic semiconductors. Section **5.1** introduces the developed off-lattice kinetic Monte Carlo model based on the Voronoi tessellation and presents the results on the role of the energetic disorder and correlations within the energetic landscape on the mobility. In section **5.2**, the presented model is utilized to study the role of spatial disorder in pentacene crystals and thin films using charge transfer integrals predicted by Machine-Learning (ML). The ML method has been developed by *Jonas Lederer* and *Michael Rinderle*, TUM. Molecular dynamics simulations have been contributed by *Alessandro Mattoni*, Cittadella Universitaria di Monserrato.

Parts of this chapter have been adapted from the following sources: 'Charge carrier mobility of disordered organic semiconductors with correlated energetic and spatial disorder,' *Phys. Chem. Chem. Phys.*, 20 (13), 8897-8908, 2018 [50] with permission from the PCCP Owner Societies; 'Machine LearningBased Charge Transport Computation for Pentacene,' *Adv. Theory Sim.*, 2 (2), 1800136, 2019 [253], ©2018 WILEYVCH Verlag GmbH & Co. KGaA, Weinheim; 'Machine-Learned Charge Transfer Integrals for Multiscale Simulations in Organic Thin Films,' *J. Phys. Chem. C* 2020, 124, 32, 1773317743 [51], adapted with permission by ©(2020) American Chemical Society.

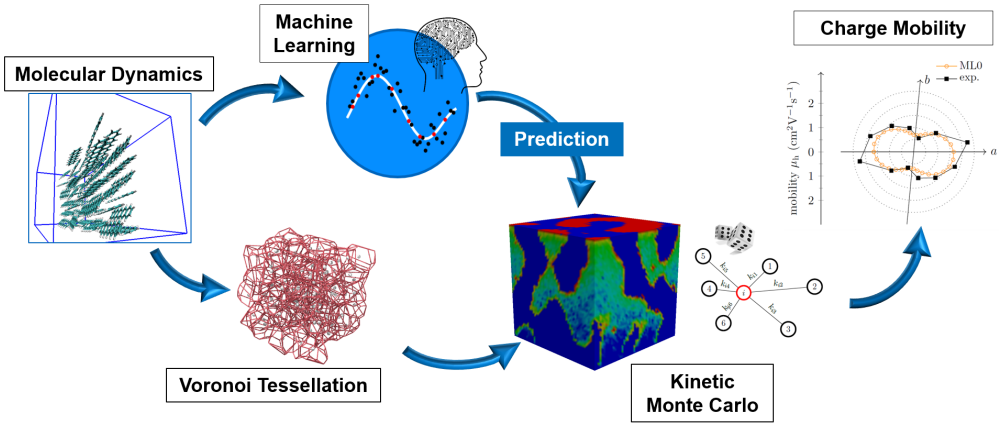

5.1 Role of Energetic and Spatial Disorder on the Charge Carrier Mobility

5.1.1 Background

Due to their unique properties, organic semiconductors, such as molecularly doped [254, 255] and conjugated polymers [256, 257], are considered to be highly feasible materials for a wide range of applications, including organic photovoltaics (OPVs) [10, 159, 258] or field-effect transistors (OFETs) [202, 259, 260]. The design and synthesis of appropriate organic materials require a deep understanding of the physical processes determining the performance of these devices. Irrespective of the type of application, the charge carrier mobility plays a key role for the applicability of organic semiconductors in electronic devices. First measurements indicated a high dependence of the mobility on several physical characteristics such as the charge carrier density, the applied electric field or a change in temperature [261, 262]. Experimentally, the mobility can be obtained *e.g.* from time-of-flight measurements [263], using linearly increasing voltage in metal-insulator semiconductor structures (MIS-CELIV) [264, 265], or pulse-radiolysis time-resolved microwave conductivity [266, 267].

A key feature of organic semiconductors compared to their inorganic counterpart is the presence of energetically and spatially disordered localized quantum states. The observable energetic disorder σ is caused by the non-crystalline arrangement of polymers or small molecules [112]. The fluctuations can be in the order of 0.1 eV [29], while systems with a reduced energetic disorder have been found recently [268]. Due to the lack of a long-range order, charge carriers are strongly localized. Transport of charge carriers in such disordered semiconductors occurs by incoherent hopping between localized quantum states which often represent molecules or conjugated segments of polymers [17, 27]. Baranovskii discusses in detail that the shape of the density of states (DOS) follows a Gaussian distribution [85], which is characteristic for the experimentally observed charge carrier dependence of the mobility [269].

A frequently discussed subject is the distribution of the disordered energy. Many investigations are modeling charge transport within uncorrelated sites, known as the Gaussian disorder model (GDM) [29, 270, 271]. A correlated disorder model (CDM) is required to describe observable characteristics like the Poole-Frenkel behavior of the charge carrier mobility [44, 271, 272]. Analytic treatments of this problem allows to derive analytic relations describing charge carrier mobility in 1D-structures [273]. The complexity of 3D-percolation paths in (un-)correlated, semi-crystalline structures requires numerical methods.

Kinetic Monte Carlo (kMC) models are frequently utilized in simulations of organic compounds [29, 46–48], in which charge transport is described by hopping of charge carriers along localized quantum states [17]. Many existing models make use of simplified cubic lattices. Structural information such as the spatial distribution of localized states and anisotropies due to e.g. $\pi - \pi$-stacking of molecules is neglected in this strong approximation. An off-lattice model is required to capture arbitrary distributions of localized sites. First publications including randomly distributed sites are based on multi-scale approaches [20, 49]. Recently, a generalization of Pasveer's well-known mobility model [270] was given using a random site model [189]. The observations made by Nenashev *et al.* emphasize the need of generalized site distributions in kMC [189].

5.1.2 Model

Here, we consider unipolar charge transport between localized sites modeled by hopping according to the Miller-Abrahams hopping rate [27]:

$$a_{i\to j} = a_0 \exp\left(-2\gamma r_{ij}\right) \exp\left(-\frac{\Delta E_{ij} + \left|\Delta E_{ij}\right|}{2k_\mathrm{B}T}\right), \tag{5.1}$$

where a_0 is the attempt-to-hop frequency, $\Delta E_{ij} = E_j - E_i$ is the difference in energy between the initial state i and the final state j, the Boltzmann constant k_B, temperature T, the inverse localization length γ and the inter-site hopping distance r_{ij}. The energy E_i at site i is obtained by

$$E_i = E_i^\mathrm{MO} + E_i^\sigma + E_i^F + E_i^C \,. \tag{5.2}$$

Here, E_i^MO is the ideal energy level of the considered molecular orbital (MO), E_i^σ is the energetic disorder, E_i^F represents the external electric potential, and E_i^C gives the Coulomb energy. The electrostatic Coulomb interaction is included using the Ewald sum [48, 211], which includes the electrostatic interaction of charge replicas in the 3D periodic system. Without any applied electric field, charge transfer is purely diffusion-based and thus there will be a negligible net current flowing in the field direction. An external electric potential E_i^F generates a gradient in the average potential of the MO energy levels, forcing an increase in the net current. To avoid any undesirable rise of mobility due to time-of-flight effects at low fields [85, 274, 275], we assume an infinite sample in all directions by applying periodic boundaries in all spatial dimensions. Charge carriers can hop across the periodic boundary, thus they stay in the simulation box, yielding a fixed charge carrier density n. The initial charge carrier density is obtained by placing charges at random positions in the simulation box. Only next-neighbor hopping is considered.

Correlated Disorder Model

The energetic landscape of an organic semiconductor plays a significant role in the charge transport and exciton dissociation [13, 85, 112]. In contrast to inorganic semiconductors, the molecular orbital energies inside an organic material are strongly disordered due to the non-crystalline arrangement of the molecules and polymers [112]. Energetic disorder values of $\sigma = 0.1\,\mathrm{eV}$ are present in many materials [29]. It is widely accepted, that the shape of the density of states (DOS) can be modeled using a Gaussian distribution [44, 85, 269, 270, 272, 276]. Some experimental observations require a correlation in the site energies, as described in the correlated disorder model (CDM) [44,271,272,277], while many studies are based on the uncorrelated, Gaussian disorder proposed by the Gaussian disorder model (GDM) [29, 270, 271].

Correlations in the energetic landscape are included based on a weighted averaging comparable to existing CDMs [44, 271]. Figure 5.1 visualizes the CDM for an organic system consisting of PCBM (black dots) and P3HT (red dots). A spatial correlation of the site energies is achieved by weighting the contribution of site energies with inversed inter-site distance. The following scheme summarizes the correlation algorithm:

1. Choose random MO energy from a Gaussian distribution with a variance σ^2

$$g(\epsilon) = \frac{N}{\sigma\sqrt{2\pi}} \exp\left(-\frac{\epsilon^2}{2\sigma^2}\right) \,. \tag{5.3}$$

The uncorrelated GDM stops here. For the CDM the following steps are required.

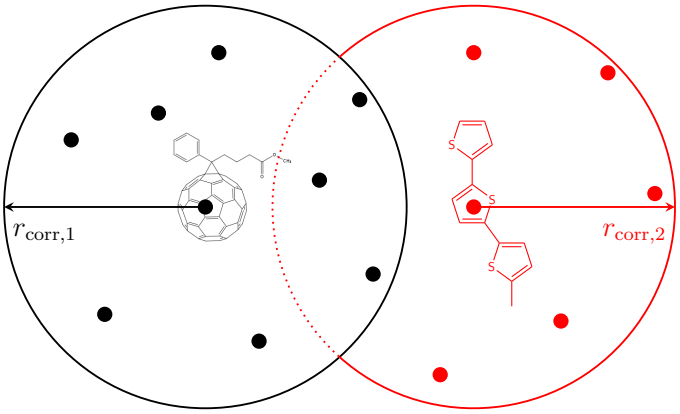

Figure 5.1 Correlation of site energies inside a blend. The black and red dots represent lattice sites of the small molecule PCBM and the polymer P3HT, respectively. A weighted average is performed over all sites of the same material type within the radius of $r_{\mathrm{corr},i}$. Reproduced from [182] under license CC BY 4.0.

2. Take a weighted average of the energy levels E_k of sites within a sphere with the correlation radius r_{corr}

$$E_i = \frac{1}{\sum_k \frac{1}{|r_{ik}|}} \sum_k E_k \frac{1}{|r_{ik}|} \,. \tag{5.4}$$

   The index k iterates over all sites within a correlation radius r_{corr} around site i, r_{ik} gives the distance between sites i and k. The resulting, correlated energies E_i are stored in an intermediate matrix. Step 2 is performed for all sites.

3. Overwrite the site energy levels with the correlated energies stored in the intermediate matrix.

4. Calculate the new energetic disorder σ^*. Rescale the site energies by

$$E_i \to E_i \sqrt{\frac{\sigma}{\sigma^*}} - \left(\sqrt{\frac{\sigma}{\sigma^*}} - 1 \right) E_i^0 \,, \tag{5.5}$$

   where E_i^0 is the ideal energy level of the MO. While the averaging procedure reduces the width of the density of states, the energetic disorder is rescaled by eq. 5.5 to restore the global disorder σ defined in step 1. This allows a comparison between different levels of correlation and avoids a reduction of the width of the Gaussian DOS.

5. To achieve an increased correlation, steps 2-4 can be repeated. Alternatively, the correlation radius r_{corr} may be increased.

Figure 5.2 shows the energetic landscape with different correlations ranging from $r_{\mathrm{corr}} = 0\,\mathrm{nm}$ (GDM) to 7.5 nm. The shape of the DOS needs to remain Gaussian, as a change of the DOS itself would result in strongly varied transport properties [85]. Figure 5.2a depicts the distribution of site energies for all configurations, and Fig. 5.2b depicts their energetic landscapes. The Gaussian DOS remains nearly unchanged for all configurations. Only a small negligible shift of the peak of CDM_2 by 7 meV towards higher energies is observed. The distribution of site energies changes and a formation of domains with locally reduced energetic disorder is obtained.

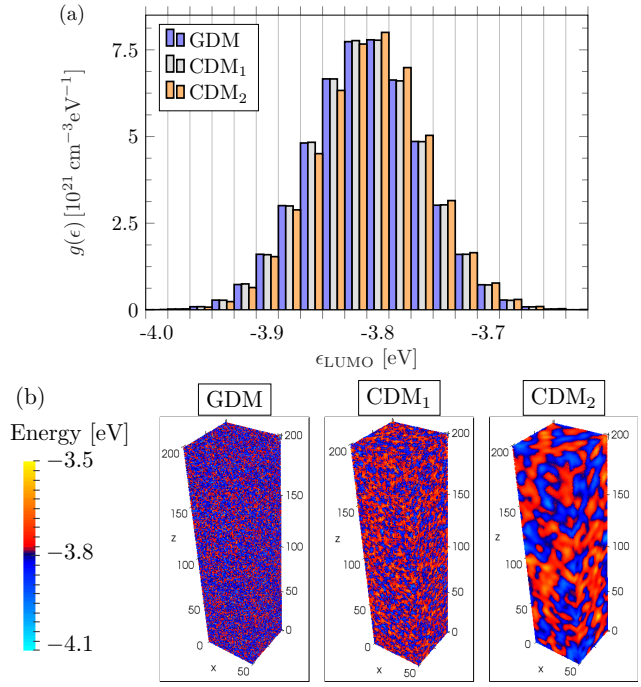

Figure 5.2 (a) Site energy distribution for the uncorrelated GDM and the two spatial correlated configurations CDM_1 and CDM_2. In the case of CDM_2 a correlation length of $r_{corr,1} \approx 2.5\,nm$ is obtained, while $r_{corr,2} \approx 7.5\,nm$ represents a strongly spatial correlated energetic landscape. (b) Energy landscape for the investigated configurations with different levels of correlation, the GDM (left), CDM_1 (mid) and CDM_2 (right). Reprinted from [50], with permission from the PCCP Owner Societies.

Voronoi Tessellation

With rising amount of computational power and powerful clusters, investigations on the structure-property relationship, especially for charge and exciton transport within organic materials, using multiscale simulations have gained rising interest in the community [20, 186, 187]. Organic materials mostly consist of amorphous or regio-regular polymers or small molecules. A cubic lattice model may not describe all experimentally observable features in its detail. To capture the molecular structure of thin films within kMC simulations, off-lattice models are required [29, 49, 188, 189]. A representative site model of the active organic layer has been implemented based on the Voronoi tessellation [190, 191]. The detailed procedure of the generation of the Voronoi tessellation and its features are described in section 3.2

Figure 5.3 visualizes the Voronoi tessellation of a small number of sites. Each localized quantum state is represented by a grey sphere. The red wires indicate the boundaries of the Voronoi cells. The shown Voronoi tessellation is obtained by a shift of the cubic lattice sites by a random distance. The shift value is drawn from a Gaussian distribution with width σ_r. Here, a standard deviation of $\sigma_r = 0.05a$ is chosen. Obviously, a strong increase in the structural disorder can be reproduced. Further geometrical information, like clustering or crystalline arrangement of the localized sites, can be easily included.

Comparing the cubic with the off-lattice approach, some obvious differences and their importance are to highlight. Due to the spatial disorder of the sites, the number of next-neighbors increases. Moreover, the major drawback of an equidistant spacing between lattice points in the cubic model [278] is overcome with the use of the Voronoi tessellation. The local distribution of lattice sites can be

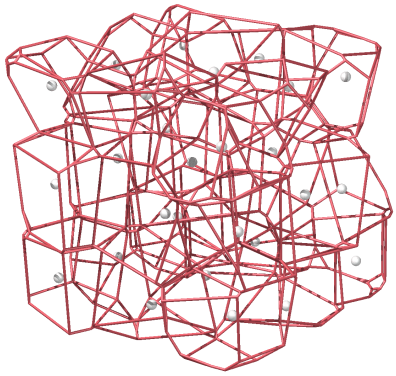

Figure 5.3 Visualization of the Voronoi tessellation of spatially disordered sites: The grey spheres represent localized quantum states, while the red wires define the space belonging to the site. Reprinted from [50], with permission from the PCCP Owner Societies.

imported from MD simulations using the center of masses of the molecules, providing a sophisticated multi-scale simulation method comparable to Refs. [20, 49]. In case of available quantum chemical simulations the localized quantum state could directly be used as the input of the sites. Herewith, the information depth of the structural alignment of e.g. polymers or small molecules down to the nanoscale can be represented on a mesoscopic level. Besides, amorphous domains in both polymers and small molecules can be explicitly investigated, which makes the study of the physical properties more realistic. In case of the exciton diffusion, non-nearest neighbors are required. The Voronoi tessellation supports a fast iteration method to obtain all neighbors within a certain radius around a site.

Existing off-lattice models take into account all adjacent molecules within a certain radius [49,279]. Depending on the density of sites, this may cause a strong increase in simulation time. Using the Voronoi tessellation, only adjacent sites are considered, which keeps the computation time feasibly low. In case of a strong disorder, a common radius might introduce the scenario that certain sites are fully disconnected from the surrounding material. This is avoided with the Voronoi tessellation. The tessellation furthermore allows the computation of local current and charge densities as a well-defined area of the faces and volume of the Voronoi cells is obtained [50]. Besides all advantages, it still is to consider that the cell boundaries are purely based on the distance between centroids and do not contain any physical information, which, depending on the modeled system, has to be evaluated carefully for the computation of local quantities.

5.1.3 Results and Discussion

First, we recapitulate the dependence of the charge carrier mobility on the electric field F, the charge carrier density n, and the energetic disorder σ within the uncorrelated Gaussian disorder model (GDM), as discussed by Pasveer *et al.* [270]. Using kMC simulations in a $50\,\mathrm{nm} \times 50\,\mathrm{nm} \times 200\,\mathrm{nm}$ single material with periodic boundaries in all spatial dimensions, we compute the average drift mobility by

$$\mu_z = \frac{\langle \mathbf{v} \cdot \mathbf{F} \rangle}{F^2}\,, \tag{5.6}$$

Table 5.1 Set of investigated parameters

Parameter [unit]	**Values**
Attempt-to-hop frequency a_0 $[1/\mathrm{s}]$	3×10^{12}
Inverse localization length γ $[1/\mathrm{nm}]$	$\{2, 10\}$
Reduced energetic disorder $\hat{\sigma}$	$\{2, 3, 4\}$
Charge carrier density n $\left[\mathrm{cm}^{-3}\right]$	$\left\{8 \times 10^{15}, 10^{18}\right\}$
Correlation lengths l_{corr} $[\mathrm{nm}]$	$\{0,\ 3,\ 12\}$
Inter-site distance a $[\mathrm{nm}]$	1
Spatial disorder σ_r $[1/a]$	$\{0.01,\ 0.05,\ 0.1\}$
Permittivity ϵ	3.5

where $\mathbf{F} = F\mathbf{e}_z$ is the external field applied along z-direction. In the following, we denote the reduced energetic disorder by $\hat{\sigma} = \sigma/(kT)$, while $k_\mathrm{B}T = 25\,\mathrm{meV}$ is fixed. An attempt-to-hop frequency of $a_0 = 3 \times 10^{12}\,\mathrm{s}^{-1}$ and an inverse localization length of $\gamma = 2\,\mathrm{nm}^{-1}$ are chosen, if not mentioned otherwise. For every $\hat{\sigma}$, simulations with three different energetic configurations are run and the mean mobility is calculated. Following this overview, we investigate both the impact of spatial correlations in energetic disorder and a spatial disorder in the site positions on the mobility. Table 5.1 summarizes the investigated parameter set.

Charge Carrier Density, Energetic Disorder and Electric Field Dependence

First, we outline the dependence of the mobility on the charge carrier density, the energetic disorder and the electric field in the GDM [29, 270]. As shown experimentally [269], the mobility can differ up to 3 orders of magnitude for different charge carrier densities. We assume typical values for the charge carrier density in OPVs and OFETs with the same active material, using experimentally observed values of $n = 8 \times 10^{15}\,\mathrm{cm}^{-3}$ and $n = 10^{18}\,\mathrm{cm}^{-3}$, respectively [280, 281]. The reduced energetic disorder $\hat{\sigma}$ is varied from 2 to 4, representing realistic disorder values in disordered organic semiconductors [268, 282]. For high charge carrier densities, we shrink the simulation box to 50 nm in z-direction to keep the simulation time low.

In Fig. 5.4, we plot μ as a function of the electric field F with different energetic disorders for both the low (left) and the high charge carrier density (right). At the investigated low charge carrier density, the mobility varies by several orders of magnitude for different disorders at low electric fields. For low $\hat{\sigma}$, the carrier mobility remains almost constant, while at high $\hat{\sigma}$ the mobility can be raised by approximately two orders of magnitude with increasing electric field. At low electric field, charges are slowed down due to the presence of energetic barriers between two sites, and transport mainly occurs by diffusion. At electric fields exceeding one σ per inter-site distance a, the energetic barriers lose their impact and charge carrier movement is dominanted by the drift field. Increasing the electric field leads to a saturation of the charge carrier velocity, thus the mobility decreases for high electric fields with $1/F$. Moreover, the curves for different $\hat{\sigma}$ almost converge at high F.

The above features are similar for both high and low charge carrier densities. The mobility shows an increase up to one order of magnitude for high charge carrier densities. Moreover, the difference in the mobility may rise up to three orders of magnitude for even higher energetic disorder [269, 270]. Thus, the mobility in different devices (*e.g.* OPVs and OFETs) can vary tremendously. Moreover, a shift of the maximum of μ towards lower fields is observed. At high n, the density of occupied sites

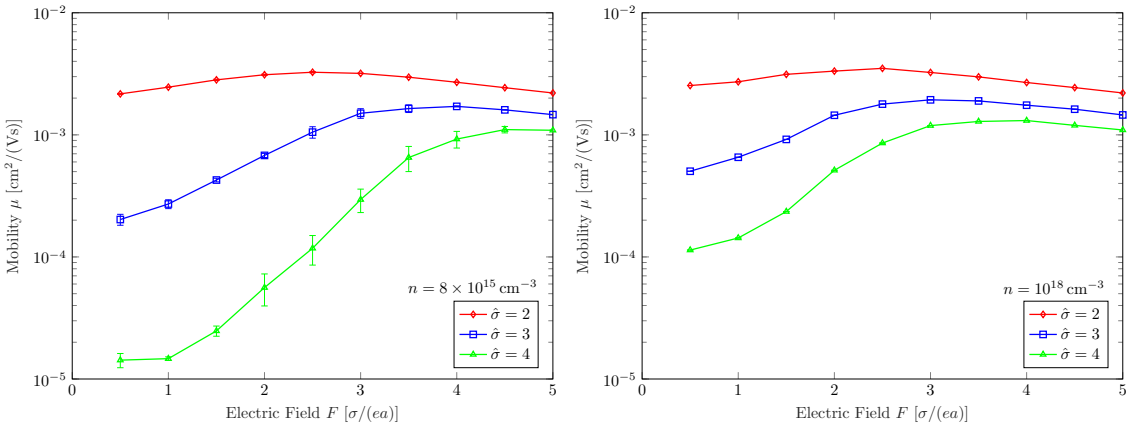

Figure 5.4 Charge carrier mobility as a function of the electric field for (left) a low charge carrier density $n = 8 \times 10^{15}\,\mathrm{cm}^{-3}$ and (right) a high charge carrier density $n = 10^{18}\,\mathrm{cm}^{-3}$ for different energetic disorders. Reprinted from [50], with permission from the PCCP Owner Societies.

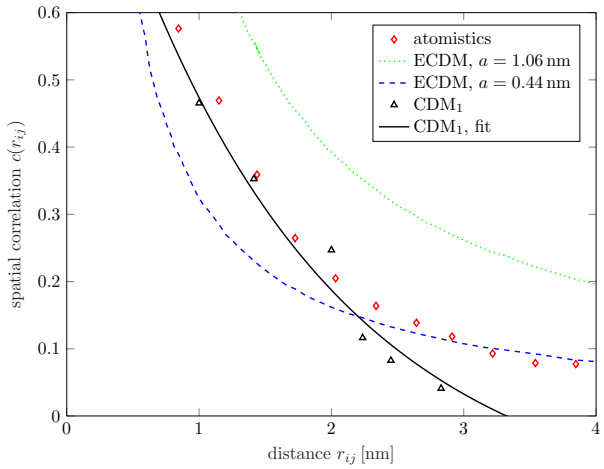

Figure 5.5 Spatial site energy correlation of the CDM$_1$ compared with the atomistic results and ECDM models extracted from Kordt *et al.* [284]. An exponential fit is used to model the correlation length in the CDM$_1$. Reprinted from [50], with permission from the PCCP Owner Societies.

close to the transport level is larger, and more sites within a small energy range are available as a hopping destination; thus the differences in energies get less important [85, 270].

Role of Correlations in the Energetic Disoder

Several researchers have implemented a correlation in the energetic disorder induced by random dipoles and studied its effect on the mobility by numerical simulations [272, 277, 283]. In our model, we induce a correlation in the energy landscape using a weighted average over all sites within a correlation radius. The implemented CDM is similar to the one Cordes *et al.* [271] and Kimber *et al.* [44] utilized for the simulation of the drift mobility in a correlated 1D-chain and 3D organic photovoltaics, respectively. We compare the charge transport properties for the uncorrelated GDM model with two levels of correlation, the weakly correlated CDM$_1$ and the strongly correlated CDM$_2$.

The spatial correlation as a function of the distance r_{ij} between sites i and j is computed by

$$c(r_{ij}) = \frac{1}{\sigma^2} \left\langle (E_i - E_i^0)(E_j - E_j^0) \right\rangle , \tag{5.7}$$

where $\langle \cdot \rangle$ denotes the arithmetic average of the product of all energies E_i and E_j between sites i and j and σ is the obtained disorder in the Gaussian DOS. The spatial correlation for the CDM_1 is shown in Fig. 5.5. An exponential fit of

$$c(r_{ij}) = -0.148 + 1.15 \exp\left(-\frac{r_{ij}}{1.623\,\text{nm}}\right) \tag{5.8}$$

is observed. The correlation length r_{corr} is taken as the distance r_{ij} which fulfills the condition $c(r_{ij}) = 0.1$. We compare the correlation with atomistic simulations [284] and the extended correlated disorder model for different lattice constants $a = 1.06\,\text{nm}$ and $a = 0.44\,\text{nm}$ [272, 277]. For a distance below 2 nm, the utilized CDM fits quite well the atomistic values. It is in the range between the ECDM curves. At distances beyond 2 nm, the obtained correlation deviates from the correlations using the dipole based CDM [284]. The correlation length of the CDM_1 is $r_{\text{corr},1} \approx 2.5\,\text{nm}$, *i.e.* the energy is correlated over a distance of more than 2 sites. For the strongly correlated CDM_2, a correlation length of $r_{\text{corr},2} \approx 7.5\,\text{nm}$ is observed. For the strongly correlated case CDM_2, an average correlation length of $r_{\text{corr},2} \approx 7.5\,\text{nm}$ is induced. Both structures are visualized in Fig. 5.2.

The field dependence of the mobility is shown for the different levels of correlation in Fig. 5.6 for (left) low and (right) high charge carrier densities. In case of the low charge carrier density, the mobility for high reduced energetic disorder $\hat{\sigma} = 4$ is increased by up to two orders of magnitude towards higher correlation. For a lower energetic disorder, the mobility increase is reduced. For CDM_1, the change in the mobility is similar to the trend observed within previous work [44, 271, 272]. Including the CDM, the mobility follows the Poole-Frenkel behavior over a larger field range for both the asymmetric Miller-Abrahams and the symmetric Marcus hopping rate [285]. It was shown that the full PF mobility dependence down to low electric fields requires the inclusion of traps [44], which is not considered here. At high electric fields, the mobility is independent of the level of correlation, as the drift component dominates. The field dependence of the mobility for high charge carrier density follows the same trend. For rising correlation, the impact of the charge carrier density, given by the Coulomb interaction, decreases as the applied field overcomes the lowered energetic site to site barriers.

Several experiments observing the Poole-Frenkel mobility [286, 287] lead to the conclusion that the site energies in the simulated materials are correlated weakly, as modeled in the CDM_1. This suggests that the CDM implemented by a weighted average is capable of describing the same effects one observes by the inclusion of random dipoles. Recently, Kordt *et al.* [284] published an interesting, sophisticated improvement of the correlation model compared to the well-known CDM based on random dipoles [277]. They utilize a distribution of dipole moments based on atomistic simulations and show that this distribution can reproduce the spatial correlation better than the commonly used ECDM. An increase in the mobility of up to one order of magnitude was observed for a large energetic disorder of $\hat{\sigma} = 7$. For lower disorders, the difference is expected to be far less such that the exact shape of the correlation function has a reduced impact on the mobility for low $\hat{\sigma}$.

In the strongly correlated CDM_2, an inversion of the field dependence of the mobility is observed for all energetic disorders. The origin of this negative field dependence is explained in the upcoming subsections by the analysis of local currents and transport energies. A negative field dependence of the mobility has been observed previously in a conjugated semiconducting polymeric system based on P3HT [288] and also in bulk heterojunctions [165, 282, 289]. So far, this negative field dependence was connected to a small energetic and a large spatial disorder, which was proposed by

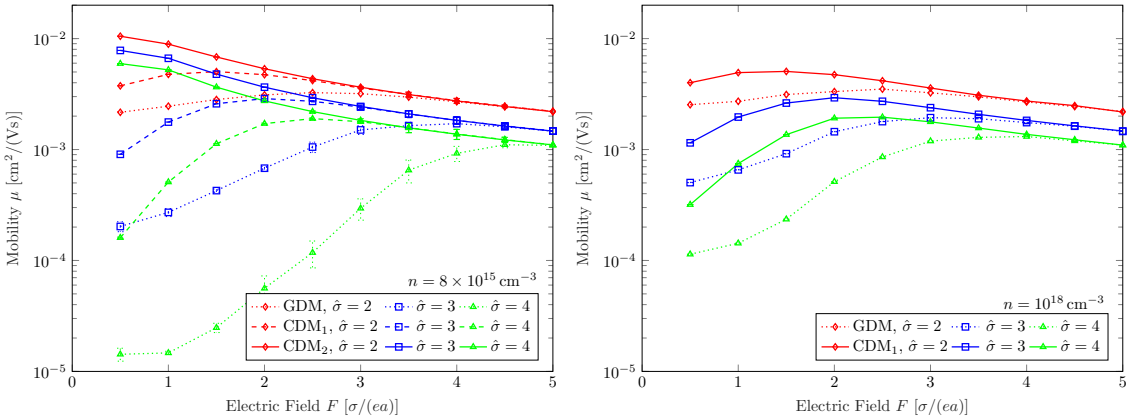

Figure 5.6 Field dependence of the mobility for a charge carrier density of (left) $n = 8 \times 10^{15}$ cm^{-3} and (right) $n = 10^{18}$ cm^{-3} with a varying level of correlation and energetic disorder. Reprinted from [50], with permission from the PCCP Owner Societies.

Bässler [29, 288]. Faster paths through the organic material and dead-ends are created. This has been originally suggested for the description of the negative differential hopping conductivity in impurity inorganic semiconductors based on a percolation model [290]. Unlike shown by other work on correlated disorder models, our simulation results of the strongly correlated organic semiconductors also provide a negative field dependence. The strong correlation lowers the energy barriers between two neighboring sites, while the width of the disorder remains constant. This results in a high charge carrier mobility at low electric fields. Our results suggest that the measurable negative field dependence may result from an increase in the spatial correlation of the energy in the regio-regular polymers rising in the highly crystalline domains.

Formation of Filamentary Currents

As already shown in existing works [291–294], current flow can be strongly filamentary. In this subsection, we study the local currents in field direction for different site energy distributions with and without spatial correlation. We show the stepwise formation of filaments in the local currents with increasing correlation and the effect of the electric field on the structure of the current filaments.

The local current density is evaluated as a site property. For every site i, we count the number of charges N_{ij} leaving site i towards site j, with the normalized distance vector $\hat{\mathbf{r}}_{ij}$ and the interface area A_{ij} between both sites. The local current density is obtained with

$$J_{\mathrm{local},i} = \sum_j \frac{N_{ij} e}{t_{\mathrm{sim}} A_{ij}} \hat{\mathbf{r}}_{ij} \cdot \mathbf{e}_z \,, \tag{5.9}$$

where $\mathbf{e}_z$ is the unit vector in z-direction and e is the elementary charge. A simulation time of $t_{\mathrm{sim}} = 10\,\mu\mathrm{s}$ is used in order to obtain a significant number of hopping events for the statistical evaluation. The interface area is obtained using the voro++ framework [192].

First, we compare the local currents of the uncorrelated GDM with both the CDM$_1$ and CDM$_2$ for an applied electric field $F = 4\,\sigma/(ea)$. The local currents J_{local} are given in Fig. 5.7. In the GDM, the local current is distributed across the organic material without showing any preferred paths. Carrier diffusion is of large importance in the case of uncorrelated site energies. In the weakly correlated CDM$_1$, small current filaments are formed. In the domains of low site energies, preferred pathways with reduced energy barriers are formed. Filamentary structures in the current are represented by the

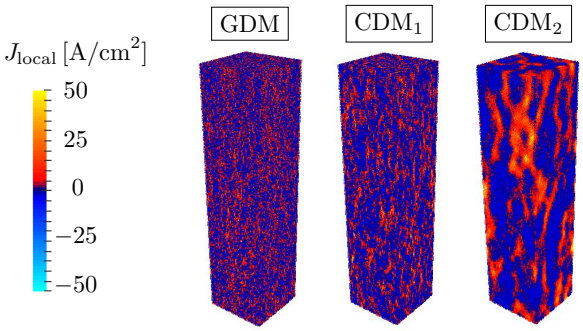

Figure 5.7 Spatial correlation dependence of the local current distribution at an electric field $F = 4\,\sigma/(ea)$ and low charge carrier density $n = 8 \times 10^{15}\,\mathrm{cm}^{-3}$. The local currents for the GDM, CDM_1 and CDM_2 are shown for a reduced energetic disorder of $\hat{\sigma} = 2$. Filament-like domains with high local current density induced by the correlation in site energies are visible in the CDM_1 and CDM_2. Reprinted from [50], with permission from the PCCP Owner Societies.

high local current domains in Fig. 5.7. This explains the observed increase in the mobility. In case of the strongly correlated CDM_2, long filaments of the local currents are formed due to the correlation in the site energies and the reduction of the energy barriers between neighboring sites. Charge transport is localized in regions with low site energies. With rising disorder, the current filaments get narrower, as the percolative paths are squeezed by the rising energetic barriers.

As shown by van der Holst *et al.* [292], a high energetic disorder σ supports the formation of filamentary structures in the charge current in case of an uncorrelated energetic disorder due to the highly percolative nature of charge transport in disordered matter. The inclusion of a short-range Coulomb interaction between the charges however yields a blocking of the percolation paths due to the Coulomb repulsion by other carriers [293]. In the shown current profiles (Fig. 5.7), an energetic disorder lower than the values investigated in Refs. [292] and [293] is chosen. Both low $\hat{\sigma}$ and Coulomb repulsion hamper the formation of filaments. In addition, our model for an organic bulk material comprises an exact treatment of the Coulomb interaction and imposes a fixed carrier density, as injection processes have been omitted. As all charge carriers will relax towards the tail of the DOS, charge trapping occurs and no filamentary structures in the currents are expected in the GDM. Van der Holst *et al.* have shown that due to the charge injection from the contact into an organic thin film device, the charge density close to the contact is very high compared to the middle organic layer. Thus, the formation of current filaments inside a thin film device strongly differs from a bulk material. With rising correlation, the filaments get broadened and the percolation paths acquire a width of a multiple of the lattice spacing [293, 294]. The effect of the Coulomb interaction is reduced, as the decrease of local currents due to a blocking of charges and the increase of current rising by a declotting effect cancel each other [293].

For the strongly correlated CDM_2, we study the dependence of the formation of current filaments on the electric field. The local currents are shown in Fig. 5.8. On the left, the local current distribution is shown for both low and high electric fields, at $F = 0.5\,\sigma/(ea)$ and $F = 5\,\sigma/(ea)$ respectively. The site energy landscape without applied external field is shown on the right part of Fig. 5.8. Already at low F, the local current is confined to regions of low site energies. Furthermore, the current is spread over a broader region between two clusters of low site energies, as diffusion mainly controls the current distribution in the low-field regime. With increasing field, domains with high local currents grow and filaments are formed. The location of the filaments correlates with energy tails in the organic semiconductor. A high external electric field delocalizes the confined charges and supports the formation of filaments across energetic barriers. These barriers, which previously separated domains

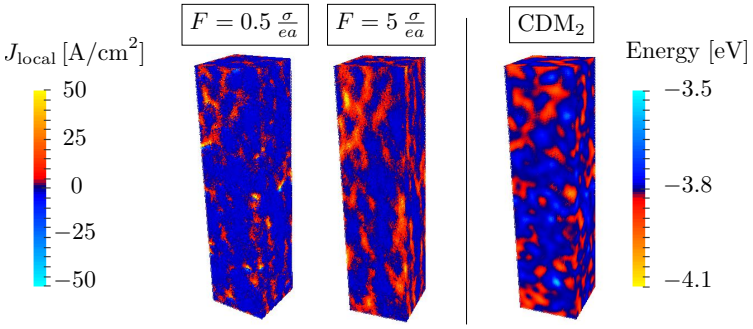

Figure 5.8 Local current distribution at low electric field $F = 0.5\,\sigma/(ea)$ (left) and high electric field $F = 5\,\sigma/(ea)$ (mid). The right part shows the site energy distribution for the CDM$_2$ configuration. Reprinted from [50], with permission from the PCCP Owner Societies.

of high local currents, now are overcome. For a high field, charge carrier transport is dominated by the drift component. Thus, the filaments are stretched in field direction.

Impact of Correlated Energy Levels on the Transport Energy

While the results in the previous section presented a picture of the formation of local filaments in the spatial phase space, the following part links the transport properties with its energy-phase space based on the theoretical concept of the transport energy. The transport energy ϵ_t plays an important role for charge transport in a Gaussian DOS [295, 296]. Charge carriers at energies higher than ϵ_t tend to relax in energy, while states below ϵ_t essentially contribute to the charge transport by transitions towards ϵ_t. In thermal equilibrium, carrier energies are distributed around the equilibrium energy $\epsilon_\infty = -\sigma^2/(kT)$. The theoretical fundamentals of the transport energy are summarized by Baranovskii [85]. The transport energy was previously studied in systems with uncorrelated and correlated energetic disorder using percolation theory [297]. Here, we investigate the effect of the correlation on the transport energy level ϵ_t based on our kMC results of the local currents through a site i.

In Fig. 5.9, we visualize the density of states contributing to a local current in field direction above the threshold current density of $J_{\text{local,th}} = 1\,\text{A/cm}^2$ for different electric fields F. For a comparison, the DOS of the site energies is provided in each plot. The distribution of activated sites is shown for all studied cases, the GDM, CDM$_1$, and CDM$_2$. Figure 5.9 depicts results for an energetic disorder of $\hat{\sigma} = 2$.

We define sites to be active for charge transport if the current density through site i exceeds the lower threshold of $J_{\text{local},th} = 1\,\text{A/cm}^2$. Based on the density of activated sites, we evaluate the transport energy ϵ_t. In Fig. 5.10a, the transport energy is shown for the different energetic configurations. The width of the DOS of activated sites σ_j is observed by a Gaussian fit. We compare σ_j with the energetic disorder σ in Fig. 5.10b in form of the normalized standard deviation σ_j/σ for all energetic configurations and electric fields F.

Due to finite size effects, there is a significant deviation from the theoretical carrier energy if one has low carrier densities and large values of energetic disorder [298, 299]. The number of sites chosen in this analysis ($N = 500000$) is significantly higher than the required number of sites to avoid dispersive transport for a reduced energetic disorder of $\hat{\sigma} = 2$ [298]. As a consequence, the impact on the transport energy and local currents are negligible. We neglect these effects and point out, that deviations from the theoretical values, observable at infinite system size, need to be taken into account

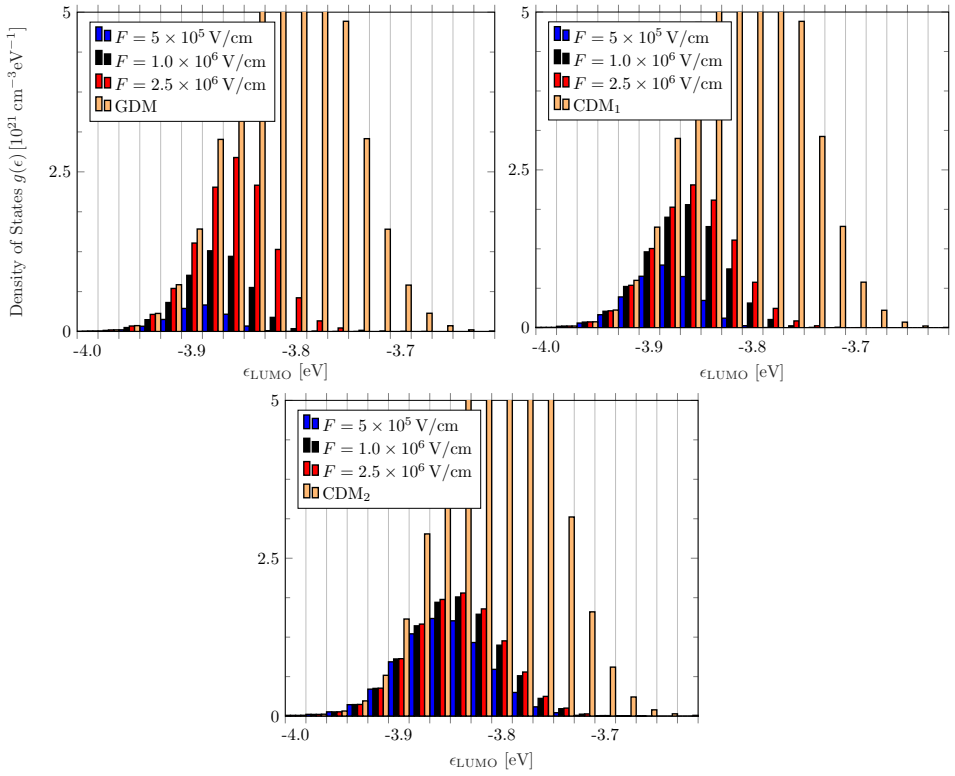

Figure 5.9 Distribution of density of activated states, defined by a lower current density threshold of 1 A/cm^2. The given distributions show the result for an energetic disorder of $\hat{\sigma} = 2$ and the charge carrier density $n = 8 \times 10^{15}\,\mathrm{cm}^{-3}$ at different electric fields F. The density of states for all sites is given for all investigated degrees of correlation: uncorrelated GDM (left), weakly correlated CDM$_1$ with $r_{\mathrm{corr}} \approx 2.5\,\mathrm{nm}$ (mid), CDM$_2$ with $r_{\mathrm{corr}} \approx 7.5\,\mathrm{nm}$ (right). Reprinted from [50], with permission from the PCCP Owner Societies.

for the higher investigated energetic disorders to obtain a quantitatively precise study of the transport properties.

First, we discuss the transport energy in the GDM. Comparable to the energetic DOS, the distribution of the transport energy can be fitted with a Gaussian distribution. The transport energy is evaluated as the mean energy level of the distribution of activated sites. For low electric field, the maximum of the distribution of activated sites is shifted to lower energy sites. The transport energy approaches $\epsilon_{\mathrm{t}} = -3.89\,\mathrm{eV}$. This energy is very close to the ideal MO energy level lowered by the theoretical equilibrium energy of $\epsilon_\infty = -0.1\,\mathrm{eV}$. With increasing electric fields, the transport energy is shifted towards the energy of $-3.86\,\mathrm{eV}$. For even higher fields, the transport energy remains constant. An increase in the activated number of sites is only observable until the maximum mobility is reached and the velocity saturates.

At low electric fields, the transport energy in the correlated configurations CDM$_1$ and CDM$_2$ reveals the same values (see Fig. 5.10). With increasing field, the rise in transport energy differs strongly from the GDM. For the CDM$_2$, ϵ_{t} shows a steep increase and approaches the level of $-3.85\,\mathrm{eV}$ within an increase of $1\,\sigma/(ea)$ in the electric field. For even higher fields, ϵ_{t} remains constant. Only the number of activated sites increases until the charge carrier velocity saturates. The distribution of activated sites for a high electric field is significantly broadened compared to the weakly correlated and uncorrelated site energies. A reason for this observation is the strong increase in correlation. Thus, neighboring sites exhibit a low difference in site energies. Only a small electric field is required

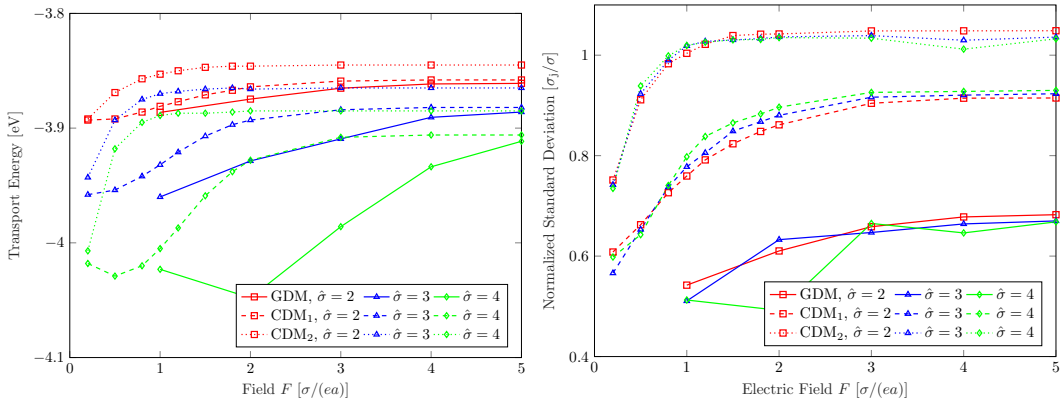

Figure 5.10 Field dependence of the (left) transport energy and (right) normalized current distribution width σ_j for the different energetic configurations and varying reduced energetic disorder $\hat{\sigma}$. Reprinted from [50], with permission from the PCCP Owner Societies.

to overcome these energetic barriers. Hence, sites higher in energy also contribute effectively to the charge transport. This was also seen in Fig. 5.8, where a high electric field stretches the filamentary currents in field direction and sites with higher energies are included in the current filaments with increasing field.

The width of the distribution of active sites, shown in Fig. 5.10b, shows the same trend for all reduced energetic disorders $\hat{\sigma}$ for same correlation. A steep broadening of the distribution of activated sites with increasing field for the CDM$_2$ compared to the CDM$_1$ can be seen.

In the CDM$_2$, the main change in the distribution of active sites is observable for low electric fields below $1\,\sigma/(ea)$. For the CDM$_1$, the distribution changes up to an electric field of $\approx 2\,\sigma/(ea)$, while the transport energy saturates at approx. $3-4\,\sigma/(ea)$ in the GDM. These electric fields were also obtained in the presented study on the field dependence of the mobility and the local currents, proving the strong correlation between the transport energy and the effective charge carrier mobility.

The study of the transport energy and the distribution of local currents gives a clear picture of the energetic phase space dominating the charge transport at the different orders of correlation. Results with different energetic disorders show a difference in the value of the transport energy, while the distribution of site energies contributing to the current is independent of the value of σ. At low electric fields, the transport energy is close to the theoretical value of the equilibrium energy. Clear differences in the charge transport properties for different site energy correlations are observable with increasing electric fields.

5.1.4 Impact of the Spatial Disorder on the Mobility

In this subsection, we discuss the impact of a spatial dislocation from the cubic lattice of the localized sites. The dislocation is modeled by a shift of the sites from the cubic lattice by a random value chosen from a Gaussian distribution with the spatial disorder σ_r. The irregular Voronoi tessellation is then calculated on the shifted sites, which gives an increased number of neighbors and a strong change in the inter-site distances. With increasing σ_r, the structure describes a rather amorphous than a crystalline material. This can be considered as a very simplified description of small molecules aligned in a disordered system. The kMC model based on the Voronoi tessellation is capable of modeling a realistic organic structure, if combined with an input from molecular dynamics as discussed in the next subsection.

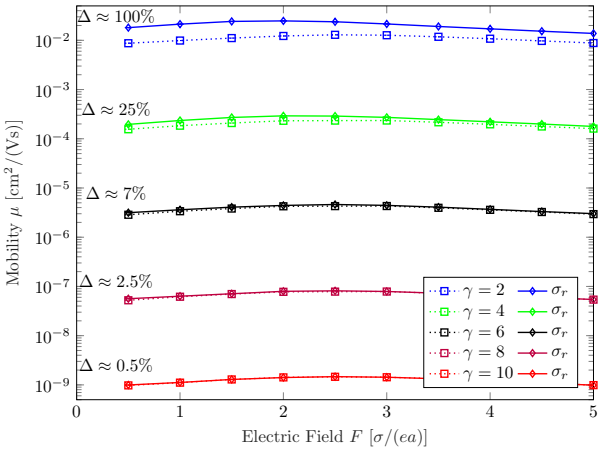

Figure 5.11 Field dependence of the charge carrier mobility for different inverse localization lengths with (solid lines) and without (dashed lines) a spatial disorder $\sigma_r = 0.01a$. All results are shown for the GDM with an energetic disorder of $\hat{\sigma} = 2$. Reprinted from [50], with permission from the PCCP Owner Societies.

In the following, we only consider the uncorrelated GDM. We investigate the effect of the spatial disorder in the range of $\sigma_r \in \{0.01a, 0.05a, 0.1a\}$ on the charge carrier mobility.

For $\sigma_r = 0.01a$, the Voronoi tessellation only slightly differs from the cubic lattice, thus no larger changes in the mobility are expected. In Fig. 5.11, the mobility is visualized in the system with and without spatial disorder. Unlike expected, the mobility was doubled for the case of the small spatial disorder at an inverse localization length of $\gamma = 2\,\mathrm{nm}^{-1}$. The increase is caused by the increased connectivity of the semiconductor sites. The small shift of a lattice site leads to a connection of additional neighbors to the Voronoi cell. These arise from the second and third nearest neighbors with the distance of $\sqrt{2}a$ and $\sqrt{3}a$, respectively, from the cubic lattice. Due to the low γ, the probability of hopping to a higher order next-neighbor needs to be taken into account. We varied γ from the low localized state with $2\,\mathrm{nm}^{-1}$ to a high localized state using $\gamma = 10\,\mathrm{nm}^{-1}$ and compared the mobility between the cubic lattice and the Voronoi tessellation with $\sigma_r = 0.01a$ (shown in Fig. 5.11). The deviation in mobility Δ is given in the graph. It is observable that the change in mobility is high for inverse localization lengths below $\gamma = 6\,\mathrm{nm}^{-1}$, while it is negligible for a higher localization.

In Fig. 5.12, the mobility is shown for different spatial and energetic disorders. We assume a localization constant of $\gamma = 10\,\mathrm{nm}^{-1}$ to avoid the discussed change in connectivity by the inclusion of the second and third next-neighbors. We assume an uncorrelated Gaussian disorder in the site energies. The results show the mobility for low charge carrier densities $n = 8 \times 10^{15}\,\mathrm{cm}^{-3}$. For high energetic disorder $\hat{\sigma} = 4$, our model shows a slight increase in mobility at low electric fields. This increase is caused by the increased connectivity in the material, such that the energetic disorder may be overcome easier. Towards high electric fields, the mobility decreases and does not reach the same mobility value which the cubic lattice model obtains in the case of saturation.

In comparison, Bässler shows in his model [29] that an inclusion of the spatial disorder, modeled by a variation in $\Gamma = 2\gamma a$, increases the mobility by several orders of magnitude and even inverts the field dependence of the mobility in the low-field portion. This is not observable in our results based on the Voronoi tessellation. In our model, a small distance r_{ij} between sites i and j implies, that the distance from j to another neighbor site $k \neq i$ is most probably larger than the cubic lattice spacing a, creating a dead-end for the charge carrier. Thus, charge carriers will be likely to hop between sites i and j several times, as they behave like charges in an energetic valley. This slows down the effective velocity in field direction and hereby leads to a reduction of the mobility. As discussed by Baranovskii [85], the

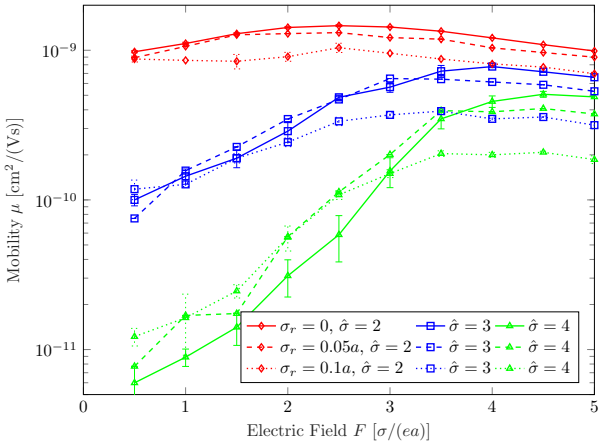

Figure 5.12 Field dependence of the mobility for different spatial disorder σ_r and reduced energetic disorder $\hat{\sigma}$ with an inverse localization length $\gamma = 10\,\mathrm{nm}^{-1}$. Reprinted from [50], with permission from the PCCP Owner Societies.

numerical model of Bässler [29] can build up a directionality of the charge hopping, as easy channels are opened for compensation of the energetic disorder. In our investigation of the Voronoi tessellation based on spatially disordered sites, these easy channels are not formed. Other works using random lattice models also did not result in a negative field dependence [49]. Not only the presence of the spatial disorder itself is of importance, the structure in the spatial arrangement of the molecular sites needs to be considered. Within a previous work [188], the negative field dependence of the mobility could be reproduced based on highly polymerized chains including conformational traps, neglecting any energetic disorder and charge-charge interactions. We showed in the previous section, that the negative field dependence in the mobility can arise due to a high correlation in the energetic disorder, which is considered to be present in the domains with an increased crystallinity.

5.2 Spatial Disorder in Pentacene Crystals and Thin Films

5.2.1 Background

One of the biggest challenge in the design of efficient organic electronics is to understand the relation between structural properties of molecular thin films and the device properties such as the charge carrier mobility. To date, the low charge carrier mobility of organic semiconductors limits the performance of electronic devices. Largest observed mobilities are in the range of $10\,\mathrm{cm}^2\mathrm{V}^{-1}\mathrm{s}^{-1}$ for crystalline pentacene [300] and rubrene [301]. The lack of insight into structure-property relationships requires detailed chemical intuition to design novel, high mobility molecules. *In silico* models are considered as promising alternatives to derive a relation between charge transport properties and structural morphologies within organic devices with high accuracies down to the atomic scale [302].

Most existing approaches focus on a specific length scale of the mentioned problem: analytic models provide an empirical picture of charge transport in disordered organic materials at the continuum scale, while neglecting the molecular details [85, 270, 303–305]; molecular dynamics (MD) and density functional theory (DFT) allow insight into packing of molecules and the electronic structure of isolated molecules, respectively. This provides detailed information on molecular length scales ($\leq$ 1 nm), however it is not feasible to obtain transport properties due to the high computational cost [186, 306]; kMC bridges different length scales by linking structural and electronic properties to

hopping rates [29, 44, 50, 182, 307]. However, accurate kMC results can only be obtained if accurate electronic structure properties are given as an input.

Multiscale methodologies bridge different length scales by combining electronic structure calculations of single molecules and molecular units, MD simulations to observe realistic morphologies, and kMC to simulate mesoscopic charge transport properties [20,49,213,308–316]. One of the fundamental property for the hopping rate of charge carriers is given by the charge transfer integral [308, 309]. Computing transfer integrals from *ab initio* requires huge computational resources for most disordered systems. Thus, the mentioned parameters are often approximated by parametrized models [44, 50]. This, however, cannot capture the sensitivity of transport to structural changes.

Machine learning (ML) has been utilized in many fields of research and engineering to tackle big data issues and to provide a powerful prediction for complex problems [317–320]. ML seems a promising route for an efficient and effective prediction of the electronic charge transfer integrals if being trained on accurate quantum chemical calculations. Within multiscale frameworks, this allows a rapid prediction without the need for any empirical parametrization.

Here, a multiscale method for the computation of charge carrier mobilities is presented. Electronic transfer integrals are predicted by Machine Learning after training on dimers obtained by MD simulations and quantum chemical computations. The kMC model, based on the Voronoi tessellation, is a key part of the model and delivers the connection between the transfer integrals in dimers with mobilities of a mesoscopic bulk / thin film of organic molecules. Here, pentacene has been used as an example. The transfer integral predicted by the ML algorithm are taken as input values into the kMC model. Here, charge carrier mobilities are computed based on the Marcus hopping model. Anisotropies of mobilities for various configurations with different degree of disorder are studied based on the ML predictions of the transfer integrals. For details on the ML model, please refer to [253].

5.2.2 Model

The integration of the developed kMC model into the multiscale framework is visualized in Fig. 5.13. The framework connects the structure of molecular systems obtained from MD, electronic structure calculations, ML for the efficient prediction of intermolecular transfer integrals, and kMC for charge transport calculations. The different components are briefly outlined in the following.

Machine Learning

Accurate prediction by ML relies on the meaningful features that are uniquely linked to their respective label [321]. A set of simple geometric features has been used to predict transfer integrals for different pentacene dimers. The dimer of two rigid molecules is uniquely described by six features: three coordinates determining the relative position, plus three angles providing the relative orientation between the molecules. This feature can be applied to any planar molecular material.

The ML is exploiting a simple kernel ridge regression (KRR) [322]. It mainly is a regularized least-squares fitting method, which links features to labels by a linear function $f(\mathbf{x}_i, \mathbf{w}) \coloneqq f_i$:

$$f_i = w_0 + \sum_{j=1}^{m-1} w_j x_{ij} = \mathbf{w}^{\mathrm{T}} \mathbf{x}_i \,, \tag{5.10}$$

with the feature vector $\mathbf{x}_i$ of a particular sample i, the number of features $m-1$, and the weight vector $\mathbf{w}$. The optimal weight vector $\hat{\mathbf{w}}$ is given by

$$\hat{\mathbf{w}} = \arg\min_{\mathbf{w}} \left[\sum_i (t_i - f_i)^2 + \frac{\lambda^{\mathrm{ML}}}{2} \mathbf{w}^2 \right] \,. \tag{5.11}$$

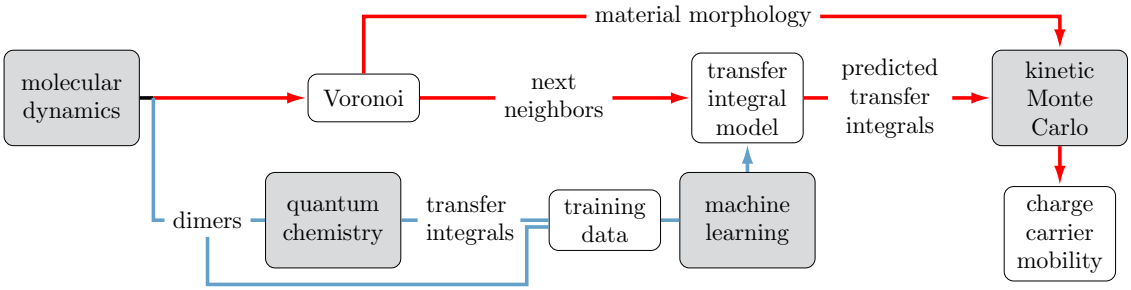

Figure 5.13 Workflow of the multiscale approach. The blue path describes the workflow of the training of the ML algorithm. Dimers, extracted from MD simulations of the disordered pentacene crystal, are used to compute the charge transfer integrals using QC simulations. The dimers in combination with the transfer integrals build the training set of the ML algorithm. Using Kernel ridge regression, a prediction model for the transfer integrals is developed. To obtain mobilities within our multiscale method (red path), we build a Voronoi tessellation based on MD snapshots. The tessellation computes next neighbors and forms a network for the charge hopping within the kMC model. For all next neighbors, the transfer integral is predicted with the ML algorithm and passed to the kMC tool. As a result, we obtain the charge carrier mobility for the given morphology and chemical structure. Reprinted from [253], with permission by ©2018 WILEYVCH Verlag GmbH & Co. KGaA, Weinheim.

The true label of sample i is given by t_i, and λ^{ML} defines the extent of regularization to avoid under-/overfitting.

A common approach to fit non-linear relationships between the features and the label is to apply the Kernel trick. It utilizes the Kernel $k\,(\mathbf{x}, \mathbf{x}')$ as a measure of similarity between the features of two samples [323]. In the presented simulations, the Gaussian radial basis Kernel is used:

$$k\,(\mathbf{x}, \mathbf{x}') = \exp\left(-\gamma^{\mathrm{ML}}\,\|\mathbf{x} - \mathbf{x}'\|_2^2\right)\,, \tag{5.12}$$

with the inverse influence radius $\gamma^{\mathrm{ML}} = 1/(2\sigma^2)$ defining to what extent the label prediction of a particular sample is influenced by other samples with similar features. This hyper-parameter allows for a smooth fitting of the data. To identify suitable values for λ^{ML} and γ^{ML}, 5-fold cross-validations is used. The performance of the ML model is discussed in [253].

Molecular Dynamics

MD simulations are performed to generated the morphology for the kMC simulations and to extract a realistic dataset of pentacene dimers for the ML training. Two different systems are studied: (i) a thermally disordered pentacene crystal, and (ii) a pentacene thin film on top of a SiO_2 substrate. From the obtained morphologies, pentacene dimers from each snapshot are computed by the Voronoi tesselation [50]. The MD procedure is briefly summarized here:

(i) MD simulations are performed using *Tinker* [324] to generate a realistic morphology for the multiscale simulations. The simulation box contains 96 pentacene molecules using low temperature bulk structure of pentacene as initial condition (see Fig. 5.14). The molecules were kept rigid, as intramolecular interactions only have little impact on the dynamics of the full system [325]. A time step length of 2 fs was taken to trace the trajectories accurately. Temperature is kept constant at 300 K applying a Berendsen thermostat algorithm. The MM3 force field is taken for the molecular mechanics simulations [326–328]. It captures the attractive interactions of non-bonded atoms by a pairwise additive van der Waals potential.

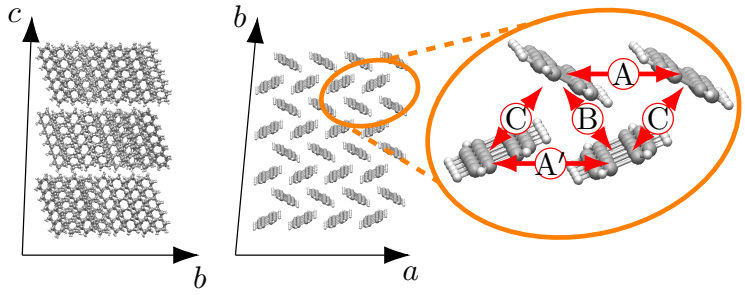

Figure 5.14 Pentacene crystal structure: The crystal is composed of stacked layers along c-direction. The molecular packing in the ab-plane obeys a herringbone pattern. In a super-cell consisting of four molecules, the major transport directions A, A′, B and C are indicated. Reprinted from [253], with permission by ©2018 WILEYVCH Verlag GmbH & Co. KGaA, Weinheim.

(ii) Morphologies of pentacene thin films are generated from classical MD to account for two relevant morphological features occurring in realistic organic thin films: (i) the orientational disorder of molecules induced by temperature and deposition dynamics; (ii) the silicon-dioxide surface that locally affects the molecular assembling with respect to the bulk. Classical molecular dynamics (MD) is a well-established tool to study the structure of organic films at finite temperature and has been successfully applied to hybrid organic-oxide interfaces within previous studies [329–331].

The hybrid interface was prepared as follows: first, 720 pentacene molecules were distributed within a box with dimension 10 nm×5.0 nm×37 nm on top of a frozen crystalline SiO_2 slab with the same lateral dimensions and a thickness of 2 nm (see Fig. 5.15, left). Pentacene molecules were randomly rotated around an axis parallel to the substrate. Periodic boundary conditions were applied in all directions. Replica along the out-of-plane direction are separated by an empty buffer greater than 2 nm. The temperature was controlled by Nose-Hoover thermostat, and equations of motion were solved with the velocity Verlet algorithm with a time step of 1 fs. The final simulation box has dimensions 10.7 nm × 5.5 nm × 18.2 nm. For the SiO_2 the Buckingham-Coulomb [332, 333] interatomic pair potential was used, and for pentacene the standard GAFF force field was used to describe organic-organic interactions [334]. Hybrid interactions are modeled using Coulomb plus dispersive interactions. Dispersive interactions are calculated by mixing rules of Lennard-Jones parameters for atoms of the substrate and the molecules [335]. All MD simulation were performed using LAMMPS [336]. This procedure generates a crystalline film having a preferential orientation of the molecular backbones, but with a sizable molecular disorder.

After a conjugate gradient minimization of simulation box (lateral dimensions only) and atomic positions, pentacene molecules were deposited on the substrate by applying constant force per atom (0.43 eV nm^{-1}) during a 0.1 ns annealing at 150 K. The obtained interface was further annealed at 300 K in the nanosecond time scale. Amorphous and mixed amorphous-crystalline films tend to recrystallize during long annealing times [337]. Since the focus of this study was on the properties of amorphous pentacene films, only the first 0.1 ns of annealing after deposition were studied in which the morphology is maximally disordered. For crystalline thin films, the hopping mechanism does not apply. The final structure is visualized in Fig. 5.15, right.

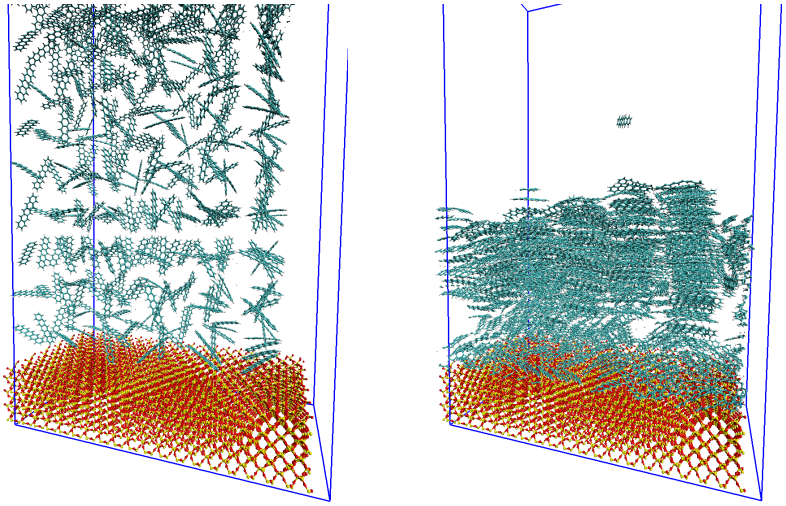

Figure 5.15 MD snapshots of the pentacene thin film on top of a SiO_2 substrate: (left) initial structure, (right) structure after 200 ps. The MD calculations were done by *Alessandro Mattoni*, Cittadella Universitaria di Monserrato. Reprinted from [51], with permission by ©(2020) American Chemical Society

Transfer Integral

In the tight-binding approach [338], electronic orbitals are assumed to be localized due to a strong interaction between electrons and nuclei in the molecules. A delocalization of the electronic states is introduced by a perturbative coupling between localized electronic orbitals. In this assumption, the single electron Hamiltonian can be written as

$$\hat{H}_{\text{el}} = \sum_i E_i \hat{a}_i^\dagger \hat{a}_i + \sum_{i \neq j} V_{ij} \hat{a}_i^+ \hat{a}_j \ , \tag{5.13}$$

where $\hat{a}_i^\dagger$ and $\hat{a}_i$ are the creation and annihilation operators of a charge on site i, respectively, and V_{ij} is the transfer integral between two molecular orbitals. The site energy E_i of a particular orbital ϕ_i is given by

$$E_i = \langle \phi_i | \hat{H}_{\text{el}} | \phi_i \rangle \ . \tag{5.14}$$

Within the frozen-core approximation, only the frontier orbitals are relevant, such that electron transport is assumed to take place in the LUMO and hole transport in the HOMO levels only. Therefore, the electronic coupling between two molecules is given by

$$V_{ij} = \langle \phi_i | \hat{H}_{\text{el}} | \phi_j \rangle \ , \tag{5.15}$$

where ϕ_i and ϕ_j are the HOMO and LUMO wave functions at site i and j, respectively [94].

The orbital wave functions are calculated using the software pDynamo [339] exploiting the semi-empirical Recife Model 1 (RM1) [340], which is a reparametrization of the modified neglect of differential overlap (MNDO) approach [341]. To avoid expensive calculations of the adiabatic monomer wave functions $\{\phi_i\}$, we exploit the dimer projection (DIPRO) method [308,309]. The main idea of the DIPRO method is to project the diabatic monomer wave functions on the dimer wave function, which are relatively easy to access. The implementation of this procedure is based on the code provided by Raos [342].

The STO-3G basis set with the LDA exchange-correlation approximation has been used to obtain the electronic structure of the dimers. Coropceanu and co-workers exploited the PW91 functional

Table 5.2 Computed absolute transfer integrals (in [meV]) corresponding to the dominant transport directions A, A′, B and C for the low-temperature bulk pentacene structure. For each direction, the Miller indices are specified. The values obtained from the semi-empirical (RM1) are compared to simulation results (DFT and tight binding (TB)) from literature [212, 343, 344].

	a	b	c	RM1	DFT [343]	DFT [212]	TB [344]	ML
A	1	0	0	17.2	37	39.68	61	17.2
A′	1	0	0	17.1	34	36.62	-	16.4
B	1	1	0	24.2	51	55.05	56	24.7
C	$\bar{1}$	1	0	36.4	85	90.69	91	36.3

with triple-ζ plus polarization basis set [309]. The latter approach gives reasonable results for the dimer properties; however, even if significantly simpler, the obtained DFT results are comparable to the reference results. The obtained transfer integrals are shown in Table 5.2. The results from RM1 underestimate the electronic coupling by about a factor of $1/2$, but are qualitatively in good agreement to the DFT results. The values predicted by ML are in good agreement with the results from RM1.

Kinetic Monte Carlo Model

Charge transport is described by a hopping process between localized electronic states. For simplicity, we assume charge carriers to be localized on molecules [343, 345]. Additionally, we assume that the transition rates are accurately described by the non-adiabatic Marcus rate given by [92]:

$$a_{i\to j} = \frac{|V_{ij}|^2}{\hbar}\sqrt{\frac{\pi}{\lambda_{ij}k_\mathrm{B}T}}\exp\left(-\frac{\left(\Delta G_{ij}+\lambda_{ij}\right)^2}{4\lambda_{ij}k_\mathrm{B}T}\right)\,, \tag{5.16}$$

with the transfer integral V_{ij}, the reorganization energy λ_{ij}, the driving force ΔG_{ij}, which represents the free energy difference between the sites i and j, Boltzmann constant k_B and temperature T.

The Voronoi tessellation is build based on the morphology of the disordered pentacene layer. We use the center of mass as our sites for the tessellation. Hopping is allowed only to the nearest-neighbors. For π-conjugated materials, representing the molecules by simple sites is justified due to the delocalization of charges across the entire molecule [9]. The ultrafast intramolecular dynamics of charge carriers on the molecule are neglected, which allows a coarse-grained description of charge transport between organic molecules.

Neglecting entropic contributions, the driving force is given as

$$\Delta G_{ij} \approx \Delta E_{ij} = E_j - E_i\,, \tag{5.17}$$

with the site energy E_i given by

$$E_i = E_i^\mathrm{MO} + E_i^F + E_i^C\,, \tag{5.18}$$

where E_i^MO is the molecular orbital energy, E_i^F is the shift of the site energy due to the external electric field, and E_i^C is the Coulomb interaction between charge carriers.

The reorganization energy arises from the conformational changes of the monomers involved in the charge transfer and from lattice distortion as well as polarization caused by the charges themselves [346]. Hence, the reorganization energy can be divided into an intramolecular and an intermolecular part [212], such that

$$\lambda = \lambda_\mathrm{int} + \lambda_\mathrm{ext}\,. \tag{5.19}$$

For oligoacenes, like pentacene, λ_{int} is found to be at least one order of magnitude larger than the external part [346, 347]. Therefore, the reorganization energy is approximated by a constant value corresponding to the internal λ_{int}.

5.2.3 Results and Discussion

Disordered Pentacene Crystal

kMC simulations are performed to obtain the angular dependence of the charge carrier mobility within pentacene. This is a good indicator for the applicability of the ML-based multiscale method as the charge transfer integrals and carrier mobility are strongly dependent on the direction of charge transport [348]. A constant electric field of $10^5\,\text{V}\,\text{cm}^{-1}$ is applied with varying direction across the ab- and bc-plane of the pentacene film.

We use the Marcus transition rate comparing two different electronic coupling models: firstly, we use a parametrized distance-dependent transfer integral given by

$$V_{ij} = V_0 \exp\left(-\gamma r_{ij}\right) \ ; \tag{5.20}$$

secondly, we use the transfer integrals predicted by ML. Since the electronic coupling decays with the radial distance between adjacent molecules, a distance-dependent parametrization is often used and provides relatively accurate estimations of the absolute values of the charge carrier mobility. However, the relative orientation between the molecules are neglected and important local information of charge transport might be lost. For the sake of clarity, all simulations are run with zero energetic disorder. The reorganization energies for holes and electrons are given by $\lambda_{\text{h}} = 98\,\text{meV}$ and $\lambda_{\text{e}} = 132\,\text{meV}$ [349]. A charge density of $6 \times 10^{16}\,\text{cm}^{-3}$ is used to reduce electrostatic interactions arising from the Coulomb interactions between charge carriers. The temperature is set to 298 K. The mobility μ is calculated using

$$\mu = \frac{\langle \mathbf{v} \rangle \cdot \mathbf{F}}{F^2} \ , \tag{5.21}$$

with the electric field $\mathbf{F}$, and the average velocity $\langle \mathbf{v} \rangle = \mathbf{d}/t_{\text{sim}}$ computed by the traveled distance $\mathbf{d} = \left(d_x,\, d_y,\, d_z\right)^T$ during simulation time $t_{\text{sim}} = 500\,\text{ns}$.

Figure 5.16 shows the anisotropy of the hole mobility μ_{h}: (a) and (c) visualize the simulation results for the ML prediction and the parametrization, respectively, within the ab-plane; (b) depicts the mobility within the bc-plane for both ML prediction and parametrization. For both simulations within the ab-plane, a comparison with experimental results of the anisotropy of the mobility within pentacene [348] is provided. Note that we have rotated the experimental mobility values as the crystal orientation could not be obtained within the experimental setup [348]. Within Figs. 5.16 (a) and (c), the same experimental results have been rotated accordingly to fit the simulation in each case. The observed mobilities are in the range of the experimental results for single crystal pentacene and show a similar anisotropy. As shown by first-principle calculations for purely crystalline pentacene [212], hole transport mainly occurs within the ab-plane. A maximum hole mobility of $1.6\,\text{cm}^2\,\text{V}^{-1}\,\text{s}^{-1}$ at 168° is obtained by the ML-based multiscale simulation, which is a factor of 10 lower with respect to the first-principle values [212]. The reduction is caused by the underestimation of the transfer integral by the semi-empirical RM1 method used for the training of the ML algorithm as discussed in the previous section. Qualitatively, the mobility shows the same anisotropy. However, we observe a rotation by 35° towards the a-axis due the underestimation of the transfer integral in the [110]-direction. Both the parametrized and the ML model show a negligible transport in c-direction. This is expected, as the distance in c-direction exceeds the intermolecular distances within the ab-plane by far [212, 300].

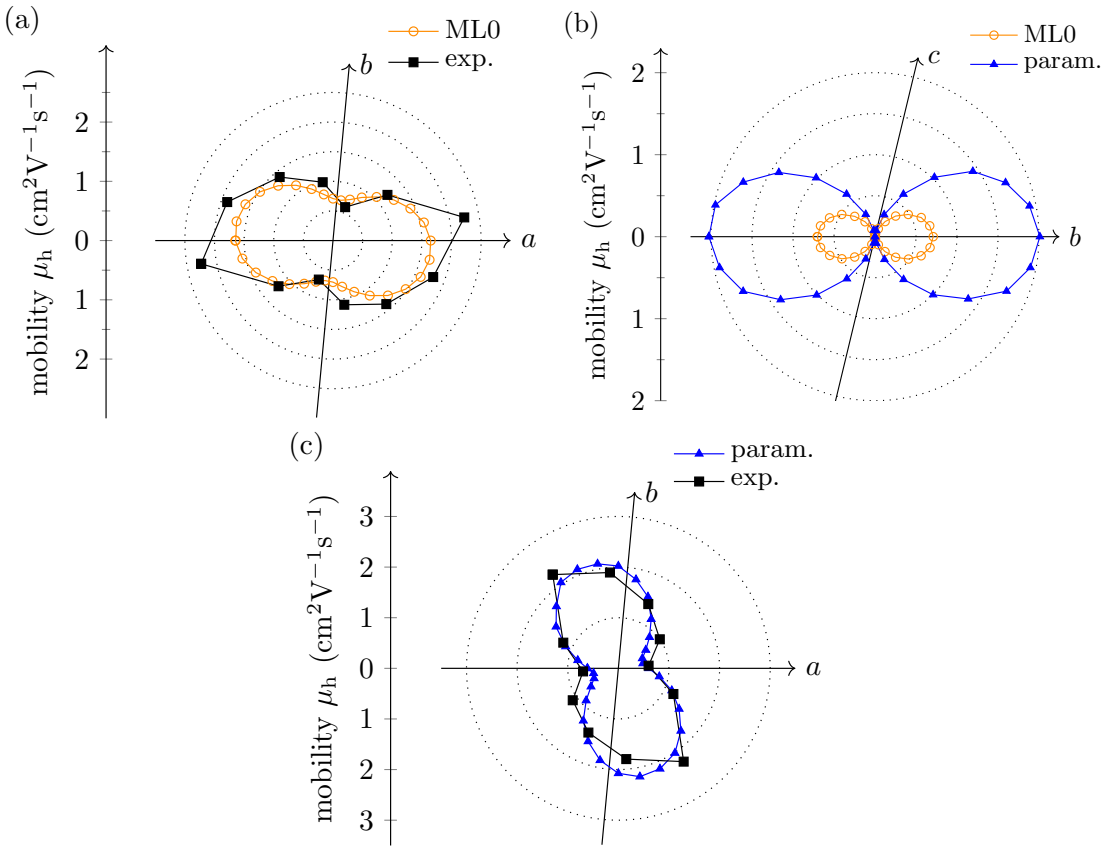

Figure 5.16 Angular dependence of hole mobility in pentacene: The hole mobility (a) in the ab-plane and (b) in the bc-plane of the pentacene crystal estimated by ML is depicted with respect to the electric field direction. Subplot (c) illustrates the angular dependence of the mobility fitted using the parametrized distance-dependent transfer integral. The results are compared with experimental data [348]. Since the orientation of the crystal could not be determined experimentally, the data are rotated to fit the simulation results best. Reprinted from [253], with permission by ©2018 WILEYVCH Verlag GmbH & Co. KGaA, Weinheim.

The parametrization based on the distance-dependent transfer integral predicts a maximum hole mobility at 188°. Interestingly, the shape of the angular dependent mobility looks similar to the observed results by both the multiscale simulations and the experiment. Using the disordered morphology and parametrized rates, the magnitude of the mobility can be fitted to observe the experimental anisotropy. However, this leads to a misinterpretation of the preferred directionality.

For the sake of completeness, the angular dependence of the electron mobility is shown for both the ab- and bc-plane in Fig. 5.17. As shown by Stehr *et al.* [212], the electron mobility in c-direction is strongly reduced due to the large spacing between the molecules. Within the ab-plane, the maximum electron mobility is $1.12\,\mathrm{cm^2\,V^{-1}\,s^{-1}}$ along the a-direction. Here, as for the holes, first-principle calculations predict a maximum mobility rotated towards the [110]-direction. Still, the resulting mobility shows the same oval shape as observed by first-principle calculations [212].

Now, mobilities are analyzed for different degrees of disorder for the given pentacene crystal. Two additional structures are generated by artificially adding a spatial disorder to the MD results to provide insight of the role of disorder and the predictability of transport properties within higher disorders. The dataset obtained by the MD snapshots is labeled as ML0, and the two additional structures generated with the artificial disorder are labeled with ML1 and ML2. An artificial disorder is added to the

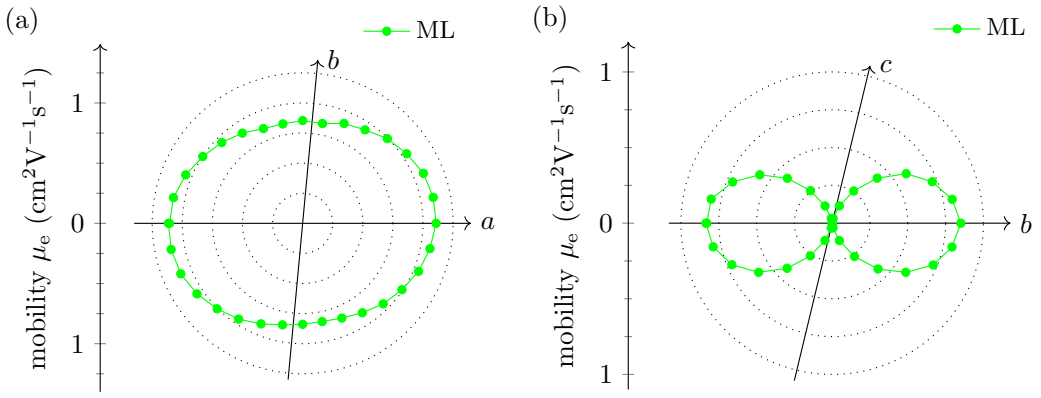

Figure 5.17 Angular dependence of the electron mobility in pentacene. The electron mobility (a) in the ab-plane and (b) bc-plane of the pentacene crystal estimated by ML is depicted with respect to the electric field direction. Reprinted from [253], with permission by ©2018 WILEYVCH Verlag GmbH & Co. KGaA, Weinheim.

Table 5.3 Datasets with varying degrees of disorder are generated, starting from the dimers obtained by molecular dynamics simulations (ML0), by adding a Gaussian-distributed shift and rotational disorder with standard deviations σ_r and σ_α, respectively. For comparison, the MAE for each dataset is given.

dataset	σ_r	σ_α	E_{MAE}
ML0	0 Å	0°	2.6 meV
ML1	0.1 Å	3°	3.9 meV
ML2	0.15 Å	4°	6.1 meV

torsional and translational degrees of freedom with random values following a Gaussian distributions with standard deviations σ_α and σ_r, respectively. The variance of the Gaussian distributions determine the degree of disorder. The respective distributions of the obtained datasets ML1 and ML2, and the MD snapshots ML0, are specified in Table 5.3.

In Figs. 5.18 (a) and (b), the distributions of the radial distance r_{dev} and orientation α_{dev} for the ML0 and ML2 dataset, respectively, are compared. The radial center of mass distance and the angular orientation deviation are shown with respect to their crystalline values. It is shown that the position of the molecules deviate from their ground state position by up to 1.5 Å and that torsion angles of up to 20° can occur. For dataset ML2, the artificially added disorder accounts for a shift towards larger radial distances and torsion angles. Figure 5.18(c) and (d) show the accuracy of the charge transfer integral with $E_{\mathrm{MAE}} = 2.6$ meV and $E_{\mathrm{MAE}} = 6.1$ meV for ML0 and ML2, respectively.

All transfer integrals are computed using the ML method. Note, that the energetic disorder of the molecular orbital energies is neglected. A higher disorder is expected to increase with the rising spatial disorder. The focus is set on the angular dependence and the ratio of the maximum to minimum mobility values as a measure of anisotropy. In Fig. 5.19, the angular dependence of the normalized hole mobility is visualized for the datasets ML0 to ML2, and the ordered pentacene crystal (cryst.). The normalization is done such that the minimum mobility is identical in each case. The neglected energetic disorder would cause a strong reduction in the absolute value of the charge carrier mobility [50], while changes in the transfer integral are expected to modify the angular anisotropy.

Despite having a decent radial and angular distribution within the dimers (cf. Fig. 5.18), the maximum normalized mobility for the ordered pentacene crystal is only slightly larger compared to the maximum value for the ML0 dataset. The directionality is slightly shifted towards the a-axis. The ratio of maximum to minimum mobility in case of the pure crystal is 2.43, while it drops subsequently

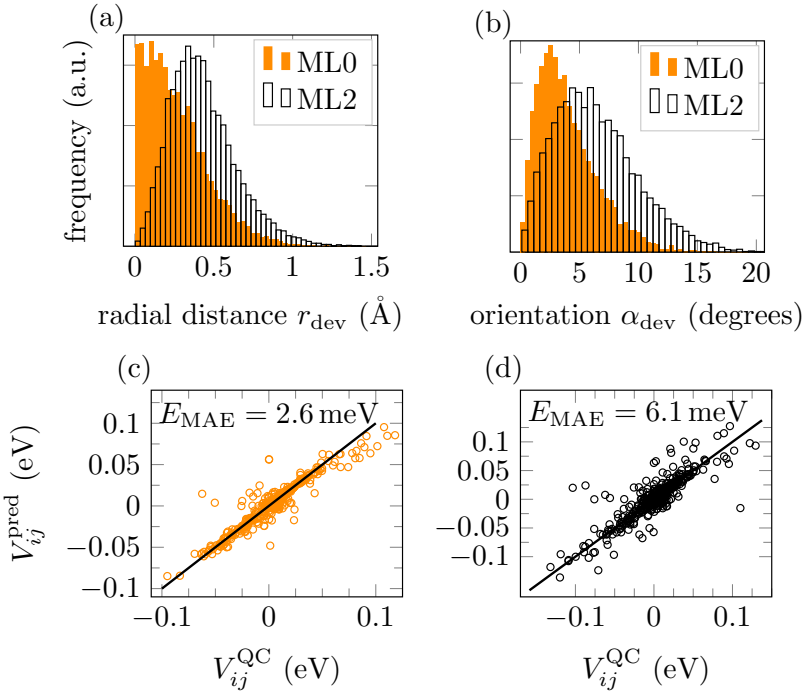

Figure 5.18 Distribution of (a) the radial distance r_{dev} and (b) orientations α_{dev} of the molecules in the disordered structure compared to the crystalline configuration. Subplots (c) and (d) show the transfer integral predictions for dimers extracted from molecular dynamics simulations without and with the artificially added disorder, respectively. Reprinted from [253], with permission by ©2018 WILEYVCH Verlag GmbH & Co. KGaA, Weinheim.

to 2.41 > 2.02 > 1.88 for the ML0, Ml1, and ML2 datasets, respectively. As a consequence, the angular dependence becomes more and more isotropic with rising disorder. The directionality of charge transport within the *bc*-plane does not significantly change within the disordered simulations ML0 to ML2.

In the study of the disorder on the mobility, the power of ML comes into play. While the resulting anisotropy in case of a weak disorder can be approximated using an ideal crystal, a rising disorder strongly alters the transfer integral due to the modifications in the torsion angles and the horizontal shift between the pentacene molecules. Thus, depending on the strength of the disorder, charge percolation paths will be strongly altered. Within the kMC model, we have ≈1 million charge transfer integrals for all next-neighbor dimers which are to be computed due to the presence of a structural disorder to achieve a high accuracy in the mobility. The computational demand for *ab initio* calculations goes far beyond reasonable simulation times, while the presented ML-based multiscale approach only requires less than 10,000 dimers to provide accurate predictions. In the following subsection, thin films with non-rigid pentacene molecules are discussed to analyze the applicability of the multiscale framework for systems of higher disorder.

Pentacene Thin Film

In the second step, the usability of the multiscale model for charge transport simulations is studied for pentacene thin films. Molecular dynamic simulations of pentacene molecules on top of a frozen SiO_2 have been performed. A short annealing time of 200 ps has been chosen to avoid the crystallization of

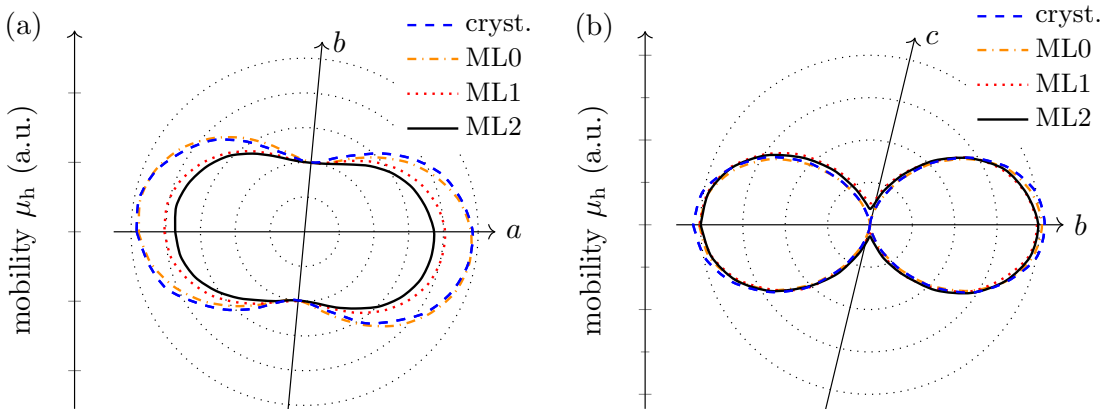

Figure 5.19 Disorder dependence of the anisotropy of the hole mobility. The hole mobility within the (a) ab- and (b) bc-plane is evaluated for the crystalline pentacene structure and the disordered crystals described in section IIIb. In all cases, the transfer integrals are estimated using the ML algorithm. Reprinted from [253], with permission by ©2018 WILEYVCH Verlag GmbH & Co. KGaA, Weinheim.

the pentacene film and to keep the thin film amorphous. The initial and final structure are shown in 5.15. The final structure is used for the simulation of the hole mobility μ_h in the xy-plane using the developed kMC model.

Despite the large spatial disorder in the morphology, the shape of the mobility anisotropy is qualitatively comparable to pentacene crystals. A comparison of the dimer distance distribution of the MD snapshot with the crystalline structure used in our previous work [253] is included in Fig. 5.20, right plot. We see many dimers along the main transport direction with short distances around 5 Å, which explains the similar shape of the mobility anisotropy. The reduced magnitude originates from the much larger disorder in the MD snapshot compared to the crystalline structure. The HOMO levels obtained by the quantum chemical calculations are taken into account. A constant electric field $F = 10^5\,\mathrm{V\,cm^{-1}}$ is applied within the $xy-$plane with varying orientation. Periodic boundaries are applied in x- and y-direction to increase the effective size of the simulation box.

The anisotropy of the mobility based on the charge transfer integrals obtained by the RM1 values is shown in Fig. 5.20. A strong anisotropy with maximum along 90° of $6.59 \times 10^{-4}\,\mathrm{cm^2\,V^{-1}\,s^{-1}}$ and a minimum of $1.34 \times 10^{-4}\,\mathrm{cm^2\,V^{-1}\,s^{-1}}$ at 180° can be seen. Interestingly, a significant anisotropy of the mobility, as observed for the crystalline pentacene, is present in this thin film. To understand this origin, the radial distribution function (RDF) of the hopping neighbors is plotted in Fig. 5.20. As short distances, the RDF of the MD snapshot shows strong similarities to the crystalline structure. The anisotropy is mainly controlled by the large transfer integrals at short distances. The RDF of the snapshot shows a significant amount of dimers at distances between 5 Å to 15 Å. These however do not seem to modify the mobility significantly due to a decrease in the transfer integrals with distance. The magnitude of the mobility is stongly reduced as the molecular orbital energies are significantly disordered within this system.

This short analysis demonstrates the capability of connecting properties of molecules and molecular thin films up to device characteristics within the presented multiscale framework.

5.3 Conclusion

In conclusion, this chapter presented a generalized picture of the role of the energetic and spatial disorder within organic semiconductors on the charge carrier mobility. The implementation of the

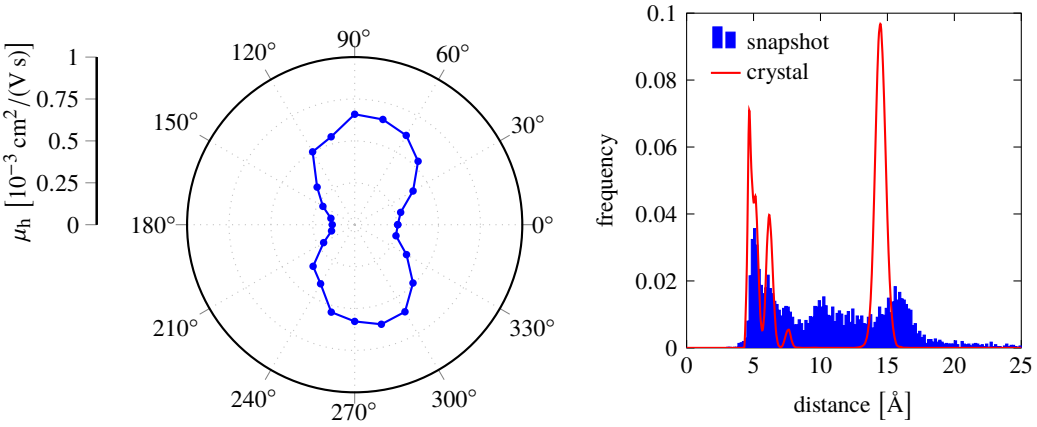

Figure 5.20 (Left) Mobility anisotropy obtained with V_{ij} from semi-empirical RM1 simulations. (Right) Radial distribution function of the molecular dynamics snapshot and crystalline pentacene. Reprinted from [51], with permission by ©(2020) American Chemical Society

Voronoi tessellation serves as the core of the kMC simulations to access field dependence or orientational dependence of the mobility within disordered organic bulk or thin films. In contrast to existing kMC studies on charge transport, the model includes a correlated disorder model (CDM) in site energies as well as the non-regular site distributions. The well-known dependence of the mobility on the electric field, charge carrier density and energetic disorder in the Gaussian disorder model was summarized. Building on this overview, two different directions were studied in detail, both dealing with disorder phenomena. First, the role of spatial correlations in site energies were studied. Based on a weighted average model, the influence of different degrees of correlations on the mobility were studied for different charge carrier densities. As a main result, filament-like conduction within the disordered organic semiconductor are observed. The formation of filaments was discussed including its field and correlation dependence. Connecting between local currents and transport energies with the distribution of activated sites yields a detailed description of charge transport in terms of both the spatial as well as the energetic phase space.

The results show that charge transport is dominated by diffusion processes up to an electric field of $\approx 1 - 2\,\sigma/(ea)$, in which the mobility is insensitive on the electric field. Above the given regime, a strong increase in mobility caused by an increasing impact of the drift component is observed. The transport energy saturates at approx. $3 - 4\,\sigma/(ea)$. For the spatially correlated disorder, charge transport is dominated by drift processes for electric fields far below $F = 1\,\sigma/(ea)$. This is due to a reduction of the energy barriers between two adjacent sites. Changes in the distribution of active sites are observable for low electric fields. For the CDM_1 changes only occur up to $F \approx 2\,\sigma/(ea)$, while for the CDM_2 a limit of $1\,\sigma/(ea)$ is observed. This suggests a strong correlation between the transport energy and the charge carrier velocity. Furthermore, the mobility is increased by orders of magnitude due to a correlation in site energies, while a strong correlation even inverts the field dependence of the mobility. This negative field dependence was measured in previous experimental studies on regular hole conducting organic materials, like *e.g.* P3HT.

Finally, the off-lattice kMC model has been integrated within a multiscale framework for charge transport simulations. The charge carrier mobility has been analyzed for thermally disordered pentacene crystals and for amorphous pentacene thin films. Transfer integrals were computed from semi-classical methods or predicted from Machine Learning for each pentacene dimer. The presented results show a vanishing orientation dependence of the mobility for higher disorder. The experimental

anisotropy could be reproduced by the multiscale simulations. Interestingly, even within the amorphous organic thin film, significant anisotropy of the mobility is observed. The framework allows a rapid computation of field dependence, density dependence as well as the anisotropy of the charge carrier mobility for both electron and hole transport.

6 Role of Energetic Disorder on the Open-Circuit Voltage in Organic Solar Cells

One major factors limiting the efficiency in organic solar cells (OSCs) is the low open-circuit voltage (V_{oc}). Existing theoretical studies link the V_{oc} with the charge transfer (CT) state and non-radiative recombination. However, also morphology and energetic disorder can have a strong impact on the V_{oc} within realistic bulk-heterojunction OSCs. This chapter presents a kinetic Monte Carlo study on the role of the energetic disorder on the maximum V_{oc}. Quasi-Fermi level splitting is calculated by tracking the occupied density of states for different energetic disorder. A special focus is set on the impact of the energetic disorder at the donor:acceptor interface as well as correlations in the site energies on the V_{oc}. The results show that the interface strongly controls the maximum V_{oc}. For a higher interface disorder, charge densities and non-geminate recombination increases, and the V_{oc} is reduced. Furthermore, the correlated morphologies show an increase in the maximum V_{oc} and a reduced impact of the energetic disorder.

Section **6.1** presents an overview on the topic of open-circuit voltage in OSCs. In section **6.2**, details on the kMC model are summarized. Section **6.3** presents and discusses the main results of the published study.

This chapter is reprinted with permission from 'Kinetic Monte Carlo Study of the Role of the Energetic Disorder on the Open-Circuit Voltage in Polymer/Fullerene Solar Cells,' *J. Phys. Chem. Lett.*, 2019, 10 (20), 6097-6104 [350]. Copyright (2020) American Chemical Society.

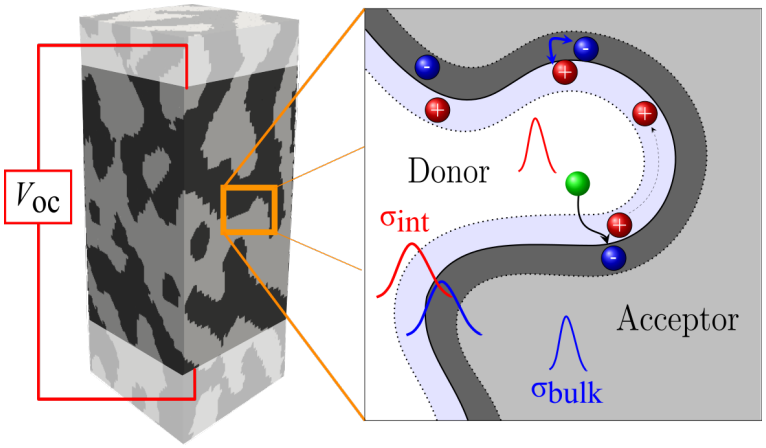

6.1 Background

In typical organic solar cells, the generation of charge carriers and their transport towards the electrodes is very efficient, which is captured by the high internal quantum efficiencies approaching 100 % [54]. However, despite the large progress in the understanding of energy losses within OSCs [23, 351–353], the low V_{oc} remains one of the major factors limiting the efficiency in OSCs. In addition to intrinsic properties of the chosen donor and acceptor semiconductors, such as the molecular frontier energy levels [354, 355], charge carrier mobilities [32, 356], and recombination dynamics [353, 357], the morphology [24,358] and the energetic disorder can have a significant impact on the V_{oc} [33,359–361]. Vandewal *et al.* showed that a reduced donor:acceptor interface area leads to an increase in V_{oc} due to a reduction in recombination channels [24]. Recently, Tang *et al.* observed a reduction in non-radiative voltage losses by tuning the active layer morphology [358]. Using additive solvents, they could significantly suppress the collection of minority charge carriers at the wrong contacts. These results agree with numerical studies of engineered morphologies [362,363]. An increase in energetic disorder can substantially reduce the V_{oc} due to the trapping behavior of the disorder-induced tail states [33]. In addition, rising carrier densities and increased illumination rates lead to a higher V_{oc} [33, 361]. Further important properties which impact the V_{oc} are summarized within the review of Elumalai and Uddin [364].

Numerical studies are frequently used to analyze device and material properties of organic solar cells and in particular their impact on the V_{oc} by solving drift-diffusion (DD) equations [32, 33]. In most DD-studies, the complex photoactive layer is reduced to a single effective medium in 1D. Here all interface properties are reduced to bulk properties. DD calculations are also possible for three-dimensional bulk-heterojunction morphologies [34], but their convergence is not guaranteed. Moreover, most DD simulation tools lack local structural information such as a correlated energetic disorder, interface properties, and the localized nature of charge carriers within OSCs. Except for a few studies [31], DD is based on equilibrium statistics which does not capture the non-equilibrium transport properties in organic semiconductors [29,365]. Kinetic Monte Carlo (kMC) methods provide an alternative for full device simulations of OSCs [44,45]. The advantage of kMC compared to DD or analytical theories is its ability of full device simulations within three-dimensional morphologies of locally strongly varying properties. In addition, it captures the non-equilibrium properties of exciton and charge transport [365]. This fact, as well as the detailed morphology, are of high importance for an accurate study of the V_{oc} within bulk-heterojunction OSCs.

In this chapter, a kMC analysis of the intrinsic V_{oc} within a bulk-heterojunction OSC is presented. The developed methodology allows to extract the maximum quasi-Fermi levels of the stand-alone bulk-heterojunction without the need of full device simulations. Thus, we avoid additional interfaces, such as transport layers and contacts, which can have a significant impact on or even dominate the V_{oc} of the full device. Our simulations focus on the role of the energetic disorder on the V_{oc} of the well-known polymer:fullerene blend formed from poly(3-hexylthiophene) (P3HT) and [6,6]-phenyl C61-butyric acid methyl ester (PCBM). The general relation between the energetic disorder and the V_{oc} is well-known both from an experimental perspective and from DD-simulations as summarized above. However, kMC has not been used so far to investigate the intrinsic limit of the V_{oc} within the standalone photoactive layer. Furthermore, we use the capabilities of a 3D kMC model to analyze the role of additional local properties for the bulk-heterojunction morphology, as sketched in Fig. 6.1. In particular, we study the impact of the energetic disorder at the donor:acceptor interface as well as a correlated energetic disorder on the maximum V_{oc}.

6.2 Kinetic Monte Carlo Model

A 3D kinetic Monte Carlo model for the simulation of the OSC including exciton and charge carrier dynamics is implemented based on established implementations [13, 44, 45, 47, 48]. The photoactive layer is represented using a $50 \times 50 \times 100\,\mathrm{nm}^3$ large Cartesian lattice with lattice spacing $a = 1\,\mathrm{nm}$. For each site, transitions are considered towards the nearest neighbors, i.e. six bonds for each site. A bulk-heterojunction morphology is generated using a spin-exchange algorithm [46]. Singlet excitons are generated within the active layer using a constant generation rate k_{gen} all over the photoactive layer. Singlet diffusion occurs by Förster resonance energy transfer (FRET). FRET is modeled using a Miller-Abrahams like rate [8, 39, 182, 362]:

$$k_{\mathrm{FRET}}(r, \Delta E_{ij}) = \tau_{\mathrm{ex}}^{-1} \left(\frac{r_{\mathrm{F}}}{r}\right)^6 \begin{cases} \exp\left(-\frac{\Delta E_{ij}}{k_{\mathrm{B}}T}\right) & \text{if } \Delta E_{ij} > 0 \\ 1 & \text{else} \end{cases} \tag{6.1}$$

with the exciton lifetime τ_{ex}, the Förster radius r_{F}, the distance r over which the energy transfer occurs, the Boltzmann constant k_{B}, temperature T, and the difference in singlet energies ΔE_{ij} between nodes i and j. As FRET is a long-range mechanism, we compute k_{FRET} to all sites with $r \leq r_{\mathrm{F}}$. The singlet decay rate is computed as the inverse of the singlet lifetime:

$$k_{\mathrm{dec}} = \tau_{\mathrm{ex}}^{-1}\,. \tag{6.2}$$

Singlet dissociation at the donor-acceptor interface can occur by an electron transfer from the excited donor molecule towards the acceptor. This process is modeled using a constant dissociation rate k_{diss} which is only activated if the singlet is located at the interface [13, 48].

Charge carriers move between adjacent sites i and j under the influence of the local site potentials E_i which are constituted by the molecular orbital energy E_i^0, the electric field E_i^F, the energetic disorder E_i^σ, and the Coulomb potential E_i^C. The Coulomb interaction is included by the Ewald summation which accounts for the interaction between all charge carriers and their periodic replica [48]. Charge transport is modeled by the Marcus hopping rate [92]:

$$k_{ij} = \frac{\left|V_{ij}\right|^2}{\hbar}\sqrt{\frac{\pi}{\lambda_{ij}k_B T}}\exp\left(-\frac{(\Delta E_{ij} + \lambda_{ij})^2}{4\lambda_{ij}k_B T}\right)\,, \tag{6.3}$$

with $\Delta E_{ij} = E_j - E_i$.

Recombination of charge carriers can occur if an electron and a hole reside on adjacent sites. Two different recombination channels are implemented: radiative and non-radiative recombination. The non-radiative recombination rate is implemented following the Marcus-Levich-Jortner relation [231]:

$$k_{\mathrm{nr}} = \frac{4\pi^2}{h} V_{\mathrm{CR}}^2 \mathrm{FC}(E_{\mathrm{CT}})\,, \tag{6.4}$$

with the electronic coupling in the recombination process V_{CR}, and the Franck-Condon weighted density of states

$$\mathrm{FC}(g) = \frac{1}{\sqrt{4\pi\lambda_{\mathrm{slow}}k_{\mathrm{B}}T}} \sum_{m=0}^{\infty} \frac{\exp(-S)S^m}{m!} \exp\left[-\frac{(g + m\hbar\omega_v + \lambda_{\mathrm{slow}})^2}{4\lambda_{\mathrm{slow}}k_{\mathrm{B}}T}\right]\,, \tag{6.5}$$

with $m \in \mathbb{N}$ being the number of the high-frequency intramolecular vibration mode $\hbar\omega_v$, the reorganization energy due to inter-molecular vibrations λ_{slow}, and the Huang-Rhys parameter S. Radiative recombination is included following Gould *et al.* [231]:

$$k_{\mathrm{rad}} = \frac{64\pi^4}{3h^3c^3} n^3 \nu_{\mathrm{av}} V_{\mathrm{CR}}^2 \Delta\mu^2\,, \tag{6.6}$$

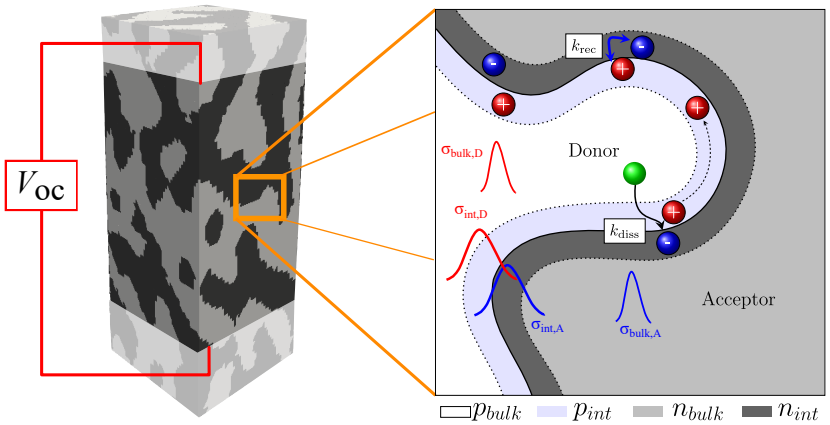

Figure 6.1 Schematic representation of the 3-dimensional bulk-heterojunction organic solar cell. We extract the energy levels of holes and electrons at the boundaries in ±15 nm distance from the z-boundaries. This is to avoid artefacts at the interfaces in z-direction as described in the main text. We analyze different energetic disorder within the bulk $\sigma_{\text{bulk,A/D}}$ and at the interface $\sigma_{\text{int,A/D}}$. Exciton (green ball) transport and dissociation as well as recombination and transport of electron (blue ball) and holes (red ball) are accounted for within the kMC model. Each site which has a neighbor of different phase is labeled as an interface site for an evaluation of the charge densities at the interface (p/n_{int}) and within the bulk (p/n_{bulk}). Reprinted with permission from [350]. Copyright (2020) American Chemical Society.

where n denotes the refractive index, c is the speed of light, $\Delta\mu$ gives the transition dipole moment, and $h\nu_{\text{av}} = E_{\text{CT}} - \lambda_{\text{slow}} - \hbar\omega_v$.

The bulk-heterojunction morphology used within this study was computed with the spin-exchange algorithm looped over 2,000 Monte Carlo steps [47], which yields an average cluster size of 13.9 nm. The resulting morphology is depicted in Fig. 6.1. All simulation parameters of the studied P3HT:PCBM blend are summarized in Tab. 6.1.

Calculation of Quasi-Fermi Energies

The open-circuit voltage is defined by the difference in quasi-Fermi levels of electrons and holes $E^e_{F,q}$ and $E^h_{F,q}$, respectively:

$$qV_{\text{oc}} = \Delta E_{F,q} = E^e_{F,q} - E^h_{F,q}\,. \tag{6.7}$$

The quasi-Fermi level $E_{F,q}$ is obtained by fitting the charge distribution function $n(E)$ to the occupied HOMO/LUMO energy levels where

$$n(E) = f(E, E_{F,q})g(E)\,, \tag{6.8}$$

with the Gaussian density of states $g(E)$ and the Fermi-Dirac distribution function $f(E, E_{F,q})$. We compute the occupied energy levels, which are made up by the site energy E_i, including the molecular orbital energy, the energetic disorder, and the Coulomb interaction. The occupied energy level is stored once a charge carrier crosses a fixed boundary at the z-planes in ±15 nm-distance from the ±-z boundary, respectively. We label each charge once its energy is stored to avoid multiple counting of the energy levels. After storing the energy, charge carriers can still move within the photoactive layer until recombination occurs or until the charge carriers are removed from the simulation box at the $\pm z$ boundary which act as sinks for charge carriers. As our goal is to study the V_{oc} of the BHJ

Table 6.1 Material parameters used in the kinetic Monte Carlo simulations.

Parameter	Value	Reference
$E^0_{\mathrm{HOMO,P3HT}}/E^0_{\mathrm{LUMO,PCBM}}$	−5.2 eV/−3.8 eV	[13]
Huang-Rhys factor S	1.37	[229]
Electronic coupling (rec.) V_{CR}	8.0 meV	[229]
Intermolecular reorganization λ_{slow}	0.11 eV	[229]
Intramolecular vibration $\hbar\omega_v$	0.186 eV	[229]
Transition dipole moment $\Delta\mu$	15 D	-
Permittivity ϵ_r	3.5	[13]
Charge transfer integral V_{ij}	1.5 meV	-
Reorganization energy λ	0.2 eV	-
Singlet lifetime τ_{ex}	0.8 ns	[362]
Singlet energy E_S	1.8 eV	[366]
Singlet disorder E_S^σ	50 meV	-
Förster radius r_{F}	1.6 nm	[362]
Dissociation rate k_{diss}	$2 \times 10^{13}\ \mathrm{s}^{-1}$	[13]

morphology without the impact of any contacts or transport layers, the blend is extended by 15 nm in both $\pm z$-direction. Assume an electron-hole pair diffusing near the boundary and the hole being removed from the simulation box. This causes an immediate jump in the potential of the electron by the Coulomb binding energy, which is an artifact due to contacts and boundaries. This is avoided as the charge carriers will live on after passing the planes at ±15 nm distance from the z-boundaries. The value is chosen to be in the range of the Bjerrum length. Beyond this radius the thermal energy is larger than the Coulomb interaction.

The constant generation rate of $k_{\mathrm{gen}} = 2\,\mathrm{nm}^{-3}\,\mathrm{s}^{-1}$ together with the relatively homogeneous phase intermixing along the z-direction yield constant charge densities within the ±15 nm-borders. Thus, constant quasi-Fermi level splitting are achieved across the film. The simulation is stopped once 20,000 electron and hole energies are stored. Even for the highest considered disorder values, equilibrated charge densities are reached within less than 20 collected electron-hole pairs.

Note that all attempts to fit the distribution functions using the standard Fermi-Dirac distributions led to inaccurate fits of the occupied density of states. In order to obtain a reliable fit of the occupation distributions, we use the concept of the effective temperature [367–369] by replacing the temperature T within the Fermi-Dirac distribution by the effective temperature T_{eff}:

$$f(E, E_{F,q}) = \left[1 + \exp\left(\frac{E - E_{F,q}}{k_{\mathrm{B}} T_{\mathrm{eff}}}\right)\right]^{-1} . \tag{6.9}$$

Baranovskii and coworkers have used the concept of effective temperature previously to describe the field dependence of the charge carrier mobilities and distributions of occupied molecular orbital energies within systems of Gaussian density of states [368, 369]. In our analysis, charge carrier diffusion is only affected by the strong Coulomb attraction as no external electric field is applied. Recently, Brigeman *et al.* provided evidence by photoluminescence (PL) spectroscopy that the thermalization of the charge transfer states within BHJ solar cells is incomplete, which means that the CT state distribution is far from equilibrium and electron-hole pairs do not thermalize before being extracted at contacts or before recombining [370]. Using the concept of the effective temperature

they were able to accurately describe the CT state PL with $T_{\text{eff}} > T_{\text{sample}}$. Moreover, they suggested a re-evaluation of the typical V_{oc} analyses, which assume equilibrated CT states, using the effective temperature accounting for the non-equilibrated CT states.

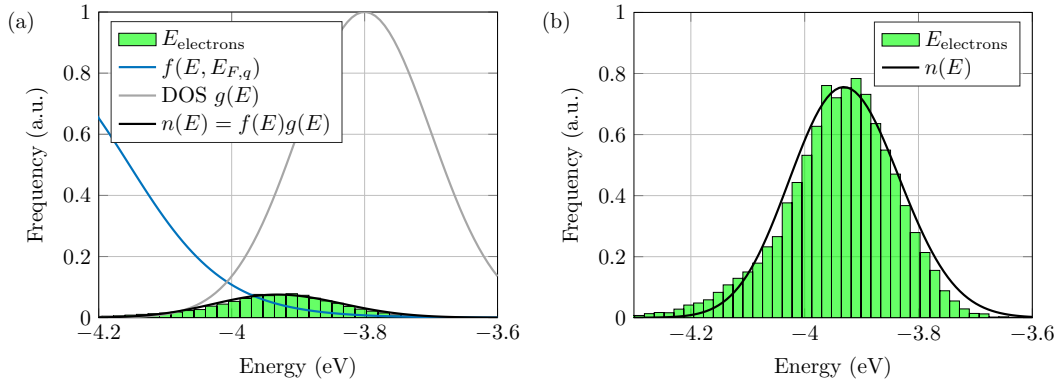

Figure 6.2 Procedure of the calculation of the quasi-Fermi energies. Subplot (a) shows the Gaussian input DOS $g(E)$, the Fermi function $f(E, E_{F,q})$, and the fit $n(E)$ to the electron energies $E_{\text{electrons}}$. In (b), $n(E)$ and the distribution $E_{\text{electrons}}$ is shown enlarged. Reprinted with permission from [350]. Copyright (2020) American Chemical Society.

Figure 6.2 visualizes the procedure for the calculation of the quasi-Fermi energy levels. Here, we consider the example of the distribution of electron energies $E_{\text{electrons}}$ for an energetic disorder $\sigma = 100\,\text{meV}$. The density of states $g(E)$ is centered around the LUMO energy of $-3.8\,\text{eV}$. The quasi-Fermi energy $E_{F,q}$ is obtained by fitting the product $n(E) = f(E)g(E)$ of the Fermi function $f(E)$ and the Gaussian DOS $g(E)$ to the distribution of $E_{\text{electrons}}$ using the *Curve Fitting Tool* within MATLAB. To obtain a reasonable fit for the high energies we use the effective temperature T_{eff} as an additional parameter. The effective temperature has been shown to capture the effect of the electrostatic interaction between charge carriers on the distributions of occupied molecular orbital energies [368].

The density of states changes within the study of higher interfacial energetic disorders. Here, a linear superposition of the bulk DOS $g_{\text{bulk}}(E)$ and the interface DOS $g_{\text{int}}(E)$ with the disorder σ_{bulk} and σ_{int}, respectively, is used:

$$g'(E) = (1 - f)g_{\text{bulk}}(E) + f g_{\text{int}}(E)\,, \tag{6.10}$$

where f gives the interface percentage within the acceptor/donor, depending on which energy distribution we aim to fit. Figure 6.3 shows the fit for the (a) hole and (b) electron energy distributions for $\sigma_{\text{bulk}} = 50\,\text{meV}$ and $\sigma_{\text{int}} = 100\,\text{meV}$. We obtain the quasi-Fermi levels of $E_{F,q}^{\text{holes}} = -4.887\,\text{eV}$ and $E_{F,q}^{\text{electrons}} = -4.076\,\text{eV}$, resulting in the quasi-Fermi level splitting of 0.811 eV. The energy tail for high hole (and low electron) energies arises due to the presence of the Coulomb interaction between the mobile charge carriers. The quasi-Fermi energy and the effective temperature are dominantly determined by the shape of the occupied energy levels at low (high) energies for the holes (electrons). The presence of the Coulomb interaction can lead to a change of the available DOS. In a previous study, it was proposed that the presence of ionized dopants can induce deep, exponential tails within the DOS changing the shape to a non-Gaussian DOS [371]. However, densities exceeding $10^{18}\,\text{cm}^{-3}$ are needed to change the DOS significantly. Within organic solar cells, the low charge carrier densities of $< 5 \times 10^{17}\,\text{cm}^{-3}$ are much lower than the available DOS of $10^{21}\,\text{cm}^{-3}$, thus only a small change in the shape of the DOS is expected. Arkhipov *et al.* consider the case of unipolar dopants [371]. In terms of organic solar cells, where bipolar charge carriers are present, the shape of the DOS is expected to be affected less.

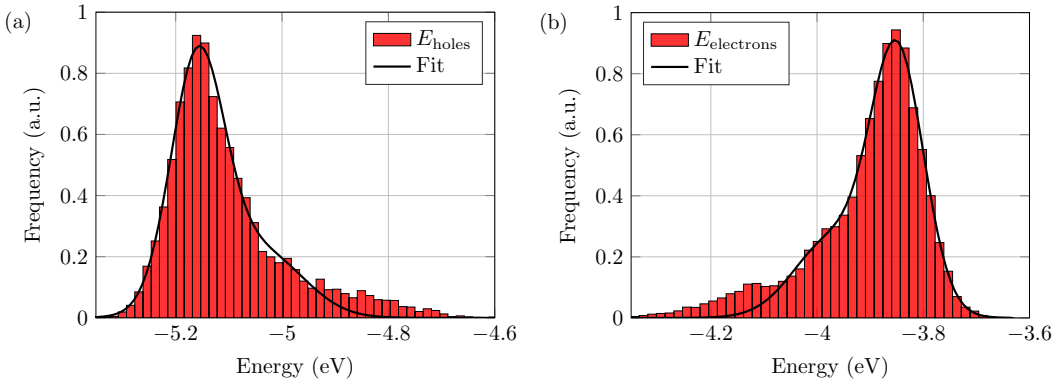

Figure 6.3 Fit of the (a) hole energy distribution and the (b) electron distribution for the bulk disorder $\sigma_{\text{bulk}} = 50\,\text{meV}$ and the interface disorder $\sigma_{\text{int}} = 100\,\text{meV}$. Reprinted with permission from [350]. Copyright (2020) American Chemical Society.

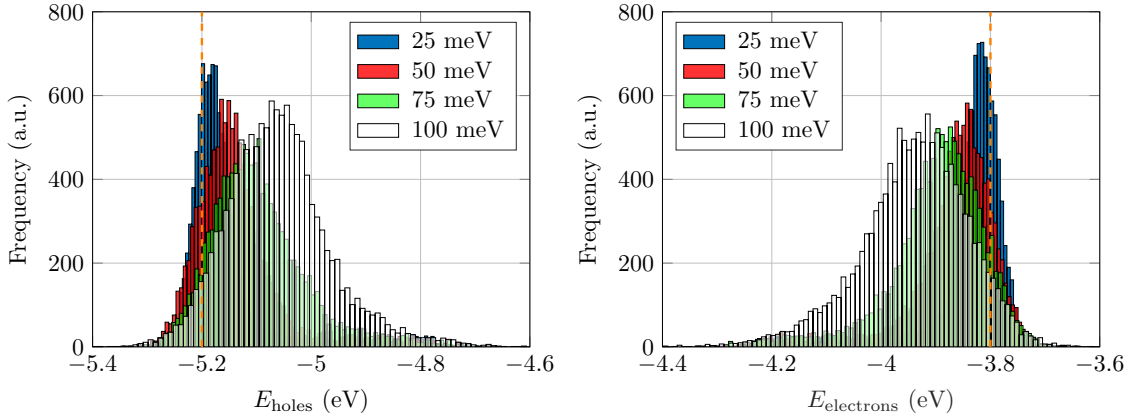

Figure 6.4 Energy distribution of collected (a) holes and (b) electrons at flat-band conditions. The energetic disorder in both the donor and acceptor is varied from 25 to 100 meV. The vertical dashed lines show the ideal HOMO and LUMO levels E^0_{HOMO} and E^0_{LUMO}, respectively. Reprinted with permission from [350]. Copyright (2020) American Chemical Society.

6.3 Results and Discussions

Role of the Energetic Disorder

First, we investigate the impact of the energetic disorder on the carrier density and the maximum open-circuit voltage. The energetic disorder is varied from 25 meV to 100 meV which are typical values for disordered organic semiconductors [372, 373]. The potential distribution of collected holes and electrons are shown in Fig. 6.4(a) and (b), respectively. Table 6.2 summarizes the quasi-Fermi energies, the average charge densities, and the effective temperature.

Several observation can be made from the distributions. For all energetic disorders, the mean site energy is lower (higher) than the ideal LUMO (HOMO) energies. This is caused by the relaxation in energy during the transport through the photoactive layer. In addition, a long tail arises from the Coulomb interacting between the strongly localized charge carriers. With rising disorder, the shift of the maximum of the distributions with respect to the ideal molecular orbital levels increase significantly. Moreover, the low (high) energy tail becomes more pronounced with increasing energetic

Table 6.2 Quasi-Fermi levels $E_{F,q}^{e/h}$ of extracted electrons (e) and holes (h) are summarized for different energetic disorder σ. $\overline{T}_{\text{eff}}$ (see eq. 6.9) gives the effective temperature, $\overline{n}$ the average charge carrier density within the photoactive layer, and ΔE_{e-h} the difference of the average hole and electron energies E_{holes} and $E_{\text{electrons}}$, respectively.

σ (meV)	$\overline{n}$ (cm^{-3})	$\overline{T}_{\text{eff}}$ (K)	$E_{F,q}^{h}$ (eV)	$E_{F,q}^{e}$ (eV)	$\Delta E_{F,q}$ (eV)	ΔE_{e-h} (eV)
25	1.44×10^{15}	460	−5.017	−4.002	1.015	1.315
50	4.76×10^{15}	624	−4.935	−4.055	0.880	1.265
75	3.44×10^{16}	728	−4.884	−4.118	0.766	1.198
100	4.12×10^{17}	840	−4.855	−4.158	0.697	1.121

disorder. At high $\sigma \geq 75$ meV, both the charge carrier mobility [50, 270], see also Fig. B.1 in the appendix, and charge separation are reduced [13]. With rising σ, both the effective temperature and the charge carrier density increase. Thus, the geminate electron-hole pairs diffuse through the photoactive layer while staying at close distances for high disorder values. This causes a large increase in the tail which can be seen at $E_{\text{HOMO}} \approx -4.95$ eV for $\sigma = 100$ meV.

Arkhipov *et al.* showed that ionized dopants add a static exponential tail and modify the shape of the density of states [28]. This causes a static change in the available input DOS. In our system, charge carriers are affected by a dynamic Coulomb field which arises due to many-body Coulomb interactions. As the Coulomb interaction adds dynamically accessible tail states, we expect a slight shift of the DOS towards lower energies. As the Fermi distribution and with this the quasi-Fermi energies describe the occupancy statistics especially at higher energies, we expect that our calculated quasi-Fermi levels provide an upper boundary of the exact quasi-Fermi levels. A quantification of this effect requires additional fitting degrees of freedom and may provide valid fitting of the occupied density of states, but due to an arbitrary and nonphysical change in the input DOS. We want to point out that the used method provides correct trends and reasonable quasi-Fermi levels, which can be seen as upper boundaries.

The difference in the quasi-Fermi levels $\Delta E_{F,q}$ drops from a value of 1.015 eV at $\sigma = 25$ meV to 0.697 eV at $\sigma = 100$ meV. The maximum $\Delta E_{F,q} = 1.015$ eV is far below both the optical bandgap of P3HT $E_{g,\text{P3HT}} = 2.2$ eV and the electrical bandgap, given by the difference in the P3HT HOMO and the PCBM LUMO level ($E_{g,el} = 1.4$ eV). The voltage loss, given by $q^{-1}(E_{g,el} - \Delta E_{F,q})$, increases with rising disorder. The nature of thermally activated charge carrier hopping leads to the observed relaxation in energy and reduces the quasi-Fermi level splitting. Both the magnitude of the quasi-Fermi levels and the trend match with the results observed from analytical and DD calculations [33]. As we assume the same charge transfer integral and reorganization energy in both the acceptor and the donor, the change in electron and hole quasi-Fermi levels is in the same order. This is expected to change for asymmetric charge transport properties as carriers within materials of better transport properties can relax on faster timescales which might even lead to a sufficient charge carrier separation or delocalization.

Role of the Interface Disorder

To model the detailed morphology of the donor-acceptor blend accurately, insights from ab-initio calculations in combination with molecular dynamic simulations are needed to obtain quantitatively correct inter-molecular transport properties as well as the on- and off-diagonal disorder. However, a full ab-initio model of the interfaces within the large photoactive layer is not feasible due to an

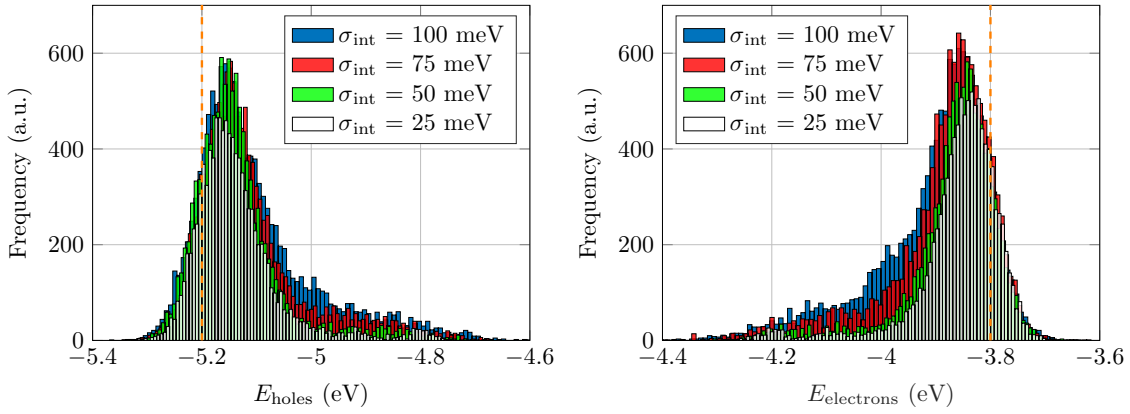

Figure 6.5 Energetic distribution of collected (a) holes and (b) electrons at flat-band conditions. The energetic disorder in both the donor and acceptor is varied from 50 to 100 meV. The vertical dashed lines show the ideal HOMO and LUMO levels E^0_{HOMO} and E^0_{LUMO}, respectively. Reprinted with permission from [350]. Copyright (2020) American Chemical Society.

enormous computational cost. Several authors have demonstrated the presence of a higher degree of spatial and energetic disorder at the bulk-heterojunction interface, which rather represents a strongly intermixed phase [374–376]. To study the impact of the interfacial disorder on the charge carrier energetics, we apply a higher energetic disorder $\sigma_{\mathrm{int}} > \sigma_{\mathrm{bulk}}$ at all interface sites as sketched in Fig. 6.1. The density of states $g'(E)$ is now given by a superposition of the bulk DOS $g_{\mathrm{bulk}}(E)$ and the interface DOS $g_{\mathrm{int}}(E)$ with the percentage f of interface sites:

$$g'(E) = f g_{\mathrm{int}}(E) + (1 - f) g_{\mathrm{bulk}}(E) \,. \tag{6.11}$$

Figure 6.5 shows the distributions of (a) hole and (b) electron energies for an interface energetic disorder varying from 25 to 100 meV at a constant disorder of $\sigma_{\mathrm{bulk}} = 50$ meV within the bulk of the photoactive layer. As shown within the previous section, the distributions of hole and electron energies are symmetric, i.e. the interface disorder does not significantly change the symmetry in charge carrier properties. The low energy tails of the distributions get more pronounced with rising σ_{int}.

In Table 6.3 we summarize the simulation results for σ_{int} varying from 25 meV, which represents a rather ordered interface, to 125 meV, representing a strongly disordered interface. For high interface disorder of $\sigma_{\mathrm{int}} \geq 75$ meV, the interface charge densities $\overline{n}_{\mathrm{int}}/\overline{p}_{\mathrm{int}}$ exceed the bulk densities $\overline{n}_{\mathrm{bulk}}/\overline{p}_{\mathrm{bulk}}$ due to the strong Coulomb binding energies. In addition, the ratio of interface to bulk densities increases from $\approx 3-4$ for $\sigma_{\mathrm{int}} = 75$ meV up to ≈ 300 at the highest disorder of 125 meV. This is mainly due to the increase in the interface densities which are raised by more than three decades, while the bulk density vary by less than one order of magnitude. For the low interface disorder $\sigma_{\mathrm{int}} = 25$ meV, the interface densities drop below the bulk densities, i.e. the role of the interfaces become less pronounced.

For a reduced interface disorder $\sigma_{\mathrm{int}} = 25$ meV, the quasi-Fermi level difference is increased to 0.938 eV. The charge carrier densities at the interface are lower than bulk densities, while for equal disorder throughout the BHJ equal densities are obtained. Thus, a reduction in σ_{int} lowers the interaction of charge carriers at the interface and the BHJ solar cell becomes bulk dominated. A decrease in $\Delta E_{F,q}$ from 0.88 eV to 0.799 eV is observed for an increase in σ_{int} from 50 meV to 125 meV. The higher interface disorder leads to an increase in interface densities; thus the energetics at the interface have a stronger impact on $\Delta E_{F,q}$. Although a higher disorder can lead to a better charge separation in the presence of an external driving force [377], it strongly decreases the maximum V_{oc}.

Table 6.3 Average hole and electron interface densities $\overline{n}_{\text{int}}$ and $\overline{p}_{\text{int}}$,respectively, and bulk densities $\overline{n}_{\text{bulk}}$ and $\overline{p}_{\text{bulk}}$ for different interfacial disorder σ_{int}. The energetic disorder in the bulk is fixed at $\sigma = 50\,\text{meV}$. The percentage of geminate recombination η_{gen} and the difference in quasi-Fermi energies $\Delta E_{F,q}$ are shown for each case.

σ_{int} (meV)	$\overline{n}_{\text{int}}$ (cm^{-3})	$\overline{p}_{\text{int}}$ (cm^{-3})	$\overline{n}_{\text{bulk}}$ (cm^{-3})	$\overline{p}_{\text{bulk}}$ (cm^{-3})	η_{gem} (%)	$\Delta E_{F,q}$ (eV)
25	3.67×10^{15}	3.45×10^{15}	1.05×10^{16}	1.02×10^{16}	95.76	0.938
50	8.74×10^{15}	8.29×10^{15}	9.54×10^{15}	9.06×10^{15}	97.42	0.880
75	5.94×10^{16}	4.84×10^{16}	1.33×10^{16}	1.30×10^{16}	97.78	0.865
100	9.12×10^{17}	7.62×10^{17}	4.11×10^{16}	3.15×10^{16}	91.47	0.813
125	7.58×10^{18}	6.21×10^{18}	2.09×10^{16}	2.01×10^{16}	83.37	0.799

Furthermore, we study the relative amount of geminate recombination η_{gem} for the different interfacial disorders. We define the probability η_{gem} as the ratio between the number of geminate recombination recombination events #gem to the total number of recombination events #rec. The given results show a decrease of η_{gen} above an interfacial disorder of $\sigma_{\text{int}} = 75\,\text{meV}$. The interface densities $\overline{n}_{\text{int}}/\overline{p}_{\text{int}}$ strongly increase, thus non-geminate charge carriers have a higher chance to meet and recombine. All of these observations show that the properties in bulk-heterojunction solar cells with strongly disordered interfaces are mainly controlled by the D:A interface due to the strong Coulomb binding for the low permittivity of $\epsilon_r = 3.5$.

Role of Correlations in the Energetic Disorder

A modification of the Gaussian disorder model [29, 270] by a correlated disorder has been used to describe observable characteristics like the PooleFrenkel mobility of charge carriers [44, 272]. In a previous publication, we showed that correlations in energetic disorder lead to filamentary charge conduction and increase the mobility by up to orders of magnitude [50]. While the impact on the carrier mobility is understood well, the role of correlations on the open circuit voltage has not been studied so far. We include correlations in the energetic disorder as described in ref. [50]. The method used to generate the spatial correlations has been presented in detail in chapter 6. In appendix B.3, the procedure to obtain the local DOS is presented. In addition, it shows the electron and hole energy distributions.

We simulate the open-circuit voltage for correlation radii l_c varying from 1 nm to 5 nm with $\sigma = 75\,\text{meV}$ and compare it with the results presented for the uncorrelated Gaussian disorder. Figure 6.6 shows the energy distribution of HOMO levels in the donor phase for different correlations from the above studied uncorrelated disorder ($l_c = 0\,\text{nm}$) up to a strong local correlation of $l_c = 5\,\text{nm}$. The extracted quasi-Fermi level differences $\Delta E_{\text{F,q}}$ are given for each investigated correlation. The distributions of electron and hole energies are given in the appendix, B.3. We observe an increase in $\Delta E_{\text{F,q}}$ from 0.766 eV to 1.015 eV. Interestingly, even a low correlation radius of $l_c = 1\,\text{nm}$ causes a substantial increase of $\Delta E_{\text{F,q}}$ to 0.906 eV. A correlation in the disorder significantly changes the local DOS without modifying the global Gaussian DOS. For the uncorrelated energetic disorder, an average charge carrier density of $3.51 \times 10^{16}\,\text{cm}^{-3}$ is obtained. With rising correlation, the average densities drop to $2.96 \times 10^{16}\,\text{cm}^{-3} > 1.97 \times 10^{16}\,\text{cm}^{-3} > 1.07 \times 10^{16}\,\text{cm}^{-3}$ from $l_c = 1\,\text{nm}$ to $l_c = 5\,\text{nm}$. While the global DOS remains unchanged with respect to the uncorrelated Gaussian DOS, charge carriers see a reduced density of states as they can move within correlated domains of high (low) HOMO (LUMO) energy levels. Figure S8 visualizes the density of electrons and holes within the acceptor and donor, respectively, for the uncorrelated DOS and the correlated DOS with $l_c = 3\,\text{nm}$.

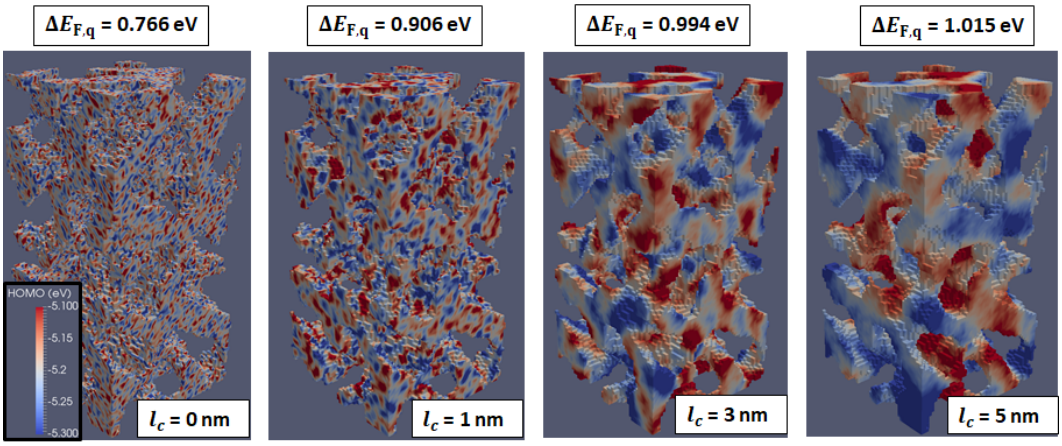

Figure 6.6 Energy landscape of the HOMO within the donor phase for varying correlated disorder from a completely uncorrelated disorder $l_c = 1\,\text{nm}$ up to a strong correlation of $l_c = 5\,\text{nm}$. The difference in quasi-Fermi levels is increased from 0.766 eV up to 1.015 eV due to the correlation in the disorder. Reprinted with permission from [350]. Copyright (2020) American Chemical Society.

While the distribution of the charge carriers in the disordered medium is rather random, clear domains of high charge carrier densities arise within the correlated structure. This is as charge carriers can move along these favorable correlated domains without the need of overcoming large barriers due to the disorder in site energies. This leads also to filamentary conduction in organic semiconductors as shown previously [50].

This resembles characteristic properties of organic semiconductors with higher crystallinity. As shown by Ripolles *et al.*, an increase in crystallinity can be beneficial for the open-circuit voltage and the device performance [378]. This is due to the strong connection of the V_{oc} with the energy distribution of the DOS at the interface [360, 378]. The available DOS strongly depends on the processing techniques and can be tuned e.g. by annealing [379, 380]. However, an increase in crystallinity can also lead to a decrease in the quasi-Fermi levels due to lower energy-gaps of pure crystals within the photoactive layer [360, 381]. The complexity of the bulk-heterojunction interface and the large degrees of freedom during processing may lead to correlated domains, however we do not expect strong energetic correlations at the interface. However, the strong impact of even lowest correlations were unexpected and may add a new control parameter to push the maximum V_{oc} to higher values. To predict and design organic semiconductors and donor:acceptor blends with high correlation lengths ab-initio methods are required. Kordt *et al.* have developed a mesoscopic method to generate Gaussian-distributed energies with predefined spatial correlations to compute accurate mobilities within organic semiconductors [284]. Such detailed atomistic inputs are beyond the scope of this work, but are of high interest to obtain a quantitatively accurate description of the energetic landscape.

6.4 Conclusion

In conclusion, we have presented a kinetic Monte Carlo analysis of the open-circuit voltage within 3-dimensional bulk-heterojunction organic solar cells. We computed the V_{oc} of the material composition neglecting the impact of additional interfaces such as contacts or selective transport layers. Thus, the results represent the maximum achievable open-circuit voltage for this specific material composition. Our analysis on the impact of the energetic disorder matches with existing numerical drift-diffusion

studies and experimentally observed trends. In addition, we focused on the role of interfaces by choosing different energetic disorders at the interface and within the bulk of the donor and acceptor. Our results show that the V_{oc} is dominated by the interfaces for an increase in interface disorder. With higher interface disorder, V_{oc} decreases significantly. This is due to the low screening of the Coulomb interaction, which causes high electron and hole densities at the interface. These results are of high importance for disordered organic solar cells as an increase in spatial and equally in energetic disorder is proposed within several theoretical and experimental studies. In addition, the impact of a correlation in the energetic disorder on the V_{oc} has been analyzed. We observe an increase in V_{oc} with rising correlation length. This increase is caused by the reduction of 'trapping'-tail states. These insights are difficult to observe within the effective medium approximation which is commonly used within drift-diffusion solvers. Thus the presented kinetic Monte Carlo study can provide new insight on the role of the local energetic disorder in organic solar cells. We expect qualitatively similar results for other BHJ solar cells besides P3HT:PCBM for which CT state dominate charge separation and recombination properties. In this case, the quantitative prediction of the V_{oc} strongly depends on the material dependent recombination and charge separation rates. High efficiency non-fullerene solar cells have been shown to be less dependent on the CT state. Note that the used model assumes fully localized charge carriers, thus it cannot account for the impact of strongly delocalized charge carriers or excitons.

7 Enhancing Exciton Diffusion in Organic Solar Cells via Triplet Sensitization

Low exciton diffusion lengths of ≤ 10 nm are a limiting factor for the efficiency of organic solar cells. To keep a high exciton dissociation yield, bulk-heterojunction morphologies of large donor:acceptor interface area are required. However, recombination losses are strongly enhanced with increased interface area. In contrast to short-living singlet excitons with lifetimes in the ns regime, triplet excitons may live up to µs to ms. Existing literature also suggests high triplet diffusion lengths within organic semiconductors. The conversion of photogenerated singlet excitons into triplet excitons via intersystem crossing using heavy-metal based compounds was previously shown by experiments to enhance the performance. Still, a detailed understanding of the detailed singlet and triplet dynamics as well as interactions are not well understood. Here, the role of triplet sensitization on the exciton lifetime and the OSC performance is studied in detail. Managing exciton lifetimes and diffusion lengths can provide an interesting approach to circumvent the tradeoff between short-circuit current and open-circuit voltage within OSCs.

Section **7.1** presents an overview on existing work on triplet sensitized organic solar cells. Section **7.2** summarizes the kinetic Monte Carlo model and excitonic processes. Sections **7.3** and **7.4** analyze the role of triplet sensitization via $Ir(ppy_3)$ phosphorescent sensitizers within bulk materials and heterojunction organic solar cells, respectively.

Contribution:
I have supervised the development of the excitonic model and conceptualized the study of triplet sensitization. Simulations in sections **7.3** and **7.4** were conducted by *Johannes Popp*, TUM, during his Master thesis under my supervision. I have led the writing of the published manuscript [362]. The content of this chapter has been adapted from 'Impact of Phosphorescent Sensitizers and Morphology on the Photovoltaic Performance in Organic Solar Cells,' *Adv. Theory Sim.*, 2 (1), 1800114, 2019 [362], ; section **7.3** is reproduced from 'Generalized Kinetic Monte Carlo Framework for Organic Electronics,' Algorithms, 2018, 11, 37 .

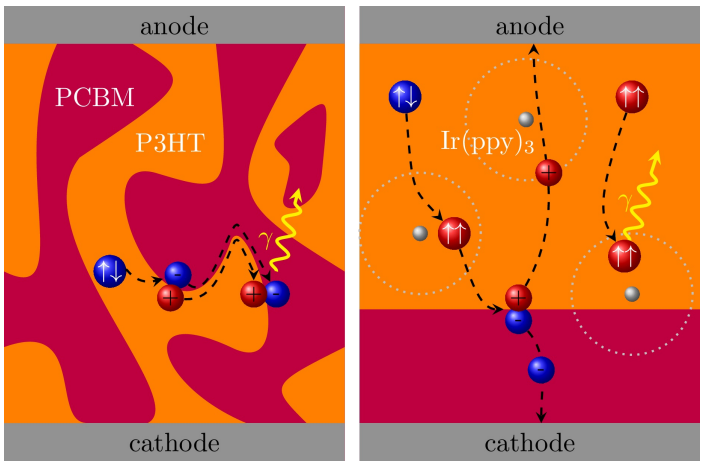

7.1 Background

To establish a solar cell with high PCE, four crucial properties need to be optimized: (1) effective light absorption under AM1.5G solar illumination; (2) exciton diffusion towards the donor-acceptor interface; (3) charge transfer state separation; (4) charge transport towards and collection at the electrodes [382–384]. The problem of the low PCE in most organic solar cells arises due to the high binding energy of the photo-generated singlet excitons. Strong electric fields or a strongly electronegative acceptor phase are required for an efficient exciton dissociation and free charge carrier generation. Typical optical absorption length of organic materials are in the range of 50 nm to 100 nm. This exceeds the short singlet exciton diffusion length $l_{\text{diff}} \approx 3$ nm to 10 nm [8,151,207,217,385,386]. In Fig. 7.1a, this issue is depicted for the bilayer solar cell: (i) excitons generated in the donor phase far from the interface will most probably decay before reaching the acceptor phase; (ii) only excitons generated in proximity to the donor-acceptor interface reach the interface by diffusion and can be dissociated into free electron-hole pairs. The use of materials with a high exciton diffusion length [384] or blended structures [10] increase the exciton dissociation yield. BHJ solar cells, as shown in Fig. 7.1b, ensure a small mean distance from the spot of the exciton generation to donor:acceptor interface due to the fine phase intermixing. Most of the excitons reach an interface (iii) and are separated, i.e., a high dissociation yield is observed [54, 144, 387]. The major disadvantage of the complex BHJ intermixing is given in the high interface area and increased energetic disorder [10]. Thus, (iv) the dissociated electron-hole pair moves along the interface and shows high recombination due to the low permittivity [13]. An alternative morphology is given by the planar-mixed heterojunction (PM-HJ). PM-HJs consist of a donor:acceptor blend sandwiched between neat donor and acceptor layers. The thickness of the single layers is preferably chosen to be equal to the exciton diffusion length to ensure a high dissociation efficiency. The PM-HJ provides a compromise between the bilayer and BHJ. Both the charge transport towards the contacts and the collection efficiency are improved due to the neat films next to the collection layers and the reduced interface area.

Another option to increase the PCE is the enhancement of the exciton diffusion length. Compared to the low singlet lifetimes and diffusion lengths, triplet excitons have a strongly increased lifetime of 1 µs to 10 µs and reach diffusion lengths of 10 nm to 100 nm [114, 207]. Previous studies have shown that the use of phosphorescent sensitizers (PS) in organic solar cells increases the exciton lifetime and diffusion length tremendously [207, 210, 388, 389]. The working principle of the doped solar cells is depicted in Fig. 7.1c: (v) doping the solar cell with the sensitizers (depicted by the red dots) increases the triplet state population due to an increased intersystem crossing of singlets into triplets in proximity to the sensitizers; (vi) triplets have a larger diffusion length and thus reach the interface with higher probability, where they are dissociated into free electron-hole pairs. This may improve the PCE despite the low donor:acceptor interface area and helps to reduce the recombination. The PCE is strongly sensitive to the PS concentration. Only a slight increase has been observed at low PS concentrations while the PCE drops for a high PS concentration [207,210]. Triplet-triplet annihilation and leakage currents have been considered as the limiting factors of the PCE. However, a deeper understanding of the interplay of the excitons with PS within organic solar cells is required to further improve the excitonic yield and PCE.

This chapter presents a kinetic Monte Carlo study on the impact of the phosphorescent sensitizers and the different morphologies on the photovoltaic performance of organic solar cells. Therefore, we use the established polymer:fullerene blends formed from poly(3-hexylthiophene) (P3HT) and [6,6]-phenyl C_{61}-butyric acid methyl ester (PCBM). Using our previously developed kinetic Monte Carlo framework [13,47,50,182], we account for all physical properties within the OSCs and explicitly treat singlet and triplet processes. We study the impact of the PS on three different morphologies:

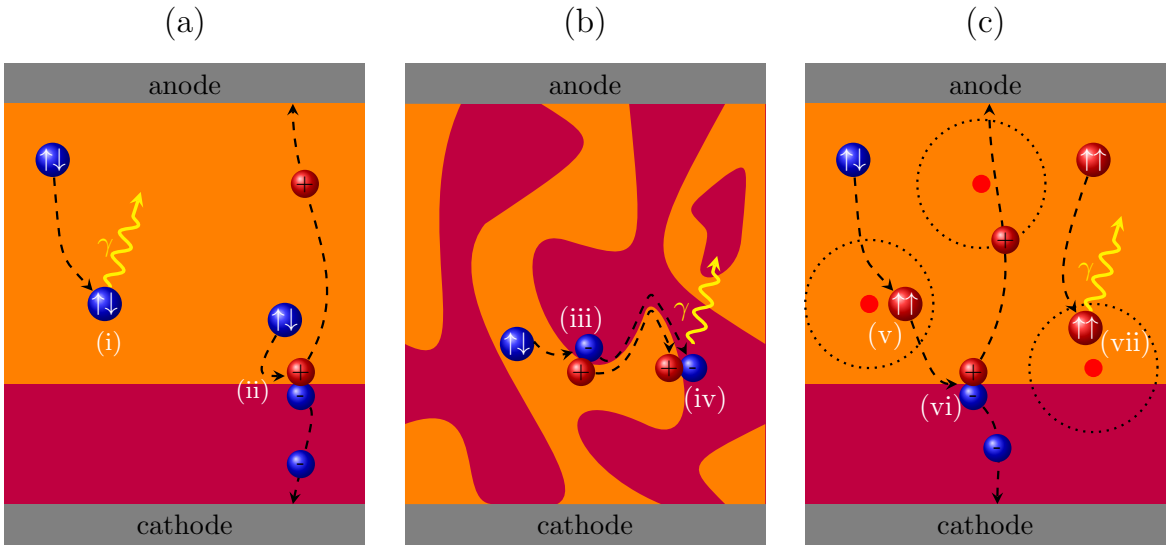

Figure 7.1 (a) Singlet exciton (↑↓) processes in a standard bilayer organic solar cell: (i) singlet exciton decay before reaching interface; (ii) dissociation and charge collection for singlets generated close to the donor:acceptor interface. Generated charge carriers will be transferred to the anode/cathode with a minimum path length. (b) Bulk-heterojunction organic solar cell: (iii) effective singlet exciton dissociation. The fine intermixing allows an efficient excitonic dissociation yield. (iv) Geminate charge recombination. (c) Bilayer solar cell with phosphorescent sensitizers (red dots): (v) intersystem crossing of singlets to triplets (↑↑) in proximity to the phosphorescent sensitizer. (vi) Triplet exciton dissociation. (vii) Enhanced decay of triplet excitons in the vicinity of a PS molecule due to high spin-orbit coupling. Reprinted with permission from [362], ©2018 WILEYVCH Verlag GmbH & Co. KGaA, Weinheim.

bilayer, planar-mixed molecular heterojunction, and bulk-heterojunction. Introducing the PS, the impact on the mean exciton diffusion length and the exciton dissociation yield is studied. Our goal is to investigate if and to which extent the photovoltaic performance of the organic solar cells can be retained while reducing the interface area and introducing PS, i.e., going towards bilayer structures doped with PS molecules. We study fac-tris(2-phenylpyridine) iridium ($Ir(ppy)_3$) as PS. Its use as a phosphorescent sensitizer in organic solar cells has been demonstrated experimentally in previous studies [210, 390] and is frequently used in highly efficient OLEDs [115, 124, 125, 391, 392].

7.2 Kinetic Monte Carlo Model - Exciton Dynamics

The presented results are obtained using our kinetic Monte Carlo (kMC) tool for organic solar cells [13, 14, 47]. We have previously extended the model presented by Albes *et al.* [47] with a detailed model of the singlet and triplet exciton dynamics and phosphorescent sensitizers [182].

In Fig. 7.2, we visualize the important excitonic processes: (a) Dexter type energy transfer (DTET); (b) Förster type resonance energy transfer (FRET); (c) exciton dissociation; (d) intersystem crossing (ISC), fluorescence and phosphorescence. The intramolecular excited states are visualized by their spin configurations on the lowest unoccupied molecular orbital (LUMO) and the highest occupied molecular orbital (HOMO). Figure 7.2d depicts the Jablonski diagram with the singlet and triplet excited states S_1 and T_1, respectively, and the singlet ground state S_0.

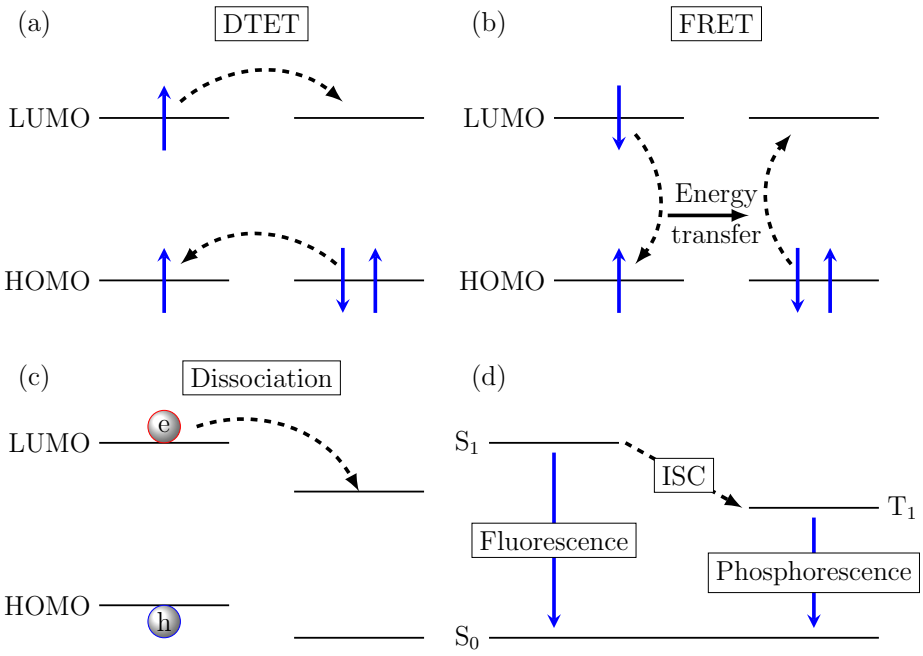

Figure 7.2 (a) Dexter type energy transfer (DTET) describing the diffusion of triplet excited states. (b) Förster resonance type energy transfer (FRET) describes the diffusion of singlet excitons. (c) Dissociation of excitons at the donor-acceptor interface. The dashed arrows highlight the simultaneous energetic transitions. (d) Jablonski diagram of the excited singlet and triplet state S_1 and T_1, respectively, and the ground state S_0. Visualization of the de-population mechanism of the exciton states: fluorescence (singlet excitons) and phosphorescence (triplet excitons). The intersystem crossing describes the transition of the singlet to triplet exciton in the proximity of the phosphorescent sensitizer. Reprinted with permission from [362], ©2018 WILEYVCH Verlag GmbH & Co. KGaA, Weinheim.

Now, we outline the fundamental physical processes of the exciton dynamics and the rate equations used within our kMC tool. For further details on the kMC method and the excitonic properties we refer to our previous publications [47, 182] and reviews on the exciton dynamics [8, 114, 225], respectively.

Förster type resonant energy transfer (FRET): Singlet exciton diffusion occurs by a non-radiative energy transfer from an excited donor to a ground state acceptor site [8]. FRET is a long-range mechanism, described by a dipole-dipole interaction, and can occur up to several nanometers [135]. The transition rate depends on the oscillator strength. As the transition of triplet excited state to the singlet ground state is a spin-forbidden process, it carries a negligible oscillator strength, and FRET can not describe triplet diffusion in general [8]. The transition rate for the singlet diffusion by FRET is described by [39, 46]

$$a_{\mathrm{FRET}} = \Gamma \left(\frac{r_{\mathrm{F}}}{r_{ij}}\right)^6 \begin{cases} \exp\left(-\frac{\Delta E_{ij}}{k_{\mathrm{B}}T}\right) & \text{if } \Delta E_{ij} > 0 \\ 1 & \text{else} \end{cases}, \tag{7.1}$$

with the thermal energy $k_{\mathrm{B}}T \approx 26\,\mathrm{meV}$, the total decay rate Γ, the Förster radius r_{F}, and the distance r_{ij} and energy difference ΔE_{ij} between the initial site i and the final site j. At $r_{ij} = r_{\mathrm{F}}$ and $\Delta E_{ij} = 0\,\mathrm{eV}$, exciton decay and FRET are equally probable. Between phosphorescent compounds, the spin-selection rules are lifted due to the strong spin-orbit coupling. This induces an oscillator strength which allows triplet excited states to diffuse by the FRET mechanism [8, 114, 223, 224]. The energy difference ΔE_{ij}

depends on the energetic distribution of exciton state energies to the sites. A Gaussian distribution with disorder σ_{ex} can be added to the energies $E^{s/t}$ of the excited states S_1/T_1. Furthermore, we account for different energies of the excited states in each material. The energy difference is then given by $\Delta E_{ij} = E_j^{s/t} - E_i^{s/t}$.

Dexter type energy transfer (DTET): DTET [133] describes triplet exciton diffusion between host molecules with negligible spin-orbit coupling. It is transmitted by an exchange coupling between the triplet donating and triplet accepting molecules and thus requires a strong spatial overlap of the wavefunction, i.e., it can only occur on short length scales [8, 225]. Its strength decays exponentially with rising distance and can be modeled using a Miller-Abrahams like rate [27, 223, 225]:

$$a_{\mathrm{DTET}} = a_{\mathrm{D}} \exp\left(-2\gamma r_{ij}\right) \begin{cases} \exp\left(-\frac{\Delta E_{ij}}{k_{\mathrm{B}}T}\right) & \text{if } \Delta E_{ij} > 0 \\ 1 & \text{else} \end{cases}, \tag{7.2}$$

with the Dexter prefactor a_{D} and the triplet exciton energy difference $\Delta E_{ij} = E_j - E_i$ of the involved sites. The energetic difference ΔE_{ij} is computed in the same way as for FRET.

Optical exciton generation: Singlet excitons can be generated optically upon absorption of a photon. The generation profile is computed by the transfer matrix method (TMM) [215–217]. With this, we account for the optical interference and absorption in the organic solar cell under the AM1.5 illumination spectrum. Due to the spin selection rules, direct optical excitation of triplets is forbidden. In the kMC simulations, we account for the attenuation in the active layer by a z-dependent optical generation profile $a_{\mathrm{opt}}(z)$ obtained by the TMM. For the BHJ solar cell, the generation rate is set equal in both the donor and acceptor material due to the lack of a complete optical model.

Electrical exciton generation: Singlet and triplet excited states can be formed by electrical excitation. Charge carriers are injected from the electrodes and diffuse through the organic material until they are attracted by their Coulomb interaction. When an electron and hole meet, they can recombine to form a singlet or triplet state depending on their spin configuration [8]. We account for the electrical exciton generation by a hopping process of an electron (hole) on a neighboring site occupied by a hole (electron). Charge hopping is modeled using the Miller-Abrahams rate [27]:

$$a_{\mathrm{el,gen}} = a_0 \exp\left(-2\gamma r_{ij}\right) \begin{cases} \exp\left(-\frac{\Delta E_{ij}}{k_{\mathrm{B}}T}\right) & \text{if } \Delta E_{ij} > 0 \\ 1 & \text{else} \end{cases}, \tag{7.3}$$

with the inverse localization length γ, the distance r_{ij} between the initial site i of the hopping charge and the final site j of the occupied molecule. To determine the final excitonic state, the involved electron and hole are labeled with a fixed spin configuration ($|\uparrow\rangle$ or $|\downarrow\rangle$). For the sake of simplicity, we assign a fixed spin-down for all the injected holes. In case of the electrons, the spin state is chosen randomly with a predefined ratio of spin-up/spin-down states. The energy difference ΔE_{ij} depends on the spin configuration of the electron-hole pair:

$$\Delta E_{ij} = E_{\mathrm{B}}^{s/t} + E_j^{\mathrm{MO}} - E_i^{\mathrm{MO}} - E_{\mathrm{CT}}\,, \tag{7.4}$$

with the singlet/triplet binding energy $E_{\mathrm{B},j}^{s/t}$, the charge transfer state energy E_{CT}, and the difference in molecular orbital energies $E_{i/j}^{\mathrm{MO}}$ at initial site i and final site j.

Intersystem crossing: The conversion of singlet into triplet excited states requires an inversion of the electron spin. Intersystem crossing is strongly enhanced close to heavy-atom molecules due to the

strong spin-orbit coupling. In our model, we account for the intersystem crossing within the material-dependent radius r_{ISC} around a phosphorescent sensitizer. If an exciton encounters this domain, the intersystem crossing rate is enabled:

$$a_{\mathrm{ISC}} = a^0_{\mathrm{ISC}} \exp\left(-\frac{2r_{i\to d}}{r_{\mathrm{ISC}}}\right) , \tag{7.5}$$

with the intersystem crossing frequency a^0_{ISC}, and the distance $r_{i\to d}$ from site i and the phosphorescent sensitizer residing at site d.

Triplet-triplet annihilation: Excited triplet states can decay monomolecularly or bimolecularly [8]. The bimolecular annihilation process, known as the triplet-triplet annihilation (TTA), describes the decay of one triplet exciton into the ground state while the second triplet is promoted to a higher excited state. The excited state relaxes by non-radiative transitions to the singlet/triplet excited states S_1/T_1. We assume the relaxation to occur immediately, i.e., we consider the following processes:

$$T_1 + T_1 \rightarrow S_0 + T_1 , \tag{7.6}$$

$$T_1 + T_1 \rightarrow S_0 + S_1 . \tag{7.7}$$

We activate the TTA if two triplet excitons reside on neighboring sites or at sensitizer molecules within the Förster radius. If the TTA occurs, one triplet decays to the ground state. In the first case, the second triplet results in a singlet/triplet with a ratio of 1:3 [154, 219]. In the second case, the resulting exciton remains in the triplet configuration. The TTA rate is modeled by [8, 219]

$$a_{\mathrm{TTA}} = 8\pi f r_{ij} D , \tag{7.8}$$

where D is the triplet diffusion constant, and f gives the probability that reaction (7.7) occurs.

Exciton decay: Excited states can decay radiatively, by fluorescence and phosphorescence, and non-radiatively. If the spins of the electron-hole pair are antiparallel, the singlet exciton can decay radiatively within a short lifetime, which is known as fluorescence. In contrast, triplet excitons can only recombine radiatively if a spin-flip occurs. As the spin selection rules forbid a spin-flip, radiative recombination (phosphorescence) of triplets occurs on a larger timescale compared to fluorescence. Exciton decay is modeled using a constant decay rate corresponding to the inverse lifetime: $a_{\mathrm{dec,s/t}} = \tau^{-1}_{\mathrm{s/t}}$. Within r_{ISC}, the triplet decay rate is raised to account for the higher spin-orbit coupling.

Exciton dissociation: The dissociation of excitons has been reported to occur on ultrafast timescales of $\approx$ fs [143, 160, 226]. It is of fundamental importance for organic solar cells to generate free charge carriers. Dissociation of excitons is the energetically inverse process of the electrical exciton generation. The dissociation is modeled as an electron or hole leaving the exciton by a hopping process from its current site i to a neighboring site j using the Miller-Abrahams rate given in eq. 7.4, where the energy difference is given by

$$\Delta E_{ij} = E_{\mathrm{MO},j} - E_{\mathrm{MO},i} + E_{\mathrm{CT}} - E^{s/t}_{\mathrm{B}} . \tag{7.9}$$

Whether the hopping charge is the electron or the hole depends on the material, at which the exciton resides.

7.3 Enhancing Exciton Diffusion in Single Organic Layers

Using the presented kMC framework, we study the impact of phosphorescent sensitizers on the exciton dynamics in an organic bulk material. We focus on the diffusion length and lifetime of excitons and analyze the number of singlets converted into triplets. With this simulation, which is of rather theoretical aspect, we aim to mimic the exciton dynamics and interplay of excitons within a single organic material without any interfaces, defects and contacts.

As for the charge transport simulation, a single material cubic lattice of $50\,\text{nm} \times 50\,\text{nm} \times 50\,\text{nm}$ with lattice constant of 1 nm and periodic boundaries in all spatial dimensions is generated. Simulations are executed for different PS volume concentrations varying from 0 vol% up to 10 vol%. As no contacts are included, charges cannot be injected or collected. Due to the lack of interfaces exciton splitting cannot occur. Singlet excitons are generated with a constant optical generation rate $a^s_{\text{gen}} = 7\,\text{s}^{-1}\text{nm}^{-3}$. Triplet excitons can be induced upon intersystem crossing close to the PS. In Table 7.1, the used simulation parameters are summarized.

In Fig. 7.3, the dependence of the average lifetime τ and effective diffusion length $L_{\text{diff,eff}}$ on the PS volume concentration c is illustrated for both singlet (a) and triplet excitons (b). The effective exciton diffusion length is determined using

$$L^{s/t}_{\text{diff,eff}} = \sqrt{\frac{\sum (\text{d}L^{s/t}_i)^2}{N^{s/t}}}\,, \tag{7.10}$$

Table 7.1 Simulation parameters for the exciton dynamics.

Description	Parameter	Value	Ref.
Common Parameters			
Phosphorescent sensitizer concentration	c	0 vol% − 10 vol%	-
Energetic disorder excitons	$\sigma^{s/t}$	0 eV	-
Inverse localization length	γ	$2\,\text{nm}^{-1}$	[46, 48]
Simulation time	t_{sim}	1 ms	-
Exciton parameters			
Optical generation rate	a^s_{gen}	$7\,\text{s}^{-1}\,\text{nm}^{-3}$	-
Hopping rate (RW)	$a^s_{\text{exh,RW}}$	$2.0 \times 10^{10}\,\text{s}^{-1}$	[47]
Singlet decay rate	a^s_{exd}	$2.0 \times 10^{9}\,\text{s}^{-1}$	[45, 48, 393]
Singlet binding energy	E^s_{B}	0.5 eV	-
ISC radius	r_{ISC}	2 nm	-
ISC rate	a^0_{ISC}	$1.0 \times 10^{12}\,\text{s}^{-1}$	-
Förster radius	$r_{\text{F,PS}}$	1.5 nm	[138]
Dexter rate	a_{D}	$2.9 \times 10^{8}\,\text{s}^{-1}$	[223]
Decay rate	$a^t_{\text{exd,PS}}$	$1.0 \times 10^{6}\,\text{s}^{-1}$	-
Decay rate host material	$a^t_{\text{exd,host}}$	$1.0 \times 10^{6}\,\text{s}^{-1}$	[151, 207]
Triplet binding energy	E^t_{B}	1.0 eV	-
TTA rate Dexter type	$a_{\text{D,TTA}}$	$2.9 \times 10^{8}\,\text{s}^{-1}$	[223]
TTA Förster radius	$r_{\text{F,TTA}}$	1.5 nm	[138]

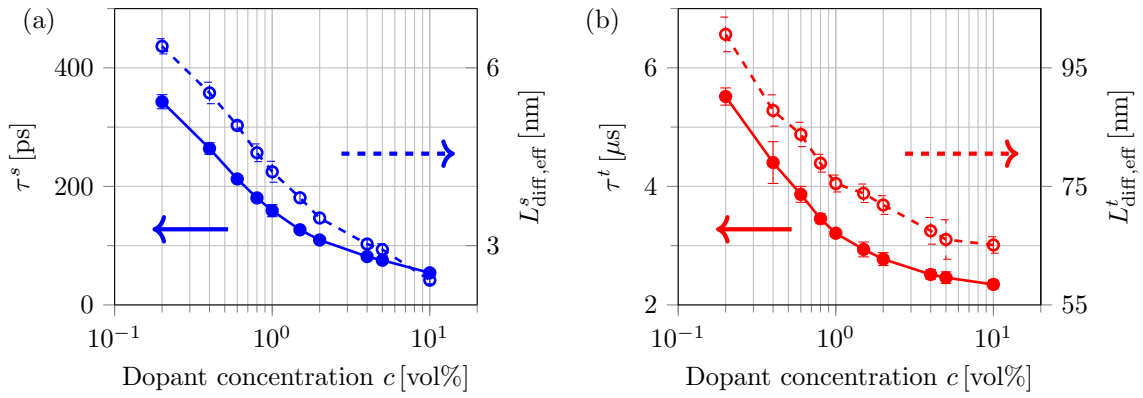

Figure 7.3 Impact of the PS volume concentration c on the average exciton lifetime τ (solid curves) and the effective diffusion length $L_{\mathrm{diff,eff}}$ (dashed curves) for (a) singlet excitons and (b) triplet excitons. Reproduced from [182] under license CC BY 4.0.

where $\mathrm{d}L_i$ is the Euclidean distance between the generation and final site of exciton i and $N^{s/t}$ denotes the number of either singlet or triplet excitons [114]. The presented results show the average effective diffusion lengths of eight configurations simulated for each PS concentration, while the error bars indicate the standard deviation. For a concentration of $c = 0\,\mathrm{vol\%}$, an average singlet exciton lifetime of $\tau^s = 501 \pm 24\,\mathrm{ps}$ is obtained, which corresponds to an effective diffusion length of $L^s_{\mathrm{diff,eff}} = 7.6 \pm 0.1\,\mathrm{nm}$. As can be seen in Figure 7.3 both τ^s and $L^s_{\mathrm{diff,eff}}$ decrease with rising PS concentrations. This is caused by the increased intersystem crossing of singlets into triplets within simulation times below the decay time. Effective triplet diffusion lengths of $L^t_{\mathrm{diff,eff}} = 101 \pm 3\,\mathrm{nm}$ are obtained for a low PS concentration, whereas for increasing PS concentrations the diffusion length decreases down to $L^t_{\mathrm{diff,eff}} \approx 65\,\mathrm{nm}$ for $c = 10\,\mathrm{vol\%}$. The average lifetime of triplets decreases from $5.5 \pm 0.1\,\mathrm{s}$ for $c = 0.2\,\mathrm{vol\%}$ to $2.3 \pm 0.1\,\mathrm{s}$ at $c = 10\,\mathrm{vol\%}$. This strong decrease in both effective diffusion length and lifetime is caused by the higher decay rates of triplets within the radius r_{ISC} around a PS. With rising volume concentration the influence of PS becomes increasingly visible.

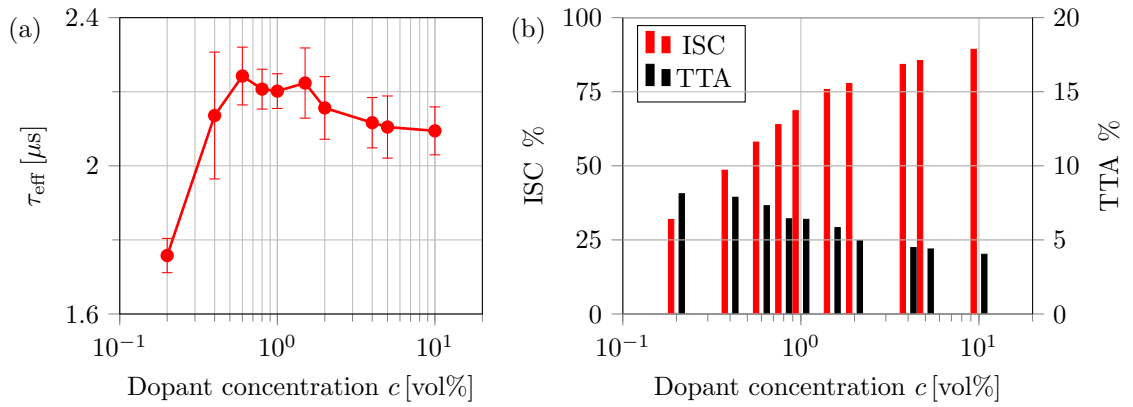

Figure 7.4 Impact of the PS volume concentration c on (a) the effective exciton lifetime and (b) intersystem crossing and triplet-triplet annihilation. The red bars show the proportion of converted triplets over the amount of optically generated singlets, the black bars represent the percentage of TTA over the amount of converted/generated triplets. Reproduced from [182] under license CC BY 4.0.

Figure 7.4 depicts the dependence of the percentage of singlets undergoing intersystem crossing and triplets annihilated by TTA on the PS concentrations. Multiple counting of singlets back-converted from triplets upon a TTA event is omitted. For a PS concentration of $c = 0.2\,\text{vol\%}$, the proportion of converted triplets to optical generated singlets is 30 %. For higher concentrations more than 80 % of singlets are converted into triplets before decaying. Figure 7.4 displays the percentage of triplets annihilated upon TTA. Starting with a ratio of 8.1 % at $c = 0.2\,\text{vol\%}$, the proportion of triplet-triplet annihilation decreases to a value of 2.3 % for $c = 10\,\text{vol\%}$. Triplet-triplet annihilation becomes unlikely for higher concentrations. The decrease in TTA can be related to the decreasing lifetime of triplets and the reduced diffusion length. Thus, the probability of triplets to meet each other decreases tremendously. This is explicitly caused by the lowering of the spin-selection rules within the strong spin-orbit coupling domains of the PSs. Higher triplet densities would significantly rise the impact of TTA. In Figure 7.4a the effective exciton lifetime defined by

$$\tau_{\text{eff}} = \text{ISC} \cdot \tau^t + (1 - \text{ISC}) \cdot \tau^s \tag{7.11}$$

is visualized. For low PS concentration the τ_{eff} increases strongly as most of the excitons are not converted into triplets. With rising c the effective lifetime rises and reaches its maximum at $c = 1\,\text{vol\%}$. Beyond the maximum the effective lifetime decreases and saturates at a value of $\tau_{\text{eff}} \approx (2.09 \pm 0.06)\,\mu\text{s}$. A similar trend is observed by Gonzales *et al.* for a doped P3HT:PCBM solar cells [207].

The results for exciton diffusion lengths and lifetime conform with experimental values within ideal material setups, documented in refs. [8, 151, 220, 394]. Similar to the trend observed in ref. [207, 390], the lifetime of excitons decreases with PS concentration. Firstly, for small PS concentration the lifetime increases tremendously in comparison to singlet lifetimes caused by the conversion of singlets to the long-living triplets. However, for higher PS concentration a quenching mechanism is observable due to the TTA and a higher decay rate. Simulations with higher triplet exciton decay rates within the ISC radius due to stronger spin-orbit coupling matches observed results for exciton lifetime trends [390]. Yang *et al.* measured decrease of the triplet exciton lifetime by a factor of 2.8 upon doping with Ir(mppy)_3 which is in the same order of magnitude of our simulation results [390].

7.4 Enhancing Exciton Diffusion within Organic Solar Cells

In this section, we present our kMC study of the impact of the morphology and doping with phosphorescent sensitizers on the photovoltaic performance of the organic solar cells. In section 7.4.2, we investigate the excitonic properties and the dissociation efficiency for the different morphologies at short circuit condition. Then, we introduce the PS with concentrations of $c \in [0\,\text{vol\%},\ 3\,\text{vol\%}]$ into the four aforementioned solar cells to improve the photovoltaic performance and analyze the drawbacks at rising sensitizer concentrations. The parameters of the PS are calibrated based on the diffusion length in the doped N, N'-bis(naphthalene-1-yl)-N, N'-bis(phenyl)-benzidine (NPD):C_{60} solar cell [210]. In section 7.4.4, we artificially design an optimized sensitizer by varying the intersystem crossing and decay rates within the sensitizer region. The aim is to find an ideal PS and donor material to improve the PCE within an organic solar cell with low recombination due to a reduced interface area.

7.4.1 Parameter Calibration

Before discussing the impact of morphology and phosphorescent sensitizers on the P3HT:PCBM solar cell performance, we need to calibrate the excitonic parameters and the properties of the sensitizer Ir(ppy)_3.

To account for a correct singlet exciton diffusion, the Förster radius needs to be calibrated. Thus, we study the diffusion length within a P3HT bulk material for an ensemble of singlets. With the decay rate of $a_{\mathrm{dec,s}} = 1.25 \times 10^9\,\mathrm{s}^{-1}$ and the Förster radius $r_\mathrm{F} = 2\,\mathrm{nm}$, we obtain the singlet exciton diffusion length of $l_{\mathrm{diff,s}} \approx 12\,\mathrm{nm}$ within P3HT, which is in the range of measured [114, 395, 396] and simulated values [397] for amorphous P3HT.

The triplet exciton diffusion length is difficult to determine experimentally. Mostly, triplet diffusion lengths are assumed to exceed the singlet diffusion length by far [398, 399]. To our knowledge, no experimental measurements on diffusion lengths within the donor material P3HT are available. Other polymers show a high spreading in the triplet diffusion length of 10 nm to 100 nm [8, 114, 207]. We use the Dexter prefactor $a_D^0 = 1.6 \times 10^9\,\mathrm{s}^{-1}$ and a decay rate of $a_{\mathrm{dec,t}} = 10^5\,\mathrm{s}^{-1}$ to obtain a triplet diffusion length of $l_{\mathrm{diff,t}} \approx 37\,\mathrm{nm}$. The observed triplet diffusion length is in good agreement with other materials used for phosphorescent sensitization [388, 389, 400]. In previous work, triplet diffusion lengths of 28 nm to 35 nm in C_{60} are obtained [114, 217]. For platinum octaethylporphyrin (PtOEP), triplet diffusion lengths of 13 nm to 30 nm are reported [114]. For further experimental data on singlet and triplet diffusion lengths the reader is referred to to the review of Mikhnenko *et al* [114].

We calibrate the rates for the phosphorescent sensitizer using the test system NPD:C_{60} [210]. As shown in appendix C.2, we use a bilayer structure doped with $\mathrm{Ir(ppy)_3}$ and study the effective exciton diffusion length and the IQE at short-circuit condition. For the given sensitizer, we use an ISC radius $r_{\mathrm{ISC}} = 2\,\mathrm{nm}$. This determines the exponential decay of the intersystem crossing rate with the distance to the PS. The intersystem crossing frequency is set to $a^0_{\mathrm{ISC}} = 10^{11}\,\mathrm{s}^{-1}$. Furthermore, we set a Dexter prefactor for the triplet diffusion to $a^0_{\mathrm{D,Ir(ppy)_3}} = 1.6 \times 10^{10}\,\mathrm{s}^{-1}$ between the PS sites and to $a^0_{\mathrm{D,P3HT}} = 1.6 \times 10^9\,\mathrm{s}^{-1}$ within P3HT. The triplet decay rates within the intersystem radius of the PS and within the donor are calibrated by measured triplet diffusion lengths [210]. Luhman *et al.* observed an increase in the exciton diffusion length from $l_{\mathrm{diff,eff}} = 6.5 \pm 0.3\,\mathrm{nm}$ to $l_{\mathrm{diff,eff}} = 11.8 \pm 0.6\,\mathrm{nm}$ by doping the solar cell with a PS weight percentage of $c = 5\,\mathrm{wt\%}$ [210]. We obtain an increase in the diffusion length from $l_{\mathrm{diff,eff}} = 6.9 \pm 0.1\,\mathrm{nm}$ at zero PS concentration to $l_{\mathrm{diff,t}} = 13.0 \pm 0.3\,\mathrm{nm}$ at $c = 0.6\,\mathrm{vol\%}$. Further information on the diffusion simulations using the NPD:C_{60} system as well as the material parameters of the P3HT:PCBM solar cell are given in the appendix C.3.

7.4.2 Impact of the Morphology on the OPV performance

In this section, we investigate the impact of the morphology on the solar cell performance at short-circuit condition. We use four different morphologies: bilayer, planar-mixed heterojunction with two different cluster sizes of 10 nm (PM-$\mathrm{HJ_{10}}$) and 20 nm (PM-$\mathrm{HJ_{20}}$), and the bulk-heterojunction. In table 7.2, the studied morphologies are visualized. We run 5 simulations for each configuration to ensure a good statistics. The presented results show the mean and standard deviation of the 5 runs. In table 7.2, the OPV parameters electron/hole collection time $\tau_{\mathrm{elc/hoc}}$, recombination ratio η_{ehr}, dissociation efficiency η_{diss}, internal quantum efficiency IQE, and short circuit current density j_{sc} are presented.

The aim of reducing the complexity of the donor:acceptor blend is to improve the charge carrier collection efficiency η_{cc} [195]. The fastest observed electron and hole collection times are $\tau_{\mathrm{elc}} = 35.5\,\mathrm{ns}$ and $\tau_{\mathrm{hoc}} = 228.9\,\mathrm{ns}$ in the case of the bilayer solar cell. By increasing the complexity of the morphology, the collection times increase due to the rising complexity in the percolation paths. Furthermore, the collection time increases as the charge pair separation is worsened by the Coulomb interaction, which results in a strong interface density [13]. From the bilayer to BHJ solar cell the charge carrier collection time is doubled. Due to the limiting dissociation efficiency in the bilayer structures, these values are insignificant. Charge collection times for the PM-HJ structures rise as expected with the complexity.

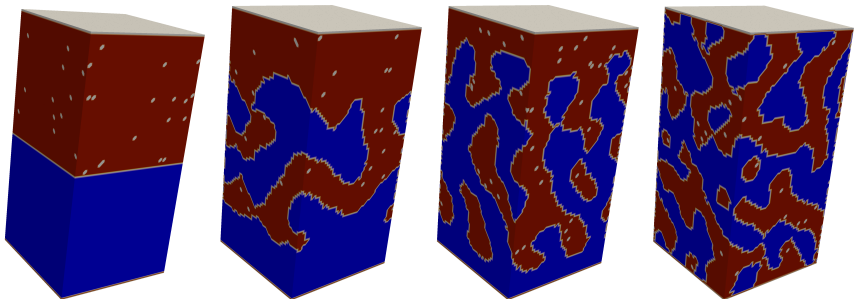

Figure 7.5 Organic solar cell morphologies from left to right: Bilayer morphology, PM-HJ with phase size of 20 nm, PM-HJ with phase size of 10 nm, and bulk-heterojunction morphology. The P3HT donor phase is given in red, the PCBM acceptor phase in blue and 0.6 vol% of $Ir(ppy)_3$ highlighted by white sites. Reprinted with permission from [362], ©2018 WILEYVCH Verlag GmbH & Co. KGaA, Weinheim.

Table 7.2 Comparison of different morphologies of the P3HT:PCBM organic solar cell modeled by a $50 \times 50 \times 100\,\mathrm{nm}^3$ simulation box with periodic boundary conditions. The electron and hole collection time τ_{elc} and τ_{hoc}, respectively, mean recombination ratio η_{ehr}, exciton dissociation efficiency η_{diss}, internal quantum efficiency IQE, and short-circuit current density j_{sc} are evaluated for pure P3HT:PCBM solar cells without phosphorescent sensitizers at short-circuit condition. Furthermore, the fill factor FF, open circuit voltage V_{oc}, and power conversion efficiency PCE are shown.

Configuration	**Bilayer**	**PM-HJ$_{20}$**	**PM-HJ$_{10}$**	**BHJ**
Interface area (nm^2)	2500	25710	44866	56917
$\tau_{\mathrm{elc}}/\tau_{\mathrm{hoc}}$ (ns)	35.5/157.9	58.8/228.9	65.1/250.9	76.5/314.1
η_{ehr} (%)	1.3	3.4	3.6	3.8
η_{diss} (%)	14.68	60.31	81.58	89.24
IQE (%)	14.45	58.30	78.46	85.34
j_{sc} ($\mathrm{mA\,cm}^{-2}$)	1.36	6.01	8.17	9.08
V_{oc} (V)	0.86	0.84	0.83	0.67
FF (%)	75.6	68.7	65.4	58.4
PCE (%)	0.91	3.46	4.45	3.56

For the chosen recombination rate $a_{\mathrm{ehr}} = 10^7\,\mathrm{s}^{-1}$, recombination is rather small for all the configurations. The bilayer solar cell shows minimal mean recombination with a ratio of $\eta_{\mathrm{ehr}} = 1.3\,\%$, whereas the heterojunction morphologies have recombination ratios above 3 %. By reducing the complexity of BHJ, a slight improvement in recombination ratio can be achieved. The small recombination ratios ensure a high charge collection efficiency $\eta_{\mathrm{cc}} \approx 100\,\%$ and thus a high IQE (IQE $\approx \eta_{\mathrm{diss}}$).

The BHJ solar cell exhibits the highest exciton dissociation efficiency $\eta_{\mathrm{diss}} = 89.24\,\%$. The PM-HJ$_{10}$ has the same cluster size as the BHJ; its dissociation efficiency is lowered by the singlet excitons lost in the neat layers at the contacts. The PM-HJ$_{20}$ provides insufficient exciton dissociation due to the larger cluster size and strongly reduced interface area. In case of the bilayer morphology, the interface area is reduced to 10 % of the PM-HJs. Thus, the IQE and short circuit current density strongly drop.

The best IQE of 85.3 % is observed for the BHJ solar cell. By a reduction of the complexity of the morphology, the IQE rises for the BHJ by a factor of 6 compared to the bilayer IQE. The bilayer solar cell has an IQE of 14.5 %. Due to the high layer thickness, most of the optically generated singlets decay before reaching an interface. This limits their efficiency despite their good charge collection

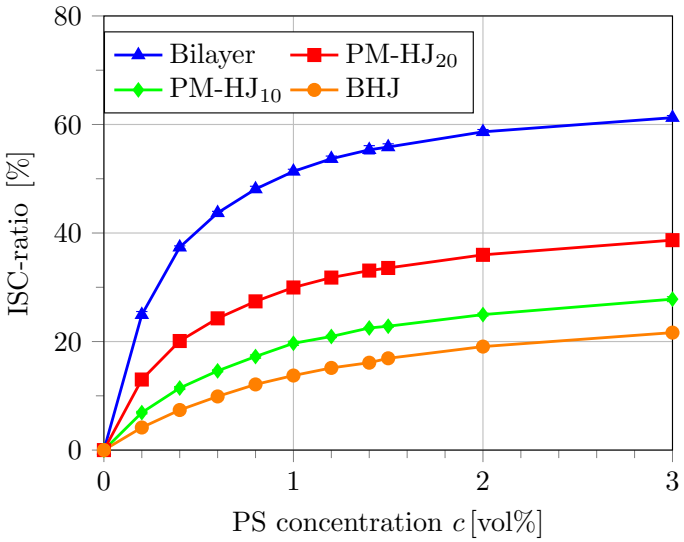

Figure 7.6 Influence of the phosphorescent sensitzer (PS) concentration on the ISC-ratio for the different morphologies: bilayer, PM-HJ$_{20}$, PM-HJ$_{10}$ and BHJ. Reprinted with permission from [362], ©2018 WILEYVCH Verlag GmbH & Co. KGaA, Weinheim.

efficiency. We obtain IQEs of 78.5 % for the PM-HJ$_{10}$ and 58.3 % for the PM-HJ$_{20}$. The increase in cluster size and homogeneous layer thickness limits exciton dissociation in the PM-HJ configurations.

Despite the low j_{sc} of the bilayer and PM-HJ solar cells, they still exhibit a good photovoltaic performance due to their high V_{oc} exceeding 0.8 V. This results in a power conversion efficiency of the PM-HJs in the range of the BHJ solar cells. The fill factor rises with reduced interface area due to a reduction in the electron-hole recombination. The PM-HJ$_{10}$ even shows an increase in the PCE of almost 1 %, while the PM-HJ$_{20}$ has a PCE comparable with the BHJ solar cell despite the halved interface area.

In summary, one can still obtain a high PCE despite a reduced interface area and current density, as the open circuit voltage and fill factor increase. In the next section, we study the impact of the phosphorescent sensitizer on the excitonic properties and solar cell performance.

7.4.3 OPV Performance Enhancement by Phosphorescent Sensitization

Now, we induce the PS molecules Ir(ppy)$_3$ with varying volume concentration $c = 0 \ldots 3$ vol% into the donor phase of the P3HT:PCBM solar cells. Singlet excitons are converted into triplet excitons by intersystem crossing in proximity to the PS sites. Triplets have a longer lifetime; however the diffusion constant is slower compared to singlets. We study the impact of the sensitizer on the effective exciton lifetime and dissociation efficiency. As optical exciton generation does not change with the sensitizer concentration, the total number of generated exciton within a certain morphology does not differ with changing c. Thus, we study the percentage of singlets and triplets reaching the interface and undergoing a dissociation. Finally, the jV curve at the optimal PS concentration is compared to the results presented in Table 7.2.

Intersystem crossing and population of triplet exciton states influence the mean exciton lifetime. Triplet excitons show typical lifetimes in the range of $\tau_t \approx 10\,\mu s$ [151, 207], whereas singlets have a mean lifetime of $\tau_s \approx 500\,ps$ [45, 207, 393]. Here, we investigate the impact of PS doping in bilayer, BHJ and PM-HJ solar cell morphologies on the effective exciton lifetime τ_{eff}. For the calculation

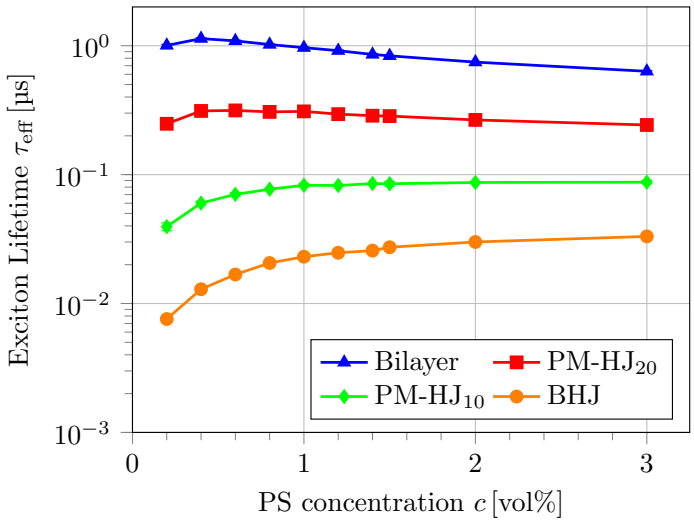

Figure 7.7 Effective exciton lifetime τ_{eff} in all four configurations. Considered decay mechanisms are decay, dissociation and triplet-triplet annihilation. Reprinted with permission from [362], ©2018 WILEYVCH Verlag GmbH & Co. KGaA, Weinheim.

of effective lifetime, we involve the lifetime of all the decayed, dissociated or annihilated excitons, regardless of their type. The effective exciton lifetime is obtained by

$$\tau_{\text{eff}} = \eta_{\text{ISC}}\tau_{\text{t}} + (1 - \eta_{\text{ISC}})\tau_{\text{s}}\,, \tag{7.12}$$

where η_{ISC} denotes the intersystem crossing ratio and $\tau_{\text{s/t}}$ the mean exciton lifetime of singlet or triplet excitons, respectively. The effective lifetimes τ_{eff} are illustrated in Fig. 7.7. Without any PS concentration, only singlet excitons are present, which yields a lifetime of hundreds of ps. The presence of phosphorescence sensitizers and ISC leads to an increase in the effective lifetime due to the long-term triplets. For all morphologies, an increase in the effective lifetime with rising PS concentration is observed. While the ISC rises with the PS concentration until saturation is observed, the effective lifetime reaches a maximum value before decreasing again. Maximum effective lifetimes of $1.1 \pm 0.1\,\mu\text{s}$ at $c = 0.4\,\text{vol\%}$ for the bilayer solar cell and $315 \pm 6\,\text{ns}$ at $c = 0.6\,\text{vol\%}$ for the PM-HJ$_{20}$ solar cell are observed. For higher PS concentrations, the effective lifetime decreases to $\tau_{\text{eff,bilayer}} = 633 \pm 9\,\text{ns}$ and $\tau_{\text{eff,PM-HJ20}} = 243 \pm 4\,\text{ns}$ at $c = 3\,\text{vol\%}$. The decrease in the lifetime with rising PS concentration c results from a higher decay rate for triplet excitons within the ISC radius r_{ISC}. The decay rate within the ISC volume has been chosen as $10^6\,\text{s}^{-1}$, i.e., ten times higher than the decay rate within the pure P3HT phase. Concerning the BHJ and PM-HJ$_{10}$, an increase of effective lifetime followed by a saturation regime is observed. The effective exciton lifetimes converge to $\tau_{\text{eff,PM-HJ10}} = 87 \pm 3\,\text{ns}$ and $\tau_{\text{eff,BHJ}} = 33 \pm 1\,\text{ns}$. Due to the high dissociation efficiency η_{diss} in these morphologies, the ISC is rather small. The increase of effective lifetime is caused by the rising intersystem crossing for increasing PS concentrations c outperforming the influence of higher triplet decay rates within the ISC-radius.

The intention of introducing PS molecules is not particularly increasing the exciton lifetime, but to enlarge the diffusion length of excitons to reach the donor:acceptor interface. Thus, the impact of the sensitizer on the diffusion length l_{diff} is studied. We focus on the mean distance; an exciton

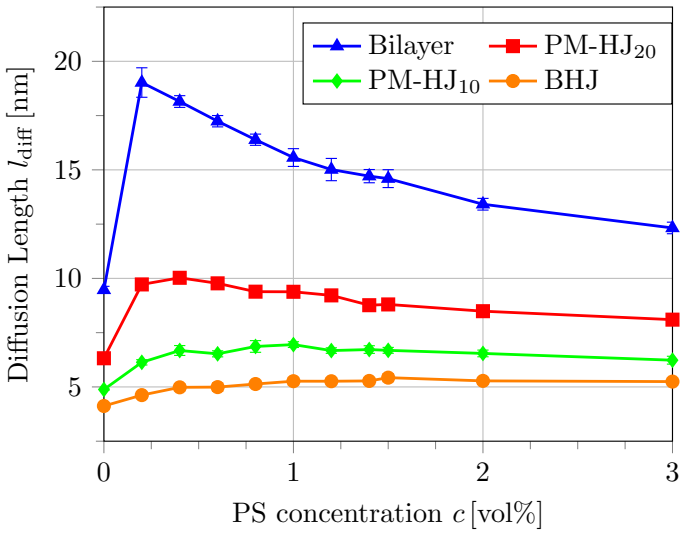

Figure 7.8 Exciton diffusion length l_{diff} of the four configurations bilayer, PM-HJ$_{20}$, PM-HJ$_{10}$ and BHJ for PS concentrations 0 vol% $\leq c \leq$ 3 vol%. Reprinted with permission from [362], ©2018 WILEYVCH Verlag GmbH & Co. KGaA, Weinheim.

diffuses through the active layer until reaching a donor:acceptor interface and dissociating to a free electron-hole pair. The mean diffusion length is calculated by [114]

$$l_{\text{diff}} = \sqrt{\frac{\sum_i \mathrm{d}l_{\text{diff},i}^2}{N}}, \tag{7.13}$$

where N gives the number of generated excitons, which have been dissociated at the P3HT:PCBM interface. Furthermore, the diffusion length $\mathrm{d}l_{\text{diff},i}$ denotes the Euclidean distance between the spot of generation and dissociation site of exciton i. The mean diffusion lengths l_{diff} for varying concentrations c and all morphologies are illustrated in Fig. 7.8.

We observe a strong correlation between the simulated diffusion lengths and the effective lifetimes. For the bilayer solar cell, a tremendous increase in diffusion length is obtained. A maximum diffusion length of $l_{\text{diff}} = 19.0 \pm 0.7$ nm is reached at $c = 0.2$ vol%. Beyond $c = 0.2$ vol%, the diffusion length decreases quickly down to 12.3 nm at $c = 3$ vol%. For the other configurations, the change in diffusion length is rather small. For the BHJ, $l_{\text{diff}} \approx 5$ nm over the full considered range of c. The high phase intermixing leads to a constant mean diffusion length before dissociation and thus shows no impact of the phosphorescent sensitizer. By comparing the two PM-HJ structures, we note that doping with PS increases l_{diff} for the PM-HJ$_{20}$ strongly. The higher cluster sizes require charges to overcome a larger distance before dissociating. Thus, one can exploit the PS to allow excitons, generated far away from the interface, to reach the P3HT:PCBM interface and dissociate. We observe a doubling of l_{diff} to values exceeding 10 nm. The distance of 10 nm corresponds to half the homogeneous layer thickness; thus, sensitization ensures higher dissociation for excitons generated in the homogeneous layers of the PM-HJ solar cells. Further details on the dissociation distribution within the PM-HJs for different PS concentrations are given in appendix C.4.

An improvement in effective exciton lifetime τ_{eff} and diffusion length l_{diff} with PS concentration strongly influences the IQE. In Fig. 7.9, the normalized IQE of the studied solar cells is shown for different PS concentrations. The bilayer structure exhibits the highest PS sensitivity, which leads to a maximum IQE increase of almost 35 % within PS concentrations $c = 0.4$ vol% and $c = 0.6$ vol%.

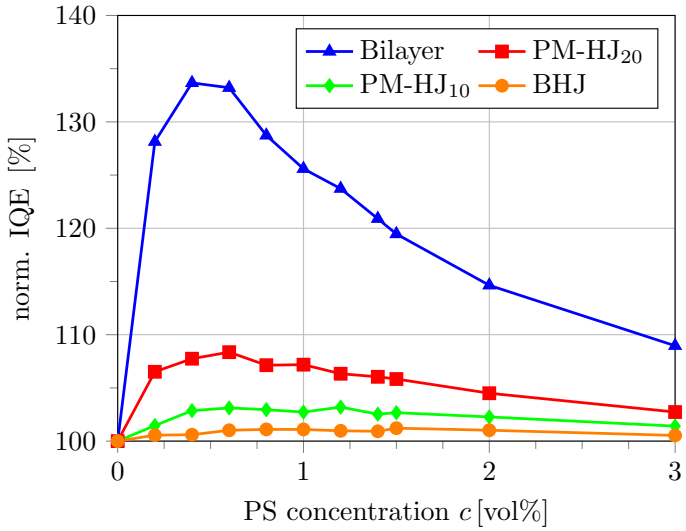

Figure 7.9 Normalized IQE for PS concentrations 0 vol% $\leq c \leq$ 3 vol%. IQE values are normalized to the IQE of the pure solar cells without any phosphorescent sensitizers. Reprinted with permission from [362], ©2018 WILEYVCH Verlag GmbH & Co. KGaA, Weinheim.

For the PM-HJ$_{20}$ at $c = 0.6$ vol%, the IQE improves by 8.4 %. For higher phase intermixing, only a small influence of the PS is observed: the PM-HJ$_{10}$ has an IQE improvement of 3 %, the BHJ solar cell IQE can be improved by 1 %. Above $c = 1$ vol%, the IQE of all configurations decreases strongly due to the increased spin-orbit coupling, which causes a faster triplet exciton decay.

To gain a better understanding of the impact of the PS on above features, we study the contributions of both singlets and triplets on the dissociated and decayed excitons. In Fig. 7.10, the share of the aforementioned transitions of singlets and triplets is visualized for all examined solar cell morphologies and $c = 0 \ldots 1$ vol%. The red and orange bars visualize the percentage of dissociated singlets and triplets, respectively, and the green and blue bars give the percentage of decayed singlets and triplets, respectively.

With rising PS concentration, the percentage of singlets participating in dissociation events drops, while triplet dissociation increases in all the investigated structures. The total dissociation yield, given by the sum of $\eta_{\text{diss,s}}$ and $\eta_{\text{diss,t}}$, increases concerning the bilayer and both PM-HJ structures. For the BHJ structure, there is only a slight improvement, and the fraction of triplet dissociation accounts for the decrease in the singlet exciton dissociation caused by the intersystem crossing. Thus, the reduced amount of singlet dissociation does not mean a loss of excitons; they are only shifted from singlet to triplet contributions. The dissociation efficiency is highest in the case of the BHJ solar cell. For zero PS concentration, almost 90 % of excitons dissociate. Inducing the sensitizers, the dissociation efficiency can be slightly increased to 90.4 % at $c = 1$ vol%. With only $\eta_{\text{diss}} = 14.7$ % at zero PS concentration, the bilayer configuration shows the least exciton dissociation. Here, the PS improves the exciton yield to $\eta_{\text{diss}} = 20$ %. The improvement in exciton dissociation due to phosphorescent sensitization is predominantly obtained by previously decayed singlet excitons, which now are converted into long-living triplet excitons. Due to the fine intermixing, the pure PM-HJ$_{10}$ structure shows a higher exciton dissociation efficiency than the PM-HJ$_{20}$ structure. Thus, the influence of phosphorescent sensitization is higher for the PM-HJ$_{20}$ structure. The dissociation efficiency for PM-HJ$_{20}$ can be improved from 60.3 % to 65.3 % for $c = 0.6$ vol%. In the PM-HJ$_{10}$ morphology, an increase from 81.6 % to 84.3 % for the optimum PS concentration $c = 0.6$ % is observed.

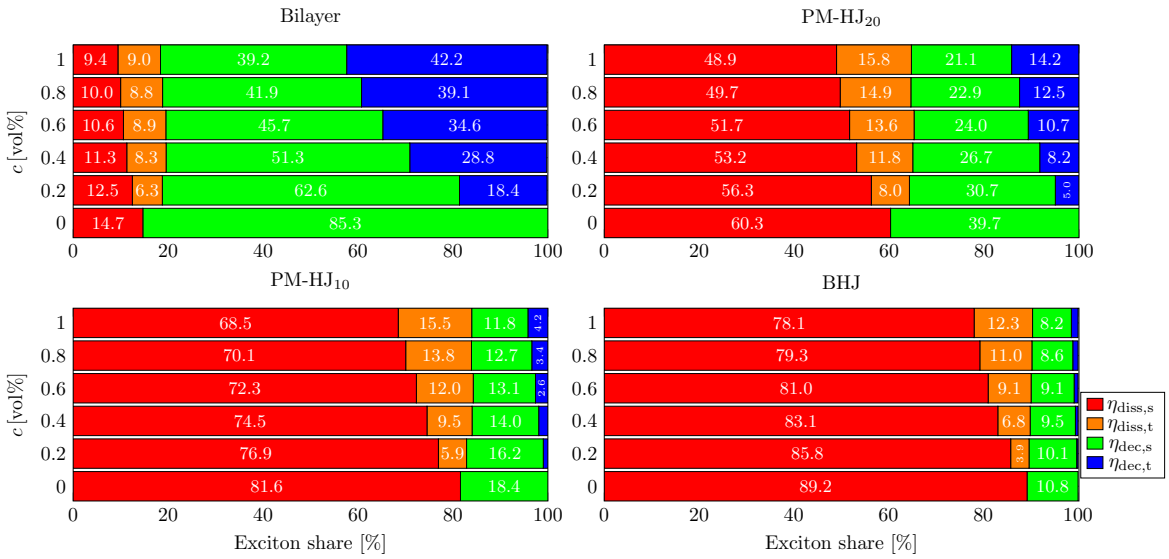

Figure 7.10 Exciton statistic of the decay (dec) and dissociation (diss) percentage of both singlets and triplets at varying phosphorescent sensitizer concentration c for the bilayer and the studied heterojunctions. Reprinted with permission from [362], ©2018 WILEYVCH Verlag GmbH & Co. KGaA, Weinheim.

Triplet-triplet annihilation is rather small and can be neglected in this statistic, as the triplet density is low and triplets do rarely encounter each other. In the bilayer cell, the fraction of triplet excitons undergoing a triplet-triplet annihilation is smaller than 1 % for a PS concentration of $c = 0.2$ % and decreases further for higher PS concentrations. For the other configurations, TTA is even smaller and cannot account for the efficiency decrease of OPVs. In comparison, triplet-triplet annihilation in OLEDs is more likely due to the high exciton densities.

So far, we have studied all properties of the excitons and the solar cells upon doping with phosphorescent sensitizers at short-circuit condition. Now, we investigate the impact of the PS on the jV-characteristics of the organic solar cells. As the highly intermixed PM-HJ$_{10}$ and BHJ show only a slight improvement in their dissociation characteristics, we only consider the bilayer and PM-HJ$_{20}$ cells. We simulate the jV-characteristics at both zero and the optimal PS concentration $c = 0.6$ vol%.

The jV-characteristics of these configurations are illustrated in Fig. 7.11. We can see two clear trends: (1) the short-circuit current density j_{sc} increases with rising interface area; (2) the open-circuit voltage V_{oc} decreases with rising complexity and interface area. The reason for the small V_{oc} in the BHJ is the absence of spatial charge separation. Electrons/holes can be collected at the opposite electrode (anode/cathode) easily due to percolation pathways through the intertwined phase (acceptor/donor) if an appropriate electric field E is applied or if the generated charge carriers are attracted by the image charge induced at the contact. In the PM-HJ morphologies, this pathway is suppressed by the pristine donor and acceptor layers between the mixed heterojunction and the electrodes. This leads to a spatial separation of charge carriers and keeps a high V_{oc}. A detailed description of the open-circuit voltage characteristics is given by Uhrich *et al* [401].

Inducing the phosphorescent sensitizers in the PM-HJ$_{20}$ solar cell, the short-circuit current density j_{sc} is raised from 6.0 mA cm^{-2} to 6.4 mA cm^{-2}. The open-circuit voltage remains at 0.84 V, while the fill factor increases from 68.7 % to 69.6 %. This results in a power increase of 8.1 % by doping the solar cell with $c = 0.6$ % of Ir(ppy)$_3$. Also, the PM-HJ$_{20}$ provides a simpler morphology with a strongly reduced interface compared to the BHJ without downgrading the PCE. In fact, the PCE of PM-HJ$_{20}$ with PS concentration $c = 0.6$ % is higher than that of the BHJ (3.56 %). Going to the even

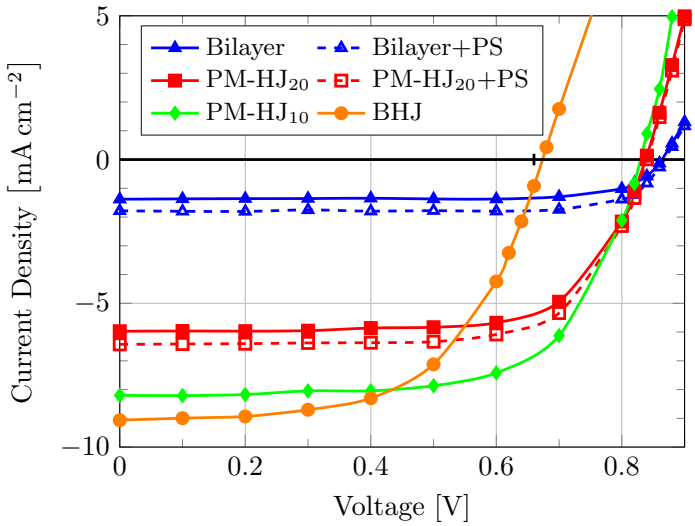

Figure 7.11 Impact of the phosphorescent sensitizers on the jV-characteristics of different morphologies. For bilayer and PM-HJ$_{20}$ configuration, zero and optimal PS concentration $c = 0.6$ vol% are illustrated. For the pure PM-HJ$_{10}$ and BHJ solar cells, the jV-curves are given. Reprinted with permission from [362], ©2018 WILEYVCH Verlag GmbH & Co. KGaA, Weinheim.

simpler bilayer structure, the power conversion increases by a factor of 34 %. This is caused by an increase of the j_{sc} from 1.4 mA cm^{-2} to 1.8 mA cm^{-2} by doping with $c = 0.6$ % of the PS. The fill factor increases from 75.6 % to 78.8 %. The PCE still is by a factor of 3 lower compared to the BHJ; however, the interface area and recombination are reduced to the minimal amount possible.

7.4.4 Influence of the Phosphorescent Sensitizer on the IQE

In the previous section, we have demonstrated that the PCE of the organic solar cells with doping by PS molecules can be enhanced by up to 34 % for the bilayer solar cell. Nevertheless, the short-circuit current density is still far below that of the BHJ solar cell. This is mainly caused by the decrease of the triplet lifetime in the ISC radius of the sensitizers based on the enhanced spin-orbit coupling. In this section, we vary this decay rate and the intersystem crossing properties of the PS molecules to study possible enhancement of the OPV performance. This may lead to a study of new sensitizer molecules for the use in OPVs. We focus on the bilayer and PM-HJ$_{20}$ morphologies and keep the PS concentration of $c = 0.6$ vol%, which shows the highest improvement in the presented studies.

First, we investigate the PS energetics to obtain high ISC-yields. To ensure a high phosphorescent sensitization, (i) the ISC yield of the PS should be high and (ii) the singlet and triplet energies of the PS need to match the host material energies. Furthermore, the HOMO level of the PS needs to be adapted to the host HOMO level to avoid hole trapping. The used PS Ir(ppy)$_3$ offers an unfavorable energy alignment to the host material P3HT. We require molecular energies of the PS molecule of $E_{\mathrm{HOMO}} = -5.2$ eV and $E_{\mathrm{LUMO}} = -3$ eV. The triplet and singlet energies are set to $E_{\mathrm{T}} = 1.6$ eV and $E_{\mathrm{S}} = 1.8$ eV to ensure a sufficient singlet transfer from P3HT to the PS with a subsequent ISC and back-transfer of the triplet to the donor. By aligning the PS energy levels, a slight improvement of ISC is obtained. A change in the ISC-ratio of $\Delta\eta_{\mathrm{ISC}} \approx 1.3$ % and $\Delta\eta_{\mathrm{ISC}} \approx 0.8$ % for the bilayer and the PM-HJ$_{20}$ solar cell, respectively, are obtained. The ISC rate within Ir(ppy)$_3$ is strong enough to ensure a high ISC yield without direct ISC on the PS sites; thus no modification in the exciton dissociation is noticed.

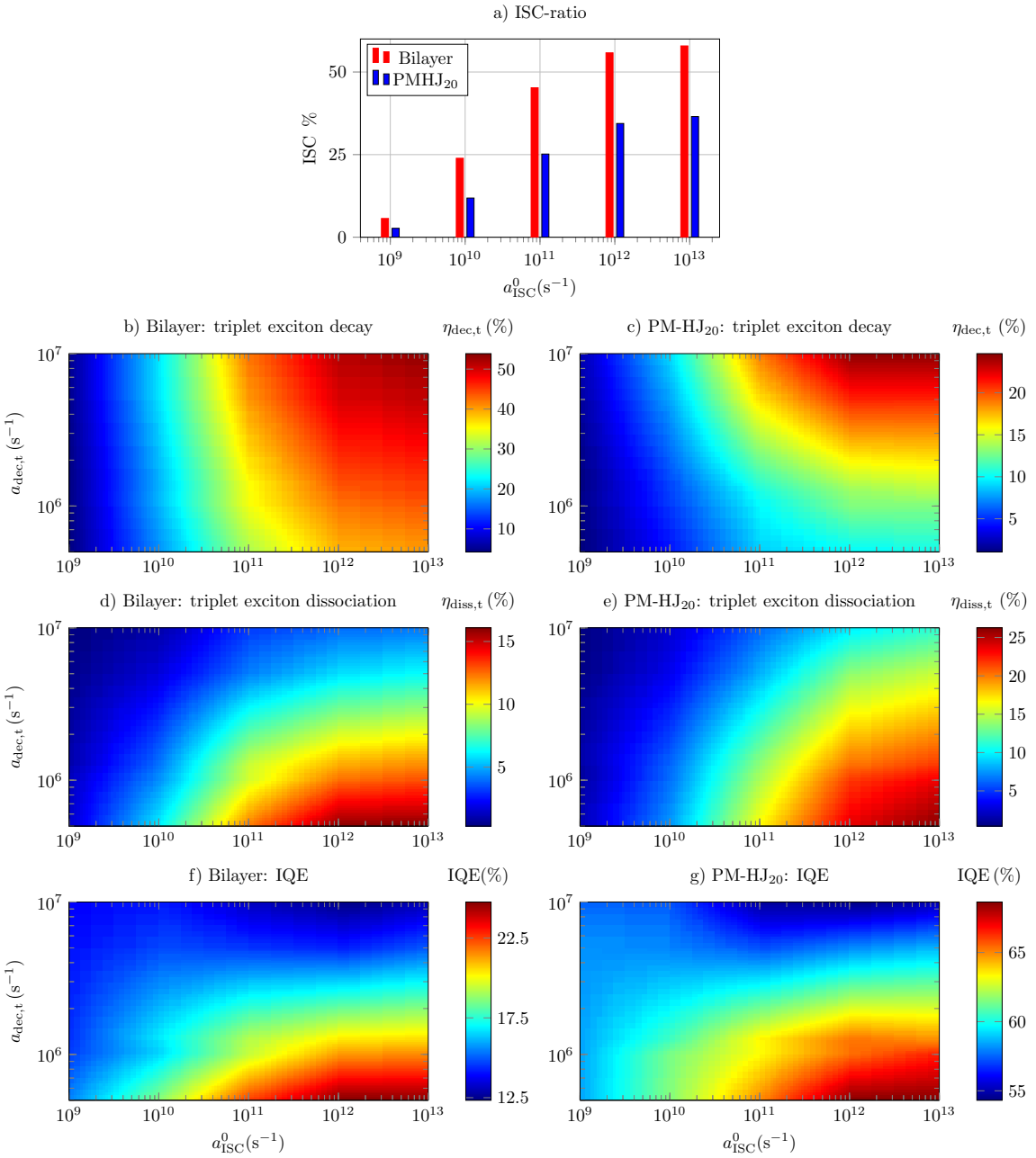

Figure 7.12 (a) Ratio of intersystem crossing from singlets to triplets for the bilayer and PM-HJ$_{20}$ for different ISC frequencies a^0_{ISC}. (b,c) Triplet decay and (d,e) dissociation as well as (f,g) the internal quantum efficiency in dependence on the triplet decay rate $a_{\mathrm{dec,t}}$ and the ISC frequency a^0_{ISC}. Results are illustrated for both the bilayer and PM-HJ$_{20}$ solar cell. Reprinted with permission from [362], ©2018 WILEYVCH Verlag GmbH & Co. KGaA, Weinheim.

Now, we focus on the interplay of the decay rate $a_{\mathrm{dec,t}}$ within the ISC radius of the PS molecules and the ISC frequency a^0_{ISC}. There is a complex interplay between this two parameters. One expects a high correlation of the ISC with the triplet exciton decay, both linked by the spin-orbit coupling of the PS molecule. We modify the ISC frequencies in the range of $1 \times 10^9\,\mathrm{s}^{-1} \leq a^0_{\mathrm{ISC}} \leq 1 \times 10^{13}\,\mathrm{s}^{-1}$ and

investigate decay rates of $5 \times 10^6\,\mathrm{s}^{-1} \leq a_{\mathrm{dec,t}} \leq 1 \times 10^7\,\mathrm{s}^{-1}$. The ISC-ratio dependency on the ISC frequency is illustrated in Fig. 7.12a. The ISC-ratio is not affected by changes in the triplet exciton decay rate. A rising ISC frequency shows a strong enhancement of the ISC ratio, i.e., singlets are converted more frequently into triplet excitons. This trend is similar to the increase in the ISC-ratio with increasing PS volume concentrations presented previously. For $a^0_{\mathrm{ISC}} = 1 \times 10^9\,\mathrm{s}^{-1}$, the ISC-ratio is minimal in both configurations. For higher ISC frequencies of $a^0_{\mathrm{ISC}} \geq 1 \times 10^{12}\,\mathrm{s}^{-1}$, the ISC-ratio exceeds 50 % for the bilayer and 30 % for the PM-HJ$_{20}$ morphology.

In Figs. 7.12b-e, the dependence of the triplet exciton decay ratio $\eta_{\mathrm{dec,t}}$ and the dissociation efficiency $\eta_{\mathrm{diss,t}}$ on the varied parameters are visualized for the bilayer and the PM-HJ$_{20}$ solar cells. Furthermore, the IQEs of both configurations are illustrated in Figs. 7.12f-g. We can divide each map into four areas. The starting point is given by the PS molecule Ir(ppy)$_3$ ($a_{\mathrm{dec,t}} = 1.25 \times 10^6\,\mathrm{s}^{-1}$ and $a^0_{\mathrm{ISC}} = 1 \times 10^{11}\,\mathrm{s}^{-1}$). Decreasing the a^0_{ISC} at constant $a_{\mathrm{dec,t}}$ lowers the ISC strongly due to the reduced spin-orbit coupling and likewise leads to a strong decrease of the IQE, i.e., the PS molecules lose their impact on the singlet excitons, they only represent traps for the charge carriers. The upper right corner represents PS molecules with high ISC frequency and high decay rates. This is reasonable as both the decay rate and the ISC frequency are expected to increase with rising spin-orbit coupling. In the uppermost right corner ($a_{\mathrm{dec,t}} = 1 \times 10^7\,\mathrm{s}^{-1}$ and $a^0_{\mathrm{ISC}} = 1 \times 10^{13}\,\mathrm{s}^{-1}$) we obtain IQEs of 13 % and 55 % for the bilayer and PM-HJ$_{20}$ cell, respectively. We obtain a decrease in IQE to values comparable to the neat OSCs. Best photovoltaic performance can be achieved with a PS which parameters tend towards the lower right corner. For $a^0_{\mathrm{ISC}} = 10^{13}\,\mathrm{s}^{-1}$ and $a_{\mathrm{dec,t}} = 5 \times 10^5\,\mathrm{s}^{-1}$, we obtain the maximum values of $\mathrm{IQE}_{\mathrm{bilayer}} = 24.7\,\%$ and $\mathrm{IQE}_{\mathrm{PM-HJ20}} = 68.7\,\%$. Here, a high ISC and subsequent triplet exciton dissociation are ensured as the loss of triplets due to decay mechanisms is lowered. Triplet dissociation efficiencies of $\eta_{\mathrm{diss,t}} \approx 16\,\%$ for the bilayer and $\eta_{\mathrm{diss,t}} \approx 26\,\%$ for the PM-HJ$_{20}$ are observed. This leads to a rather small decay ratio of $\eta_{\mathrm{dec,t}} \approx 40\,\%$ and $\eta_{\mathrm{dec,t}} \approx 11\,\%$ for the bilayer and the PM-HJ$_{20}$, respectively. In the bilayer configuration more triplets than singlets are dissociated, i.e., triplets lead to the high IQE. A good compromise in the PS parameters is given by a horizontal shift towards higher a^0_{ISC} at a constant decay rate. The IQE can be increased above 20 % for the bilayer and 65 % for the PM-HJ$_{20}$ solar cells. The triplet decay ratio increases slightly, whereas the triplet dissociation increases by a higher amount.

Finally, we investigated the impact of a change in the Dexter prefactor on triplet exciton transfer and OPV performance. Our reference are the previously shown results with Dexter prefactor $a^0_{\mathrm{D}} = 1.6 \times 10^9\,\mathrm{s}^{-1}$. The Dexter prefactor is varied to $a^0_{\mathrm{D}} = 5 \times 10^9\,\mathrm{s}^{-1}$ and $a^0_{\mathrm{D}} = 1 \times 10^{10}\,\mathrm{s}^{-1}$. The results are summarized in Table 7.3. We obtain an improvement of almost 30% for triplet exciton dissociation

Table 7.3 Diffusion length l_{diff}, exciton dissociation efficiency η_{diss}, internal quantum efficiency IQE, and short-circuit current density j_{sc} of the two configurations bilayer and PM-HJ$_{20}$ at different Dexter prefactors a^0_{D}.

a^0_{D} (s^{-1})	l_{diff} (nm)	η_{diss} (%)	IQE (%)	j_{sc} ($\mathrm{mA\,cm}^{-2}$)
Bilayer				
1.6×10^9	17.6	19.5	19.2	-1.82
5×10^9	26.4	26.7	26.4	-2.49
1×10^{10}	33.4	32.0	31.6	-2.98
PM-HJ$_{20}$				
1.6×10^9	9.7	64.9	62.8	-6.40
5×10^9	12.4	70.1	67.8	-6.95
1×10^{10}	13.7	72.2	69.9	-7.18

and a maximum internal quantum efficiency of IQE = 33.4 % for the bilayer and IQE = 72.2 % for the PM-HJ$_{20}$ at $a_{\mathrm{D}}^{0} = 1 \times 10^{10}\,\mathrm{s}^{-1}$. A small increase in the Dexter prefactor to $5 \times 10^{9}\,\mathrm{s}^{-1}$ improves the IQE by 7 % for the bilayer and 5 % in the case of the PM-HJ$_{20}$. The Dexter prefactor depends predominantly on the donor utilized in the donor:acceptor blend. Higher Dexter diffusion rates within the donor material have a higher effect on the dissociation efficiency compared to the studied decay rates $a_{\mathrm{dec,t}}$. Due to small recombination and high charge collection, the IQE correlates strongly with the dissociation efficiency and shows similar trends.

7.5 Conclusion

We have investigated the influence of different morphologies doped by phosphorescent sensitizers on the performance of P3HT:PCBM organic solar cells numerically. Based on our kinetic Monte Carlo simulation tool we have accounted for all excitonic processes and the interplay with the phosphorescent sensitizers. PS molecules were used to populate triplet excited states via intersystem crossing of optically or electrically generated singlet excitons. We studied the morphologies with different interface areas including the bulk-heterojunction, planar-mixed molecular heterojunction with a cluster size of 10 nm and 20 nm, and the bilayer solar cell. BHJ solar cells exhibit the highest exciton dissociation efficiency due to a high phase-intermixing and small cluster-sizes. However, they also reveal the highest recombination of charge transfer states due to the large interface area. Downgrading the interface area and morphology decreases the exciton dissociation yield, on the other hand, recombination and charge collection times are reduced. With the use of phosphorescent sensitizers, we obtain an increase in exciton lifetime and a higher exciton dissociation efficiency. The highest improvement in exciton diffusion lengths is observed for the bilayer configuration with the highest cluster sizes. In the BHJ and PM-HJ$_{10}$, small distances to donor:acceptor interface ensure high dissociation yield regardless of PS concentration. PS molecules only slightly improve the performance for these highly intermixed systems. By investigating the jV-characteristics of the different morphologies two significant trends are observable: (i) reducing the interface area, the short-circuit current j_{sc} decreases; (ii) the open circuit voltage V_{oc} increases with decreasing morphology complexity.

We obtained an improvement of the PCE of the PM-HJ$_{20}$ at the optimal PS concentration of $c = 0.6$ vol% to 4.45 % exceeding the PCE of the BHJ. Unless expected, the triplet-triplet annihilation is not a major concern within the OSC due to a low density of triplet excitons. The primary limitation is given by the low diffusion constant of triplets and the high decay rate in proximity to the sensitizers due to an increased spin-orbit coupling. We vary these parameters to achieve optimal PS parameters for the bilayer and PM-HJ$_{20}$ configuration. A good phosphorescent sensitizer demonstrates high ISC-frequencies and rather small increase in the lifetime of triplet excitons. The IQE can be increased to values above 20 % for the bilayer and 65 % for the PM-HJ$_{20}$ morphologies using a PS offering high ISC frequency and comparable small triplet exciton decay rates. The PCE of sensitized OPVs can be further increased by ensuring a high triplet diffusion constant D. Increasing the diffusivity of triplets by a factor of 10 allows an increase of the IQE to 31.6 % within the bilayer structure. A well designed PS and high diffusion lengths are favorable and might increase the applicability of OSCs with least possible recombination and interface area.

8 Non-Equilibrium Thermodynamics of Charge Separation in Organic Bilayers

This chapter presents a theoretical description of the non-equilibrium thermodynamics of the charge separation process at photo-excited organic bilayers. Based on the concept of stochastic thermodynamics, the kinetics of charge separation and recombination is connected with the thermodynamic properties, such as the free energy and the entropy of the separation process. We analyze the impact of energetic disorder and delocalization on the free energy, average energy and entropy for charge separation. For strong localization and high energetic disorder, free energies are close to equilibrium. A severe discrepancy in the role of delocalization to previous equilibrium studies is observed. In presence of long-range exciton separation, free energies are out of equilibrium. The theoretical results emphasize that a combination of large Gibb's entropy and low energy barriers is required for an efficient separation. Time dependent analyses of the thermodynamic properties show a significant insight into the kinetics of CT states. Energies relax with time within the given density of electronic states. This relaxation can be also seen within the entropy, which reaches maximal values after $\approx$ 10 ps, before a decrease in entropy is observed.

Section **8.1** summarizes previous studies on the free energy barrier of charge separation. Section **8.2** presents the model Hamiltonian as well as the numerical solution procedure of the master equation. In addition, the non-equilibrium and equilibrium thermodynamics is outlined. Finally, section **8.3** presents an analysis on the role of the energetic disorder and delocalization on the free energy barrier. The model Hamiltonian as well as the CT states and transition rates were provided by *Veljko Janković* and *Nenad Vukmirović*, University of Belgrade.

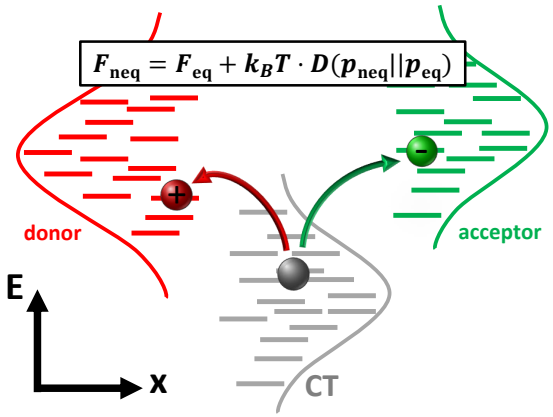

8.1 Background

Despite years of research on the fundamental properties of organic solar cells, one of their essential aspects is still not fully understood: what causes the efficient dissociation of charge transfer (CT) states into free charge carriers despite the presence of the strong Coulomb attraction? Various mechanisms have been proposed to promote CT separation. Delocalized charge carriers can efficiently escape their strong binding energy and enhance the separation of CT states due to a reduced Coulomb interaction [56, 144, 402–404]. "Hot" CT states are considered to provide a sufficient initial excess energy to overcome the binding energy [43,58,145,405]. Previous publications have suggested that the interplay of entropy with both the dimensionality of the organic semiconductor and the disorder in molecular orbital energies can lead to a strong decrease of the separation barrier [55–57,377,406]. Gregg studied the relation between the dimensionality and entropy based on the degeneracy of states W as a function of the separation distance r using the equilibrium relation $\Delta S(r) = k_B \ln W(r)$ [57]. In materials of higher dimensionality, the free energy barrier is significantly reduced due to the strong increase in available states. Hood and Kassal emphasized that the above mentioned investigation by Gregg can capture the case of semiconductors without energetic disorder, but it underestimates the energetic contribution to the free energy in case of energetically disordered organic semiconductors [55]. To account for the density of states, they calculated the free energy based on the canonical partition function assuming equilibrated CT states. The partition function is purely based on the difference between the initial and final energies of the CT states and the degeneracy of final configurations after separation. This equilibrium method predicts a reduction in free energy barrier with increased disorder σ and proposes spontaneous charge separation for $\sigma \geq 100\,\mathrm{meV}$. However, it is known that disorder can hamper charge transport and trap charge carriers. Additionally, an increased disorder impacts recombination of CT states [13]. Some authors claim that charge separation is a strongly non-equilibrium process and thus requires a non-equilibrium description [407, 408]. Giazitzidis *et al.* developed a simplified non-equilibrium description by correcting the equilibrium free energy with the probability distribution of finding a CT state at a certain distance obtained from Monte Carlo simulations [408]. Shi and coworkers emphasized that the disorder-enhanced dissociation is a non-equilibrium effect [407]. They showed a deviation between the average energy barrier obtained from the equilibrium description and the non-equilibrium energy barrier by averaging over Monte Carlo trajectories, but neglected the weighting of the energies by their population probability.

Existing studies fail to capture the non-equilibrium nature of charge separation and do not allow insight in whether and to which extent equilibrium methods provide a valid description. In this work, we between the CT separation dynamics with its fundamental non-equilibrium thermodynamic properties based on the concept of stochastic thermodynamics. Free energy differences and entropic contributions are obtained based on the stochastic formulation of the free energy [409, 410]. The stochastic free energy is derived based on the Kullback-Leibler divergence between the non-equilibrium and the equilibrium probability distribution in energy and position of CT states. The critical non-equilibrium probability is calculated by integration of the Master equation using the kinetic rates of CT states, which fulfill the detailed balance. The presented method is finally used to study the impact of energetic disorder and delocalization on the free energy.

8.2 Method

Our analysis is based on a one-dimensional model Hamiltonian of an organic bilayer. This model captures the separation dynamics of geminate CT states under the impact of energetic disorder, charge delocalization, and the interaction between charge carriers and phonons [56]. We summarize the

model Hamiltonian in appendix, D.1. CT states evolve within a phase space of available states with large energetic disorder and a variable mean distance between the wave function of the electron and the hole. In addition, transition rates k_{ji} of the phonon-assisted transport of CT states between all available states i and j, as well as lifetimes τ_i of each individual CT state i, are obtained. CT states are propagated through the phase space by solving the Master equation (see appendix D.1) [182,411]. Recombination is accounted for with rate $k_i^{\text{rec}} = \tau_i^{-1}$. CT states are considered collected once the electron and hole are fully separated in space such that their wavefunctions are sufficiently localized in a defined contact region l_c at the end of the acceptor and the donor, respectively. For further details we refer to the previous publication by Janković and Vukmirović [56].

Hood and Kassal computed the free energy for the charge separation process under the assumption of an equilibrium distribution of the CT energies using the canonical ensemble [55]:

$$F_{\text{eq}}(r) = -k_{\text{B}}T \ln Z(r)\,, \tag{8.1}$$

with Boltzmann constant k_{B}, temperature T, and partition function $Z(r)$ given by

$$Z(r) = \sum_{\{m|r_m \in [r-b/2, r+b/2)\}} \exp\left(-\beta E_m\right), \tag{8.2}$$

where $\beta^{-1} = k_{\text{B}}T$, and m denotes all CT states with distance $r_m \in [r - b/2, r + b/2)$, where r_m gives the mean distance of CT state m.

In recent years, the theory of stochastic thermodynamics has been developed and successfully applied to small-scale systems, especially to study the effect of fluctuations [409,410,412,413]. This novel theory provides a powerful description of the thermodynamics of stochastic processes governed by Markovian dynamics and can be applied to all out of equilibrium systems and processes. To study if, and to which extent, the separation of CT states occurs out of equilibrium, we formulate the stochastic free energy F_{neq} based on the Kullback-Leibler divergence $D(p||q) = \sum_m p_m \ln(p_m/q_m)$ as [409,414]:

$$\beta\left(F_{\text{neq}} - F_{\text{eq}}\right) = D\left(p_{\text{neq}}||p_{\text{eq}}\right) = \sum_m p_m^{\text{neq}} \ln\left(\frac{p_m^{\text{neq}}}{p_m^{\text{eq}}}\right) \tag{8.3}$$

where p_m^{eq} and p_m^{neq} give the equilibrium and the non-equilibrium probability for the system to be in state m, respectively. The equilibrium probability distribution is obtained based on the partition function $Z(r)$ (eq. 8.2) as $p_m^{\text{eq}} = \exp(-\beta E_m)/Z$. The (non-equilibrium) probability distribution p_{neq} can be obtained by solving the Master equation or from trajectory ensembles calculated by kinetic Monte Carlo [409]. To obtain an accurate probability distribution, we calculate the probability of being in state m by numerical integration of the Master equation [406]. The procedure is summarized in the SM.

To provide a comparable analysis to Hood and Kassal [55], we compute the non-equilibrium free energy $F_{\text{neq}}(r)$ as a function of the distance r using the Kullback-Leibler divergence of all CT states m with mean distance $r - b/2 \leq r_m < r + b/2$:

$$\beta\left(F_{\text{neq}}(r) - F_{\text{eq}}(r)\right) = \sum_m p_m^{\text{neq}} \ln\left(\frac{p_m^{\text{neq}}}{p_m^{\text{eq}}}\right)\,. \tag{8.4}$$

Here, we take $b = 5\,\text{nm}$. Rearranging Eq. 8.4 leads to the well-known expression of the free energy:

$$F_{\text{neq}}(r) = \sum_m p_m^{\text{neq}} E_m + \beta^{-1} p_m^{\text{neq}} \ln p_m^{\text{neq}} = E_{\text{neq}}(r) - TS_{\text{neq}}(r)\,. \tag{8.5}$$

Using the non-equilibrium probability distribution p_{neq} from the solution of the Master equation, we can calculate the average energy E_{neq}, which CT states pass during the separation process, as well as the entropy contribution TS_{neq} to the free energy. S_{neq} has the form of the Gibb's entropy and accounts for the accessible states during CT separation.

One major advantage of the presented model is that it allows to study the time dependence of the thermodynamic measures. To obtain the free energy of CT separation after time τ, we simply compute the probabilities $p_m(\tau)$ from initial state at t_0 until we reach $t_0 + \Delta\tau$:

$$p_m(\tau) = \frac{1}{\tau} \int_{t_0}^{t_0+\tau} p_m(t) \mathrm{d}t \,. \tag{8.6}$$

Inserting $p_m(\tau)$ in eq. 8.5 gives the free energy for CT states to separate within time-window τ.

8.3 Results and Discussion

We analyze the free energy of the charge separation process in an organic bilayer with varying energetic disorder σ and electronic transfer integrals J. We initialize the system by population of all acceptor exciton states with probabilities $p_m = \exp(-\beta E_m)/Z$, where Z gives the partition function of all acceptor exciton states m. An acceptor exciton is classified as a CT state in which both the electron and the hole are located in the acceptor region. This allows us to capture the possibility of long-range exciton separation, which has been discussed as the origin of efficient free charge generation [58,415]. All values of the model parameters are listed in Table D.1 in the appendix. The separation yields for all configurations are summarized in Table D.2.

First, we present the capabilities of the developed method by calculating the distance dependence of the free energy and its energetic and entropic contribution for a specific network of CT states shown in Fig. 8.1a. This specific configuration shows a separation yield of 44 %. Figure 8.1b shows the free energy $F(r)$ and its energetic and entropic contribution $E(r)$ and $TS(r)$, respectively, for the given configuration computed by the equilibrium method (solid line) as well as using the non-equilibrium method (dotted line). $F(r)$ shows a maximum barrier of 424 meV at 4.5 nm. The major contribution to the free energy is given by $E(r)$, which shows a similar trend as $F(r)$. The large barrier in both $F(r)$ and $E(r)$ is due to a lack of states with low energy for $r_0 \leq r \leq 9$ nm as visible in Fig. 8.1a. As the barrier is thin, long range transfer of the CT states ensures a sufficient separation. The entropy significantly reduces the free energy by up to 50 meV. In realistic 3D systems, the role of the entropy can reach values comparable to the average energies, or even dominate the energetic contribution [57]. Our non-equilibrium method shows significant deviations from the equilibrium predictions. Free energy and average energy show higher values at small distances. Due to long-range exciton dissociation, the CT states at small distances are not equilibrated which leads to a significant difference with respect to the equilibrium free energy. Beyond the energy barrier, we also see larger values in all the components. The CT state propagates along states of higher energy. As visible in Fig. 8.1a, more states are available at higher energy, which finally leads to the high entropic values above 100 meV for large CT distances.

8.3.1 Role of Energetic Disorder

A critical connection between the energetic disorder σ and free energy has been predicted based on equilibrium methodologies [55]. Here, we study the role of the energetic disorder on the free energy $F(r)$ for $\sigma \in \{50\,\mathrm{meV}, 100\,\mathrm{meV}, 150\,\mathrm{meV}\}$. Integration of the Master equation is stopped when all CT states are either recombined or extracted at the contacts. All remaining parameters are kept

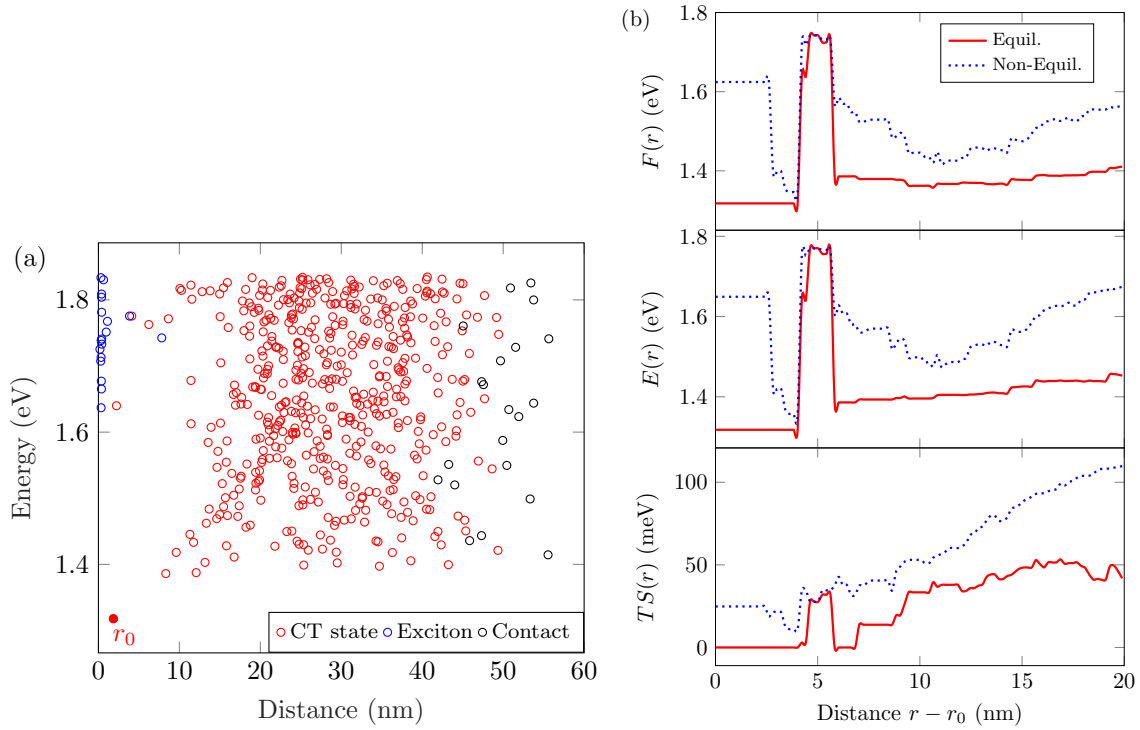

Figure 8.1 (a) Exemplary distribution of charge transfer (CT), exciton, and contact states in the distance-energy phase space. The filled scatter dot labels the CT state with smallest distance r_0. (b) Distance dependence of the free energy $F(r)$ and its contributions predicted by the non-equilibrium theory: average energy $E(r)$ and entropic contribution $TS(r)$. The solid line presents the equilibrium prediction. Dotted lines give the non-equilibrium predictions of the thermodynamic measures.

constant. For each parameter set, we take an ensemble average over 256 configurations. Figure 8.2a shows the free energy computed based on the equilibrium (solid lines) and the non-equilibrium (dashed lines) method. The equilibrium theory predicts a significant decrease in the free energy with increasing σ matching results of previous publications [55]. The origin of the decrease is mainly due to the energy, $E(r)$, which shows values comparable to the free energies. The entropy decreases with higher disorder, and remains below 50 meV for all σ. For $\sigma = 50$ meV, the Gibb's entropy shows twice and four times the value observed for $\sigma = 100$ meV and $\sigma = 150$ meV, respectively. For $\sigma \geq 100$ meV, the non-equilibrium free energy (dashed line) is close to the equilibrium free energy (solid line). Also, energy and entropy show only small deviations. The entropic contribution remains roughly constant for $r \geq 5$ nm. Entropies which do not increase with distance have been observed for 1D-systems without energetic disorder [57], but also for 2D-systems with high energetic disorder [55]. At high σ, CT states thermalize towards low energies. Equilibrated CT states can only separate by propagation through low energy states. However, the number of tail states in the CT density of states does not increase significantly with larger distance (see e.g. Fig. 8.1a). The lack of available states leads to high recombination losses. Consequently, the separation yield of excitons into free charge carriers is only 6.3 % and 14.5 % for 150 meV and 100 meV, respectively. For $\sigma = 50$ meV, we see a significant difference between the equilibrium and non-equilibrium results. The non-equilibrium free energy energy shows significantly higher values compared to the equilibrium values. Interestingly, also the Gibb's entropy increases strongly and reaches 80 meV at 20 nm. The non-equilibrium picture tells us that significantly more states are available during the CT separation than expected from equilibrium

methods. This explains the high CT separation yield of 44.8 %. During the separation, CT states do not equilibrate and efficient propagation along states of higher energies is observed.

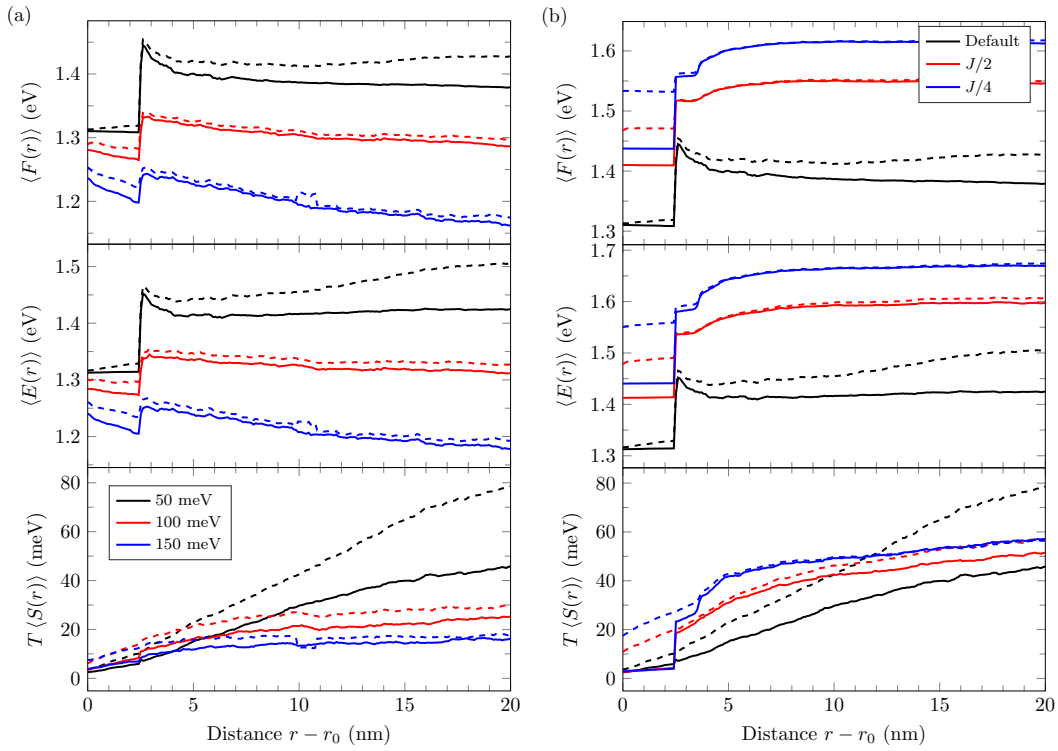

Figure 8.2 (a) Distance dependence of the free energy $F(r)$, energy $E(r)$, and entropic contribution $TS(r)$ for energetic disorder σ of 50 meV (black), 100 meV (red), and 150 meV (blue). The average $\langle\cdot\rangle$ gives the ensemble average over 256 configurations. r_0 gives the smallest distance of CT states in each configuration. (b) Impact of the charge transfer integrals J on the free energy barrier and its energetic and entropic contribution. Solid and dashed lines show results obtained from equilibrium and non-equilibrium calculations, respectively. All simulations are started with populated acceptor excitons as initial condition. The separation yields are summarized in the appendix (Table D.2).

8.3.2 Role of CT Localization

Delocalization was reported to play a significant role in the separation yield of CT states [56,377,402]. We introduce a larger localization of CT states by scaling all transfer integrals $J^{c/v}_{A/D,0/1}$ (see Fig. D.1) by a factor of $1/2$ and $1/4$. Figure 8.2b shows the distance dependence of the equilibrium (solid lines) and non-equilibrium (dashed lines) free energy and the energetic and entropic contributions. According to both methods, the free energy increases with localization. The barrier in the equilibrium free energy barrier, given by $\max_r [F(r) - F(r_0)]$, increases with stronger localization. Again, the energy follows the free energy closely. For $J/2$ and $J/4$, reduced separation yields of 30.6% and 14.7%, respectively, are observed. This matches with the observed increase in the free energy and the barrier in the average energy. For large localization, more states are available which causes an increase in the Gibb's entropy. However, due to the large energy barrier, reaching these states before recombination occurs is unlikely. In contrast to previous theoretical predictions [416], our equilibrium results emphasize that the free energy barrier decreases within larger delocalization both in the equilibrium and in the non-equilibrium picture. In ref. [416] the free energy was mainly analyzed for electron-hole distances

of less than 4 nm. In this regime, delocalization reduces states of lower energy and only few trap states remain left. This leads to the predicted increase in free energy. However, most of the efficient organic solar cells are characterized by efficient long-range exciton separation, which leads to delocalized CT states of large initial mean distance [145,402,405]. This comes closer to the model used in this work. The non-equilibrium picture presents significant differences in the free energy at small distances for higher localization ($J/2$ and $J/4$) (see Fig. 8.2b). Long-range exciton dissociation leads to a fast population of CT states at larger distances, while CT states at small distances are not equilibrated. The free energy for $r \geq 3$ nm is roughly equal for both methods. The barrier in free energy is significantly reduced with respect to equilibrium. In addition, the entropy is sufficiently high (40 - 50 meV) at large distances. This causes sufficient separation yields of 30.6 % (14.7 %) for $J/2$ ($J/4$).

8.3.3 Transient Thermodynamic Measures

So far, we only considered the ensemble averages of the free energy distributions integrated over the full timescale of the charge separation process. In contrast to the equilibrium description, the non-equilibrium thermodynamics allows insight into the time-dependence of the free energy and its energetic and entropic contributions. We obtain the time dependence of the thermodynamic measures by integration of the master equation from time $t = 0$ to a given $t = \tau$. Figure 8.3 shows the time evolution of the free energy for $\tau \in [0.1\,\text{ps}, \ldots, 1\,\mu\text{s}]$ for a disorder of $\sigma = 100$ meV. The time dependencies for all other configurations are added in Fig. D.4. The average energy $\langle E(r) \rangle$ decreases significantly with time. This resembles the relaxation of CT states within the given density of states. The equilibration process takes up to several tens of nanoseconds until the CT states are fully thermalized. The free energy seems to closely follow the trend of the average energy. Interestingly, the entropic contribution $T \langle S(r) \rangle$ increases with time between 0.1 ps and 10 ps. On such fast timescale, the CT states are still far from being thermalized. For longer timescales, i.e. when the CT states thermalize, the entropic contribution decreases again from values of 80 meV to 30 meV. This observation connects the thermodynamic measures with the relaxation of CT states in a Gaussian density of states. [85] If the CT states start far from equilibrium, the average energy is high and only a few states are accessible. Relaxation of CT states makes many more states near the maximum of the (Gaussian) DOS available. Once fully thermalized, the CT states mainly occupy tail states of the DOS. Only a few states are left which can be accessed easily without an additional driving force. Relating these results to the work of Gregg [57], we see that the effective dimensionality of accessible states changes during time due to the relaxation of CT states. This observation also allows to specify a time scale for the most efficient separation of 'hot' CT states within ≤ 1 ns. For both $\sigma = 50$ meV and $\sigma = 150$ meV, same observations are made (Fig. D.4). The time dependence of the entropy can be linked to the separation yield. In Fig. D.3, we plot the separation yield and the percentage of recombined CT states for all configurations. Within $\tau = 1$ ns, already 41.7 % (9.2 %, 1.5 %) of all CT states are separated for $\sigma = 50$ meV (100 meV,150 meV). For $\sigma = 50$ meV (100 meV), this makes 93 % (63 %) of all the separated CT states. At lowest σ (Fig. D.4a), entropy does not change after 1 ns anymore. With rising disorder, the timescales of changing entropy are much longer, which can be related to slow relaxations of CT states at higher disorder. In summary, studying the time dependence of the entropy allows to understand the most relevant time scales in which CT separation needs to occur to avoid recombination losses.

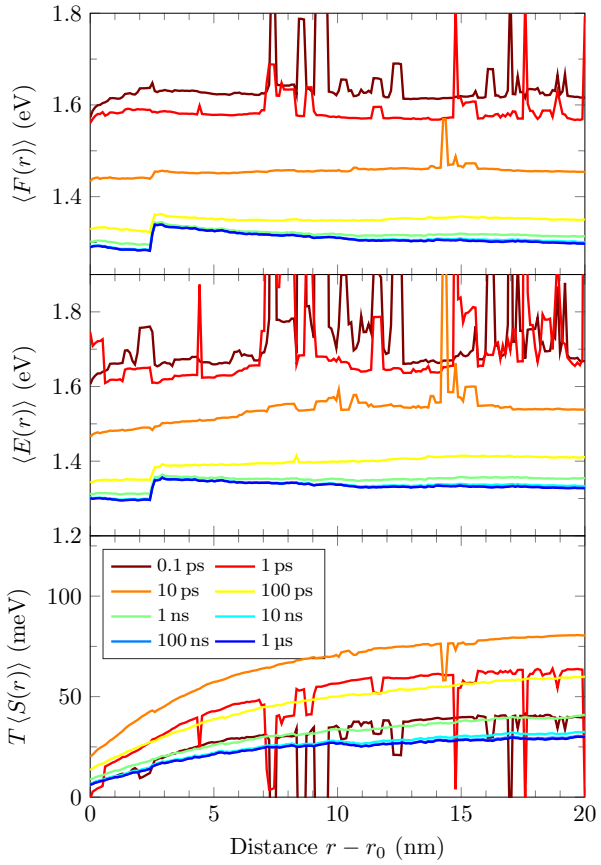

Figure 8.3 Time dependence of the free energy and its energetic and entropic contribution for $\sigma = 100\,\text{meV}$.

8.4 Conclusion

In conclusion, we have presented a theoretical description of the non-equilibrium free energy barrier for charge separation in photo-excited organic bilayers. Our methodology combines the kinetics of charge transfer (CT) state with thermodynamic properties based on the theory of stochastic thermodynamics. The presented methodology allows calculating the free energy and the Gibb's entropy for any system of Markovian dynamics. The role of the energetic disorder and delocalization has been analyzed for an organic bilayer modeled by a 1D-model Hamiltonian. Our analysis reveals discrepancies between the equilibrium and the non-equilibrium free energy predictions in the free energy and the entropy for large delocalization and low energetic disorder. Especially localized states at small distances do not thermalize due to long-range exciton dissociation, which decreases the free energy barrier with respect to the barrier equilibrated carriers are seeing. Our results emphasize that both a large Gibb's entropy and low energy barriers are required to achieve an efficient separation, while a decrease in free energy values itself does not directly correlate with an enhanced separation. The biggest novelty of the presented framework is the ability of connecting the thermodynamic measures with the CT dynamics by studying its time dependence. We showed that the entropy significantly changes during the separation timescales which makes the separation of 'hot' CT states quite efficient. After CT states thermalize, a strong reduction in entropy is observed. Insight into the time dependence of thermodynamic properties opens novel insight into physical processes and provides an interesting framework in combination with time-dependent experiments for future studies.

9 Origin of Charge Transport in Dilute Donor Organic Solar Cells

Understanding the generation of photocurrent and the transport of charge carriers within donor:acceptor morphologies is fundamental for the design of efficient OSCs. OSCs with low donor concentration, dilute donor OSCs, provide an ideal setup to study charge transport in presence of mixed and isolated phases. Electron donors are diluted with concentration below 10 wt% within a fullerene matrix. Even at donor concentrations below 0.1 wt%, a substantial photocurrent is observable. One of the main challenge is the transport mechanism of holes in absence of percolation pathways at low donor concentrations. In literature, various mechanisms have been proposed: tunneling across the fullerene matrix, back transfer to the fullerene matrix, or percolation along donor aggregates. Experimental analyses only deliver macroscopic quantities such as charge lifetimes and current densities, but they cannot reveal the transport mechanism on the nanoscale. KMC simulations provide a great alternative to study different transport mechanisms within photoactive layers with arbitrarily complex morphologies.

This chapter studies the origin of hole transport in dilute donor OSCs with low donor concentrations of 1 wt% to 5 wt%. In the following, four distinct parts are presented. Section 9.1 discusses existing studies on the charge transport mechanism in dilute donor OSCs. Section 9.2 studies the role of the polymer morphology on the photocurrent in P3HT:PC_{71}BM dilute donor OSCs at 1 wt%. In section 9.3, the contribution of the different transport mechanisms in P3HT:PC_{71}BM dilute donor OSCs is analyzed. Finally, in section 9.4, hole transport in small molecule dilute donor OSCs is studied in a joint theoretical:experimental work. Parts of this chapter have been adapted from 'Effect of Polymer Morphology in Dilute Donor Organic Solar Cells,' *J. Phys. Chem. C*, 124 (6), 3517-33528, 2020 [417] [Copyright 2020 American Chemical Society] and from 'Origin of Hole Transport in Small Molecule Dilute Donor Solar Cells', Adv. Energy Sustainability Res., 2, 2000042 [418] under the terms of the Creative Commons CC BY license.

Contributions: I have led the conceptualization and have written part of [417], and I have evaluated and visualized the back transfer mechanism (Figs. 9.2.1 and 9.2.1). Simulations in section 9.2 are contributed by *Kashif Hussain*, TUM. In section 9.3 and 9.4, I have set up the model and all simulations. I have written the theoretical part of manuscript 'Origin of Hole Transport in Small Molecule Dilute Donor Solar Cells', Adv. Energy Sustainability Res., 2, 2000042 [418]. The experimental data was provided by *Lakshmi N.S. Murthy* and *Prof. Julia W.P. Hsu* from University of Texas at Dallas. Small molecules were synthesised by *Dr. Chin-Lung Chung* and *Prof. Ken-Tsung Wong*, National Taiwan University.

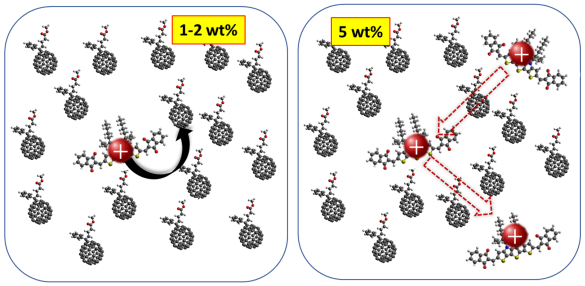

9.1 Background

Organic semiconductors have emerged as a promising material class for efficient, low cost and environmentally friendly photovoltaics. Recently, single junction organic solar cells (OSCs) reached remarkable power conversion efficiencies (PCEs) of 18 % [83, 419, 420] facilitated by the usage of novel materials, especially non-fullerene acceptors [421, 422] and increased control of film morphologies [26, 423, 424]. Understanding the generation of free charge carriers from absorbed photons is fundamental to design novel organic semiconductors and to tailor the electronic properties of interfaces in donor:acceptor blends for efficient solar cells. Despite the rapid increase in efficiencies, we are still lacking a detailed understanding of the motion of photogenerated charge carriers within the multi-faceted thin films consisting of crystalline and amorphous domains, or even strongly mixed donor:acceptor phases [425, 426].

Dilute-donor OSCs are frequently used as model systems to understand charge transport across isolated or mixed donor:acceptor phases. The active layer in dilute-donor OSCs is made of an electron donor diluted to less than 10 wt% concentration in a fullerene matrix. Despite of the low concentration of the donor material, short-circuit currents (J_{sc}) above 5 mA cm^{-2} and efficiencies above 2.5 % are observed [427–429]. Of special interest is the observation of an increased open-circuit voltage (V_{oc}) of 1.02 V at 1.2 vol% donor compared to e.g. 0.74 V at 50 vol% donor, the standard value in bulk heterojunctions, made in TAPC:C_{60} cells [428]. High V_{oc} are caused by the formation of a Schottky barrier between the fullerene matrix and a high work function anode [430]. In addition, reduced recombination [24] and ideal morphology at the extraction layers [362] can further reduce the V_{oc} losses in dilute donor OSCs.

The reduction of the donor amount raises two major challenges: (1) low exciton diffusion lengths demand a small mean distance for excitons to reach a donor-acceptor interface to dissociate into free charge carriers; (2) the lack of continuous donor networks raises the question on the physical mechanism of the charge transport. The question of the origin of hole transport has been discussed controversially in existing literature. Melianas *et al.* have analyzed the origin of hole transport in dilute-donor OSCs based on a fullerene (C_{60}) matrix containing a low content of 5 − 10 mol% α-6T donor molecules [36]. They observed hole mobilities of $\mu_h = 5 - 15 \times 10^{-5}$ cm^2 V^{-1} s^{-1}, while the electron mobility remained high ($\mu_e = 2$ cm^2 V^{-1} s^{-1}). This has been explained by a combination of Fowler-Nordheim tunneling of holes from isolated α-6T molecules to C_{60} at high electric fields and long-range tunneling ($\approx$ 4 nm) between α-6T molecules through the C_{60} matrix. However, for 1.5 mol% concentration, Fowler-Nordheim tunneling underestimates the observed hole fraction being extracted via C_{60} by quite a bit (see [36], Fig. S6a). Spoltore et al. found a correlation of hole mobilities with the relaxation energy of the donor for 18 different donor molecules, diluted at $\approx$ 6 mol% in C_{60} [60]. Their analysis showed no correlation of the CT energies with the activation energy for hole transport. Thus, hole transport was claimed to occur by long-range tunneling through several fullerene molecules based on Marcus-type hopping. Interestingly, Arrhenius-like temperature dependence of the hole mobilities were found for various donor molecules, which is typical for space charge limited currents but questions the validity of tunneling as the origin of hole transport.

The presence of donor aggregates of several tens of nanometers has been shown to produce efficient photocurrent in dilute-donor OSCs based for 10 mol% of tetraphenyldibenzoperiflanthene (DBP) as the donor and C_{70} as acceptor materials [431]. This is explained by the formation of continuous $\pi - \pi$ stacks of the planar DBP molecules which form percolation pathways for sufficient hole transport to the contacts. Donor aggregation to form percolation pathways was shown for donor concentrations larger than 5 wt% from simulated deposition using classical molecular dynamics [432] and above 10 vol% from Kelvin Probe Force Microscopy [433].

Hole back transfer from isolated donor molecules to the fullerene matrix was proposed as an alternative mechanism for the sufficient generation of photocurrent in dilute-donor P3HT:$PC_{71}BM$ solar cells [59]. Back transfer is enabled by an effective barrier lowering induced by two mechanisms: (i) the HOMO energies of isolated P3HT chains in the $PC_{71}BM$ matrix are shifted towards the HOMO level of $PC_{71}BM$, and (ii) Coulomb repulsion of trapped holes on the P3HT chains leads to an efficient back transfer. However, the morphology of the dilute P3HT chains is difficult to probe and can alter the dominant hole transport mechanism and the performance of dilute-donor OSCs [417]. In addition, the previous work assumed that exciton dissociation is independent of the driving force [59]. The driving force is given by the HOMO energy offset between the donor and acceptor molecules as well as the electrostatic interaction with charge carriers in the environment. Neglecting the driving force in the exciton dissociation rate can be partially justified in presence of large reorganization energies λ [227], which has been the case for P3HT:$PC_{71}BM$ solar cells ($\lambda \approx 0.3\,\mathrm{eV}$) [59]. For smaller λ, exciton dissociation becomes strongly dependent on the driving force. The interplay between exciton dissociation and efficient charge transport is important for the efficient operation of OSCs. Interestingly, Jiang et al. observed an increased separation of CT states into free charge carriers in dilute donor cells, while the limiting factor was due to a reduced exciton dissociation at the donor-acceptor interface [434]. Thus, a detailed understanding of both the hole transport mechanism and the role of the driving force for exciton dissociation is of importance for the optimization of dilute-donor OSCs.

9.2 Effect of Polymer Morphology in Dilute Donor OSCs

Back transfer and percolation have been proposed as the physical mechanism of hole transport in dilute donor OSCs based on polymer donors and fullerene acceptors. In a previous study [59], P3HT chains were completely dispersed in the active layer. As Albes *et al.* argued, a substantial photocurrent can arise caused by the Coulomb repulsion between holes accumulating on the donor chains, which then leads to a hole back transfer to the fullerene matrix [59]. However, it is not clear how the detailed polymer morphology affects the performance and main transport mechanism. Especially, the question on how polymer chains that provide a percolation to the anode modify the observations arises.

Here, different polymer networks are generated to study the effect of (i) the chain length and (ii) the polymer aggregation on the performance of dilute donor OSCs. For each system, three different samples of the photoactive layer were created to get a good statistics. As a study system, P3HT:$PC_{71}BM$ is used.

9.2.1 Impact of polymer chain length

First, the chain length N is varied using $N \in \{10\,\mathrm{nm}, 40\,\mathrm{nm}, 70\,\mathrm{nm}, 100\,\mathrm{nm}\}$. Figure 9.2.1 shows the short-circuit current density j_{sc} as function of the HOMO offset ΔE_{HOMO}. The error bars indicate the standard deviation for three samples. Figure 9.2 shows (a) the average hole densities and (b) the recombination efficiency for all configurations. As shown experimentally, the HOMO level within disordered P3HT is about 0.3 eV deeper than the HOMO level of ordered regioregular P3HT [435], which represents the variation in the HOMO offset which is considered here. Towards low ΔE_{HOMO}, a substantial j_{sc} of 3.1 mA cm^{-2} ($N = 10\,\mathrm{nm}$) to 3.6 mA cm^{-2} ($N = 100\,\mathrm{nm}$) is observed. Holes leave the donor by back transfer to the fullerene matrix with subsequent transfer in the ambipolar acceptor to the contact. For the shorter lengths of 10 nm to 70 nm, higher j_{sc} is produced. For $\Delta E_{HOMO} < 0.4\,\mathrm{eV}$, an exponential decrease in the hole densities is observed. This is due to an increase in the barrier between the fullerene and polymer HOMO energies, which leads to an exponential decay of the back transfer

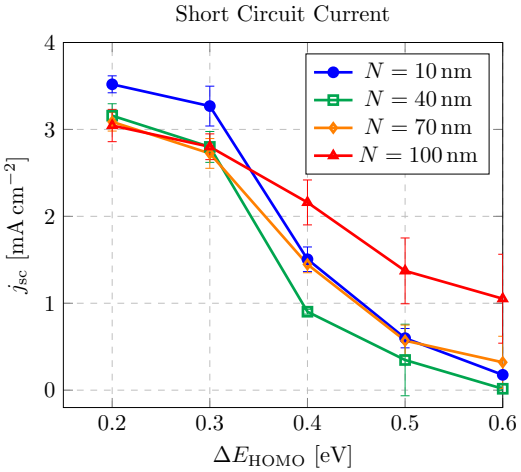

Figure 9.1 Short-circuit current density j_{sc} at various polymer lengths N for different HOMO offset ΔE_{HOMO}. Reprinted with permission from [417]. Copyright 2020 American Chemical Society.

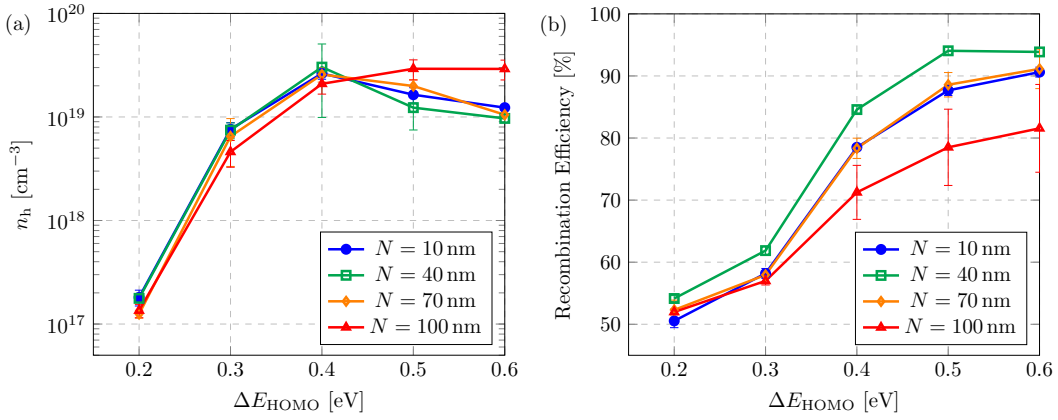

Figure 9.2 (a) Average hole density and (b) recombination efficiency at various polymer chain lengths for different HOMO level offset. Reprinted with permission from [417]. Copyright 2020 American Chemical Society.

rate. As the rate depends exponentially on the barrier, the escape becomes more and more pronounced with lowered barrier. When ΔE_{HOMO} is lowered to 0.3 eV, hole density drops to $n_h = 7 \times 10^{18}\,\mathrm{cm}^{-3}$. Lowering the HOMO offset to 0.2 eV, a small hole density $n_{\mathrm{h}} \approx 1 \times 10^{17}\,\mathrm{cm}^{-3}$ is built-up, as hole escape becomes easy at room temperature.

For $\Delta E_{\mathrm{HOMO}} \geq 0.5\,\mathrm{eV}$, holes are confined within isolated polymer chains due to the high energy barrier for back transfer. This leads to large hole densities up to $n_{\mathrm{h}} > 3 \times 10^{19}\,\mathrm{cm}^{-3}$ and recombination efficiency exceeding 90 %. Saturation is observed if nearly all the polymer sites are filled with holes, and no further exciton dissociation can occur. At steady-state, electrons surround the positive charged polymer chains due to the high Coulomb attraction leading to large recombination. For short polymer chains, the hole density is approximately $n_{\mathrm{h}} \approx 2 \times 10^{19}\,\mathrm{cm}^{-3}$. For short chains ($N \leq 70\,\mathrm{nm}$), j_{sc} decreases below 0.5 mA cm^{-2}. For longest chains, a larger j_{sc} of 1.05 mA cm^{-2} is observed.

To analyze the origin of the efficient hole escape current at low HOMO offsets, the molecular orbital energies and the Coulomb potential ϕ_C (Fig. 9.2.1a), and the electron and hole densities (Fig. 9.2.1b) are studied. The curves in (a) are extracted along the dashed line shown in the Fig. 9.2.1b. A

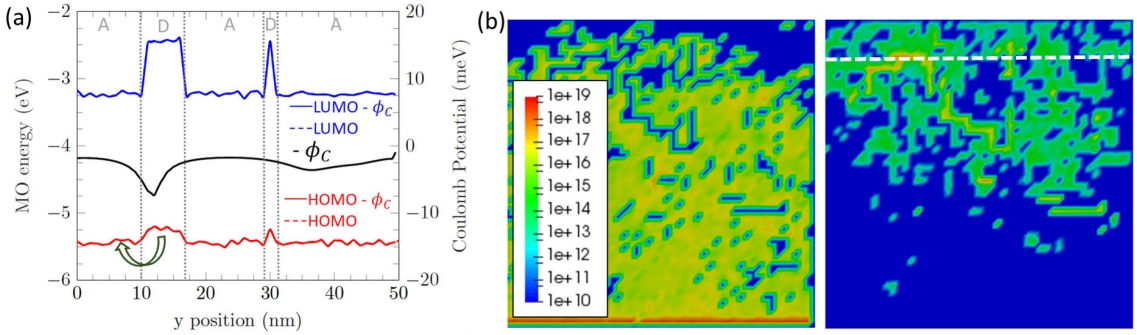

Figure 9.3 (a) Molecular orbital (MO) energies (dotted) and the Coulomb potential (black line), as well as the sum of MO energies and Coulomb potential (b) electron (left) and hole (right) densities. The colorbar shows the density in unit cm^{-3}. Reprinted with permission from [417]. Copyright 2020 American Chemical Society.

minimum Coulomb potential of less than 10 meV is observed in the donor region. Note that the molecular orbital energies (dashed lines) and the sum of MO energies and the Coulomb potential (solid lines) overlap. Despite the low Coulomb repulsion, a significant hole density all over the cell is observed (see Fig. 9.2.1b). This indicates an easy hole back transfer to the fullerene matrix. In most cases the Coulomb interaction between the geminate electron-hole pair is sufficient to induce an efficient hole back transfer.

Between $0.2\,\text{eV} \leq \Delta E_{\text{HOMO}} \leq 0.3\,\text{eV}$, j_{sc} is higher for low chain length. As the volume concentration is kept constant for each chain length, the average distance between tortuous polymer chains is increased for longer chains. Thus, less excitons dissociate in the configurations of long chain lengths. This in turn gives rise to higher exciton dissociation efficiency for chain length of $N = 10\,\text{nm}$ compared to $N = 40\,\text{nm}$ to $N = 100\,\text{nm}$. For $\Delta E_{\text{HOMO}} > 0.3\,\text{eV}$, the current density for $N = 10\,\text{nm}$ to 70 nm drop faster than for $N = 100\,\text{nm}$.

Figure 9.2.1 shows the molecular orbital energies, the Coulomb potential and the charge carrier densities for the polymer chains of length (bottom) 100 nm and (top) 10 nm. The left side of the figure shows MO energies through the active layer and the Coulomb potential (ϕ_c). In combination with the charge densities, the difference in charge density for long and short chain lengths in terms of the escaping and trapping of the charge carriers from the donor phase are explained. For long polymer chains, a minimal Coulomb potential of −0.74 eV at the position of the polymer chains is visible. The Coulomb potential in the fullerene matrix increases by −0.1 eV, reducing the effective energy barrier. Thus, holes can escape with a higher probability. In addition, once holes hop out of the chain, the shape of the Coulomb potential, especially the repulsion from the large hole density of $> 10^{19}\,\text{cm}^{-3}$ on the chain, forms a driving force away from the chain. For $N = 10\,\text{nm}$ at high ΔE_{HOMO}, a significant Coulomb potential of −1.4 eV is observed (Fig. 9.2.1c and d), shifting the potential of the holes in the donor downwards. However, as the distance between the chains is small, the Coulomb potential within and outside of the chain is reduced. If all holes fill the chains, a significant Coulomb repulsion arises. However, the interaction between the holes of neighboring chains strongly reduces the difference between the Coulomb potential on the chain and out of the chain, leading to the reduced driving force for the hole escape. This, in turn, results in a significant reduction in the current density.

The impact of the chain length on the jV curve is shown in Fig. 9.2.1a and Fig. 9.2.1 for $\Delta E_{\text{HOMO}} = 0.2\,\text{eV}$ and $\Delta E_{\text{HOMO}} = 0.5\,\text{eV}$, respectively, for $N = 10\,\text{nm}$ and $N = 100\,\text{nm}$. For low HOMO offset, holes can easily escape from the polymer chain and be effectively collected at the contacts. A slightly higher power conversion efficiency (PCE) of 0.71% is observed for $N = 10\,\text{nm}$ compared to 0.69% for $N = 100\,\text{nm}$. The higher PCE results from a higher j_{sc} of $3.37\,\text{mA}\,\text{cm}^{-2} > 2.95\,\text{mA}\,\text{cm}^{-2}$ due to

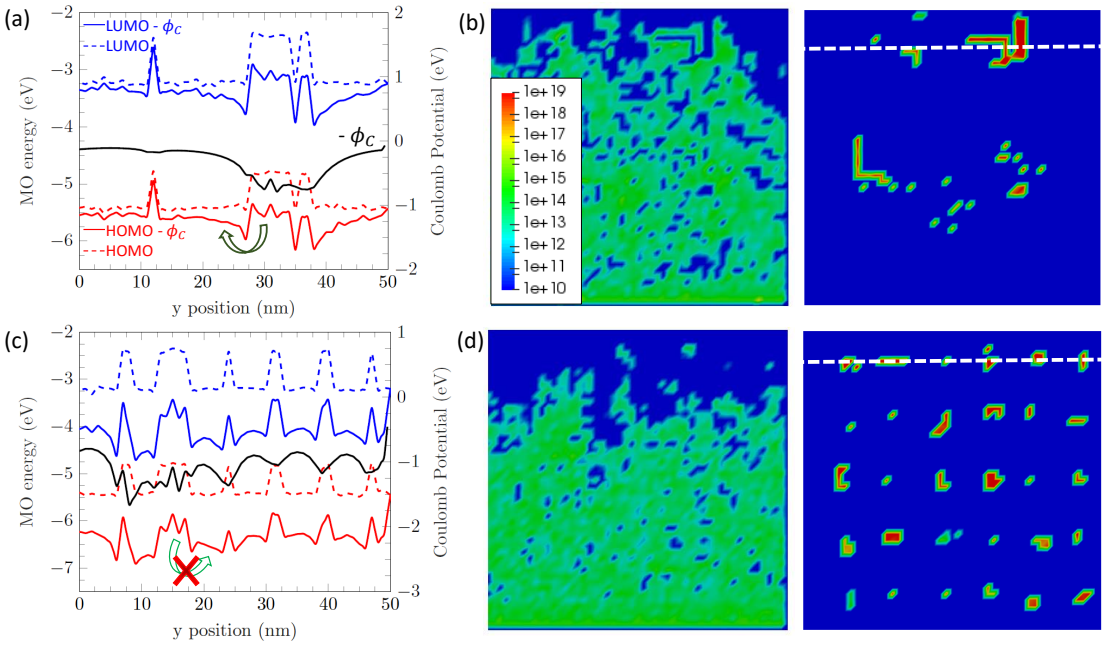

Figure 9.4 (a,c) Molecular orbital (MO) energies (dashed) and the Coulomb potential (black line), as well as the sum of MO energies and Coulomb potential (b,d) electron (left) and hole (right) densities. (a) and (b) show the results for chain length $N = 100\,\text{nm}$, and (c) and (d) represent $N = 10\,\text{nm}$. The colorbar shows the density in unit cm^{-3}. Reprinted with permission from [417]. Copyright 2020 American Chemical Society.

enhanced exciton dissociation (90 % to 75 %). At high HOMO offset (0.5 eV), holes are confined in the polymer chain for shorter chain length of 10 nm due to high energy barrier, which can be reduced using higher polymer length at same concentration, as discussed above. This results in a higher j_{sc} of $2.01\,\text{mA}\,\text{cm}^{-2} > 0.51\,\text{mA}\,\text{cm}^{-2}$, a higher V_{oc} ($0.59\,\text{V} > 0.34\,\text{V}$) and especially an increased PCE ($0.39\,\% > 0.05\,\%$) for long polymer chains. The reduced V_{oc} for short chains is caused by high recombination losses as hole back transfer is suppressed.

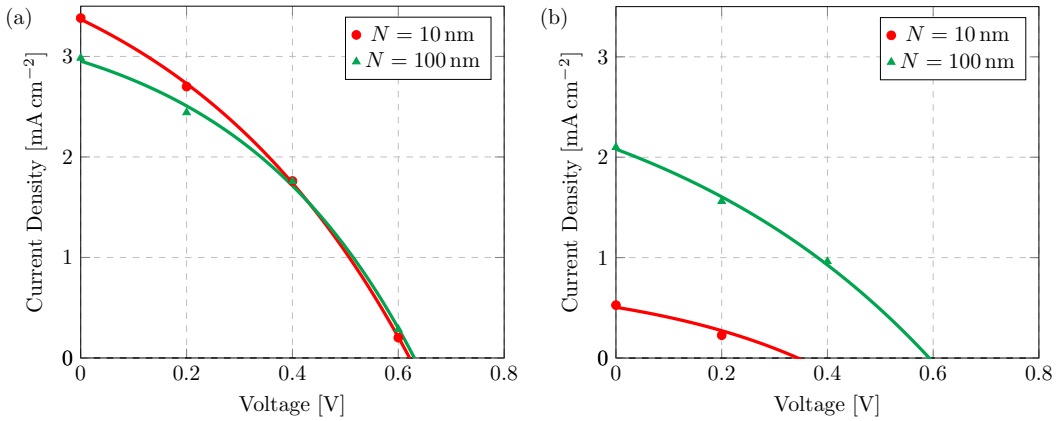

Figure 9.5 jV-characteristics at (a) 0.2 eV and (b) 0.5 eV for polymer chain lengths of $N = 10\,\text{nm}$ and $N = 100\,\text{nm}$. Solid lines show fits obtained using the Shockley equation. Reprinted with permission from [417]. Copyright 2020 American Chemical Society.

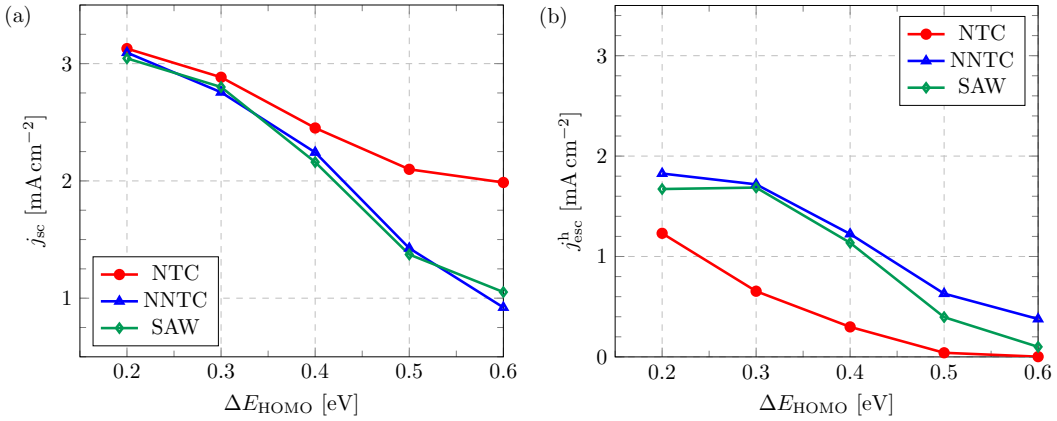

Figure 9.6 (a) Short-circuit current density j_{sc} and (b) hole escape current density j^{h}_{esc} for the SAW, NTC and NNTC morphologies at different HOMO offset ΔE_{HOMO}. Reprinted with permission from [417]. Copyright 2020 American Chemical Society.

9.2.2 Morphology study

The next part focuses on the impact of the polymer morphology. Different morphologies were created: isolated polymers (SAW), polymer network touching the contact (NTC), and polymer network not touching the contact (NNTC). All morphologies are generated with a polymer chain length of 100 nm.

Figure 9.2.2 shows the (a) short-circuit current and (b) hole escape current j^{h}_{esc} as function of the HOMO offset. j^{h}_{esc} is defined by the number of holes N_h leaving the donor region per interface area A of the heterojunction and the simulation time Δt [59]:

$$j^{h}_{esc} = \frac{q \cdot N_h}{A \cdot t_s} . \tag{9.1}$$

For small HOMO offset, holes see a low barrier for back transfer. This leads to a substantial j_{sc}. For all morphologies, j_{sc} of $\approx 3\,\mathrm{mA\,cm^{-2}}$ is reached at the low HOMO offset. For the NNTC and the SAW, no percolation paths towards the contacts exist. Thus, similar values all over the range of HOMO offsets are observed. For NTC, similar j_{sc} are observed at low HOMO offsets. However, the hole escape current density is only $\approx 1.2\,\mathrm{mA\,cm^{-2}}$. The remaining current is due to the percolation of holes which are connected to the contacts, contributing 35 % of the total j_{sc}.

Towards high HOMO offsets, NNTC and SAW morphology show a significant decrease in short-circuit and hole escape current density. j^{h}_{esc} also decreases significantly for the NTC, while the j_{sc} remains constant beyond $\Delta E_{HOMO} = 0.5\,\mathrm{eV}$ at $2\,\mathrm{mA\,cm^{-2}}$. The NTC provides sufficient percolation for holes and does not require any back transfer to the fillerene matrix. This scenario is similar to the standard BHJ morphology, however, with a strongly reduced amount of donor concentration. This makes controlling the polymer network even more critical.

Now, the jV-characteristics for the three different morphologies at $\Delta E_{HOMO} = 0.3\,\mathrm{eV}$, $0.4\,\mathrm{eV}$, and $0.7\,\mathrm{eV}$ is studied. The jV-characteristics are shown in Figure 9.2.2(a)-(c). The device characteristic parameters are summarized in Table 9.1. For this particular analysis, the work function of anode and cathode has been chosen to be $-5.5\,\mathrm{eV}$ and $-4.3\,\mathrm{eV}$, respectively, to analyze the maximum achievable V_{oc}. At $\Delta E_{HOMO} = 0.3\,\mathrm{eV}$, no difference in the jV-curves of the different morphologies is observed. The devices show a similar FF at $\Delta E_{HOMO} = 0.3\,\mathrm{eV}$ and $0.4\,\mathrm{eV}$ for all morphologies. The difference in FF at $\Delta E_{HOMO} = 0.7\,\mathrm{eV}$ is due resistive jV curve of the SAW and NNTC devices caused by the suppressed back transfer, while the NTC morphology shows an effective photocurrent along percolation pathways formed by the polymer chains.

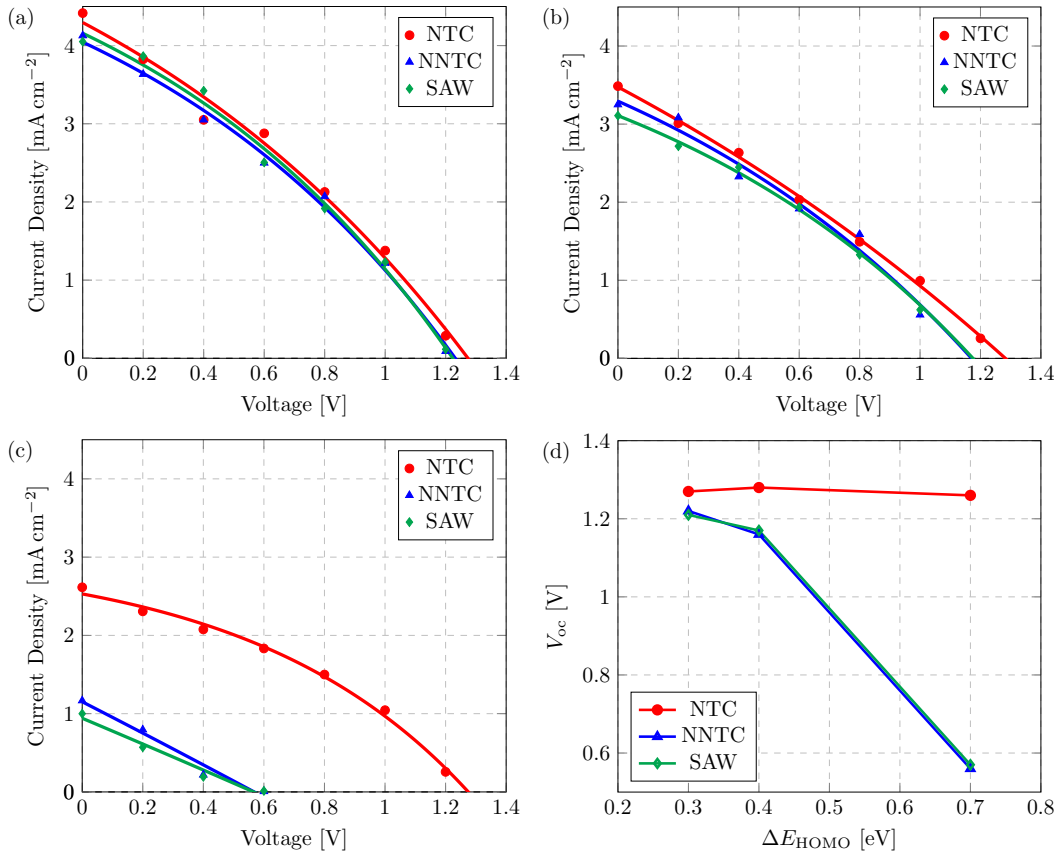

Figure 9.7 jV-characteristics at (a) 0.3 eV, (b) 0.4 eV, (c) 0.7 eV and (d) Open-circuit voltage for SAW, NTC and NNTC morphologies at different HOMO level offset. Solid lines in (a)-(c) show fits obtained using the Shockley equation. Reprinted with permission from [417]. Copyright 2020 American Chemical Society.

Table 9.1 Device parameters for SAW, NNTC and NTC morphologies.

ΔE_{HOMO} (eV)	SAW				NNTC				NTC			
	j_{sc}(mA cm^{-2})	V_{oc}(V)	FF	PCE (%)	j_{sc}(mA cm^{-2})	V_{oc}(V)	FF	PCE(%)	j_{sc}(mA cm^{-2})	V_{oc}(V)	FF	PCE(%)
0.3	4.16	1.21	0.33	1.64	4.04	1.22	0.32	1.60	4.29	1.27	0.31	1.69
0.4	3.11	1.17	0.32	1.15	3.29	1.16	0.31	1.19	3.48	1.28	0.28	1.26
0.7	0.94	0.57	0.25	0.13	1.15	0.56	0.25	0.17	2.53	1.26	0.37	1.18

For $\Delta E_{\mathrm{HOMO}} = 0.4\,\mathrm{eV}$, the trend within the jV-characteristic at low voltages is similar, while NTC shows higher currents near V_{oc}. At highest HOMO offset, V_{oc} for SAW and NNTC morphology is 0.57 V and 0.56 V, respectively, while NTC shows V_{oc} of 1.26 V. This decrease in V_{oc} for the SAW and NNTC morphologies at higher HOMO offsets is due to the increased recombination. Due to percolation within the NTC network, charges can move to the contacts and recombination stays low, which is reflected in high V_{oc}.

In a previous publication, high $j_{\mathrm{sc}} = 9.1\,\mathrm{mA\,cm^{-2}}$ was obtained within standard BHJ of a P3HT:PCBM solar cells [362]. However, V_{oc} was limited at 0.67 V. The diluted donor OSC provides a significant improvement in terms of V_{oc} as charge carriers are extracted via the fullerene matrix. Besides, charge extraction at the wrong contacts is strongly suppressed, which is one promising method to significantly enhance the V_{oc} despite using the same material system [358, 362].

9.3 Origin of Charge Transport in Dilute Polymer Donor OSCs

Section **9.2** presented a theoretical study on the role of the polymer morphology in dilute donor OSCs. To connect these results with reality, the photocurrent is studied within P3HT:$PC_{71}BM$ for donor concentrations from 1 wt% to 5 wt% by kMC simulations and compared with experimental data by Hsu and coworkers [429].

Before entering the analysis of the results, the differences to the study of Albes *et al.* [59], in the following referred to as DD1, are summarized. DD1 only studied the low P3HT concentration of 1 wt%. The molecular weight of polymer chains in DD1 was chosen as 11 kDa, which is significantly below the experimental value (37 kDa, see DD1 SI). Moreover, discrepancies in device thicknesses in experiments and kMC were present. A strong restriction in DD1 was the polymer morphology. The chains were fully isolated and strongly twisted. Also, polymers were not allowed to touch any contacts. Here, polymer chains with molecular weight of 33 kDa are used. The thickness of the photoactive layer was chosen to match the experiment [429]. Polymer chains are allowed to aggregate and to form percolation paths to contacts. In addition, less pivot steps were taken to mimic wormlike chains rather than Gaussian ones [198].

9.3.1 Kinetic Monte Carlo Method

Kinetic Monte Carlo simulations were performed to analyze the origin of the photocurrent in P3HT:$PC_{71}BM$ devices with donor concentration $n_D \in \{1, 2, 5\}$wt%. The photoactive layer is modeled by a $50 \times 50 \times 65\mathrm{nm}^3$ lattice with lattice constant of $a = 1$ nm. Periodic boundaries are applied along x and y-direction, while contacts terminate the device along the z-axis. Polymer chains are represented by 100 connected sites, which corresponds to a molecular weight of approx. 33 kDa. The chains are randomly distributed within the fullerene matrix. The number of polymer chains is chosen to match the desired concentration of the donor (1 wt% to 2 wt%). Figure 9.8 depicts the distribution of the polymers within the simulation box for the different concentrations.

The kMC model accounts for the generation of excitons, exciton diffusion and dissociation at the donor:acceptor interface, as well as charge carrier dynamics and recombination [13, 59]. The exciton diffusion rate a_{diff} is modeled by a Förster resonant energy transfer rate given by [39, 362]:

$$a_{\mathrm{diff}} = \tau^{-1} \left(\frac{r_{\mathrm{FRET}}}{r_{ij}} \right)^6 \begin{cases} \exp\left(-\frac{\Delta E_{ij}}{k_{\mathrm{B}} T} \right) & \text{if } \Delta E_{ij} > 0 \\ 1 & \text{else} \end{cases} \tag{9.2}$$

where r_{FRET} is the Förster radius, τ is the exciton lifetime, r_{ij} is the distance between initial site i and final site j, k_{B} is Boltzmanns constant, T is the temperature, and ΔE_{ij} is the energy difference.

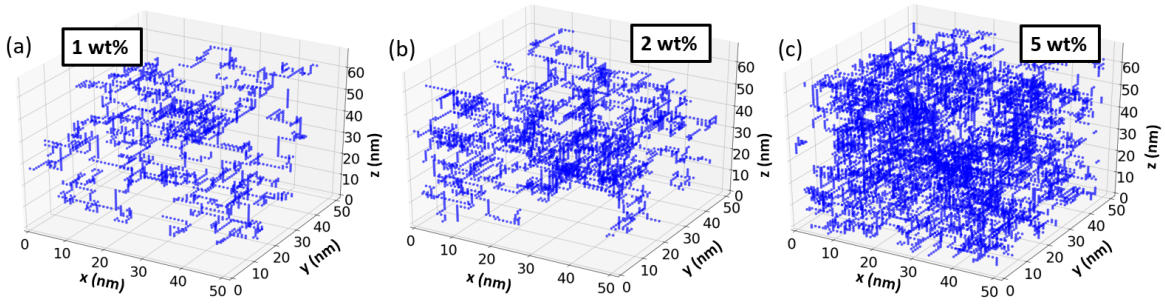

Figure 9.8 Polymer distribution within the simulation box at (a) 1 wt%, (b) 2 wt%, and (c) 5 wt% donor concentration.

All neighbors within the Förster radius are considered as possible destinations for the diffusion of excitons. Recombination of excitons is modeled as the inverse of the lifetime τ, i.e. $a_{\text{exd}} = \tau^{-1}$ [362].

Transport of photogenerated electrons and holes from the initial site i to a nearest neighbor j is modeled using the Miller-Abrahams transfer rate [27]:

$$a_{i\to j} = a_0 \exp\left(-\frac{2r_{ij}}{\alpha}\right) \begin{cases} \exp\left(-\frac{\Delta E_{ij}}{k_\text{B}T}\right) & \text{if } \Delta E_{ij} > 0 \\ 1 & \text{else} \end{cases} \tag{9.3}$$

where a_0 is the attempt-to-hop frequency, α is the localization length, r_{ij} gives the distance between sites i and j, and ΔE_{ij} the difference in the electrostatic potential. Several terms contribute to the electrostatic difference ΔE_{ij}:

$$\Delta E_{ij} = \Delta E_{ij}^{\text{MO}} + \Delta E_{ij}^{\text{C}} + \Delta E_{ij}^{\text{F}} \,. \tag{9.4}$$

$\Delta E_{ij}^{\text{MO}}$ gives the difference of the disordered molecular orbital energies (HOMO for holes, LUMO for electrons), ΔE_{ij}^{C} captures the change in Coulomb potential before and after the jump, and ΔE_{ij}^{F} is the electric field contribution from the applied voltage and the work function difference. For simplicity, a linear potential drop is taken along the z-axis. The Coulomb potential is calculated using the Ewald summation technique [48, 211], which takes into account the interaction with image charges arising due to the presence of contacts, as well as periodic replica along the x- and y-direction. Electron-hole recombination is accounted for using a constant recombination rate a_{rec} and is activated if an electron and a hole reside on adjacent sites.

As excitons dissociate by transfer of the holes from the fullerene acceptor (site i) to the donor (site j), the driving force is included in the exciton dissociation process by a Marcus transfer rate [92, 227]:

$$a_{\text{diss}} = a_{\text{d},0} \exp\left(-\frac{(\lambda + \Delta E)^2}{4\lambda k_\text{B}T}\right) , \tag{9.5}$$

where λ gives the reorganization energy, a constant dissociation prefactor $a_{\text{d},0}$, and $\Delta E = \Delta E_{\text{HOMO}} + \Delta E_{ij}^{\text{C}} + \Delta E_{ij}^{\text{F}} - E_{\text{singlet}}$, with the singlet binding energy E_{singlet}.

Tables 9.2 and 9.3 summarize the material parameters for the fullerene acceptor $PC_{71}BM$ and the P3HT polymers, respectively. To obtain an accurate exciton dynamics, the exciton diffusion properties are parametrized to match the experimentally reported diffusion length ($L_\text{D} = 5.2$ nm) and the diffusion coefficient $D = 3.6 \times 10^{-4}\,\text{cm}^2\,\text{s}^{-1}$ [114, 436]. This is of special importance to avoid an over-/underestimation of the exciton dissociation yield at low donor concentrations. To match these values, the diffusion length and exciton lifetime are simulated within a single $PC_{71}BM$ layer with periodic boundary conditions to avoid any quenching by defects or interfaces [182]. Using

Table 9.2 Material parameters for $PC_{71}BM$ within the kinetic Monte Carlo simulations.

Parameter	Value	Reference
HOMO energy	−5.85 eV	Park *et al.* [7]
LUMO energy	−3.95 eV	Park *et al.* [7]
E_{singlet}	150 meV	calculated
Singlet lifetime	1.28×10^{-10} s	Mikhnenko *et al.* [114]
Singlet diffusivity D	3.6×10^{-4} cm^2 s^{-1}	Mikhnenko *et al.* [114]
Förster radius	1.8 nm	parametrized
Localization length	0.43 nm	Gerhard *et al.* [437]
Attempt-to-hop frequency a_0	3×10^{12} s^{-1}	Albes *et al.* [59]
Recombination rate a_{ehr}	10^7 s^{-1}	parametrized
Refractive index $(n + \mathrm{i}k)$	See Fig. 9.9(a)	Pascual San-José *et al.* [438]
Generation profile	See Fig. 9.9(b)	Transfer Matrix Method
Permittivity ϵ_r	3.9	Gerhard *et al.* [437]

Table 9.3 Material parameters of P3HT polymer. All parameters which are not listed here are taken equal to the $PC_{71}BM$ values for simplicity.

Parameter	Value	Reference
Band gap	2.0 eV	[435]
Localization length	0.25 nm	parametrized
Attempt-to-hop frequency a_0	6×10^{11} s^{-1}	[14]
Dissociation rate P3HT:$PC_{71}BM$	10^{12} s^{-1}	similar values by Liu *et al.* [229]

$\tau = 1.28 \times 10^{-10}$ s and $r_{\text{FRET}} = 1.8$ nm, an accurate diffusion length of $L_{\text{D}}^{\text{kMC}} = 5.20$ nm as well as an exciton lifetime of $\tau^{\text{kMC}} = 1.27 \times 10^{-10}$ s are obtained. This gives $D^{\text{kMC}} = 3.53 \times 10^{-4}$ cm^2 s^{-1}.

The exciton generation profile was obtained from the Transfer Matrix Method (TMM) [215, 217] using the MATLAB model provided by Burkhard *et al.* [216]. The generation profile as well as the refractive index of $PC_{71}BM$ are shown in Figure 9.9(a) and (b), respectively.

9.3.2 Results and Discussion

First, the short-circuit current density J_{sc} is simulated as function of the HOMO offset between P3HT and $PC_{71}BM$. The energy level alignment can be used for comparison with experiments by Hsu and coworkers [429]. Reorganization energies λ were taken from Table 9.4.

Table 9.4 CT state energy (E_{CT}) and reorganization energy (λ) extracted from [429]. HOMO offset (ΔE_{HOMO}) is obtained by subtracting E_{CT} from the optical band gap of $PC_{71}BM$, $E_g(PC_{71}BM) = 1.75$ eV.

Donor wt%	E_{CT} (eV)	λ (eV)	ΔE_{HOMO} (eV)
1	1.49	0.25	0.26
2	1.46	0.31	0.29
5	1.46	0.37	0.29

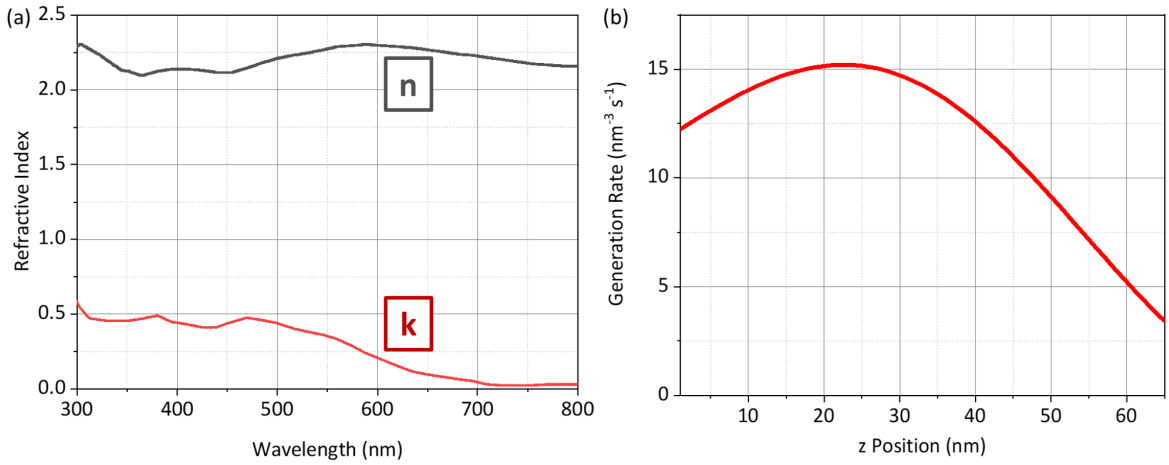

Figure 9.9 (a) Refractive index (real part n and imaginary part k) of $PC_{71}BM$ extracted from Pascual-San José *et al.* [438]. (b) Resulting generation profile $G(z)$ as a function of the z-position within the photoactive layer. Light falls in from z=0 nm. Reprinted from [418] under the terms of the Creative Commons CC BY license.

Figure 9.10 shows the J_{sc} as a function of the HOMO offset ΔE_{HOMO} for 1 wt% and 2 wt% P3HT concentration. The horizontal lines show the experimental values [429]. Previous studies on the same system did not account for the driving force in the exciton dissociation rate [59]. Consequently, a constant J_{sc} towards small ΔE_{HOMO} has been observed [59]. Interestingly, J_{sc} at 1 wt% remains roughly constant as ΔE_{HOMO} is lowered. This is due to the large reorganization energy $\lambda = 0.25$ eV [227]. At 2 wt% P3HT concentration, J_{sc} decreases as ΔE_{HOMO} approaches zero. For high $\Delta E_{HOMO} \geq 0.25$ eV, J_{sc} decreases as the back transfer of holes from the P3HT chains to the fullerene matrix is lowered. The absolute value of the short-circuit current density increases with the donor concentration. With higher wt% of P3HT, the average distance for excitons from the locations of generation to a donor:acceptor interface decreases leading to more excitons being dissociated.

Comparing the J_{sc} obtained by kMC with experiments, the HOMO offsets which match the experimental current are extracted. Experiments showed HOMO offsets of 0.26 eV and 0.29 eV for 1 wt% and 2 wt% donor concentration, respectively. The kMC results show an excellent agreement, with 0.27 eV and 0.30 eV for 1 wt% and 2 wt% P3HT concentration.

Figure 9.11 shows the simulated volume recombination rate, defined by

$$R = \frac{N_{rec}^{ngr}}{\Delta t}, \tag{9.6}$$

where N_{rec}^{ngr} is the number of nongeminate recombination events, and Δt the simulation time. Horizontal lines show the extracted recombination rates from experiments [429]. With increasing HOMO offset, R increases exponentially. This is due to an increase in the hole density due to reduced back transfer with rising HOMO offset. Beyond $\Delta E_{HOMO} = 0.35$ eV, the recombination rate saturates. At 1 wt%, the kMC results match the experimental value of 6.3×10^3 s^{-1} [59] at $\Delta E_{HOMO} = 0.26$ eV, the experimentally determined value of the HOMO offset. At 2 wt% P3HT concentration, significantly higher recombination rates are observed. The crossing point is predicted at 0.22 eV, significantly below the experimental $\Delta E_{HOMO} = 0.29$ eV. This difference may be explained by an increase in aggregation of P3HT chains with rising donor concentration, which is neglected in the kMC analysis.

To understand the importance of percolation and back transfer within these P3HT:$PC_{71}BM$ devices, both contributions are studied in detail. Figure 9.12 shows the contributions of percolation and of back transfer to the J_{sc} versus the HOMO offset. Percolation current is obtained by the fraction of holes

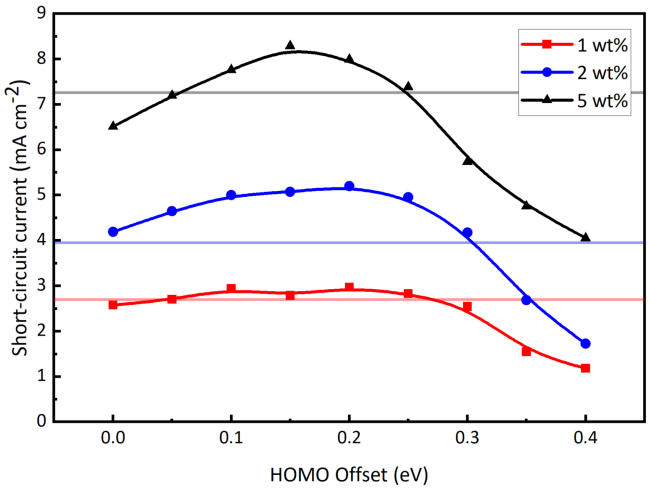

Figure 9.10 Short-circuit current density versus HOMO offset for P3HT:$PC_{71}BM$ for 1 wt% (red), 2 wt% (blue), and 5 wt% (black). The HOMO offset is defined by the difference in HOMO energies between P3HT and $PC_{71}BM$. The horizontal lines give the experimental result extracted from [429]. The solid lines are basis spline interpolations for improved readability.

which are being extracted at the anode from donor sites. The quantitative values strongly depend on the P3HT distribution within the photoactive layer. Here, the focus is set on the qualitative picture. At low HOMO offsets, back transfer dominates for both 1 wt% (Fig. 9.12a) and 2 wt% (Fig. 9.12b) P3HT concentration. Holes can be easily transferred back to the fullerene matrix. As $PC_{71}BM$ is an ambipolar material, holes are then transported to the contacts efficiently. Increasing ΔE_{HOMO} shows a rise of the percolation current. At 0.4 eV HOMO offset, 78 % (25 %) of the J_{sc} is contributed by percolation at 1 wt% (2 wt%). Clearly, back transfer dominates at the experimental observed HOMO offsets. This demonstrates that hole back transfer is sufficient to explain the origin of the photocurrent, as previously claimed by Albes *et al.* [59]. Still, even at lowest donor concentrations of 1 wt%, percolation in dilute donor OSCs with polymer donors can contribute a significant amount of current.

9.4 Origin of Charge Transport in Small Molecule Dilute Donor OSCs

9.4.1 Background

Most existing studies supporting tunneling as the hole transport mechanism in dilute donor morphologies are based on donor concentrations of 5 wt% and higher. Low crystallinity and localized charge carriers in solution processed OSCs question the validity of tunneling across up to 4-5 nm as the mechanism of hole transfer for dilution of less than 5 wt%. Back transfer in solution processed dilute donor OSCs was only studied for polymer donors, which makes conclusions difficult due to their complex morphology. Also, delocalization of charge carriers in polymer donors can strongly differ from small molecules. Even in polymers with structural disorder in the backbone and side chains, conjugation across several monomers is observed [21]. Consequently, charges can delocalize within conjugated segments of several monomer subunits. Small molecule donors with reduced tendency for aggregation and less freedom in the individual molecule morphology are needed to provide insight into the nature of hole transport. The energetic and morphological complexity in dilute-donor OSCs requires joint effort by experiments and theory to gain understanding in the hole transport mechanism for small molecule donor materials at a dilution of less than 5 wt%.

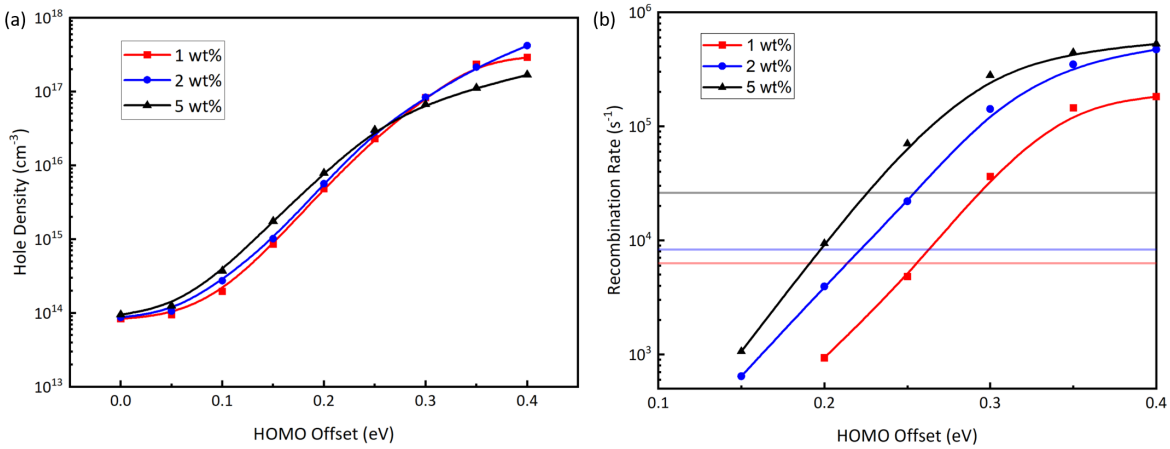

Figure 9.11 (a) Hole density versus HOMO offset for 1 wt% to 5 wt% P3HT concentration. (b) Volume recombination rate of charge carriers versus the HOMO offset extracted from kinetic Monte Carlo simulations.

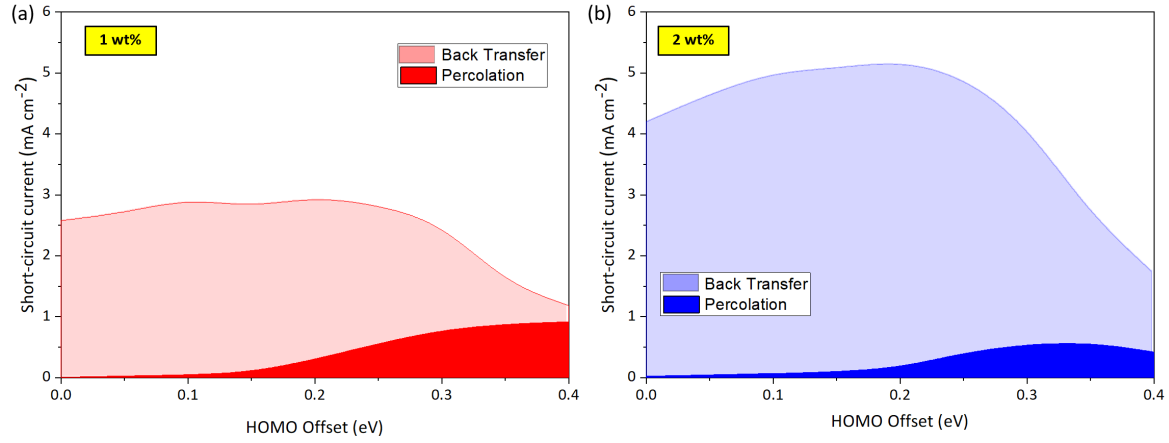

Figure 9.12 Contribution of hole back transfer and percolation to the short-circuit current density as function of the HOMO offset for (a) 1 wt% and (b) 2 wt%.

In this work, we study the origin of the photocurrent in small molecule dilute donor OSCs in a joint experimental-theoretical analysis. Kinetic Monte Carlo (kMC) simulations are performed to analyze the origin of the photocurrent in the small molecule dilute donor OSCs with considering the role of the driving force in the exciton dissociation rate. Both back transfer and long-range hopping (tunneling) are studied as potential mechanisms of hole transport. We analyze the photocurrent generation using intensity dependence measurements of the short-circuit current and characterize the device performance for a dilution of 1 to 5 wt%. We synthesize nitrogen-bridged terthiophene (NBTT) molecules with rhodanine (Rho) and 1,3-Indandione (IDD) end groups as donor molecules, and use [6,6]-phenyl-C71-butyric acid methyl ester ($PC_{71}BM$) as our acceptor molecule. A variety of such terthiophene based molecules have been applied in OSCs [439–441] and dye-sensitized solar cells [442]. NBTT shows a good miscibility with $PC_{71}BM$ because of its high affinity of the aligned sulfur atoms to fullerene, and NBTT:$PC_{71}BM$ bulk heterojunction OSCs have been demonstrated [443]. Thanks to the high solubility in the processing solvent, NBTT molecules are expected to be homogeneously distributed within the photoactive layer at 1 wt% and 2 wt% donor concentration. This minimizes the average distance between exciton generated locations in $PC_{71}BM$

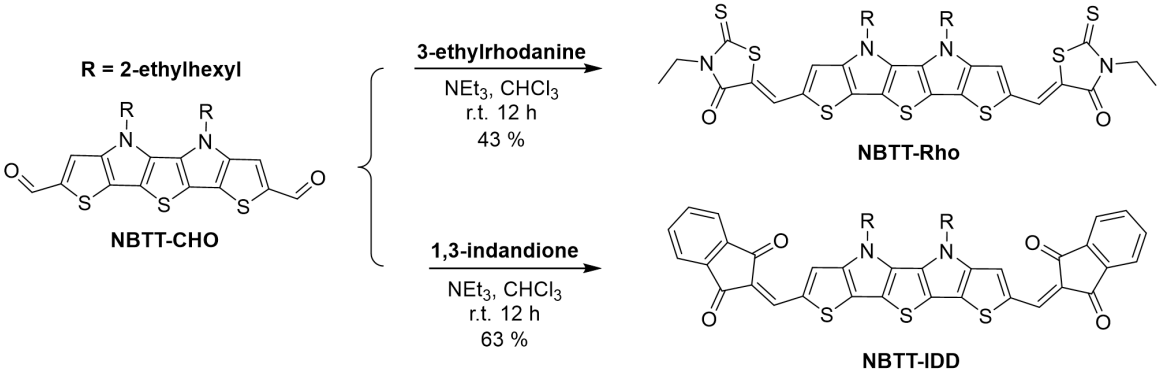

Figure 9.13 Synthetic routes to NBTT-IDD and NBTT-Rho. Reprinted from [418] under the terms of the Creative Commons CC BY license.

and nearest donor molecules. In addition, donor crystallization and percolation networks can be ruled out at such low dilution. For 5 wt% concentration, donor aggregation is observed. Hence, NBTT:$PC_{71}BM$ represents an ideal test system to study the origin of hole transport in dilute-donor OSCs at donor concentrations below 5 wt%. Our results show that the experimentally observed current densities can be explained by the back transfer mechanism. Long-range hopping provides no significant photocurrent below 5 wt%. At 5 wt%, distances between molecules become sufficiently small to allow long-range hopping.

9.4.2 Methods

NBTT Donor Molecules[1]

The syntheses of NBTT-IDD and NBTT-Rho are shown in Fig. 9.13. The dialdehyde NBTT-CHO was treated with corresponding electron-withdrawing molecules, 1,3-indandione (IDD) or 3-ethylrhodanine (Rho), in the presence of triethylamine to produce the target compounds. The electron rich NBTT core end-capped with electron deficient terminal groups renders evident charge transfer absorption. The solution of NBTT-IDD and NBTT-Rho in chlorobenzene exhibit absorption peak centered at 650 and 615 nm (Figure 9.14), respectively, indicating the higher electron-withdrawing feature of IDD group for a better intramolecular charge transfer interaction.

Device Fabrication

To understand the mechanism of hole transport in dilute donor cells with small molecules below the percolation threshold, dilute donor OSCs were prepared with varying NBTT concentration between 0 wt% and 5 wt% in a $PC_{71}BM$ matrix. All devices were fabricated in a standard OSC structure: glass/indium tin oxide (ITO)/poly(3,4-ethylenedioxythiophene):poly-(styrenesulfonate) (PEDOT:PSS)/active layer/Ca/Al. PEDOT:PSS (Heraeus Clevios AI 4083) was spin-coated onto precleaned patterned ITO (Xinyan, 15 Ω/sq) substrates at 4000 rpm for 30 s, followed by 170 °C annealing in N2 for 5 min to form the bottom hole transport layer. Appropriate weights of synthesized NBTT-IDD and NBTT-Rho molecules and $PC_{71}BM$ (Solenne BV), with a total concentration of 20 mg/mL, were dissolved in chlorobenzene (CB) and stirred overnight at 70 °C. The active layers were made by spin-coating the

[1] The synthesis of the NBTT molecules has been done by *Chin-Lung Chung* and Prof. *Ken-Tsung Wong* from the National Taiwan University.

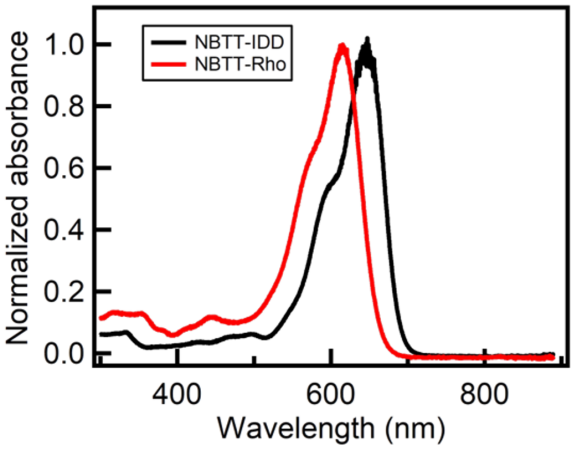

Figure 9.14 Normalized absorbance spectra of NBTT-IDD (black) and NBTT-Rho (red) in chlorobenzene solution. Reprinted from [418] under the terms of the Creative Commons CC BY license.

prepared solutions at 1000 rpm for 60 s followed by annealing at 80 °C in N2 for 10 min. The active layer thickness is approximately 65 nm. Finally, 7 nm Ca and 100 nm Al were thermally evaporated (Angstrom Engineering) to complete the devices.

Ultraviolet (UV)-Visible Absorption Spectroscopy

The UV-Vis absorbance spectra of molecules in solution (CB) and spin coated thin films were measured using an Ocean Optics USB 4000 spectrometer with a DT-mini-2-GS light source.

Photoelectron Spectroscopy in Air (PESA)

Ionization energy (IE) was measured using PESA (RKI instruments, AC2 model) with 100 nW deuterium lamp power. The resolution of PESA measurements are approximately 0.05 eV.

Current Density-Voltage Measurements

The jV measurements are performed in a N2-filled glovebox under AM1.5G 100 mW cm^{-2} illumination from a class AAA solar simulator (Abet Technologies) using a low-noise source meter (2635A, Keithley). The solar simulator intensity was calibrated using a NIST-traceable Si photodiode (Abet RR_227KG5). A 2.5 mm diameter aperture was placed in front of each device to define the illuminated area of 0.049 cm^2. 5 diodes for each condition were averaged to calculate standard deviation.

Variable Intensity Measurements

The intensity dependence on photocurrent was measured using the class AAA solar simulator described above. Neutral density filters optical density (OD) varying from 0.03 to 2 was placed between the light source and the sample to vary the intensity. The absolute intensity was measured using thermopile power meter (Ophiro, 10A model).

Table 9.5 Material parameters of NBTT donor molecules. All parameters which are not listed here are taken equal to the $PC_{71}BM$ values for simplicity. If not noted otherwise, the parameters are assumed to be equal for NBTT-Rho and NBTT-IDD.

Parameter	Value	Reference
Band gap NBTT-IDD	1.65 eV	Fig. 9.14
Band gap NBTT-Rho	1.75 eV	Fig. 9.14
Localization length NBTT-IDD	0.08 nm	parametrized
Localization length NBTT-Rho	0.1 nm	parametrized
Dissociation rate NBTT-IDD:$PC_{71}BM$	10^{12} s^{-1}	-
Dissociation rate NBTT-Rho:$PC_{71}BM$	5×10^{11} s^{-1}	similar values by Liu *et al.* [229]

External Quantum Efficiency (EQE) Spectroscopy

EQE measurements were taken at short circuit using a monochromatic light from a tungsten halogen lamp (HORIBA TRIAX-180, grating 600 groove/mm) from 400 to 1000 nm. A chopper (Tetrahertz, C-995) was used to modulate the monochromatic light at 199 Hz, and a lock-in amplifier (Standard Research System, SR830) was used to demodulate the signal. Cutoff filters at 710 and 850 nm were used to reduce the scattered light from the light source so that the weak sub-band gap EQE response was accessible. EQE measurements were quantified using an NREL-calibrated Si photodiode.

Kinetic Monte Carlo Method

Kinetic Monte Carlo simulations were performed to analyze the origin of the photocurrent in NBTT-x:$PC_{71}BM$ (x = IDD / Rho) devices with donor concentration $n_D \in \{1, 2, 5\}$wt%. Details on the used model are shown in chapter 12.3.1. Here, the main differences are summarized.

Donor molecules, represented by 3 connected sites, are distributed randomly within the fullerene matrix. No further post-processing of the photoactive layer is done to mimic the aggregation of the sulfur atoms with $PC_{71}BM$. The number of molecules is chosen to match the desired concentration of the donor (1 to 5 vol%). Figure 9.15 depicts the distribution of the small molecules within the simulation box for the different concentrations.

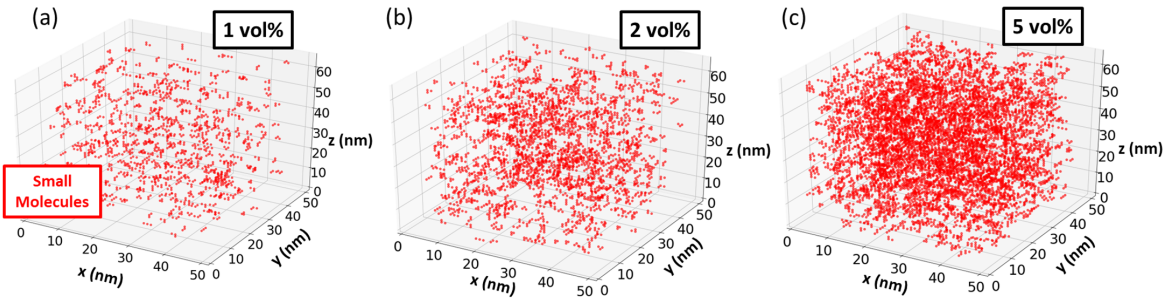

Figure 9.15 Small molecule distribution within the simulation box at (a) 1 vol%, (b) 2 vol% and (c) 5 vol% donor concentration. Reprinted from [418] under the terms of the Creative Commons CC BY license.

Tables 9.2 and 9.5 summarize the material parameters for the fullerene acceptor $PC_{71}BM$ and the donor molecules, respectively. In contrast to the polymer dilute donor study, a higher $\sigma = 75$ meV was obtained.

Table 9.6 Device parameters of NBTT-IDD:$PC_{71}BM$ devices with different donor concentrations.

NBTT-IDD (wt%)	V_{oc} (V)	J_{sc} (mA cm^{-2})	FF ( )	PCE (%)
0	0.83 ± 0.02	0.20 ± 0.00	0.31 ± 0.00	0.05 ± 0.00
1	0.77 ± 0.01	1.58 ± 0.05	0.26 ± 0.00	0.32 ± 0.01
2	0.86 ± 0.01	2.10 ± 0.05	0.27 ± 0.00	0.49 ± 0.02
5	0.84 ± 0.01	3.43 ± 0.07	0.34 ± 0.00	0.99 ± 0.02

9.4.3 Experimental Results

First, the *jV* characteristics for the NBTT-x:$PC_{71}BM$ (x = IDD / Rho) solar cells with 0 wt% (neat $PC_{71}BM$) to 5 wt% concentration of the donor molecules under 1 sun illumination is presented in Fig. 9.16. The device parameters for NBTT-IDD:$PC_{71}BM$ and NBTT-Rho:$PC_{71}BM$ are summarized in Table 9.6 and 9.7, respectively. The neat $PC_{71}BM$ devices show low J_{sc} of 0.2 mA cm^{-2} with a V_{oc} of 0.83 V. The photocurrent in the neat $PC_{71}BM$ devices is attributed to a field dissociation of excitons [444]. Adding small amounts of donor molecules enhance the J_{sc}, whereas the V_{oc} and the fill factor (FF) remain roughly constant. For the NBTT-IDD:$PC_{71}BM$ devices (Fig. 9.16a), the short-circuit current density increases monotonically with increased donor concentrations. The PCEs are determined by J_{sc} as the other device parameters are insensitive to the donor concentration. Interestingly, the J_{sc} only increases by a factor of 1.6 while donor concentration increases by a factor of 2.5 from 2 wt% to 5 wt%. NBTT-Rho:$PC_{71}BM$ devices (Fig. 9.16b) exhibit similar device parameters for 1 wt% and 2 wt% donor concentration as NBTT-IDD:$PC_{71}BM$ devices. At 5 wt% donor concentration, however, NBTT-Rho:$PC_{71}BM$ devices produce a substantially higher J_{sc}, 5.23 mA cm^{-2}, which increases the PCE to 1.55 %, significantly higher than the 5 wt% NBTT-IDD:$PC_{71}BM$ device (PCE = 0.99 %). The FF for all investigated devices remains low. Highest FF values of 0.35 were observed for the 5 wt% NBTT-IDD:$PC_{71}BM$ device. The shape of the *jV* curves in the 4th quadrant are very linear, which could signal poor charge transport properties [32].

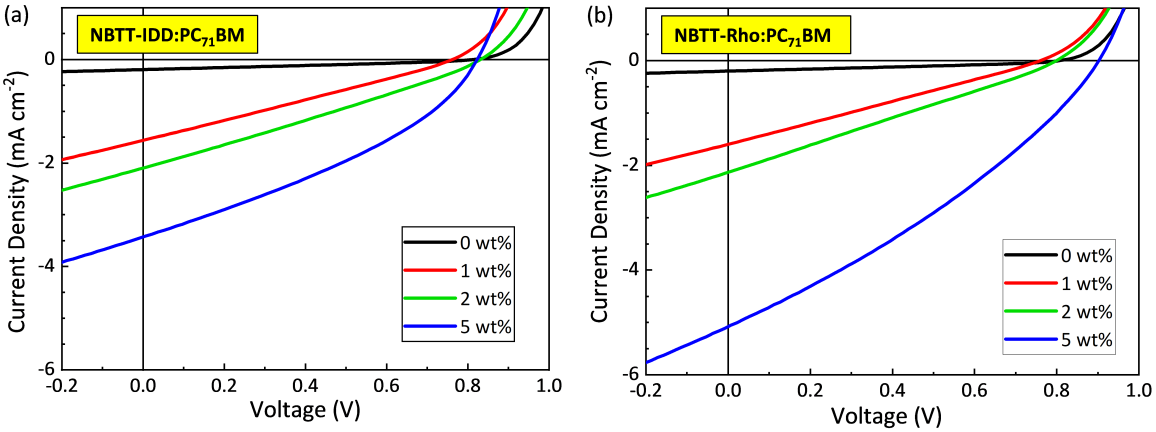

Figure 9.16 *jV* curves of (a) NBTT-IDD:$PC_{71}BM$ and (b) NBTT-Rho:$PC_{71}BM$ devices with different donor concentrations: 0 wt% (black), 1 wt% (red), 2 wt% (green), and 5 wt% (blue) under one sun illumination (AM 1.5G 100 mW cm^{-2}). Reprinted from [418] under the terms of the Creative Commons CC BY license.

CT energies, E_{CT}, are measured using low-energy EQE spectroscopy to determine the HOMO offset energies between the donor molecules and the $PC_{71}BM$. The E_{CT} represents the difference

Table 9.7 Device parameters of NBTT-Rho:$PC_{71}BM$ devices with different donor concentrations.

NBTT-Rho (wt%)	V_{oc} (V)	J_{sc} (mA cm^{-2})	FF ( )	PCE (%)
0	0.82 ± 0.01	0.20 ± 0.00	0.32 ± 0.02	0.05 ± 0.00
1	0.77 ± 0.01	1.61 ± 0.04	0.26 ± 0.00	0.32 ± 0.01
2	0.80 ± 0.01	2.17 ± 0.08	0.26 ± 0.00	0.45 ± 0.02
5	0.91 ± 0.01	5.23 ± 0.16	0.32 ± 0.00	1.55 ± 0.05

between the HOMO of the NBTT molecules and the LUMO of $PC_{71}BM$. Subtracting E_{CT} from the optical band gap of $PC_{71}BM$ ($E_g(PC_{71}BM) = 1.75$ eV) [7] provides an estimation for the HOMO offset $\Delta E_{HOMO} = E_g(PC_{71}BM) - E_{CT}$ [351]. Figure 9.17 shows the EQE spectra of (a) NBTT-IDD:$PC_{71}BM$ and (b) NBTT-Rho:$PC_{71}BM$ devices with varying concentrations. Both sets of devices show an enhanced EQE magnitude with increasing donor concentration for energies below $E_g(PC_{71}BM$. From the low energy part of the EQE spectra, the E_{CT} and the λ are extracted using a Gaussian fit [445] and summarized in Table 9.8 and 9.9. E_{CT} decreases slightly with the addition of NBTT donors in both NBTT:$PC_{71}BM$ devices. NBTT-Rho:$PC_{71}BM$ devices show lower E_{CT} values than NBTT-IDD:$PC_{71}BM$ devices. The reorganization energy λ increase with donor concentration in both NBTT:$PC_{71}BM$ devices, but remains significantly lower than observed for P3HT:$PC_{71}BM$ OSCs which have $\lambda \approx 0.3$ eV [59]. For both NBTT:$PC_{71}BM$ devices, ΔE_{HOMO} increases slightly with the donor concentration. The significance of ΔE_{HOMO} on hole transport will be discussed in **section 3.4**.

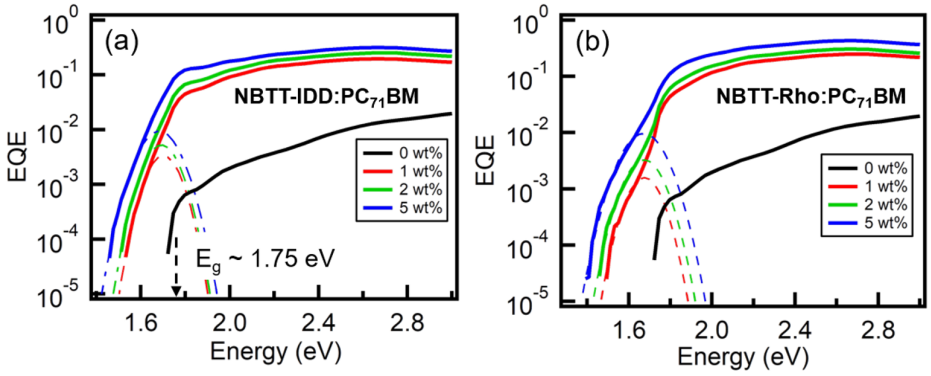

Figure 9.17 (a) External quantum efficiency (EQE) vs. wavelength, (b) EQE (plotted in log scale) vs energy of NBTT-IDD:$PC_{71}BM$ devices with varying donor concentrations: 1 wt% (red), 2 wt% (green), and 5 wt% (blue). The dashed-dotted lines in (b) show the Gaussian fit of the CT state energy. Reprinted from [418] under the terms of the Creative Commons CC BY license.

Table 9.8 Parameters extracted from the Gaussian fit of the CT state energy for the NBTT-IDD:$PC_{71}BM$ devices.

NBTT-IDD (wt%)	E_{CT} (eV)	ΔE_{HOMO} (eV)	λ (eV)
1	1.64 ± 0.01	0.11 ± 0.01	0.06 ± 0.01
2	1.62 ± 0.01	0.13 ± 0.01	0.07 ± 0.01
5	1.59 ± 0.01	0.16 ± 0.01	0.09 ± 0.01

To investigate the possible contribution of donor aggregation to the photocurrent, the absorption spectra of the NBTT:$PC_{71}BM$ devices are studied and compared with the neat $PC_{71}BM$ film. The

Table 9.9 Parameters extracted from the Gaussian fit of the CT state energy for the NBTT-Rho:$PC_{71}BM$ devices.

NBTT-Rho (wt%)	E_{CT} (eV)	ΔE_{HOMO} (eV)	λ (eV)
1	1.59 ± 0.01	0.16 ± 0.01	0.08 ± 0.03
2	1.57 ± 0.01	0.18 ± 0.01	0.1 ± 0.02
5	1.54 ± 0.01	0.21 ± 0.02	0.12 ± 0.02

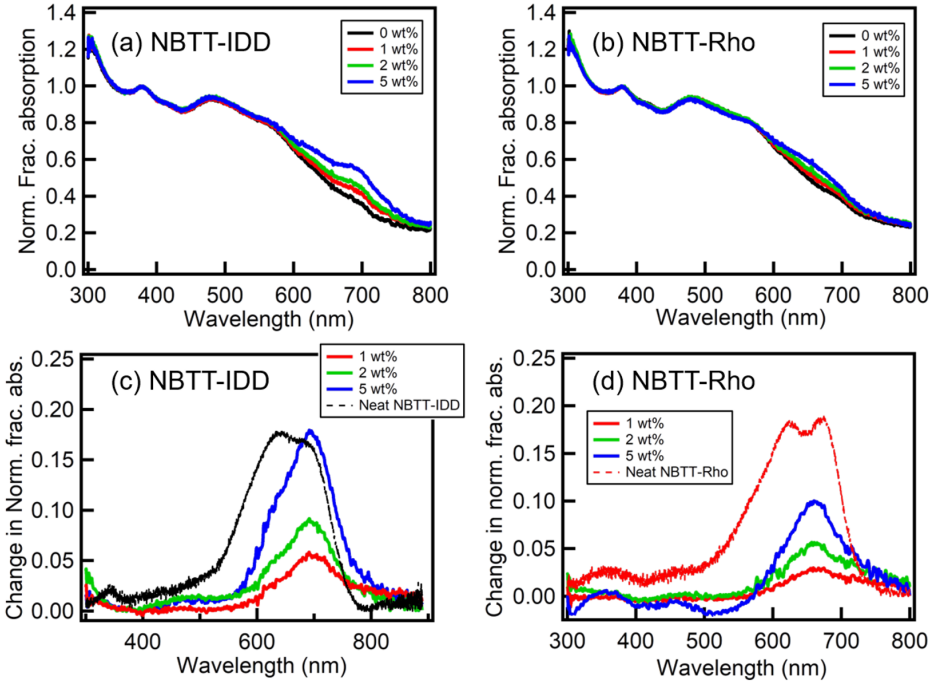

Figure 9.18 Fractional absorption spectra normalized at 380 nm of NBTT:$PC_{71}BM$ for (a) NBTT-IDD and (b) NBTT-Rho molecules with varying donor concentrations: 0 wt% (black), 1 wt% (red), 2 wt% (green), and 5 wt% (blue). The change in normalized fractional absorption of NBTT:$PC_{71}BM$ from neat $PC_{71}BM$ for (c) NBTT-IDD and (d) NBTT-Rho donors. The dashed line represents the fractional absorption of neat NBTT-IDD film (black) in (c) and neat NBTT-Rho film (red) in (d), respectively. Reprinted from [418] under the terms of the Creative Commons CC BY license.

fractional absorption spectra of NBTT-IDD:$PC_{71}BM$ and NBTT-Rho:$PC_{71}BM$ devices are shown in Fig. 9.18(a) and (b), respectively. To obtain the absorption contribution from donor, neat $PC_{71}BM$ absorption is subtracted from the dilute donor films (Fig. 9.18(c), (d)). The neat NBTT-IDD (NBTT-Rho) films show two absorption peaks at 645 & 690 nm (625 & 675 nm). For the NBTT-IDD:$PC_{71}BM$ devices, an increasing signal at ≈ 690 nm with higher donor concentration is observed, while the remaining spectrum remains constant. In the NBTT-Rho:$PC_{71}BM$ devices, a slight increase of the absorption below ≈ 660 nm is observed. The excess absorption from donor for the NBTT-IDD devices is more pronounced compared to the NBTT-Rho devices. Especially at 5 wt%, a strong peak in the absorption spectrum corresponding to the absorption edge of the NBTT molecules is visible for both the NBTT-IDD and NBTT-Rho devices. This observation indicates the possibility of donor aggregation which becomes more pronounced with increased donor concentration.

For the 5 wt% devices, J_{sc} of the NBTT-Rho:$PC_{71}BM$ devices is significantly higher than for NBTT-IDD:$PC_{71}BM$. Extracting the EQE at different wavelengths, one can distinguish the contribution of

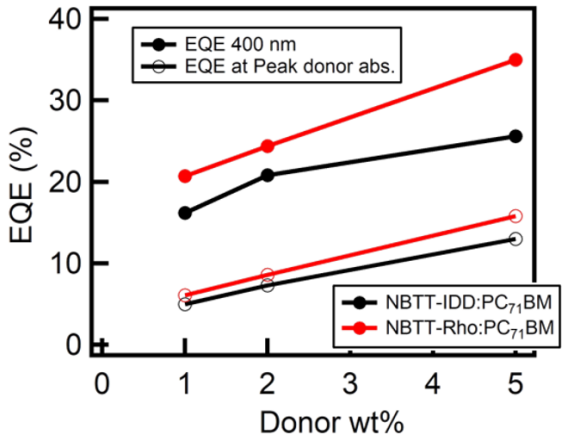

Figure 9.19 Comparison of the EQE between NBTT-IDD:$PC_{71}BM$ (red) and NBTT-Rho:$PC_{71}BM$ (black) devices as a function of the donor concentration. The filled symbols visualize the EQE extracted at 400 nm and the open symbols visualize the EQE at the peak of the donor absorption. Reprinted from [418] under the terms of the Creative Commons CC BY license.

excitons generated in the fullerene matrix and excitons generated in the donor molecules. Figure 9.19 shows the EQE for 400 nm and at the peak absorption of the donor molecules as a function of the donor concentration. EQE signals measured at the peak absorption of the donor molecules gives the efficiency of donor excitons in producing photocurrent, which show a linear increase with the donor concentration and are very similar for the two donor molecules. Even if NBTT-IDD appears to aggregate more, the aggregation does not appear to contribute to photocurrent. On the other hand, the EQE signals at 400 nm, which measure the photocurrent resulted from acceptor excitons arising from the strong absorption of $PC_{71}BM$, show a significant difference between the NBTT-IDD:$PC_{71}BM$ and the NBTT-Rho:$PC_{71}BM$ devices. For the NBTT-IDD:$PC_{71}BM$ devices, the EQE only slightly increases when going from 2 wt% to 5 wt%. The donor absorption signals have higher values in the NBTT-IDD absorption region (Fig. 9.18c), which can be explained by a stronger aggregation of the NBTT-IDD molecules, compared the NBTT-Rho absorption (Fig. 9.18d). Aggregation however can reduce the fraction of acceptor excitons, being generated in the fullerene matrix, that reach a donor:acceptor interface. This might explain the smaller increase in J_{sc} in the NBTT-IDD:$PC_{71}BM$ devices.

9.4.4 kMC Analysis of Hole Back Transfer

The experimental results show a sufficient generation of photocurrent for lowest donor concentrations of 1 wt% for both the NBTT-IDD and NBTT-Rho molecules. However, the experiments alone cannot reveal the origin of the photocurrent, especially for holes, for such low dilution. Kinetic Monte Carlo simulations [13, 182] are performed to investigate the origin of the hole transport for small molecule dilute donor OSCs using NBTT:$PC_{71}BM$ as our test system. Small molecule donors, modeled by 3 donor sites, are placed within the fullerene matrix using a self-avoiding random walk starting at random position in the simulation box. This mimics the high miscibility of NBTT molecules within the fullerene matrix.

First, the impact of the HOMO energy offset between $PC_{71}BM$ and the NBTT molecules on the short-circuit current density is studied. High short-circuit currents require the efficient separation of excitons at the donor:acceptor interface and the transport of both electrons and holes to the contacts. In

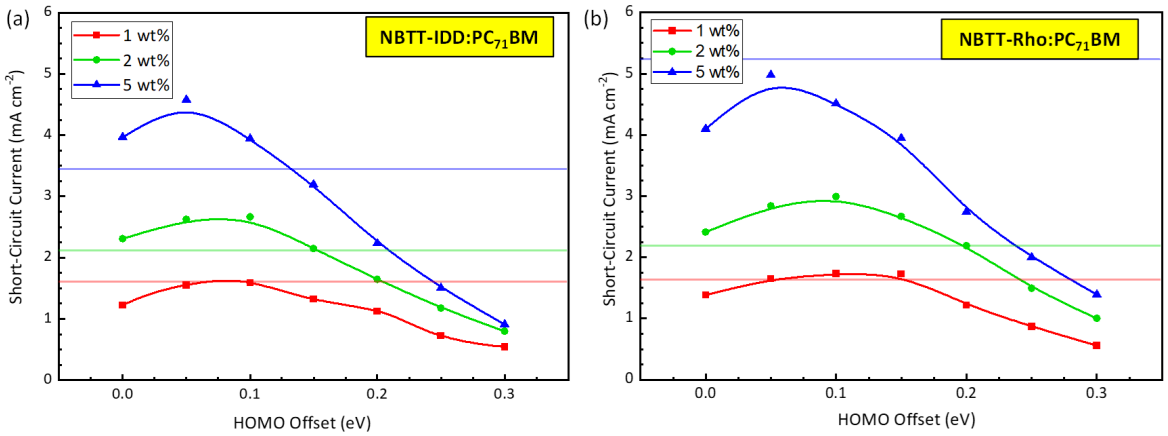

Figure 9.20 Short-circuit current density versus HOMO offset for (a) NBTT-IDD:$PC_{71}BM$, and (b) NBTT-Rho:$PC_{71}BM$ for 1 wt% to 5 wt%. The HOMO offset is defined by the difference in HOMO energies between the donor molecule and $PC_{71}BM$. The horizontal lines give the experimental results. The solid lines are basis spline interpolations for improved readability. Reprinted from [418] under the terms of the Creative Commons CC BY license.

the previous study by Albes *et al.*, the change of the HOMO level within amorphous P3HT with respect to crystalline P3HT has been used to explain the efficient hole back transfer in dilute donor OSCs [59]. However, that model did not account for the energy dependence of the separation rate of excitons. Here, the driving force is included within the separation rate using the Marcus equation [92,227]. This is of great importance as the reorganization energies for the given devices are significantly lower than for the P3HT:$PC_{71}BM$ devices. kMC calculations are performed by varying the HOMO offset while keeping the donor band gap fixed at 1.65 eV and 1.75 eV for NBTT-IDD and NBTT-Rho (see Fig. 9.14, Table 9.5), respectively. An energetic disorder of the molecular orbital energies of $\sigma = 75$ meV is assumed [446]. The reorganization energies are taken from the fits of the EQE measurements (Table 9.8 and 9.9). Hole back transfer from the donor to the fullerene matrix is the only mechanism of hole transport considered here.

Figure 9.20 shows the simulated short-circuit current densities as a function of the HOMO level offset (ΔE_{HOMO}) for (a) NBTT-IDD:$PC_{71}BM$ and (b) NBTT-Rho:$PC_{71}BM$. The horizontal lines show the experimental values of the J_{sc}. Compared to previous model that did not consider of exciton dissociation (Ref. [59], Fig. 4), J_{sc} is not constant at small ΔE_{HOMO}; instead, it decreases as ΔE_{HOMO} is lowered. This is reflected in the exciton dissociation efficiency, i.e. the fraction of excitons reaching and being dissociated at the interface, shown in Fig. 9.22a for the NBTT-IDD:$PC_{71}BM$ (solid lines) and the NBTT-Rho:$PC_{71}BM$ (dotted lines) devices. For $\Delta E_{\mathrm{HOMO}} < 0.1$ eV, the current is low because the driving force needs to be large enough to overcome the exciton binding energy of 0.15 eV, difference between the electrical (1.9 eV) and optical band gap (1.75 eV) [7,59], to allow an efficient transfer of holes from the fullerene matrix to the donor molecules. Increasing the HOMO offset increases the driving force for exciton dissociation, so the current increases as more excitons dissociate. The dependence of the dissociation efficiency on the HOMO offset is explained by the energy dependence of the electron transfer. Note that for donor:acceptor systems of higher HOMO offsets (larger driving forces), the Marcus rate might fail and the Marcus-Levich-Jortner expression needs to be used [227, 228]. For $\Delta E_{\mathrm{HOMO}} \geq 0.1$ eV, a decrease in the current density is observed because the HOMO offset presents an energy barrier for the holes to transfer back to fullerene matrix and transport to the anode. An increase in the energy barrier causes an exponential decrease in the

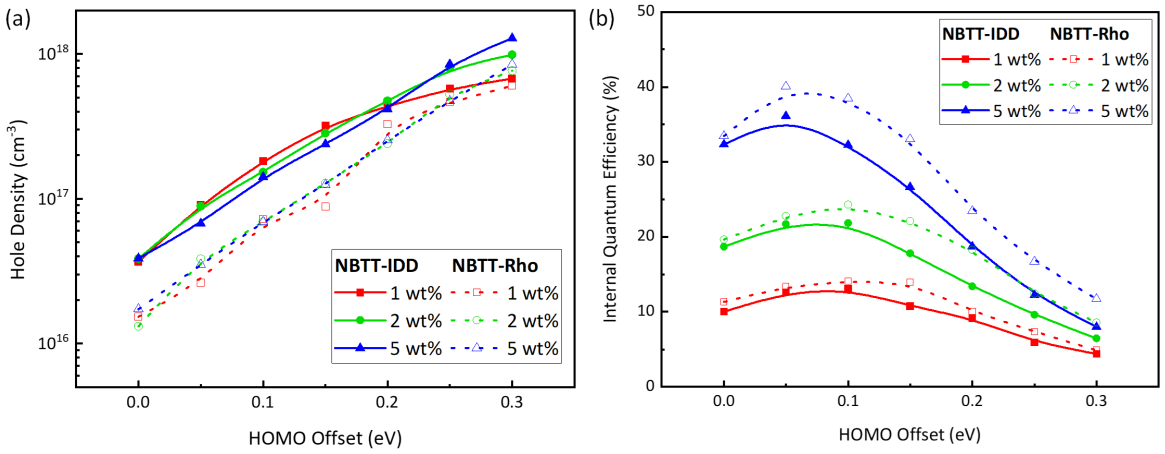

Figure 9.21 Simulation results of (a) average hole density, and (d) internal quantum efficiency versus HOMO offset. The solid lines (closed symbols) visualize the NBTT-IDD:$PC_{71}BM$ devices, dotted lines (open symbols) the NBTT-Rho:$PC_{71}BM$ devices. Reprinted from [418] under the terms of the Creative Commons CC BY license.

back-transfer rate. Consequently, holes are being trapped in the donor molecules. This leads to the increase in the density of holes in the system (see Fig. 9.21a) and recombination with electrons is enhanced [59]. Figure 9.22b visualizes the volume recombination rate R, defined as [59]:

$$R = \frac{N_{\text{rec}}^{\text{ngr}}}{\Delta t} \,. \tag{9.7}$$

$N_{\text{rec}}^{\text{ngr}}$ gives the number of electrons or holes participating in nongeminate recombination within the simulation time Δt. Increasing ΔE_{HOMO} enhances the barrier for the back transfer of holes to the fullerene matrix. Consequently, the hole density (see Fig. 9.21a) increases significantly from $10^{16}\,\text{cm}^{-3}$ to $10^{18}\,\text{cm}^{-3}$. As a result, the volume recombination rate increases for higher HOMO offsets due to the strongly enhanced hole density. For ΔE_{HOMO} above 0.1 eV, the dissociation efficiency saturates (Fig. 9.22a) while recombination of charge carriers increases (Fig. 9.22b), leading to a significant drop in the J_{sc} (Fig. 9.20). Between the discussed regimes, J_{sc} reaches peak values in the range of $\Delta E_{\text{HOMO}} = 0.050.15\,\text{eV}$.

Figure 9.20 also shows that the absolute values of the short-circuit current increase with the donor concentration, and the position of J_{sc} peak shifts to lower energy offsets with rising donor concentration. With increasing amount of donor material in the photoactive layer, the average distance for excitons from the locations of generation to a donor:acceptor interface decreases. This leads to more excitons reaching the interface which explains the increased dissociation efficiency.

Comparing the short-circuit currents obtained by our kMC study with experiments (Fig. 9.20), the HOMO level offsets which match the experimental current are extracted. For NBTT-IDD (-Rho):$PC_{71}BM$, the crossing points at high HOMO offsets are at 0.1 eV (0.16 eV) and 0.15 eV (0.2 eV) for 1 wt% and 2 wt% donor concentration, respectively. The values match very well with the HOMO offsets extracted from the CT state energies (see Table 9.8, 9.9). The increase in the HOMO offset can be explained by the increase in the reorganization energy. At 5 wt% donor concentration, our simulations predict a lower HOMO offset of 0.13 eV for the NBTT-IDD:$PC_{71}BM$ device than the experiments (0.16 eV). For NBTT:Rho-$PC_{71}BM$, J_{sc} does not reach the experimental values, especially towards high donor concentrations, the effect of aggregation of NBTT-IDD molecules may shift the energetic structure of the environment and enhance hole delocalization within aggregates.

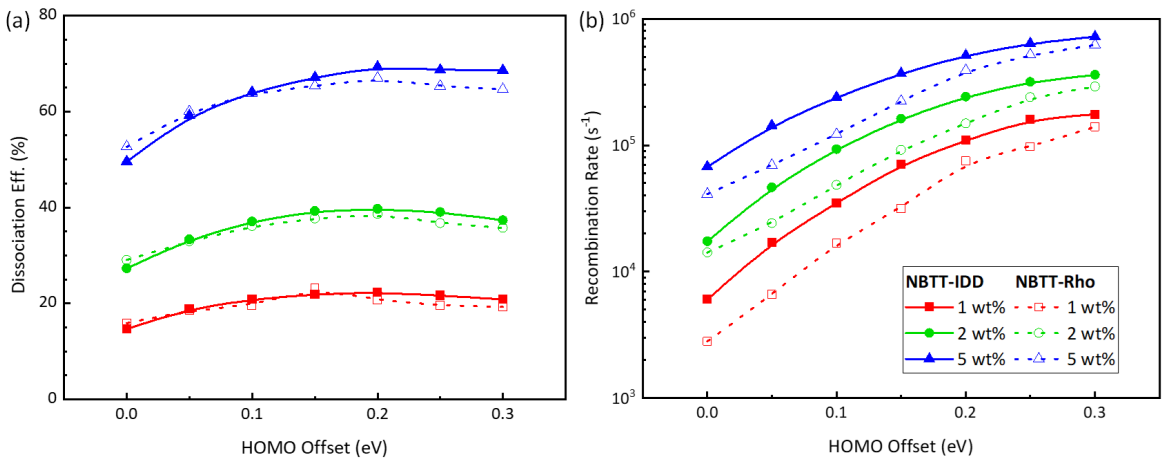

Figure 9.22 (a) Exciton dissociation efficiency and (b) volume recombination rate of charge carriers versus the HOMO offset extracted from kinetic Monte Carlo simulations. The solid lines (closed symbols) visualize the NBTT-IDD:$PC_{71}BM$ devices, dotted lines (open symbols) the NBTT-Rho:$PC_{71}BM$ devices.

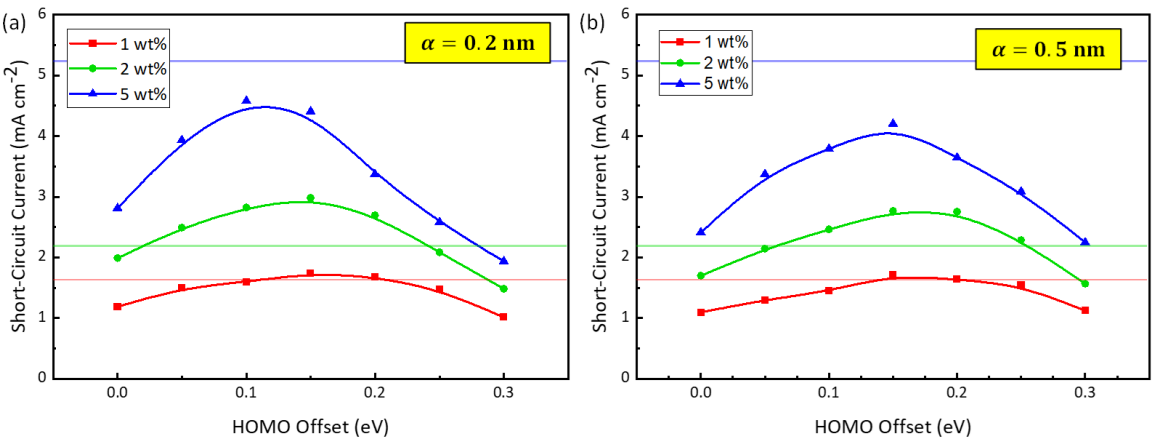

Figure 9.23 Short-circuit current density versus HOMO offset for (a) $\alpha = 0.2$ nm, and (b) $\alpha = 0.5$ nm for 1 wt% to 5 wt%. The HOMO offset is defined by the difference in HOMO energies between the donor molecule and $PC_{71}BM$. The horizontal lines give the experimental results. The solid lines are basis spline interpolations for improved readability. Experimentally measured reorganization energies of the NBTT-Rho:$PC_{71}BM$ are taken within the simulations. Reprinted from [418] under the terms of the Creative Commons CC BY license.

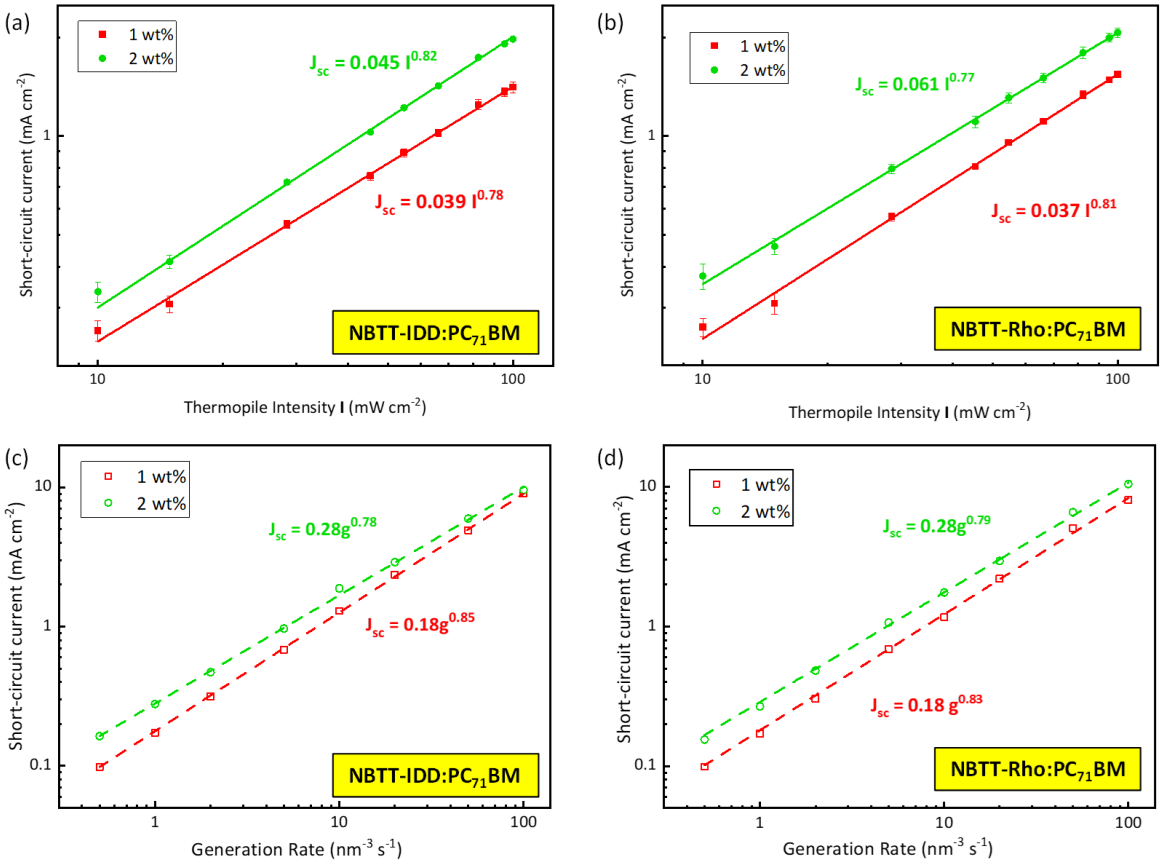

Figure 9.24 (a-b) Experimental measurements of the short-circuit current density versus light intensity for (a) NBTT-IDD:PC_{71}BM and (b) NBTT-Rho:PC_{71}BM with 1 wt% and 1 wt% donor concentration. Solid lines represent power law fits, with the values given in the inset. (c-d) Kinetic Monte Carlo simulation results of the short-circuit current density versus the generation rate for (c) NBTT-IDD:PC_{71}BM and (d) NBTT-Rho:PC_{71}BM. Reprinted from [418] under the terms of the Creative Commons CC BY license.

Surprisingly, significantly lower J_{sc} are observed in comparison to the P3HT:PC_{71}BM devices (2.5 mA cm^{-2}, ref. [59]) despite the reduced HOMO offset [59]. The energetic barrier for back transfer is significantly lower, i.e. $\approx$ 0.1 eV compared to $\approx$ 0.3 eV, which was expected to lead to higher J_{sc}. Our kMC study reveals that the difference in J_{sc} can only be explained by a significant difference in the localization of the charge carriers on the donor molecules. In P3HT, a localization length α = 0.5 nm has been observed [59]. For the NBTT-molecules, our kMC study predicts significantly lower α, i.e. stronger hole localization, of 0.1 nm (0.08 nm) for the NBTT-Rho (NBTT-IDD) molecules. In polymer donors, the conjugation length of the polymer chain strongly controls the localization of the molecular orbitals. It was shown that polymers of higher chain length have longer conjugation lengths [447]. As a result, molecular orbitals can delocalized across several conjugation lengths within polymers [448]. Forrest and coworkers showed that delocalized and localized CT states coexist in small molecule dilute-donor OSCs, mainly due to delocalization of the orbital wave functions in the fullerene phase [449]. Holes remain rather localized in the small molecule donors. Simulations with larger localization length α, i.e. holes less localized, show the experimental J_{sc} values are reached at higher HOMO offsets (Fig. 9.23).

The same J_{sc} values are observed in both the NBTT:PC_{71}BM devices despite the lower HOMO offset for 1 wt% and 2 wt% donor concentration for NBTT-IDD:PC_{71}BM. Our kMC simulation suggest that

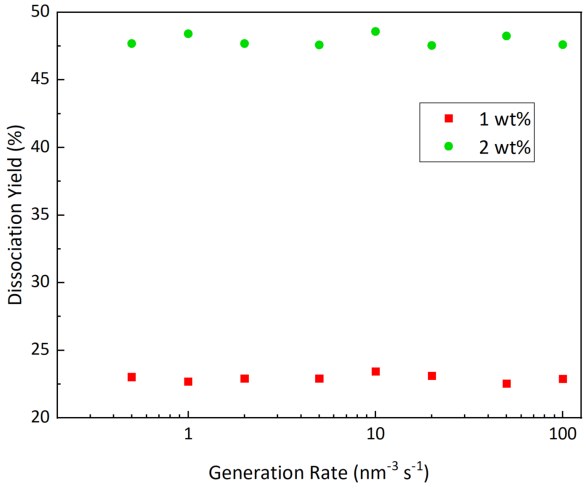

Figure 9.25 Dissociation yield vs. generation rate for the NBTT-Rho:$PC_{71}BM$ devices. Reprinted from [418] under the terms of the Creative Commons CC BY license.

this is due to (i) a stronger localization of the holes on the NBTT-IDD molecules ($\alpha = 0.08$ nm) than the NBTT-Rho molecules ($\alpha = 0.1$ nm) and (ii) a larger exciton dissociation at the NBTT-IDD:$PC_{71}BM$ interface enabled by the higher electron-withdrawing feature of the IDD group.

To further test our hypothesis of hole back transfer as the main transport mechanism for low dilution, the light intensity dependence of the short-circuit current density is studied. Hole back transfer strongly depends on the energy barrier and electrostatic interaction of charge carriers on the molecules. Thus, a non-linear dependence of the J_{sc} on the light intensity can be expected. In contrast, if hole transport occurs by tunneling, one expects a linear relation as the tunneling rate is mainly controlled by the distance between the molecules and the localization of the charge carriers.

Figure 9.24 represents the experimental (a-b) and simulation (c-d) results of the J_{sc} as a function of the light intensity. Power laws with an exponent of 0.78 (0.82) at 1 wt% (2 wt%) for NBTT-IDD and 0.81 (0.77) at 1 wt% (2 wt%) for NBTT-Rho are observed experimentally. Light intensity simulations are performed by applying a constant generation rate g across the photoactive layer with varying value. Simulations are run for the experimentally measured HOMO offsets (see Table 9.8 and 9.9) for NBTT-IDD and NBTT-Rho at 1 wt% and 2 wt% donor concentration. Note that the prefactor of the power law fits in experiment and simulation are expected to differ as the intensity of the thermopile and the generation rate are different quantities though they are proportional to each other. With the experimentally measured HOMO offset, kMC simulations predict power law exponents of 0.85 (0.78) and 0.83 (0.79) at 1 wt% (2 wt%) for the NBTT-IDD and NBTT-Rho devices, respectively. Figure 9.25 shows that the dissociation yield of excitons does not charge with the generation rate. Thus, the observed power law can only be explained by the back transfer of charge carriers. For the NBTT-Rho donor molecules, kMC results agree well with the experimental measurements. For the NBTT-IDD molecules, kMC slightly overestimates the exponents. The difference might be caused by the aggregation of donor molecules, which are neglected within these simulations. Overall, the resulting values are within the error margin of the experimental fits and parameter uncertainties of our model.

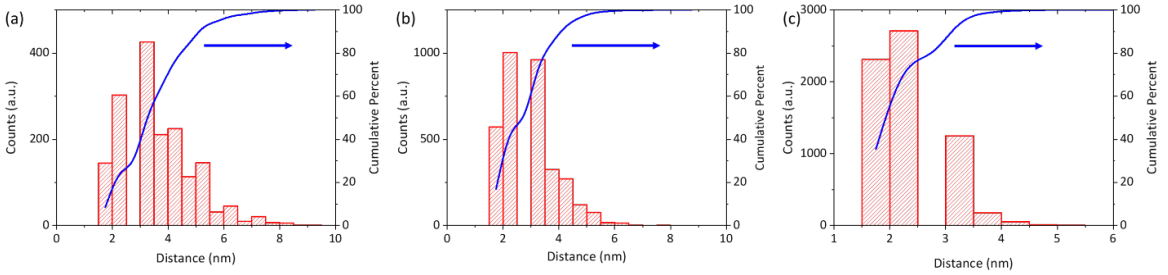

Figure 9.26 Radial distribution of donor molecules for (a) 1 vol%, (b) 2 vol%, and 5 vol%. The solid lines represent the normalized cumulative distribution. Reprinted from [418] under the terms of the Creative Commons CC BY license.

9.4.5 kMC Analysis of Long-Range Hopping

The physical origin of photocurrent in dilute donor organic solar cells with donor concentration below the percolation limit has drawn diverse proposals in recent publications [36, 59, 60, 431]. Most of the studies analyze dilute donor solar cells with donor concentrations of 5 wt% and higher, which cannot adequately answer the extreme dilution cases. Our analysis shows that a substantial photocurrent can be produced by the back transfer of holes from the small molecule donor to the fullerene matrix even for the lowest donor concentrations of 1 wt%. Once being back-transferred, holes can move through the acceptor matrix to the anode because fullerene is a known ambipolar semiconductor [59]. The simulated values of the short-circuit current density are in great agreement with the experimental measurements. The excellent match between simulation and experiment for the intensity dependence of the photocurrent further provides strong evidence for hole back transfer mechanism. Our simulations show an accurate fit of the short-circuit currents and of the intensity dependence for 1 wt% and 2 wt% at the same HOMO offset. At higher concentration (5 wt%), a shift in the crossing point of the kMC results with the experimental data towards lower HOMO offsets is observed (see Fig. 9.20).

To analyze the possible origin of this difference at larger donor concentrations, the distance between the NBTT molecules in the dilute donor cells is extracted. Figure 9.28a shows the cumulative radial distance distribution (CDF) between the NBTT molecules within the generated dilute donor OSCs. For each donor site n_i of molecule i, we calculate the minimum distance to a donor site m_j of molecule j, i.e. $d_{n_i} = \min_{k,m_k}(|r_{n_i} - r_{m_k}|_2)$. Periodic boundaries in x- and y-direction are taken into consideration. In Fig. S8, the distribution of distances is given for all donor concentrations. The CDF does not reach 100 % until past 6 nm for 1 wt%. For 2 wt%, the CDF reach 100 % at $\approx$ 5 nm, and for 5 wt% already at $\approx$ 3.5 nm. Melianas *et al.* have reported long-range tunneling of holes through a several fullerene molecules of up to 4 nm [36]. At 1 (2, 5) wt% donor concentration, there is 70 (90, 100)% probability of a donor molecule located within 4 nm of another donor molecule. Thus, long-range tunneling is not likely to contribute to hole transport for low donor concentrations of 1 wt% and 2 wt%, but might contribute to the short-circuit current at 5 wt% donor concentration.

While the discussed ranges for long-range tunneling might be possible in theory, recombination needs to be considered as a limiting factor for the lifetime of the holes. To investigate the possibility of hole transport via long-range tunneling, the kMC code is modified to allow long-range hopping across distances of up to a variable range hopping distance $r_{\mathrm{VRH}} = 4$ nm and eliminate hole back transfer to the fullerene phase. The concept of long-range hopping was studied previously by Bässler [29]. Recombination of charge carriers is allowed if electrons and holes meet on adjacent sites. Figure 9.27 shows a scheme to visualize the idea behind the long-range hopping with maximal distance r_{VRH}. The hopping rate of holes is scaled with $exp(-2r\alpha^{-1})$, with the localization length α and the distance r.

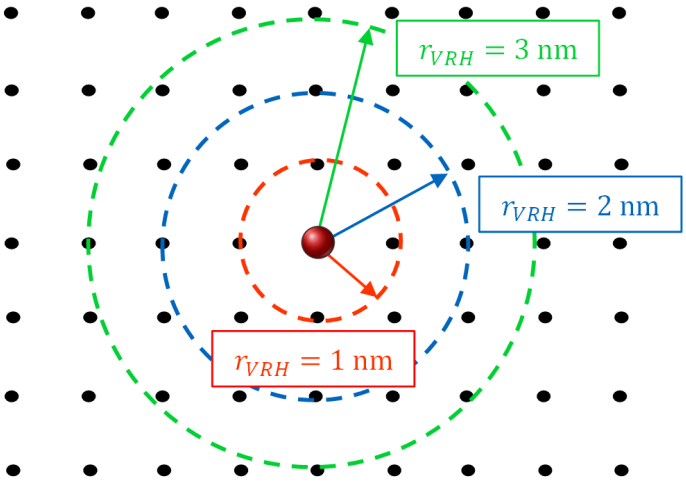

Figure 9.27 Schematic representation of the long-range hopping model. All sites within a distance of r_{VRH} are considered as possible neighbors for the long-range hopping of the charge, depicted by the red ball. Reprinted from [418] under the terms of the Creative Commons CC BY license.

The number of available sites, and with this the computational demand, scales with r_{VRH} by the power of three. Thus, r_{VRH} is limited at 4 nm to account for as many sites as possible while keeping the simulation times reasonable. Now, as hole back-transfer is eliminated, the only need for the HOMO offset is to separate excitons. The experimentally measured E_{CT} and λ for the NBTT-Rho:$PC_{71}BM$ device are used within the simulations.

Figure 9.28b shows the simulated short-circuit current densities versus localization length α for different donor concentrations with $r_{\mathrm{VRH}} = 4\,\mathrm{nm}$. For 5 wt% donor concentration, the simulations show significant current densities exceeding the experimental values for $\alpha \geq 0.7\,\mathrm{nm}$. In this range, hole transport by long-range hopping within the photoactive layer is possible. This is in line with previous literature [36, 60, 427]. Melianas *et al.* used $\alpha = 1\,\mathrm{nm}$ to explain hole transport by tunneling within α-6T:C_{60} dilute donor OSCs [36]. Towards lower localization lengths, a strong decrease in J_{sc} is observed. For $\alpha = 0.1\,\mathrm{nm}$, tunneling only results in a J_{sc} of $0.49\,\mathrm{mA\,cm^{-2}}$. Towards lower donor concentrations, hole transport via long-range hopping is strongly suppressed. For 1 wt% and 2 wt%, the experimental short-circuit current density is not reached even for the highest localization length α of 1 nm. Maximum J_{sc} of $0.32\,\mathrm{mA\,cm^{-2}}$ ($1.60\,\mathrm{mA\,cm^{-2}}$) are observed for 1 wt% (2 wt%) donor concentration. For these donor concentrations, long-range hopping cannot explain the observed current densities. At 1 wt%, only 70 % of all donor molecules have another donor molecule within distances of 4 nm. This suppresses hole transport and enhances recombination tremendously. Above, a localization length of $\alpha = 0.1\,\mathrm{nm}$ was extracted. In such strong localization, long-range hopping clearly cannot explain the experimental observations. Even for 5 wt%, one requires a high α to explain the J_{sc}. The latter cannot be excluded, as aggregation of NBTT molecules may increase α.

Note that changes in morphology as another degree of freedom which may change the picture of hole transport at high wt% due to increasing donor aggregation have been neglected. Previous studies have shown the formation of column-like percolation paths at high donor concentrations of 10 wt% [432]. However, NBTT was shown to preferentially cluster with fullerene due to the strong coupling of the aligned sulfur atoms with $PC_{71}BM$ molecules [443]. Thus, one can expect that percolation paths occur at donor concentrations of 1 wt% and 2 wt%.

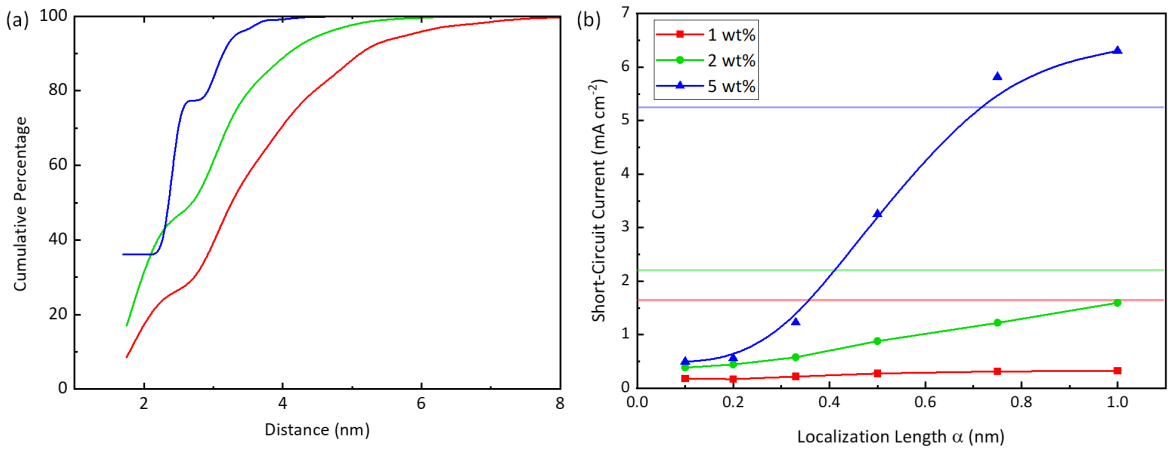

Figure 9.28 (a) Cumulative radial distance distribution of NBTT molecules within the generated dilute donor morphologies at 1 wt% (red), 2 wt% (green) and 5 wt% (blue). (b) Short-circuit current density versus localization length α with suppressed hole back transfer. Horizontal lines give the experimental short-circuit currents of the NBTT-Rho:$PC_{71}BM$ devices. Reprinted from [418] under the terms of the Creative Commons CC BY license.

9.5 Conclusion

In conclusion, the origin of photocurrent in dilute donor OSCs is analyzed for polymer donor materials (P3HT) and small molecules donors (NBTT) and $PC_{71}BM$ as the acceptor material.

For P3HT:$PC_{71}BM$ dilute donor OSCs, hole back transfer to the fullerene matrix as well as percolation along polymer chains were considered. It was shown that back transfer explains the observable short-circuit current densities. Percolation becomes the dominant contribution for large donor concentrations and high HOMO offsets. In addition, the role of the polymer morphology was highlighted. The detailed arrangement of the polymers, especially if aggregation is possible, strongly alters the preferred migration pathways. Thus, additional studies using small molecule donors were performed.

NBTT molecules were synthesized, which show a favorable mixing with $PC_{71}BM$ with reduced phase segregation between the donor and the acceptor at low concentrations. Kinetic Monte Carlo simulations were performed to study the photocurrent at short-circuit condition for 1 to 5 wt% donor concentration assuming (a) hole back transfer and (b) long-range hopping as possible transport mechanisms. At the lowest donor concentrations of 1 wt% and 2 wt%, the simulations using hole back transfer, taking into account of exciton dissociation probability, match the experimental values of the current density as well as the dependence of the current density on the light intensity. In contrast to previous studies on P3HT:$PC_{71}BM$, significant reduction in HOMO offset and current-densities are observed. kMC simulations showed that this is due to higher hole localization on the small-molecule donors. In previous studies, only the HOMO offset has been considered as a barrier for hole back transfer. Our results strongly emphasize that hole localization is another important property to be considered for an efficient hole back transfer.

For 5 wt% donor concentration, kMC simulations of the hole-back transfer show lower current densities than expected, which indicate possible contribution from long-range hopping. The average distance between the isolated donor molecules shrinks to 2-3 nanometers at 5 wt%, which makes long-range hopping feasible. kMC simulations with long-range hopping between donor molecules and suppressed hole back transfer show sufficient photocurrent generation at 5 wt% for localization lengths beyond $\alpha = 0.5$ nm. For lower donor concentrations, even high delocalization cannot reproduce the

experimental J_{sc}. This chapter demonstrates that both hole back transfer and tunneling / long-range hopping are required to explain the photocurrent. For lowest concentrations (< 5 wt%), the back transfer of holes to the fullerene matrix dominates. Towards larger concentrations, both long-range hopping and back transfer can contribute to the photocurrent.

10 Conclusion

Several aspects of organic semiconductors and organic solar cells have been addressed within this thesis. The existing kMC model [52] was extended with an improved representation of the amorphous organic semiconductors by the usage of the Voronoi tessellation. Additionally, improved models for charge carriers and excitons, especially the implementation of singlet and triplet dynamics, make the developed kMC model a versatile tool for simulating a broad spectrum of device properties and physical characteristics of organic semiconductors and organic solar cells.

The implementation of the Voronoi tessellation enabled the integration of the kMC model within a multiscale framework for the simulation of charge carrier mobilities for realistic organic thin-film morphologies. The role of the energetic disorder and especially of correlations within the disorder on the charge carrier mobility were studied. Simulations based on correlated energetic disorder showed a formation of filament-like current densities within regions of low molecular orbital energies. Moreover, a negative field dependence of the mobility with enhanced energy correlations was observed. The role of the spatial disorder was studied within (i) disordered pentacene crystals and (ii) amorphous pentacene thin films. The simulations revealed anisotropic carrier mobility within both systems. The developed model allows a fast calculation of charge carrier mobilities starting from the molecular arrangement with the Voronoi tessellation acting as the bridge between the microscopic and macroscopic worlds.

To accelerate kMC simulations, a sophisticated acceleration scheme has been developed. The presented scheme detects possible superbasins, which are trapping the system state within a small region of the available phase space, and derives adequate scaling factors depending on the physical escape rates out of the superbasin. High speed-up in CPU times is achieved while keeping the error negligibly low.

The developed model for singlet and triplet dynamics allows us to study exciton losses and analyze the possibility of enhancing exciton lifetimes using phosphorescent sensitizers. The model predicts a significant increase in lifetime and diffusion length, while triplet–triplet annihilation and shortened triplet lifetimes in the presence of the phosphorescent sensitizers act as loss mechanisms. These results help to explain previous experimental studies on the use of PS within organic solar cells. Furthermore, consideration of triplet states is crucial for blends of low energy offset. In such systems, charge transfer states may recombine into the triplet state and lead to a loss mechanism.

The role of the donor:acceptor interface on the losses in the open-circuit voltage of bulk-heterojunction OSCs has been studied theoretically for the first time using kMC. The kMC model has been adapted to track the occupied density of states. The maximum open-circuit voltage was obtained from the difference in quasi-Fermi levels, which only considered the internal blend without any undesired impact of electrodes. The results underline the dominance of the interface energetics in the open-circuit voltage. Additionally, it was proposed that an increase in the correlation of the energetic DOS can reduce the voltage losses by far.

A novel non-equilibrium description of the free energy barrier during the separation process of CT states was developed. The propagation of CT states within the phase space spanned by CT energies and mean distance was solved with the master equation. The time-dependent probabilities were used to calculate the transient free energy, entropy, and average energy. The time evolution of the average energy captures the relaxation dynamics of CT states within the energetic DOS. Interestingly,

a significant change in entropy during the CT separation process was observed. Initially, the entropy increased as more CT states were accessible. For longer timescales, a decrease in entropy was observed due to the relaxation of CT states towards the lower energetic states. This allows bridging the kinetics with the thermodynamics of CT separation.

Finally, the origin of hole transport within dilute-donor OSCs has been presented. This is relevant for an understanding of the physical mechanism of charge transport within mixed and isolated phases in the complex heterostructure morphology of OSCs. First, the importance of the polymer morphology was presented. Even if smallest amounts of percolation paths exist, holes can be transported to the contacts by percolation. The results especially highlight the important role of controlling the polymer morphology in dilute donor OSCs. Afterward, the current density was analyzed within a joint experimental-theoretical study within polymer-based dilute donor OSCs, using P3HT:$PC_{71}BM$, and within small molecule-based dilute donor OSCs, using NBTT:$PC_{71}BM$ with novel synthesized NBTT small molecules. The results show clear evidence of back transfer of holes from the donor molecules/polymers to the fullerene matrix. Tunneling could be ruled out for donor concentrations below 5 wt%. For higher donor concentrations, tunneling can contribute significantly to the transport of holes. On top of that, the significance of the hole localization for the back transfer properties has been highlighted. High localization of holes in the small molecule dilute donor was observed, which questions transport by tunneling even more.

In summary, the achievements in the presented thesis open many novel possibilities in terms of multiscale simulations and excited-state dynamics not only for OSCs but also for other optoelectronic devices such as OLEDs or organic thin-film transistors. Moreover, studies of the energy losses in the open-circuit voltage and the management of exciton losses by intersystem crossing allow new insight into the device physics and may shape future research in this direction. The developed non-equilibrium thermodynamic description of the CT separation process will help to understand the role of the CT separation dynamics and all contributing factors such as disorder, delocalization, and dimensionality on the free energy and entropy during the separation process. Furthermore, the method can be easily applied to other processes which are described by a Markovian dynamics. Finally, novel insight into the transport of charge carriers in dilute donor OSCs has been gained by joint experimental-theoretical efforts. This will help to understand the origin of photocurrent not only in dilute donor OSCs, but also in mixed and isolated phases of bulk-heterojunction OSCs.

A Supplementary Information on 'Acceleration Scheme for Particle Transport in KMC Methods'

A.1 Pseudocodes

Algorithm 1: calc_local_critical_branches

```
foreach state i in lattice do
    get position of state i;
    find maximal escape rate k_es from state i;
    get position of state j according to direction of k_es;
    store hopping channel in auxiliary vector lv;
    mark escape/critical branches;
    mark local critical branches;
    calculate critical process probability p_c and flux vector f ;
    if p_c > ξ then
        add_maximal_escape_flux();
    else
        continue;
    end
end
```

Algorithm 2: add_maximal_escape_flux

```
while true do
    find maximal escape flux f_es of hopping transitions;
    get position of state k according to direction of f_es;
    add state k to auxiliary vector lv;
    update escape/critical branches;
    update local critical states;
    save old critical process probability: p'_c = p_c;
    update critical process probability p_c and flux vector f ;
    calculate change in critical probability: Δp_c = p_c − p'_c;
    if Δp_c > 0 then
        continue;
    else
        if p'_c > ξ then
            store expanded hopping channel in lattice;
        end
        break;
    end
end
```

Algorithm 3: apply_scaling

```
1  if (α_l == 1 and α_g == 1) then
2  |  do nothing
3  else if α_l > 1 then
4  |  foreach transition k do
5  |  |  if k is local critical branch then
6  |  |  |  scale with α_l
7  |  |  else
8  |  |  |  do nothing
9  |  |  end
10 |  end
11 else if α_g > 1 then
12 |  repeat lines 4-12 with α_l → α_g and local→global
13 else
14 |  do nothing
15 end
```

Algorithm 4: update_scaling

```
1  if n^g_SB > 0 then
2  |  /* Global superbasins exist */
3  |  set global superbasin index idx_g;
4  |  if entered new global SB? then
5  |  |  initialize superbasin counters for charge carrier;
6  |  end
7  |  if idx_g> 0 then
8  |  |  increment N_sightings(idx_g);
9  |  |  calculate N_fg,limit(idx_g)= N_fg,limit(α_max(idx_g),m(idx_g));
10 |  |  if N_sightings(idx_g)> N_fg,limit(idx_g) then
11 |  |  |  m(idx_g)++;
12 |  |  |  calculate new α_g;
13 |  |  end
14 |  end
15 |  if charge left SB and no neighbor is globally critical then
16 |  |  reset N_sightings;
17 |  |  reset m(idx_g);
18 |  |  set α_g = 1;
19 |  end
20 end
21 if n^l_SB > 0 then
22 |  /* Local superbasins exist */
23 |  repeat lines 2-19 with α_g → α_l and global→local;
24 end
```

A.2 Analysis of the scaling for SIM1

A.2.1 Simulation Times

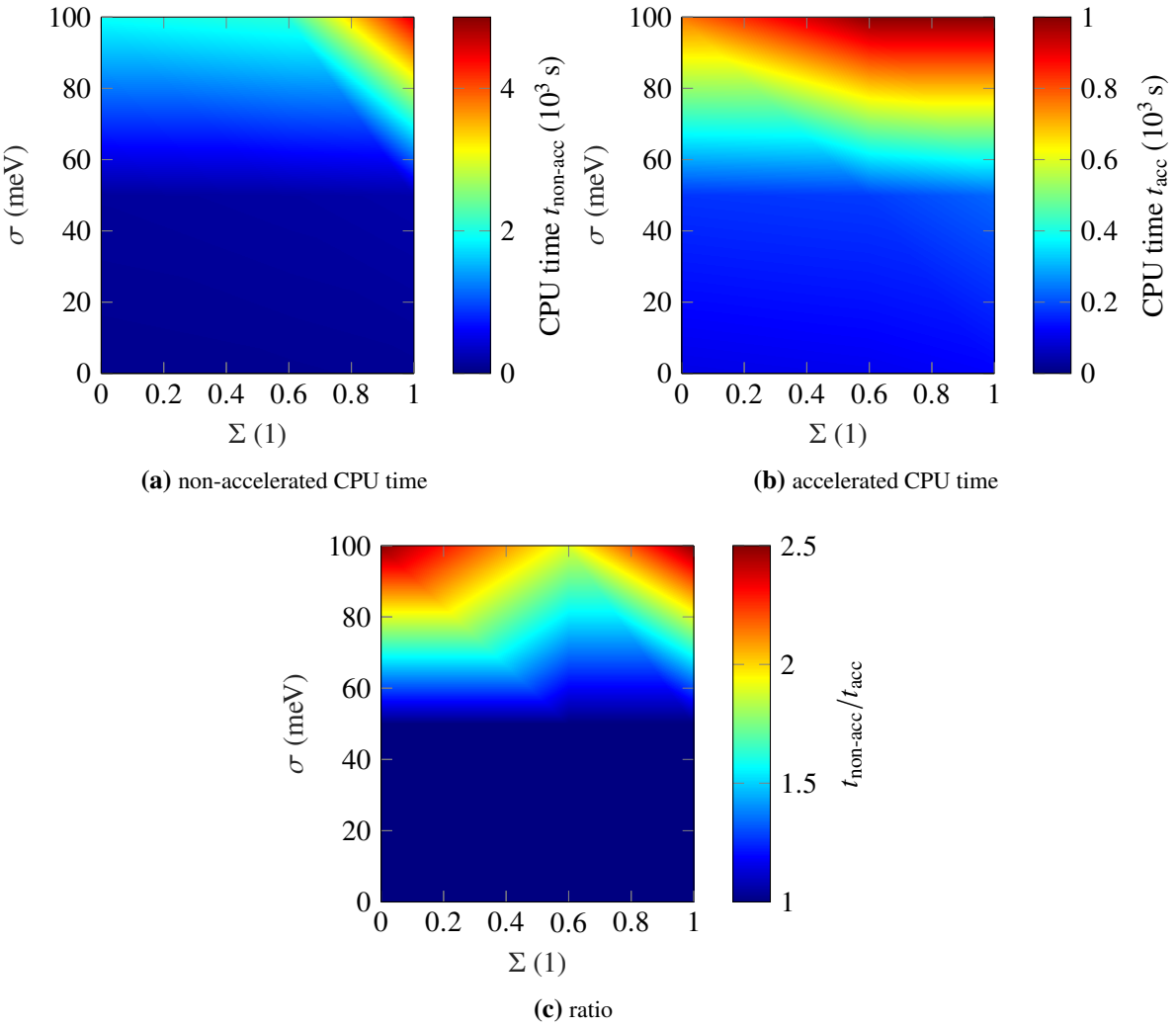

(a) non-accelerated CPU time

(b) accelerated CPU time

(c) ratio

Figure A.1 Cumulated CPU times for the mobility curve (100 time-of-flights per voltage point) with (a) the non-accelerated and (b) the accelerated kinetic Monte Carlo simulations. (c) Ratio between non-accelerated to accelerated simulation times. Used scaling parameters: $\xi = 0.75$, $\delta = 0.2$, $\kappa = 2$. Reprinted from [233], with the permission of AIP Publishing.

A.2.2 Sensitivity

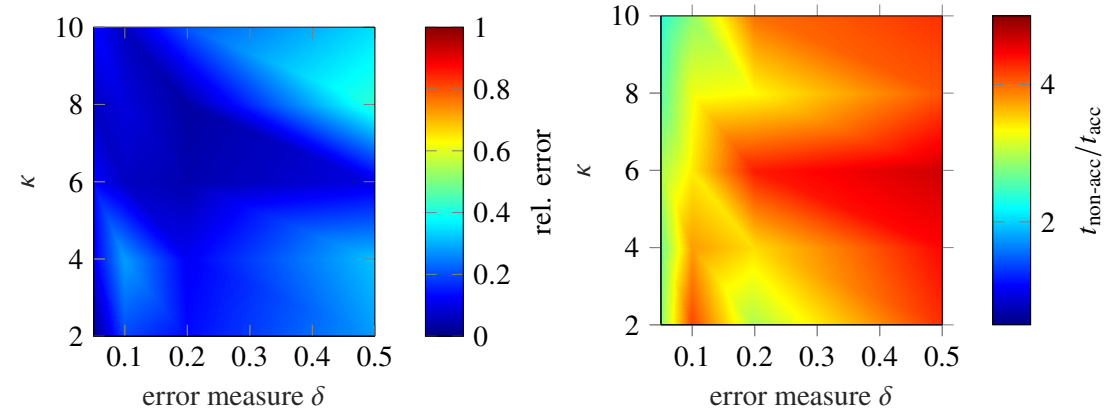

(a) $\xi = 0.75$

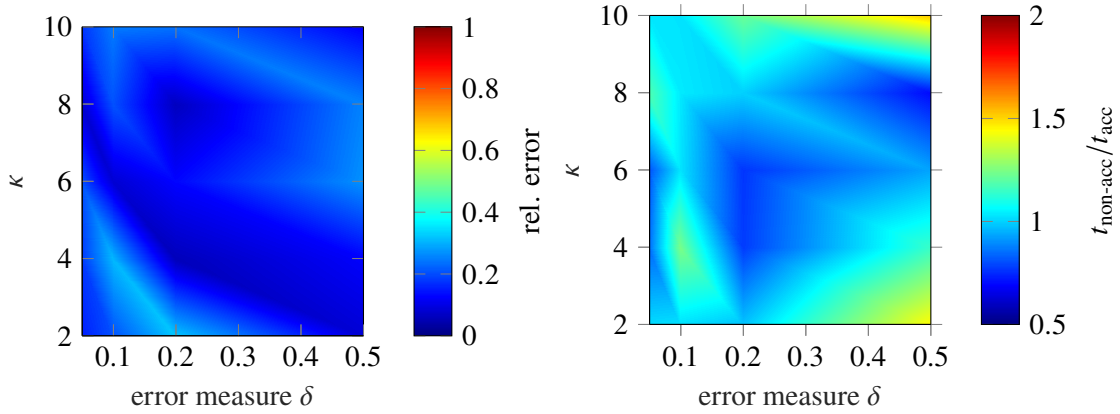

(b) $\xi = 0.85$

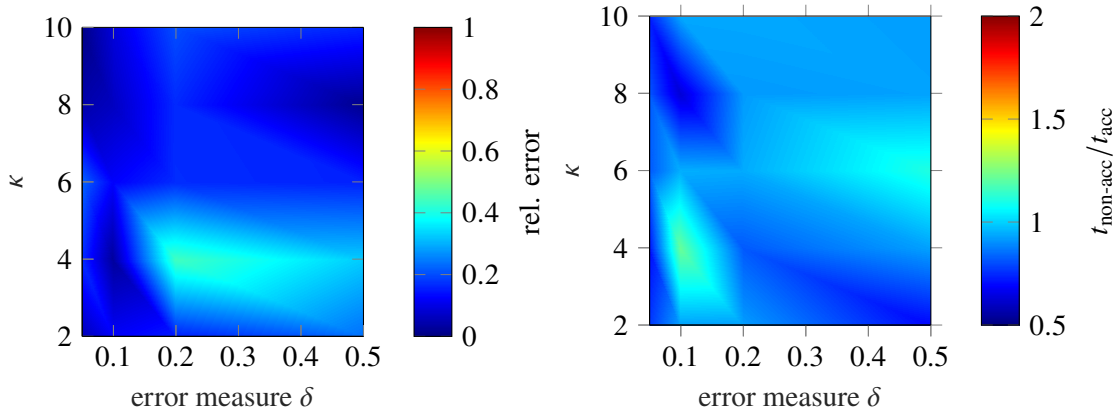

(c) $\xi = 0.95$

Figure A.2 (Left) Relative error of the average time-of-flight t_{TOF} in the accelerated with respect to the non-accelerated simulations. (Right) Acceleration in CPU times within the acceleration scheme for calculating the full mobility curve for 100 TOFs at each voltage point. The axis show the error measure δ and the scaling parameter κ. Reprinted from [233], with the permission of AIP Publishing.

A.3 Analysis of the scaling for SIM2

A.3.1 Simulation Times

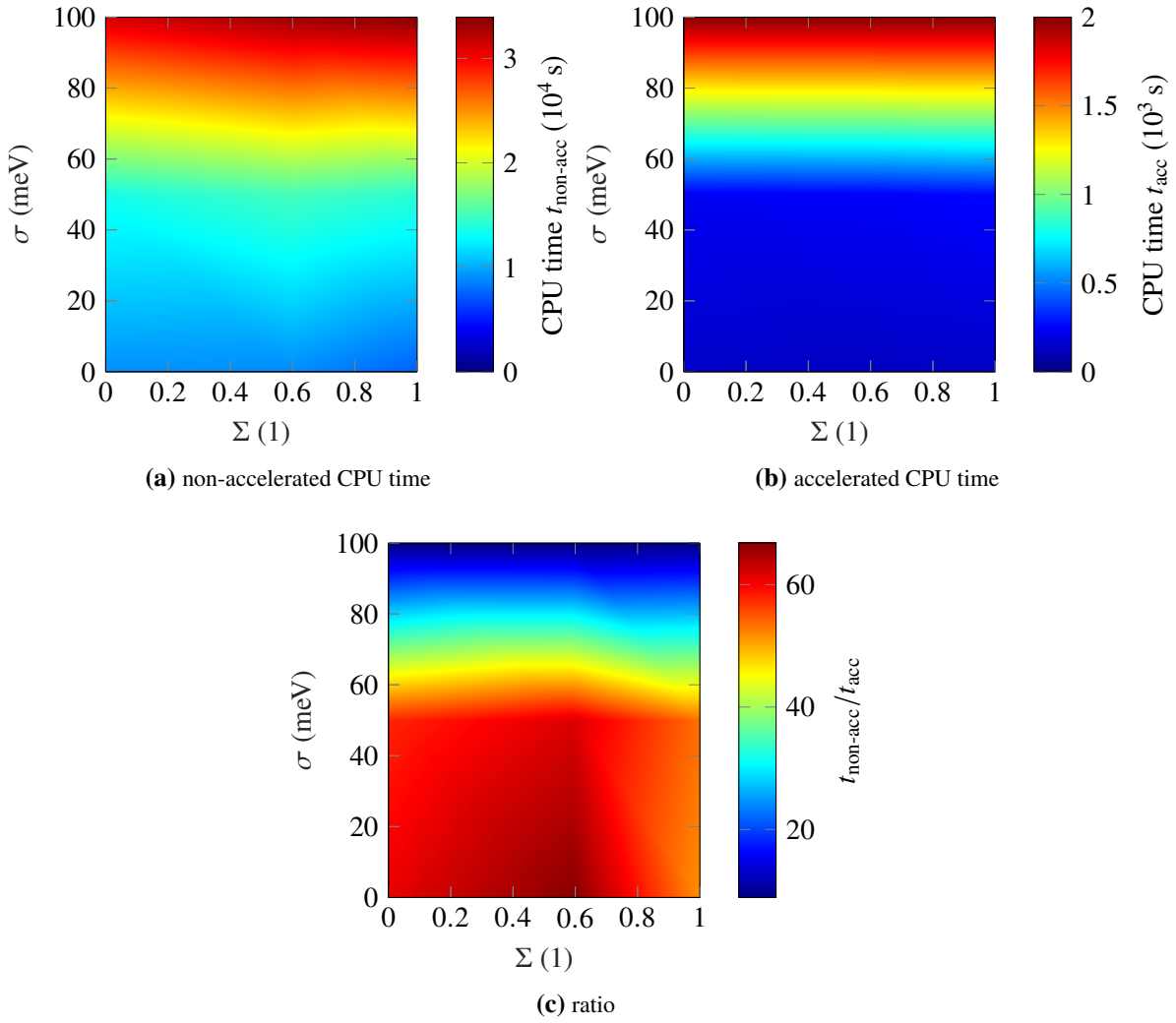

(a) non-accelerated CPU time

(b) accelerated CPU time

(c) ratio

Figure A.3 Cumulated CPU times for the mobility curve (100 time-of-flights per voltage point) with (a) the non-accelerated and (b) the accelerated kinetic Monte Carlo simulations. (c) Ratio between non-accelerated to accelerated simulation times. Used scaling parameters: $\xi = 0.75$, $\delta = 0.2$, $\kappa = 2$. Reprinted from [233], with the permission of AIP Publishing.

A.3.2 Sensitivity

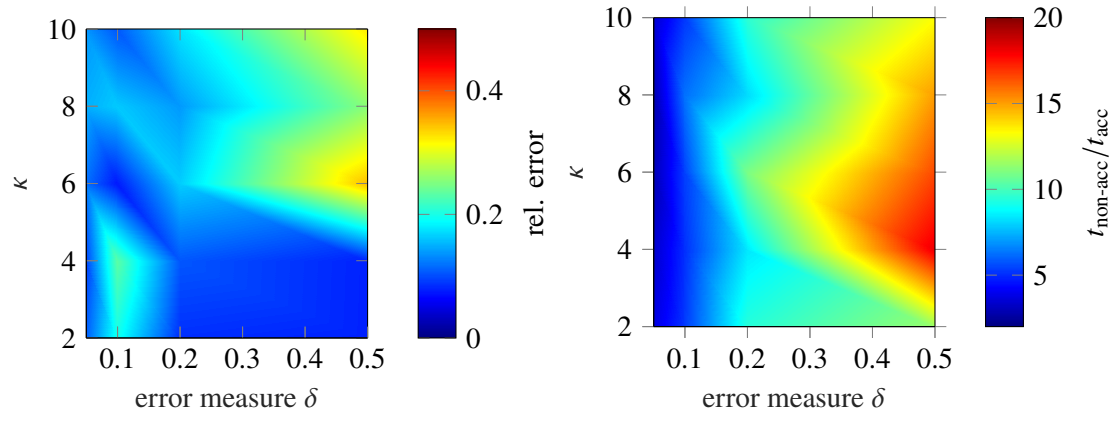

(a) $\xi = 0.75$

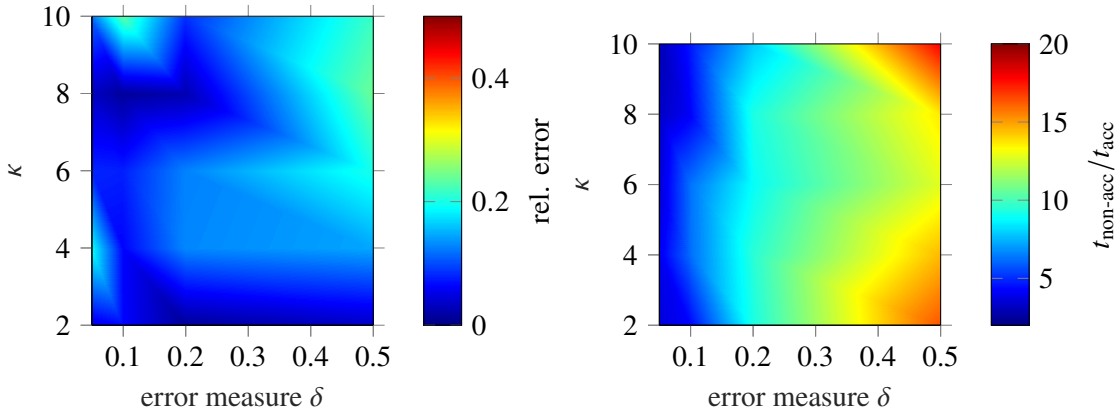

(b) $\xi = 0.85$

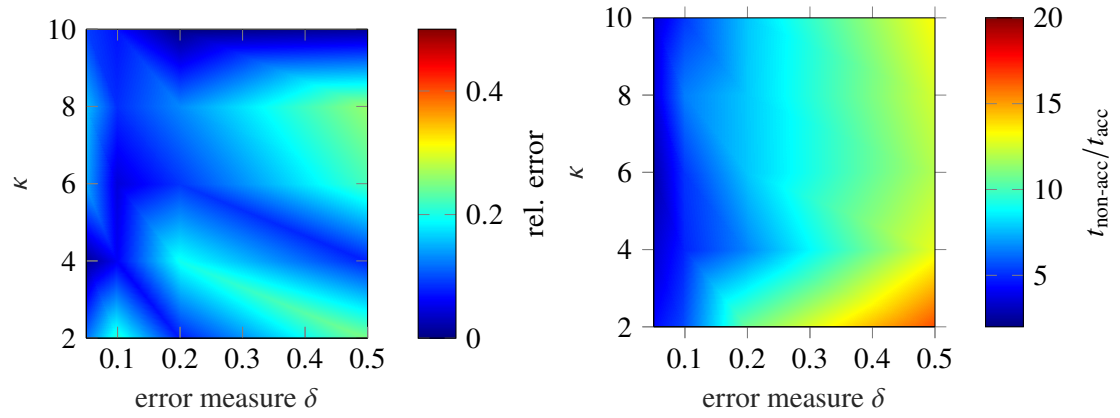

(c) $\xi = 0.95$

Figure A.4 (Left) Relative error of the average time-of-flight t_{TOF} in the accelerated with respect to the non-accelerated simulations. (Right) Acceleration in CPU times within the acceleration scheme for calculating the full mobility curve for 100 TOFs at each voltage point. The axis show the error measure δ and the scaling parameter κ. Reprinted from [233], with the permission of AIP Publishing.

B Supplementary Information on 'Role of Energetic Disorder on the Open-Circuit Voltage in Organic Solar Cells'

B.1 Mobility simulation

We simulate the mobility of charge carriers within a single material system for different electric fields and energetic disorders using our kinetic Monte Carlo model [50]. It is well known that the charge transfer integral V_{ij} is strongly dependent on the overlap of the molecular orbitals. In a simplified picture, the orientation-dependence of charge transfer integral is reduced by assuming an isotropic value. We calibrate V_{ij} to obtain a charge carrier mobility of $10^{-4}\,\mathrm{cm^2\,V^{-1}\,s^{-1}}$ at $\sigma = 75\,\mathrm{meV}$ within our kMC simulation box of 1 nm lattice spacing. A good match with the target mobility is given by a combination of the transfer integral $V_{ij} = 1.5\,\mathrm{meV}$ and reorganization energy $\lambda = 0.2\,\mathrm{eV}$, as listed in Table 1 of the main manuscript.

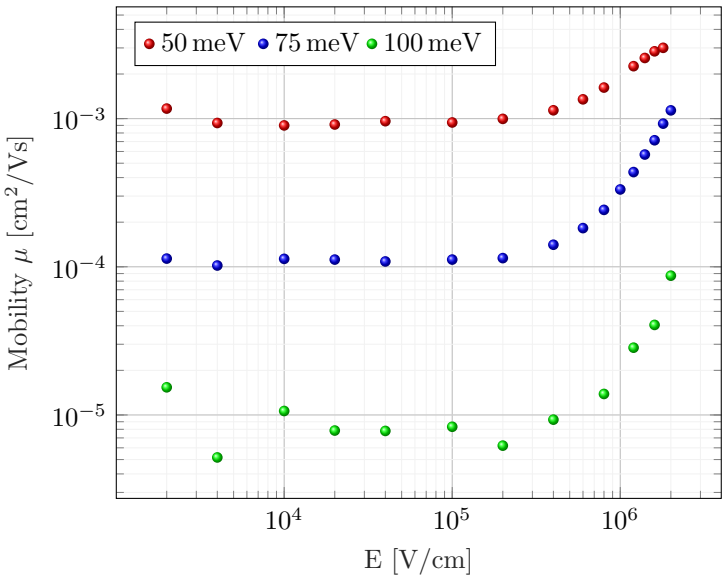

Figure B.1 Charge carrier mobility for different energetic disorder. Reprinted with permission from [350]. Copyright (2020) American Chemical Society.

The simulation results of the mobility are shown in Fig B.1. For $\sigma = 75\,\mathrm{meV}$, a mobility of $1.1 \times 10^{-4}\,\mathrm{cm^2\,V^{-1}\,s^{-1}}$ is obtained. For higher (lower) disorder of 100 meV (50 meV), the charge mobility decreases (increases) to $\approx 10^{-5}\,\mathrm{cm^2\,V^{-1}\,s^{-1}}$ ($10^{-3}\,\mathrm{cm^2\,V^{-1}\,s^{-1}}$). The mobility stays constant over a large range of electric fields up to $\approx 2 \times 10^5\,\mathrm{V\,cm^{-1}}$, before a substantial increase is observed. Here, the transport of charge carriers becomes drift-dominated, and the impact of the energetic disorder decreases. These mobilities match the experimentally observed values for regio-regular P3HT by Mauer *et al.* [450]. They observed a mobility of $\approx 2 \times 10^{-4}\,\mathrm{cm^2\,V^{-1}\,s^{-1}}$ at room temperature, which

matches to a disorder of 58 meV according to the Gaussian disorder model. In addition, a weak field-dependence has been found up to electric fields of $1.2 \times 10^5\,\mathrm{V\,cm^{-1}}$, higher fields were not examined within their analysis. A review of Laquai *et al.* summarizes several studies of charge carrier mobilities in pristine P3HT and PCBM as well as within P3HT:PCBM blends [451]. Most reported mobility values are in the range of $10^{-5}\,\mathrm{cm^2\,V^{-1}\,s^{-1}}$ to $10^{-3}\,\mathrm{cm^2\,V^{-1}\,s^{-1}}$, while the exact values strongly depend on the processing conditions as well as the regio-regularities and molecular weights of the used polymers.

B.2 Input Gaussian DOS

Figure B.2 depicts the input Gaussian density of states (DOS) and the occupied states.

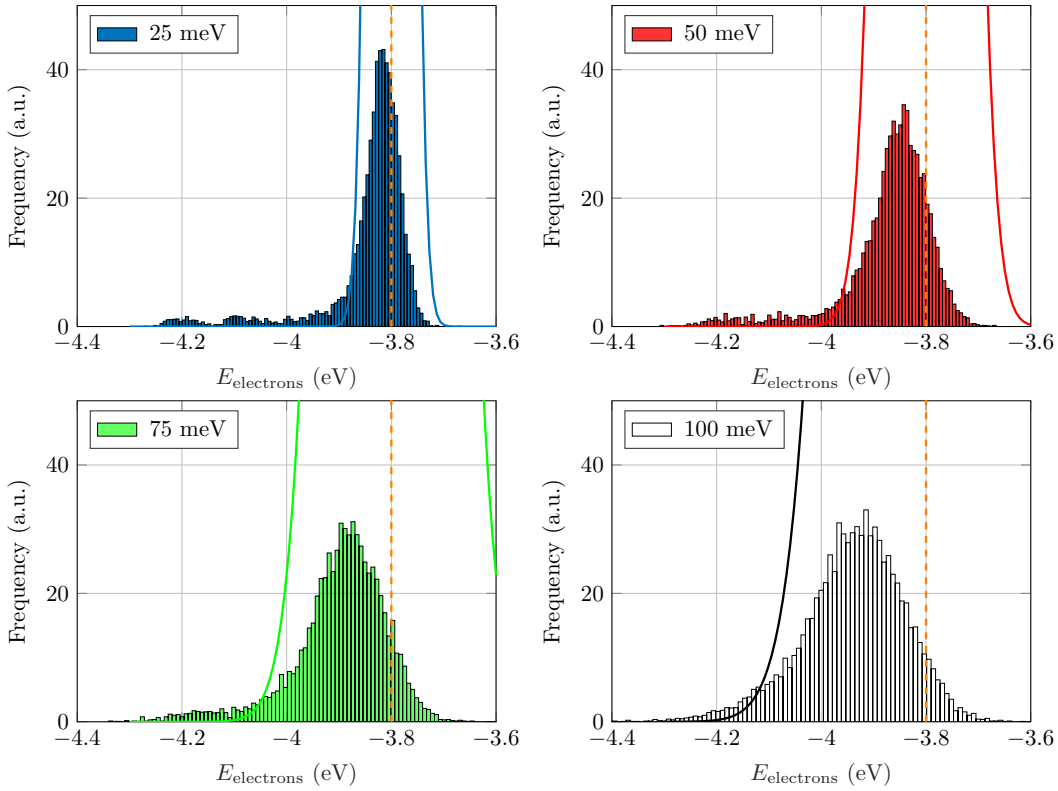

Figure B.2 Gaussian input DOS (solid lines) and electron distribution for $\sigma = 25\,\mathrm{meV}$ to $\sigma = 100\,\mathrm{meV}$. Reprinted with permission from [350]. Copyright (2020) American Chemical Society.

B.3 Energy distributions for correlated disorder

In Fig. B.3 we visualize the procedure to obtain the local density of states within the blends with spatially correlated energetic disorder.

Figure B.4 shows the fits of the local HOMO and LUMO DOS for (a) $l_c = 1\,\mathrm{nm}$, (b) $l_c = 3\,\mathrm{nm}$ and (c) $l_c = 5\,\mathrm{nm}$. To obtain the local DOS $g(E)$ we fit the density of states with a single Gaussian distribution function for $l_c = 1\,\mathrm{nm}$ to $l_c = 3\,\mathrm{nm}$, while a superposition of two Gaussian distribution function was used for the $l_c = 5\,\mathrm{nm}$ correlated BHJ.

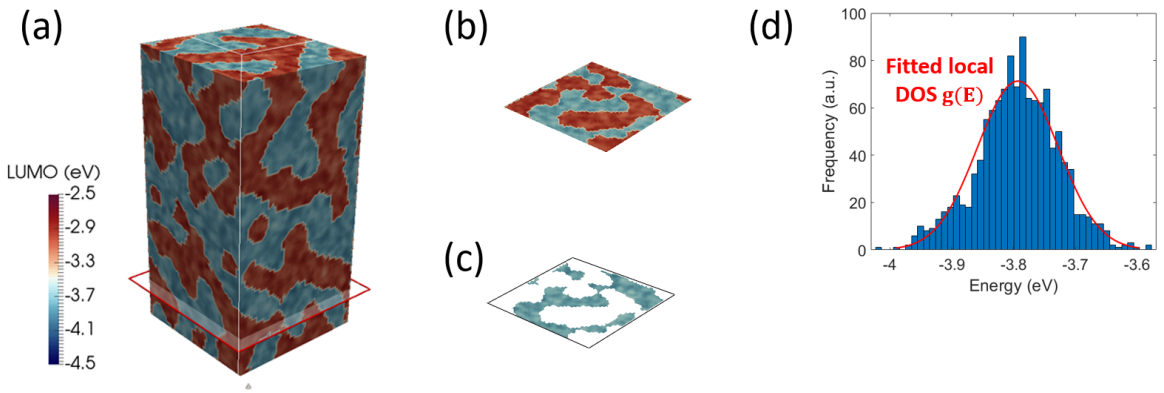

Figure B.3 Procedure of the calculation of the local DOS within the correlated BHJ morphologies. (a) LUMO distribution within the BHJ (visualized using Paraview). (b) Extracted plane at $z = 15\,\mathrm{nm}$. (c) Acceptor regions within the plane. (d) Extracted histogram showing the distribution of LUMO energies within the plane. The red curve gives the fitted local DOS $g(E)$. Reprinted with permission from [350]. Copyright (2020) American Chemical Society.

The distribution of electron and hole energies for the bulk-heterojunction with correlated energetic disorder are plotted in Fig. B.5. The correlation radius is varied from 1 nm to 5 nm.

Figure B.6 shows the local electron and hole density distributions for the uncorrelated Gaussian DOS and the correlated DOS with $l_\mathrm{c} = 1\,\mathrm{nm}$ and $l_\mathrm{c} = 3\,\mathrm{nm}$. The charge carrier density is calculated using the occupancies $X_{ijk}^{(s)}$ of all nodes, labeled by the indices ijk, at kMC step $s = 1, \ldots, N$ [47]:

$$n_{ijk} = \frac{1}{V_{ijk}} \frac{1}{t_\mathrm{sim}} \sum_{s=1}^{N} X_{ijk}^{(s)} \tau_s \,, \tag{B.1}$$

with the volume of one site $V_{ijk} = 1\,\mathrm{nm}^3$, the simulation time t_sim, and the time of kMC step τ_s. The average density is obtained by taking the arithmetic average over all nodes ijk.

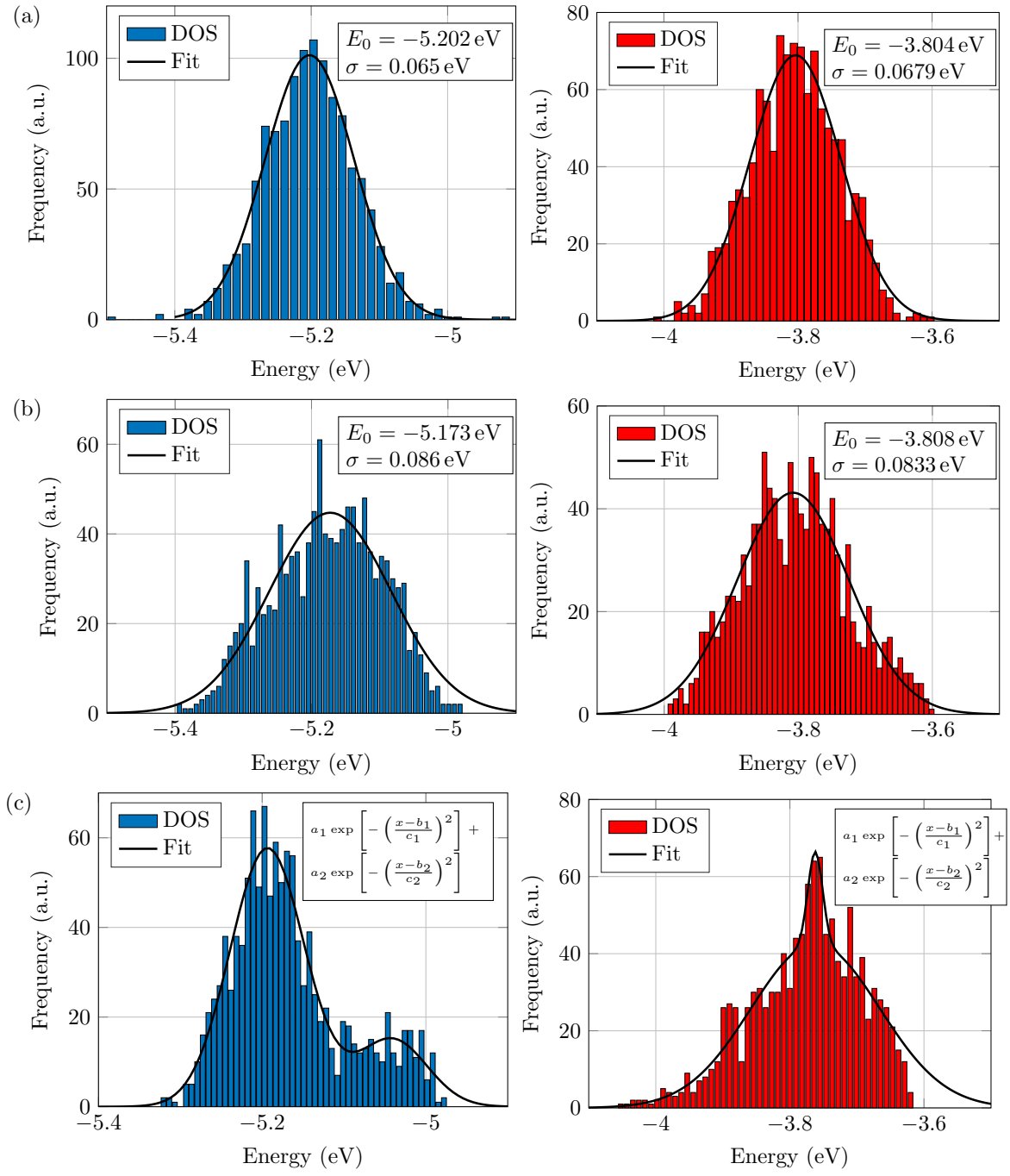

Figure B.4 Electron energy distributions for varying correlated disorder l_{corr}: (a) $l_{\text{corr}} = 1\,\text{nm}$, (b) $l_{\text{corr}} = 3\,\text{nm}$, and (c) $l_{\text{corr}} = 5\,\text{nm}$. Reprinted with permission from [350]. Copyright (2020) American Chemical Society.

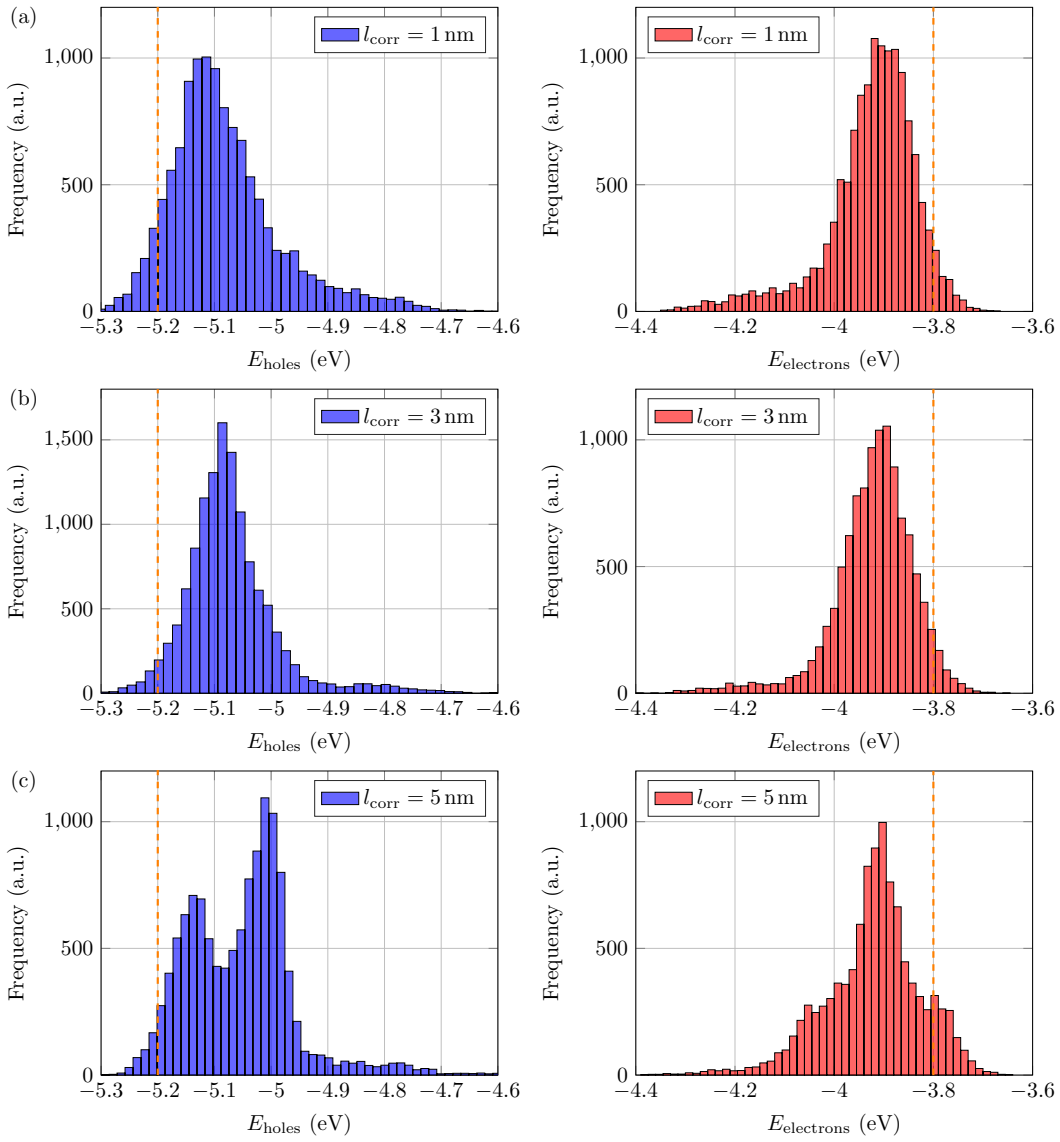

Figure B.5 Hole (left) and electron (right) energy distributions for varying correlated disorder l_{corr}: (a) $l_{\text{corr}} = 1\,\text{nm}$, (b) $l_{\text{corr}} = 3\,\text{nm}$, and (c) $l_{\text{corr}} = 5\,\text{nm}$. Reprinted with permission from [350]. Copyright (2020) American Chemical Society.

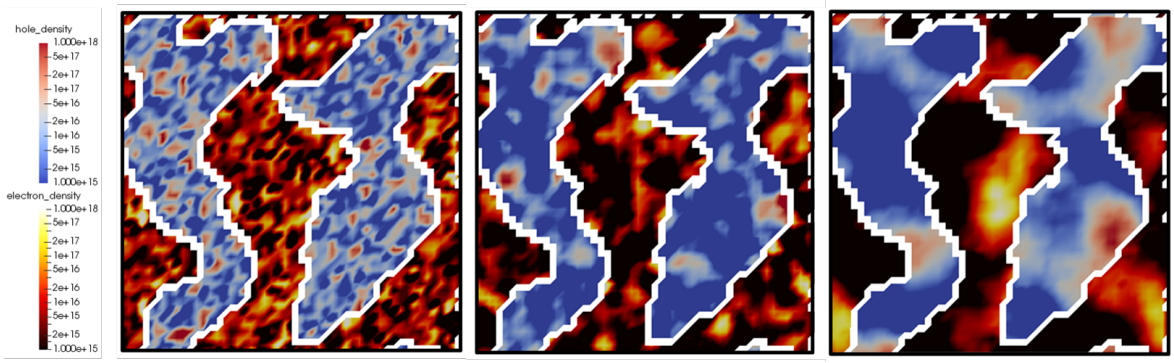

Figure B.6 Comparison of the electron and hole densities for the (left) uncorrelated Gaussian DOS and the correlated DOS with (middle) $l_c = 1$ nm and (right) $l_c = 3$ nm. Reprinted with permission from [350]. Copyright (2020) American Chemical Society.

C Supplementary Information on Phosphorescent Sensitizer Study

C.1 Morphology generation

The bulk-heterojunction (BHJ) morphology is generated using an Ising spin exchange algorithm adapted from Watkins *et al.* [46] and is based on the Metropolis Monte Carlo method. At the beginning, donor and acceptor sites are randomly distributed on the simulated grid. Each material is assigned with a spin (donor: spin-up, acceptor: spin-down). Now, spins are swapped consecutively and the energy of the corresponding configurations is computed using:

$$\epsilon = -J \sum_j (s_i s_j - 1)\,, \tag{C.1}$$

where $J = 0.5 k_\mathrm{B} T$ is the interaction energy between neighboring spins, and spins s_i can take values of +1 (up) and -1 (down). The summations are taken over spins j within a radius of $r \leq 2\,\mathrm{nm}$ around the swapped spin i. After swapping the starting configuration i to a new configuration j, the swap is accepted with a probability given by

$$P(\Delta\epsilon) = \left[\exp\left(\frac{\Delta\epsilon}{k_\mathrm{B} T}\right) + 1\right]^{-1}, \tag{C.2}$$

where $\Delta\epsilon = \epsilon_j - \epsilon_i$. This procedure is repeated several times to obtain large cluster sizes.

To generate the planar-mixed molecular heterojunction (PM-HJ), we combine a BHJ in the center of the active layer with two planar collection layers next to the contacts. To smooth the interface region between the original BHJ and the planar layers, the Ising spin exchange algorithm is run again for 300 MC steps [452], resulting in the PM-HJ shown in Fig. 7.5.

C.2 Calibration of the phosphorescent sensitizer based on the test system NPD:C_{60}

The calibration of the phosphorescent sensitizers parameters is crucial for a valid prediction of the impact of the sensitizer on the poly(3-hexylthiophene) (P3HT): [6,6]-phenyl C_{61}-butyric acid methyl ester (PCBM) solar cell. Thus, we model the N,N'-bis(naphthalen-1-yl)-N,N'-bis(phenyl)-benzidine (NPD):C_{60} solar cell including the sensitizer fac-tris(2-phenylpyridine) iridium $Ir(ppy)_3$ studied by Luhman *et al.* [210]. The cell is comprised by a 40 nm thick layer of NPD followed by a 10 nm thick layer of C_{60}. The optical generation profile is computed using the transfer matrix method. [215, 216, 453] Therefore, we used the wavelength dependent complex refractive indices of NPD, C_{60} and BCP obtained from spectroscopic ellipsometry data analysis [215, 454, 455].

We obtain the generation profile depicted in Fig. C.1a. One can see that most of the excitons are generated in the C_{60} layer. The values used for the rate parameters, energetic molecular levels, and excited states for the NPD and C_{60} are summarized in table C.1 and C.2, respectively. The used

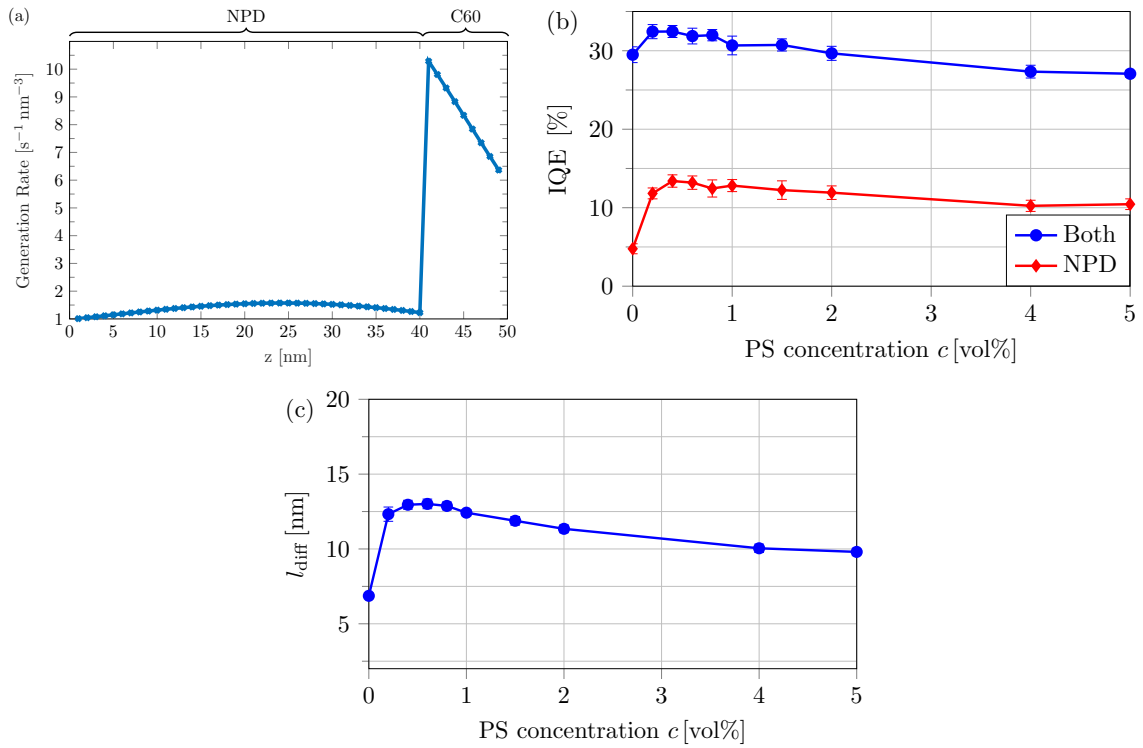

Figure C.1 (a) Optical generation profile in the NPD:C_{60} active layer. (b) IQE with exciton generation in both layers (blue) and with the suppressed optical generation of singlets in the acceptor layer C_{60} (red), both are studied for varying phosphorescent sensitizer volume concentration c. (c) Impact of c on the effective diffusion length l_{diff} of both the singlets and triplet excitons combined. Reprinted with permission from [362], ©2018 WILEYVCH Verlag GmbH & Co. KGaA, Weinheim.

parameters for the phosphorescent sensitizer $Ir(ppy)_3$ are shown in table C.3.The triplet decay rates within the intersystem radius of the PS have been calibrated with the results obtained by Luhman *et al.* [210]. They observed an increase in the exciton diffusion length from $l_{\text{diff,eff}} = 6.5 \pm 0.3$ nm to $l_{\text{diff,eff}} = 11.8 \pm 0.6$ nm using weight percentage of $c = 5$ wt% for the $Ir(ppy)_3$. In Fig. C.1c, we have depicted the change in the diffusion length l_{diff} obtained using our parameter set. The diffusion length changes from $l_{\text{diff,eff}} = 6.9 \pm 0.1$ nm to $l_{\text{diff,t}} = 13.0 \pm 0.3$ nm by introducing $c = 0.6$ vol% of $Ir(ppy)_3$. In Fig. C.1b, we show the impact of the phosphorescent sensitizer on the internal quantum efficiency (IQE) for two cases: (i) optical generation is allowed in all the layers and (ii) optical generation is only activated in the NPD. This allows us to study the impact of the PS on the IQE in the NPD layer, as most singlets are otherwise generated in the C_{60} layer. We observe in case (i) a rise of the IQE by approximately 10 % due to the higher yield of dissociated excitons coming from the thick NPD layer. If we neglect excitons generated in the C_{60} layer, the IQE can be enlarged from 5 % to approximately 13 %. Thus, the PS has a large impact on the dissociation yield concerning the NPD, however, in the total system, a slight increase is observed. This is similar to the observations by Luhman *et al.* [210].

Table C.1 Parameter α−NPD

Description	Param.	Value	Ref.
Inverse localization length	γ	$2\,\mathrm{nm}^{-1}$	-
HOMO level	E_{HOMO}	$-5.5\,\mathrm{eV}$	[210,456]
LUMO level	E_{LUMO}	$-2.4\,\mathrm{eV}$	[456]
Electron attempt-to-hop frequency	$a_{0,\mathrm{elh}}$	$2\times10^{12}\,\mathrm{s}^{-1}$	-
Hole attempt-to-hop frequency	$a_{0,\mathrm{hoh}}$	$6\times10^{11}\,\mathrm{s}^{-1}$	-
Triplet energy	E^t	$2.3\,\mathrm{eV}$	[210,457]
Singlet energy	E^s	$3.1\,\mathrm{eV}$	[210]
Triplet binding energy	E^t_{B}	$0.8\,\mathrm{eV}$	-
Singlet binding energy	E^s_{B}	$0\,\mathrm{eV}$	-
Singlet hopping rate	a^s_{RW}	$1.5\times10^{9}\,\mathrm{s}^{-1}$	[114,136,137]
Singlet dissociation rate	a^s_{diss}	$2\times10^{13}\,\mathrm{s}^{-1}$	-
Singlet decay rate	a^s_{dec}	$2.86\times10^{8}\,\mathrm{s}^{-1}$	[136,458]
Dexter rate prefactor	a^0_{D}	$1.6\times10^{9}\,\mathrm{s}^{-1}$	-
Triplet decay rate	a^t_{dec}	$1\times10^{4}\,\mathrm{s}^{-1}$	[394]

Table C.2 Parameter C_{60}

Description	Param.	Value	Ref.
Inverse localization length	γ	$2\,\mathrm{nm}^{-1}$	-
HOMO level	E_{HOMO}	$-6.2\,\mathrm{eV}$	[217,459,460]
LUMO level	E_{LUMO}	$-3.6\,\mathrm{eV}$	[459,461]
Electron attempt-to-hop frequency	$a_{0,\mathrm{elh}}$	$3\times10^{12}\,\mathrm{s}^{-1}$	-
Hole attempt-to-hop frequency	$a_{0,\mathrm{hoh}}$	$5\times10^{11}\,\mathrm{s}^{-1}$	-
Triplet energy	E^t	$1.6\,\mathrm{eV}$	[462]
Singlet energy	E^s	$2.0\,\mathrm{eV}$	[462]
Triplet binding energy	E^t_{B}	$1.0\,\mathrm{eV}$	-
Singlet binding energy	E^s_{B}	$0.6\,\mathrm{eV}$	-
Singlet hopping rate	a^s_{RW}	$2\times10^{9}\,\mathrm{s}^{-1}$	-
Singlet dissociation rate	a^s_{diss}	$2\times10^{13}\,\mathrm{s}^{-1}$	-
Singlet decay rate	a^s_{dec}	$6.25\times10^{7}\,\mathrm{s}^{-1}$	[217]
Dexter rate prefactor	a^0_{D}	$1.6\times10^{9}\,\mathrm{s}^{-1}$	[158,223]
Triplet decay rate	a^t_{dec}	$1\times10^{5}\,\mathrm{s}^{-1}$	[463]

Table C.3 Parameter $Ir(ppy)_3$

Description	Parameter	Value	Ref.
Inverse localization length	γ	$3\,\mathrm{nm}^{-1}$	[158]
HOMO level	E^{HOMO}	−5.2 eV	[210]
LUMO level	E^{LUMO}	−2.2 eV	[155, 464]
Triplet energy	E^t	2.4 eV	[125]
Singlet energy	E^s	2.6 eV	[210]
Triplet binding energy	E^t_{B}	0.6 eV	-
Singlet binding energy	E^s_{B}	0.4 eV	-
Dexter rate prefactor	a^0_{D}	$1.6 \times 10^{10}\,\mathrm{s}^{-1}$	[158, 223]
Decay rate triplet	$a_{\mathrm{dec,t}}$	$1.25 \times 10^{6}\,\mathrm{s}^{-1}$	[125]
Förster radius triplet	r^t_{F}	1.5 nm	[138]
Förster radius TTA	$r^t_{\mathrm{F,TTA}}$	1.5 nm	-
Dye ISC radius	r_{ISC}	2 nm	-
ISC frequency	a^0_{ISC}	$1 \times 10^{11}\,\mathrm{s}^{-1}$	-

C.3 Kinetic Monte Carlo model: Simulation Parameters

System setup parameters are depicted in table C.4. The simulation parameters for the P3HT:PCBM solar cell are shown in table C.5 (P3HT) and table C.6 (PCBM).

Table C.4 System setup parameters

Description	Parameter	Value	Ref.
Nodes x-direction	M_x	50	-
Nodes y-direction	M_y	50	-
Nodes z-direction	M_z	100	-
Lattice constant	l	1 nm	-
Energetic disorder orbitals	σ	50 meV	-
Energetic disorder excitons	σ_{ex}	0 eV	-
Recombination rate	a_{rec}	$1 \times 10^{7}\,\mathrm{s}^{-1}$	-
Work function cathode (Al)	Φ_{cathode}	−4.3 eV	[258]
Work function anode (ITO)	Φ_{anode}	−4.95 eV	[258]
Optical exciton generation	$a_{\mathrm{opt}}(z)$	generation profile G(z)	[215, 216, 453]
Relative permittivity	ϵ_r	3.5	[258]
PS concentration	c	0 vol% . . . 3 vol%	-
Electron injection	a_{eli}	Thermionic injection	[214]
Hole injection	a_{hoi}	Thermionic injection	[214]
Thermal energy	E_{th}	25.7 meV	-
Simulation time	δt	10 ms	-

Table C.5 Parameter P3HT

Description	Parameter	Value	Ref.
Inverse localization length	γ	$2\,\mathrm{nm}^{-1}$	[47,48]
HOMO level	E_{HOMO}	$-5.17\,\mathrm{eV}$	[47]
LUMO level	E_{LUMO}	$-3.0\,\mathrm{eV}$	[47]
Electron attempt-to-hop frequency	$a_{0,\mathrm{elh}}$	$2 \times 10^{12}\,\mathrm{s}^{-1}$	-
Hole attempt-to-hop frequency	$a_{0,\mathrm{hoh}}$	$6 \times 10^{11}\,\mathrm{s}^{-1}$	[47]
Triplet energy	E^t	$1.5\,\mathrm{eV}$	[151,152]
Singlet energy	E^s	$1.88\,\mathrm{eV}$	[148]
Triplet binding energy	E^t_{B}	$0.67\,\mathrm{eV}$	-
Singlet binding energy	E^s_{B}	$0.29\,\mathrm{eV}$	-
Singlet dissociation rate	a^s_{diss}	$2 \times 10^{13}\,\mathrm{s}^{-1}$	[47,48]
Singlet decay rate	a^s_{dec}	$1.25 \times 10^{9}\,\mathrm{s}^{-1}$	-
Förster radius singlets	r^s_{F}	$1.6\,\mathrm{nm}$	-
Dexter rate prefactor	a^0_{D}	$1.6 \times 10^{9}\,\mathrm{s}^{-1}$	[158,223]
Triplet decay rate	a^t_{dec}	$1 \times 10^{5}\,\mathrm{s}^{-1}$	[151,207]

C.4 Distribution profile of exciton dissociation within the planar-mixed molecular heterojunctions

The internal distribution of exciton dissociation processes should vary for different configurations. Within the bilayer solar cell, dissociation is only possible at the intersection layer of the donor and acceptor. In bulk-heterojunction solar cells, dissociation is possible in almost every region of the structure due to high donor-acceptor phase intermixing. More interesting is the spatial distribution of exciton distribution in the planar-mixed molecular heterojunctions (PM-HJ) configurations with neat layers of different thicknesses. Dissociation is only possible at donor-acceptor interfaces, starting approximately at the layer position $z = 10\,\mathrm{nm}$ for PM-HJ$_{10}$ or $z = 20\,\mathrm{nm}$ for PM-HJ$_{20}$.

We present the spatial distribution of the exciton dissociation within the studied PM-HJs. Figure C.2 shows a barplot of the percentage of exciton dissociation over the z direction. The exciton dissociation events of 10 layers are summarized and plotted as bars at the mean position. The values are normalized to the total number exciton dissociation events at PS concentration $c = 0\,\mathrm{vol\%}$. The bars include the fractions of both singlet and triplet exciton dissociation. Here, the dissociation distributions for different PS concentrations of $c = 0\,\mathrm{vol\%}$, $0.6\,\mathrm{vol\%}$, $1\,\mathrm{vol\%}$, $3\,\mathrm{vol\%}$ are illustrated.

At the intersection of the neat acceptor layer with the mixed heterojunction (m-HJ) layer, dissociation is rather small. The photon absorption in the acceptor material is small, and thus exciton dissociation at the acceptor neat film edge is weak. In general, an increase in dissociation is noticeable for PS concentrations in the range of $0.6\,\mathrm{vol\%} \leq c \leq 1\,\mathrm{vol\%}$. Furthermore, the dissociation share shifts more and more towards triplet exciton dissociation due to a higher intersystem crossing. In the vicinity of the neat donor layer and m-HJ intersection, a remarkable increase of dissociation events with rising PS concentration for the PM-HJ$_{20}$ is recognized. We obtain an increase of $\Delta\eta_{\mathrm{diss}} = 32\,\%$ in the layer region $75\,\mathrm{nm} \leq z < 84\,\mathrm{nm}$ for the PM-HJ$_{20}$ configuration with $c = 0.6\,\mathrm{vol\%}$. This is caused by the intersystem crossing in the 20 nm neat donor layer. Excitons exhibit higher diffusion lengths due to ISC, reach the dissociation interface and get dissociated. A majority of singlet excitons in the neat donor film, which would not reach the intersection within their lifetime, can contribute to charge carrier

Table C.6 Parameter PCBM

Description	Parameter	Value	Ref.
Inverse localization length	γ	$2\,\mathrm{nm}^{-1}$	[47,48]
HOMO level	E_{HOMO}	$-6.0\,\mathrm{eV}$	[47]
LUMO level	E_{LUMO}	$-3.8\,\mathrm{eV}$	[47]
Electron attempt-to-hop frequency	$a_{0,\mathrm{elh}}$	$3\times10^{12}\,\mathrm{s}^{-1}$	[47]
Hole attempt-to-hop frequency	$a_{0,\mathrm{hoh}}$	$5\times10^{11}\,\mathrm{s}^{-1}$	-
Triplet energy	E^t	1.5 eV	[366]
Singlet energy	E^s	1.8 eV	[366]
Triplet binding energy	E^t_{B}	0.7 eV	-
Singlet binding energy	E^s_{B}	0.4 eV	-
Singlet dissociation rate	a^s_{diss}	$2\times10^{13}\,\mathrm{s}^{-1}$	[47,48]
Singlet decay rate	a^s_{dec}	$2\times10^{9}\,\mathrm{s}^{-1}$	[47]
Förster radius singlets	r^s_{F}	1.6 nm	-
Dexter rate prefactor	a^0_{D}	$1.6\times10^{9}\,\mathrm{s}^{-1}$	-
Triplet decay rate	a^t_{dec}	$1\times10^{5}\,\mathrm{s}^{-1}$	[151,465]

generation due to ISC and long triplet exciton lifetimes. The increase in exciton dissociation at the layer intersection of the PM-HJ$_{10}$ is smaller ($\Delta\eta_{\mathrm{diss}} = 16\,\%$), as most of the optically generated singlets in the homogeneous donor layer can reach interfaces within their lifetime. For higher PS concentration $c = 3\,\mathrm{vol}\%$, the decrease of exciton diffusion length due to the lifetime contraction within the ISC radius induces degradation of dissociation yield. Triplets decay within the ISC-activated regions and the benefit of long-living triplet excitons diminishes.

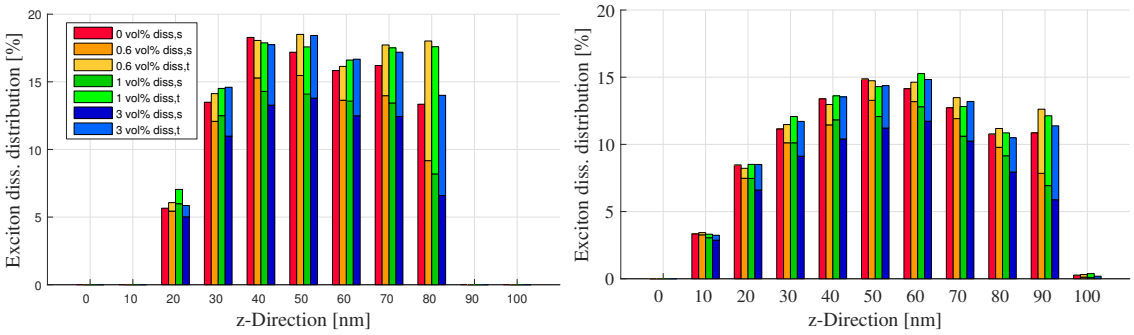

Figure C.2 Exciton dissociation distribution along the z-direction for PM-HJ$_{20}$ (left) and for PMHJ 10 nm (right). Illustrated distributions for four configurations with PS concentrations $c = 0\,\mathrm{vol}\%$, $c = 0.6\,\mathrm{vol}\%$, $c = 1\,\mathrm{vol}\%$ and $c = 3\,\mathrm{vol}\%$. Every bar is stacked. The values singlet exciton dissociation (sexds) and triplet exciton dissociation (texds) are included. Reprinted with permission from [362], ©2018 WILEYVCH Verlag GmbH & Co. KGaA, Weinheim.

C.5 Parameter study: Variation of Dexter prefactor

In Fig. C.3 the exciton share in the bilayer and PM-HJ$_{20}$ solar cell for different Dexter prefactors is shown. With increasing Dexter prefactor, triplet diffusion lengths increase and a higher dissociation of

triplet excitons are reached. Singlet dissociation and decay remain constant. The yield in dissociated triplets lowers the decay percentage, i.e., previously decayed triplets now reach the interface and contribute to the photocurrent.

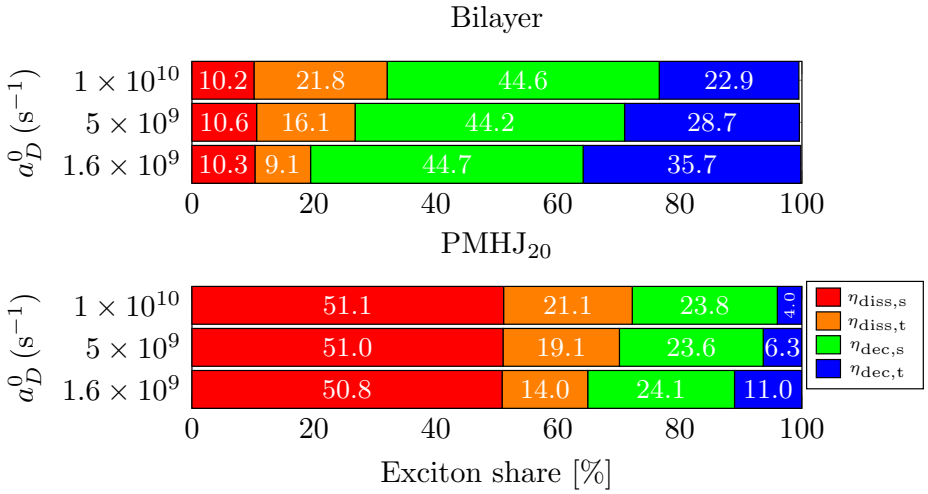

Figure C.3 Change in the distribution of singlet and triplet dissociation and decay percentage with different Dexter prefactors. At the top, the exciton share for the bilayer solar cell is depicted, the lower plot gives the exciton share for the PM-HJ$_{20}$ solar cell. Reprinted with permission from [362], ©2018 WILEYVCH Verlag GmbH & Co. KGaA, Weinheim.

C.6 *jV* characteristics for the different morphologies with and without phosphorescent sensitizers

In table C.7 the *jV* parameters presented in the paper are summarized.

Table C.7 Internal quantum efficiency IQE, open circuit voltage V_{oc}, short circuit current density j_{sc}, fill factor FF and maximum power density P_{max} for the four configurations bilayer, PM-HJ$_{20}$, PM-HJ$_{10}$ and BHJ at zero PS concentration and $c = 0.6$ vol%.

Configuration	c (vol%)	IQE (%)	V_{oc} (V)	j_{sc} (mA cm^{-2})	FF (%)	PCE (%)
Bilayer	0	14.5	0.86	1.4	75.6	0.91
Bilayer	0.6	19.3	0.86	1.8	78.8	1.22
PM-HJ$_{20}$	0	58.3	0.84	6.0	68.7	3.46
PM-HJ$_{20}$	0.6	63.2	0.84	6.4	69.6	3.74
PM-HJ$_{10}$	0	78.5	0.83	8.2	65.4	4.45
BHJ	0	85.3	0.67	9.1	58.4	3.56

D Supplementary Information on 'Non-Equilibrium Thermodynamics of Charge Separation in Organic Bilayers'

D.1 Model Hamiltonian

The organic bilayer is modeled using a 1-dimensional model Hamiltonian which has been presented in previous publications [56]. Here, we briefly outline the scheme of the model and the used parameter set.

Figure D.1 visualizes the system setup of the 1D-bilayer. The one-dimensional system consists of $2N$ sites located on a lattice with spacing a. Sites $0, \ldots, N-1$ represent the donor, sites $N, \ldots, 2N-1$ represent the acceptor of the bilayer. We account for energetically disordered HOMO and LUMO levels of the donor and acceptor with disorder σ. For the acceptor, we also include the LUMO+1 level. Transfer integrals are accounted for between all neighbor sites with different magnitude in the HOMO / LUMO levels of the acceptor and donor materials itself, as well as between the donor and the acceptor.

The model Hamiltonian is accounts for charge interaction, $\hat{H}_c$, the phonon bath, $\hat{H}_p$, and the interaction of charge carriers with the phonons, $\hat{H}_{c-p}$:

$$\hat{H} = \hat{H}_c + \hat{H}_p + \hat{H}_{c-p} \,. \tag{D.1}$$

The charge contributions are modeled by

$$\begin{aligned} \hat{H}_c = & \sum_{i\beta_i, j\beta_j} \epsilon^c_{(i\beta_i),(j,\beta_j)} c^\dagger_{i\beta_i} c_{j\beta_j} - \sum_{i\alpha_i, j\alpha_j} \epsilon^v_{(i\alpha_i),(j,\alpha_j)} d^\dagger_{i\alpha_i} d_{j\alpha_j} \\ & + \frac{1}{2} \sum_{i\beta_i, j\beta_j} V_{ij} c^\dagger_{i\beta_i} c^\dagger_{j\beta_j} c_{j\beta_j} c_{i\beta_i} + \frac{1}{2} \sum_{i\alpha_i, j\alpha_j} V_{ij} d^\dagger_{i\alpha_i} d^\dagger_{j\alpha_j} d_{j\alpha_j} d_{i\alpha_i} \\ & - \sum_{i\beta_i, j\alpha_j} V_{ij} c^\dagger_{i\beta_i} d^\dagger_{j\alpha_j} d_{j\alpha_j} c_{i\beta_i} \,. \end{aligned} \tag{D.2}$$

The Fermi operators $c^\dagger_{i\beta_i}$ ($c_{i\beta_i}$) create (annihilate) an electron on site i in single electron state β_i, $d^\dagger_{i\alpha_i}$ ($d_{i\alpha_i}$) create (annihilate) a hole on site i in single hole state α_i. The phonon bath is modeled by

$$\hat{H}_p = \sum_{i\lambda} \hbar\omega_\lambda b^\dagger_{i\lambda} b_{i\lambda} \,, \tag{D.3}$$

with the Bose operators $b^\dagger_{i\lambda}$ ($c_{i\lambda}$), site i and phonon mode λ. The interaction between the charges and the phonon bath is modeled by

$$\hat{H}_{c-p} = \sum_{i\beta_i} \sum_{\lambda} g^c_{i\beta_i\lambda} c^\dagger_{i\beta_i} c_{i\beta_i} \left(b^\dagger_{i\lambda} + b_{i\lambda} \right) - \sum_{i\alpha_i} \sum_{\lambda} g^v_{i\alpha_i\lambda} d^\dagger_{i\alpha_i} d_{i\alpha_i} \left(b^\dagger_{i\lambda} + b_{i\lambda} \right) \,, \tag{D.4}$$

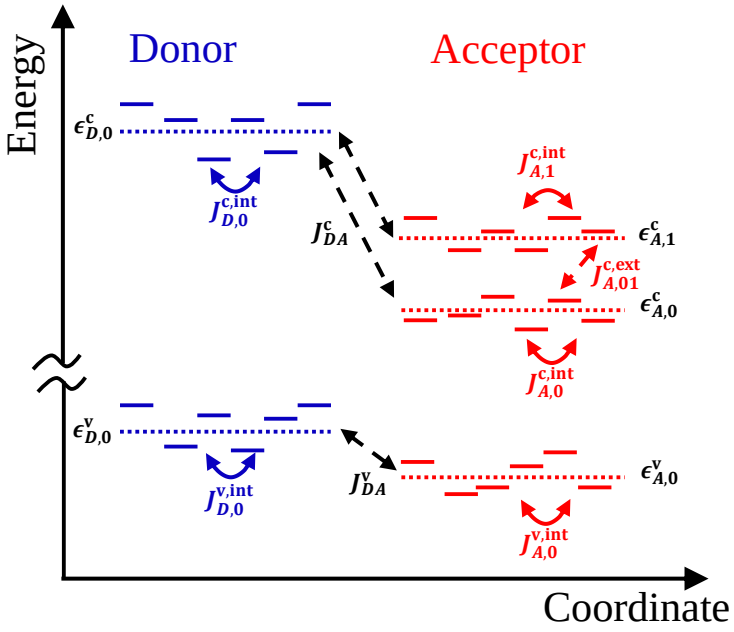

Figure D.1 Schematic of the model Hamiltonian of the organic donor:acceptor bilayer. The dotted lines highlight the different average on-site energies. Solid lines represent the actual on-site energies which vary from the average on-site energies due to the static energetic disorder. The different transfer integrals within the donor (D) and acceptor (A) as well as the coupling between the donor and acceptor (DA) are highlighted.

with the Bose operators $b^{\dagger}_{i\lambda}$ ($c_{i\lambda}$), site i and phonon mode λ.

The Coulomb interaction is approximated by the Ohno potential

$$V_{ij} = \frac{U}{\sqrt{1 + \left(\frac{r_{ij}}{r_0}\right)^2}}, \tag{D.5}$$

with $r_0 = q^2/(4\pi\epsilon_0\epsilon_r U)$, the on-site Coulomb potential U, r_{ij} the distance between sites i and j, the permittivity ϵ_r, and the elementary charge q.

The values of the model parameters used in our calculations are summarized in Table D.1.

Table D.1 Values of Model Parameters Used in Computations.

Parameter	Value
N	30
l_c	11
a (nm)	1.0
U (eV)	0.65
ϵ_r	3.0
$\epsilon^{\mathrm{c}}_{D,0}$ (eV)	2.63
$J^{\mathrm{c,int}}_{D,0}$ (eV)	0.1
$\epsilon^{\mathrm{v}}_{D,0}$ (eV)	-0.3
$J^{\mathrm{v,int}}_{D,0}$ (eV)	-0.15
$\epsilon^{\mathrm{c}}_{A,0}$ (eV)	1.565
$\epsilon^{\mathrm{c}}_{A,1}$ (eV)	1.865
$J^{\mathrm{c,int}}_{A,0}$ (eV)	0.05
$J^{\mathrm{c,int}}_{A,1}$ (eV)	0.025
$J^{\mathrm{c,ext}}_{A,01}$ (eV)	0.02
$\epsilon^{\mathrm{v}}_{A,0}$ (eV)	-1.03
$J^{\mathrm{v,int}}_{A,0}$ (eV)	-0.15
J^{c}_{DA} (eV)	0.1
J^{v}_{DA} (eV)	-0.1
σ (meV)	50
η	1.5
E_c (meV)	10
τ_0 (ps)	400
$A_{\mathrm{A/D}}$	0.5
T (K)	300

D.2 Numerical Solution of the Master Equation

The population p_m of a charge transfer state $|m\rangle$ evolves according to the Master equation:

$$\partial_t p_m(t) = \sum_{n \neq m} w_{n\to m} p_n(t) - \sum_{n \neq m} w_{m\to n} p_m(t) - \tau_m^{-1} p_m(t) \,. \tag{D.6}$$

The population of the ground state (GS) is given by the sum of all decayed states:

$$\partial_t p_{\mathrm{GS}}(t) = \sum_m \tau_m^{-1} p_m(t) \,. \tag{D.7}$$

Contact states c are assumed to be ideal. If a CT pair reaches a contact state, the charges are immediately collected into the external circuit. Thus, the population of contact states evolves as follows:

$$\partial_t p_c(t) = \sum_m w_{m\to c} p_m(t) \,, \tag{D.8}$$

where m labels all CT states. The system of rate equations can be expressed by a time-independent matrix A in matrix form:

$$\partial_t p_m(t) = \sum_n A_{n\to m} p_n(t) \,. \tag{D.9}$$

If the initial condition $p_m(0)$ is known, we can solve the time evolution as

$$p_m(t) = \langle m|p(t)\rangle = \langle m|\exp(At)|p(0)\rangle \,. \tag{D.10}$$

As described in ref. 2 [406], we can express the solution of $p_m(t)$ in terms of the eigenvalues λ_k and eigenvectors c_k of the matrix A:

$$p_m(t) = \sum_k \alpha_k \exp(\lambda_k t) c_{mk} \,, \tag{D.11}$$

where the amplitudes α_k can be found by solving the linear algebraic equations

$$p_m(0) = \sum_k \alpha_k c_{mk} \,. \tag{D.12}$$

To obtain the non-equilibrium probability of being in state m after time τ during the separation of charge carriers, we take the time-average of probability $p_m(t)$:

$$p_m^{\mathrm{neq}}(\tau) = \tau^{-1} \int_0^\tau \mathrm{d}t\, p_m(t) \,. \tag{D.13}$$

We increase τ until the probability of being in CT states drops below 10^{-20} to reach convergence of our non-equilibrium probability distribution.

D.3 Relative values of the free energy versus CT separation distance

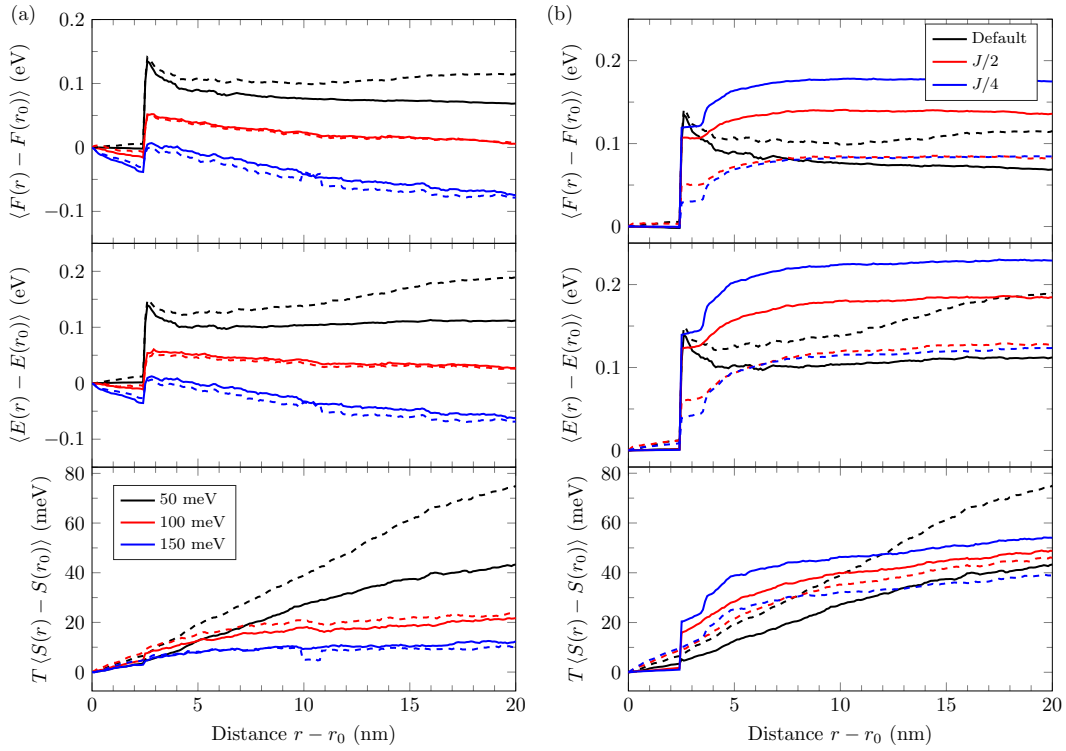

Figure D.2 (a) Distance dependence of the free energy $F(r)$, average energy $E(r)$, and entropic contribution $TS(r)$ for varying energetic disorder σ. (b) Impact of the charge transfer integrals J on the free energy and its energetic and entropic contribution. For $J/2$ and $J/4$, all transfer integrals are scaled down by a factor of 2 and 4, respectively. $\langle \cdot \rangle$ denotes an average across 256 configurations for each parameter set. The solid curves represent the predictions by the equilibrium theory, the dashed curves are obtained by the non-equilibrium theory.

D.4 Separation dynamics

Table D.2 Separation yield averaged across 256 configurations for each parameter set.

Configuration	Separation Yield (%)
Default	44.8
$\sigma = 100\,\text{meV}$	14.5
$\sigma = 150\,\text{meV}$	6.3
$J/2$	30.6
$J/4$	14.7

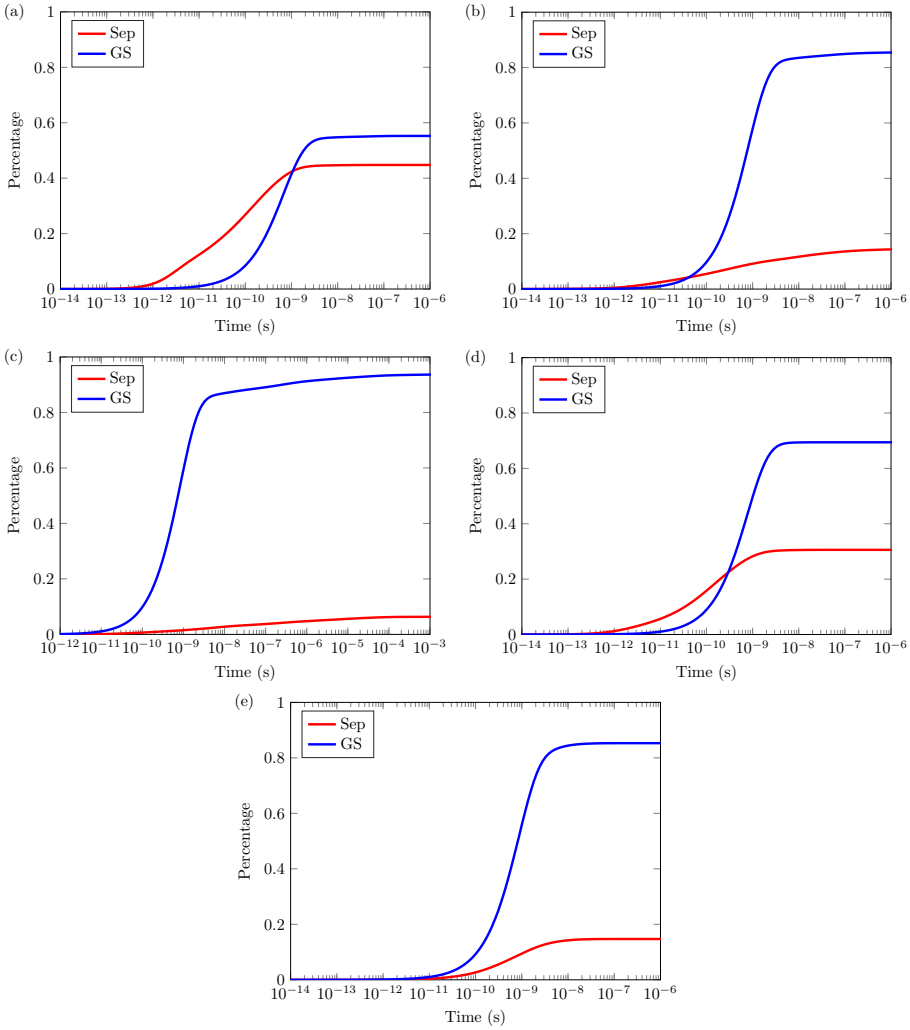

Figure D.3 Time dependence of the separation yield (Sep) and the percentage of recombined state to the ground state (GS) averaged across all 256 configurations starting from occupied acceptor exciton states. The subplots show the different configurations: (a) default, (b) $\sigma = 100\,\text{meV}$, (c) $\sigma = 150\,\text{meV}$, (d) $J/2$, (e) $J/4$.

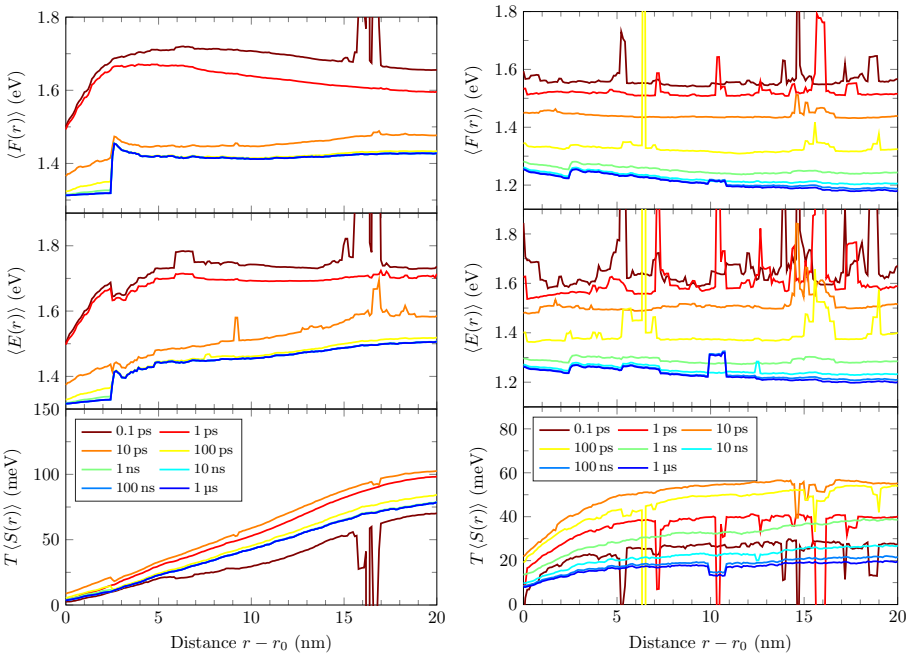

Figure D.4 Time dependence of the free energy and its energetic and entropic contribution for (left) $\sigma = 50$ meV and (right) $\sigma = 150$ meV.

List of Figures

List of Tables

Bibliography

[1] S. R. Kurtz, A. M. Leilaeioun, R. R. King, I. M. Peters, M. J. Heben, W. K. Metzger, and N. M. Haegel, "Revisiting the terawatt challenge," MRS Bull. **45**, 159–164 (2020).

[2] N. M. Haegel, H. Atwater, T. Barnes, C. Breyer, A. Burrell, Y.-M. Chiang, S. De Wolf, B. Dimmler, D. Feldman, S. Glunz *et al.*, "Terawatt-scale photovoltaics: Transform global energy," Science **364**, 836–838 (2019).

[3] E. Vartiainen, G. Masson, C. Breyer, D. Moser, and E. Román Medina, "Impact of weighted average cost of capital, capital expenditure, and other parameters on future utility-scale pv levelised cost of electricity," Progress in Photovoltaics: Research and Applications (2019).

[4] I. Fraunhofer and A. Energiewende, "Current and future cost of photovoltaics. long-term scenarios for market development, system prices and lcoe of utility-scale pv systems," Agora Energiewende **82** (2015).

[5] W. Yang, Z. Luo, R. Sun, J. Guo, T. Wang, Y. Wu, W. Wang, J. Guo, Q. Wu, M. Shi *et al.*, "Simultaneous enhanced efficiency and thermal stability in organic solar cells from a polymer acceptor additive," Nat. Comm. **11**, 1–10 (2020).

[6] J. Hou, O. Inganäs, R. H. Friend, and F. Gao, "Organic solar cells based on non-fullerene acceptors," Nat. Mater. **17**, 119 (2018).

[7] S. Park, J. Jeong, G. Hyun, M. Kim, H. Lee, and Y. Yi, "The origin of high PCE in PTB7 based photovoltaics: proper charge neutrality level and free energy of charge separation at PTB7/PC71BM interface," Sci. Rep. **6**, 1–11 (2016).

[8] A. Köhler and H. Bässler, "Triplet states in organic semiconductors," Mater. Sci. Eng., R: Reports **66**, 71–109 (2009).

[9] A. Köhler and H. Bässler, *Electronic processes in organic semiconductors: An introduction* (John Wiley & Sons, 2015).

[10] C. Deibel and V. Dyakonov, "Polymer–fullerene bulk heterojunction solar cells," Rep. Prog. Phys. **73**, 096401 (2010).

[11] A. J. Heeger, "25th anniversary article: Bulk heterojunction solar cells: Understanding the mechanism of operation," Adv. Mater. **26**, 10–28 (2014).

[12] C. W. Tang, "Two-layer organic photovoltaic cell," Appl. Phys. Lett. **48**, 183–185 (1986).

[13] T. Albes and A. Gagliardi, "Influence of permittivity and energetic disorder on the spatial charge carrier distribution and recombination in organic bulk-heterojunctions," Phys. Chem. Chem. Phys. **19**, 20974–20983 (2017).

[14] T. Albes and A. Gagliardi, "Charge pair separation dynamics in organic bulk-heterojunction solar cells," Adv. Theory Sim. p. 1800032 (2018).

[15] A. Armin, D. M. Stoltzfus, J. E. Donaghey, A. J. Clulow, R. C. R. Nagiri, P. L. Burn, I. R. Gentle, and P. Meredith, "Engineering dielectric constants in organic semiconductors," J. Mater. Chem. C **5**, 3736–3747 (2017).

[16] S. Y. Leblebici, T. L. Chen, P. Olalde-Velasco, W. Yang, and B. Ma, "Reducing exciton binding energy by increasing thin film permittivity: an effective approach to enhance exciton separation efficiency in organic solar cells," ACS Appl. Mater. Interfaces **5**, 10105–10110 (2013).

[17] P. W. Anderson, "Absence of diffusion in certain random lattices," Phys. Rev. **109**, 1492–1505 (1958).

[18] H. Oberhofer, K. Reuter, and J. Blumberger, "Charge transport in molecular materials: An assessment of computational methods," Chem. Rev. **117**, 10319–10357 (2017).

[19] S. T. Hoffmann, F. Jaiser, A. Hayer, H. Bässler, T. Unger, S. Athanasopoulos, D. Neher, and A. Köhler, "How do disorder, reorganization, and localization influence the hole mobility in conjugated copolymers?" J. Am. Chem. Soc. **135**, 1772–1782 (2013).

[20] N. Vukmirovic and L.-W. Wang, "Charge carrier motion in disordered conjugated polymers: A multiscale ab-initio study," Nano Lett. **9**, 3996–4000 (2009).

[21] M. Mladenović and N. Vukmirović, "Charge carrier localization and transport in organic semiconductors: Insights from atomistic multiscale simulations," Adv. Funct. Mater. **25**, 1915–1932 (2015).

[22] S. Ciuchi, S. Fratini, and D. Mayou, "Transient localization in crystalline organic semiconductors," Phys. Rev. B **83**, 081202 (2011).

[23] J. Benduhn, K. Tvingstedt, F. Piersimoni, S. Ullbrich, Y. Fan, M. Tropiano, K. A. McGarry, O. Zeika, M. K. Riede, C. J. Douglas, S. Barlow, S. R. Marder, D. Neher, D. Spoltore, and K. Vandewal, "Intrinsic non-radiative voltage losses in fullerene-based organic solar cells," Nat. Energy **2**, 17053 (2017).

[24] K. Vandewal, J. Widmer, T. Heumueller, C. J. Brabec, M. D. McGehee, K. Leo, M. Riede, and A. Salleo, "Increased open-circuit voltage of organic solar cells by reduced donor-acceptor interface area," Adv. Mater. **26**, 3839–3843 (2014).

[25] S. Pröller, F. Liu, C. Zhu, C. Wang, T. P. Russell, A. Hexemer, P. Müller-Buschbaum, and E. M. Herzig, "Following the morphology formation in situ in printed active layers for organic solar cells," Adv. Energy Mater. **6** (2016).

[26] S. Pröller, O. Filonik, F. Eller, S. Mansi, C. Zhu, E. Schaible, A. Hexemer, P. Müller-Buschbaum, and E. M. Herzig, "Electrophoresis assisted printing: A method to control the morphology in organic thin films," ACS Appl. Mater. Interfaces **12**, 5219–5225 (2020).

[27] A. Miller and E. Abrahams, "Impurity conduction at low concentrations," Phys. Rev. **120**, 745 (1960).

[28] V. Arkhipov and H. Bässler, "Field-dependent effective temperature of localized charge carriers in hopping systems with a random energy distribution," Philos. Mag. Lett. **69**, 241–246 (1994).

[29] H. Bässler, "Charge transport in disordered organic photoconductors a Monte Carlo simulation study," Phys. Status Solidi B **175**, 15–56 (1993).

[30] G. J. Moore, M. Causa, J. F. Martinez Hardigree, S. Karuthedath, I. Ramirez, A. Jungbluth, F. Laquai, M. Riede, and N. Banerji, "Ultrafast charge dynamics in dilute-donor versus highly intermixed TAPC:C60 organic solar cell blends," J. Phys. Chem. Lett. **11**, 5610–5617 (2020).

[31] N. Felekidis, A. Melianas, and M. Kemerink, "Nonequilibrium drift-diffusion model for organic semiconductor devices," Phys. Rev. B **94**, 035205 (2016).

[32] U. Würfel, D. Neher, A. Spies, and S. Albrecht, "Impact of charge transport on current–voltage characteristics and power-conversion efficiency of organic solar cells," Nat. Commun. **6**, 6951 (2015).

[33] J. C. Blakesley and D. Neher, "Relationship between energetic disorder and open-circuit voltage in bulk heterojunction organic solar cells," Phys. Rev. B **84**, 075210 (2011).

[34] A. Gagliardi, S. Wang, and T. Albes, "Simulation of charge carrier mobility unbalance in organic solar cells," Org. Electron. **59**, 171–176 (2018).

[35] D. Rossi, F. Santoni, M. A. Der Maur, and A. Di Carlo, "A multiparticle drift-diffusion model and its application to organic and inorganic electronic device simulation," IEEE Trans. Electr. Devices **66**, 2715–2722 (2019).

[36] A. Melianas, V. Pranculis, D. Spoltore, J. Benduhn, O. Inganäs, V. Gulbinas, K. Vandewal, and M. Kemerink, "Charge transport in pure and mixed phases in organic solar cells," Adv. Energy Mater. **7**, 1700888 (2017).

[37] C. Groves, "Simulating charge transport in organic semiconductors and devices: A review." Rep. Prog. Phys. **80**, 026502 (2017).

[38] S. Athanasopoulos, E. V. Emelianova, A. B. Walker, and D. Beljonne, "Exciton diffusion in energetically disordered organic materials," Phys. Rev. B **80**, 195209 (2009).

[39] K. Feron, X. Zhou, W. Belcher, and P. Dastoor, "Exciton transport in organic semiconductors: Förster resonance energy transfer compared with a simple random walk," J. Appl. Phys. **111**, 044510 (2012).

[40] C. Groves, R. Marsh, and N. C. Greenham, "Monte Carlo modeling of geminate recombination in polymer-polymer photovoltaic devices," J. Chem. Phys. **129**, 114903 (2008).

[41] C. Groves, R. G. Kimber, and A. B. Walker, "Simulation of loss mechanisms in organic solar cells: A description of the mesoscopic Monte Carlo technique and an evaluation of the first reaction method," J. Chem. Phys. **133**, 144110 (2010).

[42] C. Groves, "Developing understanding of organic photovoltaic devices: kinetic Monte Carlo models of geminate and non-geminate recombination, charge transport and charge extraction," Energy Environ. Sci. **6**, 3202–3217 (2013).

[43] M. L. Jones, R. Dyer, N. Clarke, and C. Groves, "Are hot charge transfer states the primary cause of efficient free-charge generation in polymer: fullerene organic photovoltaic devices? A kinetic Monte Carlo study," Phys. Chem. Chem. Phys. **16**, 20310–20320 (2014).

[44] R. G. Kimber, E. N. Wright, S. E. O'Kane, A. B. Walker, and J. C. Blakesley, "Mesoscopic kinetic Monte Carlo modeling of organic photovoltaic device characteristics," Phys. Rev. B **86**, 235206 (2012).

[45] L. Meng, Y. Shang, Q. Li, Y. Li, X. Zhan, Z. Shuai, R. G. Kimber, and A. B. Walker, "Dynamic Monte Carlo simulation for highly efficient polymer blend photovoltaics," J. Phys. Chem. B **114**, 36–41 (2009).

[46] P. K. Watkins, A. B. Walker, and G. L. Verschoor, "Dynamical Monte Carlo modelling of organic solar cells: The dependence of internal quantum efficiency on morphology," Nano Lett. **5**, 1814–1818 (2005).

[47] T. Albes, P. Lugli, and A. Gagliardi, "Investigation of the blend morphology in bulk-heterojunction organic solar cells," IEEE Trans. Nanotechnol. **15**, 281–288 (2016).

[48] M. Casalegno, G. Raos, and R. Po, "Methodological assessment of kinetic Monte Carlo simulations of organic photovoltaic devices: The treatment of electrostatic interactions," J. Chem. Phys. **132**, 094705 (2010).

[49] P. Kordt, S. Stodtmann, A. Badinski, M. Al Helwi, C. Lennartz, and D. Andrienko, "Parameter-free continuous drift–diffusion models of amorphous organic semiconductors," Phys. Chem. Chem. Phys. **17**, 22778–22783 (2015).

[50] W. Kaiser, T. Albes, and A. Gagliardi, "Charge carrier mobility of disordered organic semiconductors with correlated energetic and spatial disorder," Phys. Chem. Chem. Phys. **20**, 8897–8908 (2018).

[51] M. Rinderle, W. Kaiser, A. Mattoni, and A. Gagliardi, "Machine-learned charge transfer integrals for multiscale simulations in organic thin films," J. Phys. Chem. C **124**, 17733–17743 (2020).

[52] T. Albes, "Kinetic Monte Carlo simulations of organic solar cells," Ph.D. thesis, Technische Universität München (2019).

[53] A. Chatterjee and A. F. Voter, "Accurate acceleration of kinetic Monte Carlo simulations through the modification of rate constants," J. Chem. Phys. **132**, 194101 (2010).

[54] S. H. Park, A. Roy, S. Beaupré, S. Cho, N. Coates, J. S. Moon, D. Moses, M. Leclerc, K. Lee, and A. J. Heeger, "Bulk heterojunction solar cells with internal quantum efficiency approaching 100%," Nat. Photonics **3**, 297 (2009).

[55] S. N. Hood and I. Kassal, "Entropy and disorder enable charge separation in organic solar cells," J. Phys. Chem. Lett. **7**, 4495–4500 (2016).

[56] V. Jankovic and N. Vukmirovic, "Combination of charge delocalization and disorder enables efficient charge separation at photoexcited organic bilayers," J. Phys. Chem. C **122**, 10343–10359 (2018).

[57] B. A. Gregg, "Entropy of charge separation in organic photovoltaic cells: the benefit of higher dimensionality," J. Phys. Chem. Lett. **2**, 3013–3015 (2011).

[58] H. Bässler and A. Köhler, "Hot or cold: how do charge transfer states at the donor–acceptor interface of an organic solar cell dissociate?" Phys. Chem. Chem. Phys. **17**, 28451–28462 (2015).

[59] T. Albes, L. Xu, J. Wang, J. W. Hsu, and A. Gagliardi, "Origin of photocurrent in fullerene-based solar cells," J. Phys. Chem. C **122**, 15140–15148 (2018).

[60] D. Spoltore, A. Hofacker, J. Benduhn, S. Ullbrich, M. Nyman, O. Zeika, S. Schellhammer, Y. Fan, I. Ramirez, S. Barlow *et al.*, "Hole transport in low-donor-content organic solar cells," J. Phys. Chem. Lett. **9**, 5496–5501 (2018).

[61] R. Gross and A. Marx, *Festkörperphysik* (Walter de Gruyter GmbH & Co KG, 2018).

[62] P. Würfel and U. Würfel, *Physics of solar cells: from basic principles to advanced concepts* (John Wiley & Sons, 2016).

[63] M. Becquerel, "Mémoire sur les effets électriques produits sous l'influence des rayons solaires," Comptes rendus hebdomadaires des séances de l'Académie des sciences **9**, 561–567 (1839).

[64] C. Kittel *et al.*, *Introduction to solid state physics*, vol. 8 (Wiley New York, 1976).

[65] D. M. Chapin, C. Fuller, and G. Pearson, "A new silicon p-n junction photocell for converting solar radiation into electrical power," J. Appl. Phys. **25**, 676–677 (1954).

[66] U. Rau and T. Kirchartz, "Charge carrier collection and contact selectivity in solar cells," Adv. Mater. Interfaces **6**, 1900252 (2019).

[67] R. Brendel and R. Peibst, "Contact selectivity and efficiency in crystalline silicon photovoltaics," IEEE J. Photovolt. **6**, 1413–1420 (2016).

[68] V. Sarritzu, N. Sestu, D. Marongiu, X. Chang, S. Masi, A. Rizzo, S. Colella, F. Quochi, M. Saba, A. Mura *et al.*, "Optical determination of Shockley-Read-Hall and interface recombination currents in hybrid perovskites," Sci. Rep. **7**, 44629 (2017).

[69] M. Stolterfoht, C. M. Wolff, J. A. Márquez, S. Zhang, C. J. Hages, D. Rothhardt, S. Albrecht, P. L. Burn, P. Meredith, T. Unold *et al.*, "Visualization and suppression of interfacial recombination for high-efficiency large-area pin perovskite solar cells," Nat. Energy **3**, 847–854 (2018).

[70] B. Lim, T. Brendemühl, T. Dullweber, and R. Brendel, "Loss analysis of n-type passivated emitter rear totally diffused back-junction silicon solar cells with efficiencies up to 21.2%," IEEE J. Photovolt. **6**, 447–453 (2016).

[71] W. Shockley and H. J. Queisser, "Detailed balance limit of efficiency of p-n junction solar cells," J. Appl. Phys. **32**, 510–519 (1961).

[72] F. Coester, "Principle of detailed balance," Phys. Rev. **84**, 1259 (1951).

[73] R. King, D. Law, K. Edmondson, C. Fetzer, G. Kinsey, H. Yoon, R. Sherif, and N. Karam, "40% efficient metamorphic GaInP/GaInAs/Ge multijunction solar cells," Appl. Phys. Lett. **90**, 183516 (2007).

[74] M. Grätzel, "Dye-sensitized solar cells," J. Photochem. Photobiol. C: Photochem. Rev. **4**, 145–153 (2003).

[75] A. Hagfeldt, G. Boschloo, L. Sun, L. Kloo, and H. Pettersson, "Dye-sensitized solar cells," Chem. Rev. **110**, 6595–6663 (2010).

[76] T. Brown, A. Reale, and A. Di Carlo, "Organic and hybrid solar cells in thin film solar cells: Current status and future trends," (2011).

[77] H. Michaels, M. Rinderle, R. Freitag, I. Benesperi, T. Edvinsson, R. Socher, A. Gagliardi, and M. Freitag, "Dye-sensitized solar cells under ambient light powering machine learning: towards autonomous smart sensors for the internet of things," Chemical Science **11**, 2895–2906 (2020).

[78] U. Bach, D. Lupo, P. Comte, J.-E. Moser, F. Weissörtel, J. Salbeck, H. Spreitzer, and M. Grätzel, "Solid-state dye-sensitized mesoporous TiO2 solar cells with high photon-to-electron conversion efficiencies," Nature **395**, 583–585 (1998).

[79] M. A. Green, A. Ho-Baillie, and H. J. Snaith, "The emergence of perovskite solar cells," Nat. Photon. **8**, 506–514 (2014).

[80] N.-G. Park, "Perovskite solar cells: an emerging photovoltaic technology," Mater. Today **18**, 65–72 (2015).

[81] A. Kojima, K. Teshima, Y. Shirai, and T. Miyasaka, "Organometal halide perovskites as visible-light sensitizers for photovoltaic cells," J. Am. Chem. Soc. **131**, 6050–6051 (2009).

[82] J. Jeong, M. Kim, J. Seo, H. Lu, P. Ahlawat, A. Mishra, Y. Yang, M. A. Hope, F. T. Eickemeyer, M. Kim *et al.*, "Pseudo-halide anion engineering for α-fapbi 3 perovskite solar cells," Nature **592**, 381–385 (2021).

[83] Q. Liu, Y. Jiang, K. Jin, J. Qin, J. Xu, W. Li, J. Xiong, J. Liu, Z. Xiao, K. Sun *et al.*, "18% efficiency organic solar cells," Sci. Bull. **65**, 272–275 (2020).

[84] P. W. Atkins and R. S. Friedman, *Molecular quantum mechanics* (Oxford university press, 2011).

[85] S. Baranovskii, "Theoretical description of charge transport in disordered organic semiconductors," Phys. Status Solidi B **251**, 487–525 (2014).

[86] C. Luo, A. K. K. Kyaw, L. A. Perez, S. Patel, M. Wang, B. Grimm, G. C. Bazan, E. J. Kramer, and A. J. Heeger, "General strategy for self-assembly of highly oriented nanocrystalline semiconducting polymers with high mobility," Nano Lett. **14**, 2764–2771 (2014).

[87] T. Hasegawa and J. Takeya, "Organic field-effect transistors using single crystals," Sci. Technol. Adv. Mater. (2009).

[88] G. Kemeny and B. Rosenberg, "Small polarons in organic and biological semiconductors," J. Chem. Phys. **53**, 3549–3551 (1970).

[89] H. Tamura, M. Tsukada, H. Ishii, N. Kobayashi, and K. Hirose, "Roles of intramolecular and intermolecular electron-phonon coupling on the formation and transport of large polarons in organic semiconductors," Phys. Rev. B **86**, 035208 (2012).

[90] X. Xie, A. Santana-Bonilla, and A. Troisi, "Nonlocal electron–phonon coupling in prototypical molecular semiconductors from first principles," J. Chem. Theory Comput. **14**, 3752–3762 (2018).

[91] Y. Li, V. Coropceanu, and J.-L. Brédas, "Nonlocal electron-phonon coupling in organic semiconductor crystals: The role of acoustic lattice vibrations," J. Chem. Phys. **138**, 204713 (2013).

[92] R. A. Marcus, "Electron transfer reactions in chemistry. Theory and experiment," Rev. Mod. Phys. **65**, 599 (1993).

[93] M. D. Newton and N. Sutin, "Electron transfer reactions in condensed phases," Annu. Rev. Phys. Chem. **35**, 437–480 (1984).

[94] M. D. Newton, "Quantum chemical probes of electron-transfer kinetics: The nature of donor-acceptor interactions," Chem. Rev. **91**, 767–792 (1991).

[95] L. Landau, "On the theory of transfer of energy at collisions I," Z. Sowjetunion **1**, 88 (1932).

[96] L. D. Landau, "A theory of energy transfer II," Phys. Z. Sowjetunion **2**, 19 (1932).

[97] C. Zener, "Non-adiabatic crossing of energy levels," Proceedings of the Royal Society of London. Series A, Containing Papers of a Mathematical and Physical Character **137**, 696–702 (1932).

[98] J. Spencer, L. Scalfi, A. Carof, and J. Blumberger, "Confronting surface hopping molecular dynamics with Marcus theory for a molecular donor–acceptor system," Faraday Discuss. **195**, 215–236 (2017).

[99] A. Nitzan, *Chemical dynamics in condensed phases: relaxation, transfer and reactions in condensed molecular systems* (Oxford university press, 2006).

[100] F. Gajdos, H. Oberhofer, M. Dupuis, and J. Blumberger, "On the inapplicability of electron-hopping models for the organic semiconductor phenyl-C61-butyric acid methyl ester (PCBM)," J. Phys. Chem. Lett. **4**, 1012–1017 (2013).

[101] B. Blülle, A. Troisi, R. Häusermann, and B. Batlogg, "Charge transport perpendicular to the high mobility plane in organic crystals: bandlike temperature dependence maintained despite hundredfold anisotropy," Phys. Rev. B **93**, 035205 (2016).

[102] O. H. LeBlanc Jr, "Band structure and transport of holes and electrons in anthracene," J. Chem. Phys. **35**, 1275–1280 (1961).

[103] C. Jacoboni and P. Lugli, *The Monte Carlo method for semiconductor device simulation* (Springer Science & Business Media, 2012).

[104] Y. Cheng, R. Silbey, D. A. da Silva Filho, J. P. Calbert, J. Cornil, and J.-L. Brédas, "Three-dimensional band structure and bandlike mobility in oligoacene single crystals: A theoretical investigation," J. Chem. Phys. **118**, 3764–3774 (2003).

[105] Y. Li, Y. Yi, V. Coropceanu, and J.-L. Brédas, "Optical conductivity and optical effective mass in a high-mobility organic semiconductor: Implications for the nature of charge transport," Phys. Rev. B **90**, 245112 (2014).

[106] S. Fratini, D. Mayou, and S. Ciuchi, "The transient localization scenario for charge transport in crystalline organic materials," Adv. Funct. Mater. **26**, 2292–2315 (2016).

[107] S. Fratini, S. Ciuchi, D. Mayou, G. T. De Laissardière, and A. Troisi, "A map of high-mobility molecular semiconductors," Nat. Mater. **16**, 998–1002 (2017).

[108] S. Fratini and S. Ciuchi, "Dynamical localization corrections to band transport," Phys. Rev. Res. **2**, 013001 (2020).

[109] T. Nematiaram, S. Ciuchi, X. Xie, S. Fratini, and A. Troisi, "Practical computation of the charge mobility in molecular semiconductors using transient localization theory," J. Phys. Chem. C **123**, 6989–6997 (2019).

[110] A. Troisi and G. Orlandi, "Charge-transport regime of crystalline organic semiconductors: Diffusion limited by thermal off-diagonal electronic disorder," Phys. Rev. Lett. **96**, 086601 (2006).

[111] S. Fratini, S. Ciuchi, and D. Mayou, "Phenomenological model for charge dynamics and optical response of disordered systems: Application to organic semiconductors," Phys. Rev. B **89**, 235201 (2014).

[112] N. Tessler, Y. Preezant, N. Rappaport, and Y. Roichman, "Charge transport in disordered organic materials and its relevance to thin-film devices: A tutorial review," Adv. Mater. **21**, 2741–2761 (2009).

[113] S. D. Baranovskii, "Mott lecture: Description of charge transport in disordered organic semiconductors: Analytical theories and computer simulations," Physica Status Solidi (a) p. 1700676 (2018).

[114] O. V. Mikhnenko, P. W. Blom, and T.-Q. Nguyen, "Exciton diffusion in organic semiconductors," Energy Environ. Sci. **8**, 1867–1888 (2015).

[115] S. Reineke and M. A. Baldo, "Recent progress in the understanding of exciton dynamics within phosphorescent oleds," Phys. Status Solidi A **209**, 2341–2353 (2012).

[116] J.-W. Van der Horst, P. A. Bobbert, M. A. Michels, and H. Bässler, "Calculation of excitonic properties of conjugated polymers using the Bethe–Salpeter equation," The Journal of Chemical Physics **114**, 6950–6957 (2001).

[117] A. Köhler and D. Beljonne, "The singlet–triplet exchange energy in conjugated polymers," Adv. Funct. Mater. **14**, 11–18 (2004).

[118] A. Köhler, J. Wilson, R. Friend, M. Al-Suti, M. Khan, A. Gerhard, and H. Bässler, "The singlet–triplet energy gap in organic and Pt-containing phenylene ethynylene polymers and monomers," J. Chem. Phys. **116**, 9457–9463 (2002).

[119] A. Monkman, H. Burrows, I. Hamblett, S. Navarathnam, M. Svensson, and M. Andersson, "The effect of conjugation length on triplet energies, electron delocalization and electron–electron correlation in soluble polythiophenes," J. Chem. Phys. **115**, 9046–9049 (2001).

[120] M. Liess, S. Jeglinski, Z. Vardeny, M. Ozaki, K. Yoshino, Y. Ding, and T. Barton, "Electroabsorption spectroscopy of luminescent and nonluminescent π-conjugated polymers," Phys. Rev. B **56**, 15712 (1997).

[121] D. Beljonne, J. Cornil, R. Friend, R. Janssen, and J. Brédas, "Influence of chain length and derivatization on the lowest singlet and triplet states and intersystem crossing in oligothiophenes," J. Am. Chem. Soc. **118**, 6453–6461 (1996).

[122] D. Hertel, S. Setayesh, H.-G. Nothofer, U. Scherf, K. Müllen, and H. Bässler, "Phosphorescence in conjugated poly (para-phenylene)-derivatives," Adv. Mater. **13**, 65–70 (2001).

[123] D. Beljonne, Z. Shuai, G. Pourtois, and J. Bredas, "Spin- orbit coupling and intersystem crossing in conjugated polymers: a configuration interaction description," J. Phys. Chem. A **105**, 3899–3907 (2001).

[124] M. A. Baldo, D. O'brien, Y. You, A. Shoustikov, S. Sibley, M. Thompson, and S. Forrest, "Highly efficient phosphorescent emission from organic electroluminescent devices," Nature **395**, 151–154 (1998).

[125] M. Baldo and S. Forrest, "Transient analysis of organic electrophosphorescence: I. Transient analysis of triplet energy transfer," Phys. Rev. B **62**, 10958 (2000).

[126] J. E. Rogers, T. M. Cooper, P. A. Fleitz, D. J. Glass, and D. G. McLean, "Photophysical characterization of a series of platinum(II)-containing phenyl-ethynyl oligomers," J. Phys. Chem. A **106**, 10108–10115 (2002).

[127] F. Guo, K. Ogawa, Y.-G. Kim, E. O. Danilov, F. N. Castellano, J. R. Reynolds, and K. S. Schanze, "A fulleropyrrolidine end-capped platinum-acetylide triad: the mechanism of photoinduced charge transfer in organometallic photovoltaic cells," Phys. Chem. Chem. Phys. **9**, 2724–2734 (2007).

[128] C. Adachi, M. A. Baldo, M. E. Thompson, and S. R. Forrest, "Nearly 100% internal phosphorescence efficiency in an organic light-emitting device," J. Appl. Phys. **90**, 5048–5051 (2001).

[129] D. Beljonne, A. Ye, Z. Shuai, and J.-L. Brédas, "Chain-length dependence of singlet and triplet exciton formation rates in organic light-emitting diodes," Adv. Funct. Mater. **14**, 684–692 (2004).

[130] M. Wohlgenannt, K. Tandon, S. Mazumdar, S. Ramasesha, and Z. Vardeny, "Formation cross-sections of singlet and triplet excitons in π-conjugated polymers," Nature **409**, 494–497 (2001).

[131] M. Wohlgenannt, X. Jiang, Z. Vardeny, and R. Janssen, "Conjugation-length dependence of spin-dependent exciton formation rates in π-conjugated oligomers and polymers," Phys. Rev. Lett. **88**, 197401 (2002).

[132] G. D. Scholes, "Long-range resonance energy transfer in molecular systems," Ann. Rev. Phys. Chem. **54**, 57–87 (2003).

[133] D. L. Dexter, "A theory of sensitized luminescence in solids," J. Chem. Phys. **21**, 836–850 (1953).

[134] D. L. Dexter, R. Knox, and T. Förster, "The radiationless transfer of energy of electronic excitation between impurity molecules in crystals," Physica Status Solidi (b) **34**, K159–K162 (1969).

[135] T. Forster, "Energiewanderung und Fluoreszenz," Naturwissenschaften **33**, 166–175 (1946).

[136] W. A. Luhman and R. J. Holmes, "Investigation of energy transfer in organic photovoltaic cells and impact on exciton diffusion length measurements," Adv. Func. Mater. **21**, 764–771 (2011).

[137] R. R. Lunt, N. C. Giebink, A. A. Belak, J. B. Benziger, and S. R. Forrest, "Exciton diffusion lengths of organic semiconductor thin films measured by spectrally resolved photoluminescence quenching," J. Appl. Phys. **105**, 053711 (2009).

[138] Y. Kawamura, J. Brooks, J. J. Brown, H. Sasabe, and C. Adachi, "Intermolecular interaction and a concentration-quenching mechanism of phosphorescent Ir(III) complexes in a solid film," Phys. Rev. Lett. **96**, 017404 (2006).

[139] O. Mikhnenko, F. Cordella, A. Sieval, J. Hummelen, P. Blom, and M. Loi, "Temperature dependence of exciton diffusion in conjugated polymers," J. Phys. Chem. B **112**, 11601–11604 (2008).

[140] S. C. Meskers, J. Hübner, M. Oestreich, and H. Bässler, "Dispersive relaxation dynamics of photoexcitations in a polyfluorene film involving energy transfer: experiment and Monte Carlo simulations," J. Phys. Chem. B **105**, 9139–9149 (2001).

[141] C. Rothe and A. P. Monkman, "Triplet exciton migration in a conjugated polyfluorene," Phys. Rev. B **68**, 075208 (2003).

[142] S. T. Hoffmann, S. Athanasopoulos, D. Beljonne, H. Bässler, and A. Köhler, "How do triplets and charges move in disordered organic semiconductors? A Monte Carlo study comprising the equilibrium and nonequilibrium regime," J. Phys. Chem. C **116**, 16371–16383 (2012).

[143] S. Günes, H. Neugebauer, and N. S. Sariciftci, "Conjugated polymer-based organic solar cells," Chem. Rev. **107**, 1324–1338 (2007).

[144] C. Deibel, T. Strobel, and V. Dyakonov, "Origin of the efficient polaron-pair dissociation in polymer-fullerene blends," Phys. Rev. Lett. **103**, 036402 (2009).

[145] G. Grancini, M. Maiuri, D. Fazzi, A. Petrozza, H. Egelhaaf, D. Brida, G. Cerullo, and G. Lanzani, "Hot exciton dissociation in polymer solar cells," Nat. Mater. **12**, 29 (2013).

[146] W. Siebrand, "Radiationless transitions in polyatomic molecules. I. Calculation of FranckCondon factors," J. Chem. Phys. **46**, 440–447 (1967).

[147] G. W. Robinson and R. Frosch, "Theory of electronic energy relaxation in the solid phase," J. Chem. Phys. **37**, 1962–1973 (1962).

[148] C. Deibel, D. Mack, J. Gorenflot, A. Schöll, S. Krause, F. Reinert, D. Rauh, and V. Dyakonov, "Energetics of excited states in the conjugated polymer poly(3-hexylthiophene)," Phys. Rev. B **81**, 085202 (2010).

[149] F. Laquai, C. Im, A. Kadashchuk, and H. Bässler, "Sensitized intrinsic phosphorescence from a poly (phenylene-vinylene) derivative," Chem. Phys. Lett. **375**, 286–291 (2003).

[150] B. Xu and S. Holdcroft, "First observation of phosphorescence from π-conjugated polymers," J. Am. Chem. Soc. **115**, 8447–8448 (1993).

[151] B. Xu and S. Holdcroft, "Phosphorescence and delayed fluorescence of poly(3-hexylthiophene) films," Thin Solid Films **242**, 174–177 (1994).

[152] D. N. Congreve, J. Lee, N. J. Thompson, E. Hontz, S. R. Yost, P. D. Reusswig, M. E. Bahlke, S. Reineke, T. Van Voorhis, and M. A. Baldo, "External quantum efficiency above 100% in a singlet-exciton-fission–based organic photovoltaic cell," Science **340**, 334–337 (2013).

[153] R. Kepler, J. Caris, P. Avakian, and E. Abramson, "Triplet excitons and delayed fluorescence in anthracene crystals," Phys. Rev. Lett. **10**, 400 (1963).

[154] C. Murawski, K. Leo, and M. C. Gather, "Efficiency roll-off in organic light-emitting diodes," Adv. Mater. **25**, 6801–6827 (2013).

[155] S. Reineke, K. Walzer, and K. Leo, "Triplet-exciton quenching in organic phosphorescent light-emitting diodes with ir-based emitters," Phys. Rev. B **75**, 125328 (2007).

[156] M. A. Baldo, C. Adachi, and S. R. Forrest, "Transient analysis of organic electrophosphorescence. II. Transient analysis of triplet-triplet annihilation," Phys. Rev. B **62**, 10967 (2000).

[157] H. Van Eersel, P. Bobbert, R. Janssen, and R. Coehoorn, "Effect of förster-mediated triplet-polaron quenching and triplet-triplet annihilation on the efficiency roll-off of organic light-emitting diodes," Journal of Applied Physics **119**, 163102 (2016).

[158] H. van Eersel, P. Bobbert, R. Janssen, and R. Coehoorn, "Monte Carlo study of efficiency roll-off of phosphorescent organic light-emitting diodes: Evidence for dominant role of triplet-polaron quenching," Appl. Phys. Lett. **105**, 143303 (2014).

[159] G. Dennler, M. C. Scharber, and C. J. Brabec, "Polymer-fullerene bulk-heterojunction solar cells," Adv. Mater. **21**, 1323–1338 (2009).

[160] N. S. Sariciftci, L. Smilowitz, A. J. Heeger, and F. Wudl, "Photoinduced electron transfer from a conducting polymer to buckminsterfullerene," Science **258**, 1474–1476 (1992).

[161] C. Deibel, T. Strobel, and V. Dyakonov, "Role of the charge transfer state in organic donor–acceptor solar cells," Adv. Mater. **22**, 4097–4111 (2010).

[162] J. Liu, S. Chen, D. Qian, B. Gautam, G. Yang, J. Zhao, J. Bergqvist, F. Zhang, W. Ma, H. Ade *et al.*, "Fast charge separation in a non-fullerene organic solar cell with a small driving force," Nat. Energy **1**, 1–7 (2016).

[163] Y. Liu, J. Zhang, G. Zhou, F. Liu, X. Zhu, and F. Zhang, "Electric field facilitating hole transfer in non-fullerene organic solar cells with a negative HOMO offset," J. Phys. Chem. C **124**, 15132–15139 (2020).

[164] N. C. Giebink, G. P. Wiederrecht, M. R. Wasielewski, and S. R. Forrest, "Thermodynamic efficiency limit of excitonic solar cells," Phys. Rev. B **83**, 195326 (2011).

[165] B. Ebenhoch, S. A. Thomson, K. Genevičius, G. Juška, and I. D. Samuel, "Charge carrier mobility of the organic photovoltaic materials PTB7 and PC71BM and its influence on device performance," Org. Electron. **22**, 62–68 (2015).

[166] G. Zhang, J. Zhao, P. C. Chow, K. Jiang, J. Zhang, Z. Zhu, J. Zhang, F. Huang, and H. Yan, "Nonfullerene acceptor molecules for bulk heterojunction organic solar cells," Chem. Rev. **118**, 3447–3507 (2018).

[167] J. Yuan, Y. Zhang, L. Zhou, G. Zhang, H.-L. Yip, T.-K. Lau, X. Lu, C. Zhu, H. Peng, P. A. Johnson *et al.*, "Single-junction organic solar cell with over 15% efficiency using fused-ring acceptor with electron-deficient core," Joule **3**, 1140–1151 (2019).

[168] G. Zhang, X.-K. Chen, J. Xiao, P. C. Chow, M. Ren, G. Kupgan, X. Jiao, C. C. Chan, X. Du, R. Xia *et al.*, "Delocalization of exciton and electron wavefunction in non-fullerene acceptor molecules enables efficient organic solar cells," Nat. Comm. **11**, 1–10 (2020).

[169] A. Classen, C. L. Chochos, L. Lüer, V. G. Gregoriou, J. Wortmann, A. Osvet, K. Forberich, I. McCulloch, T. Heumüller, and C. J. Brabec, "The role of exciton lifetime for charge generation in organic solar cells at negligible energy-level offsets," Nat. Energy pp. 1–9 (2020).

[170] D. T. Gillespie, "Stochastic simulation of chemical kinetics," Annu. Rev. Phys. Chem. **58**, 35–55 (2007).

[171] F. Schwabl, *Statistische Physik* (Berlin: Springer, 2006).

[172] N. Metropolis, A. W. Rosenbluth, M. N. Rosenbluth, A. H. Teller, and E. Teller, "Equation of state calculations by fast computing machines," J. Chem. Phys. **21**, 1087–1092 (1953).

[173] M. Stamatakis and D. G. Vlachos, "Unraveling the complexity of catalytic reactions via kinetic Monte Carlo simulation: current status and frontiers," ACS Catal. **2**, 2648–2663 (2012).

[174] K. Reuter and H. Metiu, "A decade of computational surface catalysis," Handbook of Materials Modeling: Applications: Current and Emerging Materials pp. 1–11 (2018).

[175] A. Jansen and J. Lukkien, "Dynamic Monte-Carlo simulations of reactions in heterogeneous catalysis," Catal. Today **53**, 259–271 (1999).

[176] S. Piana, M. Reyhani, and J. D. Gale, "Simulating micrometre-scale crystal growth from solution," Nature **438**, 70 (2005).

[177] P. Zhu and R. Smith, "Dynamic simulation of crystal growth by Monte Carlo methodI. model description and kinetics," Acta Metall. Mater. **40**, 683–692 (1992).

[178] L. A. Zepeda-Ruiz and G. H. Gilmer, "Monte Carlo simulations of crystal growth," in "Handbook of Crystal Growth," (Elsevier, 2015), pp. 445–475.

[179] P. P. Dholabhai, S. Anwar, J. B. Adams, P. Crozier, and R. Sharma, "Kinetic lattice Monte Carlo model for oxygen vacancy diffusion in praseodymium doped ceria: Applications to materials design," J. Solid State Chem. **184**, 811–817 (2011).

[180] M. Grabowski, J. Rogal, and R. Drautz, "Kinetic Monte Carlo simulations of vacancy diffusion in nondilute Ni-X (X = Re, W, Ta) alloys," Phys. Rev. Mater. **2**, 123403 (2018).

[181] W. Young and E. Elcock, "Monte Carlo studies of vacancy migration in binary ordered alloys: I," Proc. Phys. Soc. **89**, 735 (1966).

[182] W. Kaiser, J. Popp, M. Rinderle, T. Albes, and A. Gagliardi, "Generalized kinetic Monte Carlo framework for organic electronics," Algorithms **11**, 37 (2018).

[183] D. T. Gillespie, "A general method for numerically simulating the stochastic time evolution of coupled chemical reactions," J. Comput. Phys. **22**, 403–434 (1976).

[184] A. B. Bortz, M. H. Kalos, and J. L. Lebowitz, "A new algorithm for Monte Carlo simulation of Ising spin systems," J. Comp. Phys. **17**, 10–18 (1975).

[185] M. C. Heiber and A. Dhinojwala, "Dynamic Monte Carlo modeling of exciton dissociation in organic donor-acceptor solar cells," J. Chem. Phys. **137**, 014903 (2012).

[186] A. Troisi and G. Orlandi, "Dynamics of the intermolecular transfer integral in crystalline organic semiconductors," J. Phys. Chem. A **110**, 4065–4070 (2006).

[187] J. Ren, N. Vukmirović, and L.-W. Wang, "Nonadiabatic molecular dynamics simulation for carrier transport in a pentathiophene butyric acid monolayer," Phys. Rev. B **87**, 205117 (2013).

[188] S. A. Mollinger, A. Salleo, and A. J. Spakowitz, "Anomalous charge transport in conjugated polymers reveals underlying mechanisms of trapping and percolation," ACS Cent. Sci. **2**, 910–915 (2016).

[189] A. Nenashev, J. Oelerich, A. Dvurechenskii, F. Gebhard, and S. Baranovskii, "Fundamental characteristic length scale for the field dependence of hopping charge transport in disordered organic semiconductors," Phys. Rev. B **96**, 035204 (2017).

[190] G. Voronoi, "Nouvelles applications des paramètres continus à la théorie des formes quadratiques. deuxième mémoire. recherches sur les parallélloèdres primitifs." Journal für die reine und angewandte Mathematik (Crelles Journal) **134**, 198–287 (1908).

[191] F. Aurenhammer, "Voronoi diagramsa survey of a fundamental geometric data structure," ACM Computing Surveys (CSUR) **23**, 345–405 (1991).

[192] C. Rycroft, "Voro++: A three-dimensional Voronoi cell library in C++," Chaos: An Interdisciplinary Journal of Nonlinear Science (2009).

[193] R. G. Kimber, A. B. Walker, G. E. Schröder-Turk, and D. J. Cleaver, "Bicontinuous minimal surface nanostructures for polymer blend solar cells," Phys. Chem. Chem. Phys. **12**, 844–851 (2010).

[194] E. Ising, "Beitrag zur Theorie des Ferromagnetismus," Zeitschrift für Physik **31**, 253–258 (1925).

[195] D. Wynands, B. Männig, M. Riede, K. Leo, E. Brier, E. Reinold, and P. Bäuerle, "Organic thin film photovoltaic cells based on planar and mixed heterojunctions between fullerene and a low bandgap oligothiophene," J. Appl. Phys. **106**, 054509 (2009).

[196] H. Sirringhaus, R. Wilson, R. Friend, M. Inbasekaran, W. Wu, E. Woo, M. Grell, and D. Bradley, "Mobility enhancement in conjugated polymer field-effect transistors through chain alignment in a liquid-crystalline phase," Appl. Phys. Lett. **77**, 406–408 (2000).

[197] P. Carbone and A. Troisi, "Charge diffusion in semiconducting polymers: analytical relation between polymer rigidity and time scales for intrachain and interchain hopping," J. Phys. Chem. Lett. **5**, 2637–2641 (2014).

[198] B. O. Conchuir, C. Tarantini, C. R. McNeill, S. Huttner, and A. Zaccone, "Chain-assisted charge transport in semicrystalline conjugated polymers," J. Phys. Chem. C **120**, 14539–14548 (2016).

[199] R. P. Fornari and A. Troisi, "Theory of charge hopping along a disordered polymer chain," Phys. Chem. Chem. Phys. **16**, 9997–10007 (2014).

[200] P. Vanlaeke, A. Swinnen, I. Haeldermans, G. Vanhoyland, T. Aernouts, D. Cheyns, C. Deibel, J. DHaen, P. Heremans, J. Poortmans *et al.*, "P3HT/PCBM bulk heterojunction solar cells: Relation between morphology and electro-optical characteristics," Sol. Energy Mater. Sol. Cells **90**, 2150–2158 (2006).

[201] C. R. Singh, G. Gupta, R. Lohwasser, S. Engmann, J. Balko, M. Thelakkat, T. Thurn-Albrecht, and H. Hoppe, "Correlation of charge transport with structural order in highly ordered melt-crystallized poly(3-hexylthiophene) thin films," J. Polym. Sci., Part B: Polym. Phys. **51**, 943–951 (2013).

[202] H. Sirringhaus, P. Brown, R. Friend, M. M. Nielsen, K. Bechgaard, B. Langeveld-Voss, A. Spiering, R. A. Janssen, E. Meijer, P. Herwig *et al.*, "Two-dimensional charge transport in self-organized, high-mobility conjugated polymers," Nature **401**, 685 (1999).

[203] R. H. Landau, C. C. Bordeianu *et al.*, *Computational Physics: Problem Solving with Python* (John Wiley & Sons, 2015).

[204] J. Moore, "Gel permeation chromatography. I. a new method for molecular weight distribution of high polymers," J. Polym. Sci., Part A: Polym. Chem. **2**, 835–843 (1964).

[205] S. Förster, M. Schmidt, and M. Antonietti, "Static and dynamic light scattering by aqueous polyelectrolyte solutions: effect of molecular weight, charge density and added salt," Polymer **31**, 781–792 (1990).

[206] N. Madras and A. D. Sokal, "The pivot algorithm: a highly efficient Monte Carlo method for the self-avoiding walk," J. Stat. Phys. **50**, 109–186 (1988).

[207] D. M. Gonzalez, V. Körstgens, Y. Yao, L. Song, G. Santoro, S. V. Roth, and P. Müller-Buschbaum, "Improved power conversion efficiency of P3HT:PCBM organic solar cells by strong spinorbit coupling-induced delayed fluorescence," Adv. Energy Mater. **5**, 1401770 (2015).

[208] W. Zhang, Y. Xu, H. Wang, C. Xu, and S. Yang, "Fe3O4 nanoparticles induced magnetic field effect on efficiency enhancement of P3HT:PCBM bulk heterojunction polymer solar cells," Sol. Energy Mater. Sol. Cells **95**, 2880–2885 (2011).

[209] W. Zhang, N. A. Nguyen, R. Murray, J. Xin, and M. E. Mackay, "A comparative study on the morphology of P3HT:PCBM solar cells with the addition of Fe3O4 nanoparticles by spin and rod coating methods," J. Nanopart. Res. **19**, 315 (2017).

[210] W. A. Luhman and R. J. Holmes, "Enhanced exciton diffusion in an organic photovoltaic cell by energy transfer using a phosphorescent sensitizer," Appl. Phys. Lett. **94**, 110 (2009).

[211] P. P. Ewald, "Die Berechnung optischer und elektrostatischer Gitterpotentiale," Ann. Phys. **369**, 253–287 (1921).

[212] V. Stehr, J. Pfister, R. Fink, B. Engels, and C. Deibel, "First-principles calculations of anisotropic charge-carrier mobilities in organic semiconductor crystals," Phys. Rev. B **83**, 155208 (2011).

[213] J. Kirkpatrick, V. Marcon, J. Nelson, K. Kremer, and D. Andrienko, "Charge mobility of discotic mesophases: A multiscale quantum and classical study," Phys. Rev. Lett. **98**, 227402 (2007).

[214] U. Wolf, V. I. Arkhipov, and H. Bässler, "Current injection from a metal to a disordered hopping system. I. Monte Carlo simulation," Phys. Rev. B **59**, 7507–7513 (1999).

[215] L. A. Pettersson, L. S. Roman, and O. Inganäs, "Modeling photocurrent action spectra of photovoltaic devices based on organic thin films," J. Appl. Phys. **86**, 487–496 (1999).

[216] G. F. Burkhard, E. T. Hoke, and M. D. McGehee, "Accounting for interference, scattering, and electrode absorption to make accurate internal quantum efficiency measurements in organic and other thin solar cells," Adv. Mater. **22**, 3293–3297 (2010).

[217] P. Peumans, A. Yakimov, and S. R. Forrest, "Small molecular weight organic thin-film photodetectors and solar cells," J. Appl. Phys. **93**, 3693–3723 (2003).

[218] H. van Eersel, P. A. Bobbert, and R. Coehoorn, "Kinetic Monte Carlo study of triplet-triplet annihilation in organic phosphorescent emitters," J. Appl. Phys. **117**, 115502 (2015).

[219] M. Scheidler, B. Cleve, H. Bässler, and P. Thomas, "Monte Carlo simulation of bimolecular exciton annihilation in an energetically random hopping system," Chem. Phys. Lett. **225**, 431–436 (1994).

[220] O. V. Mikhnenko, J. Lin, Y. Shu, J. E. Anthony, P. W. Blom, T.-Q. Nguyen, and M. A. Loi, "Effect of thermal annealing on exciton diffusion in a diketopyrrolopyrrole derivative," Phys. Chem. Chem. Phys. **14**, 14196–14201 (2012).

[221] A. Einstein, "Über die von der molekularkinetischen Theorie der Wärme geforderte Bewegung von in ruhenden Flüssigkeiten suspendierten Teilchen," Ann. Phys. **322**, 549–560 (1905).

[222] M. Von Smoluchowski, "Zur kinetischen Theorie der Brownschen Molekularbewegung und der Suspensionen," Ann. Phys. **326**, 756–780 (1906).

[223] R. Coehoorn, H. van Eersel, P. Bobbert, and R. Janssen, "Kinetic Monte Carlo study of the sensitivity of OLED efficiency and lifetime to materials parameters," Adv. Funct. Mater. **25**, 2024–2037 (2015).

[224] M. Mesta, M. Carvelli, R. J. De Vries, H. Van Eersel, J. J. Van Der Holst, M. Schober, M. Furno, B. Lüssem, K. Leo, P. Loebl *et al.*, "Molecular-scale simulation of electroluminescence in a multilayer white organic light-emitting diode," Nat. Mater. **12**, 652–658 (2013).

[225] A. Köhler and H. Bässler, "What controls triplet exciton transfer in organic semiconductors?" J. Mater. Chem. **21**, 4003–4011 (2011).

[226] I.-W. Hwang, D. Moses, and A. J. Heeger, "Photoinduced carrier generation in P3HT/PCBM bulk heterojunction materials," J. Phys. Chem. C **112**, 4350–4354 (2008).

[227] T. Unger, S. Wedler, F.-J. Kahle, U. Scherf, H. Bässler, and A. Köhler, "The impact of driving force and temperature on the electron transfer in donor–acceptor blend systems," J. Phys. Chem. C **121**, 22739–22752 (2017).

[228] J. Jortner, "Temperature dependent activation energy for electron transfer between biological molecules," J. Chem. Phys. **64**, 4860–4867 (1976).

[229] T. Liu and A. Troisi, "Absolute rate of charge separation and recombination in a molecular model of the P3HT/PCBM interface," J. Phys. Chem. C **115**, 2406–2415 (2011).

[230] R. Marsh, C. Groves, and N. C. Greenham, "A microscopic model for the behavior of nanostructured organic photovoltaic devices," J. Appl. Phys. **101**, 083509 (2007).

[231] I. R. Gould, D. Noukakis, L. Gomez-Jahn, R. H. Young, J. L. Goodman, and S. Farid, "Radiative and nonradiative electron transfer in contact radical-ion pairs," Chem. Phys. **176**, 439–456 (1993).

[232] J. S. Wilson, N. Chawdhury, M. R. Al-Mandhary, M. Younus, M. S. Khan, P. R. Raithby, A. Köhler, and R. H. Friend, "The energy gap law for triplet states in Pt-containing conjugated polymers and monomers," J. Am. Chem. Soc. **123**, 9412–9417 (2001).

[233] W. Kaiser, M. Gößwein, and A. Gagliardi, "Acceleration scheme for particle transport in kinetic Monte Carlo methods," J. Chem. Phys. **152**, 174106 (2020).

[234] D. T. Gillespie, "A rigorous derivation of the chemical master equation," Physica A: Statistical Mechanics and its Applications **188**, 404–425 (1992).

[235] C. Groves and N. C. Greenham, "Monte Carlo simulations of organic photovoltaics," in "Multiscale Modelling of Organic and Hybrid Photovoltaics," (Springer, 2013), pp. 257–278.

[236] L. Nurminen, A. Kuronen, and K. Kaski, "Kinetic Monte Carlo simulation of nucleation on patterned substrates," Phys. Rev. B **63**, 035407 (2000).

[237] P. Zhang, X. Zheng, S. Wu, J. Liu, and D. He, "Kinetic Monte Carlo simulation of Cu thin film growth," Vacuum **72**, 405–410 (2004).

[238] D. G. Vlachos, "A review of multiscale analysis: examples from systems biology, materials engineering, and other fluid–surface interacting systems," Adv. Chem. Eng. **30**, 1–61 (2005).

[239] M. A. Katsoulakis and D. G. Vlachos, "Coarse-grained stochastic processes and kinetic Monte Carlo simulators for the diffusion of interacting particles," J. Chem. Phys. **119**, 9412–9427 (2003).

[240] J. Dai, W. D. Seider, and T. Sinno, "Coarse-grained lattice kinetic Monte Carlo simulation of systems of strongly interacting particles," J. Chem. Phys. **128**, 194705 (2008).

[241] A. Chatterjee, D. G. Vlachos, and M. A. Katsoulakis, "Spatially adaptive lattice coarse-grained Monte Carlo simulations for diffusion of interacting molecules," J. Chem. Phys. **121**, 11420–11431 (2004).

[242] A. Chatterjee and D. G. Vlachos, "Multiscale spatial Monte Carlo simulations: Multigriding, computational singular perturbation, and hierarchical stochastic closures," J. Chem. Phys. **124**, 064110 (2006).

[243] D. T. Gillespie, "Approximate accelerated stochastic simulation of chemically reacting systems," J. Chem. Phys. **115**, 1716–1733 (2001).

[244] D. G. Vlachos, "Temporal coarse-graining of microscopic-lattice kinetic Monte Carlo simulations via τ leaping," Phys. Rev. E **78**, 046713 (2008).

[245] D. J. Higham, "Modeling and simulating chemical reactions," SIAM Review **50**, 347–368 (2008).

[246] W. Koh and K. T. Blackwell, "An accelerated algorithm for discrete stochastic simulation of reaction–diffusion systems using gradient-based diffusion and tau-leaping," J. Chem. Phys. **134**, 04B612 (2011).

[247] M. Rathinam, L. R. Petzold, Y. Cao, and D. T. Gillespie, "Consistency and stability of tau-leaping schemes for chemical reaction systems," Multiscale Model. Simul. **4**, 867–895 (2005).

[248] T. Li, "Analysis of explicit tau-leaping schemes for simulating chemically reacting systems," Multiscale Model. Simul. **6**, 417–436 (2007).

[249] M. Snyder, A. Chatterjee, and D. Vlachos, "Net-event kinetic Monte Carlo for overcoming stiffness in spatially homogeneous and distributed systems," Comput. Chem. Eng. **29**, 701–712 (2005).

[250] H. Resat, H. S. Wiley, and D. A. Dixon, "Probability-weighted dynamic Monte Carlo method for reaction kinetics simulations," J. Phys. Chem. B **105**, 11026–11034 (2001).

[251] E. C. Dybeck, C. P. Plaisance, and M. Neurock, "Generalized temporal acceleration scheme for kinetic Monte Carlo simulations of surface catalytic processes by scaling the rates of fast reactions," J. Chem. Theory Comput. **13**, 1525–1538 (2017).

[252] A. Chatterjee and D. G. Vlachos, "An overview of spatial microscopic and accelerated kinetic Monte Carlo methods," J. Comput.-Aided Mater. Des. **14**, 253–308 (2007).

[253] J. Lederer, W. Kaiser, A. Mattoni, and A. Gagliardi, "Machine learning–based charge transport computation for pentacene," Adv. Theory Simul. **2**, 1800136 (2019).

[254] W. Gill, "Drift mobilities in amorphous charge-transfer complexes of trinitrofluorenone and poly-n-vinylcarbazole," J. Appl. Phys. **43**, 5033–5040 (1972).

[255] L. Schein, A. Peled, and D. Glatz, "The electric field dependence of the mobility in molecularly doped polymers," J. Appl. Phys. **66**, 686–692 (1989).

[256] M. Abkowitz, "Electronic transport in polymers," Philos. Mag. B **65**, 817–829 (1992).

[257] A. Y. Kryukov, A. C. Saidov, and A. Vannikov, "Charge carrier transport in poly (phenylene vinylene) films," Thin Solid Films **209**, 84–91 (1992).

[258] C. Brabec, U. Scherf, and V. Dyakonov, *Organic photovoltaics: materials, device physics, and manufacturing technologies* (John Wiley & Sons, 2011).

[259] H. Klauk, "Organic thin-film transistors," Chem. Soc. Rev. **39**, 2643–2666 (2010).

[260] R. J. Kline, M. D. McGehee, and M. F. Toney, "Highly oriented crystals at the buried interface in polythiophene thin-film transistors." Nat. Mater. **5** (2006).

[261] M. Stolka, J. Yanus, and D. Pai, "Hole transport in solid solutions of a diamine in polycarbonate," J. Phys. Chem. **88**, 4707–4714 (1984).

[262] A. Peled and L. Schein, "Hole mobilities that decrease with increasing electric fields in a molecularly doped polymer," Chem. Phys. Lett. **153**, 422–424 (1988).

[263] R. Kepler, P. Beeson, S. Jacobs, R. Anderson, M. Sinclair, V. Valencia, and P. Cahill, "Electron and hole mobility in tris (8-hydroxyquinolinolato-n1, o8) aluminum," Appl. Phys. Lett. **66**, 3618–3620 (1995).

[264] G. Juška, N. Nekrašas, and K. Genevičius, "Investigation of charge carriers transport from extraction current transients of injected charge carriers," J. Non-Cryst. Solids **358**, 748–750 (2012).

[265] A. Armin, G. Juska, M. Ullah, M. Velusamy, P. L. Burn, P. Meredith, and A. Pivrikas, "Balanced carrier mobilities: Not a necessary condition for high-efficiency thin organic solar cells as determined by mis-celiv," Adv. Energy Mater. **4** (2014).

[266] J. M. Warman and P. G. Schouten, "Charge transport in mesomorphic phthalocyanines studied by pulse-radiolysis time-resolved microwave conductivity," Appl. Organomet. Chem. **10**, 637–647 (1996).

[267] A. M. van de Craats, J. M. Warman, M. P. de Haas, D. Adam, J. Simmerer, D. Haarer, and P. Schuhmacher, "The mobility of charge carriers in all four phases of the columnar discotic material hexakis (hexylthio) triphenylene: Combined TOF and PR-TRMC results," Adv. Mater. **8**, 823–826 (1996).

[268] D. Venkateshvaran, M. Nikolka, A. Sadhanala, V. Lemaur, M. Zelazny, M. Kepa, M. Hurhangee, A. J. Kronemeijer, V. Pecunia, I. Nasrallah *et al.*, "Approaching disorder-free transport in high mobility conjugated polymers," Nature pp. 348–388 (2014).

[269] C. Tanase, E. Meijer, P. Blom, and D. De Leeuw, "Unification of the hole transport in polymeric field-effect transistors and light-emitting diodes," Phys. Rev. Lett. **91**, 216601 (2003).

[270] W. Pasveer, J. Cottaar, C. Tanase, R. Coehoorn, P. Bobbert, P. Blom, D. De Leeuw, and M. Michels, "Unified description of charge-carrier mobilities in disordered semiconducting polymers," Phys. Rev. Lett. **94**, 206601 (2005).

[271] H. Cordes, S. Baranovskii, K. Kohary, P. Thomas, S. Yamasaki, F. Hensel, and J.-H. Wendorff, "One-dimensional hopping transport in disordered organic solids. I. Analytic calculations," Phys. Rev. B **63**, 094201 (2001).

[272] M. Bouhassoune, S. Van Mensfoort, P. Bobbert, and R. Coehoorn, "Carrier-density and field-dependent charge-carrier mobility in organic semiconductors with correlated Gaussian disorder," Org. Electron. **10**, 437–445 (2009).

[273] K. Kohary, H. Cordes, S. Baranovskii, P. Thomas, S. Yamasaki, F. Hensel, and J.-H. Wendorff, "One-dimensional hopping transport in disordered organic solids. II. Monte Carlo simulations," Phys. Rev. B **63**, 094202 (2001).

[274] A. Hirao, H. Nishizawa, and M. Sugiuchi, "Diffusion and drift of charge carriers in molecularly doped polymers," Phys. Rev. Lett. **75**, 1787 (1995).

[275] G. Juška, K. Genevičius, K. Arlauskas, R. Österbacka, and H. Stubb, "Charge transport at low electric fields in π-conjugated polymers," Phys. Rev. B **65**, 233208 (2002).

[276] L. Sousa, R. Volpi, D. A. da Silva Filho, and M. Linares, "Mobility field and mobility temperature dependence in PC61BM: A Kinetic Monte-Carlo study," Chem. Phys. Lett. (2017).

[277] Y. N. Gartstein and E. Conwell, "High-field hopping mobility in molecular systems with spatially correlated energetic disorder," Chem. Phys. Lett. **245**, 351–358 (1995).

[278] P. Kordt, J. J. M. van der Holst, M. Al Helwi, W. Kowalsky, F. May, A. Badinski, C. Lennartz, and D. Andrienko, "Modeling of organic light emitting diodes: From molecular to device properties," Adv. Funct. Mater. **25**, 1955–1971 (2015).

[279] B. Baumeier, O. Stenzel, C. Poelking, D. Andrienko, and V. Schmidt, "Stochastic modeling of molecular charge transport networks," Phys. Rev. B **86**, 184202 (2012).

[280] C. G. Shuttle, R. Hamilton, J. Nelson, B. C. O'Regan, and J. R. Durrant, "Measurement of charge-density dependence of carrier mobility in an organic semiconductor blend," Adv. Funct. Mater. **20**, 698–702 (2010).

[281] C. Tanase, E. Meijer, P. Blom, and D. De Leeuw, "Local charge carrier mobility in disordered organic field-effect transistors," Org. Electron. **4**, 33–37 (2003).

[282] A. M. Ballantyne, L. Chen, J. Dane, T. Hammant, F. M. Braun, M. Heeney, W. Duffy, I. McCulloch, D. D. Bradley, and J. Nelson, "The effect of poly(3-hexylthiophene) molecular weight on charge transport and the performance of polymer:fullerene solar cells," Adv. Funct. Mater. **18**, 2373–2380 (2008).

[283] D. H. Dunlap, P. E. Parris, and V. M. Kenkre, "Charge-dipole model for the universal field dependence of mobilities in molecularly doped polymers," Phys. Rev. Lett. **77**, 542 (1996).

[284] P. Kordt and D. Andrienko, "Modeling of spatially correlated energetic disorder in organic semiconductors," J. Chem. Theory Comput. **12**, 36 (2016).

[285] S. V. Novikov, D. H. Dunlap, V. M. Kenkre, P. E. Parris, and A. V. Vannikov, "Essential role of correlations in governing charge transport in disordered organic materials," Phys. Rev. Lett. **81**, 4472 (1998).

[286] L. Schein and P. Borsenberger, "Hole mobilities in a hydrazone-doped polycarbonate and poly(styrene)," Chem. Phys. **177**, 773–781 (1993).

[287] D. M. Pai and B. E. Springett, "Physics of electrophotography," Rev. Mod. Phys. **65**, 163 (1993).

[288] A. J. Mozer and N. S. Sariciftci, "Negative electric field dependence of charge carrier drift mobility in conjugated, semiconducting polymers," Chem. Phys. Lett. **389**, 438–442 (2004).

[289] A. Baumann, J. Lorrmann, C. Deibel, and V. Dyakonov, "Bipolar charge transport in poly (3-hexyl thiophene)/methanofullerene blends: A ratio dependent study," Appl. Phys. Lett. **93**, 252104 (2008).

[290] N. Van Lien and B. Shklovskii, "Hopping conduction in strong electric fields and directed percolation," Solid State Commun. **38**, 99–102 (1981).

[291] V. Rühle, A. Lukyanov, F. May, M. Schrader, T. Vehoff, J. Kirkpatrick, B. Baumeier, and D. Andrienko, "Microscopic simulations of charge transport in disordered organic semiconductors," J. Chem. Theory Comput. **7**, 3335 (2011).

[292] J. Van Der Holst, M. Uijttewaal, B. Ramachandhran, R. Coehoorn, P. Bobbert, G. De Wijs, and R. De Groot, "Modeling and analysis of the three-dimensional current density in sandwich-type single-carrier devices of disordered organic semiconductors," Phys. Rev. B **79**, 085203 (2009).

[293] J. Van der Holst, F. Van Oost, R. Coehoorn, and P. Bobbert, "Monte Carlo study of charge transport in organic sandwich-type single-carrier devices: Effects of Coulomb interactions," Phys. Rev. B **83**, 085206 (2011).

[294] E. Tutiš, I. Batistić, and D. Berner, "Injection and strong current channeling in organic disordered media," Phys. Rev. B **70**, 161202 (2004).

[295] S. Baranovskii, I. Zvyagin, H. Cordes, S. Yamasaki, and P. Thomas, "Electronic transport in disordered organic and inorganic semiconductors," J. Non-Cryst. Solids **299**, 416–419 (2002).

[296] S. Baranovskii, T. Faber, F. Hensel, and P. Thomas, "The applicability of the transport-energy concept to various disordered materials," J. Phys.: Condens. Matter **9**, 2699 (1997).

[297] J. Cottaar, R. Coehoorn, and P. Bobbert, "Scaling theory for percolative charge transport in molecular semiconductors: Correlated versus uncorrelated energetic disorder," Phys. Rev. B **85**, 245205 (2012).

[298] A. Lukyanov and D. Andrienko, "Extracting nondispersive charge carrier mobilities of organic semiconductors from simulations of small systems," Phys. Rev. B **82**, 193202 (2010).

[299] P. Kordt, T. Speck, and D. Andrienko, "Finite-size scaling of charge carrier mobility in disordered organic semiconductors," Phys. Rev. B **94**, 014208 (2016).

[300] O. D. Jurchescu, J. Baas, and T. T. M. Palstra, "Effect of impurities on the mobility of single crystal pentacene," Appl. Phys. Lett. **84**, 3061–3063 (2004).

[301] V. Podzorov, E. Menard, A. Borissov, V. Kiryukhin, J. A. Rogers, and M. E. Gershenson, "Intrinsic charge transport on the surface of organic semiconductors," Phys. Rev. Lett. **93**, 086602 (2004).

[302] D. Andrienko, *Multiscale Concepts in Simulations of Organic Semiconductors* (Springer, 2018).

[303] S. D. Baranovskii, H. Cordes, F. Hensel, and G. Leising, "Charge-carrier transport in disordered organic solids," Phys. Rev. B **62**, 7934 (2000).

[304] V. I. Arkhipov, P. Heremans, E. V. Emelianova, G. J. Adriaenssens, and H. Bässler, "Charge carrier mobility in doped semiconducting polymers," Appl. Phys. Lett. **82**, 3245–3247 (2003).

[305] M. Vissenberg and M. Matters, "Theory of the field-effect mobility in amorphous organic transistors," Phys. Rev. B **57**, 12964 (1998).

[306] A. Troisi and G. Orlandi, "Band structure of the four pentacene polymorphs and effect on the hole mobility at low temperature," J. Phys. Chem. B **109**, 1849–1856 (2005).

[307] P. M. Borsenberger, L. Pautmeier, and H. Bässler, "Charge transport in disordered molecular solids," J. Chem. Phys. **94**, 5447–5454 (1991).

[308] B. Baumeier, J. Kirkpatrick, and D. Andrienko, "Density-functional based determination of intermolecular charge transfer properties for large-scale morphologies," Phys. Chem. Chem. Phys. **12**, 11103–11113 (2010).

[309] E. F. Valeev, V. Coropceanu, D. A. da Silva Filho, S. Salman, and J.-L. Brédas, "Effect of electronic polarization on charge-transport parameters in molecular organic semiconductors," J. Am. Chem. Soc. **128**, 9882–9886 (2006).

[310] D. L. Cheung and A. Troisi, "Modelling charge transport in organic semiconductors: From quantum dynamics to soft matter," Phys. Chem. Chem. Phys. **10**, 5941–5952 (2008).

[311] B. Baumeier, F. May, C. Lennartz, and D. Andrienko, "Challenges for in silico design of organic semiconductors," J. Mater. Chem. **22**, 10971–10976 (2012).

[312] W.-Q. Deng and W. A. Goddard, "Predictions of hole mobilities in oligoacene organic semiconductors from quantum mechanical calculations," J. Phys. Chem. B **108**, 8614–8621 (2004).

[313] M. Yoneya, M. Kawasaki, and M. Ando, "Molecular dynamics simulations of pentacene thin films: The effect of surface on polymorph selection," J. Mater. Chem. **20**, 10397–10402 (2010).

[314] R. G. Della Valle, E. Venuti, A. Brillante, and A. Girlando, "Molecular dynamics simulations for a pentacene monolayer on amorphous silica," Phys. Chem. Chem. Phys. **10**, 1783–1788 (2009).

[315] S. Kubo and H. Kaji, "Parameter-free multiscale simulation realising quantitative prediction of hole and electron mobilities in organic amorphous system with multiple frontier orbitals," Sci. Rep. **8**, 13462 (2018).

[316] P. Friederich, F. Symalla, V. Meded, T. Neumann, and W. Wenzel, "Ab initio treatment of disorder effects in amorphous organic materials: Toward parameter free materials simulation," J. Chem. Theory Comput. **10**, 3720–3725 (2014).

[317] T. Mueller, A. G. Kusne, and R. Ramprasad, "Machine learning in materials science: Recent progress and emerging applications," Rev. Comput. Chem. **29**, 186–273 (2016).

[318] M. Rupp, A. Tkatchenko, K.-R. Müller, and O. A. von Lilienfeld, "Fast and accurate modeling of molecular atomization energies with machine learning," Phys. Rev. Lett. **108**, 058301 (2012).

[319] G. Montavon, M. Rupp, V. Gobre, A. Vazquez-Mayagoitia, K. Hansen, A. Tkatchenko, K.-R. Müller, and O. Anatole von Lilienfeld, "Machine learning of molecular electronic properties in chemical compound space," New J. Phys. **15**, 095003 (2013).

[320] C. M. Bishop, *Pattern Recognition and Machine Learning* (Springer-Verlag New York, 2016).

[321] L. M. Ghiringhelli, J. Vybiral, S. V. Levchenko, C. Draxl, and M. Scheffler, "Big data of materials science: Critical role of the descriptor," Phys. Rev. Lett. **114**, 105503 (2015).

[322] C. Saunders, A. Gammerman, and V. Vovk, "Ridge regression learning algorithm in dual variables," Proceedings of the 15th International Conference on Machine Learning ICML-98 (1998).

[323] T. Hofmann, B. Schölkopf, and A. J. Smola, "Kernel methods in machine learning," Ann. Stat. **36**, 1171–1220 (2008).

[324] C. E. Kundrot, J. W. Ponder, and F. M. Richards, "Algorithms for calculating excluded volume and its derivatives as a function of molecular conformation and their use in energy minimization," J. Comput. Chem. **12**, 402–409 (1991).

[325] A. Warshel and S. Lifson, "Consistent force field calculations. II. Crystal structures, sublimation energies, molecular and lattice vibrations, molecular conformations, and enthalpies of alkanes," J. Chem. Phys. **53**, 582–594 (1970).

[326] N. L. Allinger, Y. H. Yuh, and J. H. Lii, "Molecular mechanics. The MM3 force field for hydrocarbons. 1," J. Am. Chem. Soc. **111**, 8551–8566 (1989).

[327] J. H. Lii and N. L. Allinger, "Molecular mechanics. The MM3 force field for hydrocarbons. 2. Vibrational frequencies and thermodynamics," J. Am. Chem. Soc. **111**, 8566–8575 (1989).

[328] J. H. Lii and N. L. Allinger, "Molecular mechanics. The MM3 force field for hydrocarbons. 3. The van der Waals' potentials and crystal data for aliphatic and aromatic hydrocarbons," J. Am. Chem. Soc. **111**, 8576–8582 (1989).

[329] G. Mattioli, S. B. Dkhil, M. I. Saba, G. Malloci, C. Melis, P. Alippi, F. Filippone, P. Giannozzi, A. K. Thakur, M. Gaceur *et al.*, "Interfacial engineering of P3HT/ZnO hybrid solar cells using phthalocyanines: A joint theoretical and experimental investigation," Adv. Energy Mater- **4**, 1301694 (2014).

[330] C. Caddeo, R. Dessì, C. Melis, L. Colombo, and A. Mattoni, "Poly (3-hexylthiophene) adhesion on zinc oxide nanoneedles," J. Phys. Chem. C **115**, 16833–16837 (2011).

[331] C. Melis, P. Raiteri, L. Colombo, and A. Mattoni, "Self-assembling of zinc phthalocyanines on ZnO (1010) surface through multiple time scales," ACS Nano **5**, 9639–9647 (2011).

[332] B. Van Beest, G. J. Kramer, and R. Van Santen, "Force fields for silicas and aluminophosphates based on ab initio calculations," Phys. Rev. Lett. **64**, 1955 (1990).

[333] G. Malavasi, M. C. Menziani, A. Pedone, and U. Segre, "Void size distribution in MD-modelled silica glass structures," J. Non-Cryst. Solids **352**, 285–296 (2006).

[334] J. W. Ponder and D. A. Case, "Force fields for protein simulations," in "Advances in Protein Chemistry," , vol. 66 (Elsevier, 2003), pp. 27–85.

[335] M. Saba and A. Mattoni, "Simulations of oxide/polymer hybrids," Encyclopedia Nanotechnol. pp. 1–13 (2015).

[336] S. Plimpton, "Fast parallel algorithms for short-range molecular dynamics," J. Comput. Phys. **117**, 1–19 (1995).

[337] A. Mattoni and L. Colombo, "Crystallization kinetics of mixed amorphous-crystalline nanosystems," Phys. Rev. B **78**, 075408 (2008).

[338] M. Pope and C. E. Swenberg, *Electronic processes in organic crystals and polymers* (Oxford University Press:, 1999), 2nd ed.

[339] M. J. Field, "The pdynamo program for molecular simulations using hybrid quantum chemical and molecular mechanical potentials," J. Chem. Theory Comput. **4**, 1151–1161 (2008).

[340] G. B. Rocha, R. O. Freire, A. M. Simas, and J. J. P. Stewart, "RM1: A reparameterization of AM1 for H, C, N, O, P, S, F, Cl, Br, and I," J. Comput. Chem. **27**, 1101–1111 (2006).

[341] Michael J. S. Dewar and Walter Thiel, "Ground states of molecules. 38. The MNDO method. Approximations and parameters," J. Am. Chem. Soc. **99**, 4899–4907 (1977).

[342] G. Raos, "Coupling integrals for charge transfer," `https://sites.google.com/site/pdynamowiki/contributions/template1` (2013). Accessed: 2017-09-01.

[343] V. Coropceanu, J. Cornil, D. A. da Silva Filho, Y. Olivier, R. Silbey, and J.-L. Brédas, "Charge transport in organic semiconductors," Chem. Rev. **107**, 926–952 (2007).

[344] G. A. de Wijs, C. C. Mattheus, R. A. de Groot, and T. T. Palstra, "Anisotropy of the mobility of pentacene from frustration," Synth. Met. **139**, 109–114 (2003).

[345] J. H. Schön, C. Kloc, and B. Batlogg, "Universal crossover from band to hopping conduction in molecular organic semiconductors," Phys. Rev. Lett. **86**, 3843–3846 (2001).

[346] J. E. Norton and J.-L. Brédas, "Polarization energies in oligoacene semiconductor crystals," J. Am. Chem. Soc. **130**, 12377–12384 (2008).

[347] D. P. McMahon and A. Troisi, "Evaluation of the external reorganization energy of polyacenes," J. Phys. Chem. Lett. **1**, 941–946 (2010).

[348] J. Y. Lee, S. Roth, and Y. W. Park, "Anisotropic field effect mobility in single crystal pentacene," Appl. Phys. Lett. **88**, 252106 (2006).

[349] V. Coropceanu, M. Malagoli, D. da Silva Filho, N. Gruhn, T. Bill, and J. Brédas, "Hole-and electron-vibrational couplings in oligoacene crystals: intramolecular contributions," Phys. Rev. Lett. **89**, 275503 (2002).

[350] W. Kaiser and A. Gagliardi, "Kinetic monte carlo study of the role of the energetic disorder on the open-circuit voltage in polymer/fullerene solar cells," J. Phys. Chem. Lett. **10**, 6097–6104 (2019).

[351] S. M. Menke, N. A. Ran, G. C. Bazan, and R. H. Friend, "Understanding energy loss in organic solar cells: Toward a new efficiency regime," Joule **2**, 25–35 (2018).

[352] D. Veldman, S. C. Meskers, and R. A. Janssen, "The energy of charge-transfer states in electron donor–acceptor blends: Insight into the energy losses in organic solar cells," Adv. Funct. Mater. **19**, 1939–1948 (2009).

[353] M. Azzouzi, J. Yan, T. Kirchartz, K. Liu, J. Wang, H. Wu, and J. Nelson, "Nonradiative energy losses in bulk-heterojunction organic photovoltaics," Phys. Rev. X **8**, 031055 (2018).

[354] H.-Y. Chen, J. Hou, S. Zhang, Y. Liang, G. Yang, Y. Yang, L. Yu, Y. Wu, and G. Li, "Polymer solar cells with enhanced open-circuit voltage and efficiency," Nat. Photonics **3**, 649 (2009).

[355] S. Albrecht, S. Janietz, W. Schindler, J. Frisch, J. Kurpiers, J. Kniepert, S. Inal, P. Pingel, K. Fostiropoulos, N. Koch, and D. Neher, "Fluorinated copolymer PCPDTBT with enhanced open-circuit voltage and reduced recombination for highly efficient polymer solar cells," J. Am. Chem. Soc. **134**, 14932–14944 (2012).

[356] S. Albrecht, W. Schindler, J. Kurpiers, J. Kniepert, J. C. Blakesley, I. Dumsch, S. Allard, K. Fostiropoulos, U. Scherf, and D. Neher, "On the field dependence of free charge carrier generation and recombination in blends of PCPDTBT/PC70BM: Influence of solvent additives," J. Phys. Chem. Lett. **3**, 640–645 (2012).

[357] A. Maurano, R. Hamilton, C. G. Shuttle, A. M. Ballantyne, J. Nelson, B. Oregan, W. Zhang, I. McCulloch, H. Azimi, M. Morana, C. J. Brabec, and J. R. Durrant, "Recombination dynamics as a key determinant of open circuit voltage in organic bulk heterojunction solar cells: a comparison of four different donor polymers," Adv. Mater. **22**, 4987–4992 (2010).

[358] Z. Tang, J. Wang, A. Melianas, Y. Wu, R. Kroon, W. Li, W. Ma, M. R. Andersson, Z. Ma, W. Cai, W. Tress, and O. Inganäs, "Relating open-circuit voltage losses to the active layer morphology and contact selectivity in organic solar cells," J. Mater. Chem. A **6**, 12574–12581 (2018).

[359] G. Garcia-Belmonte and J. Bisquert, "Open-circuit voltage limit caused by recombination through tail states in bulk heterojunction polymer-fullerene solar cells," Appl. Phys. Lett. **96**, 48 (2010).

[360] G. Garcia-Belmonte, P. P. Boix, J. Bisquert, M. Lenes, H. J. Bolink, A. La Rosa, S. Filippone, and N. Martín, "Influence of the intermediate density-of-states occupancy on open-circuit voltage of bulk heterojunction solar cells with different fullerene acceptors," J. Phys. Chem. Lett. **1**, 2566–2571 (2010).

[361] I. Lange, J. Kniepert, P. Pingel, I. Dumsch, S. Allard, S. Janietz, U. Scherf, and D. Neher, "Correlation between the open circuit voltage and the energetics of organic bulk heterojunction solar cells," J. Phys. Chem. Lett. **4**, 3865–3871 (2013).

[362] J. Popp, W. Kaiser, and A. Gagliardi, "Impact of phosphorescent sensitizers and morphology on the photovoltaic performance in organic solar cells," Adv. Theory Simul. **2**, 1800114 (2019).

[363] S. Bi, Z. Ouyang, S. Shaik, and D. Li, "Effect of donor-acceptor vertical composition profile on performance of organic bulk heterojunction solar cells," Sci. Rep. **8**, 9574 (2018).

[364] N. K. Elumalai and A. Uddin, "Open circuit voltage of organic solar cells: An in-depth review," Energy Environ. Sci. **9**, 391–410 (2016).

[365] A. Melianas and M. Kemerink, "Photogenerated charge transport in organic electronic materials: Experiments confirmed by simulations," Adv. Mater. **31**, 1806004 (2019).

[366] S. Cook, H. Ohkita, J. R. Durrant, Y. Kim, J. J. Benson-Smith, J. Nelson, and D. D. Bradley, "Singlet exciton transfer and fullerene triplet formation in polymer-fullerene blend films," Appl. Phys. Lett. **89**, 101128 (2006).

[367] S. Marianer and B. Shklovskii, "Effective temperature of hopping electrons in a strong electric field," Phys. Rev. B **46**, 13100 (1992).

[368] F. Jansson, S. Baranovskii, G. Sliaužys, R. Österbacka, and P. Thomas, "Effective temperature for hopping transport in a Gaussian DOS," Phys. Status Solidi C **5**, 722–724 (2008).

[369] S. Baranovskii, B. Cleve, R. Hess, and P. Thomas, "Effective temperature for electrons in band tails," J. Non-Cryst. Solids **164**, 437–440 (1993).

[370] A. Brigeman, M. Fusella, B. P. Rand, and N. Giebink, "Nonthermal site occupation at the donor-acceptor interface of organic solar cells," Phys. Rev. Appl. **10**, 034034 (2018).

[371] V. Arkhipov, P. Heremans, E. Emelianova, and H. Baessler, "Effect of doping on the density-of-states distribution and carrier hopping in disordered organic semiconductors," Phys. Rev. B **71**, 045214 (2005).

[372] P. Borsenberger, R. Richert, and H. Bässler, "Dispersive and nondispersive charge transport in a molecularly doped polymer with superimposed energetic and positional disorder," Phys. Rev. B **47**, 4289 (1993).

[373] C. Poelking, K. Daoulas, A. Troisi, and D. Andrienko, "Morphology and charge transport in P3HT: A theorists perspective," in "P3HT Revisited–From Molecular Scale to Solar Cell Devices," (Springer, 2014), pp. 139–180.

[374] Y.-T. Fu, C. Risko, and J.-L. Brédas, "Intermixing at the pentacene-fullerene bilayer interface: A molecular dynamics study," Adv. Mater. **25**, 878–882 (2013).

[375] J. Xue, B. P. Rand, S. Uchida, and S. R. Forrest, "A hybrid planar–mixed molecular heterojunction photovoltaic cell," Adv. Mater. **17**, 66–71 (2005).

[376] D. Yoo, H. Song, Y. Youn, S. H. Jeon, Y. Cho, and S. Han, "A molecular dynamics study on the interface morphology of vapor-deposited amorphous organic thin films," Phys. Chem. Chem. Phys. **21**, 1484–1490 (2019).

[377] S. Athanasopoulos, F. Schauer, V. Nádaždy, M. Weiß, F.-J. Kahle, U. Scherf, H. Bässler, and A. Köhler, "What is the binding energy of a charge transfer state in an organic solar cell?" Adv. Energy Mater. **9**, 1900814 (2019).

[378] T. S. Ripolles, A. Guerrero, and G. Garcia-Belmonte, "Polymer defect states modulate open-circuit voltage in bulk-heterojunction solar cells," Appl. Phys. Lett. **103**, 243306 (2013).

[379] Y. Kim, S. A. Choulis, J. Nelson, D. D. Bradley, S. Cook, and J. R. Durrant, "Composition and annealing effects in polythiophene/fullerene solar cells," J. Mater. Sci. **40**, 1371–1376 (2005).

[380] M. B. Upama, N. K. Elumalai, M. A. Mahmud, M. Wright, D. Wang, C. Xu, and A. Uddin, "Effect of annnealing dependent blend morphology and dielectric properties on the performance and stability of non-fullerene organic solar cells," Sol. Energy Mater. Sol. Cells **176**, 109–118 (2018).

[381] K. Vandewal, W. D. Oosterbaan, S. Bertho, V. Vrindts, A. Gadisa, L. Lutsen, D. Vanderzande, and J. V. Manca, "Varying polymer crystallinity in nanofiber poly(3-alkylthiophene):PCBM solar cells: Influence on charge-transfer state energy and open-circuit voltage," Appl. Phys. Lett. **95**, 256 (2009).

[382] B. C. Thompson and J. M. Fréchet, "Polymer–fullerene composite solar cells," Angew. Chem., Int. Ed. **47**, 58–77 (2008).

[383] F. Guo, Y.-G. Kim, J. R. Reynolds, and K. S. Schanze, "Platinum–acetylide polymer based solar cells: Involvement of the triplet state for energy conversion," Chem. Commun. pp. 1887–1889 (2006).

[384] S. R. Forrest, "The limits to organic photovoltaic cell efficiency," MRS Bull. **30**, 28–32 (2005).

[385] H. Hoppe and N. S. Sariciftci, "Organic solar cells: An overview," J. Mater. Res. **19**, 1924–1945 (2004).

[386] S. M. Menke and R. J. Holmes, "Exciton diffusion in organic photovoltaic cells," Energy Environ. Sci. **7**, 499–512 (2014).

[387] V. D. Mihailetchi, H. Xie, B. de Boer, L. A. Koster, and P. W. Blom, "Charge transport and photocurrent generation in poly(3-hexylthiophene):methanofullerene bulk-heterojunction solar cells," Adv. Func. Mater. **16**, 699–708 (2006).

[388] B. P. Rand, S. Schols, D. Cheyns, H. Gommans, C. Girotto, J. Genoe, P. Heremans, and J. Poortmans, "Organic solar cells with sensitized phosphorescent absorbing layers," Org. Electr. **10**, 1015–1019 (2009).

[389] Y. Shao and Y. Yang, "Efficient organic heterojunction photovoltaic cells based on triplet materials," Adv. Mater. **17**, 2841–2844 (2005).

[390] C.-M. Yang, C.-H. Wu, H.-H. Liao, K.-Y. Lai, H.-P. Cheng, S.-F. Horng, H.-F. Meng, and J.-T. Shy, "Enhanced photovoltaic response of organic solar cell by singlet-to-triplet exciton conversion," Appl. Phys. Lett. **90**, 133509 (2007).

[391] M. Baldo, M. Thompson, and S. Forrest, "High-efficiency fluorescent organic light-emitting devices using a phosphorescent sensitizer," Nature **403**, 750–753 (2000).

[392] C. Adachi, M. A. Baldo, S. R. Forrest, and M. E. Thompson, "High-efficiency organic electrophosphorescent devices with tris(2-phenylpyridine) iridium doped into electron-transporting materials," Appl. Phys. Lett. **77**, 904–906 (2000).

[393] B. Kraabel, D. Moses, and A. Heeger, "Direct observation of the intersystem crossing in poly(3-octylthiophene)," J. Chem. Phys. **103**, 5102–5108 (1995).

[394] O. V. Mikhnenko, R. Ruiter, P. W. Blom, and M. A. Loi, "Direct measurement of the triplet exciton diffusion length in organic semiconductors," Phys. Rev. Lett. **108**, 137401 (2012).

[395] P. E. Shaw, A. Ruseckas, and I. D. Samuel, "Exciton diffusion measurements in poly (3-hexylthiophene)," Adv. Mater. **20**, 3516–3520 (2008).

[396] Y. Tamai, H. Ohkita, H. Benten, and S. Ito, "Exciton diffusion in conjugated polymers: from fundamental understanding to improvement in photovoltaic conversion efficiency," J. Phys. Chem. Lett. **6**, 3417–3428 (2015).

[397] J. A. Bjorgaard and M. E. Köse, "Simulations of exciton diffusion and trapping in semicrystalline morphologies of poly(3-hexylthiophene)," J. Phys. Chem. C **118**, 5756–5761 (2014).

[398] A. K. Thomas, J. A. Garcia, J. Ulibarri-Sanchez, J. Gao, and J. K. Grey, "High intrachain order promotes triplet formation from recombination of long-lived polarons in poly (3-hexylthiophene) J-aggregate nanofibers," ACS Nano **8**, 10559–10568 (2014).

[399] F. Steiner, J. Vogelsang, and J. M. Lupton, "Singlet-triplet annihilation limits exciton yield in poly(3-hexylthiophene)," Phys. Rev. Lett. **112**, 137402 (2014).

[400] C.-L. Lee, I.-W. Hwang, C. C. Byeon, B. H. Kim, and N. C. Greenham, "Triplet exciton and polaron dynamics in phosphorescent dye blended polymer photovoltaic devices," Adv. Func. Mater. **20**, 2945–2950 (2010).

[401] C. Uhrich, D. Wynands, S. Olthof, M. K. Riede, K. Leo, S. Sonntag, B. Maennig, and M. Pfeiffer, "Origin of open circuit voltage in planar and bulk heterojunction organic thin-film photovoltaics depending on doped transport layers," J. Appl. Phys. **104**, 043107 (2008).

[402] F.-J. Kahle, C. Saller, S. Olthof, C. Li, J. Lebert, S. Weiß, E. M. Herzig, S. Hüttner, K. Meerholz, P. Strohriegl *et al.*, "Does electron delocalization influence charge separation at donor–acceptor interfaces in organic photovoltaic cells?" J. Phys. Chem. C **122**, 21792–21802 (2018).

[403] S. Tscheuschner, H. Bässler, K. Huber, and A. Köhler, "A combined theoretical and experimental study of dissociation of charge transfer states at the donor–acceptor interface of organic solar cells," J. Phys. Chem. B **119**, 10359–10371 (2015).

[404] S. Athanasopoulos, H. Bässler, and A. Köhler, "Disorder vs. delocalization: Which is more advantageous for high-efficiency organic solar cells?" J. Phys. Chem. Lett. (2019).

[405] A. A. Bakulin, A. Rao, V. G. Pavelyev, P. H. van Loosdrecht, M. S. Pshenichnikov, D. Niedzialek, J. Cornil, D. Beljonne, and R. H. Friend, "The role of driving energy and delocalized states for charge separation in organic semiconductors," Science **335**, 1340–1344 (2012).

[406] V. Janković and N. Vukmirovic, "Energy–temporal pathways of free-charge formation at organic bilayers: Competition of delocalization, disorder, and polaronic effects," J. Phys. Chem. C **124**, 4378–4392 (2020).

[407] L. Shi, C. K. Lee, and A. P. Willard, "The enhancement of interfacial exciton dissociation by energetic disorder is a nonequilibrium effect," ACS Cent. Sci. **3**, 1262–1270 (2017).

[408] P. Giazitzidis, P. Argyrakis, J. Bisquert, and V. S. Vikhrenko, "Charge separation in organic photovoltaic cells," Org. Electron. **15**, 1043–1049 (2014).

[409] C. Van den Broeck and M. Esposito, "Ensemble and trajectory thermodynamics: A brief introduction," Phys. A **418**, 6–16 (2015).

[410] U. Seifert, "Stochastic thermodynamics, fluctuation theorems and molecular machines," Rep. Prog. Phys. **75**, 126001 (2012).

[411] D. T. Gillespie, "Exact stochastic simulation of coupled chemical reactions," J. Phys. Chem. **81**, 2340–2361 (1977).

[412] R. Rao and M. Esposito, "Nonequilibrium thermodynamics of chemical reaction networks: wisdom from stochastic thermodynamics," Phys. Rev. X **6**, 041064 (2016).

[413] T. Leonard, B. Lander, U. Seifert, and T. Speck, "Stochastic thermodynamics of fluctuating density fields: non-equilibrium free energy differences under coarse-graining," J. Chem. Phys. **139**, 204109 (2013).

[414] H. Qian, "Relative entropy: Free energy associated with equilibrium fluctuations and nonequilibrium deviations," Phys. Rev. E **63**, 042103 (2001).

[415] D. Caruso and A. Troisi, "Long-range exciton dissociation in organic solar cells," Proc. Natl. Acad. Sci. **109**, 13498–13502 (2012).

[416] A. Gluchowski, K. L. Gray, S. N. Hood, and I. Kassal, "Increases in the charge separation barrier in organic solar cells due to delocalization," J. Phys. Chem. Lett. **9**, 1359–1364 (2018).

[417] K. Hussain, W. Kaiser, and A. Gagliardi, "Effect of polymer morphology on dilute donor organic solar cells," J. Phys. Chem. C **124**, 3517–3528 (2020).

[418] W. Kaiser, L. N. Murthy, C.-L. Chung, K.-T. Wong, J. W. Hsu, and A. Gagliardi, "Origin of hole transport in small molecule dilute donor solar cells," Adv. Energy Sustainability Res. **2**, 2000042 (2021).

[419] Y. Cui, H. Yao, J. Zhang, T. Zhang, Y. Wang, L. Hong, K. Xian, B. Xu, S. Zhang, J. Peng *et al.*, "Over 16% efficiency organic photovoltaic cells enabled by a chlorinated acceptor with increased open-circuit voltages," Nat. Commun. **10**, 1–8 (2019).

[420] Y. Cui, H. Yao, L. Hong, T. Zhang, Y. Tang, B. Lin, K. Xian, B. Gao, C. An, P. Bi *et al.*, "17% efficiency organic photovoltaic cell with superior processability," Nat. Sci. Rev. (2019).

[421] H. Sun, F. Chen, and Z.-K. Chen, "Recent progress on non-fullerene acceptors for organic photovoltaics," Mater. Today **24**, 94–118 (2019).

[422] X. Zhan and S. R. Marder, "Non-fullerene acceptors inaugurating a new era of organic photovoltaic research and technology," Mater. Chem. Front. **3**, 180–180 (2019).

[423] M. Elshobaki, R. Gebhardt, J. Carr, W. Lindemann, W. Wang, E. Grieser, S. Venkatesan, E. Ngo, U. Bhattacharjee, J. Strzalka *et al.*, "Tailoring nanoscale morphology of polymer:fullerene blends using electrostatic field," ACS Appl. Mater. Interfaces **9**, 2678–2685 (2016).

[424] F. Molina-Lopez, H. Yan, X. Gu, Y. Kim, M. F. Toney, and Z. Bao, "Electric field tuning molecular packing and electrical properties of solution-shearing coated organic semiconducting thin films," Adv. Funct. Mater. **27**, 1605503 (2017).

[425] L. Ye, H. Hu, M. Ghasemi, T. Wang, B. A. Collins, J.-H. Kim, K. Jiang, J. H. Carpenter, H. Li, Z. Li *et al.*, "Quantitative relations between interaction parameter, miscibility and function in organic solar cells," Nat. Mater. **17**, 253 (2018).

[426] S. Mukherjee, C. M. Proctor, G. C. Bazan, T.-Q. Nguyen, and H. Ade, "Significance of average domain purity and mixed domains on the photovoltaic performance of high-efficiency solution-processed small-molecule bhj solar cells," Adv. Energy Mater. **5**, 1500877 (2015).

[427] E. Collado-Fregoso, S. N. Pugliese, M. Wojcik, J. Benduhn, E. Bar-Or, L. Perdigón Toro, U. Hörmann, D. Spoltore, K. Vandewal, J. M. Hodgkiss *et al.*, "Energy-gap law for photocurrent generation in fullerene-based organic solar cells: the case of low-donor-content blends," J. Am. Chem. Soc. **141**, 2329–2341 (2019).

[428] M. Zhang, H. Wang, H. Tian, Y. Geng, and C. W. Tang, "Bulk heterojunction photovoltaic cells with low donor concentration," Adv. Mater. **23**, 4960–4964 (2011).

[429] L. Xu, J. Wang, M. d. A. Villa, T. B. Daunis, Y.-J. Lee, A. V. Malko, and J. W. Hsu, "Quantitative analyses of competing photocurrent generation mechanisms in fullerene-based organic photovoltaics," J. Phys. Chem. C **120**, 16470–16477 (2016).

[430] S. Sutty, G. Williams, and H. Aziz, "Fullerene-based Schottky-junction organic solar cells: ağ brief review," J. Photonics Energy **4**, 040999 (2014).

[431] K. Ding, X. Liu, and S. R. Forrest, "Charge transfer and collection in dilute organic donor–acceptor heterojunction blends," Nano Lett. **18**, 3180–3184 (2018).

[432] T. Lee, A. Sanzogni, N. Zhangzhou, P. L. Burn, and A. E. Mark, "Morphology of a bulk heterojunction photovoltaic cell with low donor concentration," ACS Appl. Mater. Interfaces **10**, 32413–32419 (2018).

[433] J.-W. Seo, J. H. Kim, M. Kim, S.-M. Jin, S.-H. Lee, C. Cho, E. Lee, S. Yoo, J. Y. Park, and J.-Y. Lee, "Columnar-structured low-concentration donor molecules in bulk heterojunction organic solar cells," ACS Omega **3**, 929–936 (2018).

[434] W. Jiang, H. Jin, M. Stolterfoht, P. E. Shaw, R. C. R. Nagiri, N. Kopidakis, and P. L. Burn, "Loss mechanisms in fullerene-based low-donor content organic solar cells," J. Phys. Chem. C **122**, 20611–20618 (2018).

[435] W. C. Tsoi, S. J. Spencer, L. Yang, A. M. Ballantyne, P. G. Nicholson, A. Turnbull, A. G. Shard, C. E. Murphy, D. D. Bradley, J. Nelson *et al.*, "Effect of crystallization on the electronic energy levels and thin film morphology of P3HT:PCBM blends," Macromolecules **44**, 2944–2952 (2011).

[436] G. J. Hedley, A. J. Ward, A. Alekseev, C. T. Howells, E. R. Martins, L. A. Serrano, G. Cooke, A. Ruseckas, and I. D. Samuel, "Determining the optimum morphology in high-performance polymer-fullerene organic photovoltaic cells," Nat. Commun. **4**, 1–10 (2013).

[437] M. Gerhard, A. P. Arndt, M. Bilal, U. Lemmer, M. Koch, and I. A. Howard, "Field-induced exciton dissociation in ptb7-based organic solar cells," Physical Review B **95**, 195301 (2017).

[438] E. Pascual-San José, A. Sánchez-Díaz, M. Stella, E. Martínez-Ferrero, M. I. Alonso, and M. Campoy-Quiles, "Comparing the potential of different strategies for colour tuning in thin film photovoltaic technologies," Sci. Technol. Adv. Mater. **19**, 823–835 (2018).

[439] Y. N. Luponosov, J. Min, A. V. Bakirov, P. V. Dmitryakov, S. N. Chvalun, S. M. Peregudova, T. Ameri, C. J. Brabec, and S. A. Ponomarenko, "Effects of bridging atom and π-bridge length on physical and photovoltaic properties of A–π-D–π-A oligomers for solution-processed organic solar cells," Dyes Pigm. **122**, 213–223 (2015).

[440] H. Kast, A. Mishra, G. L. Schulz, M. Urdanpilleta, E. Mena-Osteritz, and P. Bäuerle, "Acceptor-substituted S,N-Heteropentacenes of different conjugation length: Structure–property relationships and solar cell performance," Adv. Funct. Mater. **25**, 3414–3424 (2015).

[441] A. Mishra, D. Popovic, A. Vogt, H. Kast, T. Leitner, K. Walzer, M. Pfeiffer, and E. Mena-Osteritz, "A–D–A-type S,N-heteropentacenes: Next-generation molecular donor materials for efficient vacuum-processed organic solar cells," Adv. Mater. **26**, 7217–7223 (2014).

[442] C.-L. Chung, C.-H. Chen, C.-H. Tsai, and K.-T. Wong, "Novel organic dyes containing N-bridged oligothiophene coplanar cores for dye-sensitized solar cells," Org. Electron. **18**, 8–16 (2015).

[443] Q. Wang, "Solution-processed small-molecule organic solar cells," Ph.D. thesis, Technische Universiteit Eindhoven (2017).

[444] T. Hahn, S. Tscheuschner, C. Saller, P. Strohriegl, P. Boregowda, T. Mukhopadhyay, S. Patil, D. Neher, H. Bässler, and A. Köhler, "Role of intrinsic photogeneration in single layer and bilayer solar cells with C60 and PCBM," J. Phys. Chem. C **120**, 25083–25091 (2016).

[445] K. Vandewal, K. Tvingstedt, A. Gadisa, O. Inganäs, and J. V. Manca, "Relating the open-circuit voltage to interface molecular properties of donor:acceptor bulk heterojunction solar cells," Phys. Rev. B **81**, 125204 (2010).

[446] F. Gao, S. Himmelberger, M. Andersson, D. Hanifi, Y. Xia, S. Zhang, J. Wang, J. Hou, A. Salleo, and O. Inganäs, "The effect of processing additives on energetic disorder in highly efficient organic photovoltaics: A case study on PBDTTT-C-T:PC71BM," Adv. Mater. **27**, 3868–3873 (2015).

[447] M. A. Ansari, S. Mohiuddin, F. Kandemirli, and M. I. Malik, "Synthesis and characterization of poly (3-hexylthiophene): improvement of regioregularity and energy band gap," RSC Adv. **8**, 8319–8328 (2018).

[448] N. Vukmirovic and L.-W. Wang, "Electronic structure of disordered conjugated polymers:polythiophenes," J. Phys. Chem. B **113**, 409–415 (2009).

[449] X. Liu, K. Ding, A. Panda, and S. R. Forrest, "Charge transfer states in dilute donor–acceptor blend organic heterojunctions," ACS Nano **10**, 7619–7626 (2016).

[450] R. Mauer, M. Kastler, and F. Laquai, "The impact of polymer regioregularity on charge transport and efficiency of P3HT:PCBM photovoltaic devices," Adv. Funct. Mater. **20**, 2085–2092 (2010).

[451] F. Laquai, D. Andrienko, R. Mauer, and P. W. Blom, "Charge carrier transport and photogeneration in P3HT:PCBM photovoltaic blends," Macromol. Rapid Commun. **36**, 1001–1025 (2015).

[452] T. Albes, B. Popescu, D. Popescu, M. Loch, F. Arca, and P. Lugli, "Kinetic Monte Carlo modeling of low-bandgap polymer solar cells," in "2014 IEEE 40th Photovoltaic Specialist Conference (PVSC)," (IEEE, 2014), pp. 0057–0062.

[453] P. Peumans, V. Bulović, and S. R. Forrest, "Efficient photon harvesting at high optical intensities in ultrathin organic double-heterostructure photovoltaic diodes," Appl. Phys. Lett. **76**, 2650–2652 (2000).

[454] B. W. DAndrade and J. J. Brown, "Organic light-emitting device luminaire for illumination applications," Appl. Phys. Lett. **88**, 192908 (2006).

[455] Z. Liu, C. Kwong, C. Cheung, A. Djurišić, Y. Chan, and P. Chui, "The characterization of the optical functions of BCP and CBP thin films by spectroscopic ellipsometry," Synth. Met. **150**, 159–163 (2005).

[456] I. Hill and A. Kahn, "Energy level alignment at interfaces of organic semiconductor heterostructures," J. Appl. Phys. **84**, 5583–5586 (1998).

[457] K. Goushi, R. Kwong, J. J. Brown, H. Sasabe, and C. Adachi, "Triplet exciton confinement and unconfinement by adjacent hole-transport layers," J. Appl. Phys. **95**, 7798–7802 (2004).

[458] Y. Kawamura, H. Sasabe, and C. Adachi, "Simple accurate system for measuring absolute photoluminescence quantum efficiency in organic solid-state thin films," Japanese J. Appl. Phys. **43**, 7729 (2004).

[459] B. P. Rand, D. P. Burk, and S. R. Forrest, "Offset energies at organic semiconductor heterojunctions and their influence on the open-circuit voltage of thin-film solar cells," Phys. Rev. B **75**, 115327 (2007).

[460] J. Yu, J. Huang, H. Lin, and Y. Jiang, "Exciton diffusion length analysis of mixed donor materials in organic solar cells by doping with phosphorescent iridium complex," J. Appl. Phys. **108**, 113111 (2010).

[461] K. L. Mutolo, E. I. Mayo, B. P. Rand, S. R. Forrest, and M. E. Thompson, "Enhanced open-circuit voltage in subphthalocyanine/C60 organic photovoltaic cells," J. Am. Chem. Soc. **128**, 8108–8109 (2006).

[462] J. W. Arbogast, A. P. Darmanyan, C. S. Foote, F. N. Diederich, R. Whetten, Y. Rubin, M. M. Alvarez, and S. J. Anz, "Photophysical properties of sixty atom carbon molecule (C60)," J. Phys. Chem. **95**, 11–12 (1991).

[463] B. P. Rand, J. Genoe, P. Heremans, and J. Poortmans, "Solar cells utilizing small molecular weight organic semiconductors," Prog. Photovoltaics: Research and Applications **15**, 659–676 (2007).

[464] G. He, M. Pfeiffer, K. Leo, M. Hofmann, J. Birnstock, R. Pudzich, and J. Salbeck, "High-efficiency and low-voltage p-i-n electrophosphorescent organic light-emitting diodes with double-emission layers," Appl. Phys. Lett. **85**, 3911–3913 (2004).

[465] K. Feron, C. Fell, L. J. Rozanski, B. B. Gong, N. Nicolaidis, W. Belcher, X. Zhou, E. Sesa, B. King, and P. Dastoor, "Towards the development of a virtual organic solar cell: An experimental and dynamic Monte Carlo study of the role of charge blocking layers and active layer thickness," Appl. Phys. Lett. **101**, 193306 (2012).

List of Own Publications and Contributions

This thesis is based on the authors work conducted in the chair *Simulation of Nanosystems for Energy Conversion*, Department of Electrical and Computer Engineering, Technical University of Munich from 2017 until 2020. Parts of this work have been published and are based on the following contributions.

Journal Publications

1. **W. Kaiser**, T. Albes, A. Gagliardi, "Charge carrier mobility of disordered organic semiconductors with correlated energetic and spatial disorder", *Physical Chemistry Chemical Physics*, 2018, 20 (13), 8897-8908

2. **W. Kaiser**, J. Popp, M. Rinderle, T. Albes, A. Gagliardi, "Generalized kinetic Monte Carlo framework for organic electronics", *Algorithms*, 2018, 11 (4), 37

3. J. Popp, **W. Kaiser**, A. Gagliardi, "Impact of phosphorescent sensitizers and morphology on the photovoltaic performance in organic solar cells", *Advanced Theory and Simulations*, 2019, 2 (1), 1800114

4. J. Lederer, **W. Kaiser**, A. Mattoni, A. Gagliardi, "Machine learningbased charge transport computation for pentacene", *Advanced Theory and Simulations*, 2019, 2 (2), 1800136

5. M. Speckbacher, M. Rinderle, **W. Kaiser**, E.A. Osman, D. Chryssikos, A. CattaniScholz, J.M. Gibbs, A. Gagliardi, M. Tornow, "Directed assembly of nanoparticle threshold-selector arrays", *Advanced Electronic Materials*, 2019, 5 (7), 1900098

6. **W. Kaiser**, A. Gagliardi, "Kinetic Monte Carlo study of the role of the energetic Disorder on the open-circuit voltage in polymer/fullerene solar cells", *The Journal of Physical Chemistry Letters*, 2019, 10 (20), 6097-6104

7. K. Hussain, **W. Kaiser**, A. Gagliardi, "Effect of polymer morphology in dilute donor organic solar cells", *The Journal of Physical Chemistry C*, 2020, 124 (6), 3517-3528

8. **W. Kaiser**, M. GöSSwein, A. Gagliardi, "Acceleration scheme for particle transport in kinetic Monte Carlo methods", *The Journal of Chemical Physics*, 2020, 152 (17), 174106

9. M. Rinderle, **W. Kaiser**, A. Mattoni, A. Gagliardi, "Machine learning the charge transfer integral for multiscale simulations in organic thin films", *The Journal of Physical Chemistry C*, 2020, 124 (32), 1773317743

10. *Editorial*: **W. Kaiser**, A. Gagliardi, "Stepping out of equilibrium: The quest for understanding the role of non-equilibrium (thermo-)dynamics in electronic and electrochemical processes", *Entropy*, 2020, 22 (9), 1013

11. A. Singh, **W. Kaiser**, A. Gagliardi, "Role of cation-mediated recombination in perovskite solar cells", *Solar Energy Materials & Solar Cells*, 2021, 221, 110912

12. **W. Kaiser**, L.N.S. Murthy, C.-L. Chung, K.-T. Wong, J.W.P. Hsu, A. Gagliardi, "Origin of hole transport in small molecule dilute donor solar cells", *Advanced Energy and Sustainability Research*, 2021, 2, 2000042

13. K. Hussain, **W. Kaiser**, A. Gagliardi, "Role of the interface and contact energetics in organic solar cells", *The Journal of Physical Chemistry C*, 2021, 125 (10), 5447-5457

14. **W. Kaiser**, E. Mosconi, A. A. Alothman, D. Meggiolaro, A. Gagliardi, F. De Angelis, "Halide-driven formation of lead halide perovskites: Insight from *ab initio* molecular dynamics simulations", *Materials Advances*, 2021, 2, 3915-3926

15. *Accepted for Publication:* **W. Kaiser**, V. Janković, N. Vukmirović, A. Gagliardi, "Non-equilibrium thermodynamics of charge separation in organic bilayers", *The Journal of Physical Chemistry Letters*, 2021

Proceedings

1. A. Gagliardi, A. Singh, **W. Kaiser**, "Simulation of ion migration in perovskite solar cells using a kinetic Monte Carlo/drift diffusion numerical model and analysis of the impact on device performance", Proceedings of International Conference on Hybrid and Organic Photovoltaics (HOPV18), 2018, DOI: `10.29363/nanoge.hopv.2018.099`

2. J. Popp, **W. Kaiser**, A. Gagliardi, "Simulation of enhanced exciton diffusion in organic solar cells with phosphorescent sensitizers" IEEE 18th International Conference on Nanotechnology (IEEE-NANO), 2018, 420-425, DOI: `10.1109/NANO.2018.8626281`

3. **W. Kaiser**, M. Rinderle, A. Gagliardi, "Impact of the level and orientation of crystallinity on charge transport in semi-crystalline organic semiconductors" IEEE 18th International Conference on Nanotechnology (IEEE-NANO), 2018, 1-2, DOI: `10.1109/NANO.2018.8626309`

4. **W. Kaiser**, N. Phung, A. Abate, A. Gagliardi, "3D Simulation of ion migration within the microstructure of perovskite solar cells", Proceedings of International Conference on Hybrid and Organic Photovoltaics (HOPV19), DOI: `10.29363/nanoge.hopv.2019.124`

5. K. Hussain, **W. Kaiser**, A. Gagliardi, "Role of interface energetics and off-diagonal disorder in bulk heterojunction organic solar cells", 2020 IEEE 20th International Conference on Nanotechnology (IEEE-NANO), DOI: `10.1109/NANO47656.2020.9183465`

Oral Talks and Poster Contributions

Oral Talks

1. J. Popp, **W. Kaiser**, A. Gagliardi, "Simulation of enhanced exciton diffusion in organic solar cells with phosphorescent sensitizers" 2018 IEEE 18th International Conference on Nanotechnology (IEEE-NANO), Cork (Ireland)

2. A. Gagliardi, J. Stanley, **W. Kaiser**, "Machine learning bandgaps of inorganic mixed halide perovskites", 2018 Materials Research Society Fall Meeting, Boston (United States of America)

3. A. Gagliardi, A. Singh, **W. Kaiser**, "Simulation of ion migration in perovskite solar cells using a kinetic Monte Carlo/drift diffusion numerical model and analysis of the impact on device performance", 2018 International Conference on Hybrid and Organic Photovoltaics (HOPV18), Benidorm (Spain)

4. **W. Kaiser**, N. Phung, A. Abate, A. Gagliardi, "3D simulation of ion migration within the microstructure of perovskite solar cells" 2019 International Conference on Hybrid and Organic Photovoltaics (HOPV19), Rome (Italy)

5. K. Hussain, **W. Kaiser**, A. Gagliardi, "Role of interface energetics and off-diagonal disorder in bulk heterojunction organic solar cells" 2020 IEEE 20th International Conference on Nanotechnology (IEEE-NANO)

6. **W. Kaiser**, D. Meggiolaro, E. Mosconi, A. Gagliardi, F. De Angelis, "*Ab initio* molecular dynamics of defect migration in lead-halide perovskite grain boundaries", 2020 Internet Conference on Theory and Computation of Halide Perovskites (ComPer)

Poster Presentation

1. **W. Kaiser**, M. Rinderle, A. Gagliardi, "Impact of the level and orientation of crystallinity on charge transport in semi-crystalline organic semiconductors", 2018 IEEE 18th International Conference on Nanotechnology (IEEE-NANO), Cork (Ireland)

2. **W. Kaiser**, J. Lederer, A. Gagliardi, "Machine learning based ab initio numerical study of charge transport within non-crystalline organic semiconductors", 2018 Materials Research Society Fall Meeting, Boston (United States of America)

3. **W. Kaiser**, A. Gagliardi, "Enhanced thermodynamic efficiency study of excitonic solar cells", 2018 International Conference on Hybrid and Organic Photovoltaics (HOPV18), Benidorm (Spain)

4. M. Rinderle, J. Lederer, **W. Kaiser**, A. Gagliardi, "Machine learning for predicting charge transfer integrals in organic thin films", 2019 European Materials Research Society Spring Meeting, Nice (France)

5. A. Gagliardi, **W. Kaiser**, "Non-equilibrium efficiency study of organic solar cells using stochastic thermodynamics", 27th International Conference on Statistical Physics 2019, Buenos Aires (Argentina)

Other Contributions of the Author

1. **W. Kaiser**, M. Kiechle, G. Ziemys, D. Schmitt-Landsiedel, S. Breitkreutz-v. Gamm, "Engineering the switching behavior of nanomagnets for logic computation using 3-D modeling and simulation", *IEEE Transactions on Magnetics*, 2017, 53 (6), 1-4

2. **W. Kaiser**, M. Haider, J.A. Russer, P. Russer, C. Jirauschek, "Generalized Langevin theory for Josephson parametric amplification" 2017 IEEE MTT-S International Microwave Symposium (IMS), 1181-1184

3. **W. Kaiser**, M. Haider, J.A. Russer, P. Russer, C. Jirauschek, "Quantum theory of the dissipative Josephson parametric amplifier", *International Journal of Circuit Theory and Applications*, 2017, 45 (7), 864-881

4. **W. Kaiser**, M. Haider, J.A. Russer, P. Russer, C. Jirauschek, "Markovian dynamics of Josephson parametric amplification", *Advances in Radio Science*, 2017, 15, 131-140

5. **W. Kaiser**, M. Kiechle, G. Ziemys, D. Schmitt-Landsiedel, S. Breitkreutz-v. Gamm, "Micromagnetic simulation of nanomagnets with geometry-tuned domain wall nucleation", *Journal of Physics: Conference Series*, 2017, 903 (1), 012052

6. V. Ahrens, S. Breitkreutz-v. Gamm, S. Mendisch, **W. Kaiser**, M. Kiechle, M. Becherer, "Focused ion beam irradiation for generation of skyrmionic bubble like structures", *Journal of Magnetism and Magnetic Materials*, 2021, 523, 167591

Acknowledgments

Looking back at the last three years, it feels like a 100 m hurdle race rather than a marathon. I can say that there have been way more ups than downs, which would not have been possible without the help and support of many important people.

I acknowledge the funding of my doctoral studies, conferences and the international research stay by the TUM International Graduate School of Science and Engineering (IGSSE) by the German Research Foundation (Deutsche Forschungsgemeinschaft, DFG). Further, I thank the excellence clusters 'Nanosystems Initiative Munich' and '*e*-Conversion' for partially funding conferences.

First of all, I would like to thank Prof. Alessio Gagliardi for giving me the chance and trusting in me to work on this thesis (and several other projects). Thanks for countless hours of discussions, many visionary ideas and thoughts, for giving me the freedom to explore my ideas, and of course, for the weekly suggestion of new series – I will be busy watching series for the next years. I want to thank you for the wide range of experience I have gained during the PhD: teaching several tutor exercises and lab courses, visiting many interesting conferences (and countries/continents), discussions with many collaborators, supporting in terms of proposals, and supervising many many students. I not only want to thank you, but I want to wish you all the best for your Machine Learning factory, and I hope you will keep producing many fascinating ideas.

Further, I want to thank the other members of my examining committee: Prof. Dr. Egger for co-examining and the chair Prof. Dr. Wolfrum.

I further thank Prof. Christian Jirauschek and Dr. Michael Haider from the Computational Photonics group, as well as Dr. Stephan Breitkreutz and Prof. Markus Becherer for guiding 'my first steps' into the scientific world during my Master studies. Stephan, I learned a lot from discussions with you, and I am fascinated by how structured you approached puzzling topics and urgent deadlines. Markus, thanks for always having an open door and motivational words when I was stuck with my work. You are a great help and motivator for all students. Christian, unfortunately, I had to reject your offer for the PhD position in your group, but I can gladly say that it was the right choice for me and my future way. Thank you for your support and your trust during my Master Thesis, and your mentorship during the PhD. A special thanks to Michael, you were a great supervisor and amazing friend from the beginning. I am impressed by your knowledge, your support helped me a lot during my Master thesis, and I have been able to use plenty of that during my PhD.

I want to express my gratitude to many of my collaborators: Prof. Eva Herzig; thank you, Eva, for the discussions and your help in the IGSSE project. A great thanks to Lakshmi N.S. Murthy, Prof. Julia W.P. Hsu, Dr. Chin-Lung Chung, and Prof. Ken-Tsung Wong for synthesizing novel molecules and the experimental support in the dilute donor study. A special thanks to Julia for your fast and precise responses and your contribution with interesting data and questions. A great thanks to all other collaborators: Prof. Antonio Abate, Prof. Nenad Vukmirović, Dr. Veljko Janković, Dr. Nga Phung, Prof. Marc Tornow, Dr. Maximilian Speckbacher.

Many thanks to Prof. Filippo De Angelis, Dr. Edoardo Mosconi, and Dr. Daniele Meggiolaro from the CNR / Universita degli Studi di Perugia, and all the other colleagues for the very interesting research stay. I enjoyed working with you a lot, and I was able to learn a lot of materials science and especially *ab initio* methods.

I thank my former students for great discussions, amazing effort to improve the simulation tool, and for patience with the paper writing. A special thanks to Johannes Popp, Jonas Lederer, Michael Rinderle, Karin Thalmann, and Manuel GöSSwein. I think all of you have contributed with codes and simulations to various parts of this thesis. I really appreciated working with you, and I wish you all the best for your future.

A special thanks to all my colleagues from the SNE for being great colleagues and great friends! When I joined the group in April 2017, we were still a small group. Tim and Mohammed, thank you a lot for making my start in the group that easy, for the plenty of lunch breaks at Zitronengras, and especially the evening activities after work. Also, a great thanks to Mohammed for reading all my (*waay to long*) paper drafts =). A special thanks also to Michael Rinderle for being a great friend and sharing my complaints about all kinds of stuff in our office. Many thanks to Marlon, Kashif, Ajay, and Felix for the great collaboration during the PhD and interesting discussions in our seminar sessions.

Also, I would like to express my gratitude to the committee members of the ICMST for organizing plenty of fun nights at the institute: Michael R., Michael H., Simon, Martina, Mark, Johannes! I hope to get plenty of invitations as an invited speaker to the up-coming events and, of course, the Nano Christmas parties. A special thanks to Chief Editors Michael, Elisabeth and Anna for plenty of great barbecue afternoons and beer garden sessions. I wish you all the best for your small family.

There is no thesis without the support of close friends outside of the office. A big thanks and a big hug to Felix Reinfurt, Patrick Lammering, and André Ferreira Marques for being great friends. Felix, in the past nine years, we have shared plenty of memories together with up's and down's in both of our way. Thanks for the support, discussions, celebrations, or board-game nights throughout all the years. Patrick, even if you are a BVB fan, we have spent many evenings and weekends throughout the past years. I am thankful for your open doors and your support, especially when you kept me from working on the weekends! André, a great thanks for bringing fun and joy in each and every visit (and before tjat during the weekends, i.e. Wednesday to Sunday, during our Master studies). You will be a great, relaxed group leader :D. To Johannes Schwenger, Theo FlöSS, Sven Böhl: Even if we did not see each other that often during the past three years, thanks a lot for your friendship, your support, and for taking time when I am back home once every 2-3 months.

Last but definitely not least, a few words in German ... an meine Familie, meine Eltern und meinen Bruder Kevin: Tausend Dank für die Unterstützung in jeder möglichen Situation in den vergangenen Jahren. Ohne euch wäre all dies nicht möglich gewesen. Ihr habt mir immer den Rücken freigehalten und in den stressigsten Situationen bestmöglichst unterstützt. Ich bin froh, dass es euch gibt!